

Evolution of the Kibali Granite-Greenstone Belt, North East Democratic Republic of the Congo, and Controls on Gold Mineralisation at the Kibali Gold Deposit

Philip Joel Bird

A thesis submitted in partial fulfilment of the requirements of Kingston University London for the award of the degree of Doctor of Philosophy

March 2016



Abstract

The Kibali Granite-Greenstone Belt is located in the Northeast Democratic Republic of the Congo and is host to significant gold mineralisation in the form of the Kagaraba-Chaffeur-Durba (17 Moz Au), Pakaka (1.2 Moz Au), Mengu (0.7 Moz Au) and Pamao (0.7 Moz Au) ore bodies. The greenstone belt is composed of variably metamorphosed metasediments, banded iron formations and basalts intruded by 2.63-2.64 Ga igneous plutons ranging in composition from gabbroic to granitic. The greenstone belt is bounded to the south by the Upper Congo Granitic Massif, a polyphase intrusive complex dated to 2.62-2.64 Ga, and to the north by the West Nile Gneiss, a granitic gneiss complex dated to 985 Ma. The Kibali Granite-Greenstone Belt and Upper Granitic Massif are thought to have formed as part of an arc/back-arc complex that was active along the northern margin of the Proto-Congo Craton during the Neoproterozoic. The lithologies of the Kibali Granite-Greenstone Belt are thought to have been accreted to the northern margin of the craton at approximately 2.63 Ga. The West Nile Gneiss is hypothesized to have collided with, and overthrust, the Kibali Granite-Greenstone Belt in the period 600-400 Ma. This event is thought to have occurred as part of the Oubanguidic orogeny in which the Saharan Metacraton and Congo Craton came together. This event is hypothesized to have reactivated old structures in the Kibali Granite-Greenstone Belt and resulted in large-scale fluid flow which has been recorded in the U:Pb zircon record as a regional lead loss event, and by U:Pb monazite in the ore systems.

Mineralisation in the Kibali Granite-Greenstone Belt is characterised by a pyrite(\pm gold)+arsenopyrite+chalcopyrite+pyrrhotite (\pm marcasite) assemblage occurring as both disseminated and vein-style mineralisation, hosted in deformed and altered volcano-sedimentary conglomerates, basalts and banded iron formation. Localised deformation of the host lithologies during regional metamorphism is thought to have created high permeability Fe-phyllosilicate-rich zones into which ascending CO₂-rich fluids were focused. Interaction of these fluids with the Fe-rich host lithologies resulted in the widespread development of an Fe-carbonate (ankerite \pm siderite)+quartz \pm aluminoceladonite alteration assemblage. Gold transporting fluids are inferred to have been H₂S-rich, interacting with the Fe-rich host and alteration phases to form the Fe-sulphide-rich assemblage and deposit gold. Re:Os pyrite data indicate that mineralisation formed at approximately 2 Ga with a reactivation of the mineralising system identified through U:Pb monazite dating, occurring at 600-500 Ma.

Acknowledgments

This project was jointly funded by Kingston University and Randgold Resources Ltd. Additional funding was provided in the form of a NIGFSC research grant under which radiogenic and stable isotope data were obtained.

I would like to thank Kevin Attree, Richard Giddens, Ian Gill, Simon Crust, Vanessa Pashley, Allison McDonald for their technical assistance throughout the project. Adrian Boyce, Ian Millar, Iain MacDonald, Nick Roberts, James Lambert-Smith, Andrew Miles, Alan Hastie, Andreas Hahn, David Holder, Andrew Rankin, Andrew Allibone and Carlos Alonso Vargas for many stimulating discussions on a variety of geological subjects and their general assistance in the undertaking of this project.

I would like to thank the staff at Randgold resources and the Kibali Gold project without whom this project would not have been possible, in particular David Lawrence, Reinet Harbridge, Paul Harbridge, Joel Holliday, Jono Lawrence, Charles Creasey.

In addition I would like to thank Marc Lane, Paul Whiteside, Edward Morrow, Patrick Moore, Jon Hunt, Stephen Collett, Micheal Roberts, Andrew Bedford, Robert Bird, Michelle Bird and Kayleigh Richards for their friendship and support

Finally I would like to thank my supervisor Peter J. Treloar for his contribution, support and guidance throughout the project.

Table of Contents

Abstract

Acknowledgements

Table of Contents

List of Figures

List of Tables

Chapter 1. The Kibali Granite Greenstone Belt and Kibali Gold Project	1
1.1 Introduction	1
1.1.1. Study Area	2
1.1.2 Existing knowledge	3
1.2 The Democratic Republic of the Congo	3
1.3 The Kibali Gold Project	4
1.3.1 Deposit History	5
1.4 Project aims and Objectives	6
Chapter 2. Geology of the Archean cratons and Proterozoic mobile belts around the North East Margin of the Congo Craton	9
2.1 The Cratonic Architecture of Africa	9
2.2. The Congo-Tanzania Cratonic Mass	9
2.2.1 The Bomu-Kibalian Block	12
2.2.2 The Northern Uganda Terrane	13
2.2.3 The Northwest Tanzania Terrane	15
2.2.4 The Lake Victoria Terrane	15
2.2.5 The Central Tanzania Region	18
2.3 Proterozoic Mobile Belts	18
2.4 Formation and Evolution of the geological terranes of East Africa	20
2.5 Gold Deposits of Central and East Africa	24

2.5.1 Gold endowment in the Northeast Congo (Bomu-Kibalian-Block)	24
2.5.2 Gold Endowment in Tanzania	26
2.5.2.1 The Lake Victoria Region	26
2.5.2.2 The Central Tanzania Region	28
2.5.3 Gold Endowment in Uganda	28
2.5.3.1 Busia Gold district	28
2.5.3.2 Mubende Gold District	30
2.5.3.3 Buweju-Mashonga gold district	30
2.5.3.4 Karamoja Gold district	30
2.6 Summary	31
Chapter 3. The Formation of Orogenic Gold deposits	32
3.1 Orogenic Gold deposits	32
3.1.1 Geological and Temporal distribution of Orogenic Gold	34
3.1.2 Host Structures	36
3.1.3 Host Lithologies	38
3.1.4 Host Rock Alteration	38
3.1.5 Deformation characteristics and the effect on host rock permeability	39
3.2 Fluid Sources	40
3.2.1 Metamorphic Devolatilisation	41
3.2.2 Magmatic exsolution	44
3.3 Complexing of Gold	44
3.3.1 Precipitation of gold from solution	45
3.4 Summary	47

Chapter 4. Lithological characteristics of the Kibali Granite-Greenstone Belt and its neighbouring geological terranes; The West Nile Gneiss and Upper Congo Granitic Massif.	48
4.1 Introduction	48
4.2 Sampling procedure and analytical technique	48
4.3 The Kibali Granite-Greenstone Terrane	49
4.3.1 Kibalian metasediments	49
4.3.1.1 Volcano-sedimentary ‘conglomerates’	52
4.3.1.2 Silicified Volcaniclastic rocks	54
4.3.1.3 North Kibalian Schists	56
4.3.1.4 Eastern Quartz-Biotite schists	56
4.3.2 Banded Iron Formations	59
4.3.3 Kibalian basalts	61
4.3.4 Igneous intrusive units	63
4.3.4.1 Kokiza Gabbro	63
4.3.4.2 Ambarau Granodiorite	63
4.3.4.3 Kalimva Granite	68
4.3.4.4 Sessenge Granite	71
4.4 Upper Congo Granite Massif	72
4.4.1. Watsa-A	72
4.4.2. Watsa –B	77
4.4.3. Watsa-C	81
4.4.4. Undifferentiated Intrusive Lithologies	84
4.4.5. Boundary Massifs	86
4.5. West Nile Gneiss	89
4.6 Discussion	94
4.6.1 Kibali Granite-Greenstone Belt	94
4.6.1.2 Chlorite Geothermometry	96
4.6.2. Kibali Belt Intrusions	96

4.6.3. Upper Congo Granitic Massif	98
4.6.4. The West Nile Gneiss	100
4.6.5. Late Aluminoceladonite Alteration	100
4.6.6. The Kibali Belt as an Archean Greenstone Belt	101
4.7. Conclusions	102

Chapter 5. Classification and tectonic discrimination within the Upper Congo Granite Massif and Kibali Granite Greenstone belt through the use of geochemical data. 103

5.1 Introduction	103
5.2 Methodology	103
5.3 Results	105
5.3.1 Major and Trace Element Composition	105
5.3.1.1 Kibali Granite-Greenstone Belt; Felsic Intrusive/Extrusive Units	106
5.3.1.2 Kibali Granite-Greenstone Belt; Mafic Intrusive/Extrusive Units	110
5.3.1.3 Upper Congo Granite Massif: Felsic Intrusive units	111
5.3.1.4 Upper Congo Granite Massif: Mafic Intrusive/Extrusive units	113
5.4. Discussion	114
5.4.1 Element Mobility	114
5.4.2 Classification of Igneous Lithologies	116
5.4.3 Co-genetic Origin Between Terranes	117
5.4.4 Petrogenesis and Tectonic Affinity	120
5.4.4.1 Felsic Suite	120
5.4.4.2 UCG Mafic Intrusives	121
5.4.4.3 Mafic Suite	124
5.4.5 Slab and Mantle Component Affinity	125
5.4.5.1 Slab Component	125
5.4.5.2 Mantle Component	125
5.4.6 Geodynamic setting	128

5.5 Conclusions	132
Chapter 6. Geochronological constraints on the origins and evolution of the Kibali Granite-Greenstone belt and bounding terranes, NE Democratic Republic of Congo	133
6.1 Introduction	133
6.2 The Uranium-Lead Decay System and its Geochemical Behaviour	133
6.3 Sample Preparation and Analytical Technique	135
6.4 Results	138
6.4.1 Upper Congo Granite	138
6.4.1.1 Sample: W13	138
6.4.1.2 Sample WP06	138
6.4.1.3 Sample H4	140
6.4.1.4 Sample W10	141
6.4.2 Kibali Granite-Greenstone Belt	141
6.4.2.1 Sample: MK01	141
6.4.2.2 Sample: AT4	142
6.4.2.3 Sample: AMB1	142
6.4.2.4 Sample H1	143
6.4.3 West Nile Gneiss	145
6.4.3.1 Sample: NZ03	145
6.4.3.2 Sample: NZ07	146
6.5 Discussion	147
6.5.1 The Upper Congo Granitic Massif	147
6.5.2 The Kibali Granite-Greenstone Belt	148
6.5.3 The West Nile Gneiss Complex	149
6.5.4 Regional lead loss event	150
6.5.5 Geochronological Evolution of the Kibali Granite Greenstone Belt and Neighbouring terranes	150

6.5.6 Implications for the Development of Au Mineralisation	151
6.6 Conclusion	151
Chapter 7. Textural and compositional characteristics of wall rock alteration and sulphide mineral phases of the major gold deposits in the Kibali Granite-Greenstone Belt; Insights into the factors affecting the distribution of mineralisation	153
7.1 Introduction	153
7.2 Methodology	153
7.3 Structural setting and deposit morphology	155
7.4 Karagba-Chaffeur-Durba (KCD)	158
7.4.1 Host Lithologies	158
7.4.2 Hydrothermal Alteration	159
7.4.3 Mineralisation Styles	167
7.4.4. Ore Mineralogy	169
7.4.4.1Pre-Ore stage	169
7.4.4.2 Ore Stage	169
7.4.4.3 Gold mineralisation	172
7.4.4.4 Post Ore stage	172
7.5 Mengu	175
7.5.1 Host lithologies	175
7.5.2 Alteration	175
7.5.3 Mineralisation styles	176
7.5.4 Ore Mineralogy	182
7.5.4.1Pre-Ore Stage	182
7.5.4.2 Ore stage	182
7.5.4.3 Gold Mineralisation	182
7.5.4.4 Post ore stage	185
7.6 Pakaka	186

7.6.1 Host lithologies	186
7.6.2 Alteration	186
7.6.3 Mineralisation styles	192
7.6.4 Ore Mineralogy	192
7.6.4.1 Pre-ore stage	192
7.6.4.2 Ore stage	195
7.6.4.3 Gold Mineralisation	195
7.6.4.4 Post ore stage	195
7.7 Pamao	196
7.7.1 Host lithologies	196
7.7.2 Alteration	196
7.7.3 Mineralisation styles	199
7.7.4 Ore Mineralogy	199
7.7.4.1 Pre-Ore phase	199
7.7.4.2 Ore Phase	204
7.7.4.3 Au Mineralisation	206
7.7.4.4 Post-Ore Phase	206
7.8 Discussion	208
7.8.1 Comparative mineralogy	208
7.8.2 Geothermometry	211
7.8.3 Mineralisation model	217
7.8. Conclusions	220
Chapter 8. $\delta^{34}\text{S}$ characteristics of the Karagba-Chaffeur-Durba (KCD) deposit and other significant gold resources in the Kibali Granite-Greenstone Belt	222
8.1 Introduction	222
8.2 The Sulfur Isotope System	222
8.3 Sampling and Analytical Techniques	224
8.4 Results	225

8.5 Discussion	232
8.6 Conclusions	233
Chapter 9. Constraining the age of mineralisation at the Kibali Gold project: U-Th-Pb dating of monazite	234
9.1 Introduction	234
9.2 Structure and Chemistry of Monazite	234
9.3 Sample Preparation and Analytical Technique	235
9.4 Results	237
9.4.1 Karagbe-Chaffeur-Durba (KCD)	237
9.4.1.1 Sample: PB12-D05	237
9.4.1.2 Sample: PB12-D10	237
9.4.1.3 Sample: PB12-D12	239
9.4.1.4 Sample: 2013-D39	240
9.4.1.5 Sample: 2013-D57	240
9.4.2 Pakaka Deposit	244
9.4.2.1 Sample: PB12-PK12	244
9.4.3 Pamao Deposit	247
9.4.3.1 Sample: PB12-PM02	247
9.4.3.2 Sample: 2013-PM12	248
9.5 Discussion	251
9.5.1 Age of monazite formation	251
9.5.1.1 Karagba-Chaffeur-Durba (KCD)	251
9.5.1.2 Pakaka	252
9.5.1.3 Pamao	252
9.5.2 Monazite Age as Proxy for Mineralisation Age	253
9.5.3 Single Region Wide Event vs Discrete Individual Events	254
9.5.4 Representative of True Mineralisation Age?	254
9.6 Conclusion	255

Chapter 10. Re:Os Pyrite constraints on the formation of mineralisation at the Karagba-Chaffeur-Durba (KCD) orogenic gold deposit, NE Democratic Republic of the Congo	257
10.1 Introduction	257
10.2 The Re:Os Isotopic System	257
10.3 Sampling and Analytical Technique	258
10.4 Results	260
10.5 Discussion	263
10.6 Conclusions	265
Chapter 11. Evolution of the Kibali Granite-Greenstone Terrane, NE Democratic Republic of the Congo, and Controls on Gold Mineralisation at the Kibali gold deposit	266
11.1 Formation and Evolution of the Kibali-Granite-Greenstone Belt and Neighbouring Terranes	266
11.2 Controls on Gold Mineralisation	267
11.3 Conclusions	268
11.4 Further Work	270
12. References	272

Supplementary materials

Appendix 1: Sample Details

Appendix 2: EDS data; regional lithologies

Appendix 3: Geochemical Data

Appendix 4: U-Pb Zircon Data

Appendix 5: EDS data; ore deposits

Appendix 6: U-Pb Monazite data

List of Figures

Chapter 1. The Kibali Granite Greenstone Belt and Kibali Gold Project

Figure 1.1 The Democratic Republic of the Congo. 1

Figure 1.2 Sketch Map displaying the study area showing the three major geological terranes and significant gold deposits. 2

Chapter 2. Geology of the Archean cratons and Proterozoic mobile belts around the North East Margin of the Congo Craton.

Figure 2.1 The major geochronological units of the Congo/Tanzania Craton and surrounding terranes in East and Central Africa and the incidence of significant gold mineralisation. 10

Figure 2.2 Map of the bedrock geology of Africa, outlining the major subdivisions of the crust. 11

Figure 2.3 The major geological units of the NE Congo craton (Bomu-Kibalian-North Ugandan Block) and associated Palaeozoic mobile belts. 14

Figure 2.4 Major geological divisions of the Tanzanian craton and surrounding Proterozoic-recent mobile belts. 17

Figure 2.5 Reconstruction of the African section of the Rodinia Supercontinent displaying the location of the Grenvillian orogenic belts. 22

Figure 2.6 Reconstruction of the Gondwana supercontinent. 23

Figure 2.7 Geological map of the Bomu-Kibalian block displaying the location of gold bearing Neo-Archean Granite-Greenstone belts and the location of known major gold deposits. 25

Figure 2.8 Geological map of the Tanzanian Craton displaying the location of the significant gold camps. 27

Figure 2.9 Geological map of Uganda displaying the location of the known gold deposits and gold districts within Uganda. 29

Chapter 3. The Formation of Orogenic Gold deposits

Figure 3.1 Schematic diagram showing the deposit types formed during the different phases of accretionary constructional settings. 33

Figure 3.2 Temporal distribution of the formation of orogenic gold compared to the rate of crustal formation 35

Figure 3.3 Correlation between periods of orogenic gold formation, Atmospheric Oxygen % and crustal development. 36

Figure 3.4 Schematic diagram of the southeast Alaska region illustrating the relationship between rapid dewatering of the crust and ore forming processes due to changes in tectonic regime. 37

Figure 3.5 Variation in $\delta^{34}\text{S}$ values in orogenic gold deposits over time in comparison to the variation in seawater sulphate values over time. 42

Figure 3.6 Schematic diagram displaying possible setting of modern orogenic gold formation. 43

Figure 3.7 Percentage distribution of gold(I) species as a function of solution composition and temperature at 500 bar. 46

Chapter 4. Lithological characteristics of the Kibali Granite-Greenstone Belt and its neighbouring geological terranes; The West Nile Gneiss and Upper Congo Granitic Massif

Figure 4.1 Geological map of the Kibali Granite greenstone terrane and neighboring Upper Congo Granitic Massif and West Nile Gneiss terranes, displaying the major lithological units and sample locations discussed in this chapter. 50

Figure 4.2 Airborne Electromagnetic susceptibility data over part of the Kibali Granite-Greenstone belt and neighboring terranes 51

Figure 4.3 XPL Photomicrographs illustrating the range of textures observed in the Kibalian metasedimentary volcano-sedimentary conglomerates. 53

Figure 4.4 XPL Photomicrographs display mineral textures identified in the silicified volcaniclastic units. 55

Figure 4.5 Photographs displaying selected members of the North Kibalian Schists and Eastern Biotite Schists.	57
Figure 4.6 XPL Photomicrographs illustrating mineral textures identified in the high grade meta-sediments in the Eastern part of the Kibali belt.	58
Figure 4.7 Photographs displaying selected examples of Ironstones from the Kibali Granite-Greenstone Belt	60
Figure 4.8 XPL Photomicrographs illustrating mineral textures identified in the Kibalian basalts.	62
Figure 4.9 Photographs displaying selected members of the Kibalian intrusives.	64
Figure 4.10 Photomicrographs illustrating mineralogical and textural characteristics identified in the Kokiza and Ambarau intrusions	65
Figure 4.11 Discrimination diagrams displaying composition of amphibole and phyllosilicate mineral phases within analyses from the Kokiza gabbroic pluton.	66
Figure 4.12 Ternary classification diagrams displaying the range of compositions identified in the feldspar and phyllosilicate mineral phases in the Ambarau Granodiorite.	67
Figure 4.13 XPL Photomicrographs illustrating mineralogical and textural characteristics identified in samples from the Kalimva and Sessenge granitic intrusions.	69
Figure 4.14 Ternary discrimination diagrams displaying compositional variations in the feldspar and phyllosilicate mineral phases analysed from the Kalimva and Sessenge Granitoid intrusions	70
Figure 4.15 Photographs displaying selected members of the Watsa-A and Watsa-B intrusive bodies.	74
Figure 4.16 XPL Photomicrographs displaying mineralogical and textural characteristics identified within the Watsa-A unit.	75
Figure 4.17 Discrimination diagrams illustrating the compositional characteristics of mineral phases within the Watsa-A unit.	76
Figure 4.18: XPL Photomicrographs illustrating mineralogical and textural characteristics identified in the Watsa-B unit.	79

Figure 4.19 Ternary discrimination diagrams displaying compositional variation of selected mineral phases present in the Watsa-B unit	80
Figure 4.20 XPL Photomicrographs displaying textural and mineralogical characteristics identified in the Watsa-C unit.	81
Figure 4.21 Photographs displaying selected members of the Watsa C unit, The undifferentiated intrusives and boundary massifs in the Upper Congo Granitic Massif	82
Figure 4.22 Discrimination diagrams displaying compositional characteristics of selected mineral phases in the Watsa-C unit	83
Figure 4.23 XPL Photomicrographs displaying mineralogical and textural characteristics identified in the ‘undifferentiated’ lithologies to the south of the Watsa igneous complex.	85
Figure 4.24 Photomicrographs displaying textural and mineralogical characteristics identified within the boundary massif.	86
Figure 4.25 Ternary discrimination diagrams of selected minerals displaying the range of compositional data identified in the undifferentiated lithologies (Watsa-D) and boundary massifs.	87
Figure 4.26 XPL Photomicrographs illustrating minerals and textures identified within samples from the West Nile Gneiss.	90
Figure 4.27 Photomicrographs of Sample NZ06 displaying minerals and textures present within highly deformed examples of the West Nile Gneiss collected adjacent to the contact with the Kibali Granite-greenstone terrane.	92
Figure 4.28 Ternary diagrams displaying compositional ranges of feldspar and phyllosilicate phases from selected samples of West Nile Gneiss.	93

Chapter 5. Classification and tectonic discrimination within the Upper Congo Granite Massif and Kibali Granite Greenstone belt through the use of geochemical data

Figure 5.1 Map of the Kibali Granite-Greenstone Belt and neighboring terranes displaying the locations of the samples utilised in the geochemical study.	104
--	-----

Figure 5.2 Bivariate plots displaying geochemical data for samples from the Kibali Granite-Greenstone Belt	107
Figure 5.3 REE diagrams displaying the chondrite normalised REE concentrations of the major lithological groups from the Kibali Granite-Greenstone Belt and the Upper Congo Granite Massif	108
Figure 5.4 NMORB normalised extended trace element diagrams displaying data from the intrusive and extrusive felsic lithologies from the Kibali Granite-Greenstone Belt	109
Figure 5.5 NMORB normalised extended trace element diagrams displaying data from the intrusive and extrusive mafic lithologies from the Kibali Granite-Greenstone Belt	111
Figure 5.6 Bivariate plots displaying geochemical data for samples from the Upper Congo Granite massif	112
Figure 5.7 NMORB normalised extended trace element diagrams displaying data from the intrusive felsic lithologies from the Upper Congo Granite Massif	114
Figure 5.8 NMORB normalised extended trace element diagrams displaying data from the intrusive and extrusive mafic lithologies from the Upper Congo Granite Massif	115
Figure 5.9 Th and Co concentrations plotted against Zr demonstrating relative immobility of these elements. A and B; Kibali Granite-Greenstone Belt. C and D; Upper Congo Granite Massif.	118
Figure 5.10 Th/Co classification diagram for data from the Kibali Granite-Greenstone Belt (upper) and the Upper Congo Granitic Massif (Lower).	119
Figure 5.11 Nb/Ta discrimination diagram displaying data from the Kibali Granite-Greenstone Belt and Upper Congo Granite Massif. After Foley et al (2002).	122
Figure 5.12 Mineral vector diagram displaying data from the UCG mafic intrusives.	123
Figure 5.13 Ce/Ce* crustal input discrimination diagram (after Hastie et al, 2013), displaying geochemical data from the Kibali Granite-Greenstone Belt and Upper Congo Granitic Massif.	127
Figure 5.14 Nb-Zr mantle wedge discrimination diagram displaying geochemical data from the Kibali Granite-Greenstone Belt and Upper Congo Granitic Massif.	129
Figure 5.15 Th-Nb mantle input discrimination diagram, after Pearce (2008), displaying geochemical data from the Kibali Granite-Greenstone Belt and Upper Congo Granite Massif	129

Figure 5.16 Geo-tectonic reconstruction of the early evolution of the Kibali Granite-Greenstone Belt. A: Subduction and metasomatism of the overlying mantle wedge, slab melting and formation of overlying island arc crust. B: Crustal thinning and initiation of back-arc spreading. C: Continued back-arc basin developments, Magmas generated at the subducting slab and in the enriched mantle intrude the overlying back-arc basalt/sediment package 131

Chapter 6. Geochronological constraints on the origins and evolution of the Kibali Granite-Greenstone belt and bounding terranes, NE Democratic Republic of Congo

Figure 6.1 Locations of samples used in U:Pb study. 137

Figure 6.2 Cathodo-luminescence images of selected zircons from samples W10, W13, WP06 and H4 from the Upper Congo Granitic massif showing the range of morphologies and internal features identified within the samples 139

Figure 6.3 Wetherill concordia diagrams displaying data for samples analysed from the Upper Congo Granitic massif. Inset diagrams display concordia age calculated from samples with discordance <1% 140

Figure 6.4 Cathode Luminescence images of selected zircons analysed in this study from the Kibali Granite-Greenstone belt showing the range of morphologies and internal features identified within the samples 144

Figure 6.5 Wetherill concordia diagrams displaying data for samples analysed from the Kibali granite-Greenstone Belt Inset diagrams display concordia age calculated from samples with discordance <1%. 145

Figure 6.6 Cathodo-Luminescence images of selected zircons from samples NZ03 and NZ07 from the West Nile Gneiss showing the range of morphologies and internal features identified within the samples. 146

Figure 6.7 Wetherill concordia diagrams displaying data for samples analysed from the West Nile Gneiss Inset diagram display concordia age calculated from samples with discordance <1% (sample NZ03) and <2% (Sample NZ07). 148

Chapter 7. Textural and compositional characteristics of wall rock alteration and sulphide mineral phases of the major gold deposits in the Kibali Granite-Greenstone Belt; Insights into the factors affecting the distribution of mineralisation

Figure 7.1 Geological map of the Kibali Granite-Greenstone Belt displaying the location of known gold occurrences and the hypothesized position of the KZ structure	154
Figure 7.2 Cross section of the Karagba-Chaffeur-Durba (KCD) deposit displaying the position of major lithological units, alteration halo, faults and mineralised lodes.	156
Figure 7.3 Long section through the Karagba-Chaffeur-Durba (KCD) deposit displaying the north east dipping attitude of the host lithologies, F2 fold axis and mineralised lodes.	157
Figure 7.4 Core samples displaying the characteristics of the volcano-sedimentary conglomerate lithologies at the KCD deposit	160
Figure 7.5 Photomicrographs showing deformational and mineralisation characteristics in the lithologies at the KCD deposit:	161
Figure 7.6 Ternary diagrams displaying compositional variations in Fe-Carbonate alteration minerals at the four major deposits	165
Figure 7.7 Ternary diagrams displaying compositional variations in phyllosilicate alteration minerals at the four major deposits.	166
Figure 7.8 Mineralisation styles identified at the KCD gold deposit	168
Figure 7.9 Vein and replacement style mineralisation identified in the banded iron formations:	169
Figure 7.10 XPL Photomicrographs displaying selected examples of vein style mineralisation at the KCD gold deposit	170
Figure 7.11 Paragenetic diagram illustrating the developmental sequence of the major mineral phases including alteration assemblages, sulphide mineralisation and selected accessory phases identified at the Karagba-Chaffeur-Durba deposit	171
Figure 7.12 RFL Photomicrographs displaying the relationship between the major sulphide mineral phases at identified at the Karagba-Chaffeur-Durba (KCD) deposit.	173

Figure 7.13 RFL Photomicrograph displaying the occurrences of gold and its relationship to the pyrite sulphide mineral phases at the Karagba-Chaffeur-Durba deposit	174
Figure 7.14 Core samples from the Mengu deposit displaying the localized deformation of the volcano-sedimentary conglomerate lithologies:	176
Figure 7.15 XPL Photomicrographs illustrating host lithology, alteration and mineralisation microtextural characteristics in selected samples from the Mengu deposit:	177
Figure 7.16 Core images displaying mineralisation styles identified in samples from the Mengu deposit:	181
Figure 7.17 Paragenetic diagram illustrating the developmental sequence of the major mineral phases including alteration assemblages at the Mengu deposit	183
Figure 7.18 RFL Photomicrographs illustrating the relationship between sulphide phases observed at the Mengu Deposit.	184
Figure 7.19 Photomicrographs illustrating the relationship of gold mineralisation to the major pyrite phases; at the Mengu deposit	185
Figure 7.20 Core images displaying range of deformational characteristics identified in the volcano-sedimentary conglomerates at the Pakaka deposit.	187
Figure 7.21 XPL Photomicrographs displaying deformation, alteration and mineralisation textures identified in the volcano-sedimentary units at the Pakaka deposit	188
Figure 7.22 Core images illustrating the mineralisation styles identified at the Pakaka deposit.	191
Figure 7.23 Paragenetic diagram illustrating the relative timing of the major alteration, sulphide and accessory minerals in the samples from the Pakaka deposit	193
Figure 7.24 RFL Photomicrographs illustrating the relationship between the major sulphide phases identified at the Pakaka deposit	194
Figure 7.25 Core samples displaying the range of deformation identified within the volcano-sedimentary conglomerates at the Pamao deposit.	197
Figure 7.26 XPL Photomicrographs displaying deformation and alteration characteristics in the host lithologies at the Pamao deposit.	198

Figure 7.27 Core images displaying mineralisation styles identified in core from the Pamao deposit:	200
Figure 7.28 XPL Photomicrographs displaying alteration and mineralisation textures identified in samples from the Pamao deposit.	204
Figure 7.29 Paragenetic diagram illustrating the relative timing of the major alteration, sulphide and accessory phases in the samples from the Pamao deposit	205
Figure 7.30 RFL Photomicrographs illustrating the relationship between the major sulphide phases in the samples from the Pamao deposit	207
Figure 7.31 Arsenopyrite geothermometry diagram redrawn from Sharp et al (1985) displaying data from the Karagba-Chaffeur-Durba deposit.	213
Figure 7.32 Arsenopyrite geothermometry diagram redrawn from Sharp et al (1985) displaying data from the Mengu deposit.	214
Figure 7.33 Arsenopyrite geothermometry diagram redrawn from Sharp et al (1985) displaying data from the Pakaka deposit	215
Figure 7.34 Arsenopyrite geothermometry diagram redrawn from Sharp et al (1985) displaying data from the Pamao deposit	216
Figure 7.35 Schematic diagram illustrating the reaction weakening and hydrothermal hardening mechanisms hypothesised to have influenced the formation of mineralisation in the deposits at the Kibali Gold Project	219

Chapter 8. $\delta^{34}\text{S}$ characteristics of the Karagba-Chaffeur-Durba (KCD) deposit and other significant gold resources in the Kibali Granite-Greenstone Belt

Figure 8.1 $\delta^{34}\text{S}$ ranges for terrestrial sulfur reservoirs and selected orogenic gold deposits from the Archean, Proterozoic and Phanerozoic.	223
Figure 8.2 Histograms displaying $\delta^{34}\text{S}$ data from the KCD, Mengu, Pakaka and Pamao gold deposits	231

Chapter 9. Constraining the age of mineralisation at the Kibali Gold project: U-Th-Pb dating of monazite

Figure 9.1 Selected electron micrographs demonstrating mode of occurrence of monazite crystal phase within samples from the KCD deposit.	238
Figure 9.2 Terra-Wasserburg plots of data generated during the analysis of material from the Karagba-Chaffeur-Durba (KCD) gold deposit	241
Figure 9.3 Mean Standard weighted distribution plots for samples PB12-D05, PB12-D10 and PB12-D12	242
Figure 9.4 Mean Standard weighted distribution plots for samples 2013-D39 and 2013-D57.	243
Figure 9.5 Thorium vs uranium and Th/U vs age plots for all data from KCD, Pakaka and Pamao deposits	245
Figure 9.6 Electron micrographs showing the mode of occurrence of monazite phases within samples from Pakaka and Pamao.	246
Figure 9.7 Terra-Wasserburg plots of uncorrected data generated during the analysis of material from the Pakaka gold deposit.	246
Figure 9.8 Mean Standard weighted distribution plots of data from the Pakaka gold deposit.	247
Figure 9.9 Terra-Wasserburg plots of uncorrected data generated during the analysis of material from the Pamao gold deposit	249
Figure 9.10 Mean Standard weighted distribution plots for samples from the Pamao gold deposit	250
Figure 9.11 MSWD averages for all samples from the KCD, Pakaka and Pamao deposits	253

Chapter 10. Re:Os Pyrite constraints on the formation of mineralisation at the Karagba-Chaffeur-Durba (KCD) orogenic gold deposit, NE Democratic Republic of the Congo

Figure 10.1 Model-1 regression for all samples from the KCD gold deposit	262
Figure 10.2 Model-1 regression of selected data from the KCD gold deposit	262
Figure 10.3: Model-1 regression of analytical data for samples PB17 and PB19	263

List of tables

Chapter 4. Lithological characteristics of the Kibali Granite-Greenstone Belt and its neighbouring geological terranes; The West Nile Gneiss and Upper Congo Granitic Massif.

Table 4.1 Representative EDS analysis of major mineral phases identified in lithologies of volcano-sedimentary origin within the Kibali granite-Greenstone Belt.	54
Table 4.2 Representative EDS analysis of major minerals identified in the North East Kibalian schists (sample H1) and eastern Quartz-Biotite Gneiss (Sample 116-29).	59
Table 4.3 Representative EDS analyses of the major mineral phases identified in samples from the Kokiza Gabbroic pluton.	66
Table 4.4 Representative EDS analysis of the major mineral phases identified in the samples from the Ambarau Granodiorite.	67
Table 4.5 Representative EDS analysis of the major mineral phases identified in the Kalimva and Sessenge granitoids.	70
Table 4.6 Representative EDS analysis of major mineral phases identified within the lithologies from the Watsa-A unit.	77
Table 4.7 Representative EDS analysis of the major mineral phases identified in the Watsa-B unit.	80
Table 4.8 Representative EDS analysis of the major mineralogical components identified in the Watsa-C unit.	83
Table 4.9 Representative EDS analysis of the major mineral phases identified in the Watsa-D lithologies (upper section) and Boundary Massifs (lower section).	88
Table 4.10 Representative analysis of mineral compositions within the West Nile Gneiss.	93
Table 4.11 Selected examples of chlorite compositions and calculated formation temperatures from the volcano-sedimentary conglomerates of the Kibalian metasediments	97

Chapter 7. Textural and compositional characteristics of wall rock alteration and sulphide mineral phases of the major gold deposits in the Kibali Granite-Greenstone Belt; Insights into the factors affecting the distribution of mineralisation

Table 7.1 Representative analysis of chlorite from deformed volcano-sedimentary conglomerates at the Karagba-Chaffeur- Durba deposit.	162
Table 7. 2Representative analysis of Fe-Carbonate alteration minerals identified in samples from the Kargaba-Chaffeur-Durba deposit.	163
Table 7.3 Representative analysis of aluminoceladonite phyllosilicates identified in alteration assemblages at the Karagba-Chaffeur-Durba deposit	164
Table 7.4 Representative analyses of chlorite identified in deformed volcano-sedimentary conglomerates at the Mengu deposit	178
Table 7.5 Representative analyses of Fe-carbonate alteration minerals identified at the Mengu deposit	179
Table 7.6 Representative analyses of aluminoceladonite alteration minerals identified at the Mengu deposit	180
Table 7.7 Representative analyses of chlorite minerals in deformed volcano-sedimentary conglomerates from the Pakaka deposit	189
Table 7.8 Representative analyses of Fe-Carbonate alteration minerals identified in samples from the Pakaka deposit	190
Table 7.9 Representative analyses of aluminoceladonite alteration minerals at the Pakaka deposit	190
Table 7.10 Representative analyses of chlorite minerals in deformed volcano-sedimentary conglomerates at the Pamao deposit	201
Table 7.11 Representative analyses of Fe-Carbonate alteration minerals identified at the Pamao deposit	202
Table 7.12 Representative analyses of Alluminoceladonite alteration minerals at the Pamao deposit	203

Table 7.13 Summary of the major features of the KCD, Mengu, Pakaka and Pamao deposits	209
---	-----

Chapter 8. $\delta^{34}\text{S}$ characteristics of the Karagba-Chaffeur-Durba (KCD) deposit and other significant gold resources in the Kibali Granite-Greenstone Belt

Table 8.1 Sample and analytical results for material from the Karagba-Chaffeur-Durba (KCD) deposit. $\delta^{34}\text{S}$ values are presented as ‰ VCDT	226-227
--	---------

Table 8.2 Sample and analytical results for material from the Mengu deposit. $\delta^{34}\text{S}$ values are presented as ‰ VCDT	228
---	-----

Table 8.3 Sample and analytical results for material from the Pakaka deposit $\delta^{34}\text{S}$ values are presented as ‰ VCDT	229
---	-----

Table 8.4 Sample and analytical results for material from the Pamao deposit. $\delta^{34}\text{S}$ values are presented as ‰ VCDT	230
---	-----

Chapter 10. Re:Os Pyrite constraints on the formation of mineralisation at the Karagba-Chaffeur-Durba (KCD) orogenic gold deposit, NE Democratic Republic of the Congo

Table 10.1: Samples collected and tested as part of the Re-Os study of the Karagba-Chaffeur-Durba (KCD) gold deposit	259
--	-----

Table 10.2: Re-Os analytical data for samples from the KCD gold deposit	261
---	-----

Chapter 1. The Kibali Granite-Greenstone Belt and Kibali Gold Project

1.1 Introduction

The geological terranes of the Northeast Democratic Republic of Congo (DRC) contain some of the least explored granite-greenstone belts on Earth, and constitute some of the most prospective terranes for gold mineralisation. The Kibali Granite-Greenstone Belt (KGGB) is located in the Northeast DRC (Fig. 1.1) and is host to the Kibali gold project, including the giant Karagba-Chaffeur-Durba (KCD) deposit and multiple satellite deposits (Randgold, 2010). This study aims to examine the geological, geochemical and geochronological characteristics of the KGGB, in addition to investigating the characteristics of significant gold mineralisation contained within the belt. This introduction will review the extent of the study area, the history of gold mining and research in the Kibali, and will outline the specific aims and objectives of the study.



Figure 1.1: The Democratic Republic of the Congo; the location of the Kibali gold project is indicated by the red star (modified after United Nations, 2011).

1.1.1 Study Area

The study area (Fig. 1.2) is located in the central portion of the east-west trending Kibali Granite-Greenstone Belt in Northeast DRC, approximately 100 km from the border with South Sudan and 300 km from the border with Uganda. The study area is limited to the territory covered by the Randgold Resources Ltd Kibali gold permit area and includes the central part of the KGGB, and parts of the West Nile Gneissic (WNG) and the Upper Zaire Granitoid Massif (UZG) (Fig. 1.2). Gold mineralisation occurs principally in the western part of the license area, focused around the giant KCD deposit with the Mengu, Pakaka and Pamao deposits constituting the main satellite deposits.

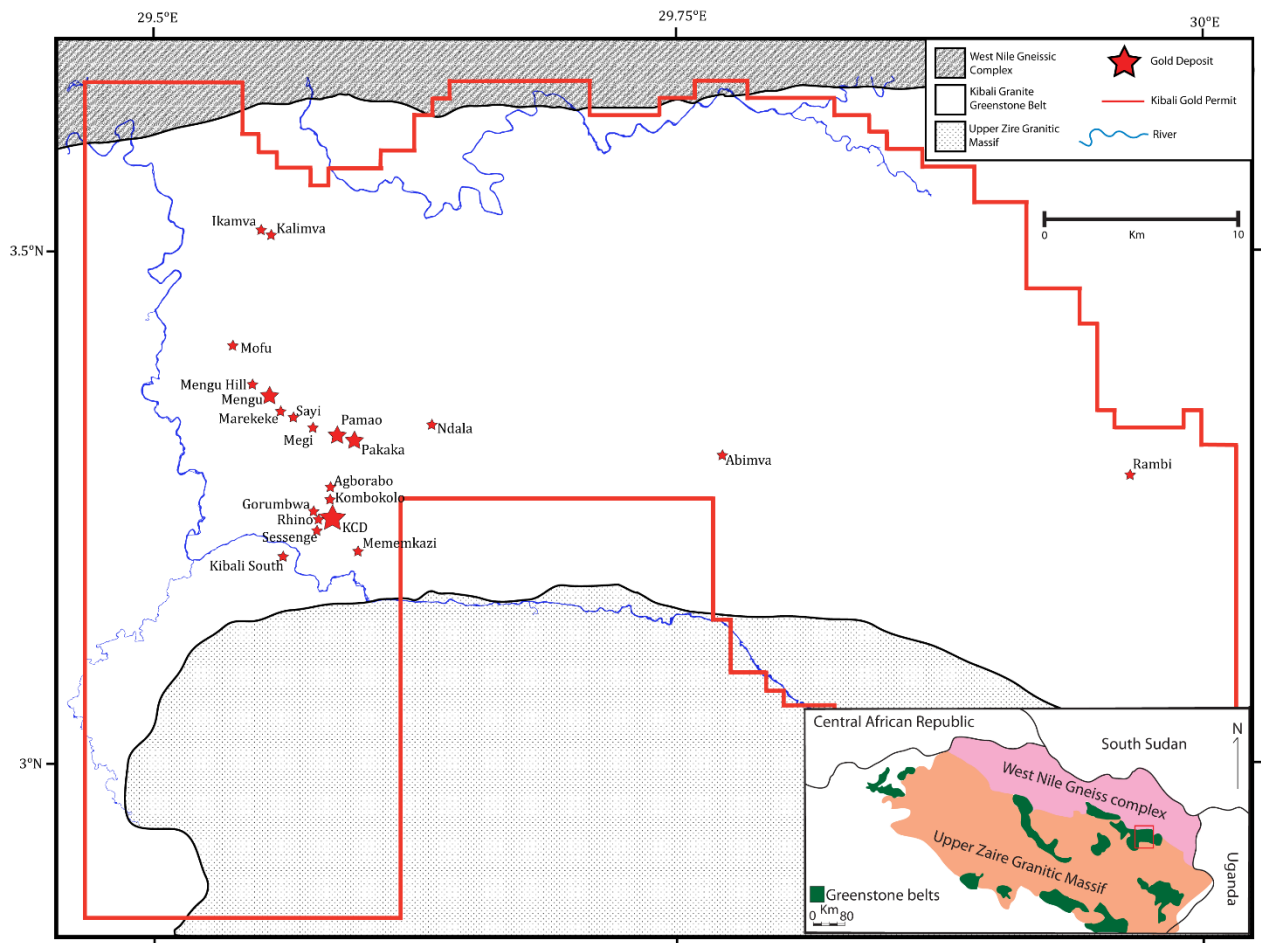


Figure 1.2: Sketch map displaying the study area showing the three major geological terranes and significant gold deposits. Inset; regional map showing location of the study area (red box) and extent of the major geological terranes (Redrawn from Lavreau, 1984).

1.1.2 Existing Knowledge

Despite significant gold resources having been identified and extraction taking place for almost a century (Section 1.3.1), there have been few detailed studies of the KGGB and its gold resource. Published material has focused on the gold resource within the KGGB, initially described in Woodtli (1961) who examined the Agborabo and Gorumbwa deposits, describing them as ‘gold impregnation deposits’ (Chapter 2). The characteristics of the gold resources were later reviewed by Lavreau (1973) and Lavreau (1984) as part of a review of the gold deposits of the Northeast DRC (Chapter 2). Prior to the commencement of this study, an investigation into the mineral assemblage within the KCD was conducted at Kingston University by Dr D. Lawrence and established an initial paragenesis for the KCD deposit. The geological characteristics of the KGGB were reviewed in brief by Woodtli (1961) and Lavreau (1984) (Chapter 2), consisting of field descriptions of the lithological units. A review of the geology of the Bomu-Kibalian block, including the units of the Kibalian sequence of which the Kibali belt is the type descriptor, was included in the reviews of Cahen and Snelling (1966) and Cahen et al. (1984). Randgold Resources Ltd has conducted extensive work as part of their continuing program of exploration and extraction of the gold resource within the KGGB. This consists of extensive regional mapping, investigation of the structural characteristics and documentation of the ore reserves.

At the inception of this study, the working hypothesis is that the Kibali Granite-Greenstone Belt is Archean in age, with gold mineralisation hypothesised to have formed during the Archean when the West Nile Gneiss was thrust over the KGGB and Upper Congo Granitic Massif.

1.2 The Democratic Republic of the Congo

The Democratic Republic of the Congo, located in central Africa (Fig. 1.1), covers 2.3 million km² and has a population of 62.4 million (United Nations, 2007). The DRC is one of the most mineral rich nations in the world, the country’s share of global production being estimated at 51% cobalt, 25% of industrial diamonds and 14% of gem quality diamonds, 14% of tantalum and 3% of both copper and tin (KPMG, 2014). These production statistics are underpinned by vast mineral reserves which are estimated to constitute, as a proportion of global reserves: 45% of cobalt, 25% of diamonds and 3% of copper, in addition to significant gold reserves which are estimated to be the 10th largest globally (KPMG, 2014). Despite this vast potential wealth, the country is one of the least developed in the world, having been ranked 186 on the Human Development Index (United Nations Development Programme, 2014).

The nation’s earliest routes stem from Henry Morten Stanley’s expedition of 1877, in which he claimed the region as the personal possession of Emperor Leopold II of Belgium, consolidating the region into the

Congo Free State in 1885 (United Nations, 2007; Kisangani and Bobb, 2010). This period was marked by mass exploitation of the region's natural resources (principally rubber and ivory) by slave labour, and is infamous for the terrible conditions experienced by the native population (Kisangani and Bobb, 2010). The Congo Free State was abolished in 1908 following international pressure and restructured as a colony of Belgium, renaming it the Belgian Congo (United Nations, 2007; Kisangani and Bobb, 2010).

The colonial period ended in 1960, following rioting in several cities (United Nations, 2007). Elections were held in May 1960 with full independence formally achieved on 30th June 1960, as 'The Republic of the Congo' (Kisangani and Bobb, 2010). The elections marked the beginning of the Congo crisis in which several provinces announced their secession from the government, international powers vied for dominance, and private mercenary militias poured into the country (Kisangani and Bobb, 2010). In September 1960, President Lumumba was overthrown in a military coup led by Colonel Joseph Mobutu who, by 1965, reasserted control of the nation, declaring himself president (United Nations, 2007).

The First Congo War began in 1997, following tensions in neighbouring Rwanda. Zairian armed forces and Hutu militias clashed with Tutsi militias who were allied with opposition groups under the leadership of Laurent-Desire Kabila. This culminated in Mobutu fleeing the country and Kabila ascending to the presidency on 20th May 1997 (United Nations, 2007; Kisangani and Bobb, 2010). The subsequent peace was short-lived, with the 'Movement for the Liberation of the Congo's; supported by Ugandan and Rwandan forces attacking in August 1998 (United Nations, 2007). Zimbabwe and Angola supported the Kabila government and one of the most devastating wars in recent history began. This war is infamous for the rush to take control of the nation's great mineral wealth with its diamond, gold, zinc, copper and coltan resources being extensively looted (Kisangani and Bobb, 2010).

President Kabila was assassinated in 2001 and succeeded by his son Joseph Kabila, who called for multilateral peace talks culminating in the Sun City agreement of May 2002. President Kabila would share power with the principal faction leaders, militia forces would be incorporated into the nation's armed forces and all foreign forces would leave the region (United Nations, 2007; Kisangani and Bobb, 2010). In the time since, Joseph Kabila has been elected president twice and, despite continued conflicts in the Nord Kivu and Sud Kivu regions, relative stability has returned to the region.

1.3 The Kibali Gold Project

The Kibali Gold Project is a joint venture between Randgold Resources Ltd, AngloGold-Ashanti Ltd and the Offices des Mines d'Or de Kilo-Moto (OKIMO), with Randgold the senior partner and operator (Randgold, 2010). The Kibali Gold Project is the largest African gold-only project outside of South Africa and is one of

the largest gold deposits under development in the world. The Project is centred on the Karagba-Chaffeur-Durba (KCD) deposit with an estimated 17 Moz Au. A number of smaller satellite deposits have been identified across the region, though principally cluster to the north and northwest of the KCD site (Fig. 1.2). The most significant of these satellite deposits are Mengu (1.1 Moz), Pakaka (0.7 Moz) and Pamao (0.5 Moz) (Randgold, 2010).

1.3.1 Deposit History

Gold was first identified in the northeast DRC by Australian prospectors in 1903, including placer deposits in the Kibali river area (then known as the Moto deposit) and the Kilo deposit to the east (Randgold, 2010). Extraction of gold from alluvial and gold impregnation deposits (Woodtli, 1954) began in 1906 and over the next 50 years, an estimated 11Moz Au was extracted (Randgold, 2013). In 1926, the Belgian government founded the Société des Mines d'Or de Kilo-Moto (SOKIMO) to oversee operations across the Kilo and Moto (Kibali). Mining occurred principally during the 1950s in open pit works at the Durba and Sessenge sites, with underground works at the Agborabo and Gorumbwa sites (Randgold, 2013). Following independence in 1960, mining activities rapidly declined, with production dominated by artisanal workings and small alluvial workings (Randgold, 2013). SOKIMO was reorganised in 1966 to 'Offices des Mines d'Or de Kilo-Moto' (OKIMO) and continued overseeing the minor workings over the next forty years (Randgold, 2013).

In 1996, Barrick Gold Corporation (BGC) acquired exploration rights over the Kilo-Moto regions in a joint venture with OKIMO (Randgold, 2010). BGC defined a large soil anomaly at the Kibali site and, in 1998, entered into a joint venture with AngloAmerican Corp (AAC) to define the resource, with AAC acting as principal operator (Randgold, 2013). BGC/AAC conducted exploration drilling at the KCD and Pakaka deposits, with results indicating a resource of 2 Moz at Kibali (Randgold, 2013). Following the outbreak of the Second Congo War in August 1998, BGC/AAC withdrew from the DRC and formally returned the concession to OKIMO in 2000 (Randgold, 2010).

Ugandan troops in support of the rebel group 'Rally for Congolese Democracy' (Rassemblement Congolais pour la Démocratie, RCD) occupied Durba, taking control of the Gorumbwa, Durba and Agborabo mines (Human Rights Watch, 2005). Ugandan forces are estimated to have removed approximately 35,000 oz Au over four years. Ugandan forces ordered the reopening of the underground workings at Gorumbwa in late 1998 and the open pit at Durba in July 1999, removing existing OKIMO personnel (Human Rights Watch, 2005). In December 1998, the Gorumbwa mine was the centre of an outbreak of Marburg haemorrhagic fever, linked to poor conditions within the mine, killing in excess of 50 mine workers in the Durba village (Human Rights Watch, 2005).

In an attempt to hasten extraction of gold at Gorumbwa, Ugandan forces employed explosives, conducting more than 50 blasts in December 1999, resulting in the destruction of supporting pillars and the collapse of the Gorumbwa mine in December 1999 (Human Rights Watch, 2005). The collapse killed an estimated 100 artisanal workers and resulted in widespread flooding of the area, destroying the most significant gold resource at the time (Human Rights Watch, 2005). In 2002, Ugandan forces began withdrawing from the Durba area, leaving control of it to the RCD-ML rebel group. This group was incorporated into the national government following the Sun City agreement in 2002 and the establishment of the transitional government in 2003 brought the area back under the control of Kinshasa (Human Rights Watch, 2005).

From 2006 to 2009, Moto gold completed a series of feasibility studies on the Kibali deposit and on 15th October 2009, Randgold Resources Ltd and AngloGold Ashanti Ltd jointly acquired all shares of Moto gold (Randgold, 2010). Following further acquisitions, at the end of 2009, Randgold Resources and AngloGold increased their share in the project to 45% each, with the remaining 10% controlled by OKIMO (Randgold, 2010). Since 2009, Randgold Resources Ltd have been the principal operator of the Kibali gold project, taking the project from post feasibility to pouring first gold in Q3 2013, with extensive open pit and underground operations under continued development.

1.4 Project Aims and Objectives

With the discovery and subsequent extraction of the world class Kibali gold deposit, there has been a renewed impetus for study of the geological characteristics and history of the Kibali Granite-Greenstone Belt. This study aims to generate the first significant data for both the Kibalian orogenic gold deposits and, from a regional perspective, the Kibalian Granite-Greenstone Belt and its neighbouring terranes, the West Nile Gneiss and Upper Congo Granitic Massif. The study is therefore divided into two distinct themes:

1. Investigation of the characteristics and origins of the Kibali Granite-Greenstone Belt and its relationship to the neighbouring terranes.
2. Investigation of the characteristics and formation of the Kibali gold resource, focussing on the KCD, Mengu, Pakaka and Pamao deposits.

Through satisfying these two investigative themes and combining the data from each, we aim to generate the first geological history of the Kibali Granite-Greenstone Belt and place the development of the gold mineralisation into this geological context.

While establishing the geological characteristics and history of the Kibali Granite-Greenstone Belt will be in itself invaluable, the geographical position of the Kibali Granite-Greenstone Belt lends this data a broader degree of significance. The Kibali Granite-Greenstone Belt lies on the northern edge of the Congo craton at the northwest end of a series of approximately northwest-southeast orientated granite-greenstone belts that extend across the Northeast DRC, Uganda and Tanzania (Chapter 2). The data collected in this study will allow us to develop the first geological model for the formation and evolution of the Kibali Granite-Greenstone Belt and place this into the broader context of the formation and evolution of the East African Granite-Greenstone terranes.

The position of the Kibali Granite-Greenstone Belt on the northern edge of the Congo craton also provides an opportunity to examine the role of Paleoproterozoic orogenesis in the region. The Oubanguide orogeny (part of the broader Pan-African orogeny (Chapter 2)) has been identified on the northern margin of the Congo craton in the Central African Republic and northern Uganda but is yet to be identified in the Bomu-Kibalian block. By examining our data it may be possible to identify, for the first time, the influence of this Paleoproterozoic event in the DRC. In order to achieve the goals outlined above, the following data sets will be generated and utilised in developing models for the formation of the Kibali Granite-Greenstone Terrane:

1. Classification of the lithologies present within the Kibali Granite-Greenstone Belt and surrounding terranes, the West Nile Gneiss and Upper Zaire Granite Massif.
2. Geochemical data to examine the origins, evolution and relationship between the major geological terranes.
3. Generate accurate dates for the major geological terranes and use them to constrain the geological evolution of the Kibali Granite-Greenstone Belt.

Orogenic gold deposits have been extensively studied and their mechanisms of formation are reasonably well constrained (Chapter 3). The orogenic gold deposits of the Kibali Granite-Greenstone Belt display a number of unusual characteristics that are of significance. Orogenic gold deposits are typically associated with large trans-crustal shear zones, deposits occurring in 2nd and 3rd order structures, however the deposits within the Kibali Granite-Greenstone Belt display no such association and are instead hosted within a sequence of thrust stacked metasediments. This places the deposits in a minority, with the Macraes flats deposits in New Zealand being the only other significant deposit to display such an association. The data collected from the Kibali deposits will be significant in examining the mechanisms through which these atypical orogenic gold deposits are formed. In examining the gold deposits of the Kibali Granite-Greenstone Belt, the following data will be generated and used to interpret their formation:

1. Data regarding the compositions, abundances and mode of occurrence of the mineralised sulphide phases, alteration assemblages and host rocks ranging from textural observations to compositional data.
2. Stable isotope data to examine the origin and evolution of the fluids and materials involved in the development of mineralisation.
3. Radiogenic isotope analysis of mineralised material or minor phases texturally associated with mineralisation to determine the age of formation and place into the context of the regional geological evolution.

The Kibali Granite-Greenstone Belt presents an almost unique opportunity in modern geology to examine an essentially unexplored 'Archean' granite-greenstone belt and gold deposits. Develop the first models for their formation and evolution and provide essential data on the evolution of the region as a whole.

Chapter 2. Geology of the Archean Cratons and Proterozoic mobile belts around the North East margin of the Congo Craton

2.1 The Cratonic Architecture of Africa

The African continent consists of deep rooted Archean Cratons and Cratonic fragments sutured together by the Palaeozoic mobile belts (Fig. 2.1, 2.2). Five major Cratonic blocks are present, the West African, East Sahara, Congo, Tanzanian and Kalahari Cratons each being composed of aggregated Cratonic fragments ranging in age from 3.6 to 2.5 Ga (Fig. 2.2) (Begg et al., 2009). The collision, rifting and subsequent re-collision of the Archean Cratons as part of the supercontinent cycle has resulted in multiple orogenic events and the formation of a series of Proterozoic mobile belts (Begg et al., 2009). Of principal interest to this study are the Cratonic units of East and Central Africa: the Tanzanian, Ugandan, East Saharan and the north east part of the Congo Craton and the three major Proterozoic mobile belts formed during the Eburnean, Grenvillian and Pan-African orogenic cycle (Fig. 2.2).

The geological terranes of North East Democratic Republic of Congo (DRC) form part of a block of Neo/Mesoarchean material that extends into Uganda and Tanzania and constitutes the north eastern section of the Congo Craton (Fig. 2.1). The margins of this Archean Cratonic block have been extensively modified by successive cycles of rifting and orogenesis across the Proterozoic and Phanerozoic eons and as such possess a complex geological history. The Kibali Granite-Greenstone Belt and associated terranes of the Northeast DRC are amongst the least investigated in the world and as such information regarding their characteristics and formation are limited. The associated Archean terranes of Uganda and Tanzania have been the subject of significant investigation and the majority of existing knowledge regarding the evolution of the Archean Cratons and Proterozoic mobile belts have been derived from these studies.

This chapter will examine the existing knowledge regarding the characteristics of the Archean Cratons and Proterozoic mobile belts in order to establish a geochronological framework for the evolution of the region.

2.2 The Congo-Tanzania Cratonic Mass

The Congo Craton is thought to consist of four geologically distinct areas of Archean basement, the Gabon-Cameroon Shield, Kasai Shield, Angolan Shield and Bomu-Kibalian Block (Begg et al., 2009) (Fig. 2.2).

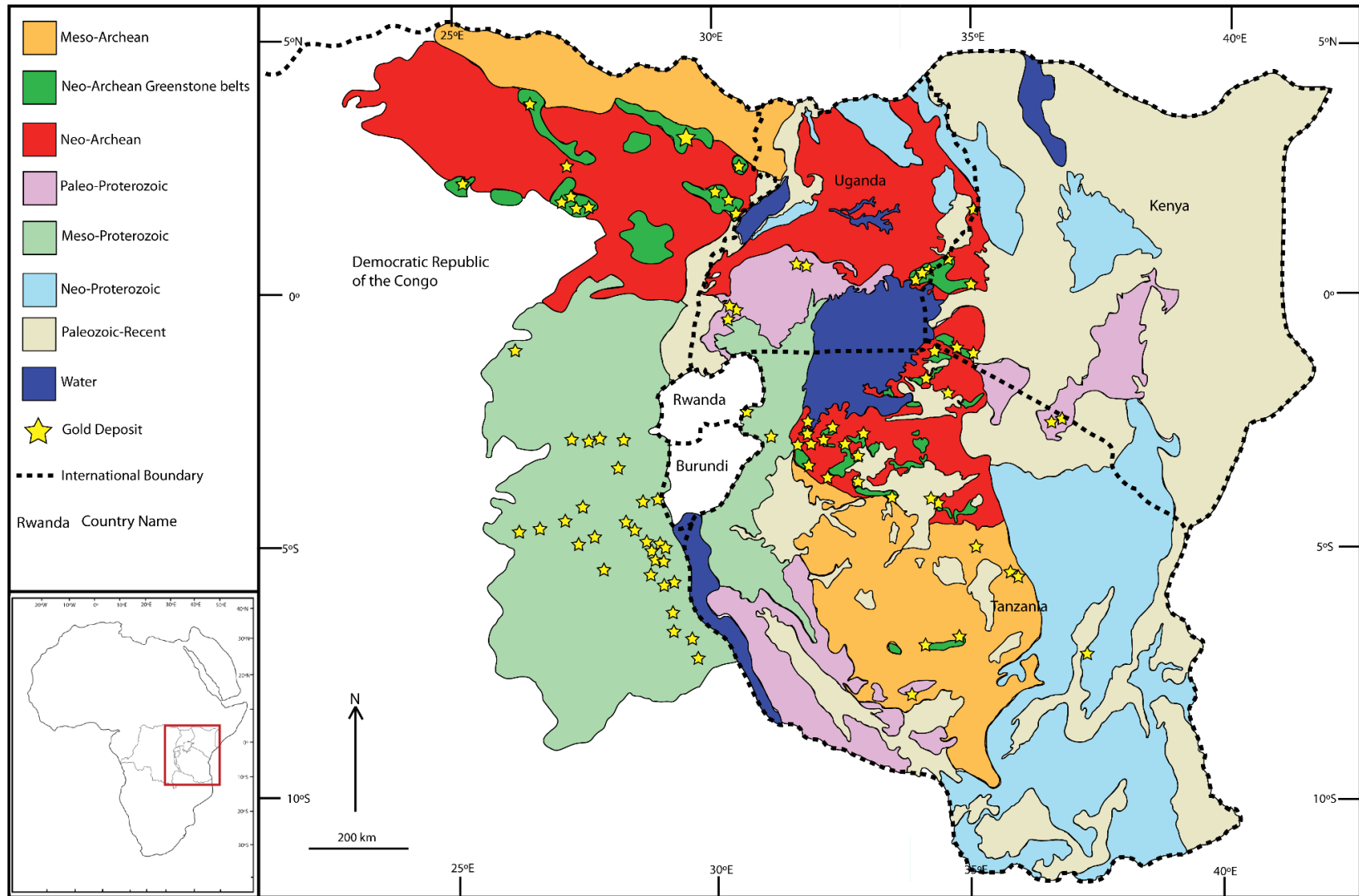


Figure 2.1: The major geochronological units of the Congo/Tanzania Craton and surrounding terranes in East and Central Africa and the incidence of significant gold mineralisation, Modified after Kabete et al., 2012; Kabete et al., 2012b; Nyakecho and Hagemann, 2014; Westerhoff et al., 2014; Lavreau, 1984.

The Tanzanian Craton, located east of the Congo Craton between the eastern and western arms of the East African rift and extends under Tanzania and southern Uganda, has generally been regarded as a separate Craton although recent research has suggested that it was part of a proto-Congo cratonic mass before post Archean rifting occurred and may still be connected at depth (Link et al., 2010).

The North East Congo Craton is divided into two major units, The Bomu-Kibalian Block of the DRC with its corollary units in the West Nile Block of Uganda, and the North Uganda basement terrane (Fig. 2.3) (Begg et al., 2009; Westerhoff et al., 2014). The Tanzanian Craton is formed of three distinct terranes, the West Tanzania Terrane in Uganda; Northern Block of Tanzania and southern Uganda and The Southern Block of Tanzania (Fig. 2.4) (Begg et al., 2009; Westerhoff et al., 2014). The two Cratonic masses are hypothesised to be sutured together along the Nakasongalo discontinuity in central Uganda (Fig. 2.3) (Westerhoff et al., 2014).

2.2.1 The Bomu-Kibalian Block

The Bomu-Kibalian Block is divided into three major units: the Bomu in the north west extending from North East DRC into the Central African republic; the Kibalian extending south west from the border of the Central African Republic to the Ugandan border and the West Nile Gneiss formation which correlates with the West Nile block of North East Uganda (Fig. 2.3) (Cahen and Snelling, 1966; Westerhoff et al., 2014). Data collected during a small number of reconnaissance surveys during the 1960's and 1980's indicates that the Kibalian consists of two geological terranes, the Kibalian Greenstone Belts and the Upper Congo Granitic Massif (Fig. 2.3) (Cahen and Snelling, 1966).

The Upper Congo Granitic Massif is composed of orthogneisses and multiple intrusive complexes which display internal zoning from alkaline microcline granites to diorite with rare oligoclase, andesine and labradorite (Cahen and Snelling, 1966). Three distinct generations of material have been identified within the Upper Congo Granitic Massif (Cahen et al., 1984). The first generation consists of tonalities, diorites and granodiorites dated between 2894 ± 67 Ma and 2725 ± 77 Ma with evidence for lead loss events at 2336 Ma and 303 Ma (Cahen et al., 1984). The second generation is composed of medium to coarse quartz monzonites that are observed intruding the first generation and dated between 2510 ± 64 Ma and 2411 ± 127 Ma (Cahen et al., 1984). The third generation consists of potassic granites and pegmatites of which limited knowledge exists (Cahen et al., 1984). The orthogneiss units of the Upper Congo Granitic Massif are held to be reworked monzonites of the second generation and, to a lesser extent, tonalities of the first generation (Cahen et al., 1984).

The Kibalian Granite-Greenstone Belts occur as narrow 10 km wide and 30 to 60 km long belts and include the Isiro, Tina, Kibali, Zani, Kilo, Mambasa, Ngayu, Panga and Tele belts (Fig. 2.3) (Lavreau, 1984). The Kibalian Granite-Greenstone Belts are composed of variable actinolite-talc-sericite-biotite-graphitic schists, grading to amphibolite with hypothesised proximity to the underlying Upper Congo Granitic Massif (Cahen and Snelling, 1966). Sedimentary and metasedimentary lithologies have been variably altered by carbonate assemblages and are interbedded with basalts and extensive banded iron formation horizons (Cahen and Snelling, 1966). These metasedimentary units are hypothesised to be of volcano-sedimentary origin (Cahen and Snelling, 1966) and have been divided into an upper and lower Kibalian based on the estimated ratio of volcanic/sedimentary material (Lavreau, 1984). The Upper Kibalian has a volcanic/sedimentary ratio of approximately 1, volcanic components are composed of andesites and non-typical ocean tholeiites, intruded by granitoids of the second generation (Cahen et al., 1984; Lavreau, 1984). The Lower Kibalian possesses a high volcanic/sedimentary ratio with volcanic rock being dominated by oceanic tholeiites and high Mg basalts, intruded by tonalitic material of the first generation of intrusives (Cahen et al., 1984; Lavreau, 1984). The Lower Kibalian is more widespread having been correlated across multiple greenstone belts while the Upper Kibalian is known only from outcrops in the Kibali, Ngayu and Zani greenstone belts (Cahen et al., 1984; Lavreau, 1984). The Kibalian greenstone belts are cut by a number of poorly constrained north-north east – south-south west orientated shear belts correlated to the Rwenzori tectonic episode (~2 Ga) which cut the Kibalian Granite-Greenstone Belts and the Upper Congo Granitic Massif where associated with the belts (Lavreau, 1984).

The West Nile Gneiss (-West Nile block) extends across the northern edge of the Kibalian terrane from the DRC into North West Uganda (Fig. 2.3). The terrane consists of variable Mesoarchean metasedimentary granulite- granite-charnockitic gneisses and granitoids dated between 3.42 and 3.07 Ga (Cahen and Snelling, 1964; Mantarri et al., 2011; Mantarri, 2014; Westerhoff et al., 2014). These are overlain in places by thin belts of metavolcanics and metasediments dated between 2.64 and 2.57 Ga and interpreted as accretionary terranes that have been correlated with the Kibalian greenstone belts (Cahen and Snelling, 1964; Mantarri et al., 2014; Westerhoff et al., 2014).

2.2.2. The North Uganda Terrane

The North Uganda Terrane comprises the northern section of the Ugandan basement and is separated from the neighbouring West Nile Block by the ~1 Ga north – south trending Madi-Igisi belt and from the West Tanzania Terrane by the mid-crustal Nakasongalo discontinuity formed prior to 2.6 Ga (Fig. 2.3) (Westerhoff et al., 2014).

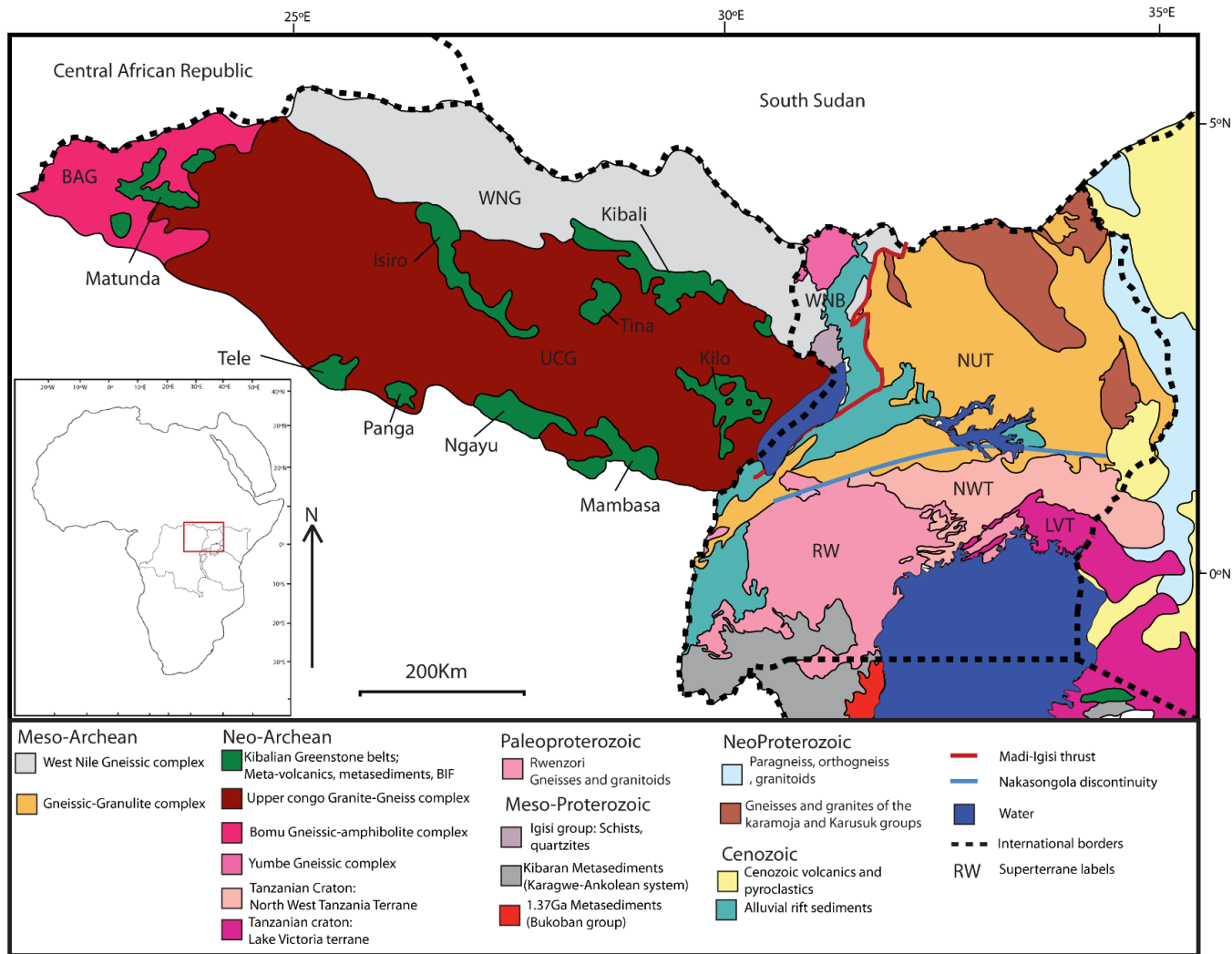


Figure 2.3: The major geological units of the NE Congo Craton (Bomu-Kibalian-North Ugandan Block) and associated Palaeozoic mobile belts. BAG: Bomu Amphibolite Gneiss UCG: Upper Congo Granite Massif WNG: West Nile Gneiss WNB: West Nile Block NUT: North Uganda Terrane NWT: North West Tanzania Terrane RW: Rwenzori Belt; LVT: Lake Victoria Terrane. Compiled from Lavreau, (1984); Kabete et al. (2012a) and Westerhoff et al. (2014).

The Northern Uganda Terrane is dominated by deformed Mesoarchean and Neoproterozoic granodiorites and tonalites occurring with highly deformed gneisses and migmatites (Nyakecho and Hageman, 2014) and has been divided into two major geological units, the Karuma Complex: a north west-south east orientated belt of Mafic to Felsic granulites (Westerhoff et al., 2014) dated to 2991 ± 9 Ma (Mantari et al., 2014); the Amura Group: consisting of deformed supracrustal gneisses and mafic metavolcanics; and a series of granitoids, metagabbros and gneisses of uncertain origin (Westerhoff et al., 2014) which have been dated to a window of 2732 ± 6 Ma to 2611 ± 6 Ma (Mantari et al., 2014).

2.2.3. The Northwest Tanzania Terrane

The North West Tanzania Terrane is the northern most part of the Tanzanian Craton and outcrops principally between Lake Kyoga and Lake Victoria though is thought to extend from South West Uganda on the border of Tanzania to the Kenyan border north of Lake Victoria in the east (Fig. 2.3, 2.4) (Nyakecho and Hageman, 2014). The West Tanzania Terrane is bounded on the south by the Lake Victoria terrane and to the north by the mid-crustal Nakasongalo discontinuity delineating the boundary with the Northern Uganda Terrane (Westerhoff et al., 2014).

The Terrane is dominated by granite-gneisses, migmatites and deformed granitoids (Nyakecho and Hageman, 2014). These units have been divided into four major units, migmatitic TTG gneisses, the Tororo suite; consisting of a series of granitoids and gneissic granites and granodiorites dated to 2644 ± 10 Ma with inherited cores dated between 2.92 and 2.73 Ga (Mantari et al., 2014); the Kampala suite; consisting of variably deformed granitoids and orthogneisses including quartz monzodiorite dated to 2.62 ± 0.2 Ga (Schumann et al., 2004); and the Kiboga suite; consisting of variable porphyritic granites, the Naluvule feldspar porphyry which has been dated at 2.49 Ga (Mantari et al., 2014) and the Lutukuma granite which has been dated at 2.49 Ga (Mantari et al., 2014; Westerhoff et al., 2014).

2.2.4. The Lake Victoria Terrane

The Lake Victoria terrane extends from south east Uganda southward into Tanzania where it dominates the northern part of the country around the shores of Lake Victoria. The Lake Victoria Terrane is composed of three major geological terranes the East Lake Victoria Superterrane, Mwanza-Lake Ayasi Superterrane and the Lake Nyanza Superterrane (Fig. 2.4) (Kabete et al., 2012a).

The East Lake Victoria Superterrane extends from SE Uganda into north east Tanzania and consists of a series of east-west orientated Archean greenstone belt (from north to south), The Busia-Kakamega Terrane, the North Mara Terrane, Mara-Mobrama terrane, Musoma-Kilimafadha terrane and Ukerewe-Maswa-Serengete terrane (Kabete et al., 2012a) with varying levels of cover by the ~ 2.6 Ga siliciclastic sediments

of the Kavidorian Supergroup (Manya, 2002; Westerhoff et al., 2014), Neoproterozoic sediments, Neogene volcanics and lake sediments (Kabete et al., 2012a; Westerhoff et al., 2014). The greenstone terranes are composed of mafic volcanic rocks, calc-alkaline felsic volcanics basalts, metasediments and ironstones metamorphosed to greenschist facies (Manya et al., 2006; Westerhoff et al., 2014) separated by granitoid-gneisses (Kabete et al., 2012a), granites and rare amphibolites (Manya et al., 2006). A progressive increase in age of the greenstone belts, moving north to south, is identified with the Northern most Busia-Kakamega Terrane dated to 2.63-2.59 Ga and the southernmost Musoma-Kilimafadha Terrane dated to 2.72-2.69 Ga (Kabete et al., 2012a, 2012b; Mantarri, 2014; Westerhoff et al., 2014).

The Mwanza-Lake Eyasi Superterrane lies directly south of the Lake Victoria Superterrane and consists of, from northwest to south east, the Mwana-Magu Terrane, Malite-Ngorongoro Terrane and Iaida-Haidan Terrane (Kabete et al., 2012a). The Mwana-Magu and Malite-Ngorongoro Terranes consists of amphibolite to granulite facies metamorphic rocks intruded by abundant synorogenic granitoids and K-Feldspar rich granites with extensional reworking along the eastern edge associated with the East African Orogen (Kabete et al., 2012a).

The Lake Nyanza Superterrane consists of a series of east-west orientated terranes, from northwest to south east, The Sukamaland Terrane, The Kahama-Mwadui Terrane, The Nzega-Sekenke Terrane and Singida-Mayamaya Terrane (Kabete et al., 2012a). The Sukamaland and Nzega-Sekenke Terranes consist of folded and faulted greenstone belts composed of metavolcanics, metasedimentary rocks and BIFS bounded by granitoids and gneisses (Manya and Moboko, 2003; Kabete et al., 2012a). The Kahama-Mwadui Terrane separates the two major greenstone belts and is marked by an absence of greenstone lithologies and is largely covered by Neogene sediments (Kabete et al., 2012a). The Kahama-Mwadui Terrane is composed of a migmatite gneiss series intruded by a series of northwest-southeast trending K-feldspar granitoids thought to have intruded along the suture between continental fragments (Kabete et al., 2012a). The Singida-Mayamaya Terrane is composed of granitoid gneisses and thin amphibolite facies greenstone belts consisting of: amphibolite schists; porphyritic andesites; schistose dolerites and rhyolites (Kabete et al., 2012a). The geochronological characteristics of the Lake Nyanza Superterrane are complex, the Sukamaland and Kahama-Mwadui Terranes show a progressive increase in age from northeast to southwest. The Sukamaland Greenstone Belts are dated to 2.82-2.69 Ga and the Kahama-Mwadui Terrane dated to 3.11 Ga with 2.76-2.65 Ga granitoids (Borg and Krogh, 1999; Manya and Moboko, 2003; Chamberlain and Tosdal, 2007; Kabete et al., 2012b). The Nzega-Sekenke Terrane displays a similar range of ages to the Kahama-Mwadui Terrane with detrital ages between 3.1-2.6 Ga and magmatic ages ranging between 2.75-2.68 Ga (Chamberlain and Tosdal, 2007; Kabete et al., 2012b).

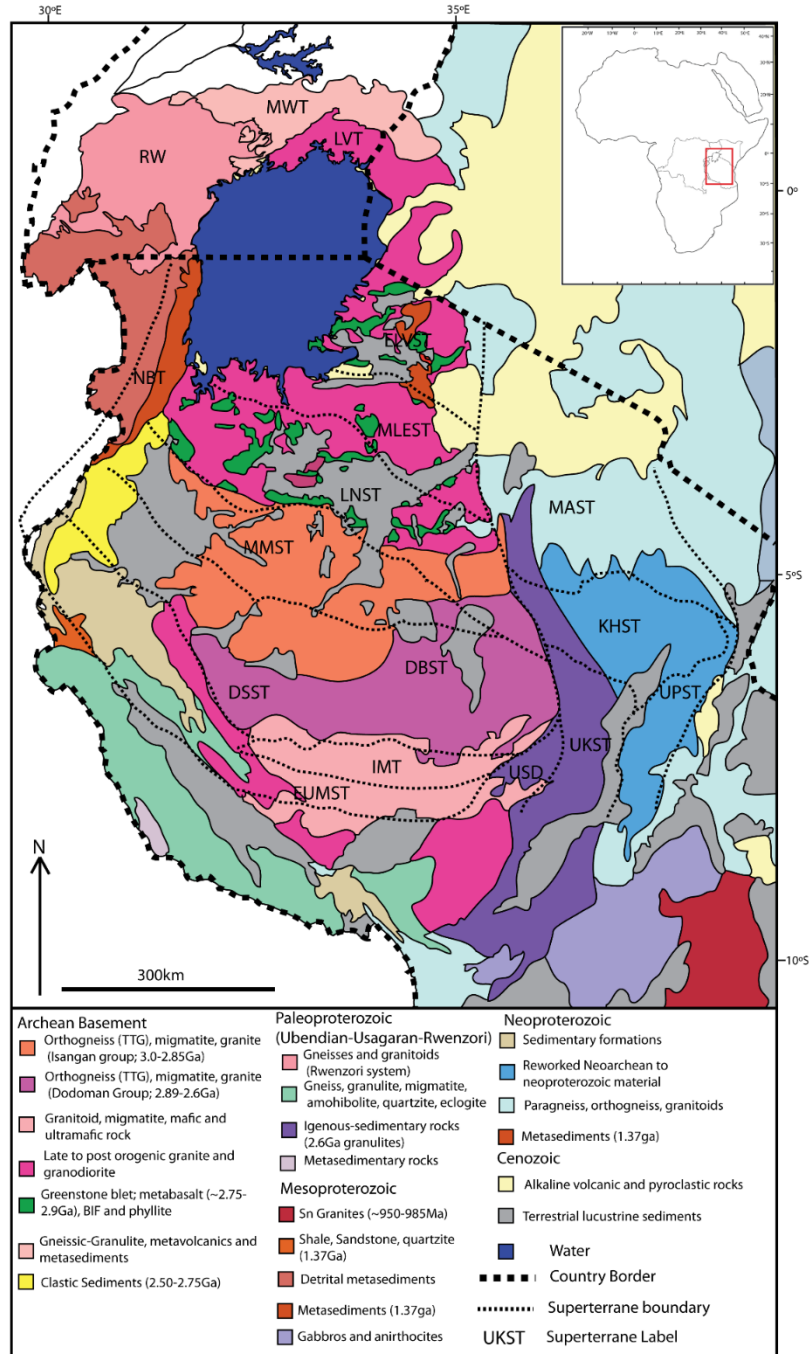


Figure 2.4: Major geological divisions of the Tanzanian Craton and surrounding Proterozoic-recent mobile belts; Tanzanian Craton: Lake Victoria Region: NWT-North West Tanzania Terrane; LVT-Lake Victoria Terrane; ELVST-East Lake Victoria Super Terrane; MLEST-Mwanza-Lake Eyasi Superterrane; LNST-Lake Nyanza Super Terrane; *Central Tanzania Region*: MMST-Moyowosi-Manyoni Superterrane; DSST-Dodoma Schist Superterrane; DBST-Dodoma Basement Superterrane; IMT-Isanga-Mtera Terrane; EUST-Eastern Ubendian-Mtera Superterrane; *Northwest Tanzanian Orogen*: NBT-Nyakahura-Burigi Terrane; *Southern East African Orogen*: USD-Usagaran domain; UKST-Usagara-Ukaguru Terrane; UPST-Uluguru-Pare Terrane; KHST-Kilindi-Hadeni Superterrane; MAST-Mbulu-Masai Superterrane. Compiled from Kabete et al. (2012a, 2012b) and Westerhoff et al. (2014)

The Singida-Mayamaya Terrane is younger than the terranes directly north of it, granitoids adjacent to the minor greenstone belts having been dated to 2.68 Ga (Kabete et al., 2012b)

2.2.5. The Central Tanzania Region

The Central Tanzania region forms a belt of Mesoarchean terranes, constituting the southernmost part of the Tanzanian Craton, and consists of the Moyowosi-Manyoni Superterrane, Dodoma basement/Dodoma schist Superterrane and the East Ubendian-Mtera Superterrane (Fig. 2.4) (Kabete et al., 2012a). The Moyowosi-Monveni Superterrane consists of two principal crustal blocks, the east-west orientated Moyowosi-Uyowa Terrane composed of synorogenic biotite granitoids and orthogneissic migmatites, and the north west-south east orientated Tabora-Manyoni Terrane composed of orthogneissic migmatites and late K-feldspar granitoids (Kabete et al., 2012a). The Dodoma basement Superterrane is composed of the Dodoma Gneissic and Undewa-Ilangali Terranes (Kabete et al., 2012a). The Dodoma Gneissic Terrane is composed of east-west trending schist and gneissic belts confined within granitoid basement rocks consisting of tonalite-trondhjemite-granodiorite (TTG) gneisses and felsic-dioritic intrusives (Kabete et al., 2012a). The Undewa-Ilangali Terrane is more varied consisting of greenschist to amphibolite facies greenstone belts and extensive TTG gneisses, diorites and syn-kinematic K-feldspar granitoids (Kabete et al., 2012a). The Dodoma Schist Superterrane is made up of the Kaliua-Inyonga Terrane and the Malagasya-Rungwa Terrane (Kabete et al., 2012a). The Malagasya-Rungwa Terrane is composed of deformed K-Feldspar granitoids, alkali feldspar granitoids and granodiorite gneisses contains a number of greenstone composed of mafic-amphibolite greenstones and dioritic-gabbroic sills (Kabete et al., 2012a). The Central Tanzania region is the oldest part of the Tanzanian Craton with units of the Undewa-Ilangali Belt having returned detrital ages of 4013-3604 Ma and extensive volcanism recorded in the period 2815-2660 Ma (Kabete et al., 2012b).

2.3 Proterozoic Mobile Belts

The margins of the Archean Cratonic fragments have been extensively reworked by Proterozoic rifting and orogenesis resulting in the formation of Proterozoic mobile belts (Fig. 2.2, 2.3 & 2.4). The Proterozoic Mobile belts of East Africa are attributed to the three major supercontinent forming events, the Eburnean cycle forming the Colombia supercontinent (2.1-1.8Ga), the Grenvillian cycle forming the Rodina supercontinent (1Ga) and the Pan-African cycle during the assembly of Gondwana (Zhao et al., 2004; Westerhoff et al., 2014). The Proterozoic Mobile belts are dominated by reworked Archean Cratons and accretionary lithologies having formed during the collision of the Archean Cratonic fragments (Begg et al., 2009).

The Eburnean terranes form a continuous belt encircling the Tanzanian Craton and consisting of the (from north west moving anticlockwise) Rwenzori, Ruizian, Ubendian and Usagaran belts (Fig. 2.2) and are associated with the suturing of the Tanzania and Congo Cratons (Westerhoff et al., 2014). Of these belts the Rwenzori is the most significant to this study, occurring in South West Uganda overlying lithologies of the Tanzanian Craton and Bomu-Kibalian Block. The Rwenzori Belt consists of basement material overlain by metasediments and metavolcanics of the Buganda Group, both units being intruded by syn and post-kinematic granitoids (Westerhoff et al., 2014). Late kinematic plutonic granitic units intruding the Rwenzori terranes have been dated between 1987-1848 Ma (Nagudi et al., 2001; Westerhoff et al., 2014).

Grenvillian terranes consist of the Kibaran Belt extending from the Kibara Mountains of Eastern Congo to South Western Uganda (Fig. 2.2, 2.3, 2.4). The Grenvillian terranes are composed of folded and metamorphosed terrigenous sedimentary and metasedimentary rocks including sandstones, slates, ironstones, quartzites, mica schists and thrust transported carbonaceous schist, phyllites and clastic-sedimentary rocks overlying Archean basement (Kabete et al., 2012a; Nyakecho and Hagemann, 2014; Westerhoff et al., 2014). These have been intruded by multiple generations of mafic to ultramafic layered intrusions, dyke swarms and syn-kinematic A-type granites (Nyakecho and Hageman, 2014; Makitie et al., 2014; Westerhoff et al., 2014).

Lithologies attributed to Grenvillian orogenesis are also identified obscuring the boundary of the North Uganda Terrane and West Nile Block in the Madi-Igisi Belt (Westerhoff et al., 2014). The Madi-Igisi Belt (Fig. 2.3) is composed of intermediate metavolcanic rocks, quartzites and metapelites, dacitic metatuffs, metasedimentary schists and gneisses, banded ironstones, amphibolites and meta-basalts (Westerhoff et al., 2014). The Kibaran Belt lithologies record metasedimentary detrital ages ranging from 2.07-1.75 Ga and multiple intrusive events at 1.57-1.45 Ga, 1.37 Ga, 1.25 Ga and 0.98 Ga (Buchwaldt et al., 2008; Makitie et al., 2014; Nyakecho and Hageman, 2014; Westerhoff et al., 2014). The Madi-Igisi Belt records a more limited range of age data with detrital ages derived from mafic metatuffs and metasedimentary schists at 984-977 Ma (Mantarri et al., 2014; Westerhoff et al., 2014).

Two major Pan-African orogenic belts are identified in the region, the north-south orientated East African Orogen (Fig. 2.2) formed during the collision of East and West Gondwana and the east-west orientated Oubanguide belt (Fig. 2.2) formed during the collision of the Saharan Craton and Congo Craton. The East African Orogen extends along the eastern margin of the Tanzanian Craton and Congo Craton and consists of thrust transported and reworked Archean basement, ophiolites (consisting fragments of the Neoproterozoic Mozambique ocean), metasediments and syn-collisional magmatic arc granites (Vearncombe et al., 1983; Ries et al., 1992 ; Mantarri et al., 2011; Kabete et al., 2012a; Westerhoff et al., 2014). Ophiolite terranes

attributed to the pre-Pan-African Mozambique Ocean have been dated at 830 Ma and provide an upper limit on the formation of the belt (Vearncombe, 1983). Reworked Archean metasedimentary lithologies have been dated returning metamorphic ages from 737 to 584 Ma and syn-orogenic granitoids are dated to 737-593 Ma (Reis et al., 1992; Mantarri, 2014; Westerhoff et al., 2014). The Oubanguide belt extends east-west across central Africa from Nigeria to South Sudan where it intersects the East African Orogen, between the Congo Craton and Saharan MetaCraton (Begg et al., 2009). The position of the Kibali Granite-Greenstone Belt along the suture between the West Nile Gneiss and the Bomu-Kibalian block makes the Oubanguide orogeny potentially highly significant to this study. The Oubanguide belt consists of thrust sheets composed of 2 Ga gneisses and 1.6 Ga granitoids thrust southwards over the Congo Craton (Begg et al., 2009; Abdelsalam et al., 2011). Syn-orogenic granitoids are identified intruding the thrust sheets of the West Nile Block and have been dated to 659-595 Ma (Begg et al., 2009; Mantarri, 2014; Westerhoff et al., 2014).

2.4 Formation and Evolution of the Geological Terranes of East Africa

The geological history of East Africa is defined and dominated by successive cycles of rifting and orogenesis along the margins of the Archean Cratonic fragments. The two major Archean crustal fragments, the Bomu-Kibalian block/North Uganda Terrane and the Tanzanian Craton, are hypothesised to have formed independently across the Meso to Neoproterozoic. Of the two the Bomu-Kibalian Block/North Uganda Terrane is less understood and is hypothesised by Westerhoff et al. (2014), based on studies of the Ugandan West Nile Block, to have formed prior to 3.08 Ga, before being buried and metamorphosed under granulite to amphibolite facies conditions in the period 3.00 to 2.86 Ga (Westerhoff et al., 2014). This period of metamorphism is followed by the emplacement at 2.63 Ga of the mafic and sedimentary lithologies thought to derive from oceanic basins, island arcs and accretionary wedges (belonging to the war group, see above) which overthrust the basement and are thought to mark a period of island arc accretion (Westerhoff et al., 2014).

Available evidence indicates the Tanzanian Craton is the older of the two major Archean units with detrital zircon ages ranging from 4.0-3.2 Ga in the Dodoma basement and between 3.6-3.2 Ga in the West Tanzania Terrane indicating its formation across the Mesoarchean (Schumann et al., 2004; Kabete et al., 2014a). Multiple models have been proposed for the subsequent evolution of the Tanzania Craton during the Archean with the two phase model of Pinna et al. (2004) being the dominant model at the time of writing. Pinna et al. (2004) defined two major Archean orogenic events; The Dodoman orogeny (2.93-2.85 Ga) characterised by subduction, slab melting and TTG accumulation in the southwest of the Craton with coeval oceanic and back arc crust formation along the northern margin of the Craton; and the Victorian orogeny (2.8-2.6 Ga) consisting of three sequential accretionary tectonic events related to the formation of greenstone

belts in the Lake Victoria Superterrane (Pinna et al., 2004) and the West Tanzania Terrane (Westerhoff et al., 2014). This two phase model for the Archean evolution of the Tanzania Craton has been further supported by subsequent studies including the work of Kabete et al. (2012a), Westerhoff et al. (2014) and Sanislav et al. (2014), who defined the peak of crustal growth during the Victorian orogeny at 2.7 Ga (Sanislav et al., 2014). The collision and suturing of the Archean Cratonic fragments into a single mass, the Proto-Congo Craton (Tack et al., 2010), is hypothesised by Westerhoff et al., (2014) to have occurred in two phases; the collision and suturing of the Bomu-Kibalian Block with the West Tanzania Terrane between 2.64-2.61 Ga (Ruotoistenmaki, 2014; Westerhoff et al., 2014), and the collision and suturing of these units to the northern margin of the Tanzanian Craton at 2.59-2.55 Ga. (Westerhoff et al., 2014).

The subsequent evolution of the Bomu-Kibalian-Tanzanian Cratonic mass is dominated by successive cycles of rifting and orogenesis. Rifting of the proto Congo Craton occurred in the period 2.15-2.0 Ga with two distinct rifts forming, a north-south orientated ocean basin extending along the western margin of the Tanzanian Craton (lithologies of the Usagaran-Ubendian fold belt) and an approximately east-west basin generated through the reactivation of the suture between the Tanzanian and Congo Cratons (lithologies of the Rwenzori fold belt) (Westerhoff et al., 2014). Closure and inversion of these basins occurred in the period 2.0-1.9 Ga during the Eburnean Orogen (Zhao et al., 2004) and formation of the Colombia supercontinent with orogenesis ending approximately 1.85 Ga with the intrusion of post kinematic granitoids (Westerhoff et al., 2014).

Fragmentation and rifting of the Colombian supercontinent began during the period 1.85-1.75 Ga resulting in the dispersal of the Archean Cratons (Pedreira and deWaele, 2008)). During this time the Congo Craton remained stable experiencing only intra-cratonic rifting and magmatism (Tack et al., 2010). This rifting resulted in the formation of the intra-cratonic Kibaran trough during the period 1.55-1.20 Ga, coinciding spatially with the north-south orientated Eburnean suture zone extending along the western margin of the Tanzanian Craton and rifting between Bomu-Kibalian Block and the North Uganda Terrane (Tack et al., 2010).

During the Grenvillian orogenic cycle, culminating in the assembly of the Rodinia super-continent and orogenesis along the eastern margin of the Congo Craton (Fig. 2.5). Inversion of the intra-cratonic Kibaran trough formed the Kibaran belt, a southwest-northeast orientated belt extending from South East DRC to Uganda (Fig. 2.5), obscuring the Eburnean suture zone (Westerhoff et al., 2014), and the north-south orientated Madi-Igisi belt which thrust westwards over the margin of the Bomu-Kibalian block (Fig. 2.5) (Westerhoff et al., 2014). This orogenic event also resulted in the reactivation of shear structures within the Eburnean Rwenzori fold belt and the Bomu-Kibalian block (Lavreau, 1984; Westerhoff et al., 2014).

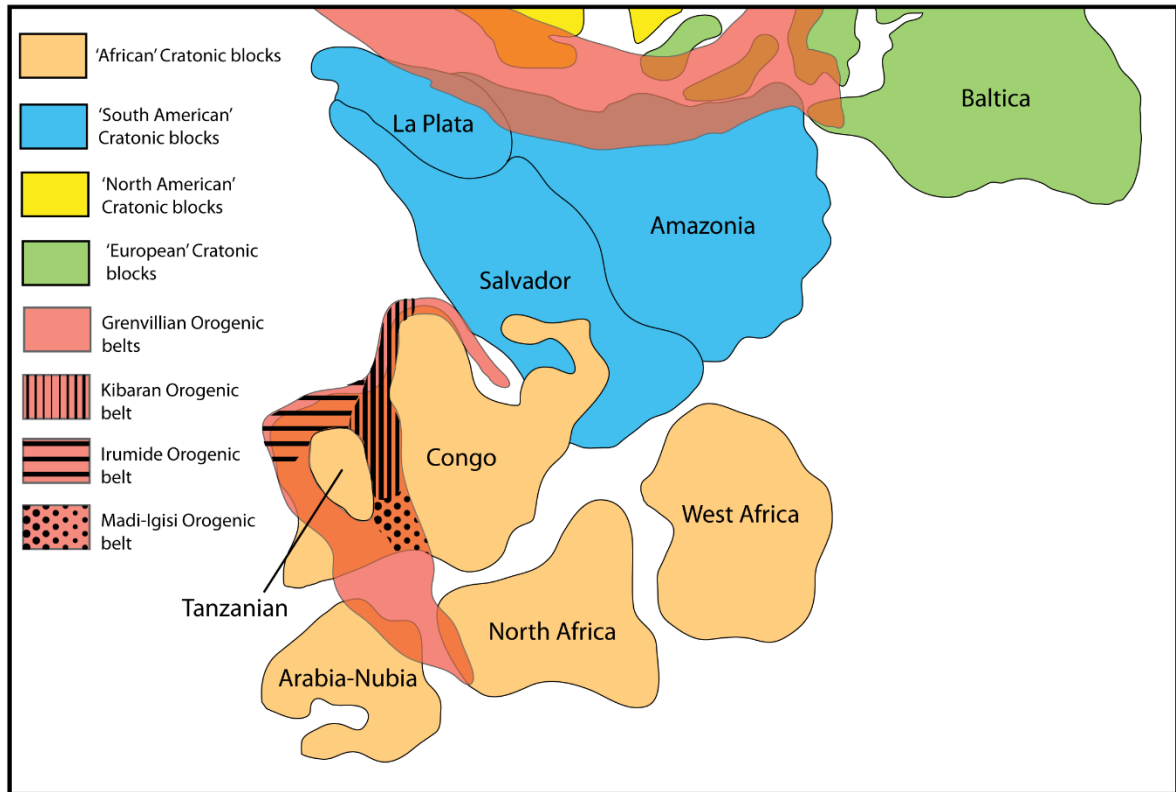


Figure 2.5: Reconstruction of the African section of the Rodinia Supercontinent displaying the location of the Grenvillian orogenic belts (Modified after Li et al. (1995))

The period 850-750 Ma is characterised globally by the rifting and dispersion of the Rodinia supercontinent, during this time the Congo Craton remained intact and experienced no significant intra-cratonic rifting (Tack et al., 2010).

During the Pan-African orogenic cycle and assembly of Gondwana the Congo Craton occupied a central position (Fig. 2.6). The other continental masses assembled around the outer edges of the Congo Craton which is therefore encircled by orogenic belts of Pan-African age (Begg et al., 2009; Westerhoff et al., 2014). The Pan-African orogenic belts are attributed to, in the case of the East African Orogen, the collision between East and West Gondwana (Begg et al., 2009; Westerhoff et al., 2014), and in the case of the Oubanguides, the collision of the northern margin of the Congo Craton and the Saharan Meta-Craton (Fig. 2.6) (Abdelsalam et al., 2011).

The East African Orogen occurs down the eastern edge of the Tanzanian Craton (Fig. 2.6) and is interpreted as having polycyclic development across the period 830 Ma to 470 Ma (Westerhoff et al., 2014).

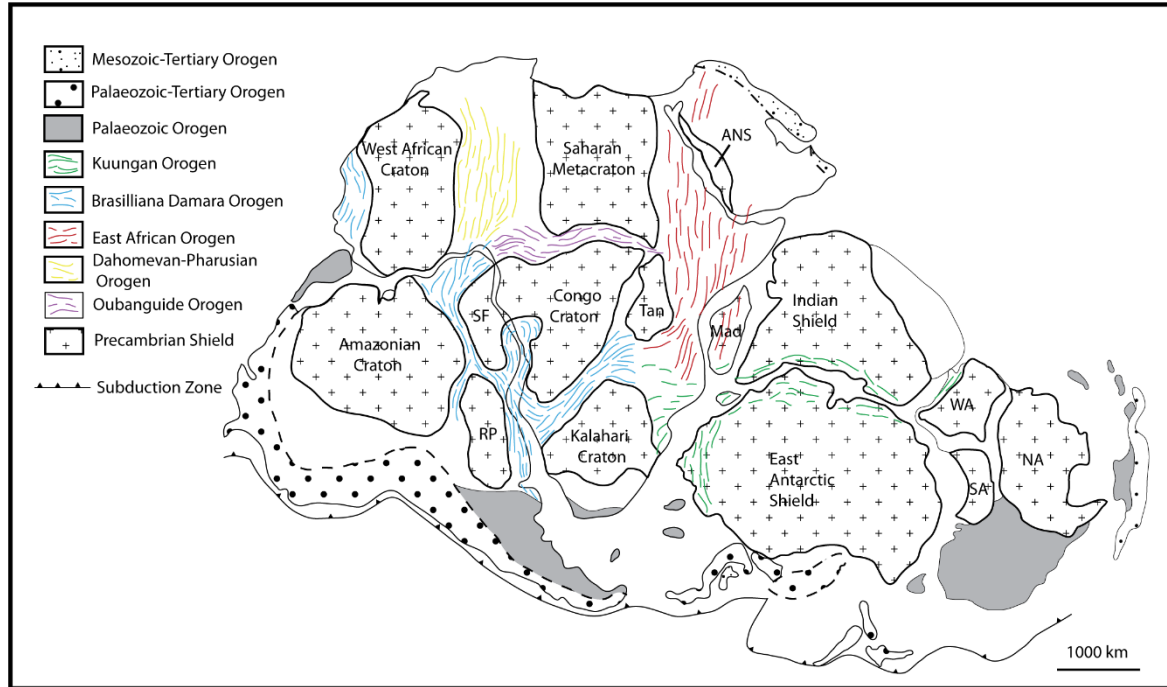


Figure 2.6: Reconstruction of the Gondwana supercontinent. The Congo/Tanzanian Cratons occupy a central position and is encircled by the Pan-African orogenic belts (Modified after Gray et al. (2008)).

Four distinct phases of development have been identified in the East African Orogen; the Samburuan-Sabachian between 830-800 Ma, The Baragoian-Barsaloian event between 630-570 Ma, and the Loldakian and Kipsangian events occurred in the period 580-470 Ma (Westerhoff et al., 2014).

The Oubanguide orogenic event occurred due to the collision of the Saharan Metacraton and north margin of the Congo Craton forming an east-west orientated belt extending along the length of the northern margin of the Congo Craton (Fig. 2.6) (Abdelsalam et al., 2002; Begg et al., 2009). Westerhoff et al. (2014) correlated this event with the emplacement of the 0.69 Ga Granites and 0.66 Ga granodiorites in northern Uganda. The final docking of the Saharan Metacraton and the Congo/Tanzania Cratons is hypothesised to have occurred in the period 501 to 490 Ma (Abdelsalam et al., 2002; Pin and Poivedin, 1987; Westerhoff, et al., 2014). Evidence for a Craton wide tectonothermal event associated with the development of the Pan-African orogenic belts is characterised by lead loss within zircon data (Kabete, 2012a; Mantarri, 2014; Westerhoff et al., 2014). This is identified within the West Tanzania terrane at 0.8-0.79 Ga and within the Lake Victoria terrane at 0.68-0.6 Ga and is attributed to the development of the East Africa Orogen (Kabete, 2012a; Westerhoff et al., 2014), and at 0.69 Ga in the West Nile block and between 0.8 Ga and 0.6 Ga within the North Uganda terrane that has been attributed to the development of the Oubanguide orogeny (Mantarri, 2014).

2.5 Gold Deposits of Central and East Africa

The Neoproterozoic terranes of north east Democratic Republic of Congo, Tanzania and Uganda are host to a number of auriferous greenstone belts while the Proterozoic mobile belts around the edges of the Cratonic masses are host to a small number of orogenic gold deposits. This section aims to examine the characteristics of the major gold-bearing terranes and to briefly examine the characteristics of the gold deposits they contain.

2.5.1. Gold Endowment in the Northeast Congo (Bomu-Kibalian Block)

The Bomu-Kibalian Block is one of the most poorly studied Archean terranes in the world with few academic or industry studies conducted. As such the existing information regarding the gold endowment of the Bomu-Kibalian Block is limited but with the discovery of the massive Kibali gold deposit it is potentially one of the most prospective gold terranes in the world.

Gold mineralisation is strongly associated with a series of greenstone belts (Fig. 2.1, 2.7) which are divided into two groups; the Ganguan and the Kibalian (Lavreau, 1984). The Ganguan Greenstone Belts lie at the western edge of the Bomu-Kibalian block within the Bomu gneissic series (Lavreau, 1984) and include the Matunda and Bili belts which are composed of metamorphosed quartzites, slates, talcschists and diabases on a folded gneissic basement, gold having been extracted from talc schist units (Lavreau, 1984). The Kibalian greenstone belts, including the Kibali (formerly Moto), Kilo, Isiro, Tina, Mambaso, Ngayu, Panga and Tele belts, are a more significant source of gold having produced significant amounts of gold from both placer and lode deposits (Lavreau, 1984). Of these belts the Kibali and Kilo are most significant being the site of the two most established mining operations, the Kilo mines and the giant Kibali gold mines with which this project is principally concerned. The Kibali Granite-Greenstone Belt hosts the most significant gold resources within the Bomu-Kibalian Block, including the Karagba-Chaffeur-Durba deposit (17 Moz Au), Mengu (1.5 Moz Au), Pakaka (1 Moz Au) and Pamao (0.5 Moz Au). Mineralisation within the Kibali Granite-Greenstone Belt has been historically described variably as impregnated, disseminated and stratabound deposits (Lavreau, 1984). These deposits are characterised by a proximity to 'itabirite horizons' and hosted within a volcano sedimentary series with the more mafic deposits containing extensive pillow lava basalts (Lavreau, 1984). All deposits are described as being altered to sericite-chlorite-ankerite schist, lacking gold hosted within quartz veins and notable for the volume and high grade of the ore (Lavreau, 1984). The three most historically important deposits within the Kibali Granite-Greenstone Belt are the Durba (part of the current Karagba-Chaffeur-Durba project), Gorumbwa and Agborabo ore bodies.

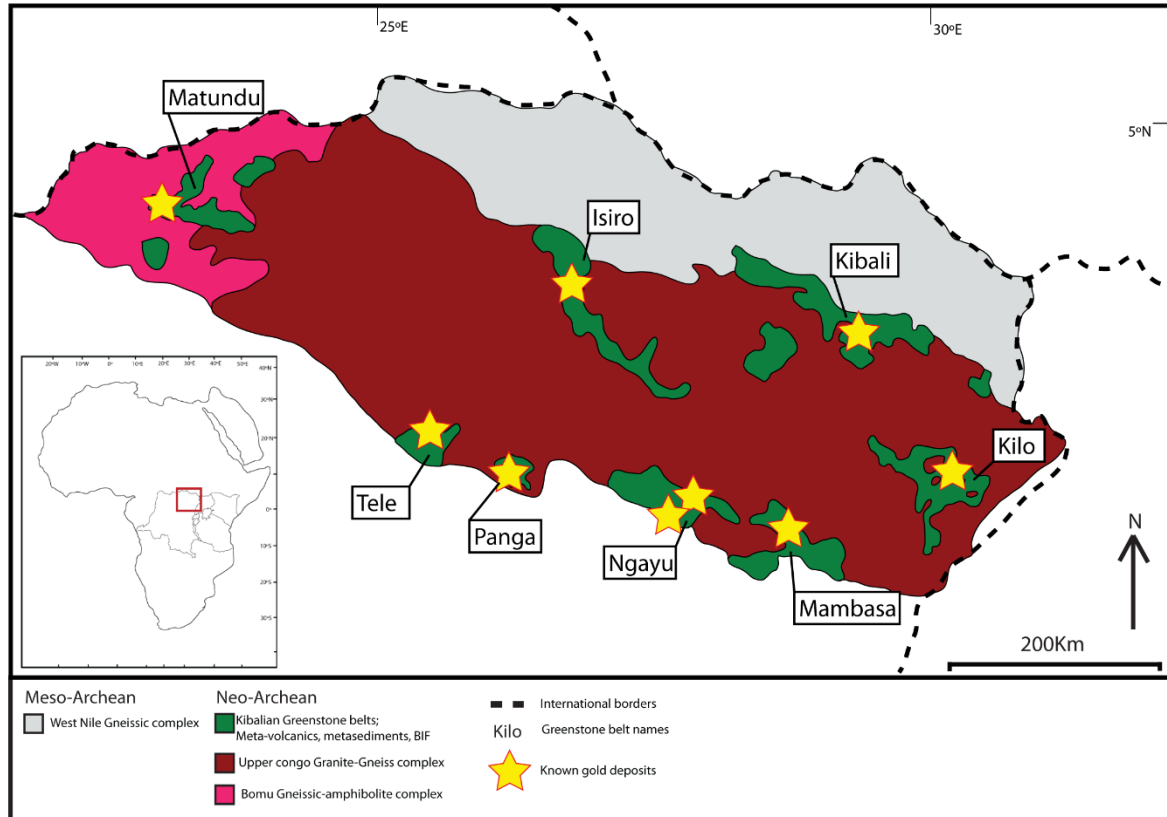


Figure 2.7: Geological map of the Bomu-Kibalian block displaying the location of gold bearing Neoproterozoic Granite-Greenstone Belts and the location of known major gold deposits (Modified after Lavreau (1984))

These three deposits are described as north-northeast dipping tabular and cylindrical lodes controlled by the ‘main foliation’ within the greenstones host (Lavreau, 1984). Similar examples of stratabound mineralisation have been identified in the Ngayu Greenstone Belt with limited extraction having taken place at the Yindi, Adumbi and Angukuluku deposits (Lavreau, 1984). The controls on mineralisation within the North East DRC are poorly understood with only limited opportunities for research over the last few decades. Lavreau (1984) suggested a link between mineralisation and a series of northeast-southwest orientated shear structures that bisect the greenstone belts and surrounding Bomu and West Nile units (Lavreau, 1984).

While the majority of gold produced in the North East of the DRC has come from the lode and vein deposits present within the Kibali and Kilo Greenstone Belts, numerous ‘placer’ style deposits have produced significant amounts of gold from the other greenstone belts and historically within the Kibali and Kilo Greenstone Belts as well. Placers are associated with the sediment cover overlying the main mineralised lodes and fluvial transported sediments geographically associated with the main deposits (Lavreau, 1984). These placer deposits represent reworking of Au bearing regolith with the source lode frequently identified several km upstream (Lavreau, 1984).

2.5.2. Gold endowment in Tanzania

2.5.2.1 The Lake Victoria region

The Lake Victoria region is host to all the major Tanzanian gold deposits (Fig. 2.8) and is typified by greenschist to lower amphibolite greenstone belts (Kabete et al., 2012b). The most significant district is the Geita Greenstone Belt which is host to 10 separate gold deposits including the Sanza-Geita, Nyamulilima-Samena and Kukuluma-Matandani camps all containing approximately 900 t Au (Kabete et al., 2012b) and, most significantly, the world class Nyankanga deposit (6.3 Moz at 5.42 g/t (open pit) and 1.2 Moz at 8.12 g/t (underground)) (Sanislav et al., 2014a). The Geita Greenstone Belt consists of an east-west trending greenstone belt bounded by west northwest-east southeast trending 2660-2620 Ma granite and granitoid-gneisses to the north and south (Kabete et al., 2012a; Sanislav et al., 2014a).

The Geita Greenstone Belt is composed of mafic metavolcanics (of interpreted MORB-like affinity (Sanislav et al., 2014a)), banded ironstones, turbiditic metasediments and volcanoclastics intruded by volumetrically dominant diorite dykes/sills and granitoids (Sanislav et al., 2014a). The Geita Greenstone Belt is cut by northwest-southeast orientated shear zones and east northeast-west southwest thrust faults which are associated with the mineralised lodes (Kabete et al., 2012b).

The world class Nyankanga gold deposit is hosted within the Geita Greenstone Belt, in a sequence of magnetite rich sediments consisting of interbedded sandstone-siltstones intercalated with chert and conglomeratic sandstones overlain by turbiditic sediments (Sanislav et al., 2014b). The sedimentary sequence has been intruded by multiple generations of diorite, lamprophyre and quartz-feldspar porphyry with the entire sequence being metamorphosed to greenschist facies (Sanislav et al., 2014b). The deposit is bisected by the Nyankanga Shear zone and the host lithologies have been extensively deformed with eight generations of deformation having been identified (Sanislav et al., 2014b). Three distinct alteration zones have been identified, a distal zone characterised by a chlorite-epidote-calcite±actinolite-pyrite±pyrite assemblage, a transitional zone characterised by a biotite-chlorite-calcite±pyrite assemblage and a proximal zone characterised by a quartz-calcite-dolomite/ankerite-hematite-pyrite-biotite assemblage (Sanislav et al., 2014b). Gold mineralisation is identified within late calcite-quartz-biotite-chlorite±pyrite veins in the proximal alteration zone and are associated with D3 fold hinges (Sanislav et al., 2014b). Mineralisation is hypothesised by Sanislav et al. (2014b) to have formed through the ascent of deep sourced fluids along the Nyankanga shear zone with the iron rich lithologies acting as a chemical trap triggering gold deposition (Sanislav et al., 2014b). The timing of mineralisation is still debated with recent work (Sanislav et al., 2014b) suggesting mineralisation formed during multiple reactivations of the Nyankanga shear zone.

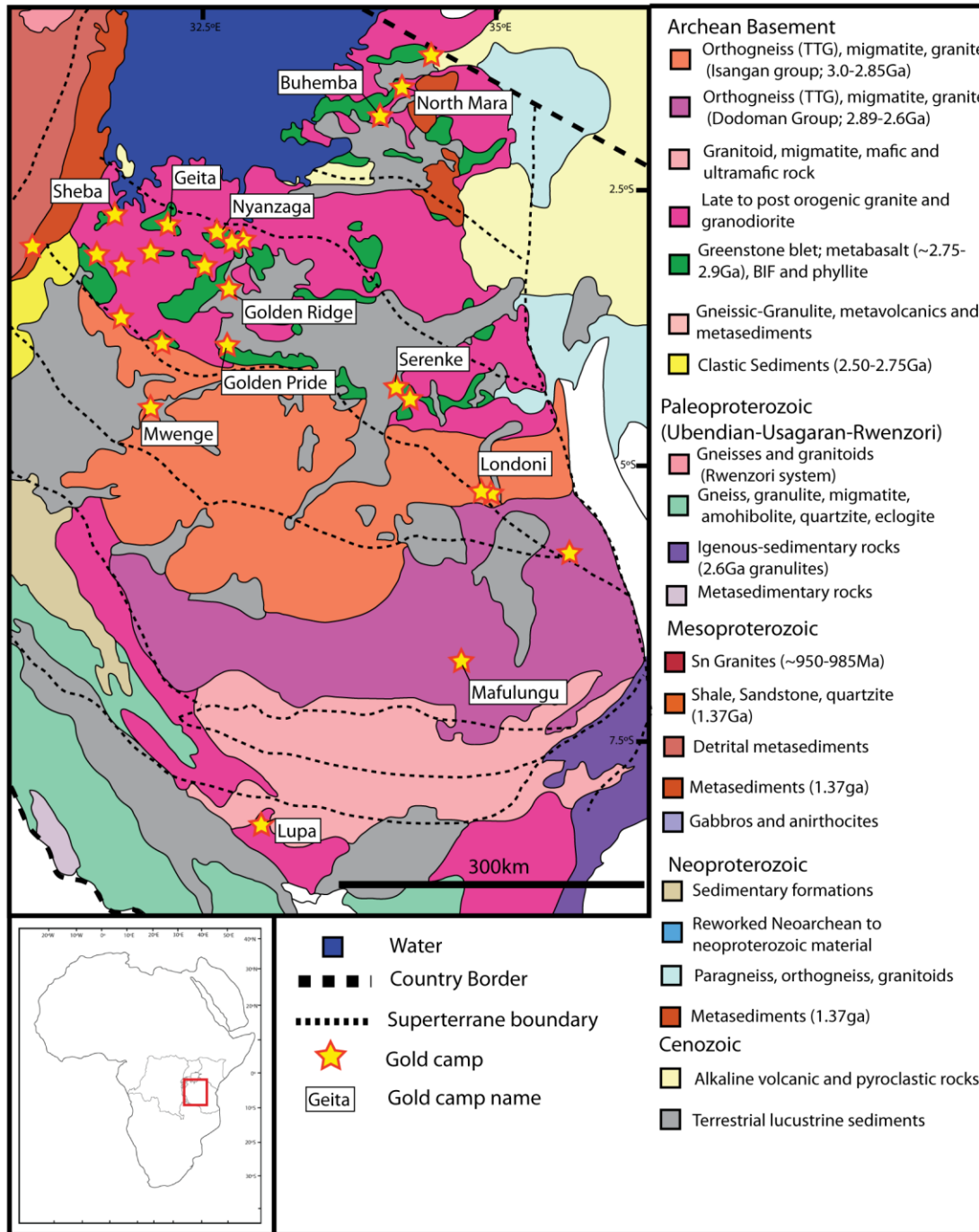


Figure 2.8: Geological map of part of Tanzania Craton displaying the location of the significant gold camps (Modified after Kabete (2012a, 2012b)).

2.5.2.2. The Central Tanzania region

The Central Tanzania region is host to small hypozonal gold systems hosted within high grade metamorphic rocks such as Moyowosi-Manyoni Goldfields, Madengi Hills and Dodoma Schist Goldfields in addition to the mesozonal Mazoka gold system hosted within an uplifted juvenile granite-greenstone terrane (Fig. 2.8) (Kabete et al., 2012a).

Gold within the Moyowosi-Manyoni Goldfield is typified by the Mwenge deposit, hosted within foliated amphibolite-biotite granite gneiss cut by multiple east northeast-west southwest orientated shear zones associated with intense potassic, silica and pyrite alteration (Kabete et al., 2012a). Gold mineralisation occurs within multiple sub metre thick laminated quartz veins within the east northeast-west southwest shear zones. The most significant deposit within the Central Tanzania region is the Mazoka prospect within the Dodoma schist goldfield. Mineralisation is hosted within an east-west orientated Neoproterozoic granite-greenstone belt, composed of shear foliated dolerites, basaltic andesite volcano-sedimentary rocks and BIF units with multiple zones of mylonite and protomylonite, bounded by Mesoarchean TTG and granitoid gneiss units, separated by east-west trending crustal scale bounding structures (Kabete et al., 2012b).

2.5.3 Gold endowment in Uganda

Four gold districts have been identified within Uganda (Fig. 2.9), The Busia gold district, The Mubende gold district, The Buweju-Mashonga gold district and the Karamoja gold district with several other regions of alluvial gold including the West Nile Belt (Nyakecho and Hageman, 2014). These regions and the features of notable gold deposits within each are reviewed below.

2.5.3.1. Busia gold district

The Busia gold district lies within the Neoproterozoic Busia-Kakamega Greenstone Belt, the northernmost belt of the Nyanzian-Kaviriondo Supergroup, in the South East corner of Uganda (Nyakecho and Hageman, 2014). Within the Busia gold district the Nyanzian Supergroup has been metamorphosed to greenschist facies with regional development of chlorite and biotite though locally banded iron formations and basalt have been metamorphosed to epidote rich amphibolite facies (Nyakecho and Hageman, 2014). Rocks within the greenstone belt have been extensively folded, with regional fold axis orientated north east, with major north east-south west orientated faults often showing late reactivation (Nyakecho and Hageman, 2014). Gold mineralisation occurs as both vein hosted and alluvial deposits. Quartz gold veins are hosted within carbonate altered mafic volcanics occurring within structurally controlled shear zones (Nyakecho and Hageman, 2014). The Tira mine is the principal mine within the Busia gold district and the only underground operation active in Uganda (Nyakecho and Hageman, 2014). The Tira mine is hosted by

metasediments (shales, phyllite, sandstone and quartzite), metabasalts and metadolerites intruded by multigenerational K feldspar rich granites (Nyakecho and Hageman, 2014). North-south trending sub-vertical ductile shear zones host gold mineralisation within fault parallel veins up to 2 m in thickness referred to as reefs (Nyakecho and Hageman, 2014).

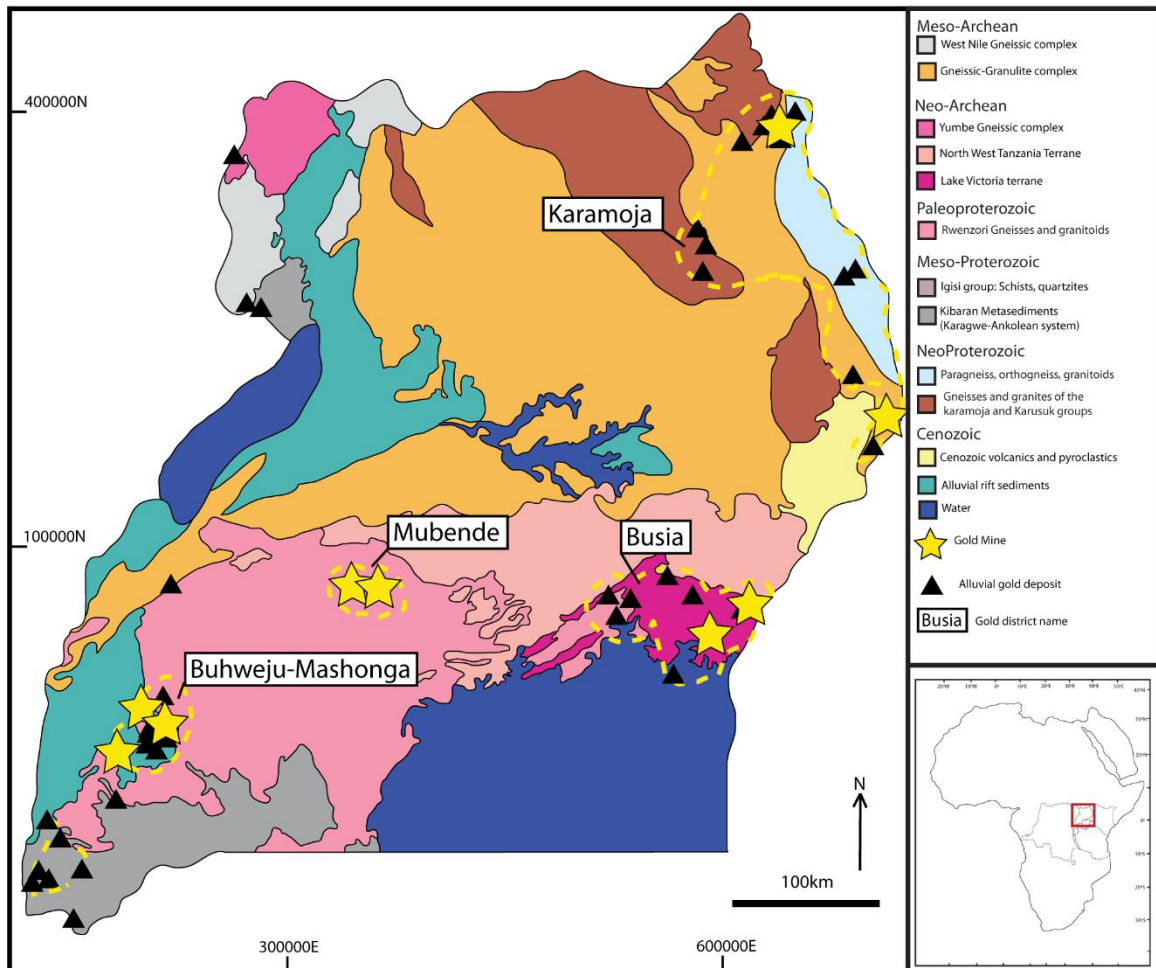


Figure 2.9: Geological map of Uganda displaying the location of the known gold deposits and gold districts within Uganda (Modified after Nyakecho and Hagemann (2014)).

2.5.3.2. Mubende gold district

The Mubende gold district sits within the Buganda meta-volcano-sedimentary unit in the Palaeozoic Rwenzori belt and within the Paleoproterozoic post Rwenzori sediment platform in central Uganda (Nyakecho and Hageman, 2014). The Mubende district is structurally complex with west north west-east south east trending fault zones crosscut by northeast-southwest trending faults and late north northeast-south southwest trending faults (Nyakecho and Hageman, 2014). Known gold mineralisation within the Mubende gold district is focused around the Kamalenge and Kisita mines (Nyakecho and Hageman, 2014). The Kista and Kamalenge mines are hosted within interbedded metasandstones with mineralisation controlled by a ductile shear zones striking northwest-southeast and dipping southwest with mineralisation hosted within quartz-hematite-albite veins and in heavily altered surrounding wall rock (Nyakecho and Hageman, 2014).

2.5.3.3. Buweju-Mashonga gold district

The Buweju-Mashonga gold district sits within the Palaeozoic Rwenzori fold belt and post Rwenzori Buganda group in South West Uganda (Nyakecho and Hageman, 2014). Within the Buhweju-Mashonga district the Rwenzori fold belt and Buganda group have been extensively folded and faulted, with two major fault sets being identified, major north east-south west orientated vertical faults and late northwest-southeast orientated sub-vertical faults (Nyakecho and Hageman, 2014). Multiple gold occurrences are recorded and currently being worked within the Buhweju-Mashonga district including the Mashonga Mine, Kitaka mine, Buckley's reef and Anderson's reef (Nyakecho and Hageman, 2014). The Mashonga mine is located in the South West of the district with gold occurring in situ in the central reef and as alluvial gold (Nyakecho and Hageman, 2014). The mineralised gold reef cuts across muscovite schist and kaolinised granite which have been locally mylonitised with veins controlled by east northeast-west southwest sub-vertical shear zone (Nyakecho and Hageman, 2014). The Kitaka mine is located in the North West of the district. Mineralisation is hosted within a northeast-southwest orientated brittle-ductile shear zone that cuts meta-granodiorite and meta-dolerite (Nyakecho and Hageman, 2014). Mineralisation within the shear zone occurs as a network of cross cutting quartz-carbonate-galena±chalcocite±pyrrhotite±gold veins (Nyakecho and Hageman, 2014).

2.5.3.4. Karamoja gold district

The Karamoja gold district sits within the Karamoja and Karasuk groups, consisting of imbricated thrust slices composed of sedimentary biotite gneiss, granite gneiss and quartzites defined by north-south orientated thrusts (Nyakecho and Hageman, 2014). Rocks within the Karamoja gold district display a sub-vertical north-south orientated variably dipping foliation interpreted as evidence of north-northwest plunging

isoclinal folding and are cut by northeast-southwest orientated fault structures (Nyakecho and Hageman, 2014). Gold mineralisation is reported within metasedimentary lithologies, occurring as quartz lenses within north-south trending shear zones (Nyakecho and Hageman, 2014). A notable deposit is the Lopedo gold mine located in the North East of the district, gold mineralisation occurring as quartz veins and disseminates within wall rock associated with north-south orientated shear zones cutting Neoproterozoic granite gneisses (Nyakecho and Hageman, 2014).

2.6 Summary

The geological history of East Africa has been dominated by successive cycles of rifting and orogenesis which have shaped its geological characteristics and evolution. The Proto-Congo Craton coalesced during the Meso-Neoproterozoic through a series of accretionary orogenic events. These events formed a cratonic block composed of thin granite-greenstone belts surrounded by granite-gneiss massifs that today make up the Tanzanian Craton and Bomu-Kibalian Block. This process of terrane accretion and cratonisation was completed by the end of the Neoproterozoic with the subsequent 2.5 Ga being characterised by cycles of rifting and orogenesis both intracratonic and along the cratonic margins. Three major orogenic cycles are identified in the lithologies of East Africa with the Colombian, Rodinian and Gondwanan orogenic cycles having had a major impact on the geological characteristics of East Africa. These orogenic cycles saw the formation of new lithological units and the deformation and modification of the cratonic blocks resulting in the complex geological history that is identified today.

Gold mineralisation is identified across East Africa with world class gold deposits being identified in the North East Democratic Republic of the Congo (Bomu-Kibalian Block) and Tanzania (Tanzanian Craton) while multiple small deposits have been identified and worked in both countries in addition to deposits in Uganda and Kenya. Though geological terranes of multiple type and age are host to gold mineralisation the Neoproterozoic granite-greenstone belts across the Bomu-Kibalian Block (Kibalian Granite-Greenstone Belts) and Tanzanian Craton (Geita Greenstone Belt) are the most notable host terranes. Neoproterozoic granite-greenstone belts are a significant host of orogenic gold deposits across the world, these terranes possessing favourable structural, chemical and lithological characteristics in addition to enhanced preservation potential (Chapter 3) that makes them ideal terranes to host significant gold resources. The major deposits of East Africa, such as the Karagba-Chaffeur-Durba and Nyankanga deposits, display similar geological characteristics including an association with iron rich sediments and similar metallogenic and mineralogical distributions. These characteristics are however distinctive of the orogenic gold, arising from the fundamental mechanisms by which these deposit types form (Chapter 3), rather than being characteristic of East African gold deposits.

Chapter 3. The Formation of Orogenic Gold Deposits

Long lived orogenic systems and terranes are host to a wide range of mineral deposit types and constitute some of the most mineralogically diverse and economically significant terranes in the world (Bierlein et al., 2010; Groves et al., 2003). The accretion of crustal elements, including allochthonous crustal fragments, oceanic plateaus, juvenile arc material and ophiolite sequences, results in multiple large first order structures along the terrane boundaries and the injection of juvenile material into the margin, providing the ideal conditions for the formation of ore mineralisation (Bierlein et al., 2010). In these long-lived accretionary terranes, the evolving geological system progresses from constructional stage to orogenic stage to post orogenic phase (Fig. 3.1), with the evolving geological conditions facilitating the formation of different mineralising systems (Bierlein et al., 2010). Orogenic gold systems develop during the late stages of terrane accretion (Fig. 3.1) as a result of high thermal flux and fluid generation during stabilisation and ‘cratonisation’ of accreted terranes (Bierlein et al., 2010).

3.1 Orogenic gold deposits

‘Orogenic gold’ deposits constitute a distinct class of mineral deposit that occur across ~3 Ga of Earth’s history (Goldfarb et al., 2001). These deposits are characterised and grouped together on the basis of a number of common geological characteristics, including deformed and metamorphosed host lithologies (typically greenschist facies), carbonate-sulfide±sericite±chlorite alteration, low salinity CO₂-rich fluids, quartz/carbonate gangue material and a geotectonic and spatial association with large scale compressional to transpressional structures developed at historic convergent tectonic margins (Groves et al., 1992, 2003, 2005; Goldfarb et al., 2001). Individual deposits, however, display significant variations in host lithologies and formation temperatures and pressures which vary from upper-mid crustal conditions (200 °C-650 °C and 1-5 Kbar) (Groves et al., 1992, 2003, 2005; Goldfarb et al., 2001). Orogenic gold deposits are one of the most important producers of gold, accounting for 32% of all historical gold production (Frimmel, 2008). The crustal continuum model (Groves et al., 1992, 2003, 2005; Goldfarb et al., 2001) has long been the preferred model development of these deposits. In this model, orogenic gold deposits are formed during convergent plate tectonics throughout a 25 km crustal interval and in lithologies ranging from prehnite-pumpellyite to granulite facies with mineralisation occurring syn-peak metamorphism (Groves et al., 1992). Improved understanding of the characteristics and mechanisms involved in the formation of orogenic gold systems have led to the continuum model being challenged and significant developments have been

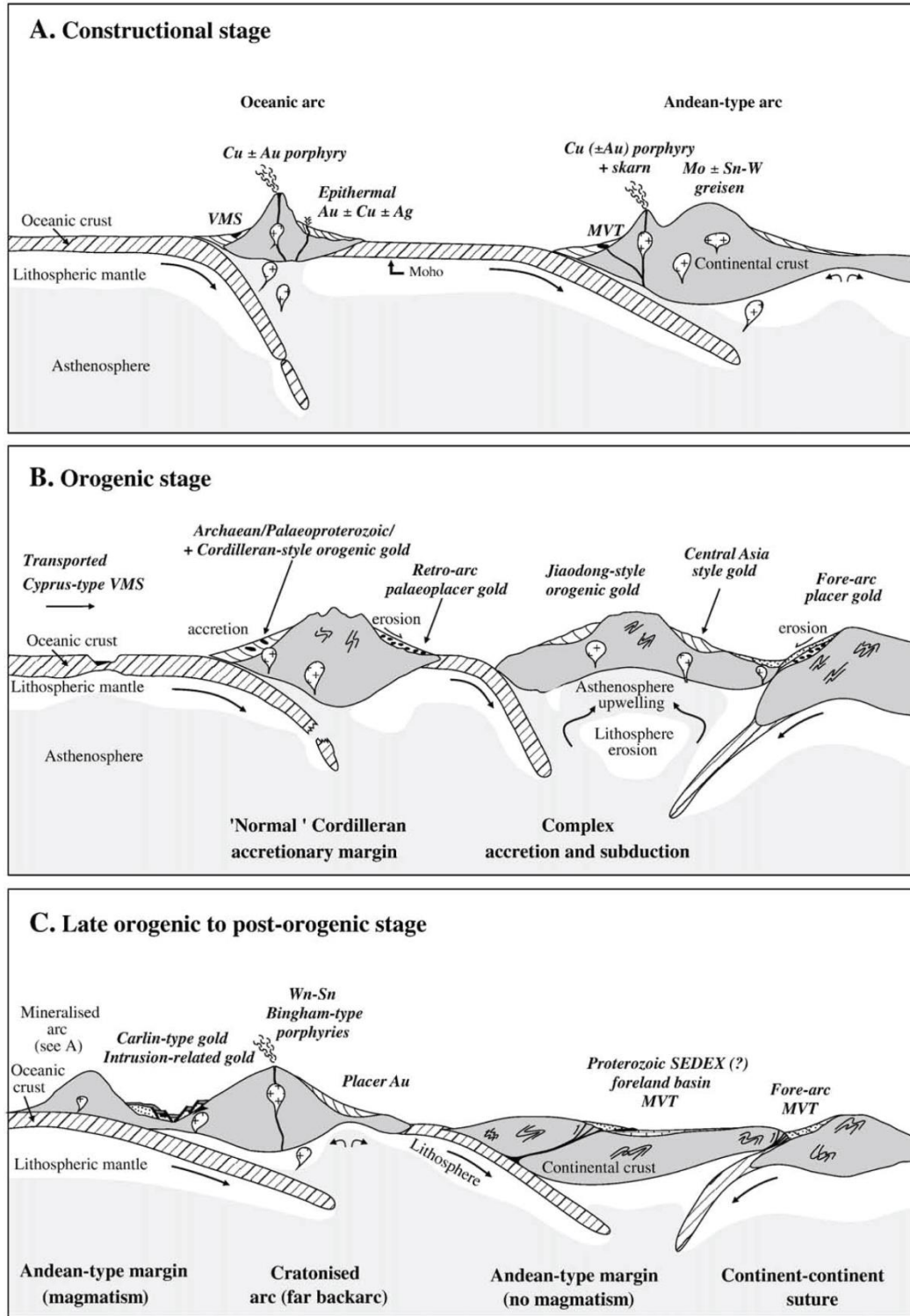


Figure 3.1: Schematic showing the deposit types formed during the different phases of accretionary constructional settings. Orogenic gold deposits are hypothesized to form during the orogenic stage (Panel B) during terrane accretion (Bierlein et al., 2010)

made, with a metamorphic devolatilization model now being favoured. The characteristics of orogenic gold deposits and the current theories and debate regarding their formation are discussed here.

3.1.1 Geological and Temporal Distribution of Orogenic Gold

Orogenic gold deposits are identified within orogenic terranes throughout Phanerozoic and Proterozoic mobile belts and Archean cratonic blocks across the world (Goldfarb et al., 2001). Three distinct periods of gold formation are identified within the geological record at 2.8-2.5 Ga, 2.1-1.8 Ga and 0.57 Ga to recent (Goldfarb et al., 2001).

The distribution of orogenic gold is linked to the global supercontinent cycle (Fig. 3.2), the distribution of gold deposits paralleling the development of juvenile continental crust (Condie, 1998; Condie and Aster, 2010; Groves et al., 2005; Cawood et al., 2013). It is estimated that approximately 75% of juvenile continental crust developed during two 'supercontinent' formation events at 3.0-2.5 Ga and 2.15-1.65 Ga (Condie, 1998). This corresponds with established Archean and Paleoproterozoic orogenic gold forming events, while the incidence of orogenic gold from the Phanerozoic coincides with the assembly of the Gondwana and Pangea supercontinents and terrane accretion in modern times (Goldfarb et al., 2001). A major exception to this distribution is the lack of orogenic gold deposits associated with the formation of the Rodinia supercontinent between 1.0-1.3 Ga (Goldfarb, 2001).

Two distinct models are proposed for the apparent temporal distribution of orogenic type gold deposits: 1) Distribution by preservation (Groves et al., 2005) and, 2) Variations in ocean oxygenation and associated uptake of gold in biogenic pyrite (Tomkins, 2013). Differing preservation potentials of Archean and Paleoproterozoic tectonic processes versus modern tectonic processes are attributed to the under-plating of Archean and Paleoproterozoic by buoyant subcontinental lithospheric mantle, giving them a high preservation potential (Groves et al., 2005). The transition during the Mesoproterozoic to modern style plate tectonics changed the preservation potential of orogenic gold deposits (Groves et al., 2005). Modern-style orogenic belts are underlain by negatively buoyant subcontinental lithospheric mantle and undergo significant uplift and erosion, resulting in the destruction of orogenic gold deposits formed across the Mesoproterozoic-Neoproterozoic (1.6-0.57 Ga) period (Groves et al., 2005). The abundance of deposits within the Phanerozoic between 600-50 Ma is a result therefore of crustal exhumation, mid crustal levels taking approximately 50 Ma to reach the surface during uplift and being completely eroded before approximately 600 Ma (Groves et al., 2005).

Tomkins (2013) links the distribution of orogenic gold with the evolution of Earth's atmosphere, particularly the two major global oxidation events (Fig. 2.3) (Tomkins, 2013).

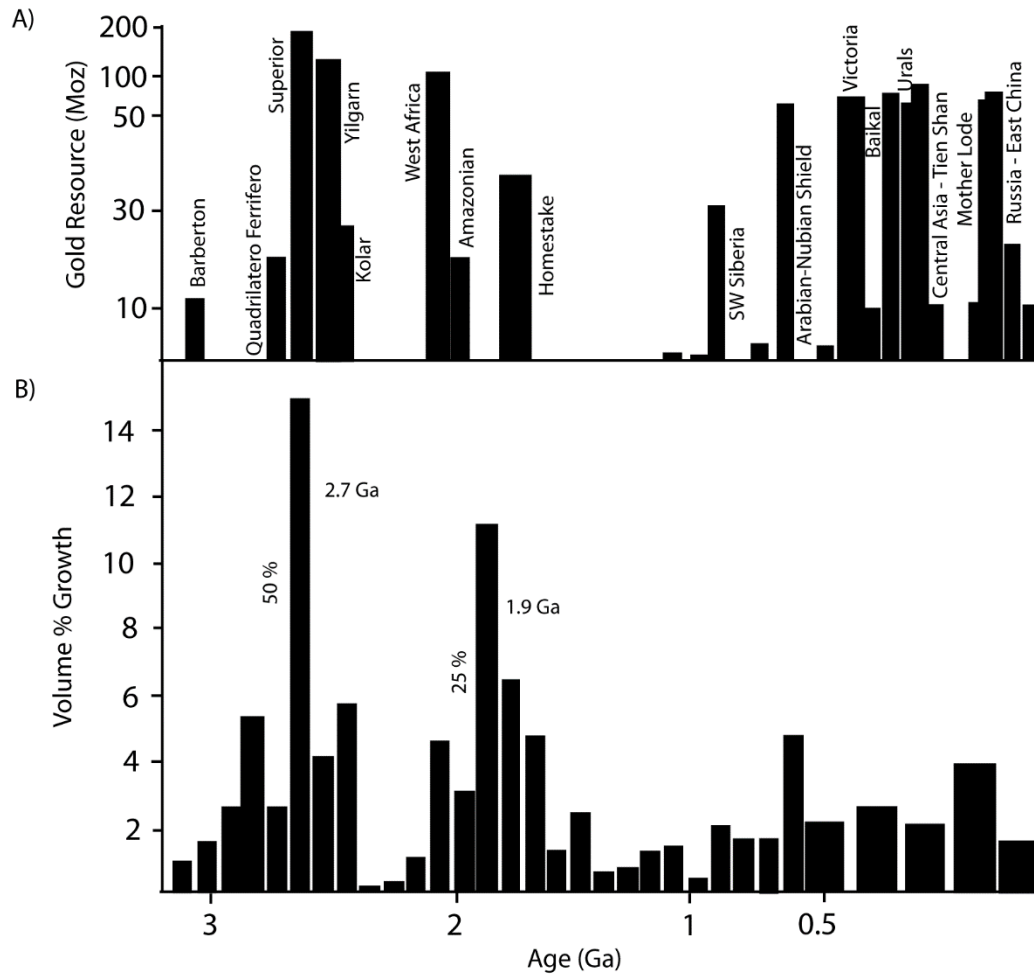


Figure 3.2: Temporal distribution of the formation of orogenic gold (Upper) compared to the rate of crustal formation (Lower) (Goldfarb et al., 2001)

Following the first great oxidation event (GOE 1) (at 2.45 Ga), the oceans were reduced relative to modern conditions, preventing the transport of gold to the necessary depth for the formation of sedimentary pyrite (Tomkins, 2013). The relative paucity of orogenic gold deposits following GOE I is therefore attributed to the deficiency in sufficiently gold enriched source lithologies across this period (Tomkins, 2013). Following the second great oxidation event (GOE 2) (at 635 Ma), the increased abundance of atmospheric oxygen increased the solubility of gold within the oceans, allowing extensive uptake of gold into pyrite and creating rich source lithologies for the development of gold deposits during Phanerozoic orogenesis (Tomkins, 2013).

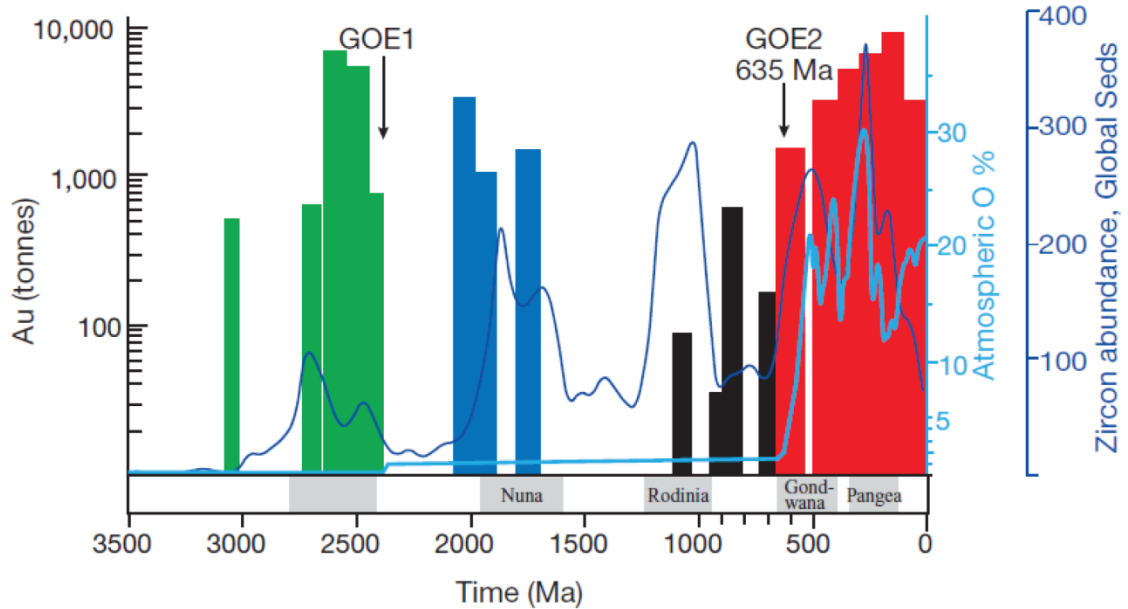


Figure 3.3: Correlation between periods of orogenic gold formation, Atmospheric Oxygen % and crustal development (represented by zircon abundance in global sediments) (Tomkins, 2013)

3.1.2 Host Structures

Orogenic gold deposits show strong association with large first order trans-crustal terrane bounding faults or docking structures between two contrasting geological terranes (Goldfarb et al., 1992; McCuaig and Kerrich, 1998; Bierlien and Crowe, 2000; Groves et al., 2003). First order structures are typically high angle anastomosing brittle-ductile ‘shear’ structures, ranging from sub vertical to sub horizontal. They display a protracted episodic movement and reactivation and can be several hundred kilometres in length with fault zones being several hundred metres in width (McCuaig and Kerrich, 1998; Bierlein and Crowe, 2000; Goldfarb et al., 2005; Phillips and Powell, 2010). These 1st order trans-crustal shear zones focus fluids produced at depth, in high volume source regions, into low volume sites of mineralisation (Phillips and Powell, 2010). Gold mineralisation occurs within subordinate 2nd or higher order splays along the edges of the main terrane bounding structures

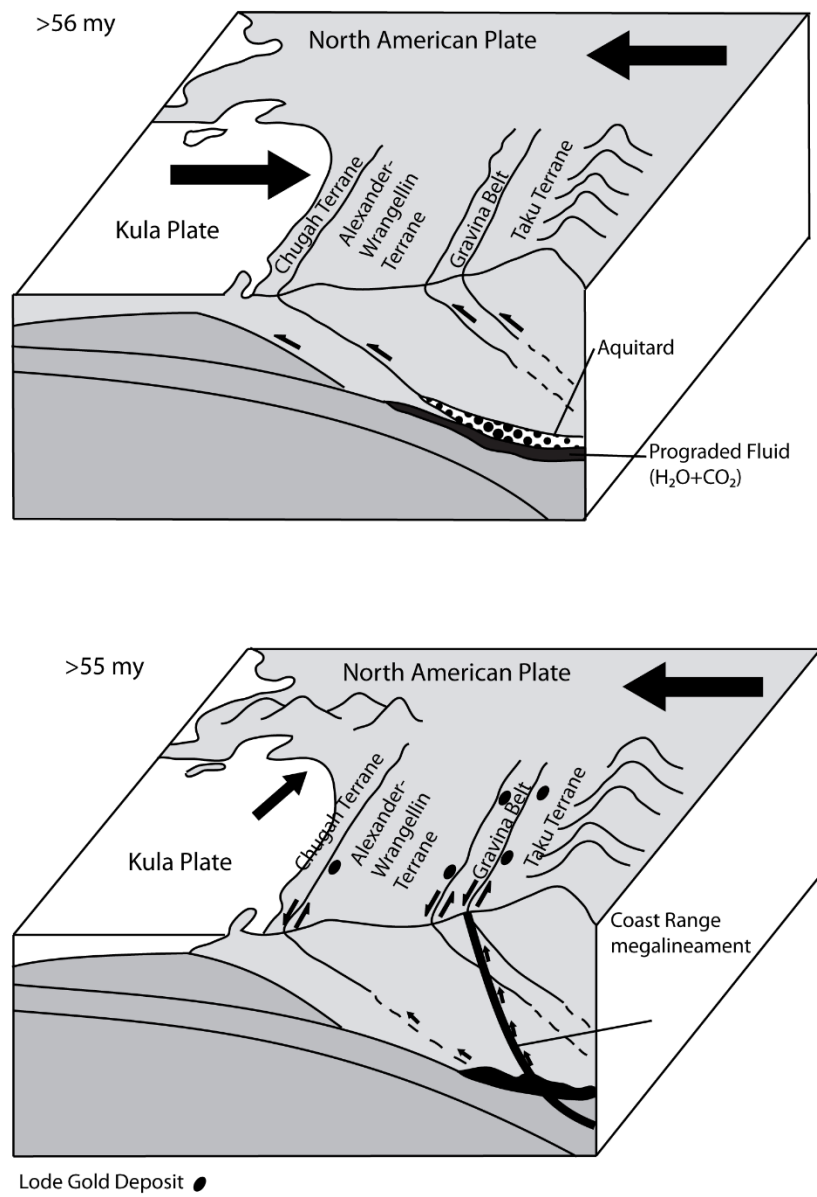


Figure 3.4: Schematic diagram of the southeast Alaska region illustrating the relationship between rapid dewatering of the crust and ore forming processes due to changes in tectonic regime. The convergent tectonic regime traps metamorphic fluids due to low permeability. Change in parity to trans-current tectonics c.55 Ma triggers rapid dewatering and ascent of hydrothermal fluids (Bierlein and Crowe, 2000)

(Groves et al., 2003; Goldfarb et al., 2005; McCuaig and Kerrich, 1998). The siting of gold within higher order splays is linked to changes in physiochemical conditions within these structures. These include: reduction in fluid volume and increase in concentration of gold within a fluid (Groves et al., 2003) and increased permeability and fluctuation in fluid pressure (McCuaig and Kerrich, 1998; Groves et al., 2005). These changes occur due to the brittle character of the higher order structures compared to the aseismic continuous ductile deformation within the first order structures (McCuaig and Kerrich, 1998; Groves et al., 2003)

Focussing of fluid into high order structures is thought to occur through fault valve action and the corresponding fluctuations in the volume of fluid flow and fluid pressures (Sibson et al., 1988; Sibson, 1990, 2004; Goldfarb et al., 2005). Variations in the regional stress field and the transition of major fault systems from high angle reverse faults accommodating shortening to strike-slip transpressional tectonics (Fig. 3.4) is considered by some to be a vital part of this process and the development of gold mineralisation (Sibson et al., 1988; Bierlein and Crowe, 2000; Sibson, 2004; Goldfarb et al., 2005; Phillips and Powell, 2010)

3.1.3 Host Lithologies

Host lithologies within orogenic gold systems are diverse and are noted to vary with time. In the Archean and Proterozoic host rocks are dominated by oceanic basalts, felsic to mafic arc rocks and clastic marine sediments, while Phanerozoic deposits are hosted within turbiditic successions interspersed by intermediate-mafic volcanic units (Bierlein and Crowe, 2000; Groves et al., 2003; Tomkins, 2013). A subset of Phanerozoic deposits are hosted within volcano-sedimentary successions, thought to be analogous to typical Archean greenstone environments (Bierlein and Crowe, 2000). Host lithologies are in all cases metamorphosed, with terranes displaying moderate to high temperature-low to moderate pressure metamorphism typified by sub-greenschist to amphibolite facies lithologies. The majority of world class orogenic gold resources are hosted within greenschist facies lithologies (Groves et al., 2003), although some Archean orogenic gold deposits occur within amphibolite grade terranes (Groves et al., 1992).

3.1.4 Host Rock Alteration

Hydrothermal alteration is ubiquitous with orogenic gold deposits, forming as ascending fluids experience chemical and isotopic metasomatic reaction with the wall-rocks (McCuaig and Kerrich, 1998). Alteration within orogenic gold deposits is typified by enrichment of K, Rb, S, H₂O, SiO₂ and CO₂ (Groves et al., 1998; Phillips and Powell, 2010), manifesting as quartz, carbonate, micas, albite, chlorite, scheelite and tourmaline alteration (McCuaig and Kerrich, 1998; Phillips and Powell, 2010). Enrichment in Au, Ag, As,

Sb also occurs with variable enrichment of Te, Se, W, Mo, Bi and B and low level enrichment in Cu, Zn and Pb (Groves et al., 2003; Goldfarb et al., 2001; McCuaig and Kerrich, 1998).

Alteration shows a strong lateral zonation between proximal and distal assemblages (Groves et al., 1998), with alteration varying by a number of controls: 1) tectonic regime and resultant stress field; 2) the fluid/rock ratio; 3) compositional variations within the host lithology; 4) compositional variations in the hydrothermal fluid such as Eh, pH, activity of individual elements and salinity; 5) temperature at which alteration occurs; 6) pressure at which alteration occurs; 7) equilibrium and disequilibrium conditions (McCuaig and Kerrich, 1998). These variables constitute a complex interplay of fluid/wall rock reactions that affect the final characteristics of the alteration assemblage. Fluid/wall rock reaction typically occurs through three mechanisms: migration of fluid along fractures and micro-cracks, and migration of fluid along grain boundaries and ionic diffusion through pore fluids (McCuaig and Kerrich, 1998). Which process dominates is determined by the permeability of the host lithology, migration along micro-cracks dominating in high permeability environments while diffusion dominates in low permeability environments (Ridley and Diamond, 2000).

3.1.5 Deformation Characteristics and the Effect on Host Rock Permeability

The range of fabrics and structures observed within orogenic gold systems are intrinsically linked to the rheological characteristics of the host lithology and the regional thermal and stress fields present during their development (McCuaig and Kerrich, 1998). The presentation of deformation fabrics is dependent on: 1) the rheological properties of the host rock, such as grain size and the susceptibility of the rock to adopt isotropic/anisotropic fabrics (rocks rich in phyllosilicates are highly susceptible while quartz, feldspars and carbonates are resistive); 2) the precipitation of minerals as part of the developing alteration assemblages; 3) regional variables such as fluid pressure, temperature and strain rate (McCuaig and Kerrich, 1998).

Brittle behaviour, characterised by faults and cataclasis, dominates at low confining pressures and temperatures with high strain rates (McCuaig and Kerrich, 1998). With increasing depth, and increasing temperature and confining pressure, ductile behaviour dominates, with deformation initially occurring as steady state deformation by pressure solution, and transitioning to dynamic re-crystallisation by dislocation glide mechanisms at upper greenschist-amphibolite facies conditions (Kerrich and Allison, 1978; McCuaig and Kerrich, 1998).

Alteration of wall rock material and the development of alteration mineral phases has a significant effect on deformation mechanisms and associated fabrics through the processes of 'strain softening' and 'hydrothermal hardening'. The growth of phyllosilicates (chlorite, biotite, and muscovite) through

hydrolysis of mafic minerals under strain imparts a fabric to the deforming lithology, reducing wall rock competency and mechanical anisotropy (McCuaig and Kerrich, 1998). Increased permeability under strain in zones of low mechanical competency focuses fluid flow and deformation causing further alignment of phyllosilicate minerals and enhancing the effect of 'strain softening' (McCuaig and Kerrich, 1998). In ductile environments, strain is subsequently preferentially accommodated within phyllosilicate dominated areas and in brittle environments, hydraulic fractures open preferentially along and parallel to the developed fabric (McCuaig and Kerrich, 1998). Precipitation of isotropic anhydrous minerals such as quartz, carbonates and albite, by fluids migrating through the zones of enhanced permeability, has the converse effect, increasing competency, lowering permeability and restricting fluid infiltration, promoting brittle behaviour through a process known as 'hydrothermal hardening' (McCuaig and Kerrich, 1998).

Multiple generations of deformation under strain and hydraulic fracturing within deposits indicate such behaviour is cyclic and is linked to fluid over-pressuring (McCuaig and Kerrich, 1998). High fluid pressures counteract increased confining pressures, enabling rocks under ductile confining pressures and temperatures to behave in a brittle manner through fluid over-pressuring and allowing hydraulic fractures to form and increase permeability (Sibson, 1990, 2004). The deformation mechanisms and characteristics discussed above have a direct bearing on the form of mineralisation developed within the system. Distinctly different styles of mineralisation are identified in brittle, brittle-ductile and ductile environs (Goldfarb et al., 2005). In brittle conditions, mineralisation styles are dominated by stockworks and breccias representative of multiple events of cataclasis with individual quartz grains remaining mostly un-deformed (Goldfarb et al., 2005). Under ductile conditions, at high temperatures and pressures, mineralisation occurs as bedding parallel vein structures showing a high degree of deformation, and replacement textures and disseminated lodes with quartz grains in the host lithologies and veins showing a high degree of recrystallisation and deformation (Goldfarb et al., 2005).

3.2 Fluid Sources

Study of orogenic gold systems has shown that the fluids involved in their formation display a relatively uniform composition, typically low salinity with 5-6 wt% NaCl being typical, outliers up to 10 wt% NaCl (Bierlein and Crowe, 2000), near neutral pH, mixed aqueous-CO₂ fluids ranging from 5-50 mole% CO₂ with associated CH₄ (below 5 mole percent) and trace N₂ (Bierlein and Crowe, 2000). Multiple models have been proposed as the source of fluids within orogenic systems, including: (1) metamorphic devolatilization of the orogenic stack (Ridley and Diamond, 2000; Phillips and Powell, 2010; Tomkins, 2010; Yardley and Cleverley, 2013); (2) exsolution of fluids from crystallising felsic igneous bodies (De Ronde et al., 2000; Ridley and Diamond, 2000); (3) fluids ascending from the upper mantle (Taylor, 1979; Cameron, 1988;

Groves et al., 1992); (4) exsolution of fluids from gold-rich lamprophyre magmas (Rock et al., 1989) and; (5) deep circulating meteoric fluids (Nesbitt, 1988; Jenkin et al., 1994; Large et al., 2011). While elements of each model may have played a role in the development of orogenic gold deposits across the world, the metamorphic devolatilization model is the most widely accepted and invoked model at present.

3.2.1 Metamorphic Devolatilisation

The metamorphic devolatilisation model proposes that fluids are generated by the breakdown of hydrous and carbonate minerals deep within an orogenic stack at the greenschist-amphibolite transition, during prograde metamorphism (Ridley and Diamond, 2000; Phillips and Powell, 2010; Tomkins, 2010; Yardley and Cleverley, 2013). These fluids then ascend through the crust along structural conduits, transporting dissolved gold to the site of deposition (Phillips and Powell, 2010; Yardley and Cleverley, 2013). The conditions at the greenschist-amphibolite facies transition are also favourable for the breakdown of pyrite to pyrrhotite, liberating sulphur and gold in the process (Tomkins, 2010).

While a metamorphic origin is widely accepted, significant debate exists as to which lithologies within a metamorphic stack are the ultimate origin of fluids, sulphur and gold that form orogenic gold deposits. Several lithologies common within accretionary terranes have been identified as potential candidates for metamorphic devolatilization, including mafic successions (Bierlein et al., 2006; Phillips and Powell, 2010; Pitcairn et al., 2015), carbonaceous shales (Large et al., 2009; Large et al., 2011; Tomkins, 2010; Gabourey, 2013) and non-carbonaceous pelitic successions (Pitcairn et al., 2006; Pitcairn et al., 2010; Tomkins, 2010).

Carbonaceous shales are known to be enriched in Au and sulphur through pyrite formed by sulphate reduction in the oceans, and models show that at the greenschist-amphibolite transitions they are capable of producing significant volumes of fluid and sulphur (Large et al., 2011; Tomkins, 2010). The low abundance of carbonaceous shales within accretionary sequences however prevents them from generating sufficient fluid volumes to produce giant orogenic gold deposits (Tomkins, 2010). Tomkins (2010) proposed that fluid produced by devolatilisation of carbonaceous shales can act to enhance the devolatilisation and breakdown of pyrite within the more voluminous pyrite-bearing psammitic successions (Tomkins, 2010). The importance of these sedimentary successions is highlighted by Gabourey (2013), who identified ethane (C₂H₆) derived from carbonaceous material within orogenic gold fluids in host lithologies where carbonaceous shales are unknown, indicating their presence at depth. Chang et al. (2008) further showed that the $\delta^{34}\text{S}$ signatures of orogenic gold deposits across the Phanerozoic correlate with the seawater sulphate

curve (Fig. 3.5), indicating that sulphur is principally sourced from fixation of sulphur in the deep ocean (Chang et al., 2008; Gabourey, 2013).

Like carbonaceous lithologies, basaltic material has been shown to be enriched in Au and capable of producing significant volumes of fluid and sulphur at the greenschist-amphibolite facies transition (Pitcairn et al., 2014). Low volumes of basaltic material within Phanerozoic deposits combined with low As contents within fluids sourced from these lithologies lowers their potential as source rocks (Bierlein and Crowe, 2000; Tomkins, 2010; Pitcairn et al., 2014). Basalts however may be an important source in Archean and Proterozoic accretionary belts where basalt is more abundant (Tomkins, 2010). The necessary conditions for the production of fluid through devolatilization of metamorphic materials, high temperature and low pressure, constrain the settings in which orogenic gold deposits can potentially form (Tomkins, 2010). Tomkins (2010) identified three scenarios in which the necessary conditions are present: (1) inverted back arc basins; (2) accretionary wedges above subduction zones and; (3) accretionary terranes composed of recently active volcanic arcs (Fig. 3.6) (Tomkins, 2010).

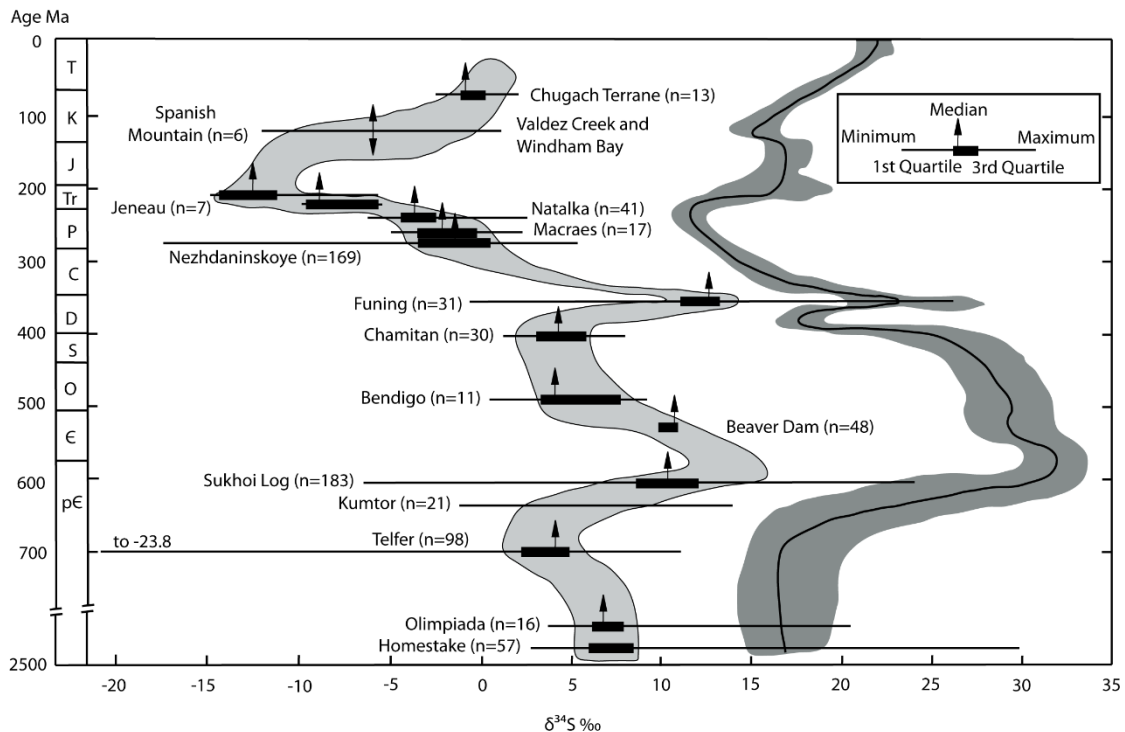


Figure 3.5: Variation in $\delta^{34}\text{S}$ values in orogenic gold deposits over time in comparison to the variation in seawater sulphate values over time (Chang et al., 2008)

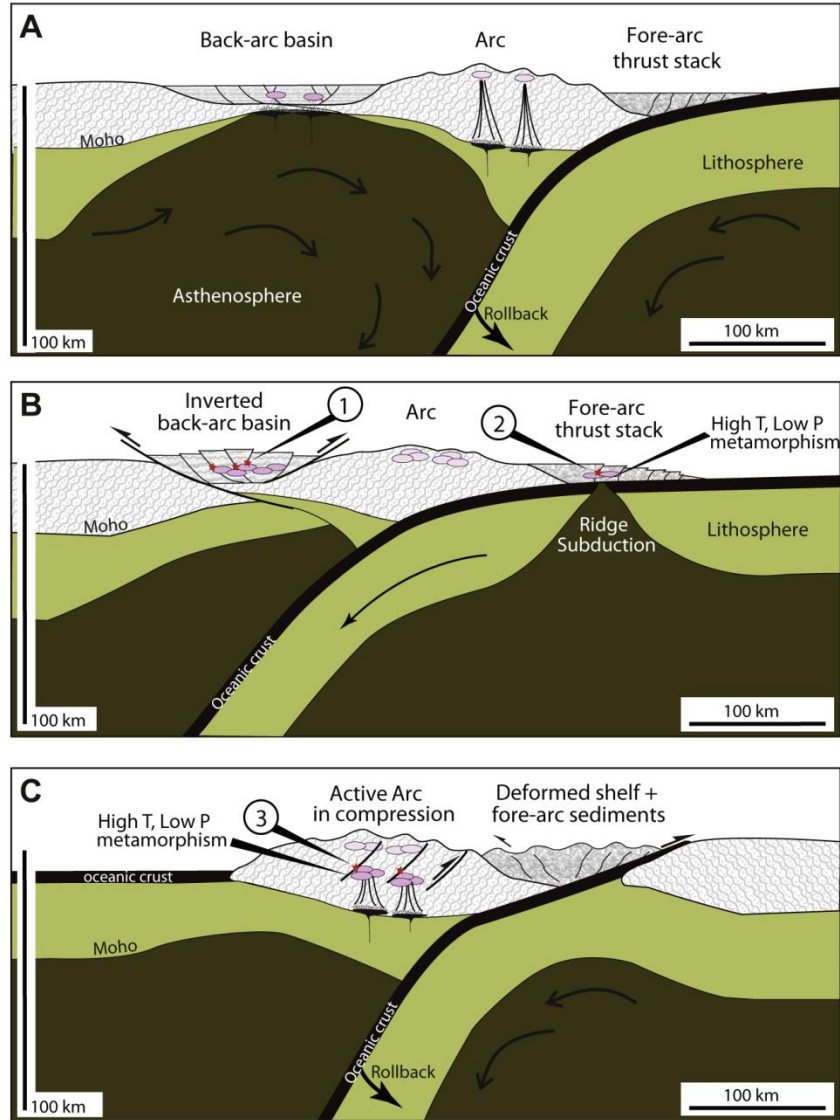


Figure 3.6: Schematic diagram displaying possible setting of modern orogenic gold formation. A) Development of a back arc basin due to slab roll back, allowing development of sequences of primitive sediments, volcanics, and carbonaceous sediments to develop in area of lower crustal melting and high heat flow. B) Basin inversion generates felsic magmas within the mid crust creating widespread high T-Low P metamorphism and orogenic gold formation in newly active compressional setting. Ridge subduction (right) facilitates partial melting of the accretionary wedge with continued convergence allowing felsic magmas to be retained in the mid crust driving regional high T-Low p metamorphism and the development of orogenic gold. C) Arc-Continent collision switches arc from dilation to compressional stress regime trapping felsic magmas in the mid crust resulting in High T-Low P metamorphism, in the presence of suitable source rocks orogenic gold systems may develop however low thermal flux limits the amount of mineralisation that may develop (Tomkins, 2010).

3.2.2. Magmatic Exsolution

The magmatic model considers fluids generated by exsolution during the crystallisation of granitic magmas. As gold is incompatible during crystallisation, it is concentrated into the fluid phase (Ridley and Diamond, 2000). The high temperature and low pressure conditions present at convergent tectonic boundaries are conducive to the generation of granitic melts, and large granitic bodies are commonly associated with orogenic gold deposits, (Powell et al., 1991). Study of fluids exsolving from active granitic bodies has established that magmatic fluids are rich in elements that are also enriched in orogenic gold deposits, and show isotopic values similar to those identified within some orogenic gold deposits (Taylor, 1979; De Ronde et al., 2000). However the magmatic model was widely rejected due to problems regarding the ability of granitic magmas to generate the necessary volume of CO₂-rich, low salinity fluids, a lack of concordant ages between granitic emplacement and development of mineralisation, and the occurrence of orogenic gold deposits in terranes where no magmatic bodies were present (Burrows and Spooner, 1989; Barley and Groves, 1990; Cline and Bodnar, 1991; Koons and Craw, 1991). The magmatic model has been re-examined following the work of Xue et al. (2013), who concluded that a magmatic source was most likely for deposits within Archean greenstone belts based on $\Delta^{33}\text{S}$ compositions of orogenic gold veins in Australia's Yilgarn craton (Xue et al., 2013). Xue et al. (2013) interpreted $\Delta^{33}\text{S}$ values around zero as being indicative of a mantle, derived sulphur source and attributed this to granitic bodies derived from the mantle but rejected the possibility of mantle derived basalts based on their low abundance in the mineralised area (Xue et al., 2013). As mantle derived basalts have been demonstrated as possessing similar $\Delta^{33}\text{S}$ values (Labidi et al., 2014) and fluid migration up sequence away from the source is well established (McCuaig and Kerrich, 1998), this author expresses doubts regarding this interpretation.

3.3 Complexing of Gold in Solution

Experimental investigation into the solubility of gold under conditions approximating natural hydrothermal systems has shown that the dominant complex varies with temperature, chloride/sulphur concentration and pH (Fig. 3.7) (Stefansson and Seward, 2004). Sulphide complexes dominate at low temperatures except, in solutions with low sulphide concentrations when chloride and oxide complexes increase in importance. At 400°C, the dominant species is dependent on the composition of the aqueous phase. In dilute sulphide and chloride solutions the hydroxide complex dominates and in dilute sulphide but chloride-rich systems, the hydrochloride complex dominates below a pH of 4 and the hydroxide complex continues to dominate above pH of 4. In solutions rich in both chloride and sulphide ions, the hydrosulphide complex dominates at all but the lowest pH values (Stefansson and Seward, 2004).

In the context of real world systems, typical crustal rock possess greater sulphur abundance (~0.1%) compared to chlorine (~200 ppm) and under typical greenschist metamorphic conditions, dehydration reactions will produce dilute aqueous, low Cl, high S fluids (McCuaig and Kerrich, 1998). These low salinity fluids are not conducive to base metal (Cu, Pb, Zn etc) complexing and transport but provide abundant sulphide to transport gold as a bi-sulphide complex ($\text{Au}(\text{HS})_2$) (see above) (McCuaig and Kerrich, 1998).

3.3.1 Precipitation of Gold from Solution

The precipitation of gold from solution requires changes in the physicochemical conditions at the site of ore deposition and the destabilising of the gold complex. This can be achieved through (1) adiabatic or conductive cooling of the fluid; (2) interaction between ore fluids and wall-rock; (3) phase separation due to pressure changes; (4) flash vaporisation due to rapid pressure fluctuations, fluid mixing, boiling and chemisorption (McCuaig and Kerrich, 1998; Mikucki, 1998; Williams-Jones et al., 2009).

Phase separation and fluid-rock interaction are the dominant mechanisms invoked in the deposition of gold from solution. Phase separation occurs as a result of drops in pressure, such as those theorised to occur during fault-valve tectonics, or due to chemical changes caused by mixing with graphitic rocks or CH_4 fluids (Mikucki et al., 1998). Pressure drops result in increased pH and oxygen fugacity within the pore fluid (Mikucki et al., 1998). This results in partitioning of sulphur into the vapour phase, leading to the precipitation of gold through the destabilisation of the $\text{Au}(\text{HS})_2$ complex (McCuaig and Kerrich, 1998). The interaction between hydrothermal fluids and wall rocks at the site of deposition is the most significant mechanism by which precipitation of gold from solution takes place during the formation of orogenic gold. This mechanism operates by the sulphidisation of Fe-rich wall rock lithologies or by oxidising the ore-bearing fluids during interaction with the host rock or meteoric fluids held within the wall rock (Neall and Phillips, 1987; Williams-Jones et al., 2009). This process involves the sulphide ligand in the gold transporting complex being consumed through reaction with Fe-silicates, oxides or sulphides in the wall rock, resulting in the destabilising and associated precipitation of Au within the wall rock (McCuaig and Kerrich, 1998, Williams-Jones et al., 2009). Where Fe-Sulphides form within vein structures, iron is removed from the wall rocks, resulting in the formation of ferromagnesian silicates and carbonates in the wall rock surrounding the vein (McCuaig and Kerrich, 1998). In lower temperature deposits, it is considered possible that precipitation of gold may occur through the reaction of CO_2 or Ca with MgO-rich wall rocks (Mikucki, 1998). Graphitic lithologies can also act as a strong control, with primary ore fluids reacting with carbon to produce methane, resulting in phase separation within the fluid (McCuaig and Kerrich, 1998).

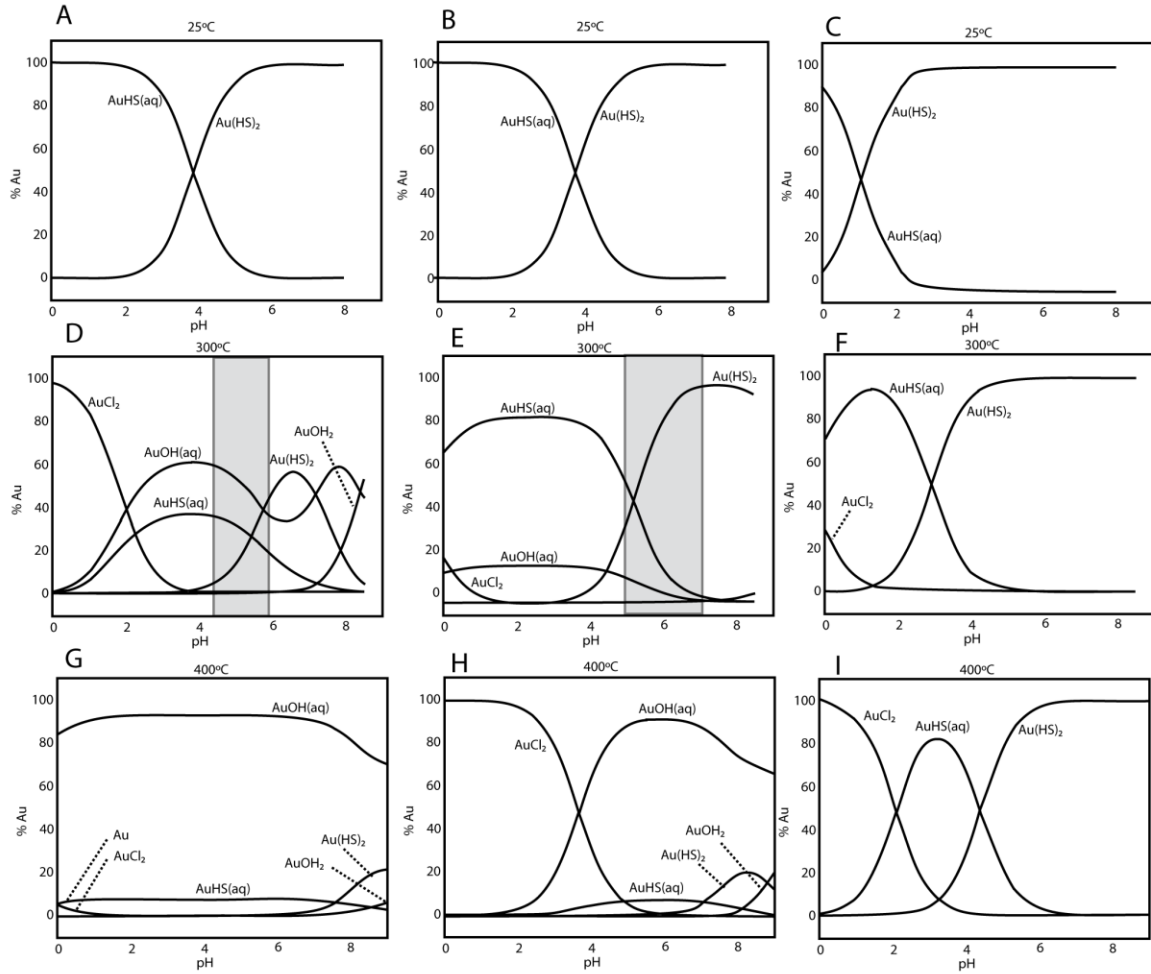


Figure 3.7: Percentage distribution of gold(I) species as a function of solution composition and temperature at 500 bar. A and G; mS_{total} and $mCl=0.001$, B and H; $mS_{total}=0.001$ and $mCl=0.5$, D; $mS_{total}=5 \times 10^{-4}$ and $mCl_{total}=0.61$, E; $mS_{total}=0.004$ and $mCl_{total}=0.03$, C, F and I; $mS_{total}=0.5$ and $mCl=0.5$. A-C: at temperature 100°C and mCl - to 0.5 mol kg^{-1} , gold(I) sulphide complex dominate at all pH's. D-F: at 300°C sulphide complex dominates except at low sulphide concentrations and in chloride-rich solutions where $AuOH(aq)$ and $AuCl_2^-$ dominate. G-I: At 400°C dominant gold complex is insensitive to solution composition, in dilute sulphide and chloride solutions (g) $AuOH(aq)$ dominates, in dilute sulphide but chloride-rich solutions $AuCl_2^-$ dominates at low pH and $AuOH(aq)$ at high pH, in sulphide and chloride-rich solutions $AuCl_2^-$, $AuHS(aq)$ and $AuHS^{2-}$ are all significant at different pH values. (Stefansson and Seward, 2004)

3.4 Summary

Orogenic gold deposits are a diverse group, displaying a range of lithological, metamorphic, structural, geochemical and mineralogical characteristics. This diverse group of deposits have been classified together on the basis of distinct similarities in the composition of mineralizing fluids (being low salinity fluids with near neutral pH), the interpreted structural setting (association with large scale crustal shears) and geotectonic setting (at interpreted historical convergent tectonic margins). While debate has existed as to the processes that facilitate the formation of orogenic gold deposits, in particular the source of the fluids and metals, the weight of evidence currently favours a metamorphic origin, fluids being produced through metamorphic devolatilization at evolving convergent margins during orogenesis. Secular variations in plate tectonics and the relative distribution of specific lithotypes, both across time and between individual orogenic events, may therefore explain the differences between individual orogenic gold deposits. The variations in host and source lithologies, transitioning from igneous dominated in Archean deposits to sediment dominated in modern deposits, and isotopic characteristics, $\delta^{34}\text{S}$ values closely tracking the $\delta^{34}\text{S}$ seawater sulfate curve, are two notable example of these variations across time. The similarities between orogenic gold deposits are a result of the fundamental mechanisms through which these deposits were formed. In this respect, the production of gold-bearing fluids at depth through metamorphic devolatilization, a process that has remained consistent throughout geologic time regardless of host lithology, may be considered the most significant factor in the formation of orogenic gold that ties together all known deposits. The crustal thickening associated with convergent tectonics, through terrane accretion and orogenesis, creates the ideal high temperature-low pressure conditions in which fluids of this type may be produced in addition to creating a structural architecture that channels them to the site of ore deposition. This fact is reflected by the distribution of orogenic gold deposits within metamorphic lithologies, hypothesized to have formed at historical convergent tectonic settings. While the metamorphic model has gained widespread acceptance in recent years, significant debate remains as to the principle source lithology, with basalts, black shales and metapelites all considered potentially significant. These lithologies are common constituents of orogenic belts and ultimately may all contribute fluids and metals during metamorphic devolatilization. The dominant source likely varies between individual orogenic gold systems depending on the available lithologies. The work of Tomkins (2013), however, has highlighted the potential importance of black shales as both a source lithology and a catalyst, triggering enhanced devolatilization in other potential source lithologies.

Chapter 4. Lithological Characteristics of the Kibali Granite-Greenstone Belt and its Neighbouring Geological Terranes; The West Nile Gneiss and Upper Congo Granitic Massif.

4.1 Introduction

The Kibali Granite-Greenstone Belt (KGGB) and its neighbouring geological terranes, the Upper Congo Granitic Massif (UCG) and West Nile Gneiss (WNG) have been the subject of limited geological study over the last century. The major geological units are currently poorly described, with the available data reviewed in Chapter 2. The area covered by this study extends across the three major geological terranes, providing an opportunity to examine the physical characteristics of each and the relationship between them. Below the physical and petrological characteristics of the principle lithological units within the three major terranes are examined and discussed in relation to the formation and evolution of the Kibali Granite-Greenstone Belt.

4.2 Sampling procedure and analytical technique

Regional sampling was undertaken during three field seasons between 2012 and 2014 in conjunction with the Kibali Gold project exploration department. A total of 83 lithological samples were collected from across the study area (Fig. 4.1). Samples were collected from, where possible, un-weathered material and each assigned a unique identification number. The geographical position and elevation at which each was collected was also recorded in addition to any further relevant field observations. Samples were examined in hand specimen and assigned a preliminary classification. Polished thin sections were produced from a subset of the available samples, providing a minimum of one section from each of the major lithological divisions identified. Petrological and mineralogical analyses were conducted using a combination of transmitted light microscopy and Energy Dispersive System (EDS) microprobe analysis. Transmitted light microscopy was conducted by petrographic microscope while mineral compositions were determined using a Zeiss EVO 50 Scanning Electron Microscope and X-ACT Energy Dispersive System (EDS) detector with data handling performed by the Oxford Instruments INCA analytical suite. EDS analysis was performed with an accelerating voltage of 20 kV, beam current of 1.5 nA and detector process time of 4 seconds. Prior to each analytical session signal intensity was measured by a Faraday cup until the variation in signal intensity fell below 1%. A pure albite standard was utilised to calibrate the detector at the beginning of each analytical session and a cobalt standard was periodically used to calibrate beam intensity throughout each analytical session.

4.3 The Kibali Granite-Greenstone Belt

The KGGB terrane dominates the study area constituting an approximately 70 km wide east-west trending belt bounded to the north by the WNG and to the south by the UCG (Fig. 4.1). The geographical extent of the belt can be observed by examining regional airborne electromagnetic susceptibility (EM) data (Fig. 4.2). The high susceptibility units of the KGGB are bisected along an approximately east-west line by the low susceptibility WNG terrane in the north. The boundary with the UCG is less well defined but is again characterised by a transition from high susceptibility units in the KGGB to low susceptibility units in the UCG with a narrow zone of high conductivity defining the boundary between the two terranes (Fig. 4.2). The geological map of the KGGB presented in this study (Fig. 4.2) represents a combination of data collected by the author and the staff in the exploration department of the Kibali Gold project.

The KGGB is composed of thrust stacked metasediments, banded iron formations and basalts displaying varying degrees of metamorphism, the metamorphic grade varying from sub-greenschist in the west to amphibolite facies in the east. The metasediments are intruded by a series of gabbroic to granitic plutons. The structural characteristics of the belt are poorly constrained at this time, studies of the structural characteristics having focussed on the area around the major gold deposits (reviewed in Chapter 7). At a regional scale two major structural sets have been identified through examination of geophysical data and limited ground truthing; a set of northeast-southwest orientated sub-vertical shear zones (Allibone, 2015; Lavreau, 1984), and northwest-southeast striking thrust faults that dip approximately 25 to 30 degrees in a northeast direction (Allibone, 2015). The characteristics of the major geological units identified during the field study are presented here.

4.3.1 Kibalian metasediments

The Kibalian metasediments include all lithologies of interpreted sedimentary origin identified within the Kibali Granite-Greenstone Belt. As a result this group has extremely variable characteristics ranging from greenschist facies volcano-sedimentary conglomerates in the western part of the study area to quartz-biotite gneisses at its eastern end. The lithologies that comprise this unit are some of the most significant within the KGGB, being host to the giant Karagba-Chaffeur-Durba (KCD) deposit and the smaller Mengu, Pakaka and Pamao deposits.

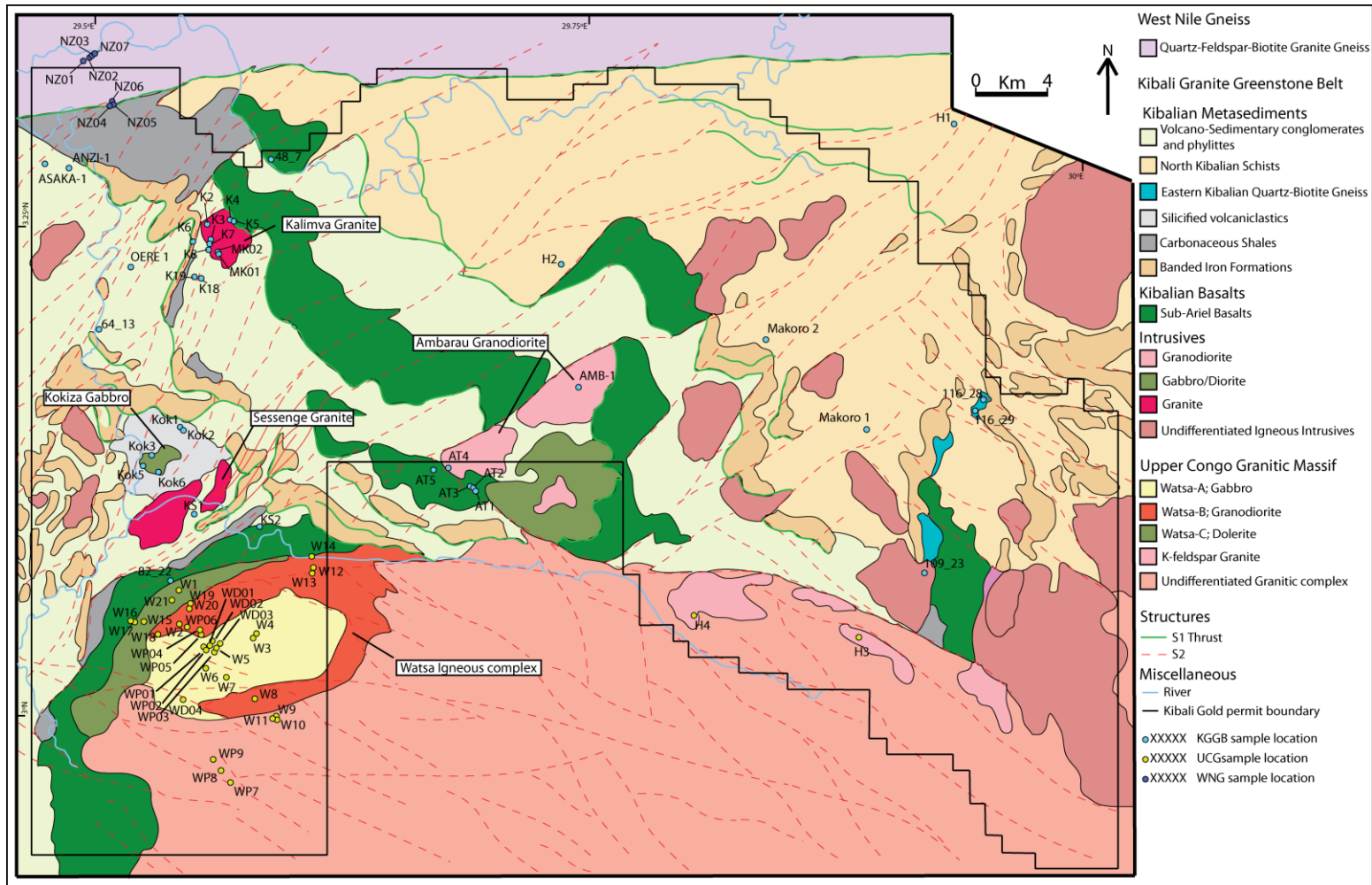


Figure 4.1: Geological map of the Kibali Granite-Greenstone Belt and neighboring Upper Congo Granitic Massif and West Nile Gneiss terranes, displaying the major lithological units and sample locations discussed in this chapter.

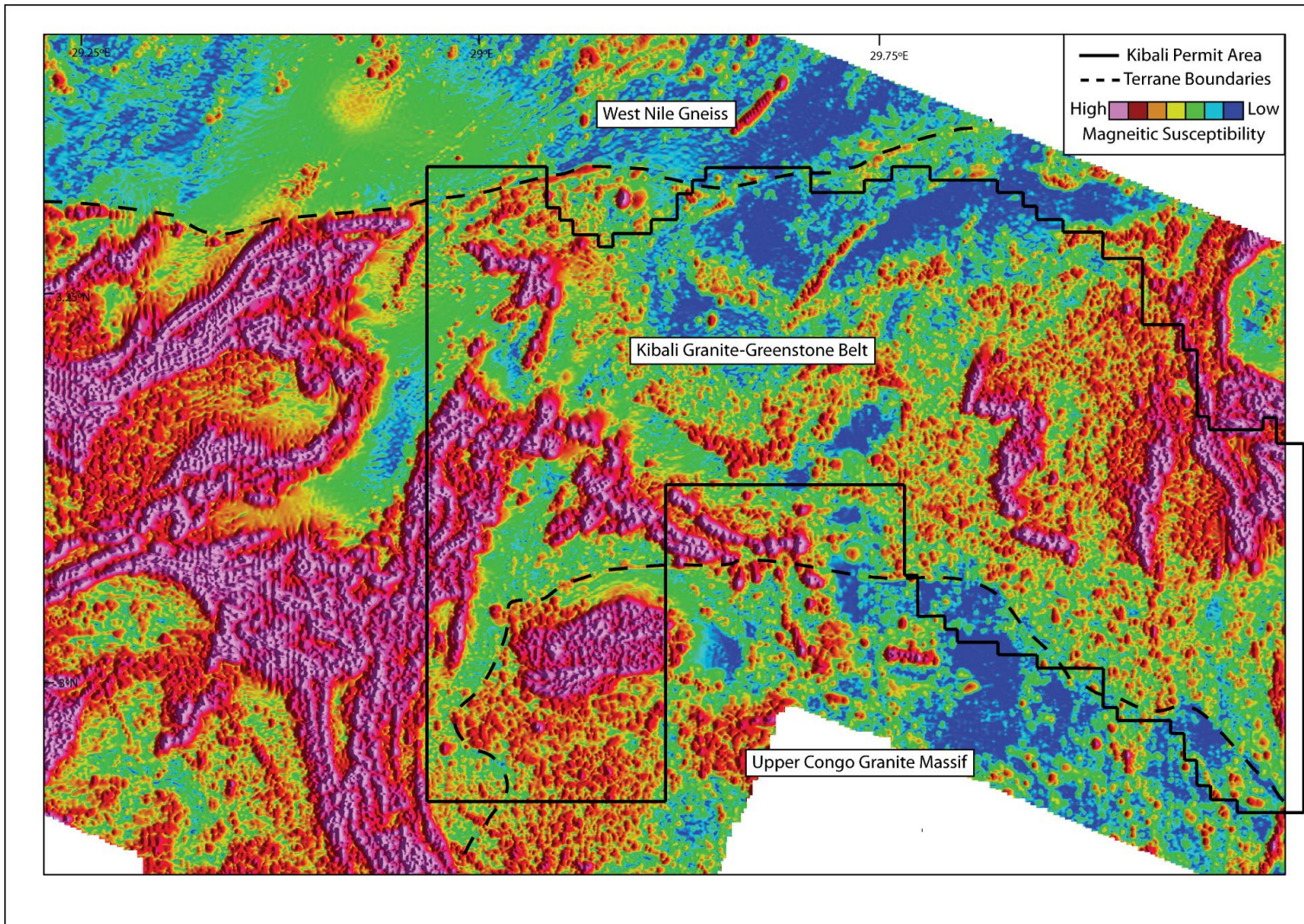


Figure 4.2: Airborne Electromagnetic susceptibility data over part of the Kibali Granite-Greenstone Belt and neighboring terranes (Provided by Randgold Resources Ltd)

4.3.1.1 Volcano-Sedimentary Conglomerates

Volcano-sedimentary lithologies, comprising conglomerates and fine-grained sediments, are identified in outcrop and drill core in the eastern part of the Kibali Granite-Greenstone Belt, extending across a significant part of the eastern half of the study area (Fig. 4.1 and 4.2). The volcano-sedimentary conglomerates are characterised by quartz-feldspar clasts hosted within a fine crystalline phyllosilicate groundmass. The relative proportions of clast to groundmass and the physical characteristics of these phases vary between samples (Fig. 4.3). Clast material ranges in size from 1 mm to 5 cm and is compositionally diverse, consisting of reworked sedimentary and igneous material.

Clasts of sedimentary origin are composed of fragments of ironstone and reworked conglomeratic and fine sedimentary material. Reworked conglomerate clasts consist of rounded feldspar crystals in a fine quartz groundmass and are only rarely observed. Clasts consisting of fine crypto-crystalline sedimentary material occur in association with the reworked conglomerate material and in rare cases display sedimentary layering. Clasts of igneous origin consist of angular feldspar laths within a fine quartz-rich groundmass. While displaying similar mineral components to the identified reworked sedimentary clasts these are distinguished on the basis of the well-formed angular morphology of the feldspar crystals. Based on the available sample set the material of igneous origin is the more abundant clast material. Clast morphology is predominantly rounded to sub-rounded though ironstone fragments are typically angular to sub-angular. The clast material is hosted in all cases within a groundmass composed of aligned phyllosilicate minerals, chlorite and aluminoceladonite (Fig. 4.3 and Table 4.1). These wrap around the clasts where deformation is significant. The total proportion of clast material varies between samples from 90% (clast supported) of the sample to <1% (matrix dominated).

Fine-grained sediments lacking any coarse clasts are included in this volcano-sedimentary package. These sediments are homogenous, fine-grained to cryptocrystalline in hand specimen and display a strong foliation. The mineralogy of these units consist of <10 µm quartz and aluminoceladonite. The relative proportion of these two phases varies between samples. In all cases, the volcano-sedimentary lithologies display evidence of deformation, although the degree of deformation is variable between samples. Deformation is principally distinguished by the deformation of the clast material and alignment of the clasts and associated phyllosilicate groundmass minerals along their long axis (Fig. 4.3), imparting a strong foliation to the samples. Increased deformation is characterised by the deformation of the clast material with associated re-crystallisation of the feldspar mineral phase to fine quartz and stretching the clasts parallel to the foliation orientation. In the fine sedimentary material deformation is indicated by the alignment of the phyllosilicate minerals within the samples imparting a phyllitic texture to the samples.

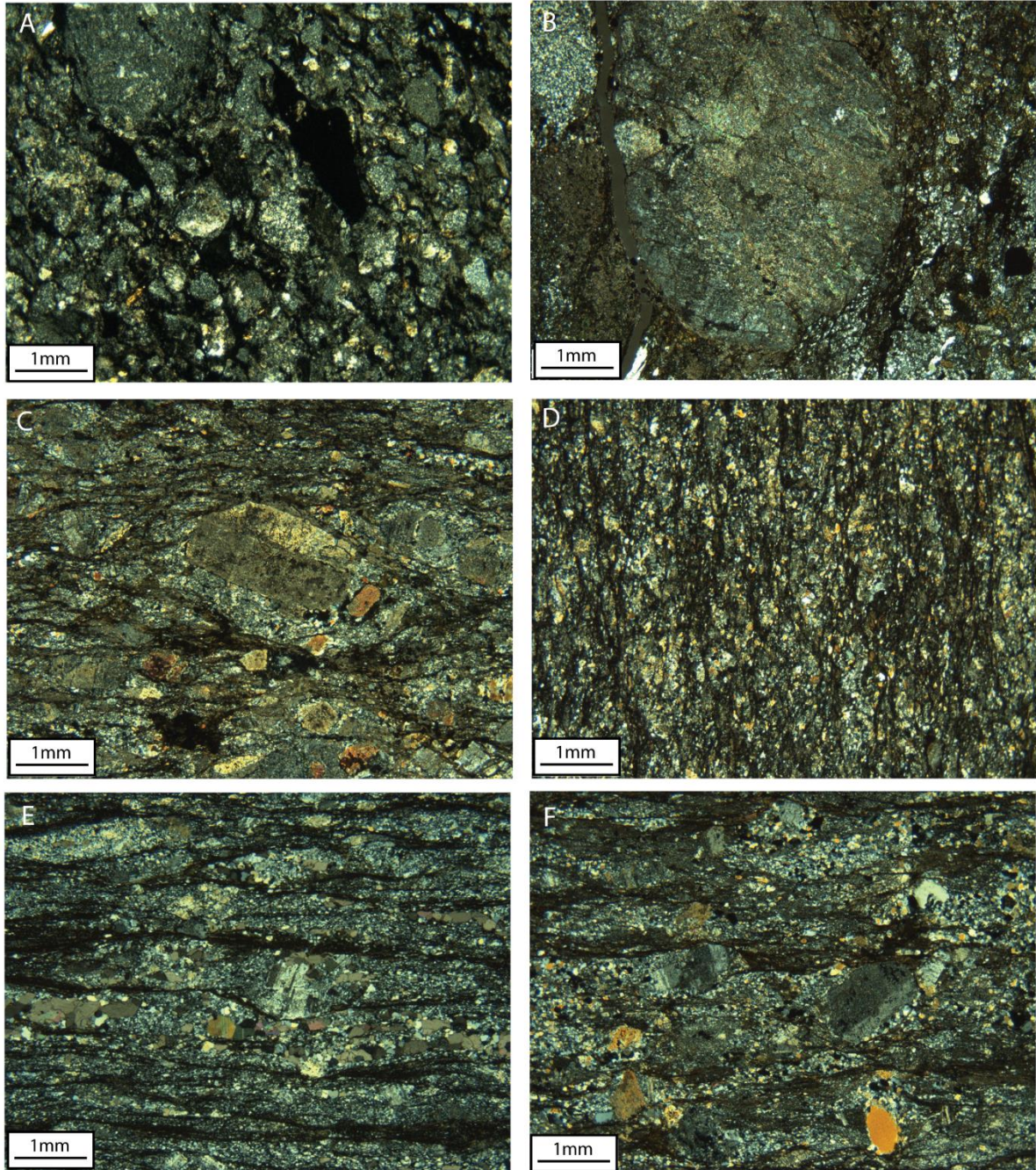


Figure 4.3: CPL photomicrographs illustrating the range of textures observed in the Kibalian metasedimentary volcano-sedimentary conglomerates. A (Upper left); Sample ZB10: irregular rounded to sub-rounded clasts consisting of reworked sedimentary material with interstitial chlorite zones. B (Upper right); Sample Kissanga South 1: Large rounded clasts consisting of reworked sedimentary material hosted in a groundmass composed of fine quartz and chlorite/aluminoceladonite. C (Middle left); Sample K18: stretched and elongated 0.5-2 mm clasts composed of large angular feldspar crystals and fine quartz, clasts are separated by thin chlorite-rich bands aligned parallel to the direction of deformation. D (middle right); Sample K19: 0.5mm stretched and elongated irregular quartz-rich clasts with parallel orientated phyllosilicate-rich intraclast areas. E (Bottom left); Sample Anzi 1: Highly elongated quartz clasts composed of fine primary quartz and 0.5 mm feldspar crystals with extensive recrystallisation to secondary quartz. Deformed clasts form a series of parallel quartz 'bands' separated by dense chlorite/aluminoceladonite-rich layers. F (Bottom right); Sample Oere-1: Deformed quartz-feldspar clasts with interstitial chlorite/aluminoceladonite-rich layers. Rounded feldspar crystals occur at the edges of the clasts with quartz forming a trail extending away to the left.

Table 4.1: Representative EDS analysis of major mineral phases identified in lithologies of volcano-sedimentary origin within the Kibali granite-Greenstone Belt

Sample	Site	SiO ₂	TiO ₂	Al ₂ O ₃	FeO	MnO	MgO	CoO	K ₂ O	Na ₂ O	Total	Mineral
wt%												
K18	1-C	70.09		18.65						11.64	100.37	Plagioclase
K18	2-D	69.79		18.63						11.43	99.85	Plagioclase
K18	1-D	26.41		20.21	25.57		14.98	0.21			87.38	Chlorite
K18	2-M	35.70		25.73	12.94		7.82				82.19	Chlorite
K18	1-K	49.99	0.38	26.87	3.63		2.40		10.36		93.63	Al-celadonite
K18	2-O	48.77		26.85	4.10		2.44		9.44		91.61	Al-celadonite
K19	1-A	70.18		18.80						11.68	100.65	Plagioclase
K19	2-B	69.54		18.96						11.59	100.09	Plagioclase
K19	1-N	31.21	38.21	1.46	0.94						100.05	Sphene
K19	1-O	31.50	37.65	1.43	0.49						99.17	Sphene
K19	1-E	26.25		19.61	25.30		14.97	0.09			86.22	Chlorite
K19	2-E	26.18		19.57	25.20		14.72				85.66	Chlorite
K19	1-G	49.31		26.68	3.86		2.40		9.03		91.28	Al-celadonite
K19	1-J	49.14	0.67	27.28	4.12		2.21		9.99		93.42	Al-celadonite
Kis-S-1	1-E	69.32		18.34						11.90	99.56	Plagioclase
Kis-S-1	3-B	69.15		18.36						11.54	99.04	Plagioclase
Kis-S-1	1-F	23.21		18.93	39.89		4.15				86.18	Chlorite
Kis-S-1	3-H	24.04		19.09	40.95		4.13	0.26			88.47	Chlorite
Kis-S-1	1-O	46.84	0.45	26.59	6.16		1.18		10.04		91.26	Al-celadonite
Kis-S-1	3-O	47.30	0.28	26.62	6.30		1.29		9.91		91.71	Al-celadonite
Oere-1	1-E	70.16		19.01						11.59	100.76	Plagioclase
Oere-1	2-A	69.39		19.03						11.72	100.33	Plagioclase
Oere-1	3-L	26.96		21.47	27.70	0.30	12.30				88.73	Chlorite
Oere-1	3-N	26.22		20.98	27.64	0.29	11.90				87.03	Chlorite
Oere-1	1-O		98.89		0.40						99.29	rutile
Oere-1	2-O		99.71		0.56						100.27	rutile
Oere-1	1-L	47.50	0.54	29.43	3.44		2.01		9.42	0.31	92.66	Al-celadonite
Oere-1	2-G	48.44	0.71	30.02	2.73		1.70		9.83	0.37	93.80	Al-celadonite

4.3.1.2 Silicified Volcaniclastic rocks

Silicified volcaniclastic rocks are identified in the eastern part of the study area (Fig. 4.1) in the vicinity of the Kokiza gabbroic pluton (Fig. 4.1). The characteristics of the silicified volcaniclastics vary with proximity to the Kokiza gabbroic pluton. Distal to the Kokiza pluton the silicified volcaniclastics occur as pale white-grey, homogenous cryptocrystalline material hosting rare (but notable) well-formed 1 cm pyrite cubes. Adjacent to the Kokiza gabbro the silicified material consists of 10-40 cm angular-sub-angular lithic fragments set in a cryptocrystalline matrix (Fig. 4.4). The lithic fragments align along their long axis and in

places the larger fragments are imbricated, the direction of alignment/imbrication pointing away from the Kokiza gabbroic pluton (Fig. 4.4). The silicified cryptocrystalline material is composed of quartz (60%); equigranular 10-20 μm elongated sub-rounded crystals, and aluminoceladonite (40%); dark ‘fibrous’ masses with no individually discernible crystals (Fig. 4.4). The micaceous phases delineate a foliation not observable in hand specimen. The groundmass is cut by a number of late 0.25-0.5 mm quartz veins that are observed exploiting and cross-cutting the pre-existing foliation (Fig. 4.4).

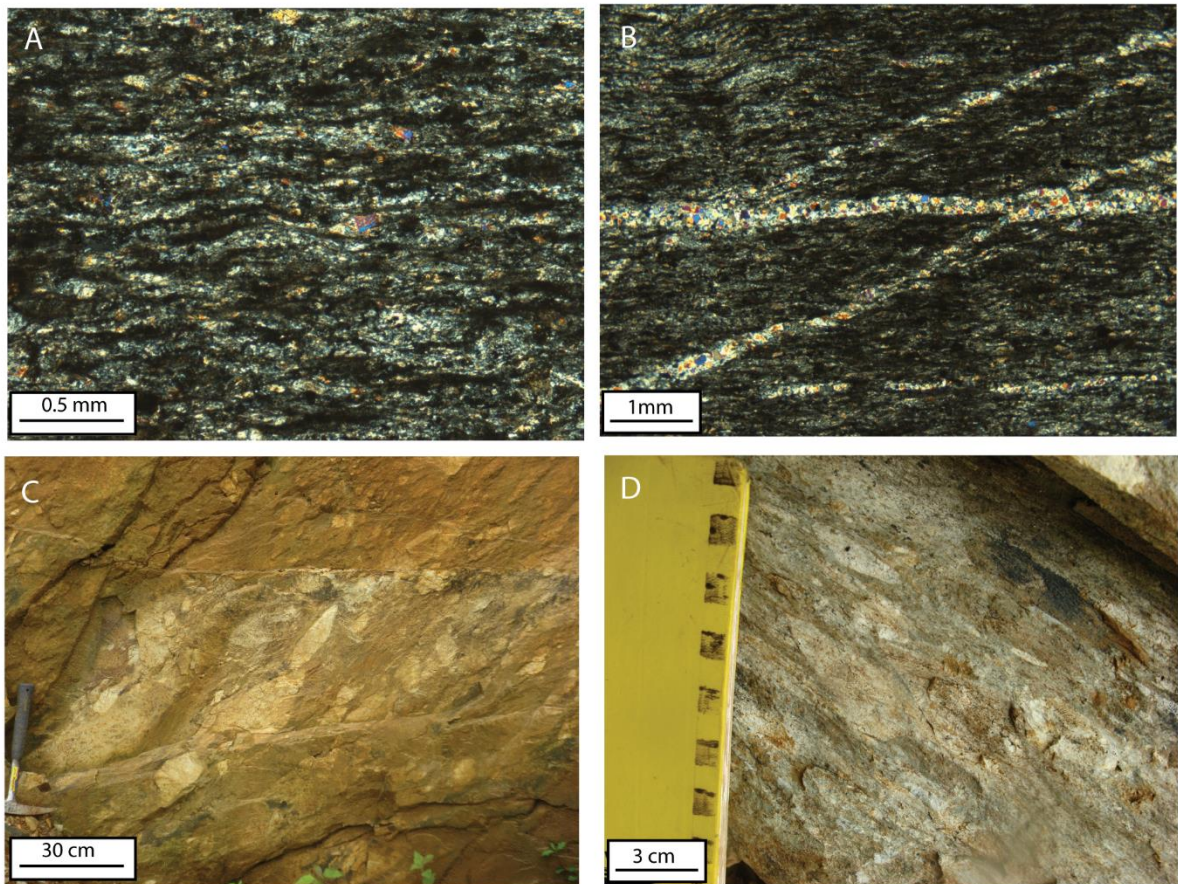


Figure 4.4: CPL Photomicrographs display mineral textures identified in the silicified volcanoclastic units. A (upper left); Sample Kokiza-1: <0.1 mm quartz crystals overprinted by ‘black’ bands composed dense aluminoceladonite with minor ankerite. Aluminoceladonite bands are approximately parallel with a distinct undulation; the quartz groundmass shows some alignment of crystals with long axis orientated parallel to aluminoceladonite bands. B (upper right); Sample 64_13; Fine quartz groundmass overprinted by aluminoceladonite bands (as observed in sample Kokiza 1) bisected by an array of sub mm veins composed of ~ 0.1 mm quartz crystals. C (Bottom left); Photograph displaying large imbricated fragments within a fine silicified groundmass adjacent to the Kokiza pluton. D (Bottom right); Photograph showing 1-5 cm deformed clastic fragments hosted in a fine silicified groundmass adjacent to the Kokiza pluton.

4.3.1.3 North Kibalian Schists

Schistose lithologies probably extend across the north central and eastern part of the KGGB, although due to low levels of exposure only three isolated outcrops are identified, H1 in the north east, H2 in the centre of the study area, and sample Makoro 2 in the eastern part of the study area (Fig. 4.1). The North Kibalian schists consist of white-yellow fine, crystalline material composed predominantly of 0.5-1 cm thick quartz-rich bands interspersed by thin (2-4 mm) layers of micaceous material (Fig. 4.5). The samples display a minor crenulation, this being best displayed where mica is abundant within the samples.

Petrological observations show sample H1 to be dominated by quartz (90%), occurring as irregular anhedral sub-angular to sub-rounded interlocking crystals, and rare discontinuous bands of biotite (10%), occurring as acicular to irregular sub-angular 0.25-1 mm crystals (Fig. 4.6). Rare plagioclase feldspar crystals, occurring as irregular sub-rounded 0.25-0.5 mm crystals with variably developed lamellae twinning, are identified within the quartz groundmass. These plagioclase crystals have been extensively recrystallised by the dominant quartz phase (Fig. 4.6). In comparison sample H2 is characterised by alternating bands of parallel orientated quartz (70%) occurring as marginally elongated to sub-angular 50-200 μm crystals, and Aluminoceladonite (30%), forming 20-500 μm thick bands of 10-40 μm acicular crystals with a 'flowing' crenulated appearance (Fig. 4.6).

4.3.1.4 Eastern Quartz-Biotite schists

Quartz biotite schists are identified at the eastern end of the study area outcropping in the area between the easternmost north-south orientated curving ironstone ridges (Fig. 4.1). The gneisses are tightly folded with folds ranging in size from 5 cm on hand specimen scale to 1m at outcrop scale with the folds being picked out by the prominent quartz-rich layers (Fig. 4.5). The quartz-biotite schists consist of fine-grained to crypto-crystalline minerals consisting of alternating bands of 0.25 cm to 5 cm quartz and 1-5 cm black-brown layers of mixed biotite-quartz composition (Fig. 4.6). The gneisses are composed of parallel-orientated quartz (40%), characterised by sub angular anhedral 50-500 μm crystals, plagioclase feldspar (10%), occurring as elongated sub-rounded anhedral 50-200 μm crystals, and biotite (40%); acicular 100-500 μm crystals forming 50-100 μm wide foliae (Fig. 4.6). The parallel bands of quartz-feldspar and biotite are tightly folded on the millimetre scale, this being most conspicuously visible in the behaviour of the biotite phase (Fig. 4.6). Quartz and feldspar crystal size increases significantly within the 'fold' hinges to up to five to times larger than in the general groundmass (Fig. 4.6).



Figure 4.5: Photographs displaying selected samples of the North Kibalian Schists and Eastern Quartz-Biotite Schists A (Upper left); Sample 116-28: Eastern quartz-biotite schist displaying tightly folded alternating quartz and biotite -rich layers. B (Upper right); photograph showing outcrop of the eastern quartz-biotite schist demonstrating tight folds, with folding defined by prominent quartz-rich layers (white-grey) that stand proud of the surface. C (Lower left); North Kibalian schists - cut section of sample H1 displaying quartz-rich (yellow-white) composition with thin undulating discontinuous layers of biotite defining layering and crenulation within the sample. D (bottom right); North Kibalian schists- cut section of sample H2 displaying poorly defined alternating layers of quartz-rich (red/yellow-white) and mica-rich (black-green) material.

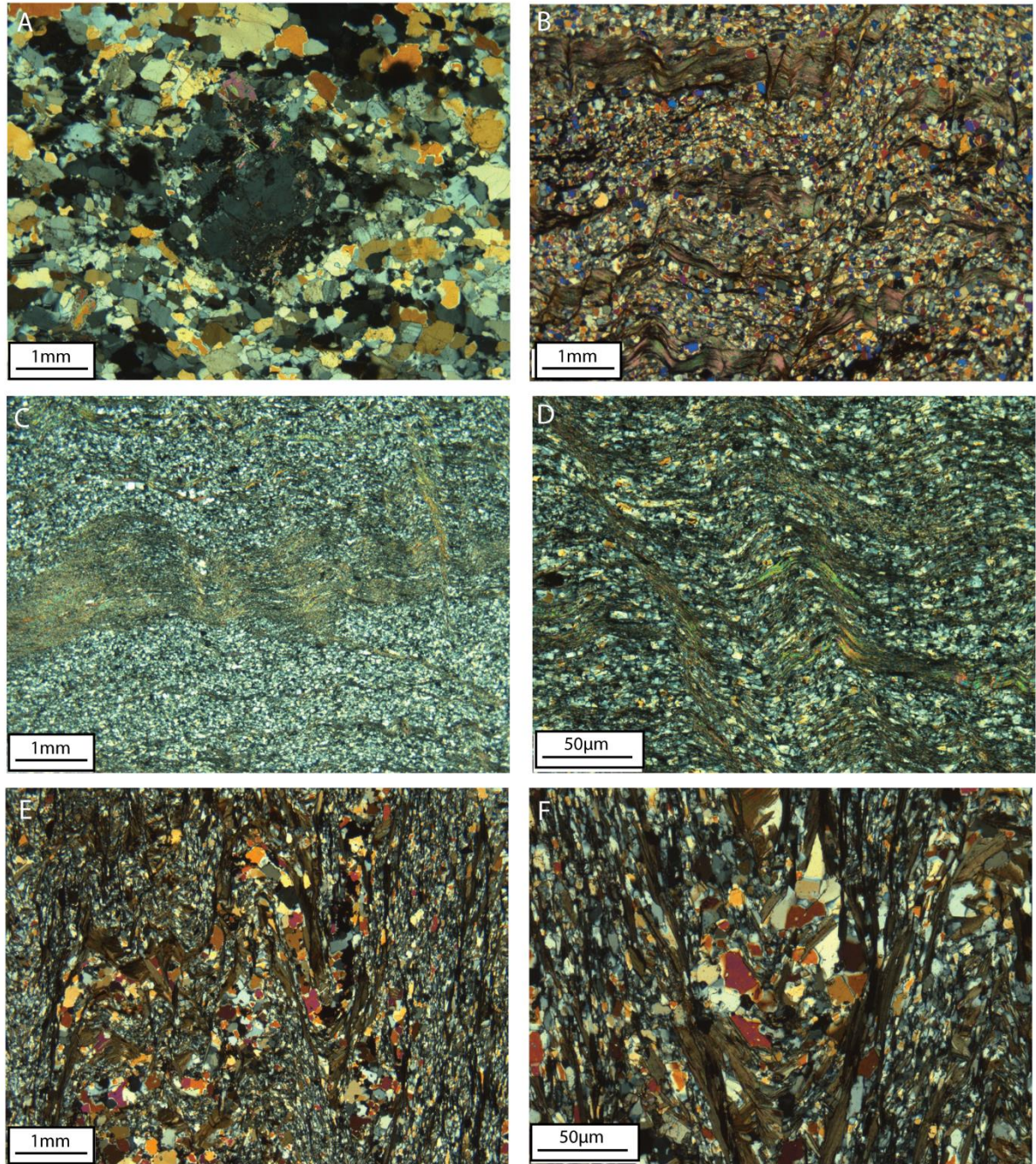


Figure 4.6: CPL Photomicrographs illustrating mineral textures identified in the high-grade meta-sediments in the Eastern part of the Kibali belt. A (Upper left); Sample H1: Quartz-feldspar-biotite schist- deformed plagioclase feldspar crystals hosted in a quartz/feldspar groundmass with rare aluminoceladonite and biotite crystals forming thin layers cutting across the sample parallel to the long axis of the quartz crystals. B (Upper right); Sample H2: Quartz-Aluminoceladonite schist- Alternating quartz and aluminoceladonite-rich layers with parallel crystal alignment and poorly developed crenulation preserved in the aluminoceladonite-rich layers. C (Middle left) and D (Middle right); Sample Makoro-2: Quartz-aluminoceladonite schist: Alternating layers of fine quartz and aligned aluminoceladonite, aluminoceladonite layers display a poorly developed crenulation. E (Bottom left) and F (Bottom right); Sample 116-28 – Quartz Biotite amphibolite: Layered quartz-biotite closed microfolds mirroring outcrop scale characteristics.

Table 4.2: Representative EDS analysis of major minerals identified in the North East Kibalian shcists (sample H1) and eastern Quartz-Biotite Gneiss (Sample 116-29)

Sample	Site	SiO ₂	TiO ₂	Al ₂ O ₃	FeO	MnO	MgO	CaO	K ₂ O	Na ₂ O	BaO	Cr ₂ O ₃	CoO	Total	Mineral
wt%															
116-29	1-E	65.40		22.11				3.83		9.60				100.94	Plagioclase
116-29	2-D	65.33		22.00				3.96		9.59				100.88	Plagioclase
116-29	1-I	38.21	2.04	17.12	15.45		12.57		9.07					94.46	Biotite
116-29	2-J	38.78	2.03	17.35	15.33		12.63		9.02					95.15	Biotite
116-29	1-N		53.06		44.63	1.59							0.32	99.60	Rutile
116-29	2-Q		52.75		45.45	1.48							0.20	99.89	Rutile
116-29	2-N	24.93		19.98	18.88		17.17					0.28		81.23	Chlorite
116-29	2-S	26.94		21.23	19.03		18.97					0.30		86.47	Chlorite
H1	1-C	65.40		18.17					14.76	0.53	0.63			99.49	Plagioclase
H1	2-D	66.47		20.80				2.69		10.10				100.07	Plagioclase
H1	1-B	65.85		21.46				2.86		10.04				100.21	Orthoclase
H1	1-R	65.90		18.13					15.04	0.62	0.57			100.25	Orthoclase
H1	1-F	36.89	2.24	16.56	21.33	0.37	7.81		9.04					94.24	Biotite
H1	2-S	39.19	2.16	16.86	20.09	0.40	7.99		8.34					95.03	Biotite
H1	2-P	47.82	0.44	29.62	2.55		1.55		10.17					92.17	Al-celadonite
H1	2-Q	48.14	0.37	27.97	2.99		2.01		10.21					91.69	Al-celadonite

4.3.2 Banded Iron Formations

Banded iron formations are some of the most distinctive units within the Kibali Granite-Greenstone Belt forming a series of elevated ridges rising up from the surrounding terrane. Banded iron formations are identified in multiple locations across the KGGB (Fig. 4.1), and defined on field observations and by a series of high magnetic susceptibility structures on airborne geophysics (Fig. 4.2). The ironstones occur as two parallel discontinuous sets of southwest-northeast orientated ironstone ridges on the southern margin of the belt, an M shaped set of ridges east the Kalimva granite (Fig. 4.1), an approximately W shaped set of ridges in the east central part of the belt and two north-south orientated curving sets of ironstone ridges in the far east of the belt (Fig. 4.1). Further banded iron formations have been identified in the Kibali Granite-Greenstone Belt outside of the area under investigation based on airborne geophysics, with the region immediately west of the study area containing abundant ironstone ridges (Fig. 4.1 and 4.2).

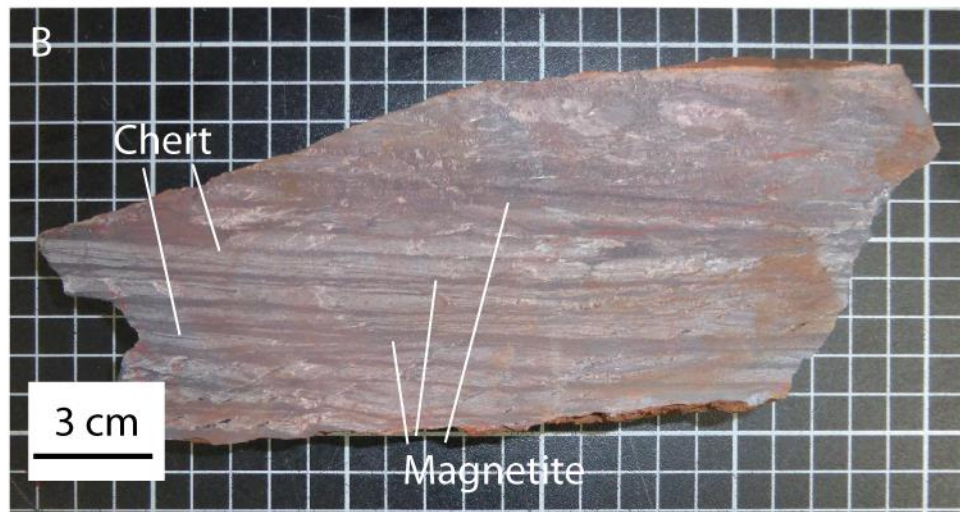
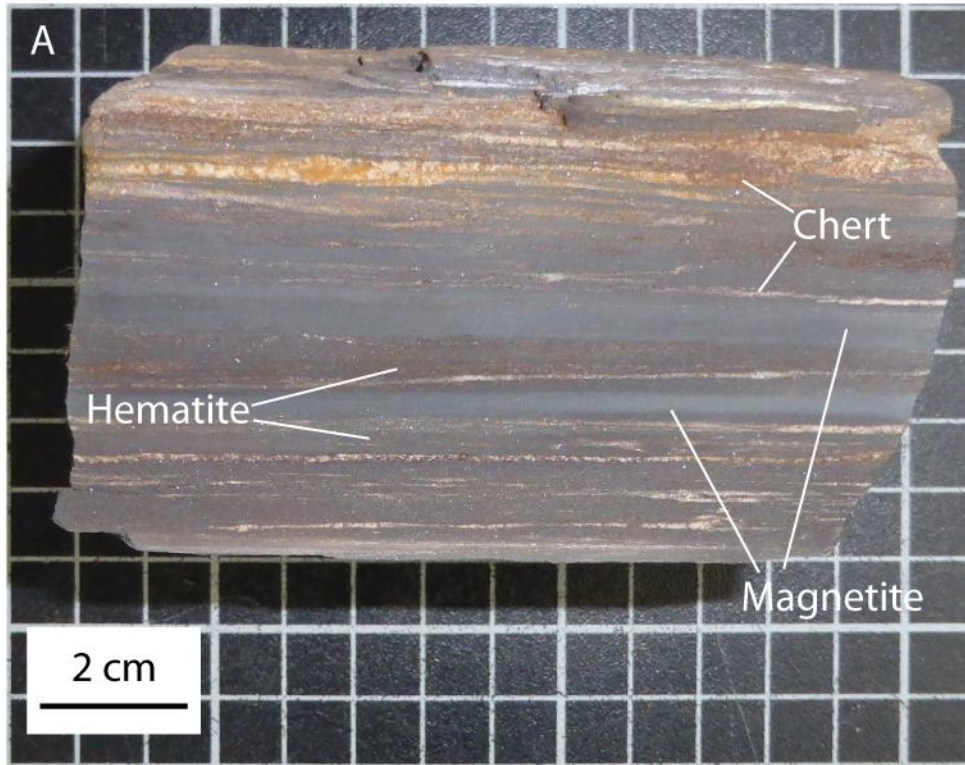


Figure 4.7: Photographs displaying selected examples of Ironstones from the Kibali Granite-Greenstone Belt. A: Sample PB12-KK01; banded ironstone consisting of layers of magnetite (dark grey), chert (white/yellow) and Hematite (Dark Red). Chert layers are host to weathered pyrite crystals (orange colouration). B: Sample PB12-M06; banded ironstone consisting of alternating layers of chert (grey/white layers) and magnetite (dark grey layers). Red colour in parts of the sample is the result of surface oxidization.

Banded iron formations typically consist of alternating Fe-rich and quartz-rich layers, the abundance of quartz being highly variable between individual samples (Fig. 4.7). Fe-rich examples are composed of 0.5-1 cm layers of magnetite and hematite with multiple layers of 1-4 mm quartz-rich 'chert' bands (Fig. 4.7 A). Quartz-rich layers are bedding parallel but vary in thickness along their length and may be discontinuous. These quartz-rich layers are host to sub-mm pyrite crystals (though heavily weathered) and display a strong association with hematite-rich layers, quartz-rich layers always being surrounded by hematite-rich layers. At maximum the quartz-rich layers are observed constituting approximately 70% of the lithology (Fig. 4.7 B). These quartz-rich lithologies consist of 0.5-2 cm thick crypto-crystalline quartz layers separated by 1-5 mm bands of fine crystalline magnetite (Fig. 4.7).

4.3.3 Kibalian Basalts

Basaltic material is identified across the study area, being present in the area around the Atekoma granodiorite (Samples AT1 and 5), around the north western edge of the Upper Congo Granitic massif (Samples KS2 and 82_22) and in an isolated sample (46_7) in the north of the study area (Fig. 4.1). Though only identified in a small number of outcrops the basaltic units are projected, based on airborne geophysical characteristics (basalts returning medium to high (green/red) values, Fig. 4.2), to extend under a significant part of the KGGB, forming a series of northwest-southeast orientated units across the western end of the study area (Fig. 4.1). The Kibalian basalts have a melanocratic, fine crystalline appearance in hand specimen with distinctive pillow structures identified in south of the Atekoma Granodiorite and in core from the Pakaka gold deposit.

The Kibalian Basalts display variable mineralogy. Sample 48-7, collected in the north of the study area (Fig. 4.1), is dominated by plagioclase feldspar, occurring as 0.1-0.25 mm interlocking rectangular laths, and amphibole, occurring as highly irregular space filling 0.5-3 mm amorphous masses occluding the feldspar mineral phase with significant late iron-magnetite phase occluding plagioclase and amphibole (Fig. 4.8). Basalts from the southern part of the belt are dominated by plagioclase, occurring as 0.1mm laths randomly orientated forming a dense groundmass, with amphibole occurring as highly irregular space filling crystals occluding the dominant plagioclase mineral phase (Fig. 4.8 C and D) or being completely absent (Fig. 4.8 E and F), the basalt being dominated by plagioclase feldspar in these cases. The basaltic lithologies display varying degrees of post crystallisation alteration, characterised by recrystallisation of plagioclase feldspar to aluminoceladonite mica. Mica alteration occurs as <0.1 mm acicular randomly orientated crystals (Fig. 4.8), replacing the feldspar laths, the amphibole component remains unaltered.

Alteration is extensive throughout the basaltic samples but it reaches peak intensity in the samples collected from the Atekoma area (Fig. 4.8 E) where the sample has the appearance of being completely altered, little of the original feldspar material remaining.

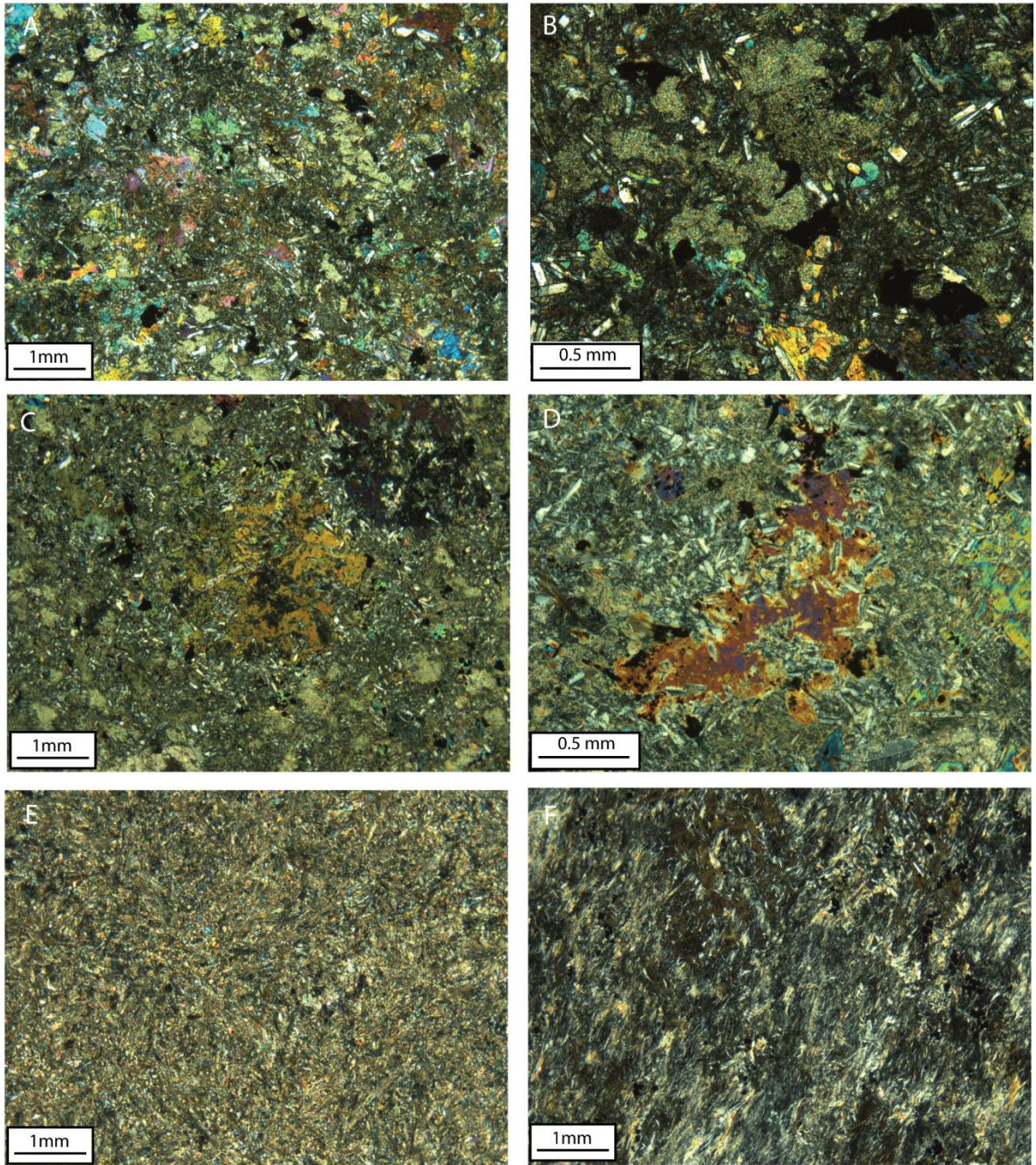


Figure 4.8: CPL Photomicrographs illustrating mineral textures identified in the Kibalian basalts A (Upper left) and B (Upper right); Sample 48-7 - Sub-aerial basalt: Irregular multi-coloured amphibole phenocrysts hosted within a dense groundmass composed of well-formed feldspar laths and amorphous amphibole C (Middle left) and D (Middle right); Sample 82_22 - Sub-Arial Basalt: Highly irregular amphibole space filling crystals occluding parts of a dense feldspar-amphibole groundmass. E (Bottom left); Sample Atekoma-1, Fine crystalline basaltic material extensively altered by late K-mica alteration, principally altering the plagioclase mineral component. F (Bottom Right); Sample Atekoma-5, Basalt:

4.3.4 Igneous intrusive units

4.3.4.1 Kokiza Gabbro

The Kokiza Gabbro is located to the west of the KCD gold deposit adjacent to Kokiza village (Fig. 4.1). The intrusion constitutes a small hill with few accessible outcrops that have been deeply weathered. The intrusion is known from two un-weathered samples of igneous material, Kokiza 3 and Kokiza 5, collected from the base and upper part of the hill respectively (Fig. 4.1). The intrusion is doleritic, consisting of coarse melanocratic crystals forming a homogenous interlocking mass (Fig. 4.8). Where heavily weathered the gabbro is dark green in colour. The intrusion is characterised by an amphibole-plagioclase-epidote assemblage (Fig. 4.10 and Table 4.3). Amphibole phenocrysts (40%) occur as irregular elongated sub-hedral 0.4-1 mm crystals occluding rare epidote (5%) which occurs as 100-200 μm subhedral sub-rounded crystals. The amphibole and epidote phases are hosted within a groundmass composed of plagioclase feldspar (55%) (Fig. 4.10 and Table 4.3) occurring as highly irregular anhedral space filling crystals. Extensive post-crystallisation alteration is present throughout the lithology with replacement of the plagioclase feldspar phase by epidote, occurring as 50-100 μm irregular anhedral sub-rounded crystals, and less commonly quartz which occurs as 50 – 100 μm irregular anhedral sub-rounded crystals (Fig. 4.9). On the western flank of the Kokiza intrusion a series of large boulders composed of alternating layers of tourmaline and quartz were identified (Fig. 4.9). This material is variable with individual bands ranging in thickness from 0.5-15 cm in thickness, with tourmaline crystals orientated perpendicularly to the layering.

4.3.4.2 Ambarau Granodiorite

The Ambarau Granodiorite intrusion is identified in the centre of the study area and is known from two locations, AMB1 and AT4 (Fig. 4.1). Although the two outcrops are separated by a significant distance they are considered to be part of a single intrusion based on similar mineral characteristics and a low susceptibility geophysical anomaly linking the areas where the samples were collected (Fig. 4.2). The samples are characterised by a two phase mineralogy comprising. 1-2 mm plagioclase feldspar laths with amorphous interstitial quartz (Fig. 4.8). Plagioclase feldspar phenocrysts (Fig. 4.10) range in composition from albite to oligoclase (Fig. 4.11 and Table 4.4), forming 0.5-2 mm euhedral laths and sub-angular crystals varying in abundance from 60% in sample AT4 to 20% in sample Amb-1 (Fig. 4.10). The groundmass is composed of quartz occurring as 200-400 μm irregular anhedral sub-rounded to sub-angular interlocking crystals, and biotite which forms 100-400 μm anhedral highly irregular space filling crystals (Fig. 4.10). The quartz phase varies in abundance, being inversely proportional with the plagioclase feldspar phase, ranging in abundance from 40 to 70%. Within sample Amb-1 quartz is principally observed replacing the feldspar mineral phase (Fig. 4.9).



Figure 4.9: Photographs displaying selected samples of the Kibalian intrusives A (Upper left); Sample K3 collected from the Kalimva intrusion, coarse crystalline leucocratic material with extensive weathering on the outer surfaces. B (Upper right); Sample S08; Section of drill core from the Sessenge intrusion consisting of fine crystalline translucent grey material with fine filament like structures of mica bisecting the core. C (middle left); Sample At-4; Coarse white-grey crystalline granodiorite with highly weathered surfaces. D (middle right); Sample Amb-1; Heavily weathered coarse crystalline white-grey granodiorite. E (Bottom left); Sample Kokiza-3; Fine to medium crystalline melanocratic dolerite collected from the upper part of the Kokiza intrusion. F (bottom right); Photograph displaying boulder identified on the western slope at the Kokiza intrusion consisting of massive tourmaline (black) and quartz (red) layers.

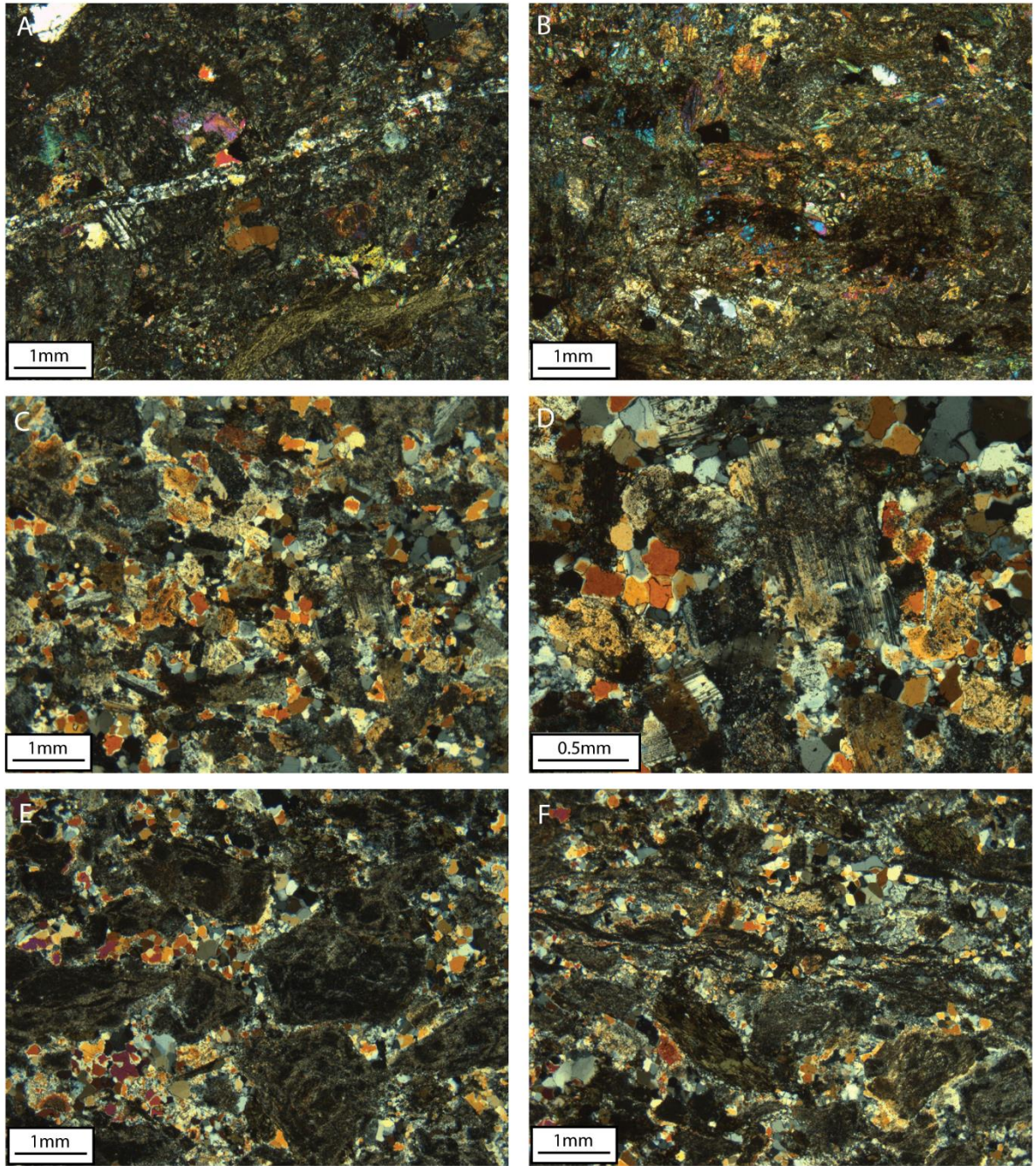


Figure 4.10: CPL Photomicrographs illustrating mineralogical and textural characteristics identified in the Kokiza and Ambarau intrusions. A (sample Kokiza-3) & B (Sample Kokiza 5); irregular amphibole and epidote hosted within a groundmass of highly altered plagioclase feldspar. C&D; Sample Ambarau-1, Highly altered plagioclase feldspar crystals hosted within a quartz-rich groundmass with extensive replacement of feldspar by secondary quartz (image D). E&F; Sample Atekoma-4, large altered plagioclase feldspar crystals hosted within quartz/secondary quartz groundmass. Image F shows mica-rich 'shears' that bisect sample At-4.

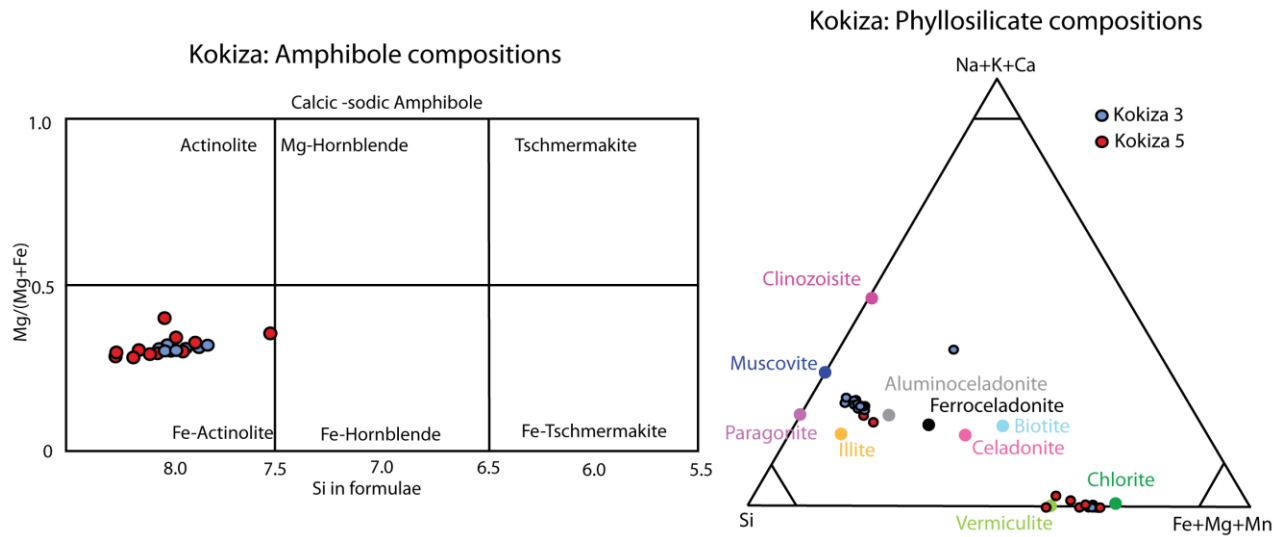


Figure 4.11: Discrimination diagrams displaying composition of amphibole and phyllosilicate mineral phases within analyses from the Kokiza gabbroic pluton

Table 4.3: Representative EDS analyses of the major mineral phases identified in samples from the Kokiza Gabbroic pluton

Sample	Site	SiO ₂	Al ₂ O ₃	FeO	MnO	MgO	CaO	K ₂ O	Na ₂ O	Total	Mineral
wt%											
Kokiza 3	2-B	69.03	19.09				0.55		11.88	100.56	Plagioclase
Kokiza 3	1-B	69.47	19.23				0.30		11.66	100.66	Plagioclase
Kokiza 3	1-H	56.40	0.89	12.98		16.04	12.64			98.94	Amphibole
Kokiza 3	2-D	56.09	0.95	13.09		15.68	12.40			98.22	Amphibole
Kokiza 3	1-N	37.68	22.05	12.86			22.41			95.01	Epidote
Kokiza 3	2-L	39.06	22.99	13.23			23.34			98.63	Epidote
Kokiza 3	2-N	27.67	19.53	24.67	0.48	16.11				88.47	Chlorite
Kokiza 3	2-O	26.94	18.84	24.12	0.45	15.85				86.20	Chlorite
Kokiza 3	2-P	49.84	31.09	1.91		1.70		10.03		94.56	Al-celadonite
Kokiza 3	2-Q	50.20	29.24	2.71		2.27		10.37		94.80	Al-celadonite
Kokiza 5	2-B	69.74	18.73						11.98	100.44	Plagioclase
Kokiza 5	1-D	58.23	0.89	12.59		16.47	12.71			100.89	Amphibole
Kokiza 5	2-C	57.08	0.71	12.45		16.50	12.54			99.28	Amphibole
Kokiza 5	1-N	38.72	22.40	12.88			22.96			96.96	Epidote
Kokiza 5	1-O	38.76	22.74	12.64			22.88			97.02	Epidote
Kokiza 5	2-J	27.77	18.80	23.88	0.51	17.04				88.00	Chlorite
Kokiza 5	2-L	27.45	19.56	25.06		16.34				88.41	Chlorite
Kokiza 5	2-O	50.29	29.74	4.10		2.04		9.28		95.45	Al-celadonite
Kokiza 5	2-P	54.47	24.24	4.61		3.94		9.51		96.77	Al-celadonite

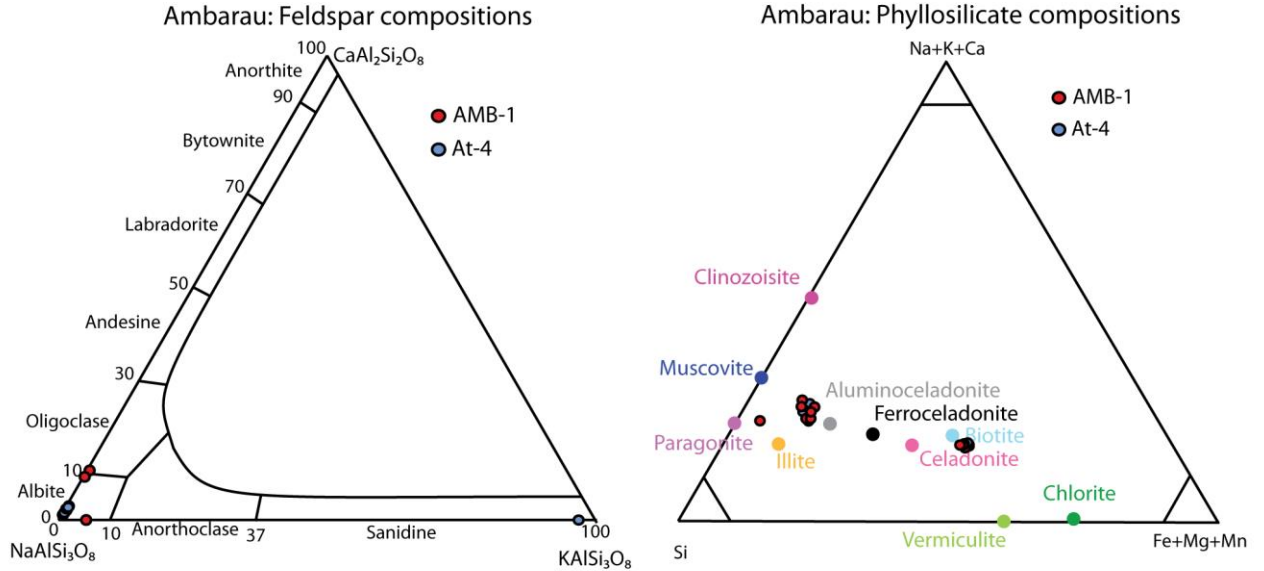


Figure 4.12: Ternary classification diagrams displaying the range of compositions identified in the feldspar and phyllosilicate mineral phases in the Ambarau Granodiorite

Table 4.4: Representative EDS analysis of the major mineral phases identified in the samples from the Ambarau Granodiorite

Sample	Site	SiO ₂	TiO ₂	Al ₂ O ₃	FeO	MgO	CaO	K ₂ O	Na ₂ O	Total	Mineral
wt%											
AMB-1	1-E	70.66		19.32			0.47		10.94	101.39	Plagioclase
AMB-1	2-G	69.90		18.82					11.76	100.48	Plagioclase
AMB-1	1-I	50.38		27.61	3.23	2.79		10.35		94.36	Al-celadonite
AMB-1	1-P	39.03	0.88	15.14	18.11	12.22		9.34		94.74	Al-celadonite
AMB-1	1-N	38.51		23.01	11.58		23.07			96.17	Epidote
AMB-1	2-N	40.58		23.80	8.62		21.16			94.17	Epidote
At-4	1-E	69.53		19.21			0.55		11.39	100.68	Plagioclase
At-4	2-F	67.68		20.36			1.98		10.87	100.89	Plagioclase
At-4	1-I	52.09		26.45	3.27	3.19		10.39		95.39	Al-celadonite
At-4	1-J	50.95		28.32	3.73	2.78		10.01		95.79	Al-celadonite
At-4	2-O	37.71		21.36	12.83		22.40			94.30	Epidote
At-4	2-M	37.71		22.76	11.70		22.47			94.65	Epidote

Further post crystallisation alteration is identified throughout the intrusion with the replacement of plagioclase feldspar phase by Al-celadonite (Fig. 4.12) occurring as 5-10 µm acicular crystals that form aggregates within the plagioclase feldspar (Fig. 4.10).

4.3.4.3 Kalimva Granite

The Kalimva Granitoid outcrops in the north west of the study area (Fig. 4.1), and comprises a series of small hills. The intrusion consists of leucocratic medium to coarse crystalline material (Fig. 4.9) characterised by a plagioclase-quartz-biotite assemblage with minor epidote and extensive alteration (Fig. 4.13). Plagioclase (Of average composition Ab:97.3 (Fig. 4.14 and Table 4.6)) is the dominant mineral phase accounting for 75% of the observed mineralogy forming 1-3 mm euhedral angular to sub-angular crystals. The interstitial spaces are dominated by 0.1-1 mm irregular anhedral quartz crystals which have a bi modal distribution of crystal size. Fine 10-20 µm crystals occur along the outer edges of the plagioclase feldspar crystals and large irregular quartz crystals occur where there is a greater 'open space' between the plagioclase crystals (Fig. 4.13). 50-200 µm euhedral angular crystals of biotite and irregular anhedral 200-400 µm space filling crystals of epidote are identified throughout the groundmass (Fig. 4.13). Quartz shows undulate extinction that may be indicative of having formed as an alteration assemblage during deformation. The presence of fine quartz crystals along the edge of the plagioclase feldspar crystals indicates a significant proportion of the quartz is the result of replacement of feldspar. Further post crystallisation alteration is present within the sample with 10-30 µm irregular anhedral epidote crystals, and 5-10 µm acicular aluminoceladonite crystals (Table 4.5), preferentially replacing the plagioclase feldspar.

Sample K4 was collected from the upper part of the intrusion, adjacent to a thrust plane that bisects the intrusion. This sample displays similar mineralogical characteristics, being comprised of a quartz-plagioclase-biotite assemblage (Fig. 4.12), but displays extensive deformation (Fig. 4.10). Sample K4 consists of 0.5-1.5 mm euhedral angular plagioclase crystals (average composition Ab:98 (Fig. 4.10 and Table 4.6)), set in groundmass composed of 10-20 µm equigranular sub-angular interlocking quartz crystals which is cut by irregular 'strands', composed of 5-10 µm acicular biotite and aluminoceladonite crystals (Fig. 4.13). The quartz and mica components are observed deforming around the feldspar crystals, though no significant rolling or deformation of the feldspar crystals themselves is noted. The large plagioclase feldspar crystals are observed being variably altered by quartz, similar in appearance to the groundmass, irregular 20-40 µm sub angular epidote crystals, and 5-10 µm acicular crystals forming aggregate masses of aluminoceladonite crystals (Fig. 4.13).

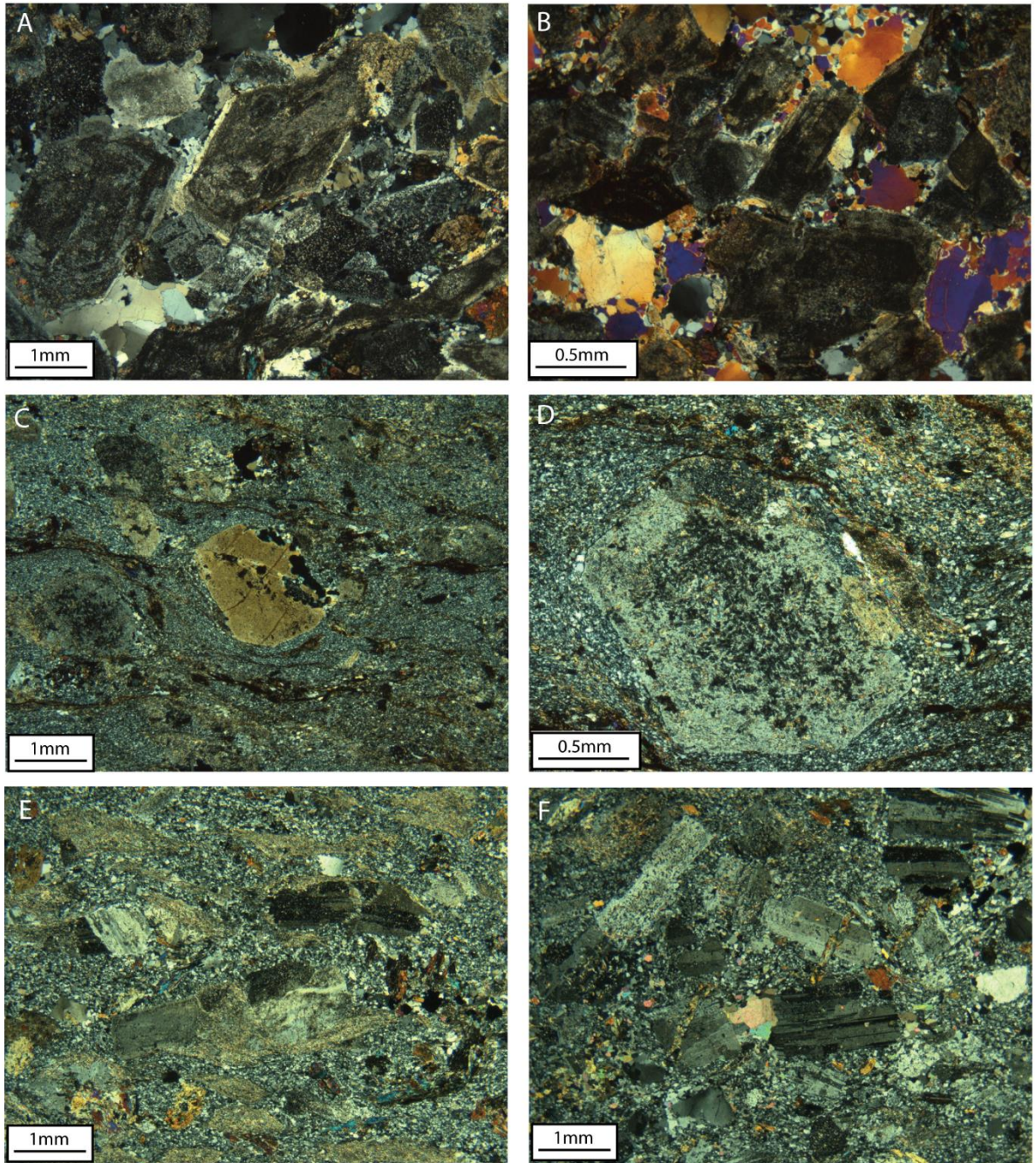


Figure 4.13: CPL Photomicrographs illustrating mineralogical and textural characteristics identified in samples from the Kalimva and Sessenge granitic intrusions. A (Sample MK01) & B (Sample MK02); Angular well-formed plagioclase crystals replaced by late K-mica with extensive development of secondary quartz between plagioclase crystals. C&D; Sample K4, Angular plagioclase feldspar phenocrysts hosted within a fine crystalline groundmass of quartz and feldspar. Thin bands of biotite cut across the sample and wrap around the plagioclase phenocrysts, shown in detail in Image D. E & F; Sample S08, partially altered plagioclase feldspar crystals hosted within quartz/secondary quartz groundmass with areas overprinted by sericite mica. Orientation of feldspar crystals imparts fabric to parts of the material, image E showing aligned feldspars with image F showing more randomly orientated crystals.

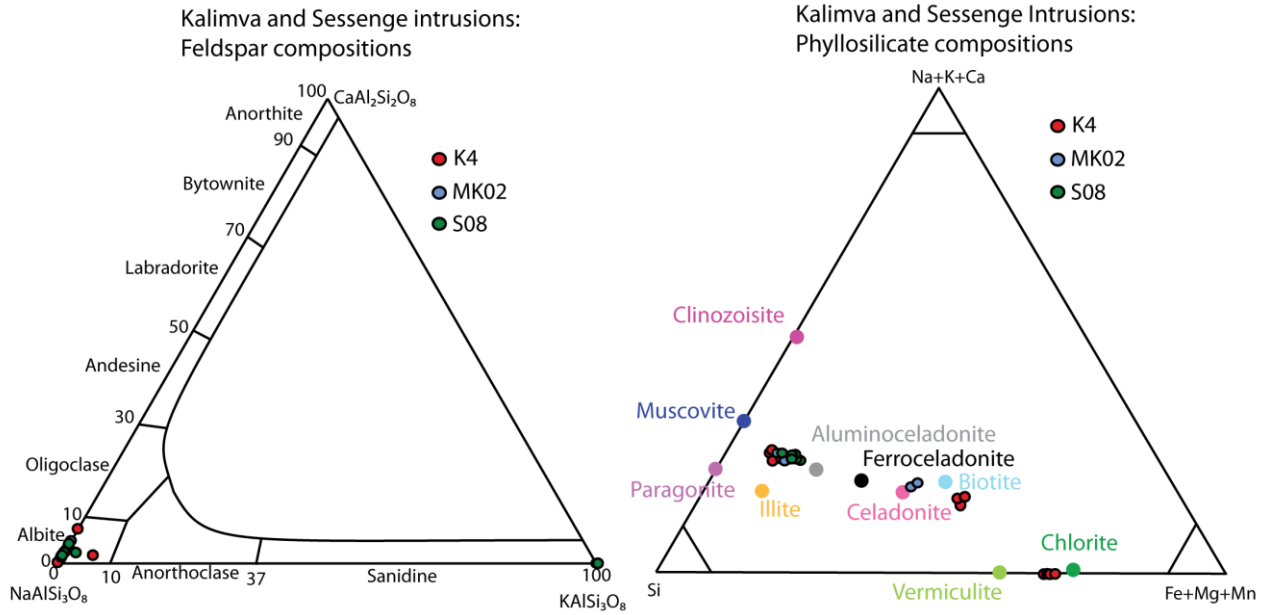


Figure 4.14: Ternary discrimination diagrams displaying compositional variations in the feldspar and phyllosilicate mineral phases analysed from the Kalimva and Sessenge Granitoid intrusions

Table 4.5: Representative EDS analysis of the major mineral phases identified in the Kalimva and Sessenge granitoids

Sample	Site	SiO ₂	TiO ₂	Al ₂ O ₃	FeO	MnO	MgO	CaO	K ₂ O	Na ₂ O	Total	Mineral
wt%												
K4	1-D	69.46		18.77						12.03	100.26	Plagioclase
K4	2-E	68.57		19.55				1.04		11.47	100.62	Plagioclase
K4	1-K	50.01		25.91	3.14		2.76		10.64		92.45	Al-celadonite
K4	2-I	51.68		25.90	3.26		3.00		10.78		94.62	Al-celadonite
K4	1-Q	39.11		25.73	7.78			23.21			95.84	Epidote
K4	2-M	40.00		25.88	7.53			23.16			96.57	Epidote
K4	2-Q	54.22		2.76	14.51	0.36	13.95	12.63	0.26	0.63	99.31	Chlorite
MK02	1-C	69.64		19.10				0.30		11.82	100.86	Plagioclase
MK02	2-E	69.12		19.39				0.90		11.35	100.75	Plagioclase
MK02	1-N	37.60	0.91	15.71	18.75		10.21	0.39	7.50		91.08	Al-celadonite
MK02	2-I	48.96		30.00	2.27		1.72		10.43		93.38	Al-celadonite
MK02	2-N	38.07		22.03	13.04	0.47		21.97			95.56	Epidote
MK02	2-O	38.52		20.81	14.38			22.94			96.64	Epidote
S08	2-G	69.53		19.02						11.70	100.26	Plagioclase
S08	2-L	69.96		19.24						11.54	100.74	Plagioclase
S08	2-M	50.49		24.36	3.97		3.54		10.39		92.74	Al-celadonite
S08	2-N	50.97		25.36	3.31		3.23		10.48		93.36	Al-celadonite
S08	2-P	38.45		21.58	13.09			22.65			95.78	Epidote
S08	2-R	38.37		23.24	10.56			22.98			95.15	Epidote

4.3.4.4 Sessenge Granite

The Sessenge granitic intrusion is identified in the south west of the study area, west of the KCD deposit and in close proximity to the Kokiza gabbroic pluton (Fig. 4.1). The Sessenge granite is characterised by a quartz-feldspar mineralogy with significant alteration and replacement by aluminoceladonite (Fig. 4.13). Plagioclase feldspar porphyroblasts form 0.5-1 mm sub-angular crystals displaying both lamellae and simple twinning and are set in a groundmass composed fine 10-20 μm equigranular sub-angular quartz crystals (Fig. 4.13). The plagioclase porphyroblasts are aligned along their long axis with the quartz groundmass deforming around the feldspar crystals, the two defining a distinct foliation throughout the sample. The granite shows significant alteration with abundant late aluminoceladonite mica (Fig. 4.13).

Aluminoceladonite occurs as 1-5 μm acicular crystals principally identified modifying the plagioclase feldspar crystals, extensively replacing the outer edges of the crystals with rare aluminoceladonite occurring within the plagioclase crystals. The aluminoceladonite phase is strongly aligned in the same orientation as plagioclase porphyroblasts and deformed quartz groundmass. The granite is cut by a number of highly irregular 1mm wide 'veins' composed of 'coarse' 0.1-0.2 mm irregular sub-rounded quartz crystals. These veins are host to small amounts of sulphides, pyrite being the dominant species occurring as highly irregular 0.05-0.5 mm crystals which is occluded by rare pyrrhotite, occurring as irregular angular 0.4 mm crystals. These veins are bisected by the late aluminoceladonite alteration.

4.4 Upper Congo Granite Massif

The Upper Congo Granitic Massif is one of the major constituents of the Bomu-Kibalian Block, which surrounds and hosts the Kibalian Granite-Greenstone Belts. The Kibali Granite-Greenstone Belt, located on the northern edge of the Bomu-Kibalian Block, is bordered by the UCG on its eastern, western and southern sides. In the vicinity of the study area the UCG is identified to the south of the KGGB, a 'lobe' of the UCG projecting northward, the KGGB extending around its northern and western edges (Fig. 4.1). The study area excludes the majority of this northward projection with only its western edge, comprising the igneous complex around Watsa, and isolated granitic massifs along its northern boundary available for study. The Watsa igneous complex consists of a central 'mafic' intrusion surrounded by a ridge of granodioritic material. The Watsa igneous complex is the most accessible part of the UCG in the study area and was the focus of the sampling (Fig. 4.1) programme. Further samples were collected from two large igneous massifs identified in the east of the study area on the boundary between the UCG and the KGGB. Sample locations are displayed in and figure 4.1 and further data is available in Appendix 1. The geological units identified in the Upper Congo Granitic Massif are discussed below.

4.4.1. Watsa-A

The central (low elevation) 'core' of the Watsa igneous complex is composed of coarsely crystalline melanocratic igneous material (Fig. 4.15) dominated by plagioclase feldspar with varying amounts of amphibole and pyroxene. The unit is compositionally variable with a broad trend of reduction in crystal size with increasing elevation and a corresponding transition in mineralogy from feldspar-amphibole-pyroxene at low elevations to feldspar dominated at high elevations, these variations in compositional and textural characteristics are examined below.

Samples collected at low elevations are characterised by a plagioclase-amphibole-pyroxene mineral assemblage (Fig. 4.16) although the proportion of each phase is highly variable. Plagioclase feldspar poor examples, such as sample WP03, are characterised by an amphibole (50%)-clinopyroxene (20%)-plagioclase feldspar (20%) mineral assemblage. Magnesian amphibole (edenite (Fig. 4.17)) is the most abundant and well-formed of the mineral phases present and occurs as 20-200 μm irregular rounded to sub-rounded crystals with generally poorly developed cleavage. A second species of amphibole, ranging in composition from hornblende to tschermakite (Fig. 4.17), is identified occurring in the groundmass as 2-6 mm irregular anhedral masses with well-developed 120 degree cleavage plains (Fig. 4.16). That the second amphibole phase crystallised late in the sequence, is shown by it occluding the edenite and plagioclase phases. Plagioclase feldspar (Labradorite (Fig. 4.17 and Table 4.6) occurs as partially developed irregular sub-hedral 1-2 mm in size with prominent lamella twinning and frequently occluding the Edenite phase.

Clinopyroxene occurs as large 0.5-3 mm interstitial masses displaying irregular crystal morphology controlled by the pre-existing amphibole mineral phase. This morphology is similar to that of the hornblende-tschermakite phase, and is differentiated from the latter by its distinctive cleavage angles and colouration.

Plagioclase feldspar-rich rocks from low elevations, here characterised by Sample W7 (Fig. 4.16), display only rare amphibole and pyroxene. Plagioclase feldspar accounts for 90% of the mineral assemblage occurring as both groundmass and phenocrysts. Rare plagioclase feldspar phenocrysts, occurring as 2-4 mm modified laths, are hosted within a groundmass dominated by plagioclase feldspar, occurring as 0.5-1 mm randomly orientated interlocking euhedral to subhedral laths displaying both simple and complex twinning. Amphibole constitutes approximately 10% of the observed mineralogy with crystals occurring as 20-50 μm subhedral sub-rounded irregular forms occupying interstitial positions between the interlocking feldspar groundmass. Secondary quartz, occurring as highly irregular interstitial material 0.5 mm in size and displaying undulating extinction indicating it formed during post crystallisation mineral phase.

At higher elevations feldspar becomes the dominant component and pyroxene minerals are no longer identified. Mineral assemblages consisting instead of plagioclase feldspar-amphibole \pm epidote (Fig. 4.15 and Table 4.6), the proportion of each phase varying between samples. Feldspar 'poor' varieties, here represented by Sample WP02, consist of plagioclase feldspar (60%) and amphibole (30%) with minor epidote (10%). Plagioclase feldspar occurs as 1-3mm randomly orientated interlocking euhedral feldspar laths. Amphibole (edenite) constitutes approximately 30% of the mineral assemblage, crystals being subhedral and ranging in size from 0.5-1 mm with well-developed internal cleavages, occupying the interstitial sites between the feldspar crystals. Minor epidote is also identified within the sample occurring as irregular subhedral crystals 1-3 mm in size and displaying a similar habit to the interstitial amphiboles. Feldspar 'rich' examples, here represented by Sample W5 (Fig. 4.16), consist of interlocking feldspar crystals with interstitial amphiboles. High relief hornblende-tschermakite constitutes approximately 15% of the sample occurring as 0.5-1 mm irregular subhedral to anhedral crystals with a prominent fracture and poorly developed internal cleavage and is identified throughout the sample. This edenitic amphibole is occluded throughout the sample by plagioclase feldspar which is the dominant mineral phase within the sample comprising approximately 80% of the observed mineral assemblage, dominating the groundmass. Feldspar crystals are 1-3 mm subhedral to euhedral laths with well-developed internal lamella twinning. The feldspar crystals form a randomly orientated interlocking crystal mass. A second late sodium-bearing amphibole phase is identified, accounting for approximately 5% of the mineral phases, within the groundmass occurring as highly irregular 1-2 mm anhedral masses occupying interstitial spaces between the feldspar groundmass.

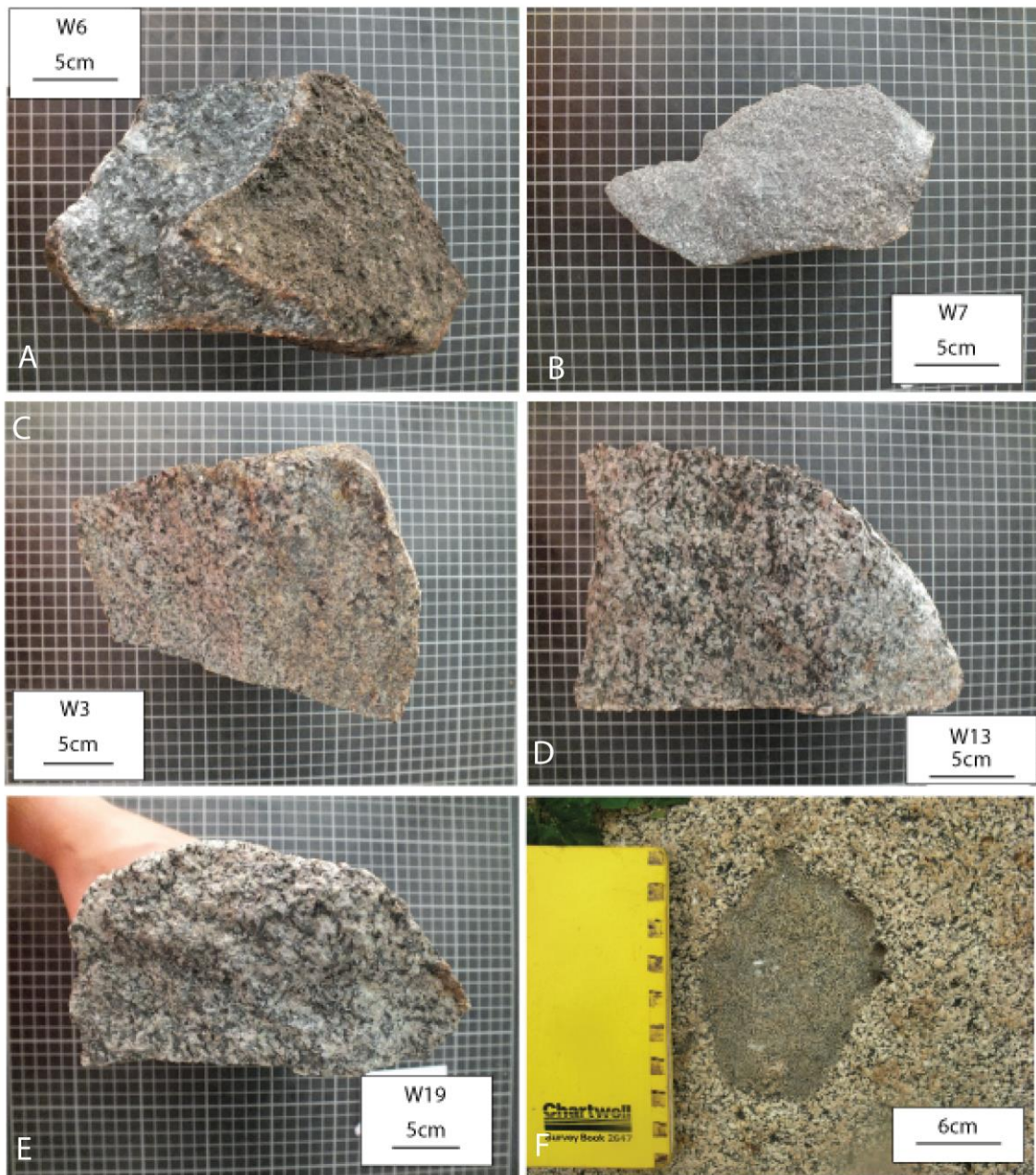


Figure 4.15: Photographs displaying selected samples from the Watsa-A and Watsa-B intrusive bodies. A (upper left); Sample W6: Coarse crystalline dark grey interlocking pyroxene crystals with minor coarse white feldspar collected from the lower elevations of the Watsa-A intrusive body. B (Upper right); Sample W7: Coarse crystalline grey pyroxene and white interlocking feldspar crystals collected from the higher elevations of the Watsa-A intrusive body. C (middle left): Coarse crystalline white-grey granodiorite collected from the outlier of the Watsa-B above the Watsa-A lithology. D (middle right) Sample W13 and E (bottom left) Sample W19; Coarse crystalline white-grey granodiorite material collected from the northern and western parts of the Watsa B intrusion. F (bottom right); Photograph displaying enclave of fine crystalline melanocratic igneous material identified within an outcrop of the Watsa-B intrusion.

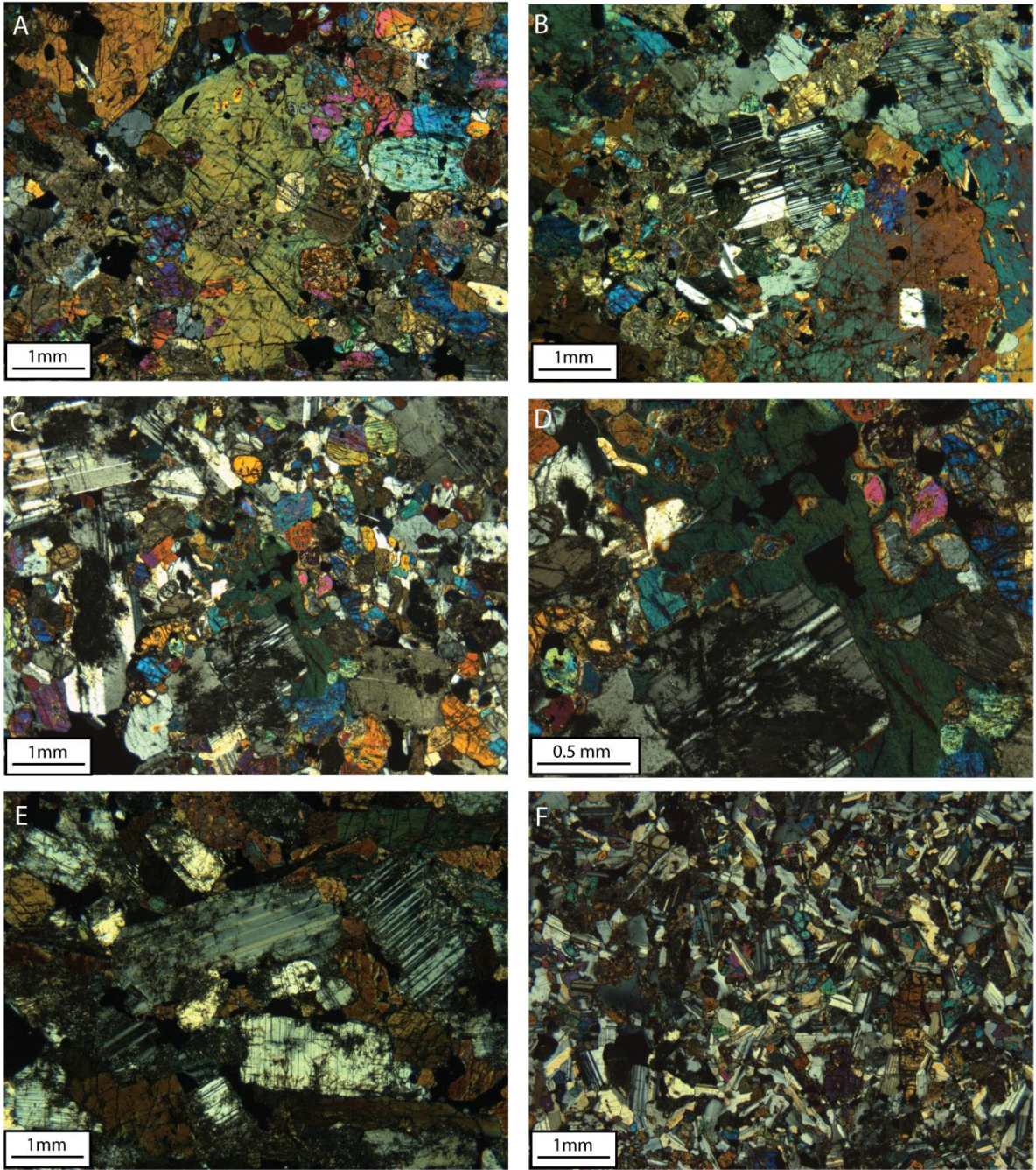


Figure 4.16: CPL Photomicrographs displaying mineralogical and textural characteristics identified within the Watsa-A unit. A&B; sample WP03 illustrating pyroxene-rich material at low elevations within the Watsa-A unit, Irregular sub-rounded amphiboles are surrounded by abundant irregular large pyroxene crystals and rare irregular plagioclase feldspar crystals. C&D; Sample W7 illustrating plagioclase feldspar-rich lithologies from low elevations, Large euhedral plagioclase feldspar laths ocluding rounded amphiboles with minor interstitial irregular pyroxenes. E; Sample WP02, Interlocking plagioclase feldspar crystals with interstitial irregular amphiboles. F; Sample W5, Interlocking plagioclase feldspar crystals hosting irregular amphibole and epidote.

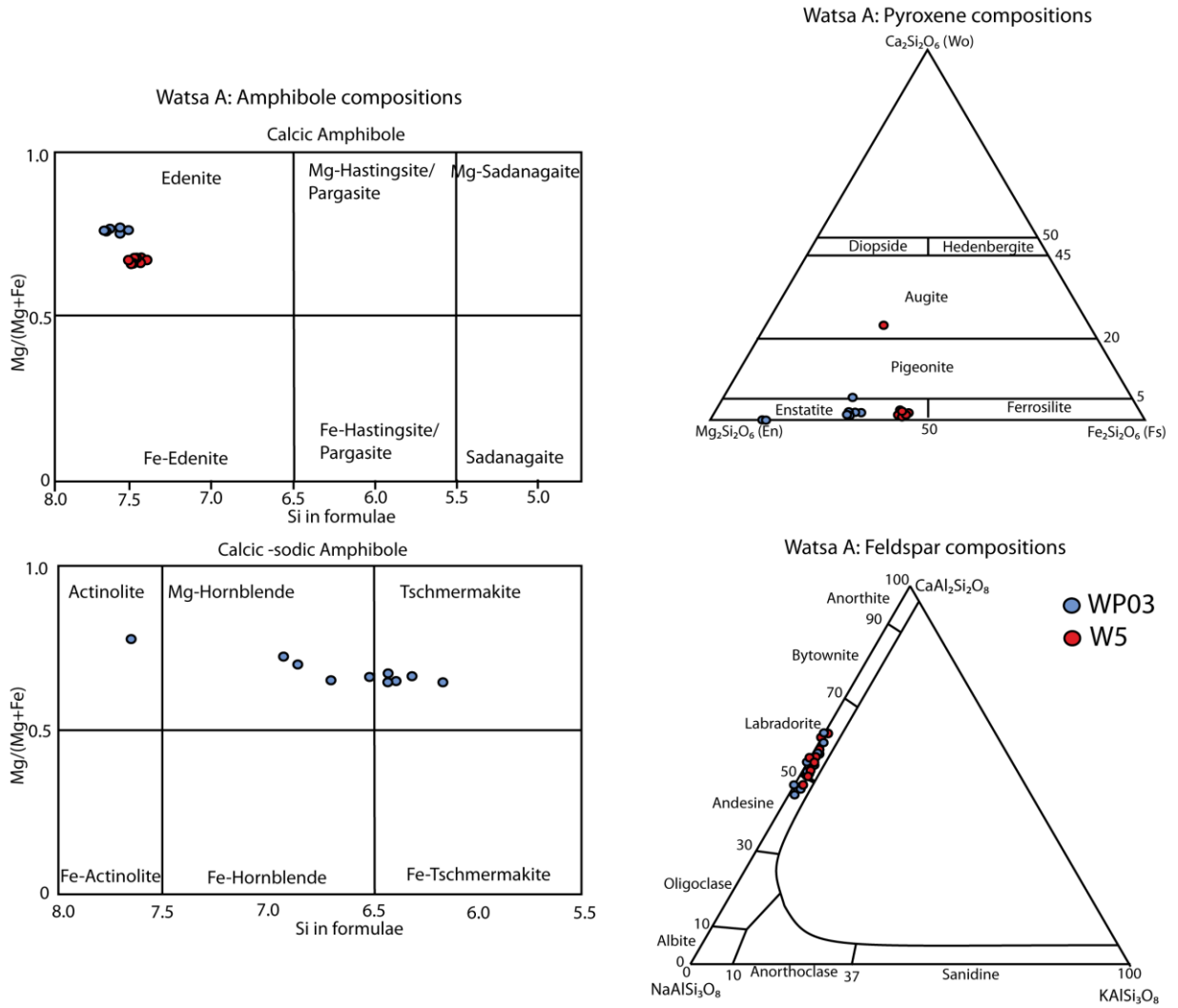


Figure 4.17: Discrimination diagrams illustrating compositional characteristics of mineral phases within the Watsa-A unit

Table 4.6: Representative EDS analysis of major mineral phases identified within the lithologies from the Watsa-A unit

Sample	Site	SiO ₂	TiO ₂	Al ₂ O ₃	FeO	MnO	MgO	CaO	K ₂ O	Na ₂ O	Total	Mineral
wt%												
WP03	1-C	56.56		26.56	0.31			9.68		6.00	99.11	Plagioclase
WP03	1-Q	55.21		28.33	0.34			11.36	0.22	4.87	100.33	Plagioclase
WP03	1-E	38.69		22.91	12.41	0.51		22.10			96.62	Amphibole
WP03	2-K	44.54	2.75	9.04	12.25		13.20	11.24	0.85	1.84	95.70	Amphibole
WP03	1-L	53.56	0.42	1.69	7.82	0.37	14.78	21.71		0.53	100.88	Pyroxene
WP03	2-J	52.99	0.54	2.01	7.77		14.22	21.86		0.61	100.00	Pyroxene
WP03	2-A	61.04		1.36	7.18		25.46				95.04	Chlorite
WP03	2-H	60.57		1.10	6.89		25.32				93.88	Chlorite
W5	1-D	56.57		27.45				11.21	0.30	5.27	100.80	Plagioclase
W5	2-D	54.31		28.62	0.34			12.50		4.67	100.43	Plagioclase
W5	1-G	52.78	0.34	1.45	10.90		12.77	21.39		0.47	100.10	Amphibole
W5	2-G	53.24	0.46	1.27	11.16		12.71	21.35			100.19	Amphibole
W5	1-O	52.50			26.56	0.58	18.70	0.69			99.03	Pyroxene
W5	2-P	56.68		1.32	15.53		15.35	11.44			100.32	Pyroxene

Significant post crystallisation aluminoceladonite alteration is present within the sample, preferentially replacing the plagioclase feldspar crystals within the groundmass (Fig. 4.16). All samples from the Watsa-A unit display a high proportion, up to 10%, of metals (including magnetite and pyrite) forming irregular angular to sub-angular crystals between the major silicate mineral components.

4.4.2. Watsa –B

The ‘mafic’ core of the Watsa igneous complex is surrounded by a rim of leucocratic, coarsely crystalline granodiorite intrusive rocks (Fig. 4.1 and Fig. 4.15). The rim is inferred to extend around the northern, eastern and southern edges of the Watsa-A unit. The Watsa-B unit displays consistent plagioclase feldspar-quartz-amphibole mineral assemblage across all samples (Fig. 4.18). Feldspars constitute 70% of the assemblage forming 2-8 mm euhedral to subhedral laths. Two distinct varieties of feldspar are distinguished based on the style of twinning and the presence of late aluminoceladonite alteration. Perthitic twinned orthoclase constitutes 40% of the feldspar crystals, these crystals being the largest and most well-formed with only minor late aluminoceladonite alteration. The remainder is composed of plagioclase feldspar, distinguished by extensive aluminoceladonite alteration and relic internal lamellae zoning (Fig. 4.18). This

heavily altered plagioclase shows variable morphologies with euhedral crystals being rare and is compositionally variable ranging from albite to oligoclase (Fig. 4.19 and Table 4.7).

Amphibole constitutes approximately 15% of the mineral assemblage, its characteristics varying between the samples. Amphibole within sample W2 occurs as well-formed euhedral to subhedral rectangular and kite shaped crystals with well-developed internal cleavage, the crystals predating and being occluded by the plagioclase feldspar phase. By contrast amphibole within samples W8 and WP06 is secondary post-dating the feldspar phase, filling the interstitial sites and is poorly formed with crystals typically being 0.5-1 mm sub-hedral to anhedral.

Quartz comprises approximately 10% of the samples and is typically identified within the samples in association with the plagioclase feldspar displays undulating extinction. Chlorite accounts for 5% of the mineral assemblage and is commonly identified in association with the secondary quartz mineral phase. Chlorite occurs as 0.05-0.2 mm irregular crystals which form aggregate masses of crystals up to 2 mm in size occurring around the edges of, and between, quartz crystals. Late aluminoceladonite alteration, consisting of 10-20 μm acicular crystals, is identified throughout the samples from the Watsa-B unit altering the well-formed plagioclase feldspar crystals.

Rare enclaves of fine crystalline melanocratic igneous material (Fig. 4.15 f) is identified within the Watsa-B intrusive unit. These xenoliths were only observed in a single location but were locally abundant. The nature of the outcrop in which the xenoliths were identified prevented proper sampling of this material, the enclaves occurring in the centre of broad flat and curved faces of outcrop, however this material appears to be of similar composition to the Watsa-C lithology discussed below.

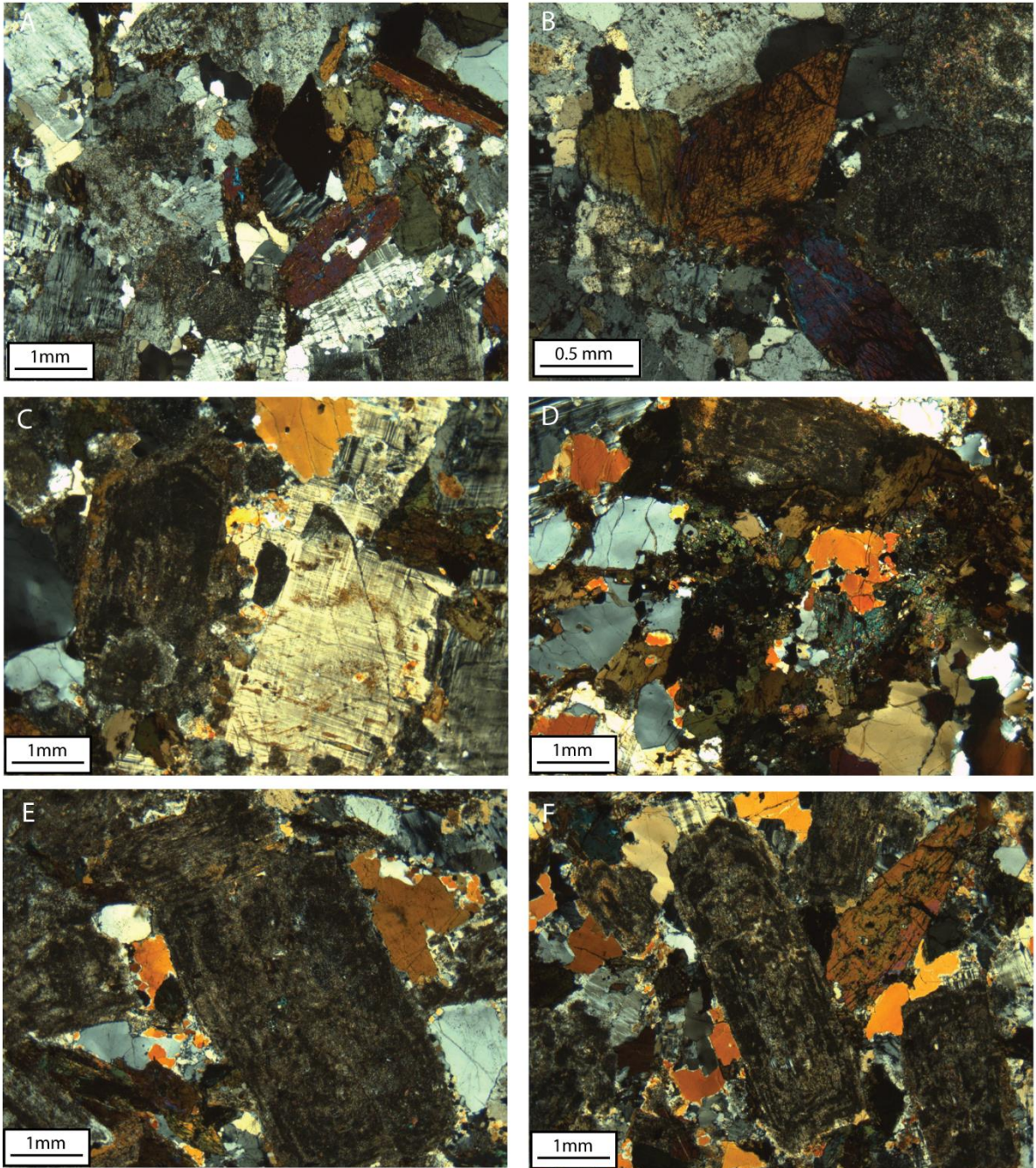


Figure 4.18: CPL Photomicrographs illustrating mineralogical and textural characteristics identified in the Watsa-B unit. A&B; Sample W2 euhedral kite shaped and simple twinned amphiboles occluded by irregular plagioclase (dark grey colour) and orthoclase feldspar (displaying perthitic twinning). C&D; Sample W8, feldspar rich groundmass composed of plagioclase (dark grey colour) and orthoclase (displaying perthitic twinning) with extensive replacement of feldspar by secondary quartz and late chlorite. E (Sample W13) & F (Sample W20) Interlocking plagioclase feldspar crystals with minor amphibole and extensive replacement of feldspar by secondary quartz. The dark grey colouration of plagioclase feldspar in all images is caused by extensive late aluminoceladonite alteration.

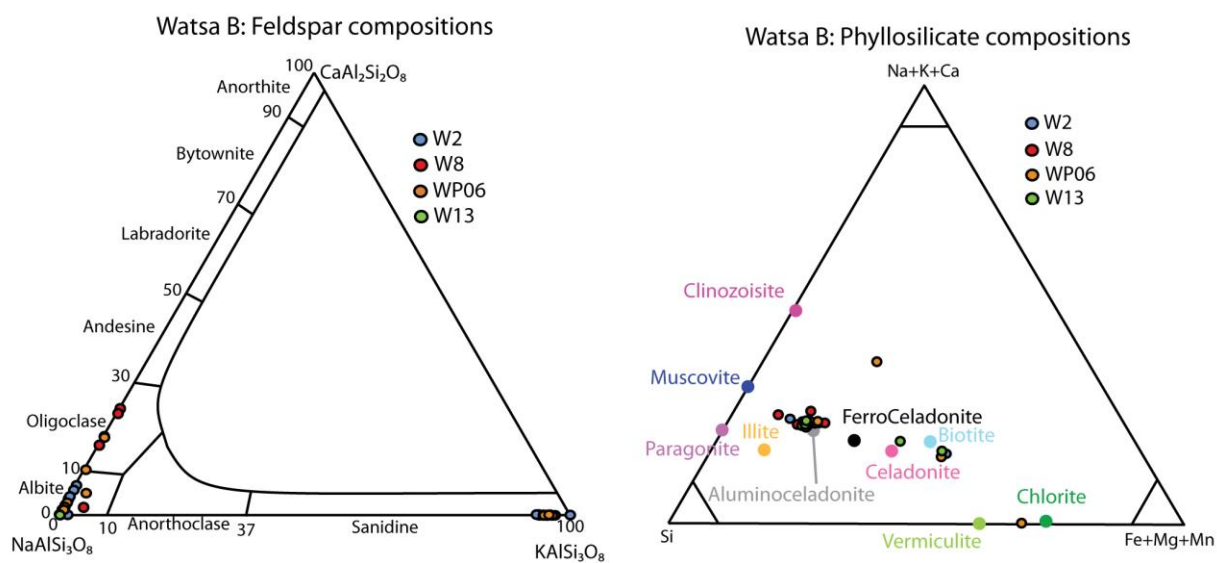


Figure 4.19: Ternary discrimination diagrams displaying compositional variation of selected mineral phases present in the Watsa-B unit

Table 4.7: Representative EDS analysis of the major mineral phases identified in the Watsa-B unit

Sample	Site	SiO ₂	TiO ₂	Al ₂ O ₃	FeO	MnO	MgO	CaO	K ₂ O	Na ₂ O	Total	Mineral
wt%												
W2	1-C	69.54		18.85				0.22		11.44	100.05	Plagioclase
W2	1-L	66.16		17.67					15.35		99.19	Orthoclase
W2	1-T	38.61		21.73	13.16	0.35		22.12			95.97	Amphibole
W2	1-R	50.37		25.37	4.65		3.17		10.60		94.16	Al-celadonite
W8	2-E	68.25		19.61	0.36			0.36	0.67	10.99	100.26	Plagioclase
W8	1-P	66.72		17.91					15.28	0.67	100.58	Orthoclase
W8	1-O	38.52		21.46	13.35	0.36		22.63			96.32	Epidote
W8	1-S	47.84		25.44	5.98		2.81		10.26		92.33	Al-celadonite
WP06	2-E	68.11		18.77				0.43		11.76	99.06	Plagioclase
WP06	2-K	48.50	1.05	5.71	14.60	0.43	12.96	11.58	0.56	1.35	96.74	Amphibole
WP06	2-N	65.20	0.39	17.59					15.07	0.44	98.68	Orthoclase
WP06	2-R	38.27		22.40	12.20			22.49			95.37	Epidote
WP06	2-Q	37.85		21.86	12.22			22.34			94.27	Chlorite
W13	2-H	70.11		19.06				0.23		11.69	101.10	Plagioclase
W13	2-M	38.81		22.12	12.56			22.69			96.17	Amphibole
W13	1-R	50.91	0.55	26.09	5.28		3.15		10.15		96.13	Al-celadonite

4.4.3. Watsa-C

Fine, crystalline leucocratic material (Fig. 4.21) is identified around the northwest edge of the Watsa igneous complex occupying the highest part of the 'ridge' around the core of the Watsa complex and the external slope on the western side of the igneous complex. The unit is known from two samples, W15 and W21, both samples being characterised an amphibole-plagioclase-sphene assemblage with minor quartz and extensive post-crystallisation alteration (Fig. 4.20 and Table 4.9). Plagioclase feldspar (45%); 0.2-1 mm euhedral to subhedral 'laths' of albitic composition (Fig. 4.22 and Table 4.9), and amphibole (45%); 0.5-2 mm subhedral to euhedral sub-angular to angular crystals ranging in composition from Fe-actinolite to hornblende (Fig. 4.22 and Table 4.9), dominate the sample forming an interlocking randomly orientated crystal mass (Fig. 4.20). The remainder of the groundmass is composed of sphene (5%); euhedral angular 100-300 μm rhombus crystals, and quartz; highly irregular anhedral 100-200 μm crystals, that where observed is recrystallising the feldspar component. Extensive alteration is identified throughout with chlorite and epidote observed replacing both plagioclase feldspar and sphene (Fig. 4.20).

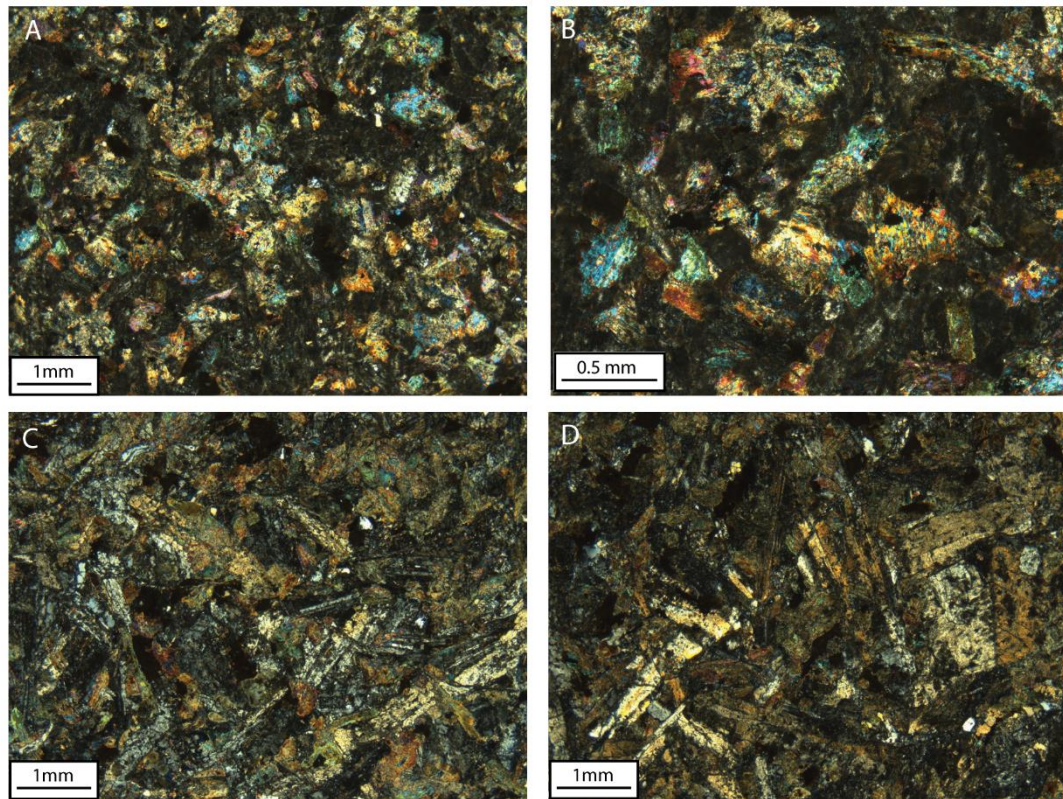


Figure 4.20: CPL Photomicrographs displaying textural and mineralogical characteristics identified in the Watsa-C unit. A&B; Sample W15, irregular amphibole crystals hosted within groundmass composed of highly altered plagioclase feldspar and minor sphene. C&D; Sample W21, Irregular Amphibole crystals hosted within groundmass composed of 1 mm feldspar laths with minor alteration by chlorite.

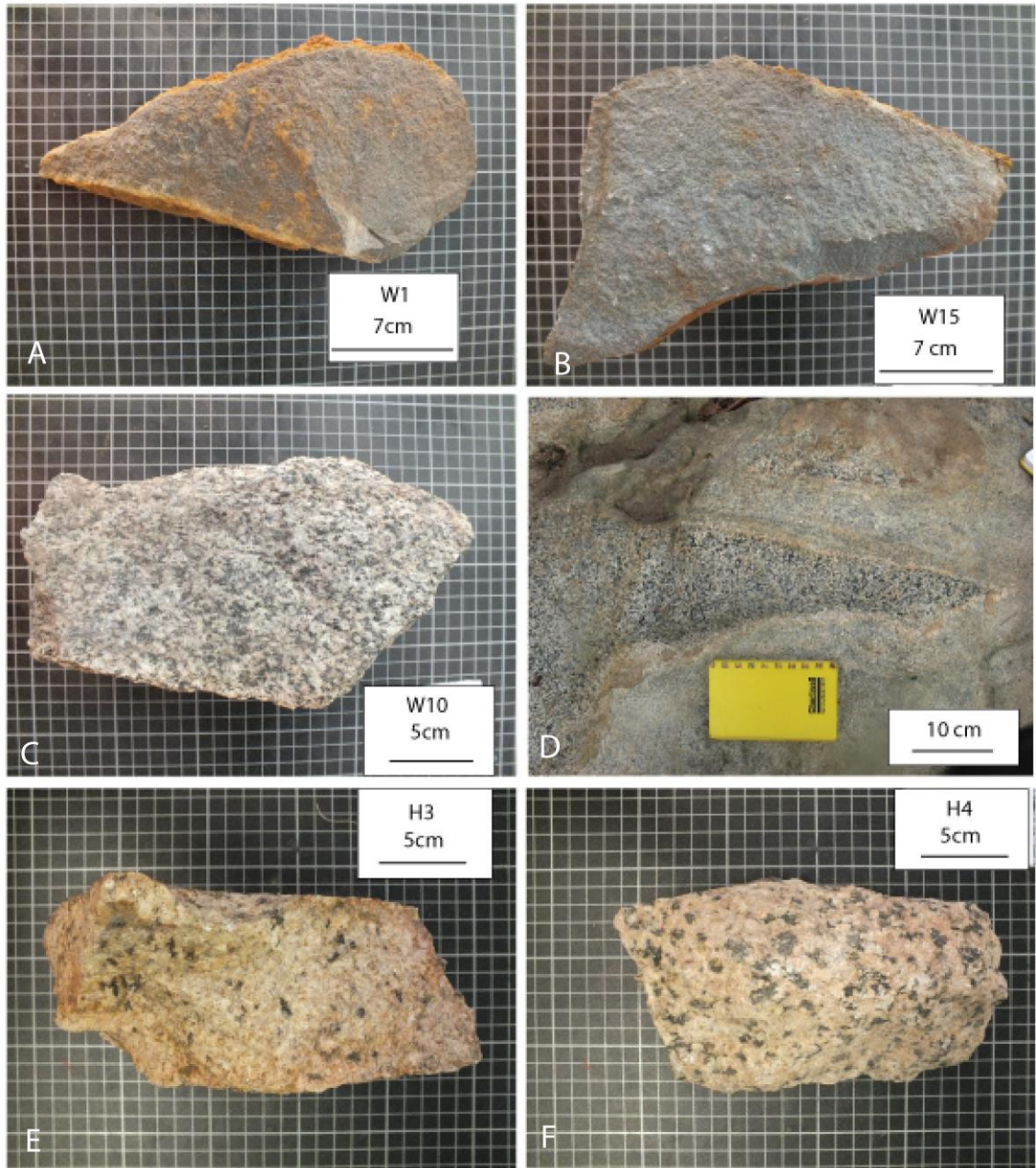


Figure 4.21: Photographs displaying selected samples from the Watsa C unit, The undifferentiated intrusives and boundary massifs in the Upper Congo Granitic Massif. A (Upper left), sample W1, and B (Upper right), Sample W15; Fine crystalline melanocratic igneous material collected from the Watsa-C intrusive body. C (middle left): Sample W10 :Coarse crystalline White-grey granitic material collected from the undifferentiated units to the south of the Watsa igneous complex. D (Middle right); Photograph showing the contact between two intrusive units from the undifferentiated intrusive lithologies to the south of Watsa igneous complex. Medium to coarse crystalline yellow-white granitic material on the right hand side of image intruding coarse crystalline white-grey granodiorite material on the left of the image. E (bottom left), sample H3, and F (bottom right), Sample H4: Coarse crystalline K-feldspar-rich granitic material from the 'boundary massifs' along the boundary between the UCG and the KGGB.

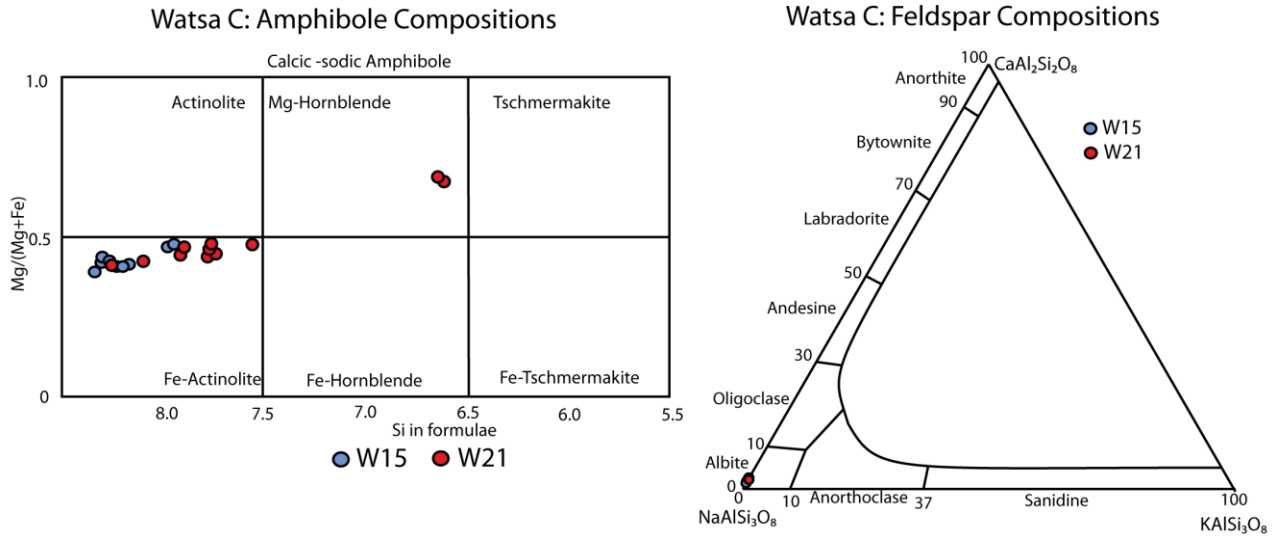


Figure 4.22: Discrimination diagrams displaying compositional characteristics of selected mineral phases in the Watsa-C unit

Table 4.8: Representative EDS analysis of the major mineralogical components identified in the Watsa-C unit

Sample	Site	SiO ₂	TiO ₂	Al ₂ O ₃	FeO	MnO	MgO	CaO	K ₂ O	Na ₂ O	V ₂ O ₅	Total	Mineral
wt%													
W15	1-B	69.38		19.33				0.38		11.38		100.46	Plagioclase
W15	2-C	69.84		19.12				0.37		11.50		100.83	Plagioclase
W15	1-F	54.50		2.12	16.25	0.40	12.83	12.36				98.46	Amphibole
W15	2-E	53.35		3.02	18.32	0.36	11.56	12.17				98.79	Amphibole
W15	1-K	31.48	39.22	0.98	0.30			28.52				100.51	Sphene
W15	2-K	31.72	37.79	1.51	0.72			28.32				100.06	Sphene
W15	1-Q	39.42		25.21	9.20			23.30				97.12	Epidote
W15	2-O	41.55		25.83	6.84			21.69		0.49		96.41	Epidote
W21	1-C	77.46		14.64				0.38		8.83		101.31	Plagioclase
W21	2-E	67.83		18.84				0.51		11.65		98.83	Plagioclase
W21	1-J	39.65		25.17	9.18			23.68				97.68	Amphibole
W21	2-N	53.01		2.72	17.32	0.33	12.18	12.16				97.72	Amphibole
W21	1-G	31.90	32.30	3.99	1.48			27.75			1.66	99.07	Sphene
W21	2-F	31.10	37.55	1.52	0.58			27.79				98.53	Sphene
W21	2-S		52.32		43.47	3.27						99.06	Rutile
W21	2-T		52.18		43.24	3.50						98.93	Rutile
W21	2-L	26.79		18.20	27.89	0.34	12.90		0.48			86.59	Chlorite
W21	2-M	27.14		18.00	28.04	0.38	13.00					86.56	Chlorite

4.4.4. Undifferentiated intrusive lithologies

The UCG south of the Watsa igneous complex is currently not separated into specific lithological units. The lithologies within this area are known from six samples which display similar characteristics though slight variations are noted. The majority of the samples (WP07, WP08, WP09, W9, W11) are characterised by a coarse crystalline plagioclase (80%)-amphibole (10%)-quartz (10%) assemblage (Fig. 4.21 and Fig. 4.23) and classified as granodiorites. Plagioclase feldspar (albitic in composition (Fig. 4.25 and Table 4.9) is the dominant mineral phase forming 1-5 mm euhedral-subhedral interlocking crystals. The interstitial spaces between the large plagioclase crystals are occupied by 0.5-1 mm angular amphibole crystals, rare highly irregular anhedral 1 mm space filling crystals K-feldspars displaying perthitic twinning, and 0.1-2 mm irregular anhedral space filling quartz crystals (Fig. 4.23). Quartz within the groundmass displays undulating extinction indicative of formation under deformation.

Granitic intrusive material, characterised by sample W10 (Fig. 4.22) is identified intruding granodiorite (Sample W9). The granites are characterised by a coarse crystalline leucocratic appearance (Fig. 4.21). The mineral assemblage is characterised by plagioclase-orthoclase-quartz with extensive recrystallisation by quartz, amphibole and aluminoceladonite (Fig. 4.23 and Table 4.9). Plagioclase (albitic composition (Fig. 4.23 and Table 4.9)) occurs as 1-3 mm angular to sub-angular crystals constituting 40% of the observed mineralogy. The plagioclase crystals occur in groundmass composed of 0.5-1.5mm irregular anhedral orthoclase crystals displaying perthitic twinning (Constituting 30% of the sample) and Quartz, irregular a 0.1-0.5 mm space filling crystals constituting 20% of the sample. The quartz phase displays undulate extinction in all observed crystals. Secondary amphibole has altered the granitic material post crystallisation, amphibole constituting approximately 10% of the mineralogy and occurring as 1-1.5 mm subhedral crystals within the groundmass. Both the granodiorites and granites display extensive post crystallisation alteration with the development of aluminoceladonite and epidote. In both phases alteration displays a similar mode of occurrence forming aggregates of irregular 10-20 μm crystals preferentially replacing the large plagioclase feldspar crystals.

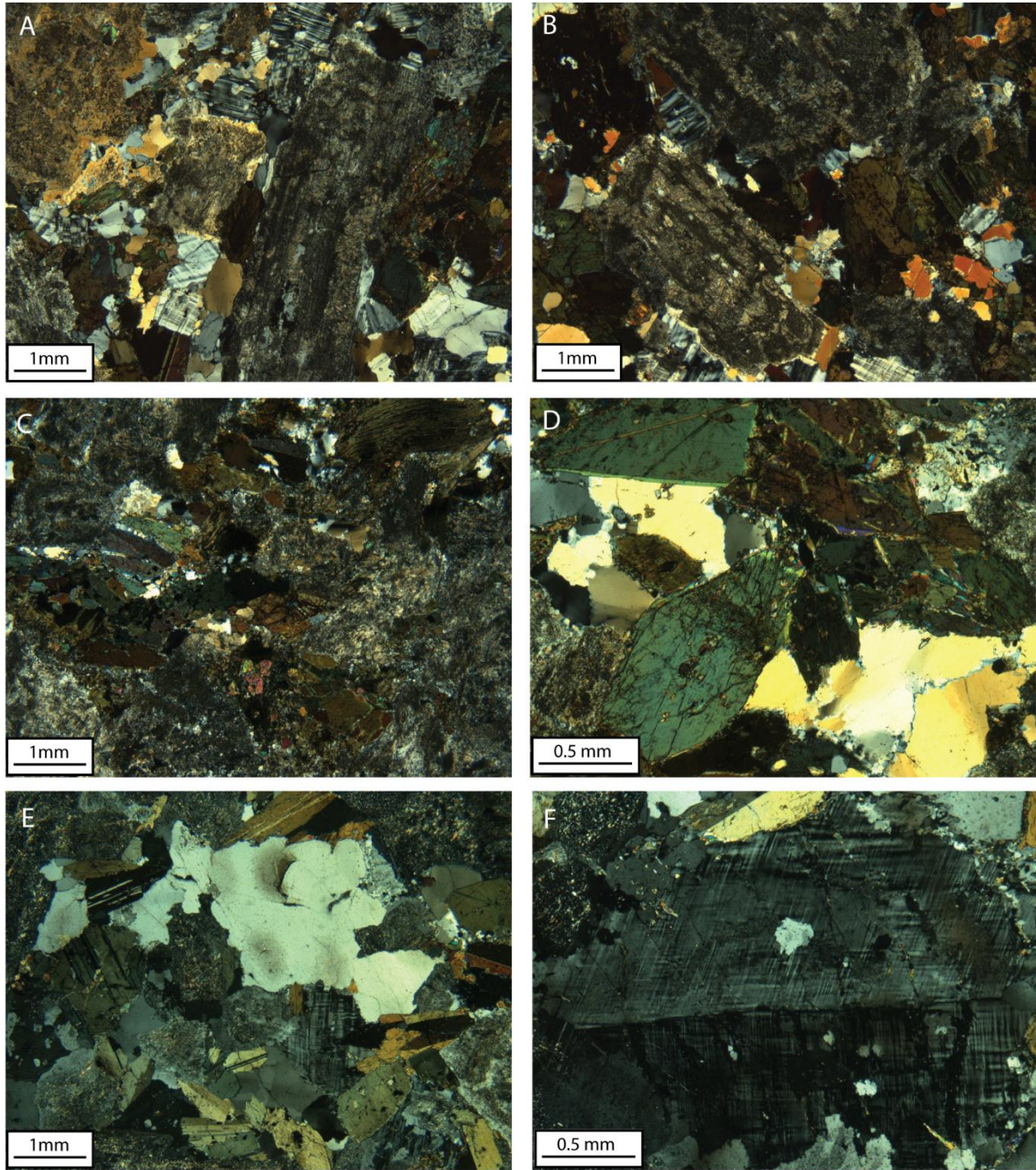


Figure 4.23: CPL Photomicrographs displaying mineralogical and textural characteristics identified in the 'undifferentiated' lithologies to the south of the Watsa igneous complex. A&B; Granitic material from Sample W10, Large plagioclase feldspar laths hosted in a groundmass composed of irregular orthoclase (perthitic twinning), secondary quartz and biotite with rare amphibole. C&D (sample WP07) and E&F (Sample WP09, Granodiorite material composed of kite shaped amphibole crystals, heavily altered plagioclase feldspar (dark grey mottled colour) and rare orthoclase (displaying perthitic twinning) with extensive secondary quartz replacing plagioclase and orthoclase feldspar. All samples display extensive late alterations of plagioclase feldspar by aluminoceladonite mica.

4.4.5. Boundary Massifs

Two large granitic massifs are identified along the northern margin of the Upper Congo Granitic massif adjacent to the inferred contact with the KGGB (Fig. 4.1). These massifs form steep sided plateaus that rise up from the surrounding terrane. Samples H3 and H4 were collected from atop two of these granitic massifs (Fig. 4.1) and consist of coarse crystalline quartz-plagioclase-K feldspar rocks (Fig. 4.21). The granitic massifs are characterised by an orthoclase (60%)-plagioclase (20%)-quartz (20%) assemblage with a number of minor phases and extensive late mica alteration (Fig. 4.23). Orthoclase phenocrysts (average composition 95Or:5Ab (Fig. 4.25) is the dominant phase occurring as large 1-10 mm euhedral to subhedral angular 'laths' displaying variably developed fine perthitic twinning (Fig. 4.24).

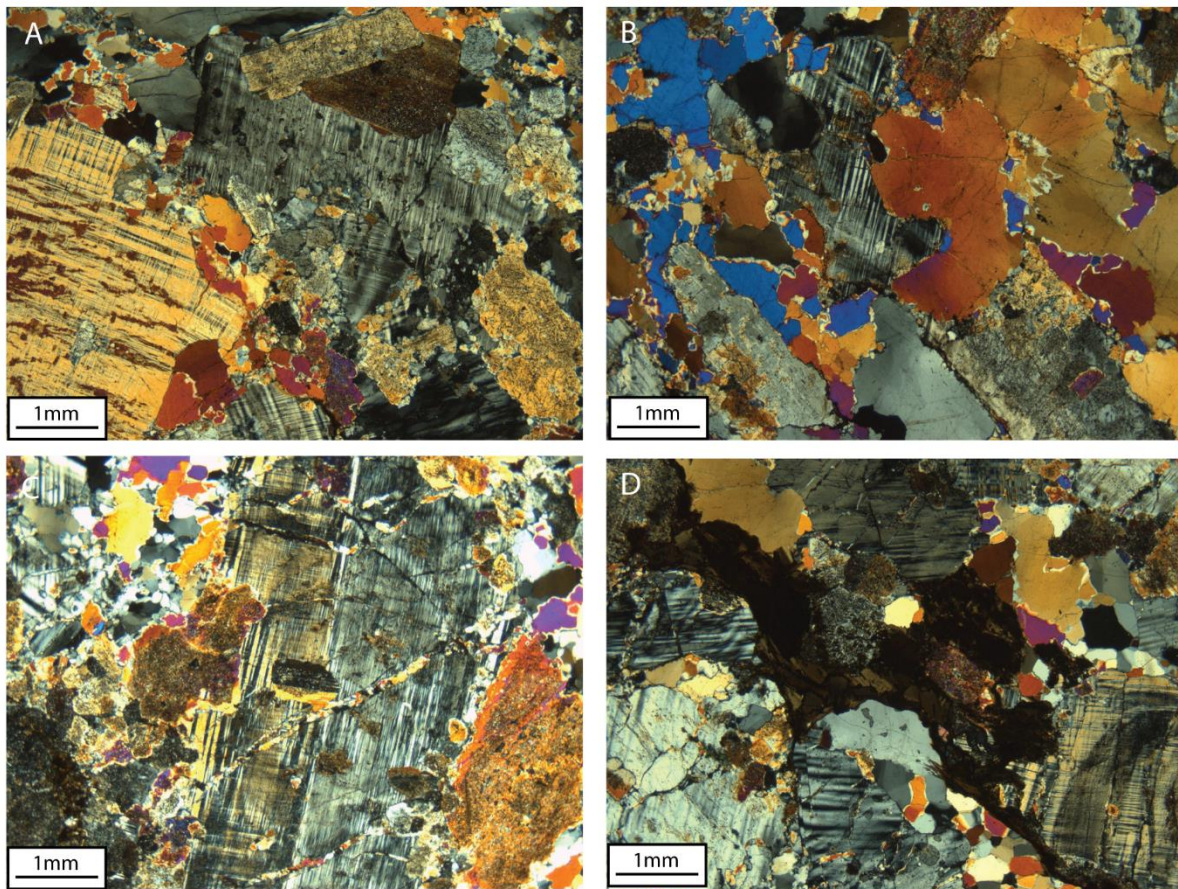


Figure 4.24: CPL Photomicrographs displaying textural and mineralogical characteristics identified within the boundary massif. A&B (Sample H3) and C&D (Sample H4), both samples display large irregular orthoclase phenocrysts (displaying variably developed perthitic twinning) hosted in a groundmass composed plagioclase laths and abundant secondary quartz which is replacing the plagioclase and orthoclase phases. Aluminoceladonite alteration is extensively modifying the plagioclase crystals giving them a mottled grey colouration in places and irregular chlorite (image D) occurring between feldspar crystals in association with secondary quartz

The orthoclase crystals are set within a groundmass composed of plagioclase feldspar, occurring as highly irregular anhedral 0.1-2 mm crystals of albitic composition (Fig. 4.24, 4.25 and Table 4.9), and quartz, occurring as irregular 0.1-2 mm anhedral crystals, forming space filling between the large orthoclase crystals (Fig. 4.24). The quartz within the groundmass displays two distinct morphologies, large highly irregular anhedral crystals in association with plagioclase feldspar within the groundmass and fine sub-rounded equigranular crystals occurring along the outer edges of the orthoclase crystals. Both morphologies of quartz possess distinct undulating extinction. Rare biotite occurs as isolated irregular 200 μm crystals within the groundmass, typically in association with the epidote and chlorite alteration phases. Post crystallisation alteration is extensive within the sample with epidote and chlorite being abundant. Epidote is highly variable ranging from 10-20 μm sub-rounded isolated crystals within the groundmass to 2-3 mm aggregate masses replacing the groundmass. Chlorite is commonly associated with epidote and occurring as rare 200 μm sub-angular crystals. Rare monazite is observed as fracture filling occurring along the edges of the epidote and mica alteration phases.

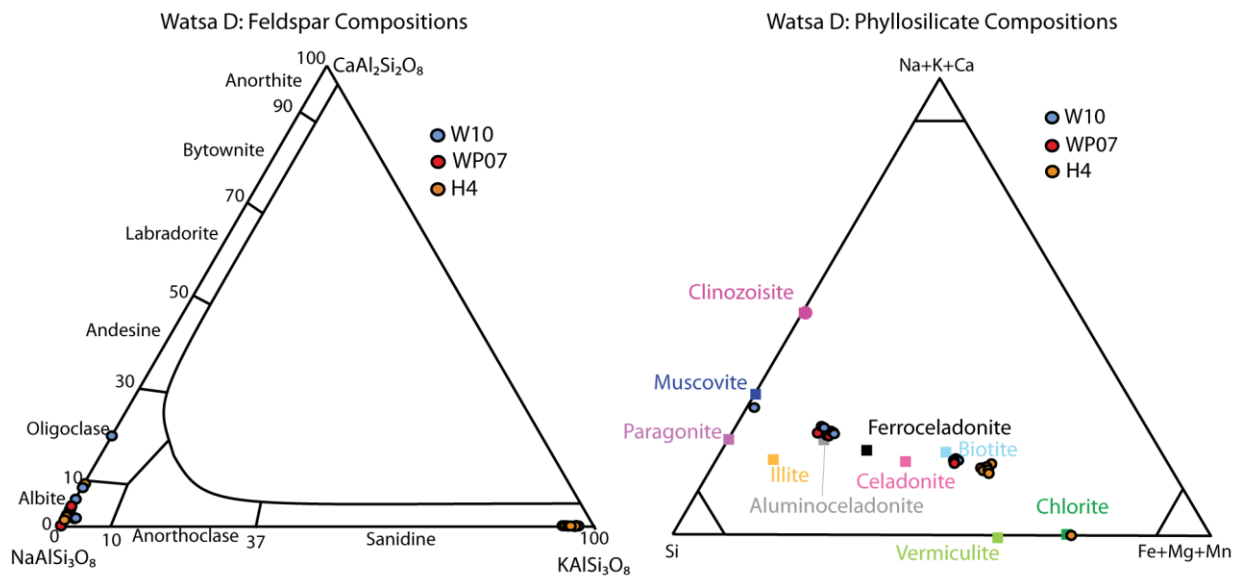


Figure 4.25: Ternary discrimination diagrams of selected minerals displaying the range of compositional data identified in the undifferentiated lithologies (Watsa-D) and boundary massifs.

Table 4.9: Representative EDS analysis of the major mineral phases identified in the Watsa-D lithologies (upper section) and Boundary Massifs (lower section)

Sample	Site	SiO ₂	TiO ₂	Al ₂ O ₃	Fe ₂ O ₃	MnO	MgO	CaO	K ₂ O	Na ₂ O	Total	Mineral
wt%												
W10	1-C	69.74		19.16				0.61		11.47	100.97	Plagioclase
W10	2-E	68.45		20.08				1.27		11.27	101.07	Plagioclase
W10	1-G	65.88		18.05					14.93	0.62	100.19	Orthoclase
W10	2-K	66.31		18.14					15.01	0.62	100.08	Orthoclase
W10	1-J	48.84	1.21	6.24	15.15	0.44	12.83	11.48	0.71	1.42	98.33	Amphibole
W10	2-I	48.34	1.04	6.69	16.57	0.43	12.17	11.92	0.62	1.22	99.00	Amphibole
W10	1-P	32.02	37.34	2.34	0.50			28.81			101.02	Sphene
W10	1-Q	31.28	37.98	1.26	0.77			28.43			99.72	Sphene
W10	1-R	47.18		27.40	5.67		2.45		10.50		93.20	Al-celadonite
W10	2-Q	46.54		36.07	0.58				9.92	0.56	93.68	Al-celadonite
WP07	1-F	69.09		19.09				0.34		11.90	100.42	Plagioclase
WP07	2-F	68.27		18.92				0.64		11.74	99.56	Plagioclase
WP07	1-R	38.40		23.49	10.24			22.65			94.78	Amphibole
WP07	2-P	39.24	0.57	14.05	16.41		14.04		9.06		93.37	Amphibole
WP07	1-O	45.42		23.86	8.35		4.81		9.96		92.41	Epidote
WP07	2-O	48.11		24.21	5.44		3.18		10.12		91.67	Epidote
WP07	1-K	46.16	1.29	6.93	16.50	0.39	11.34	11.24	0.76	1.40	96.01	Al-celadonite
WP07	2-K	46.94	0.77	6.35	15.67	0.45	12.28	11.12	0.62	1.41	95.61	Al-celadonite
H4	1-C	66.22		18.06					14.91	0.52	100.70	Orthoclase
H4	2-F	66.02		17.59					15.39	0.38	99.37	Orthoclase
H4	1-G	68.62		18.96				0.47		11.65	99.71	Plagioclase
H4	2-J	69.91		19.16				0.54		11.41	101.03	Plagioclase
H4	2-N	39.35		24.64	9.97			22.88			96.84	Amphibole
H4	2-O	38.72		24.61	9.81			23.14			96.28	Amphibole
H4	1-M	38.98		24.94	8.86			23.04			95.82	Epidote
H4	2-O	38.69		24.97	9.02			23.23			95.90	Epidote
H4	1-J	36.11	1.67	15.89	28.09	0.47	4.32		8.66		95.22	Al-celadonite
H4	2-M	35.13	1.57	16.06	28.39	0.31	4.28		8.49		94.22	Al-celadonite

4.5. West Nile Gneiss

The West Nile Gneiss (WNG) occupies the most northerly part of the study area and is the most enigmatic of the three terranes under investigation having historically been poorly studied and possessing no known significant gold deposits. Outcrops attributed to the WNG are identified in the north west of the study area in two principle locations (Fig. 4.1), the area immediately adjacent to the interpreted boundary between the WNG and the KGGB. As with the KGGB the level of exposure is poor, outcrops being principally identified where cuttings have been made during the construction of canals and roads. A total of six samples of gneissic material were collected (Fig. 4.1), sample details are displayed in Appendix 1.

The samples collected in the vicinity of the Nzoro power plant are characterised by a quartz-feldspar-biotite assemblage (Fig. 4.27). The gneisses consist of poorly formed white feldspar masses hosted within a cryptocrystalline grey coloured groundmass flecked cut by sub mm bands of dark micaceous material. The gneisses display a distinct foliation, the long axis of the irregular feldspar masses aligning parallel to the orientation of the mica bands. The gneisses consists of plagioclase feldspar porphyroclasts; compositionally ranging from albite to oligoclase (Fig. 4.28) ranging from 1-3 mm in size. The porphyroclasts are hosted within a groundmass consisting of quartz, plagioclase feldspar, orthoclase feldspar, biotite and epidote (Fig. 4.26). Quartz forms 50% of the groundmass, occurring as irregular anhedral crystals ranging in size from 10 μm -1 mm (Fig. 4.26). Orthoclase (average composition 94.7Or:5.3Ab) and plagioclase feldspar components are intergrown within the groundmass, both phases presenting highly irregular anhedral 20 μm -1 mm crystals constituting approximately 30% of groundmass material (Fig. 4.26). Biotite constitutes 15 % of the groundmass, forming euhedral acicular 10-400 μm crystals, and is predominantly identified as 5-10 μm wide bands cutting across the section parallel to foliation with additional 10-20 μm long biotite crystals occurring sporadically throughout the groundmass (Fig. 4.26).

Epidote accounts for the remaining 5% of the groundmass forming highly irregular sub-rounded crystals ranging in size from 200-400 μm and is commonly identified intergrown with biotite, and surrounding large monazite crystals, which occur as 50-500 μm sub-angular zoned crystals. Zircon displays a similar morphology to the monazite phase, occurring as sub-angular zoned 50-500 μm rectangular crystals scattered throughout the groundmass. Fluoroapatite is rarely identified, where it is observed it forms 50-100 μm rounded crystals associated with the biotite-rich bands.

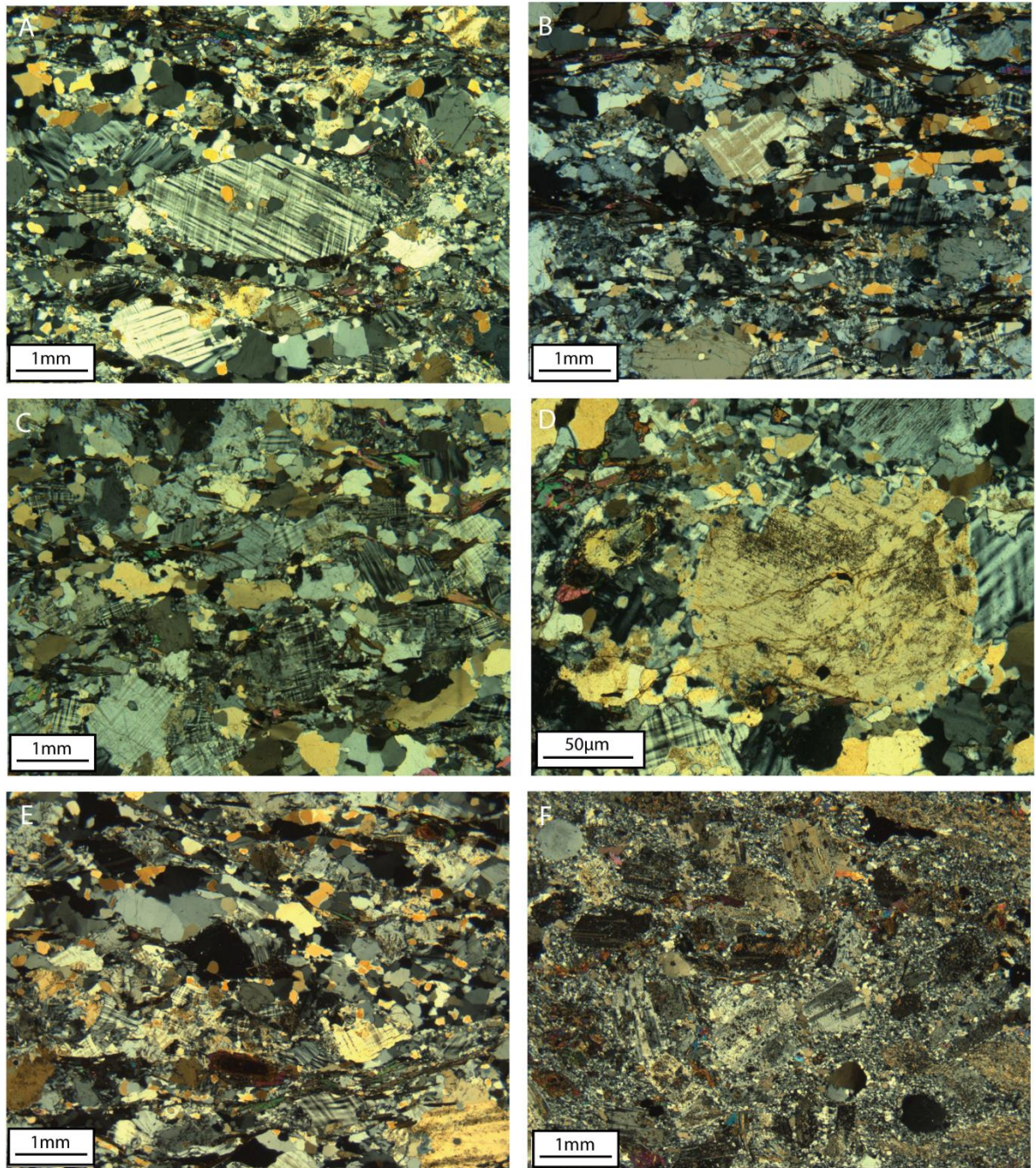


Figure 4.26: CPL Photomicrographs illustrating minerals and textures identified within samples from the West Nile Gneiss: A-E (A: Sample NZ01; B: Sample NZ03, C & D: Sample NZ02, E: Sample NZ07): Segregated bands of plagioclase-orthoclase feldspar and quartz. Compositional bands are separated by thin biotite horizons defining a strong foliation with quartz-feldspar groundmass aligning parallel to their orientation. Plagioclase porphyroclasts (A, B and D) are hosted within feldspar-rich segregations, displaying a range of morphologies, the groundmass deviating around the porphyroblasts. F (sample NZ07): Angular to sub-angular plagioclase feldspar phenocrysts hosted in a fine equigranular quartz-feldspar groundmass. Plagioclase feldspar phenocrysts and groundmass component have been extensively altered by late aluminoceladonite alteration.

A well-developed planar foliation is present throughout the material from the WNG, the porphyroclasts and groundmass components displaying elongation parallel to the biotite-rich bands. Segregation of mineral components is also present with quartz and feldspar-rich bands, ~ 0.5 mm in width, typically separated by biotite crystals (Fig. 4.26). Aluminoceladonite alteration is observed throughout the WNG occurring as aggregate masses of 10-20µm acicular crystals altering biotite within the biotite-rich bands and the feldspar crystals. Where observed replacing plagioclase feldspar the aluminoceladonite preferentially replaces specific twins within the feldspar crystals.

While the gneisses typically display little variation in composition, sample NZ07 shows internal heterogeneity with areas 1-2 cm in width consisting of 0.5-1 mm feldspar phenocrysts hosted within a quartz groundmass consisting of equigranular anhedral 5-10µm interlocking crystals (Fig. 4.26). Aluminoceladonite alteration is identified within these areas extensively replacing the feldspar phenocrysts and as 1mm masses embedded within the groundmass, though these are thought to represent feldspar-rich areas that have been extensively altered.

The degree of deformation and mineral segregation observed within the gneisses is higher in the samples collected along the boundary with the KGGB. The interpreted boundary between the two terranes consists of a high deformation zone characterised by sample NZ06. Sample NZ06 was collected adjacent to this boundary and is characterised by the presence of subhedral potassium feldspar porphyroclasts ranging in size from 1-5 mm with symmetrical quartz-rich strain shadows occurring at the ends of the larger porphyroclasts (Fig. 4.27). The outer edges of the 'porphyroclast' masses are extensively replaced by plagioclase feldspar with additional 100-200 µm masses of plagioclase also being identified throughout the groundmass (Fig. 4.27). The groundmass is composed of parallel bands of segregated quartz/feldspar and mica. Quartz within the groundmass occurs in two distinct morphologies; highly irregular elongated anhedral crystals ranging in size from 20-150 µm in length which form 10-20 µm thick bands running across the sample; and fine equigranular sub-rounded 5 µm crystals. Aluminoceladonite within the groundmass occur as 10-50 µm acicular euhedral crystals that form thin bands varying in thickness from 10-50 µm. Epidote crystals occurring as subhedral 50-150 µm sub-angular crystals, are identified throughout the sample in close association with the Aluminoceladonite bands. Extensive late aluminoceladonite alteration is present throughout the sample, distinguished from the k-mica within the groundmass by its finer crystal size (<5 µm), overprinting the k-mica-rich bands and to a lesser extent the orthoclase porphyroblasts (Fig. 4.27).

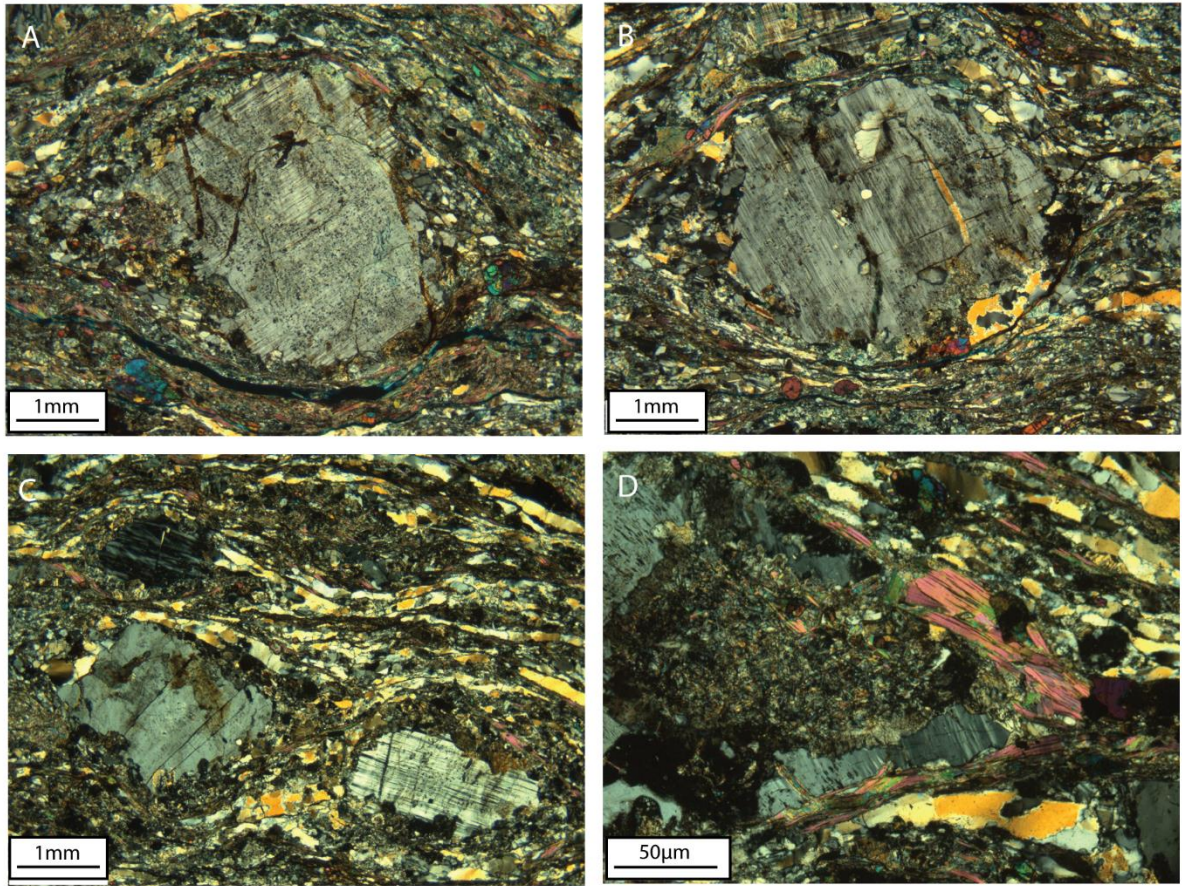


Figure 4.27: CPL Photomicrographs of Sample NZ06 displaying minerals and textures present within highly deformed examples of the West Nile Gneiss collected adjacent to the contact with the Kibali Granite-greenstone terrane. All images show orthoclase feldspar porphyroclasts hosted within alternating quartz-feldspar-rich and aluminoceladonite-rich parallel bands defining a strong foliation throughout the sample and deviating around the Orthoclase feldspar porphyroclasts. Images A and B show quartz-rich zones of recrystallisation at each end of the feldspar porphyroclasts extending out parallel to the foliation plane. Image D shows alteration of the feldspar porphyroclasts by aggregate masses of fine acicular aluminoceladonite.

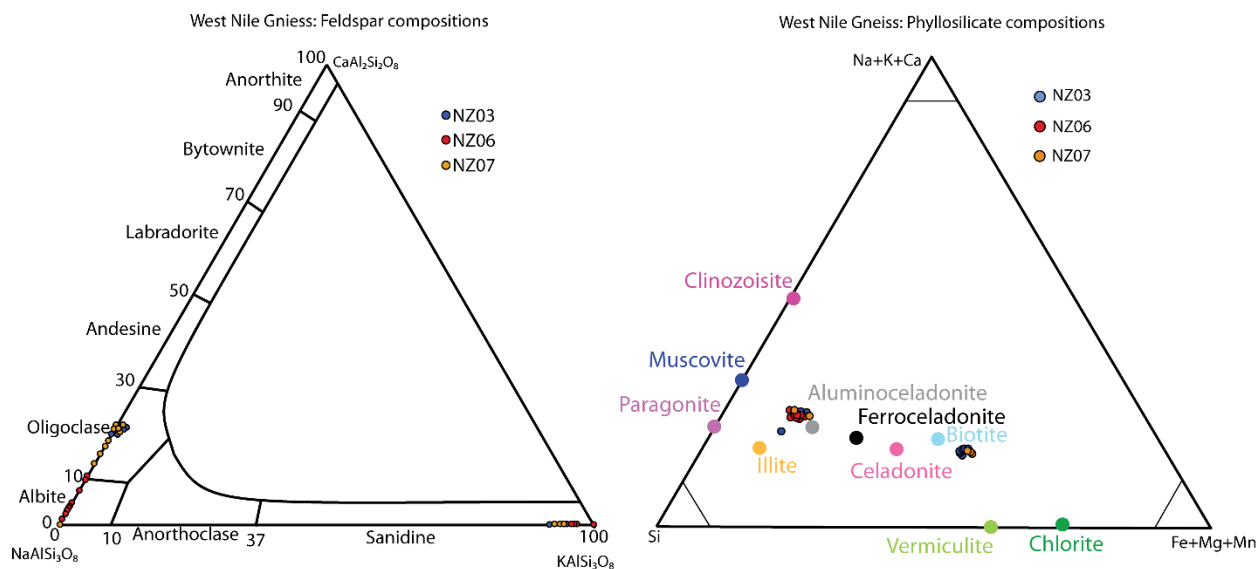


Figure 4.28: Ternary diagrams displaying compositional ranges of feldspar and phyllosilicate phases from selected samples of West Nile Gneiss

Table 4.10: Representative analysis of mineral compositions within the West Nile Gneiss

Sample	Site	SiO ₂	TiO ₂	Al ₂ O ₃	FeO	MnO	MgO	CaO	K ₂ O	Na ₂ O	BaO	Total	Mineral
wt%													
NZ03	2-A	63.65		22.08				4.46	0.28	9.04		99.50	Plagioclase
NZ03	2-P	64.26		22.28				4.64	0.26	9.19		100.64	Plagioclase
NZ03	1-G	65.69		17.58					15.28	0.59		99.14	Orthoclase
NZ03	2-J	65.62		17.72					15.15	0.42		98.91	Orthoclase
NZ03	1-L	37.97		22.55	11.16			22.68				94.36	Epidote
NZ03	2-F	38.25		23.10	10.92	0.43		22.77				95.46	Epidote
NZ03	1-K	36.61	3.38	14.22	23.86	0.40	7.33		9.17			94.97	Al-celadonite
NZ03	3-K	37.07	3.24	14.33	22.50	0.55	8.30		9.26			95.25	Al-celadonite
NZ06	1-O	68.42		19.17				1.00		11.22		99.81	Plagioclase
NZ06	2-C	69.04		19.37				0.86		11.43		100.70	Plagioclase
NZ06	1-B	65.92		17.89					15.15	0.48		99.43	Orthoclase
NZ06	2-F	66.70		17.94					15.09	0.47	0.65	100.84	Orthoclase
NZ06	1-E	38.10		22.58	10.53			22.81				94.02	Epidote
NZ06	2-J	38.84		23.02	10.95			22.96				95.78	Epidote
NZ06	1-H	49.11	1.02	24.74	4.22		2.92		10.39			92.40	Al-celadonite
NZ06	2-O	48.29	0.77	27.23	4.48		2.39		10.37			93.52	Al-celadonite

4.6 Discussion

Examination of the major lithological units within the three geological terranes, The Kibali Granite-Greenstone Belt, Upper Congo Granitic Massif and West Nile Gneiss, has demonstrated their strongly contrasting lithological characteristics. The Kibali Granite-Greenstone Terrane and Upper Congo Granitic Massif also show a significant amount of internal variability. These contrasting characteristics are indicative of differing geological origins and evolutions between the three terranes. The characteristics of the three terranes are here discussed with the aim of addressing the origin and evolution of the region.

4.6.1 Kibali Granite-Greenstone Belt

The Kibali Granite-Greenstone belt is the most complex and varied of the three terranes, with lithologies of volcano-sedimentary (Kibali metasedimentary package), chemo-sedimentary (banded iron formations), extrusive igneous and intrusive igneous origin being widely identified and displaying a range of deformational and metamorphic characteristics. The KGGB is dominated by the Kibalian metasediments. These comprise two main groups, the interbedded volcano-sedimentary conglomerates in the western part of the study area, and the fine crystalline schists in the central and eastern parts of the belt. In considering the environment in which the KGGB developed, the volcano-sedimentary conglomerates are more useful, being less deformed and metamorphosed relative to the schists in the eastern end of the belt and therefore displaying characteristics more similar to their original compositions.

The volcano-sedimentary conglomerates display a wide range of clast sizes and proportions (relative to the matrix) ranging from coarse clast-supported to clast deficient matrix-supported examples. These variations indicate an evolving depositional environment. Variation in the erosional environment is further supported by the diversity of clast types identified. These range from reworked 'sedimentary' conglomerate to angular fragments of ironstone and clasts of intrusive igneous material. These may include igneous material from the adjacent Upper Congo Granite Massif with the presence of ironstones and reworked conglomerates suggesting erosion of prior existing volcano-sedimentary lithologies formed within the Kibali Belt depositional environment. If it is assumed that the proto-Kibali depositional basin was oceanic, then changes in relative sea level may provide a plausible mechanism by which the range of observed material may be generated. Relative sea level variation would expose differing lithologies to littoral and terrestrial erosional processes while simultaneously altering the relative depth of the depositional environment from shallow marine environments, depositing coarse clast-rich material, to deep water environs, depositing fine-grained clastic sediments and mudstones. The hypothesized oceanic environment is supported by the presence of banded iron formations within the KGGB. These lithologies forming in deep water environments extending from the continental shelf out into the abyssal plane (Gross, 1996). The fine laminations, discontinuous

layering and abundant silicate-rich horizons within the ironstones are consistent with the characteristics of Algoma type banded iron formations formed during the Neoproterozoic in deep water environments with associated hydrothermal activity (Gross, 1996). Algoma type banded iron formations are typically associated with and interbedded with volcanic lithologies, turbidites and pelitic sediments (Gross, 1996) which is consistent with the lithologies observed within the KGGB.

The silicified volcanoclastic rocks identified in the western part of the study area, while being classed as part of the Kibali metasediments, display strongly contrasting characteristics, lacking the characteristic rounded and deformed clasts and chlorite-rich matrix, and may represent material of a different origin. The silicified volcanoclastics lack the foliated clast and micaceous matrix texture instead being dominated by fine cryptocrystalline silica. These silicified volcanoclastics display a strong spatial association with the Kokiza gabbroic intrusion. Angular imbricated fragments angled away from the intrusion and the gradation from large fragments adjacent to the intrusion to cryptocrystalline homogenous material distal to the intrusion indicates this lithology is linked to the emplacement of the Kokiza gabbroic intrusion.

The Kibalian metasediments have been extensively metamorphosed with two distinct metamorphic assemblages identified, separating the belt into the western sub-greenschist to greenschist facies lithologies and the central and eastern higher grade schists. The sub-greenschist to greenschist facies material comprises the variable volcano-sedimentary conglomerates identified across the western part of the belt, the metamorphic assemblage being typified by a chlorite+aluminoceladonite+quartz(\pm albite) mineral assemblage with deformation and stretching of clast material. The central and eastern schists are characterized by a biotite(\pm aluminoceladonite)+plagioclase+quartz mineralogy displaying strong segregation of minerals into parallel layers, indicating that higher pressure and temperature conditions affected the central and eastern parts of the belt, and that metamorphism took place at a greater depth than in the western part of the belt.

Cahen and Snelling (1966) described the Kibalian metasedimentary package as consisting of actinolite-talc-sericite-biotite-graphitic schists interbedded with basalts and banded iron formations (Chapter 2). This description is broadly consistent with the observations made above on the Kibalian metasediments. However, this study identified chlorite as being a significant component within the volcano-sedimentary conglomerates in the eastern part of the belt with actinolite and talc not being identified. Cahen et al. (1984) and Lavreau (1984) divided the Kibalian metasediments into an Upper Kibalian and Lower Kibalian on the basis of the ratio of sedimentary to volcanic material. The Upper Kibalian having a volcanic/sedimentary ratio of approximately 1 and the Lower Kibalian possessing a higher volcanic to sedimentary ratio (Cahen et al., 1984, Lavreau, 1984). The observations above indicate that the sedimentary component is dominant

within the study area, suggesting that it is part of the Upper Kibalian. However, the lack of exposure and vague descriptions provided in the literature of the two divisions means that this classification remains tenuous.

4.6.1.2 Chlorite Geothermometry

Chlorite is a useful mineral in estimating temperatures at which metamorphism has occurred as its composition varies systematically with temperature of formation. Here we employ the chlorite geothermometers developed by Cathelineau (1988) and Jowitt (1991), both methods examining the variations in Al(IV) occupancy of the tetrahedral site with temperature, though calculating them using different techniques. Chlorite compositions from the metamorphosed volcano-sedimentary conglomerates vary in composition with pycnochlorite, daphnite, brunsvigite and ripidolite species identified (Table 4.11). Using the method of Cathelineau (1988) returns chlorite formation temperatures ranging from 294°C to 354°C (interquartile range=315-349°C), with an average value of 318°C. Using the method of Jowitt (1991) returns chlorite formation temperatures ranging from 298°C to 370°C (interquartile range=320-358°C), with an average value of 326°C.

4.6.2. Kibali Belt Intrusions

The intrusive igneous bodies identified in the study area can be divided into two distinct groupings on the basis of their differing mineralogical compositions. The two groups are the 'mafic intrusives' consisting of the Kokiza gabbro (pyroxene-amphibole-plagioclase assemblage), and the 'felsic intrusives' consisting of the Ambarua granodiorite (amphibole-plagioclase-quartz assemblage) and the Kalimva and Sessenge granitic intrusions (quartz-plagioclase-biotite assemblage). Whether these intrusions represent an evolving igneous source at depth is not possible to determine solely on the basis of field and mineralogical observations, an examination of their geochemical characteristics is required in order to establish if these intrusions are related (Chapter 5). The intrusive generations are presented above in order of evolving composition. However, the true chronological relationship between the units cannot be determined based on field and petrological observations alone. The granodioritic and granitic intrusive phases identified may correspond to similar material identified within the UCG, particularly the Watsa-B intrusive and the undifferentiated intrusive units, however to confirm this will require detailed examination of the geochemical characteristics of each intrusive. The studies of Cahen et al. (1984) and Lavreau (1984) favoured describing the intrusives within the Kibalian belts in terms of those identified in the neighbouring UCG, but provided insufficient detail to correlate the observations made above with their conclusions.

Table 4.11: Selected examples of chlorite compositions and calculated formation temperatures from the volcano-sedimentary conglomerates of the Kibalian metasediments

Sample	K18	K18	K19	K19	Kis-S-1	Kis-S-1	Kis-S-1	Oere-1	Oere-1	Oere-1
Site	3-J	3-K	1-H	1-I	1-F	1-I	3-F	1-L	1-M	2-I
SiO ₂	27.04	27.19	26.55	28.49	23.21	22.87	23.52	25.08	26.63	25.61
Al ₂ O ₃	19.47	20.11	18.87	20.58	18.93	18.89	18.94	20.04	21.07	20.43
Fe ₂ O ₃	1.16	1.66	0.48	2.28	0.32	0.33	0.59	0.61	2.56	0.90
FeO	23.69	22.79	24.97	22.55	39.60	38.88	38.56	27.51	23.48	27.33
MnO	0.00	0.00	0.00	0.00	0.00	0.00	0.00	0.00	0.29	0.31
MgO	15.14	14.78	15.40	14.90	4.15	4.18	4.43	12.37	11.81	12.26
H ₂ O*	11.29	11.33	11.24	11.66	10.23	10.12	10.27	10.92	11.13	11.09
Total	97.77	97.86	97.94	100.45	96.44	95.29	96.31	96.53	96.97	97.93
Si	5.73	5.73	5.66	5.82	5.44	5.41	5.49	5.50	5.70	5.53
Al ^{iv}	2.27	2.27	2.34	2.18	2.56	2.59	2.51	2.50	2.30	2.47
Al ^{vi}	2.60	2.75	2.41	2.81	2.67	2.69	2.70	2.69	3.05	2.74
Ti	0.00	0.00	0.00	0.00	0.00	0.00	0.00	0.00	0.00	0.00
Cr	0.00	0.00	0.07	0.00	0.00	0.00	0.00	0.00	0.00	0.00
Fe ³⁺	0.18	0.26	0.08	0.35	0.06	0.06	0.10	0.10	0.41	0.15
Fe ²⁺	4.20	4.02	4.45	3.85	7.76	7.70	7.52	5.04	4.20	4.93
Mn	0.00	0.00	0.00	0.00	0.00	0.00	0.00	0.00	0.05	0.06
Mg	4.78	4.64	4.89	4.54	1.45	1.48	1.54	4.04	3.77	3.94
OH*	16.00	16.00	16.00	16.00	16.00	16.00	16.00	16.00	16.00	16.00
Total	35.77	35.67	35.90	35.56	35.93	35.93	35.87	35.87	35.48	35.82
Fe/Fe+Mg	0.48	0.48	0.48	0.48	0.84	0.84	0.83	0.56	0.55	0.56
Variety	pycnochlorite	pycnochlorite	pycnochlorite	pycnochlorite	daphnite	daphnite	daphnite	ripidolite	brunsvigite	ripidolite
T (°C)-Cathelineau (1988)	303.95	303.79	314.89	288.68	350.93	354.25	342.91	340.99	308.87	336.29
T (°C)-Jowett (1991)	308.40	308.12	319.51	293.01	366.91	370.08	358.56	347.89	315.18	343.25

The deformation identified in the upper part of the Kalimva granite and to a lesser degree in the Ambarau granodiorite indicates that the 'intrusive' units have undergone post-crystallisation modification. The high level of vegetation, and resulting low levels of rock exposure, has resulted in the contacts between the 'intrusive' material and the surrounding meta-sediments being obscured, with the exception of the upper contact of the Kalimva intrusion. As a result, there remains doubt as to whether the 'intrusions' are in situ or are fragments of the original intrusive bodies that have been transported to their current location during thrusting and deformation of the KGGB. The deformation observed in the Kalimva and Ambarau intrusions indicates these units were 'intruded' prior to the final stage of deformation within the Kibali belt and were subsequently modified and potentially transported. The lack of observed deformation within the Kokiza and Sessenge intrusions would therefore indicate that they intruded the meta-sediments after the final deformation event. However, without observing the edges of the intrusions and the relationship to the surrounding meta-sediments it is not possible to reach any firm conclusions.

4.6.3. Upper Congo Granitic Massif

Within the Upper Congo Granite Massif (UCG) three distinct lithological groupings are distinguished based on mineralogical characteristics; 'Mafic intrusives' consisting of the central Watsa-A body, 'Mafic extrusives' consisting of Watsa-C unit and 'Felsic intrusives' consisting of the Watsa B, Undifferentiated lithologies and boundary massifs.

The Watsa-A intrusive body is the most complex of the units identified in the Watsa complex and displays a variable mineralogy, transitioning from a pyroxene-amphibole-plagioclase mineralogy at low elevations to a plagioclase feldspar-amphibole±epidote mineralogy at higher elevations with a corresponding reduction in crystal size. Though the unit varies in composition, it is assumed to represent a single intrusion on the basis of the strong geophysical response observed in the airborne magnetic susceptibility survey. This would suggest crystallisation from an evolving melt, the composition of the crystallizing phase moving from pyroxene to plagioclase and the crystallised phase sinking through the melt to form the differing lithologies. The available lithological material and degree of exposure is insufficient to confirm this hypothesis, requiring further detailed geochemical analysis to confirm a shared origin for the varied mineralogies that constitute the Watsa-A intrusive body. The Watsa-B unit is compositionally much simpler with all samples being characterised by a plagioclase feldspar-quartz-amphibole mineral assemblage.

The relationship between the Watsa-A and Watsa-B units is of interest. The granodioritic Watsa B units potentially constitute the upper and most evolved part of the Watsa-A unit. The positioning of the granodioritic samples that constitute the Watsa B body indicate that this body surrounds the Watsa A unit, being identified to the north, west, south and above the Watsa-A lithologies. However, there are several

indications that these two units are not genetically related. The Watsa B unit returns a strongly contrasting geophysical response (Fig. 4.2) in comparison to the Watsa A intrusive. Furthermore the Watsa-B lithologies display a larger crystal size than that observed in the Watsa-A samples. Geochemical characteristics will provide further insight into the relationship between the Watsa-A and Watsa-B intrusive bodies.

The Watsa-C unit has an amphibole-plagioclase-sphene mineralogy with a fine crystal size that strongly contrast with both the Watsa-A and Watsa-B intrusive bodies. The xenoliths of fine melanocratic material identified within the Watsa-B unit are similar in appearance to the Watsa-C unit, suggesting that the Watsa-C unit predates the intrusion of the Watsa-B unit. The granodioritic lithologies within the ‘undifferentiated’ intrusives identified to the south of the Watsa igneous complex are compositionally and texturally similar to the granodioritic material that comprise the Watsa-B unit and likely represent the southern extension of this unit. The K-feldspar-rich boundary massifs, identified to the east of the Watsa complex adjacent to the Kibali River and the boundary between the UCG and KGGB, represent the most compositionally evolved intrusive units identified in the UCG. Due to their geographical isolation it is not possible to determine the timing of these intrusions relative to the intrusives of the Watsa igneous complex.

The multiple intrusive generations discussed above likely correspond to those outlined in Cahen and Snelling (1966), who described the UCG as composed of orthogneisses and multiple intrusive complexes. Three generations of intrusive are briefly described by Cahen et al. (1984), the first consisting of tonalites, diorites and granodiorite, the second consisting of quartz monzonites and the third consisting of potassic granites and pegmatites. The lack of detailed information makes correlating the ingenuous units described above with those of Cahen et al. (1984) difficult. The first generation possibly corresponding to the Watsa-B unit, both being described as granodioritic, while the second generation possibly corresponds to the K-feldspar-rich boundary intrusions, whose mineralogy is consistent with a quartz monzonite. The third generation, described as potassic granites and pegmatites (Cahen et al., 1984) is more difficult to correlate with little information available. The Granitic intrusive material (Sample W10) described as part of the ‘undifferentiated intrusives’ is K-feldspar-bearing and is a likely candidate for the third generation described by Cahen et al. (1984).

The low level of exposure, obscuring the contact between the major intrusive phases in the UCG, makes determining the relationships between the intrusive phases challenging. Geochemical and geochronological techniques will be utilised later in this study to further investigate the relationship between the major intrusive phases.

4.6.4. The West Nile Gneiss

The West Nile Gneiss is the least well examined of the three major terranes identified in the vicinity of the Kibali Gold project. Though extending across the entire northern margin of the KGGB the key characteristics have been established based only on a small number of samples collected in a relatively small geographical area. As such the described characteristics and any interpretation made from them may not represent the 'terrane' as a whole.

The West Nile Gneiss is characterized by plagioclase feldspar 'phenocrysts' hosted within a groundmass composed of quartz- K-feldspar – biotite and minor epidote, with a strong parallel alignment of minerals though only limited segregation of the minerals. The West Nile Gneiss is considered to be an orthogneiss, the quartz-feldspar dominated mineralogy reflecting the original granitic composition. This is further reinforced by the presence of rare 'un-deformed' enclaves within the samples from the WNG which possess a porphyritic granitic texture and mineralogy. The increased deformation and metamorphism, characterized by large K-feldspar porphyroblasts hosted within a strongly segregated plagioclase-quartz-aluminoceladonite groundmass, identified in the WNG near the interpreted boundary with the KGGB suggests a second stage of deformation related to the thrusting of the WNG over the variably metamorphosed packages of the KGGB. This interpretation, of the WNG over-thrusting the KGGB, disagrees with the description of the WNG provided by Cahen and Snelling (1966) who considered the WNG to underlie the KGGB, forming the basement material.

Mantarri (2014) and Westerhoff et al. (2014) also described the West Nile Gneiss in Uganda as underlying meta-sedimentary terranes they correlated with the Kibalian of the Bomu-Kibalian block [the correlation between units within the West Nile Block of Uganda (Mantarri, 2014; Westerhoff et al., 2014) and the Bomu-Kibalian block and West Nile Gneiss within the NE DRC is still a matter of debate]. Despite this, the strongly contrasting mineralogical, geophysical and metamorphic characteristics between the WNG and KGGB, observed faulting along the boundary between the two terranes and associated deformation of the WNG, indicates that in the vicinity of the KGGB the WNG is thrust over the KGGB.

4.6.5. Late Aluminoceladonite Alteration

As illustrated and discussed above the three terranes display strongly contrasting characteristics, however a common observation made across the three terranes is the presence of late aluminoceladonite alteration. Aluminoceladonite alteration presents, in all cases, as <10 µm acicular crystals occurring as late recrystallisation of the plagioclase feldspar mineral phase, both the phenocrysts and groundmass components in the granitoid/granite-gneiss lithologies and clast and matrix components within the Kibalian

metasediments. The intensity of the alteration varies between the individual lithologies but shows a broad trend of increased aluminoceladonite alteration in those samples collected near the boundaries between the three terranes, such as in the basaltic samples from the Atekoma region, Watsa-B granodiorites from the northern part of the UCG, and the heavily deformed West Nile Gneiss material adjacent to the contact with the KGGB. This possibly indicates that the boundary structures between the terranes were the conduit of the hydrating fluid. The presence of this alteration style in all three of the terranes indicates the event responsible occurred at a point where the three terranes had been assembled into their current geographical relationship, this is in contrast to the differing styles of metamorphism identified in the WNG and KGGB, suggesting these terranes were separate during peak metamorphism.

4.6.6. The Kibali Belt as an Archean Greenstone Belt

Archean Granite-Greenstone Belts have been identified in Archean cratons on every continent and have been extensively studied, in part because of their economic significance, but also for the insight they have provided into the characteristics of the ancient Earth. The lithological package that comprises the Kibali Granite-Greenstone Belt, a mix of interbedded metasediments, banded iron formations and basalts, are consistent with those identified in greenstone belts around the world (Anhaeuser, 2014). The majority of Granite-Greenstone belts are dominated by volcanic lithologies (Sylvester et al., 1997), including the famed East Pilbara terrane in Western Australia (Hickman and Van Kranendonk, 2012) and the Murchison terrane in South Africa (Viljoen, 1979; Vearnecombe et al., 1992). Within these belts sedimentary lithologies, consisting of banded iron formations, shales and greywackes, constitute less than 5% of the material within the belts (Anhaeuser, 2014) and are principally confined to the upper part of the greenstone sequences, considered to have formed after the cessation of volcanic activity (Brandl et al., 2006; Nijman et al., 2010; Hickman and Van Kranendonk, 2012; Anhaeuser, 2014).

Archean greenstone belts with a high proportion of sedimentary material, similar to that observed in the KGGB, have been identified and include the Slave Province in Canada (Padgham, 1985). Sedimentary lithologies within greenstone belts, be it in sedimentary dominated or volcanic dominated belts, display a wide range of compositions ranging from volcanogenic sediments associated with mafic-ultramafic and calc-alkaline-felsic volcanism to facies of sedimentary origin including deep water, shallow marine and terrestrial environments, including sediments of conglomerate-quartz-arenite, carbonates, conglomerate-wacke-pelite and conglomerate-arenite-pelite associations (Erikson et al., 1997; Anhaeuser, 2014).

Regional metamorphism is ubiquitous within Archean greenstone belts with metamorphism ranging from prehnite-pumpellyite facies to greenschist facies and up to amphibolite facies (Anhaeuser, 2014) The degree of metamorphism experienced has been linked to the size of the sedimentary belts, smaller greenstone belts

generally displaying higher grade metamorphism, typified by schistose lithologies, due to the increased proximity, and associated elevated geotherm, to the surrounding granitic and gneissic terranes (Block et al., 2013; Anhaeusser, 2014). In the case of the KGGB this UCG constitutes the surrounding granitic terranes, this being most evident when the regional geology map (Chapter 2) is examined, the narrow Kibalian greenstone belts being surrounded by the massive Upper Congo Granitic massif. This pattern of narrow volcano-sedimentary greenstone belts surrounded by massive granitic complexes is common to greenstone terranes (Anhaeusser, 2014) including the Yilgarn and Pilbara cratons of Western Australia (Barley, 1997; Hickman, 2012); the Zimbabwe (Blenkinsop et al., 1997), Tanzanian (Borg and Shackleton, 1997) and Kapvaal cratons (Brandl et al., 2006) in Africa; and the Slave Province (Padgham, 1985) in Canada. The granitic terranes consist of multiple intrusive phases with a wide range of compositions having been identified including plagioclase-trondhjemites, hornblende-tonalite gneisses, TTG granodiorites, monzogranites and syenogranites (Robb et al., 1986; Anhaeusser, 2010, 2014), a suite of lithologies similar to those observed along the northern margin of the UCG.

5. Conclusions

The Kibali Granite-Greenstone Belt consists of a mixed package of meta-sedimentary lithologies of volcano-sedimentary origins, banded iron formations and basaltic units that have undergone greenschist to low amphibolite facies metamorphism. The Kibali Granite-Greenstone Belt is bounded to the south by the Upper Congo Granitic Massif, a polyphasic intrusive complex that surrounds the Kibalian greenstone belts, and to the north is overthrust by the West Nile Granite-Gneisses. The Kibali Belt is hypothesized to have formed in an evolving oceanic basin that varied from sub-aerial terrestrial to deep ocean depositional environments and was subsequently accreted along the northern margin of the Bomu-Kibalian block.

The West Nile Gneiss remains enigmatic, its physical and mineralogical characteristics strongly contrasting with those observed in the Kibali Granite-Greenstone Belt and the Upper Congo Granitic Massif, with the late aluminoceladonite alteration being the only common factor between the three terranes. The lithologies within the Kibali Granite-Greenstone Belt and Upper Congo Granitic massif, and the relationship between the two terranes, are consistent with lithologies reported from other granite-greenstone terranes around the world. Condie (2015), recently highlighted the need to conduct a multidisciplinary study when examining possible greenstone belts and to be confident in describing the Kibali Granite-Greenstone Belt and the broader Bomu-Kibalian block as an Archean Granite-Greenstone terrane will require further study, particularly of the geochemical and geochronological characteristics of the terranes, to further clarify the origins and relationship between the three major terranes.

Chapter 5. Classification and tectonic discrimination within the Upper Congo Granite Massif and Kibali Granite Greenstone Belt through the use of geochemical data

5.1. Introduction

The major lithological units within the Kibali Granite-Greenstone Belt (KGGB), Upper Congo Granite Massif (UCG) and West Nile Gneiss were classified petrographically in Chapter 4. In this chapter these units are classified geochemically. The geochemical characteristics of Archean greenstone belts have been studied worldwide have been used to infer a range of geotectonic settings, including island arcs, analogous to modern day systems (Taylor and McLennan, 1985) and mantle plumes (Stein and Hoffmann, 1994). Here the geochemical characteristics of the major igneous units within the KGGB and UCG are presented and used to infer the geotectonic conditions under which the KGGB and UCG formed. This study focuses on samples of igneous origin from across the Kibali Granite-Greenstone Belt and Upper Congo Granite Massif (sample positions are displayed in Fig. 5.1). By focussing on the igneous lithologies it will be possible to provide accurate quantitative classifications of their lithotype and through modelling of the trace-element components determine the palaeo-tectonic setting in which they formed.

5.2. Methodology

Samples for geochemical analysis were selected from the available regional sample (Fig. 5.1) set, the locations of samples utilised in the geochemical study are displayed in Figure 5.1. For each sample approximately 1 kg of material was taken and external weathered surfaces trimmed to remove weathered material or obvious contamination. Clean samples were broken down to approximately 3x3 cm fragments using a hydraulic rock splitter and crushed using a Fritz jaw crusher to fine gravel. Crushed material was placed in an agate ring mill and processed until the material was reduced to a homogenous powder. Samples were prepared for analysis and analysed by inductively coupled plasma optical emission spectrometry (ICP-OES) and inductively coupled plasma mass spectrometry (ICP-MS) at Cardiff University. Analytical procedures followed those presented in McDonald and Viljoen (2006), these are reviewed below.

For each sample 2 g of powdered material was weighed and heated to 900 °C to release volatile components (H₂O, CO₂), the ignited residue was then weighed again in order to determine loss on ignition (LOI) values for each sample. Precisely 0.100 g of ignited residue was weighed for each sample and combined with 0.400 g of Li-metaborate flux in a Pt-Rh crucible and approximately 0.5 ml of 25%

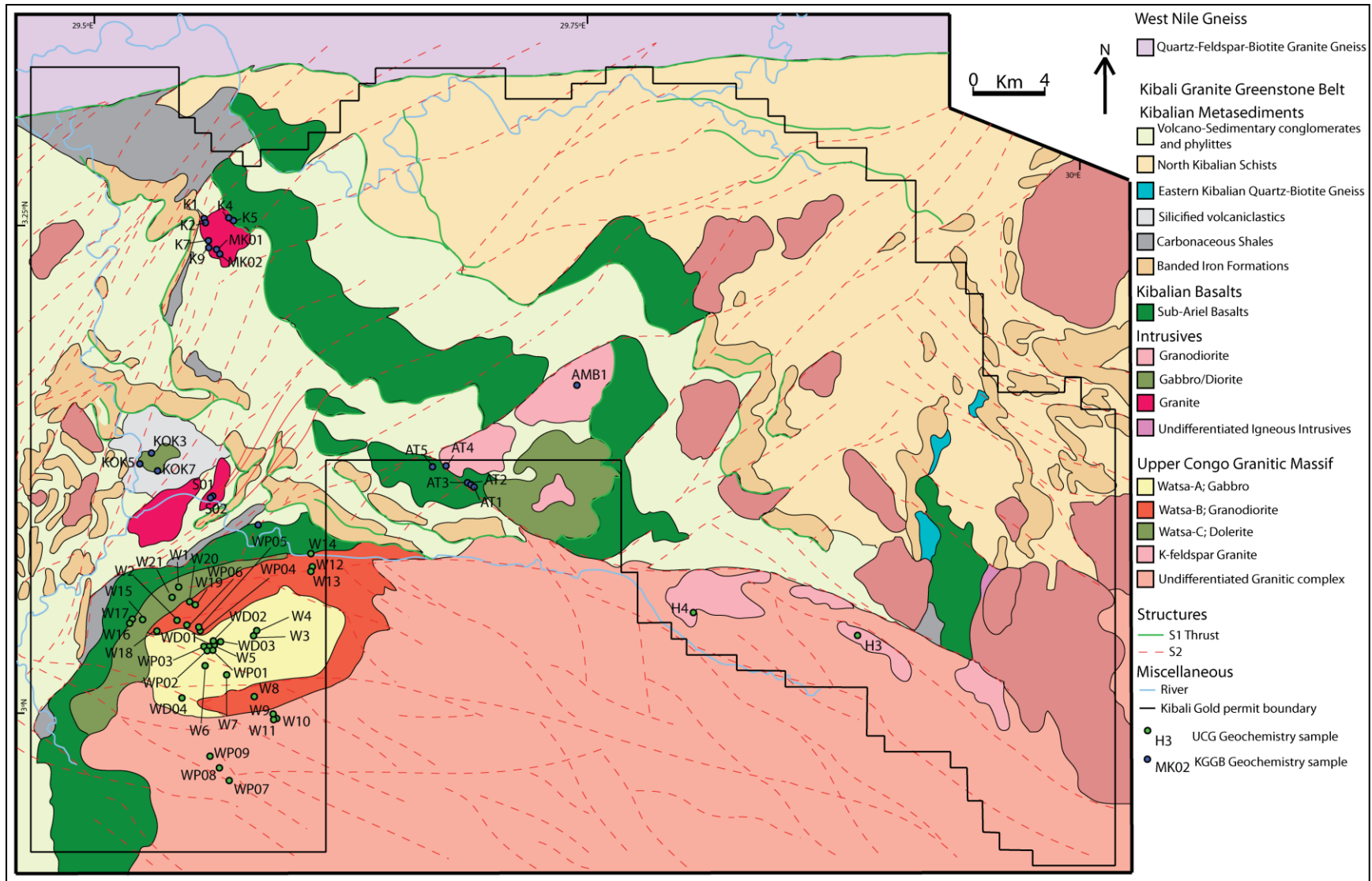


Figure 5.1: Map of the Kibali Granite-Greenstone Belt and neighboring terranes displaying the locations of the samples utilised in the geochemical study.

lithium iodide solution was added as a non-wetting agent. Samples were fused by propane burner using on a Claisse Fluxy automated fusion system. Fused melt was poured into 50 mL of 4 % HNO₃ in a Teflon beaker and agitated by magnetic stirrer until all fused glass fragments were dissolved. Following complete dissolution the solution was spiked with 1 mL of a 100 ppm Rh solution, to act as an internal standard, and diluted with 18.2 MΩ deionised water to a volume of 100 mL. These solutions were used for both ICP-OES and ICP-MS analysis.

Concentrations of the major rock forming components Si, Ti, Al, Fe, Mg, Mn, Ca, K, Na and P, and trace-element components Ni, Cu, Co, Cr, Ba, Sr, Zr, Y, Sc and V were determined using as JY Horiba Ultima2 ICP-OES system. Trace-element and rare earth element concentrations (REE, Ti, V, Cr, Mn, Co, Ni, Ga, Rb, Sr, Y, Zr, Nb, Ba, Hf, Ta, Th and U) were analysed using a ThermoElemental X series (X7) ICP-MS system. To facilitate analysis the fused solution was diluted by a factor of 10 with 2 % HNO₃ and spiked with 5 ppb of internal In and Tl standards to correct for instrumental drift. For both analytical methods calibration was performed using reagent blacks and solutions of international certified reference materials DTS-1, W2, BIR1, MRG1, JA2, STM-1 and JG3, spiked with 1 ppm Rh internal standard to correct for instrumental drift. As an external check on instrumental drift one standard solution was analysed after every six unknowns. Accuracy was assessed by analysis of CRM's JB1a and JG1a prepared as unknowns in each batch of samples.

5.3. Results

5.3.1 Major and Trace-element Composition

Based on petrological observations (Chapter 4) the igneous samples were divided into subdivisions based on their felsic/mafic characteristics. These subdivisions provide a useful framework in which to discuss the geochemical data and are here adopted. Here we present the major and trace-element characteristics of the lithologies from the KGGB and UCG. Geochemical data is here described in brief, full table of data is available in Appendix 3.

Trace-element data is presented as bivariate plots of selected elements ranging from low to high ionic potential against the zirconium concentrations. Ionic potential is defined as the ratio between the charge of an ion and its radius. Low Field Strength Elements (LFSE) with a relatively small charge and large radius have a low ionic potential, relative to High Field Strength Elements (HFSE) which generally have a higher charge and smaller radius. The LFSE are considered susceptible to mobilisation through fluid interaction and weathering, being complexed and transported as hydrated oxyions (Cann, 1970; Pearce, 1996). With

increasing ionic potential the degree of mobility decreases with the HFSE and Rare Earth elements (REE) considered the most immobile and therefore stable in geological systems.

Zirconium has an ionic potential 4+ and is largely immobile in most geological systems. When plotted against a known immobile element such as Zr, co-genetic data will yield linear trends for moderate to highly incompatible elements and diffuse 'clouds' of data for elements with a higher degree of mobility due to the effects of post-crystallisation alteration (Cann, 1970; Hastie et al., 2013). Trace-element compositions are also presented as NMORB normalised extended trace-element diagrams, NMORB values presented in Sun and McDonough (1989) were selected based on the inferred oceanic basin setting of the lithologies from the KGGB (Chapter 4). Rare earth element data is presented normalised to C1 Chondrite values from Sun and McDonough (1989). In describing the data the subscripts CN (chondrite normalised) and NM (NMORB normalised) are utilised to indicate where data has been normalised.

5.3.1.1 Kibali Granite-Greenstone Belt: Felsic Intrusive/Extrusive Units

The felsic intrusive lithologies range in composition from 64.6 to 69.8 wt% SiO₂, 0.03 to 0.05 wt% MgO, 2.30 to 4.19 wt% CaO and 1.00 to 3.55 wt% K₂O with trace-element concentrations ranging from 0.6 to 2.0 ppm U, 26.6 to 63.8 ppm Ce, 88.6-125.3 ppm Zr and 0.8-1.6 ppm Dy. The felsic extrusive lithologies range in composition from 50.96 to 57.13 wt% SiO₂, 4.14 to 8.43 wt% MgO, 10.53 to 16.39 wt% CaO and 0.08 to 1.42 wt% K₂O with trace-element concentrations ranging from 0.8 to 2.2 ppm U, 51.04 to 231.7 ppm Ce, 140.7 to 194.9 ppm Zr and 2.9 to 6.7 ppm Dy.

Plots of selected trace-element concentrations against Zr (Fig. 5.2) shows the data forming a single positive linear trend progressing from low concentrations in the felsic intrusive to higher concentrations in the felsic extrusive samples, this trend being most prominent in those plots illustrating the HFSE. The KGGB intrusive and extrusive units display similar REE distribution patterns with negative gradients and relative depletion of the MREE and HREE relative to the LREE (Fig. 5.3 D). In detail, La/Sm_{CN} range from 3.33 to 4.92, La/Yb_{CN} range from 20.97 to 28.48 and Tb/Yb_{CN}= 1.75 to 2.45. All samples display a negative Eu anomaly (Fig. 5.3 D) with Eu/Eu* (Eu*=((Sm_{CN}+Gd_{CN})/2)) values ranging from 0.75 to 0.92. The intrusive felsic data display consistent REE distributions with the exception of sample K5. Sample K5 displays a lower degree of fractionation of the MREE and HREE relative to the LREE characterised by, La/Sm_{CN}= 2.57 to 2.84, La/Yb_{CN} =11.92 to 14.91 and Tb/Yb_{CN}=1.74 to 2.08 (Fig. 5.3 D). The NMORB normalised extended trace-element distribution patterns of the intrusive felsic lithologies display enrichment of the LFSE relative to HFSE (and NMORB), the HFSE being depleted relative to NMORB (Fig. 5.4 A-B). Negative anomalies occur in Nb (Nb/La_{NM}=0.14 to 0.31), Ta, Ti, Th and U concentrations forming a 'plateau' with the distribution patterns in all samples bar one.

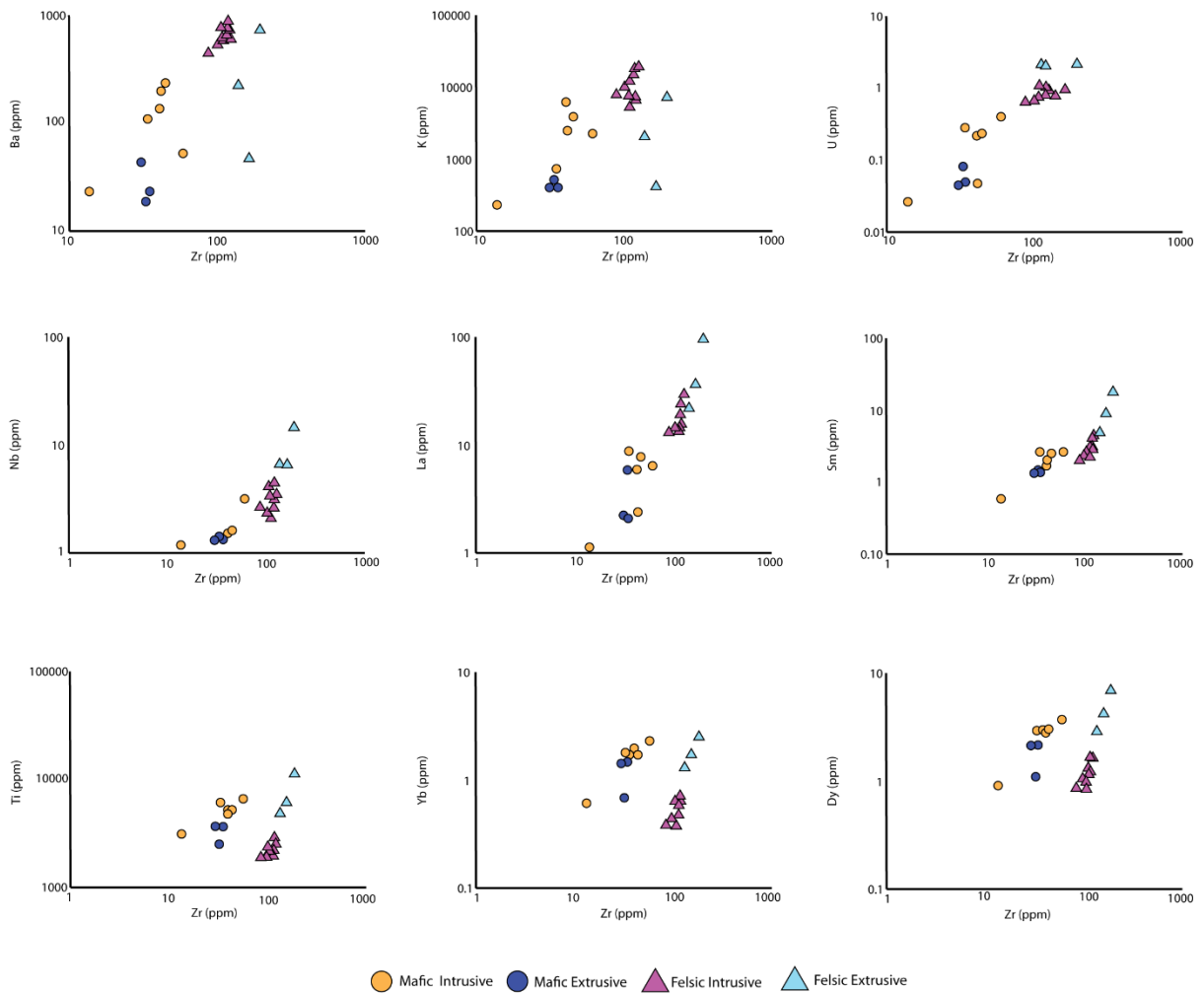


Figure 5.2: Bivariate plots displaying geochemical data for samples from the Kibali Granite-Greenstone Belt.

Positive anomalies are identified in the concentration of La, Sr and Gd (Fig. 5.4). Six of the intrusive felsic samples (Fig. 5.4 A)) display elevated Ta content relative to Nb ($Ta/Nb_{NM}=1.73$ to 2.45). Sample K5 shows significant enrichment of the LFSE and HFSE, the HFSE values being comparable in concentration to NMORB (Fig. 5.4 B), with negative Nb, Ta, Ti, Sr, Zr and Hf anomalies. NMORB normalised trace-element distribution patterns for the extrusive felsic lithologies display enriched LFSE relative to NMORB with concentrations of the HFSE approximating NMORB (Fig. 5.4 C). Negative Nb, Ta and Ti anomalies are identified ($Nb/La_{NM}=0.18$ to 0.31) with positive anomalies in La, Ce, Eu and Gd (Fig. 5.4 C).

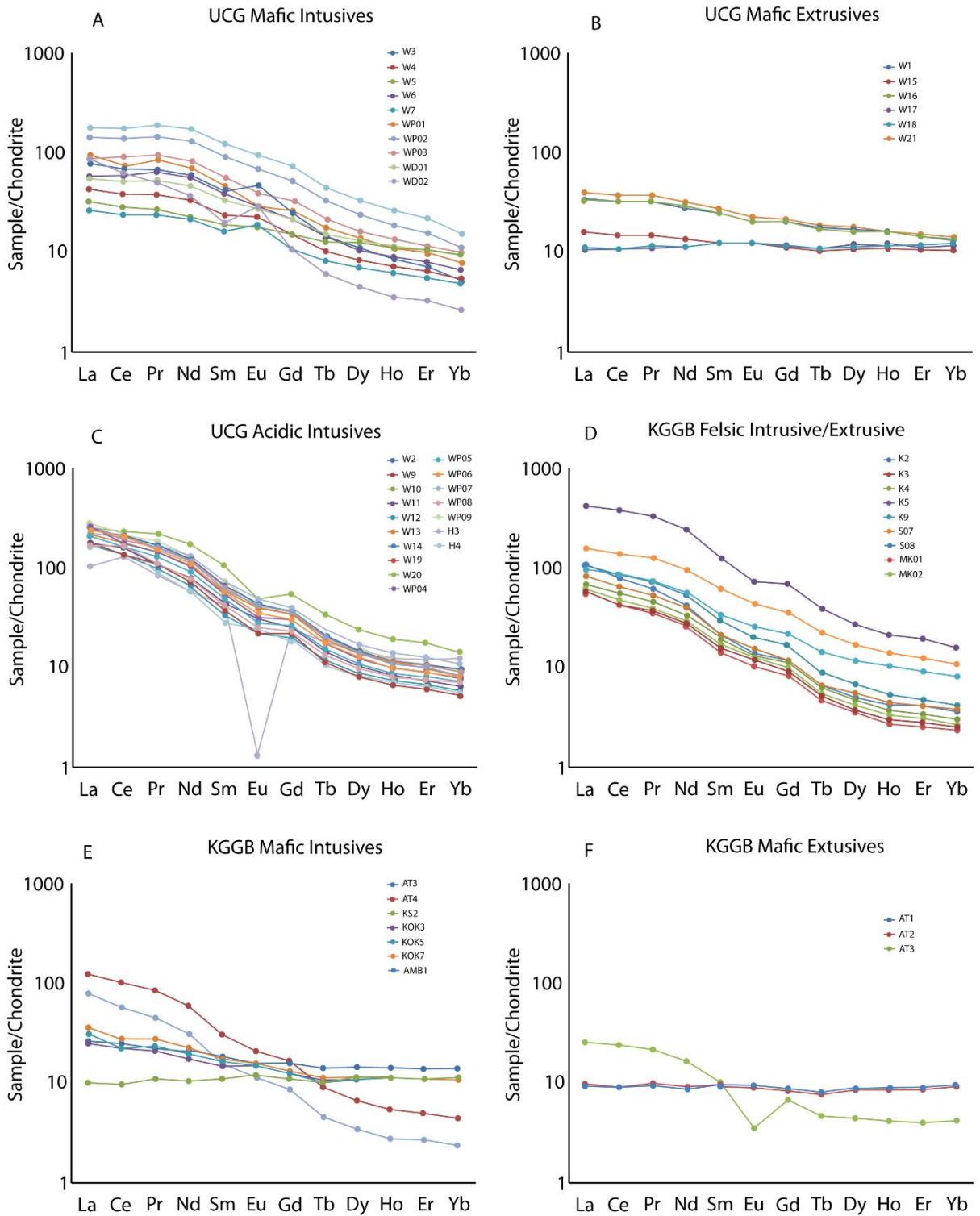


Figure 5.3: REE diagrams displaying the chondrite normalised REE concentrations of the major lithological groups from the Kibali Granite-Greenstone Belt and the Upper Congo Granite Massif.

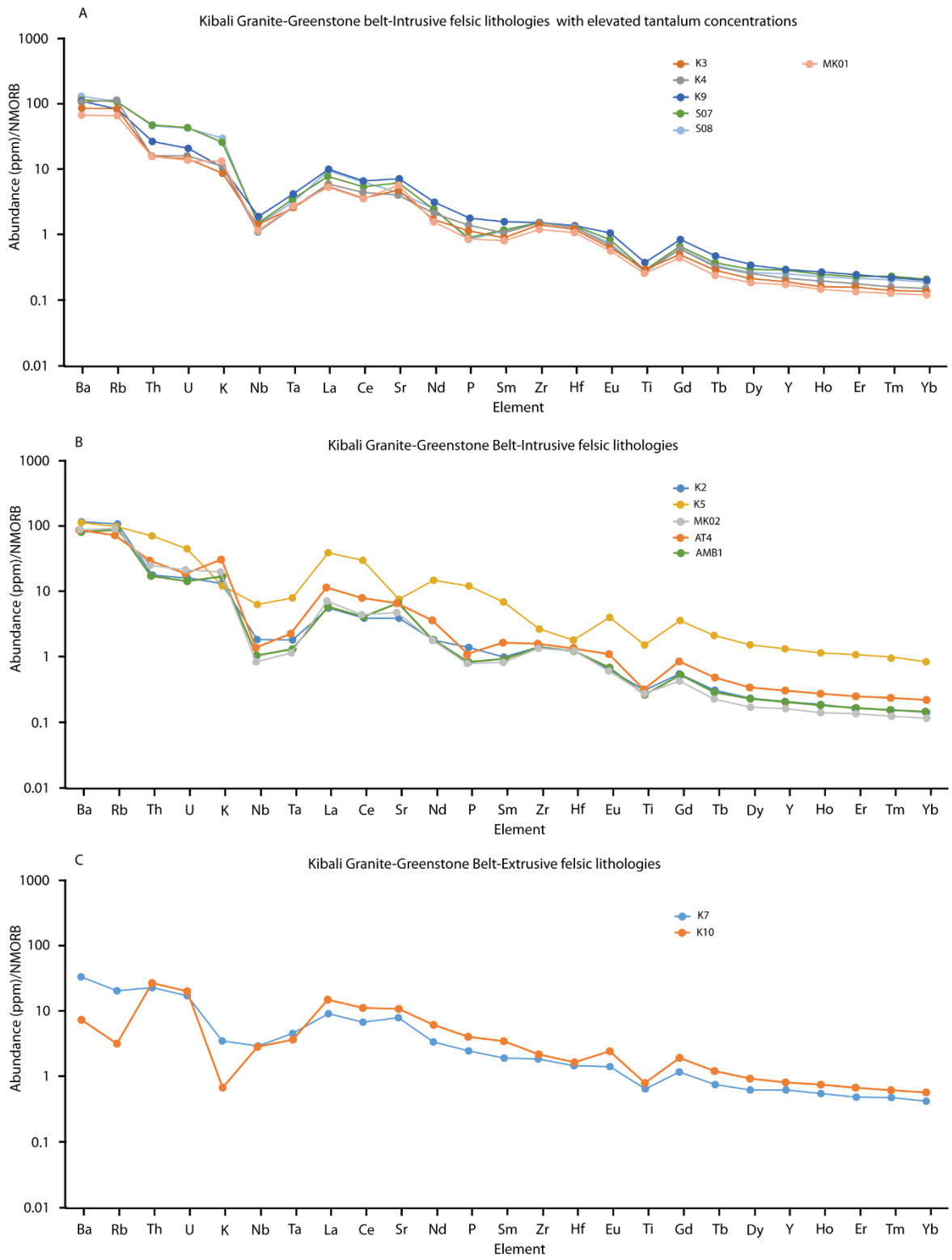


Figure 5.4: NMORB normalised extended trace-element diagrams displaying data from the intrusive and extrusive felsic lithologies from the Kibali Granite-Greenstone Belt

5.3.1.2 Kibali Granite-Greenstone Belt; Mafic Intrusive/Extrusive Units

The mafic intrusive lithologies range in composition from 45.84 to 50.58 wt% SiO₂, 2.64 to 8.30 wt% MgO, 8.96 to 13.41 wt% CaO and 0.04 to 1.17 wt% K₂O with trace-element concentrations ranging from 0.03 to 0.40 ppm U, 6.07 to 17.31 ppm Ce, 13.9 to 60.5 ppm Zr and 0.9 to 3.5 ppm Dy. The mafic extrusive lithologies range in composition from 43.86 to 48.42 wt% SiO₂, 7.93 to 19.11 wt% MgO, 5.75 to 14.00 wt% CaO and 0.07 to 0.09 wt% K₂O with trace-element concentration ranging from 0.05 to 0.08 ppm U, 5.5 to 15.07 ppm Ce, 31.4 to 35.1 ppm Zr and 1.1 to 2.1 ppm Dy. Plots of the trace-element concentrations against Zr (Fig. 5.2) show the intrusive and extrusive mafic data plot in the same geochemical space and define an approximately linear trend. This linear trend initially aligns with the trend formed by the felsic lithologies when the LFSE are plotted, however the two trends diverge with increasing ionic potential (Fig. 5.2).

REE patterns (Fig. 5.3e) for the intrusive mafic lithologies are characterised by elevated LREE relative to the HREE with significant fractionation of the middle and heavy REE, in detail, La/Sm_{CN}=1.47 to 4.06, La/Yb_{CN}=1.88 to 28.52, Tb/Yb_{CN}=0.85 to 1.04. Sample KS2 is the exception, displaying a flat REE pattern (Fig. 5.3E) characterised by La/Sm_{CN}=0.90, La/Yb_{CN}=0.88 and Tb/Yb_{CN}=0.88. The extrusive mafic lithologies display two distinct REE distribution patterns. Samples AT1 and AT2 show flat REE patterns (Fig. 5.3F) characterised by La/Sm_{CN}=0.95 to 1.05, La/Yb_{CN}=0.98 to 1.08 and Tb/Yb_{CN}=0.85 to 0.86. In contrast sample AT5 displays significant fractionation of the HREE relative to the LREE (Fig. 5.3F) characterised by La/Sm_{CN}=2.51, La/Yb_{CN}=6.14 and Tb/Yb_{CN}=1.10 with a significant negative Eu anomaly (Eu/Eu*_{CN}=0.41). NMORB normalised extended trace-element distribution patterns of the Intrusive mafic lithologies show MFSE-HFSE (P-Yb) concentrations comparable to NMORB (Fig. 5.5A). The LFSE are enriched relative to NMORB with negative anomalies observed in the concentrations of Nb (Nb/La_{NM}=0.16 to 0.67), Ta, U and Th and positive anomalies in La and Sr (Fig. 5.5a). The data for the extrusive mafic lithologies shows LFSE and HFSE concentrations comparable to NMORB with the elements of lowest ionic potential (Ba, Rb) displaying enrichment relative to MORB (Fig. 5.5b).

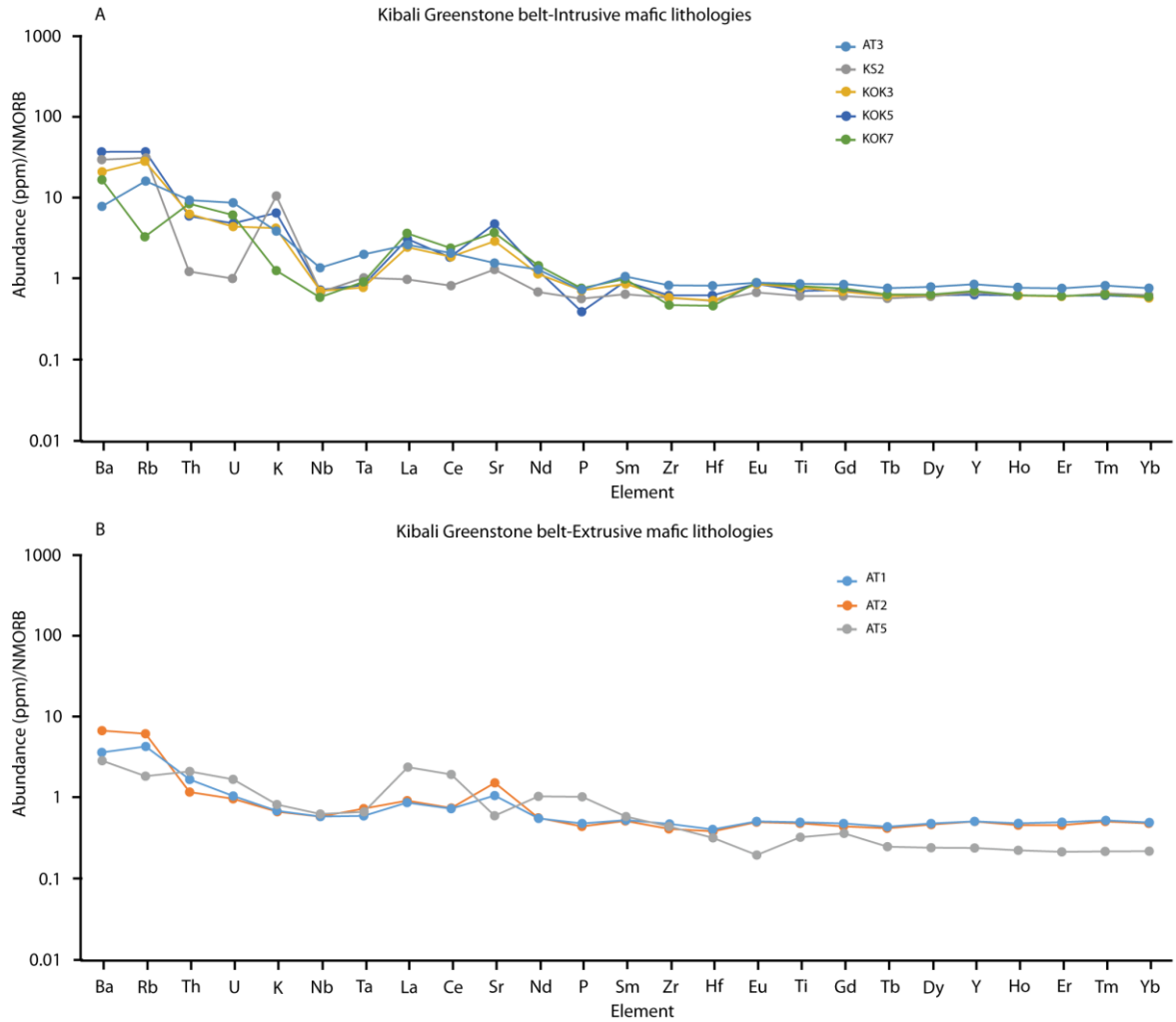


Figure 5.5: NMORB normalised extended trace-element diagrams displaying data from the intrusive and extrusive mafic lithologies from the Kibali Granite-Greenstone Belt

5.3.1.3 Upper Congo Granite Massif: Felsic Intrusive Units

The felsic intrusive lithologies from the UCG range in composition from 55.59 to 77.88 wt% SiO₂, 0.13 to 6.73 wt% MgO, 0.47 to 11.17 wt% CaO and 1.41 to 3.23 wt% K₂O with trace-element concentrations ranging from 0.8 to 3.9 ppm U, 78.5 to 132.7 ppm Ce, 109.2 to 303.9 ppm Zr, and 1.9 to 5.8 ppm Dy. Plots of the trace-element concentrations against Zr (Fig. 5.6) show the felsic intrusive lithologies form a cluster of data when the LFSE are considered becoming more linear, though retaining a high degree of scatter, when the HFSE are examined.

REE patterns (Fig. 5.3 C) display a negative gradient, the LREE being significantly enriched relative to the MREE and HREE (La/Sm_{CN}=2.04 to 5.68, La/Yb_{CN}=8.26 to 32.56, Tb/Yb_{CN}=1.43 to 2.27). Negative Eu

anomalies are observed in all samples, being relatively minor in the majority ($\text{Eu}/\text{Eu}^*_{\text{CN}}=0.73$ to 1.04) with sample H3 possessing a significantly larger negative Eu anomaly ($\text{Eu}/\text{Eu}^*_{\text{CN}}=0.03$) (Fig. 5.3 C). Trace-element concentrations form a tight grouping when normalised against NMORB (Fig. 5.7) with only minor variations between samples. The data defines a shallow negative trend with LFSE enriched relative to NMORB and HFSE concentrations below NMORB values (Fig. 5.7). Negative excursions are identified in Nb, Ta, Ti ($\text{Nb}/\text{La}_{\text{NM}}=0.07$ to 0.42), Th and Sr with a positive anomaly identified in the Gd concentrations (Fig. 5.7).

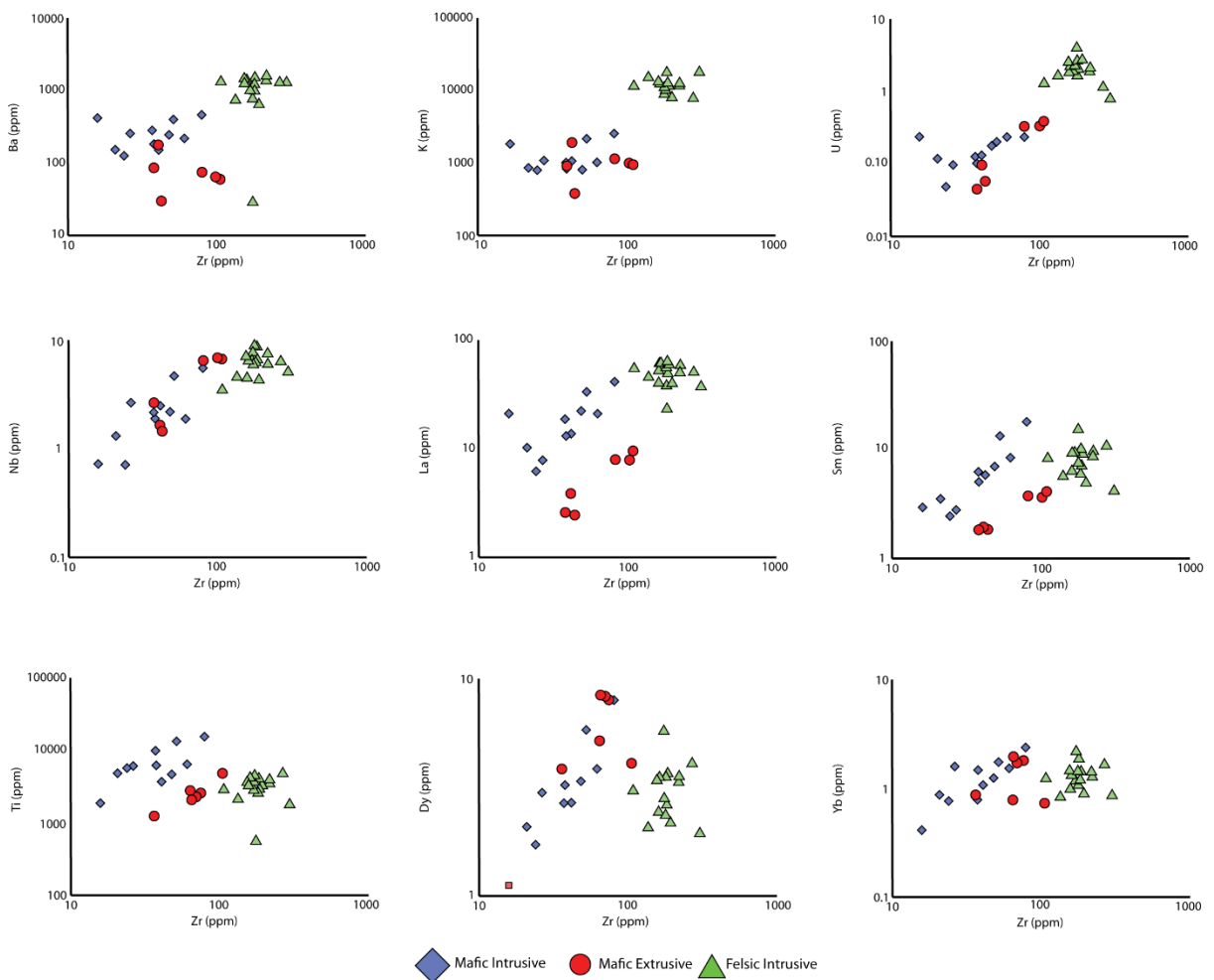


Figure 5.6: Bivariate plots displaying geochemical data for samples from the Upper Congo Granite massif

5.3.1.4 Upper Congo Granite Massif: Mafic Intrusive/Extrusive Units

The Intrusive mafic lithologies range in composition from 44.16 to 53.06 wt% SiO₂, 3.55 to 14.27 wt% MgO, 9.30 to 15.63 wt% CaO and 0.14 to 0.38 wt% K₂O with trace-element concentrations ranging from 0.05 to 0.2 ppm U, 14.6 to 105.6 ppm Ce, 15.8 to 80.3 ppm Zr and 1.1 to 8.0 ppm Dy. Bi-variate plots against Zr (Fig. 5.6) shows the Mafic intrusive lithologies form a single linear trend when the LFSE and HFSE are examined. The position of this trend relative to the UCG felsic intrusive data set varies forming a single positive linear trend with Intrusive felsic lithologies when the LFSE are examined, but with increasing ionic potential the trends separate being approximately parallel when the HFSE are considered (Fig. 5.6).

REE patterns display a shallow negative gradient (Fig. 5.3 A) with a low degree of fractionation in the LREE characterised by La/Sm_{CN}=1.4 to 1.97 with an outlier at La/Sm_{CN}=4.41. Greater fractionation is observed in the MREE and HREE (Fig. 5.3 A), characterised by La/Yb_{CN}=5.39 to 32.96 and Tb/Yb_{CN}=1.24 to 2.96. Samples W3, W4, W7 and W8 display positive Eu anomalies (Eu/Eu*_{CN}=1.21 to 1.88) (Fig. 5.3 A). Trace-element data, normalised to NMORB, displays enrichment of the LFSE and MFSE with the HFSE showing concentrations at approximately NMORB values (Fig. 5.8 A-B). Negative anomalies are observed in Nb (Nb/La_{NM}= 0.03 to 0.37), Ta, Ti, Th, U, Zr and Hf concentrations (Fig. 5.8 A-B). Positive anomalies are identified in the concentrations of Eu and Gd within all samples (Fig. 5.8 A-B). The samples divide into two distinct groups based on the presence of a significant positive Sr anomaly and coexisting positive La anomaly (Fig. 5.8 A-B). The samples that display the positive Sr anomaly are also marginally depleted in the MFSE and HFSE relative to the other samples.

The extrusive mafic lithologies range in composition from 48.03 to 51.10 wt% SiO₂, 5.43 to 9.06 wt% MgO, 10.59 to 16.39 wt% CaO and 0.07 to 0.34 wt% K₂O with trace-element concentrations ranging from 0.05 to 0.3 ppm U, 6.6 to 23 ppm Ce, 38.2 to 107.7 ppm Zr and 2.7 to 4.4 ppm Dy. Bivariate diagrams show the extrusive mafic data occupying the same geochemical space as the intrusive mafic lithologies when the LFSE are considered. Examining the MFSE and HFSE however shows that with increasing ionic potential the two data sets separates out forming independent trends (Fig. 5.6). This is most apparent in plots of La, Sm and Ti against Zr (Fig. 5.6).

REE patterns define two distinct trends (Fig. 5.3 B). Samples W15, W17 and W18 define flat trends with only minor fractionation of the MREE and HREE (Fig. 5.3) characterised by La/Sm_{CN}=0.86 to 1.27, La/Yb_{CN}=0.84 to 1.50 and Tb/Yb_{CN}=0.89 to 0.97. Samples W1, W16 and W21 show significant fractionation of the MREE and HREE relative to the LREE (Fig. 5.3 B), characterised by La/Sm_{CN}=1.34 to 1.44, La/Yb_{CN}=2.41 to 2.78 and Tb/Yb_{CN}=1.23 to 1.32. Trace-element concentrations normalised to

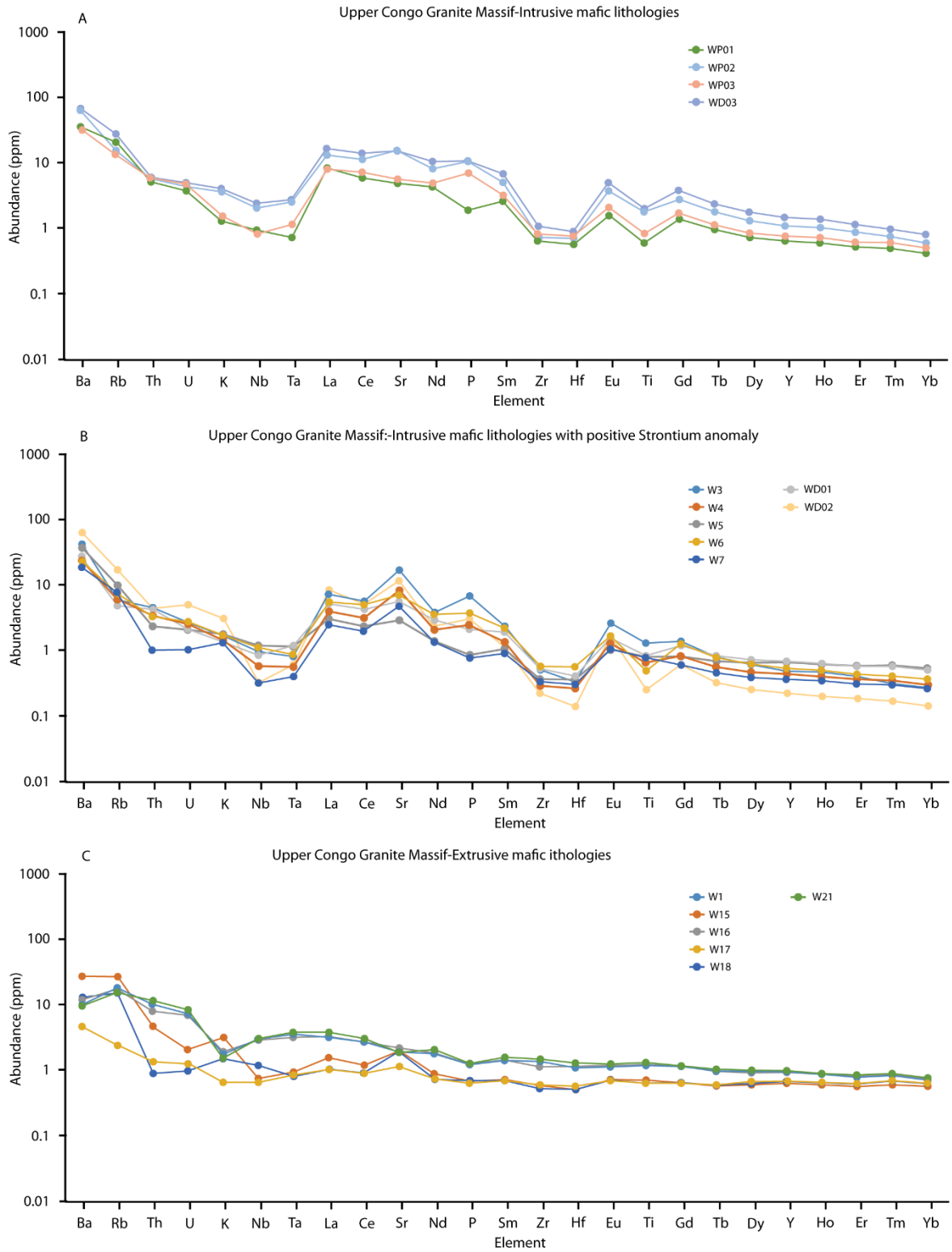


Figure 5.8: NMORB normalised extended trace-element diagrams displaying data from the intrusive and extrusive mafic lithologies from the Upper Congo Granite Massif

of the elements of lowest ionic potential elements have been significantly modified through post crystallisation effects. This is attributed to a combination of regional metamorphism and the development of widespread alteration assemblages associated with regional fluid flow (Chapter 4). Conversely the majority of the MFSE and all of the HFSE elements are considered to have not been modified by the regional metamorphism and alteration and instead representing original magmatic concentrations.

5.4.2 Classification of Igneous Lithologies

Geochemical data provides an independent quantitative mechanism by which to classify lithologies. Multiple methods of classifying igneous rocks exist, including the Total alkali-silica (TAS) (Peccerillo and Taylor, 1976; Le Bas et al., 1986) and QAPF (utilising recalculated CIPW norms). The above bi-variate plots (Fig. 5.2 and 5.6) demonstrated that elements of low ionic potential have been mobilised, hypothesised to be a result of regional alteration. This mobility within the elements of low ionic potential precludes the use of the classification schemes listed above, the geochemical characteristics of the intrinsic variables (Si, Al, K, Na etc.) utilised by these diagrams having been significantly modified. The medium and high field strength elements are however considered immobile in the system, representing primary concentrations and making them suitable for use in geochemical classification.

Here the Th-Co method developed by Hastie et al. (2013) is utilised. While thorium is always considered as an immobile element (Jolly et al., 2006; Escuder Viruete et al., 2007; Hastie et al., 2007; Escuder Viruete et al., 2011), Cobalt is not typically considered immobile within geological systems. Hastie et al. (2007) highlighted the compatibility of Cobalt with chlorite, Fe-Ti oxides and amphibole during metamorphism and strong absorption onto iron and manganese oxyhydroxides during tropical weathering processes as indicators of its low mobility (Hastie et al., 2007). The Th-Co diagram developed by Hastie et al. (2007) acts as a proxy for the widely used TAS diagram. Hastie et al. (2007) demonstrated that Thorium is the most immobile element that behaves non-conservatively in subduction environments, behaviour in a similar manner to potassium, and that cobalt shows an inverse correlation with SiO₂ (Hastie et al., 2013).

The behaviour of Th and Co in the data sets from the KGGB and UCG have been examined by plotting thorium concentrations against zirconium (Fig. 5.9 A-D). Plots of Th values display a series of overlapping positive linear trends while plots of Co values show a series of scattered, approximately linear trends. While not an ideal correlation the data shows a lower degree of scatter than that observed in the LILE elements making it more favourable for use in the classification of lithologies.

The Th-Co classification scheme divides the data from the KGGB into two broad clusters (Fig. 5.10 A), correlating to the felsic (12 samples) and mafic (8 samples) subdivisions. The felsic intrusive lithologies

range from 1.8 to 8.5 ppm Th and 7.7 to 23.6 ppm Co and plot across three compositional fields, calc-alkaline diorite (5 samples), high-k diorite (1 sample) and calc-alkaline granite (4 samples) (Fig. 5.10 A). The felsic extrusive lithologies range in composition from 2.7 to 3.2 ppm Th and 17.9 to 28.9 ppm Co, both samples plotting as calc-alkaline andesite (see Fig. 5.10 A). The felsic intrusive lithologies range in composition from 0.1 to 1.0 ppm Th and 32.4 to 58.6 ppm Co plotting as calc-alkaline gabbro (4 samples) and island arc tholeiite gabbro (1 sample) (Fig. 5.10 A). The felsic extrusive lithologies range in composition from 0.1 to 0.2 ppm Th and 44.0 to 97.8 ppm Co, plotting in the island arc tholeiite basalt (2 samples) and calc-alkaline basalt (1 sample) fields (Fig. 5.10 A).

The samples from the UCG display a similar bi-modal distribution to that observed in the KGGB correlating to the 'felsic' and 'mafic' subdivisions. The felsic intrusive samples range in composition from 4.4 to 17.6 ppm Th and 0.4 to 27.2 ppm Co plotting across the high K diorite (13 samples) and high K Granite (4 samples) fields (Fig. 5.10 B). The mafic extrusive samples range in composition from 0.10 to 1.3 ppm Th and 38.2 to 50.2 ppm Co plotting within the calc-alkaline basalt (4 samples) and island arc tholeiitic basalt (2 samples) fields (Fig. 5.10). The mafic intrusive samples range from 0.1 to 0.7 ppm Th and 6.9 to 56.3 ppm Co plotting as calc-alkaline gabbro (4 Samples), island arc tholeiitic gabbro (3 samples), island arc diorite (3 samples) and island arc granite (1 sample) (Fig. 5.10 B).

5.4.3 Co-genetic Origin Between Terranes

Examination of the trace-element distribution patterns for the four major sample groups highlights a number of similarities between the lithologies from the two terranes.

The felsic intrusive lithologies from the two terranes both display significant fractionation of the HFSE relative to the LFSE (Fig. 5.3) (UCG intrusive felsic average $\text{La/Yb}_{\text{CN}}=25.83$, KGGB intrusive felsic average $\text{La/Yb}_{\text{CN}}=25.56$) with NMORB normalised trace-element diagrams from both terranes displaying significant negative Nb, Ta and Ti anomalies (UCG intrusive felsic average $\text{Nb/La}_{\text{NM}}=0.15$, KGGB intrusive felsic average $\text{Nb/La}_{\text{NM}}=0.189$) and positive Gd anomalies (Fig. 5.4 and 5.7). The KGGB extrusive lithologies possess similar NMORB trace-element distribution with the negative Nb, Ta and Ti anomalies (average $\text{Nb/La}_{\text{NM}}=0.25$) being present (Fig. 5.4). However the degree of fractionation between the LREE and HREE is notably less (average $\text{La/Yb}_{\text{CN}}=13.42$) (Fig. 5.3). Due to the similarities between the trace-element distribution of the KGGB intrusive/extrusive felsic lithologies and the UCG felsic lithologies, it is considered probable that these units originated in similar tectonic settings.

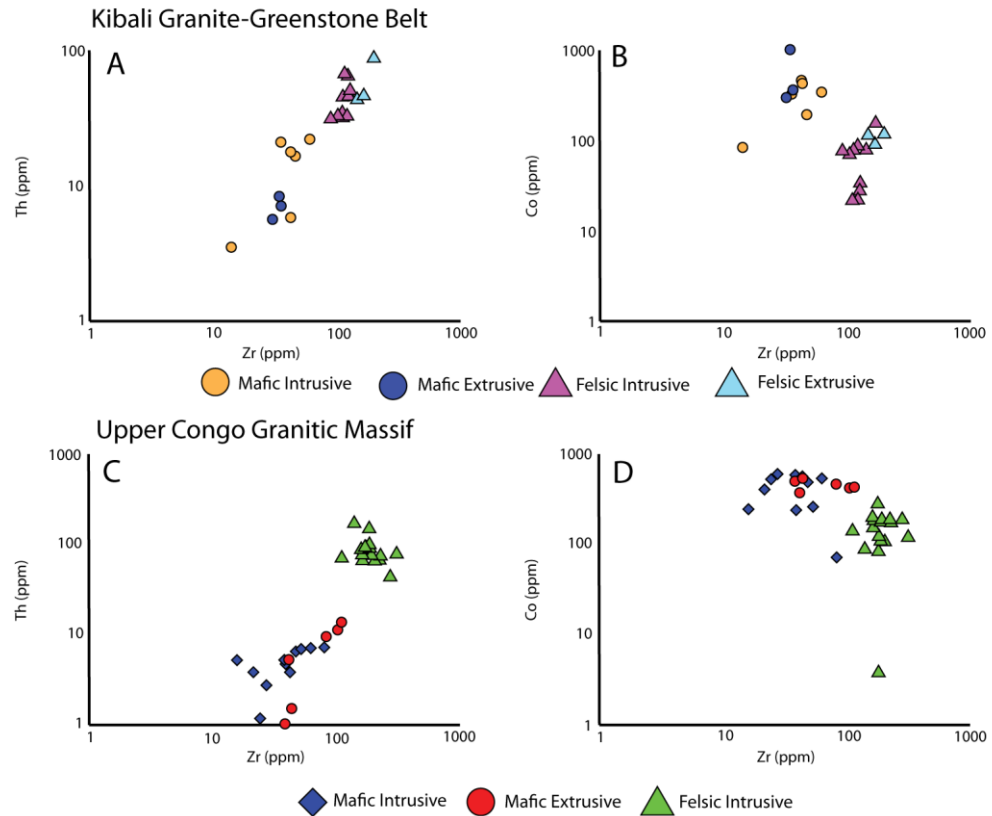


Figure 5.9: Th and Co concentrations plotted against Zr demonstrating relative immobility of these elements. A and B; Kibali Granite-Greenstone Belt. C and D; Upper Congo Granite Massif.

Based on this inferred co-genetic origin these units are considered to represent a single large ‘felsic suite’ and shall be discussed as such below.

The UCG intrusive mafic lithologies display some similarities to the felsic suite discussed above with REE plots displaying a negative gradient indicating fractionation of the HREE relative to the LREE (Fig. 5.3) though the degree of fractionation is significantly less (average $La/Yb_{CN}=11.25$). The trace-element distribution patterns also show similar characteristics with distinct negative Nb, Ta and Ti anomalies (average $Nb/La_{NM}=0.15$) and minor positive Gd anomalies (Fig. 5.8). The mafic intrusive lithologies do however show a number of differing characteristics.

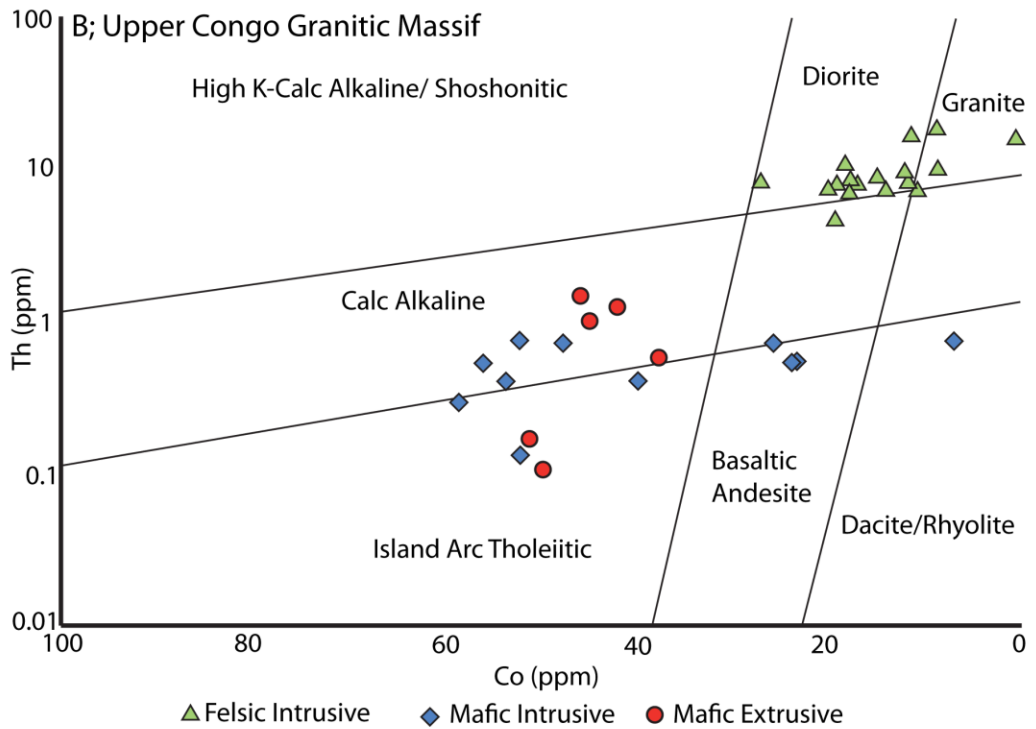
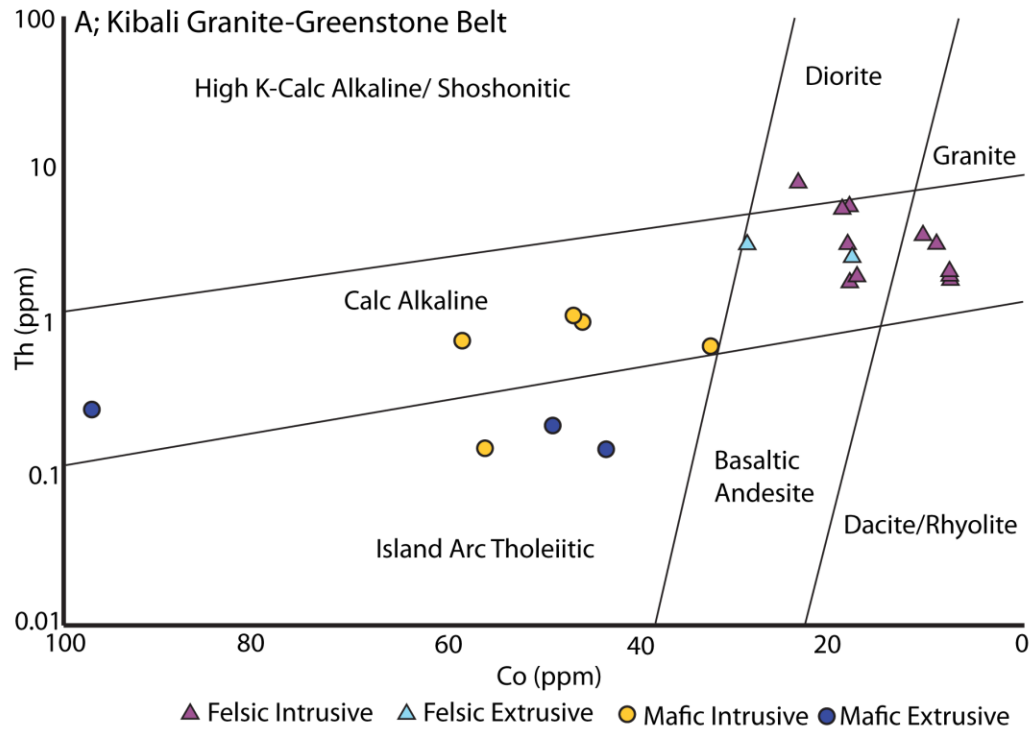


Figure 5.10: Th/Co classification diagram for data from the Kibali Granite-Greenstone Belt (upper) and the Upper Congo Granitic Massif (Lower). Field lines and labels from Hastie et al. (2007).

The UCG intrusive mafic lithologies display significant negative Zr, Hf, Th and U anomalies and positive Sr and Eu anomalies (Fig. 5.8). Despite some similarities in the trace-element behaviour the UCG mafic intrusives have distinct characteristics that indicate a significantly different evolution from the lithologies of the felsic suite and so are considered to have an independent evolutionary history to the ‘felsic suite’ lithologies from the KGGB and UCG.

The UCG extrusive mafic lithologies and KGGB intrusive/extrusive mafic lithologies) display a number of similar characteristics. Multi-element plots for these lithologies show NMORB like concentrations of the MFSE and HFSE (Fig. 5.5 and 5.8) but with variable enrichment in the LFSE and LILE. While significant variations are observed within each data set the similar enrichment of the LFSE and MFSE observed within the individual sample divisions are thought to indicate the samples share a similar origin and so are discussed below as the ‘mafic suite’.

5.4.4 Petrogenesis and Tectonic Affinity

5.4.4.1 Felsic Suite

The lithologies of the felsic suite are characterised by fractionation of the HFSE and negative anomalies of Nb, Ta and Ti (Fig. 5.4 and 5.7). These geochemical features are characteristic of modern subduction zone partial melts (Pearce and Peate, 1995) with this geodynamic setting thought to be relevant for the lithologies of the ‘felsic suite’. Negative Nb, Ta and Ti anomalies are consistent with residual Fe-Ti oxides (ilmenite, rutile) acting as refractory phases during partial melting at source (Stolz et al., 1996). Enrichment (relative to NMORB) of the LILE, LFSE and MFSE is linked to the enrichment of the overlying mantle wedge by fluids exsolved from a descending slab at a subduction zone (Elliott, 2003; Pearce and Stern, 2006). Fractionation of the HREE is indicative of a residual refractory phase(s) in the source region. The HREE are preferentially partitioned by a number of minerals with amphibole, clinopyroxene and garnet being the most significant (Davidson et al., 2013). Clinopyroxene favourably partitions the LREE, amphibole the MREE and garnet the HREE (Davidson et al., 2013). The ‘felsic suite’ suite shows a greater degree of fractionation in the MREE (average $Sm/Tb_{CN}=3.08$) compared to the HREE (average $Tb/Yb_{CN}=2.04$) suggesting residual amphibole has had a more significant effect. While partitioning of the MREE and HREE in to residual amphibole and garnet at source is favoured the same effect can be achieved through fractional crystallisation of amphibole during ascent through the crust (Pearce and Peate, 2005).

The subdivision of samples that display elevated Ta concentrations, relative to Nb ($Nb/Ta=7.10$ to 10.10) (Fig. 5.4), is unusual as these two elements are normally regarded as behaving identically in geochemical systems due to their similar size and ionic potential (Foley et al., 2002). The trace-element patterns (Fig. 5.4)

indicate that the behaviour of Nb and Ta has become uncoupled resulting in low Nb/Ta ratios. Fractionation of Nb and Ta is widely identified within Archean TTG terranes and has been linked to the melting of amphibolites containing low-Mg amphiboles within the subducting slab (Foley et al., 2002), facilitated by the elevated geothermal gradients during the Archean. Alternatively Stolz et al. (1996) proposed that low Nb/Ta values, $Nb/Ta < 14$, can be generated through partial melting of an HFSE depleted mantle source which would also result in HFSE concentrations below NMORB values (Stolz et al., 1996). Stolz et al. (1996) also found that low Nb/Ta ratios (~ 8) can be generated through partial melting of pelitic sediments containing biotite, with residual rutile again controlling Nb/Ta variations (Stolz et al., 1996).

High Zr/Sm ratios in the samples from the felsic suite ($Zr/Sm=28.22$ to 46.38) support the low Mg amphibole melting mechanism proposed by Foley et al. (2002) who demonstrated high Zr/Sm ratios accompanying high Nb/Ta values in Archean TTG material (Foley et al., 2002). This subset of the samples represents the most extreme example of Nb/Ta decoupling in the 'Felsic suite'. The Nb/Ta values in the lithologies of the 'felsic suite' are in general low ($Nb/Ta=7.19$ to 27.50 with average $Nb/Ta=14.04$) with variable Zr/Sm ratios ($Zr/Sm=10.50$ to 48.02) (Fig. 5.12). These data indicate that the felsic suite was generated through melting associated with low-Mg amphibolites in a subducting slab and is consistent with observations made on the trace-element distribution patterns.

The extrusive igneous lithologies while displaying the features characteristic of island arc subduction melting display notable enrichment in the MFSE and HFSE relative to the felsic intrusive lithologies and a notably lower degree of fractionation, average $La/Yb_{CN}=13.42$ compared to the intrusive lithologies (Fig. 5.4 and 5.7). Average $La/Yb_{CN}=25.70$. Lower fractionation between the LREE and HREE can be explained through two distinct mechanisms, a higher proportion of melting at source or the samples represent a highly evolved end member, the incompatible elements having been concentrated into this last melt fraction.

5.4.4.2 UCG Mafic Intrusives

The Nb, Ta and Ti anomalies ($Nb/La_{NM}=0.03$ to 0.37) and significant fractionation of the HREE ($La/Yb_{CN}=5.8$ to 32.9) identified in the UCG mafic intrusives are consistent with formation at an island arc subduction zone. The mechanisms that result in these characteristics having been discussed above (Section 5.4.4.1). The NMORB normalised trace-element distribution patterns (Fig. 5.8) do however show a number of significant differences from the felsic suite indicating a distinct independent evolutionary history. Petrological observations (Chapter 4) showed the UCG intrusive mafic lithologies possess a distinctive mineralogy dominated by plagioclase feldspar with varying proportions of intercumulus amphibole and orthopyroxene. The positive Eu and Sr anomalies (Fig. 5.8) are indicative of fractional crystallisation and accumulation of plagioclase, Eu and Sr preferentially partitioning into the feldspar phase (Drake and Well,

1973). The concentrations of Th, U, Zr and Hf may also be explained through this mechanism, these elements not readily partitioning into the plagioclase mineral phase and the samples being poor in phases such that would readily partition these elements, such as zircon (Chapter 4). Calculated mineral vectors (Fig. 5.12) show the UCG mafic samples evolving along lines defined by fractional crystallisation of plagioclase and orthopyroxene consistent with the petrological and trace-element observations.

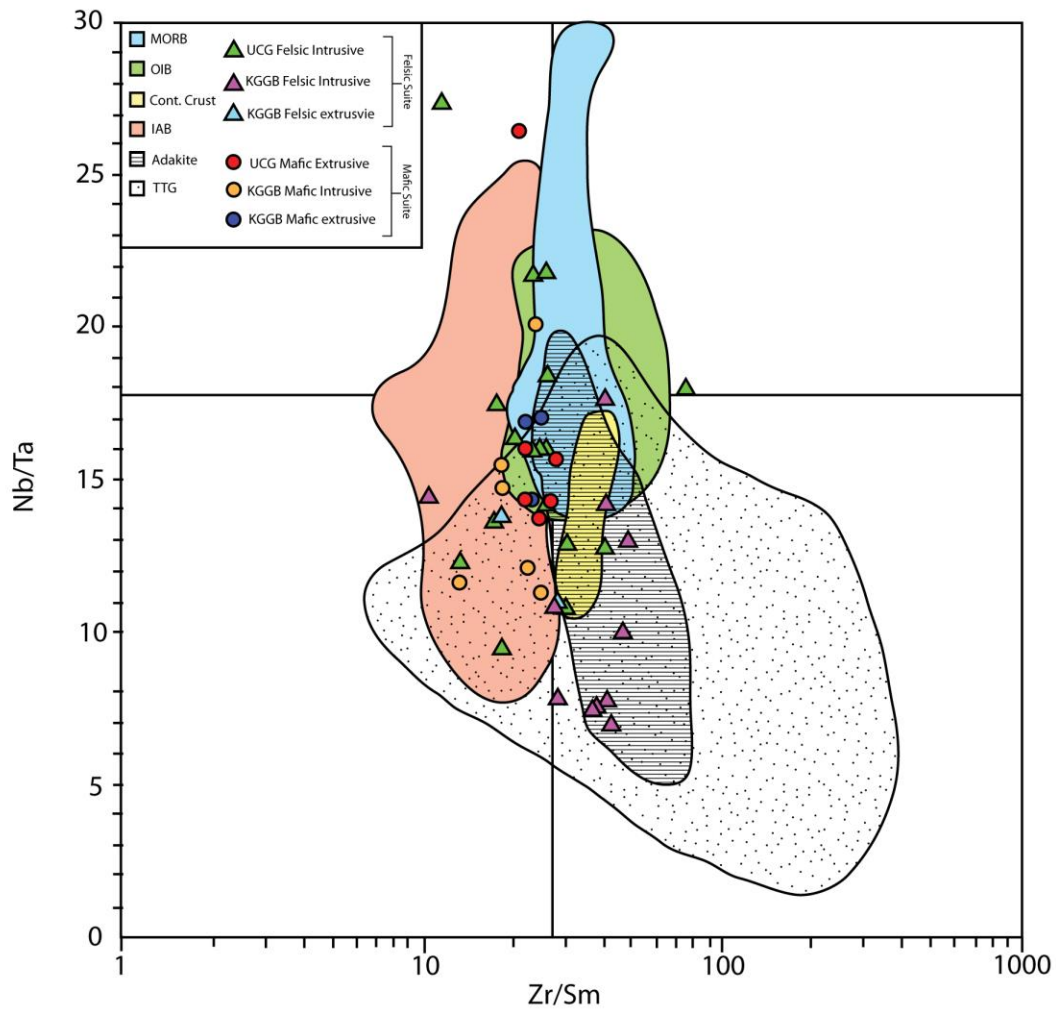


Figure 5.11: Nb/Ta discrimination diagram displaying data from the Kibali Granite-Greenstone Belt and Upper Congo Granite Massif. After Foley et al. (2002). MORB= mid ocean ridge basalt; OIB=ocean island basalt; Cont. Crust= Continental crust; IAB= island arc basalt; TTG=tonalite-trochhjemite-granodiorite

The Eu and Sr anomalies are variable within the samples and likely represent the varying proportions of plagioclase/orthopyroxene/clinopyroxene mineral phases in individual samples (Chapter 4). The low degree of fractionation across the LREE (Fig. 5.3) is linked to the presence of orthopyroxene, derived from the intercumulus melt fraction, the LREE favourably partitioning (relative to the MREE and HREE) into this

mineral phase during crystallisation. The relationship between the UCG mafic intrusives and the UCG felsic intrusive lithologies, whether the felsic lithologies represent the upper part of the magma chamber in which the mafic ‘cumulates’ formed, is difficult to establish with the geochemical data providing contrasting evidence.

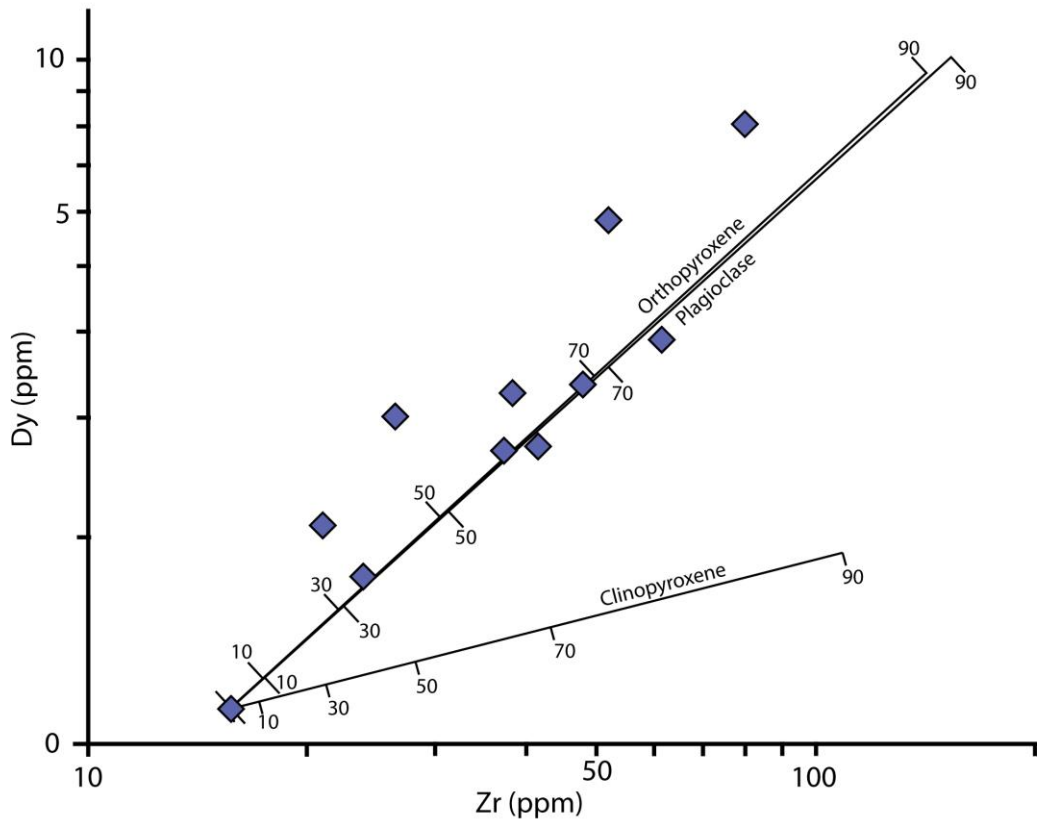


Figure 5.12: Mineral vector diagram displaying data from the UCG mafic intrusives. Mineral vector lines show composition of residual fluid after n% fractional crystallisation. Mineral vectors were calculated by Rayleigh Fractionation utilizing partition coefficients from Rollinson (2003) and starting composition of the least evolved samples within the UCG mafic intrusive samples.

REE distribution (Fig. 5.3) shows some of the UCG felsic intrusive lithologies possess minor positive Eu anomalies, as would be expected if these units represent crystallisation of the remaining melt following significant plagioclase fractionation. The bivariate plots (Fig. 5.6) however show the two divisions forming two distinct trends which would typically indicate they are unrelated. The unusual trace-element characteristics of the UCG mafic intrusives resulting from the atypical crystallisation history, highlighted by the distinctive trace-element distribution pattern, is likely to have resulted in the trace-element concentrations within the samples being unrepresentative of the original magmatic compositions. Due to

these constraints it is not possible at this time to draw firm conclusions regarding the relationship between the felsic and mafic intrusive lithologies within the UCG.

5.4.4.3 Mafic Suite

The mafic suite lithologies are characterised by MFSE and HFSE concentrations comparable to NMORB (Fig. 5.5 and Fig. 5.8) with variable enrichment in the LILE and LFSE. The ‘flat’ trace-element distribution patterns observed in samples AT1, AT2, W15, W17 and W18 (concentrations at approximately NMORB values) are characteristic of melts produced at mid ocean spreading centres through bulk melting of the mantle (Pearce and Stern, 2006). Variable enrichment of the LILE is observed within these samples and is attributed to alteration effects, the development of muscovite, as opposed to being a magmatic component.

The KGGB mafic intrusives and samples AT3, W1, W16 and W21 display HFSE concentrations (Fig. 5.5 and 5.8) consistent with formation at a mid-ocean ridge. The LFSE and LILE characteristics of these samples display notable enrichment relative to MORB, inconsistent with formation at a mid ocean spreading centre. Enrichment of the LILE and LFSE/LREE is typically related to melts produced in a mantle wedge which has been enriched in the LFSE through interaction with fluids related to a subducting oceanic slab (Elliott, 2003; Pearce and Stern, 2006).

Examining the NMORB normalised trace-element distribution (Fig. 5.5 and 5.8) shows the Nb-Ta anomaly characteristic of Island arc melts. These lithologies display a mixed MORB/ARC signature consistent with melting of a metasomatised mantle wedge enriched in the LILE and LFSE (Elliott, 2003; Pearce and Stern, 2006). The similarities in the trace-element distribution characteristics of the LILE and LFSE between the enriched mafic lithologies and the lithologies of the felsic suite, Positive La and Sr anomalies with low Th/U ratios (Fig. 5.5 and 5.8), suggests the source of the LILE/LFSE component in both suites is a subducting slab. These characteristics are consistent with melt formation in an evolving back-arc environment (Pearce and Stern, 2006; Hastie et al., 2013).

The varying degree of enrichment ranging from values consistent with MORB (Average $\text{La}/\text{Sm}_{\text{CN}}=0.99$) to those displaying ARC-like LILE and LFSE (Average $\text{La}/\text{Sm}_{\text{CN}}=1.96$) suggests an evolving back arc system. Studies of modern island arcs have shown that the degree of LILE and LFSE enrichment decreases with increasing distance from the subducting slab (Pearce and Stern, 2006; Hastie et al., 2013).

5.4.5 Slab and Mantle Component Affinity

5.4.5.1 Slab Component

The trace-element distribution patterns from the KGGB and UCG have shown varying tectonic affinity ranging between island-arc/back-arc subduction zone and mid ocean spreading centre with a number of samples illustrating mixed composition between the two. These different trace-element distribution patterns indicate differing degrees of input from the major elemental reservoirs, the subducting slab and associated sediments (crustal component) and the underlying mantle (mantle wedge). Studies of modern island arc and associated back arc sequences in the Caribbean (Hastie, 2009; Hastie et al., 2013) have utilised trace-element modelling to assess the relative mantle and slab component in the melt source region. Application of these discrimination techniques to the data for the Kibali Granite-Greenstone Belt and Upper Zaire Granite massif allows us to examine the origins of certain elements and assess the contribution of slab and mantle components to the melts that formed the igneous lithologies.

The Ce/Ce* vs Th/La diagram ($Ce^* = La^{2/3} \times Nd^{1/3}$) developed by Hastie et al. (2013) specifically examines the crustal component derived from a subducting ocean slab and overlying sediments. Due to the atypical crystallisation history of the UCG mafic intrusive lithologies the trace-element concentrations are no longer representative of the original magmatic composition and as such further application of discriminant diagrams will not yield significant data. The felsic lithologies define a cluster of data across the volcanic and continental detritus fields (Fig. 5.13), this being consistent with the interpreted island arc origin where material derived from the overlying volcanic arc being entrained during the subduction process. The lithologies of the mafic suite form an array of data extending from the ideal NMORB composition to the volcanic detritus field. NMORB compositions can be explained through two distinct mechanisms, melting of uncontaminated mantle material or melting of a subducting slab dominated by mid ocean ridge basalts with little or no external input of material (Hastie et al., 2013). The data shows varying degrees of sediment flux from the subducting slab, consistent with the origin of the melts in an evolving back arc system.

5.4.5.2 Mantle Component

To examine the composition of the mantle wedge component in island arc systems it is necessary to examine elements which will not have been significantly affected by the interaction of slab derived fluids with the mantle wedge. Pearce and Peate (1995) demonstrated that Nb, Zr and Y are not mobilised by slab derived fluids and as such will represent the composition of the mantle wedge. These elements were utilised by Fitton et al. (1997) in the development of the Nb/Y-Zr/Y discrimination diagram to differentiate between MORB and OIB origins.

The 'felsic suite' forms an approximately horizontal array (Fig. 5.14) extending away to the right of the lower tram line indicating a MORB or island-arc/back-arc related MORB like mantle component (Fitton et al., 1997). This observation supports the interpretation that these rocks were formed through subduction related melting. The Mafic suite form a cluster of data at lower Nb/Y and Zr/Y ratios plotting around the lower tramline (Fig. 5.14) and extending left to the area between the tram lines. This position indicates an ocean island origin for the mantle component within these samples (Fitton et al., 1997).

The apparent OIB component is counter to the tectonic distinctions derived from the observation of the trace-element distribution patterns for these lithologies and as such it is important to examine the validity of this interpretation for the available samples. The lithologies under investigation from the UCG and KGGB are considered to have formed during the Archean (Chapter 6). The Nb/Y-Zr/Y discrimination diagram were constructed using modern Icelandic rocks. As such the question of whether the same geological and geochemical processes were operating during the Archean is significant when discussing these discrimination diagrams. Condie (2005) demonstrated that Archean basalts from all tectonic environments consistently plot within the OIB field and proposed that relatively unfractionated mantle with negligible shallow depleted component was responsible for this (Condie, 2005). This would have the effect of moving the 'tram lines' to the left on this diagram. Taking this shift in to account would place the data from the 'felsic suite' within the MORB field.

Pearce (2008) further developed the discrimination diagram concept and improve resolution between different tectonic environments by plotting Nb/Yb (mantle proxy) against Th/Yb (crustal proxy) (Fig. 5.15). Utilising the (Th/Yb) vs (Nb/Yb) discrimination diagram shows the lithologies of the felsic suite plot above the MORB OIB array (Fig. 5.15). This indicates the Th component is dominated by the effect of interaction with Th derived from slab flux (Pearce, 2008). The lithologies of the mafic suite form a diffuse cluster with Nb/Yb compositions between N-MORB and E-MORB with Th/Yb ratios varying in concentration (Fig. 5.15). This distribution is consistent with a back arc basin environment, the degree of enrichment relative to NMORB varying with the dominance of the subduction component (Pearce, 2008). In this scenario MORB concentrations are generated where the inflowing mantle is not significantly affected by the subduction component (Pearce, 2008), in effect with increased proximity to the subducting slab, the subduction component dominates over the mantle component.

Ce/Ce*-Crustal input discrimination

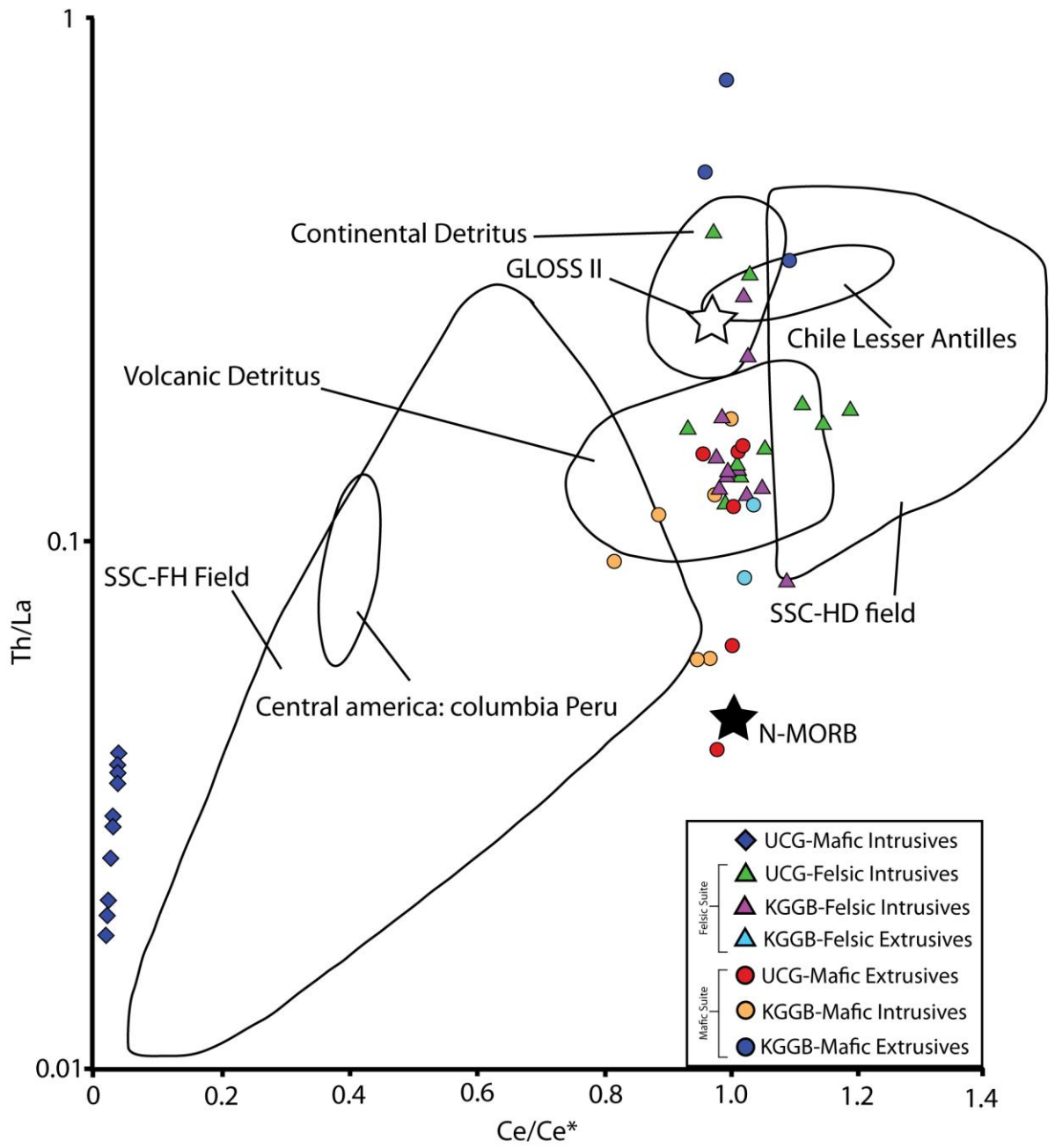


Figure 5.13: Ce/Ce* crustal input discrimination diagram (after Hastie et al., 2013), displaying geochemical data from the Kibali Granite-Greenstone Belt and Upper Congo Granitic Massif.

5.4.6. Geodynamic Setting

Examination of the trace-element components from the KGGB and UCG has demonstrated that the igneous lithologies display characteristics indicative of a range of tectonic environments. The 'felsic suite' and the UCG mafic lithologies show characteristics consistent with formation through subduction related melting at an island arc. Variations in the trace-element distribution of these samples are attributed to crystallisation effects in evolving magmas. These variations are particularly apparent in the UCG Mafic lithologies where the crystallisation and accumulation of plagioclase feldspar have preferentially retained trace-elements compatible in this phase. Due to the consistent similarities in the HFSE distribution, particularly the presence of the notable Gd anomaly (Fig. 5.3, 5.4, 5.5 and 5.7), the lithologies are interpreted as having formed in the same subduction system. Variations in the source are however discernible between the lithological divisions.

Variations in the composition of the descending slab and resultant slab flux are thought to be the primary mechanism by which variations in the geochemical characteristics have arisen. The mafic suite present a range of characteristics from MORB like to intermediate MORB/island-arc/back-arc (Fig. 5.5 and 5.8). Enrichment of the mobile and LILE with otherwise MORB concentrations is associated with melts produced in modern back arc settings where mid ocean ridge melting of mantle material enriched by interaction with fluids produced from a nearby subducting slab. The varying degree of enrichment identified in the mafic suite indicates an evolving back arc system. The distance to the subducting slab reaching a maximum distance sufficient to produce MORB type melts with negligible slab flux.

The physical relationship between the intrusive and extrusive lithologies provides further constraints on the geochemical evolution of the KGGB. The extrusive lithologies are inferred to have formed within the same active oceanic basin system as the sedimentary and BIF component however the 'intrusive' felsic and mafic complexes are interpreted as intruding this sediment pile and as such must have formed after significant back arc spreading and sedimentation had already occurred.

Applying these constraints it is possible to construct a model for the geotectono-chemical evolution of the KGGB (Fig. 5.16). Descending oceanic lithosphere at an active convergent margin exsolved fluids which metasomatised the overlying mantle wedge triggering partial melting of the slab generating magmas of typical 'arc affinity' which ascend to form arc crust (Fig. 5.16a). Arc magmas are emplaced within the overlying arc crust forming multi-generation intrusive complexes with varying crystallisation processes. Slab roll back and convection of the mantle wedge causes thinning of the overlying arc crust which transitions to true ocean ridge spreading.

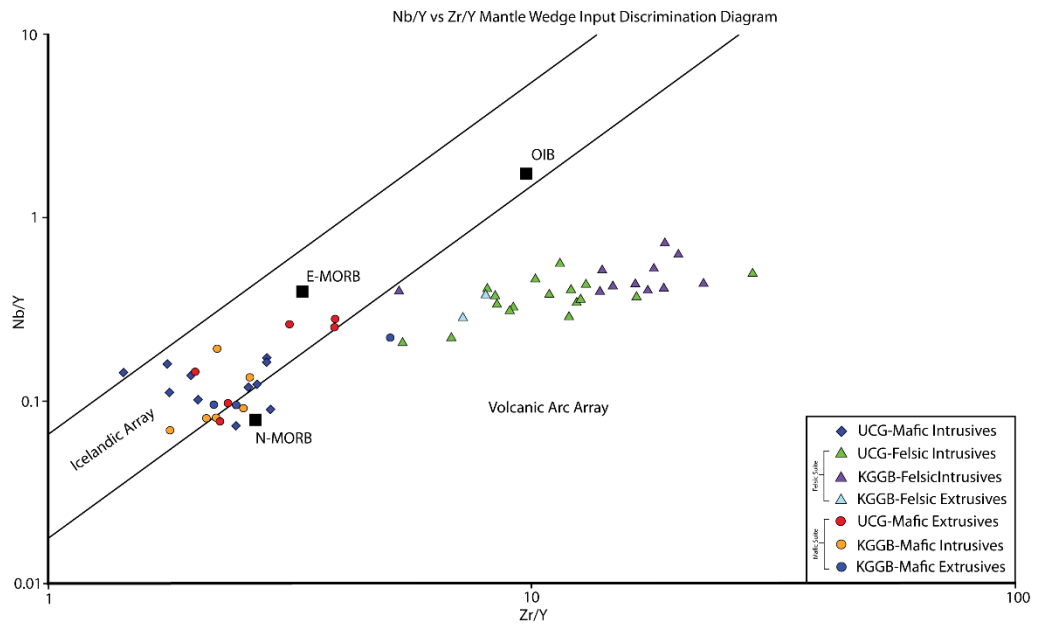


Figure 5.14: Nb-Zr mantle wedge discrimination diagram displaying geochemical data from the Kibali Granite-Greenstone Belt and Upper Congo Granitic Massif. After Fitton et al., 1997.

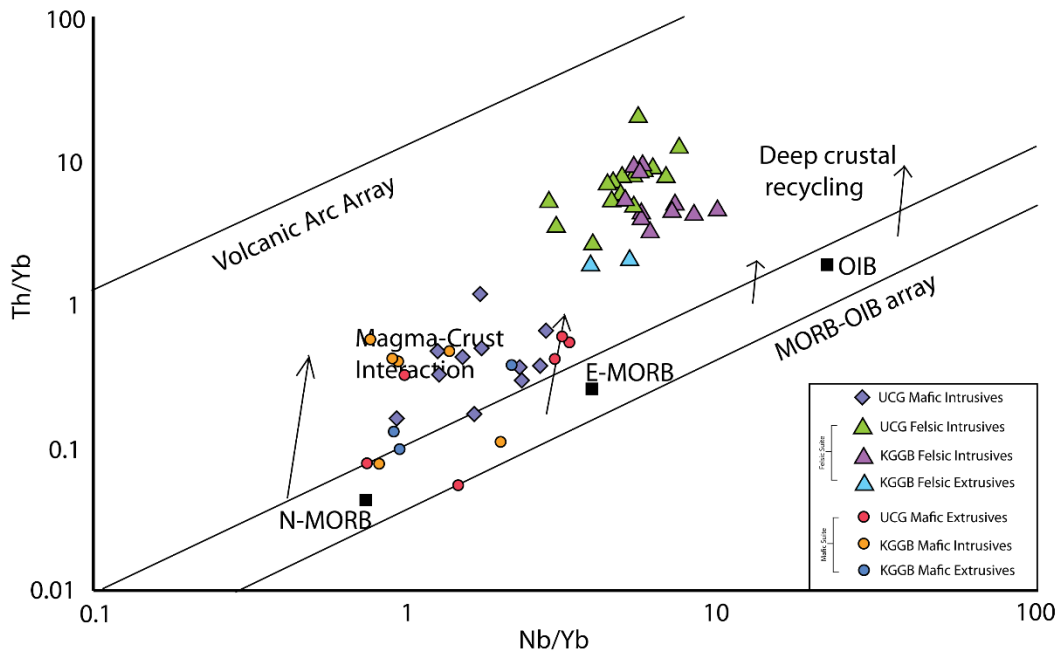


Figure 5.15: Th-Nb mantle input discrimination diagram, after Pearce (2008), displaying geochemical data from the Kibali Granite-Greenstone Belt and Upper Congo Granite Massif.

Decompression melting of the metasomatised mantle at this new spreading centre generates basalts of mixed MORB/ARC characteristics (Fig. 5.16B). Back Arc basin development continues, forming an oceanic basin with active formation of varied sedimentary lithologies and BIF with interleaved basalts. Back arc extension and basalt formation continued until the metasomatised mantle wedge no longer contributed a significant LREE component, producing basalts of typical MORB composition. Continued melt production from the descending slab, producing magmas of island-arc type, and the metasomatised mantle, producing magmas of mixed island-arc/MORB, resulted in the formation of the intrusive lithologies within the basalt/sediment package, similar to the formation of modern rear arc sea-mounts (Fig. 5.16c). The geochemical data do not provide any insight on the transition from extensional back arc tectonics to the compressional convergent tectonics necessary to create the characteristics observed within the Kibali Granite-Greenstone Belt in modern times.

The presence of a back arc basin system also has significant implications for the gold mineralisation present within the KGGB. Tomkins (2013) identified the tectonothermal conditions present during the closure and associated thrusting of back arc basin systems as favourable to the development of orogenic gold systems. The presence of elevated LILE, linked to the development of alteration assemblages, across the samples from both terranes suggests a region wide alteration event, though the relationship of this to the development of the Kibali Granite-Greenstone Belt and Upper Congo Granitic Massif (and potentially gold mineralisation) is not apparent from the geochemical data. Geochemical studies of the Sukumaland (Manya and Maboko, 2003), Iramba-sekenke (Manya and Maboko, 2008) and Musoma-Mara (Manya et al., 2006) greenstone belts in northern Tanzania have identified island Arc and Back Arc characteristics similar to that observed within the KGGB. Cook et al. (2015) hypothesised an oceanic plateau (plume) origin for basalts of the Kiziba formation (Sukamaland Terrane) that display similar flat REE patterns with minor LREE enrichment. The interpretation put forward by Cook et al. (2015) may be relevant when considering the extrusive basaltic from the KGGB and UCG however the evolving arc scenario is still preferred given the strong association with samples of clear Arc and intermediate Arc/MORB composition. Though the relationship between the granite-greenstone belts of the Bomu-Kibalian block and northern Tanzania are debated, the KGGB belt is here hypothesised to represent the north-west continuation of this Neo-Archean trend, the granite-greenstone terranes accreting along the northern margin of a Mesoarchean cratonic route (unknown in the Congo craton but well documented in the as the Dodoma basement terranes in Tanzania (Kabete et al., 2012a).

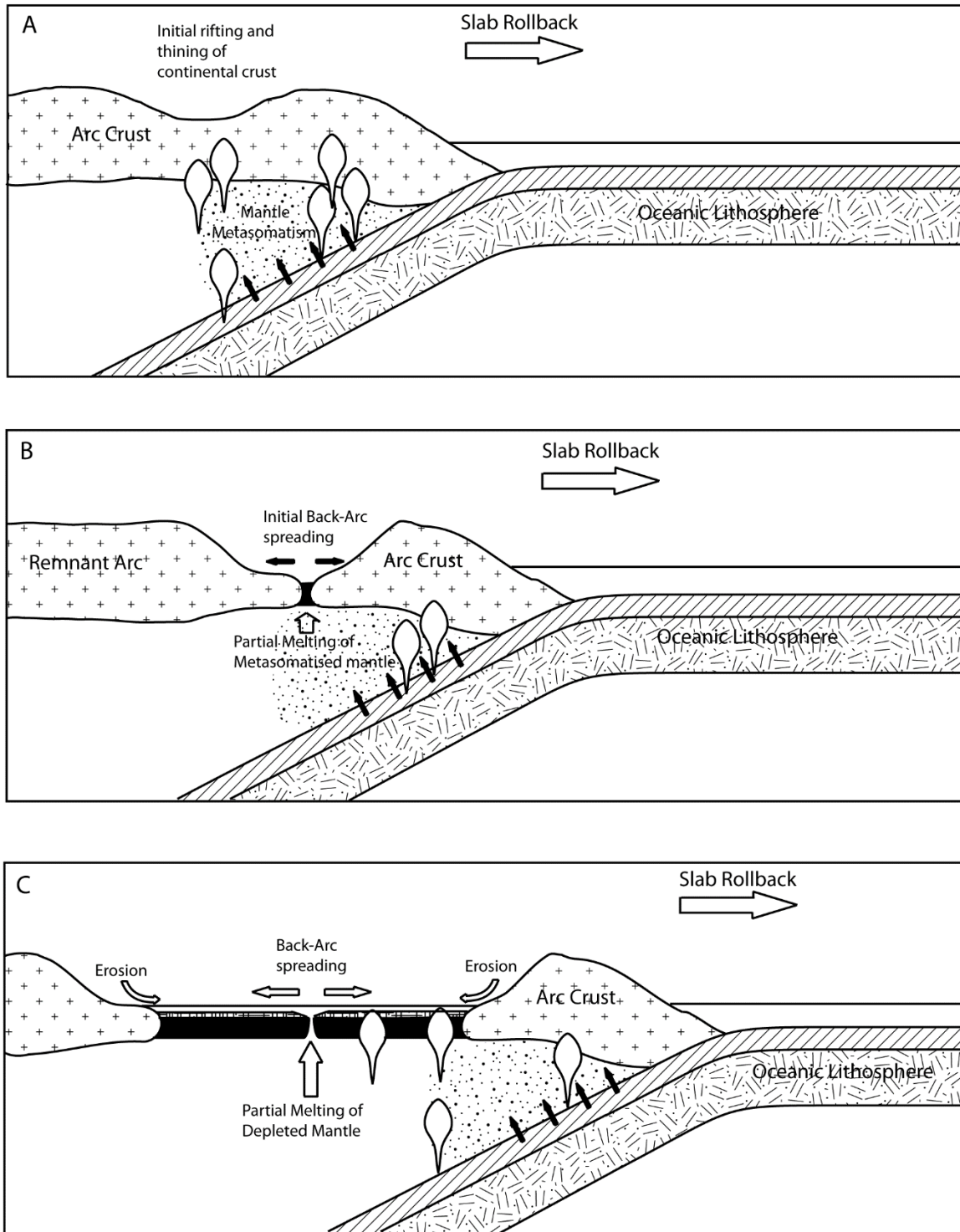


Figure 5.16: Geo-tectonic reconstruction of the early evolution of the Kibali Granite-Greenstone Belt. (A) Subduction and metasomatism of the overlying mantle wedge, slab melting and formation of overlying island arc crust. (B) Crustal thinning and initiation of back-arc spreading. (C) Continued back-arc basin developments, magmas generated at the subducting slab and in the enriched mantle intrude the overlying back-arc basalt/sediment package.

5.5. Conclusions

The geochemical characteristics of the igneous lithologies from the Kibali Granite-Greenstone Belt and the Upper Congo Granitic Massif have provided essential information regarding the formation and evolution of these two terranes. Geochemical classification of the igneous lithologies shows a bimodal distribution of compositions ranging from island arc-tholeiite basalts and calc-alkaline intrusions to granitic and dioritic lithologies. Trace-element characteristics have been interpreted as indicating the two terranes share a common origin having formed in a geotectonic environment analogous to modern evolving arc/back-arc systems. Felsic intrusive lithologies from both terranes display geochemical characteristics consistent with formation in an island arc environment above an active subduction zone, this geodynamic scenario being hypothesised to exist along the northern edge of the Bomu-Kibalian block and extending southwest into Tanzania during the Neoproterozoic. The basic lithologies from the Kibali Granite-Greenstone Belt and Upper Congo Granitic Massif display geochemical characteristics consistent with MORB and intermediate compositions between MORB and modern Island Arc lithologies. This range of compositions is interpreted to indicate the basic lithologies formed in an evolving basin adjacent to the active subduction zone above which the Island-Arc lithologies formed.

Chapter 6. Geochronological constraints on the origins and evolution of the Kibali Granite-Greenstone Belt and bounding terranes, NE Democratic Republic of Congo

6.1 Introduction

Understanding the relationship between the Kibali Granite-Greenstone Belt (KGGB) and its neighbouring terranes, The Upper Congo Granitic Massif (UCG) and the West Nile Gneiss Complex (WNG) is key to developing a coherent geological history for the development of the region. Geochemical characteristics of intrusive units within the KGGB and UCG demonstrate that the two terranes were formed in similar geotectonic environments, in this case a magmatic arc-back arc system, and it is hypothesised that they formed coevally (Chapter 5). The West Nile Gneiss Complex remains enigmatic and its relation to the hypothesised arc system is poorly understood. To constrain the evolution of the KGGB U:Pb zircon geochronology has been utilised to determine the geochronological characteristics of the Kibali Granite-Greenstone Belt, West Nile Gneiss Complex and Upper Congo Granitic Massif.

6.2 The Uranium-Lead Decay System and its Geochemical Behaviour

The uranium-lead decay system has been extensively utilised over the last century to determine absolute ages for, initially, uranium-bearing lithologies and following improvements in analytical technique absolute ages based on in-situ analysis of individual uranium-bearing minerals. The decay series displays a number of characteristics that make its use preferred in geochronological investigations. Uranium occurs as three naturally occurring isotopes; ^{238}U , ^{235}U and ^{234}U , all three being radioactive parents of decay chains ending in stable lead isotopes (Faure and Mensing, 2005). ^{238}U is the most abundant species accounting for 99.27% of Uranium and decays through the Uranium series by emission of 8 alpha particles and 6 beta particles through a sequence including ^{234}U to ^{206}Pb with a half-life of 4.468×10^9 years. ^{235}U decays through the actinium series by the emission of seven alpha particles and four beta particles to ^{207}Pb with a half-life of 2.45×10^5 years (Faure and Mensing, 2005).

The behaviour of Uranium within geochemical systems facilitates its inclusion into specific minerals achieving concentrations sufficient to facilitate analysis. Uranium isotopes exist in a tetravalent oxide state (4^+) and under oxidizing conditions form the uranyl ion UO_2 (2^+). Uranyl compounds are highly soluble in water making Uranium a highly mobile element under oxidising conditions. Uranium behaves as an

incompatible lithophile element in geological systems and during partial melting is concentrated in to the melt phase (Faure and Mensing, 2005), resulting in the continental crust becoming enriched over time as a result of the progressive geochemical differentiation of the upper mantle (Faure and Mensing, 2005). The major rock forming silicate minerals possess negligible concentrations of uranium, it being concentrated in the melt until the later phases of crystallisation at the point where the melt is also saturated accessory phases such as zircon. As a result significant concentrations of uranium are present in accessory minerals where it is either a principle component, as in Uraninite, or replacing elements, as in Zircon, Monazite, Apatite, Xenotime and sphene (Faure and Mensing, 2005).

Zircon is a common accessory mineral in felsic igneous and metamorphic rocks, its physical and chemical durability combined with the ability to incorporate trace elements has led to its widespread application in geochronological studies (Finch and Hanchar, 2003). Zircon ($ZrSiO_4$) is composed of isolated SiO_4 tetrahedra linked by ZrO_8 polyhedra through sharing of oxygen along polyhedra edges and corners. Substitution of uranium and thorium occurs through the substitution of the Zr^{4+} atom for U^{4+} and Th^{4+} in the ZrO_8 polyhedra (Finch and Hanchar, 2003). Substitution of U and Th in to the crystal lattice is possible due to the matching valence of Uranium and Thorium ions under oxidising conditions and the similar ionic radii, $U^{4+}=1.00 \text{ \AA}$ $Th^{4+}=1.05 \text{ \AA}$, compared to Zr^{4+} (0.84 \AA) (Finch and Hanchar, 2003; Hoskin and Schaltegger, 2003). Non-Radiogenic lead is predominantly excluded from crystallising zircon due to differing valence (Pb^{2+}) and large ionic radius (1.29 \AA) making it incompatible in the formation of O_8 polyhedra (Hoskin and Schaltegger, 2003). A vital component in application of zircon as a geochronometers is the robustness of the U-Pb zircon isotope system. Experimental studies have determined the Pb closure temperature of zircon to be above 900°C indicating that U-Pb ratios and the ages derived from them are unlikely to be modified or reset through thermal effects alone (Lee et al., 1997). Multiple mechanisms have been identified through which modification of the crystal lattice disrupts the isotopic constituents, principally through Pb loss, have been identified including radiation damage, fracturing due to differential lattice expansion, pressure release, recrystallization, self-annealing, chemical reaction and leaching/alteration by fluids (Lee et al., 1997). These mechanisms are thought to only operate at low temperatures (Schoene, 2013) and which is operating in a specific instance must be assessed on an individual basis and it is necessary to establish if the discordance possesses any geological significance (Schoene, 2013; Tilton, 1960).

6.3 Sample Preparation and Analytical Technique

To develop a geochronological model for the Kibali Granite-Greenstone Belt and to further constrain its relationship to the two major bounding terranes, the West Nile Gneiss and Upper Congo Granite Massif, it is necessary to analyse material from each of the three geological terranes. Zircon crystals were initially identified in thin sections from intrusive igneous lithologies from the UCG and KGGB and in metamorphic lithologies from the KGGB and WNG. These initial observations significantly informed sample selection, favouring those samples with abundant zircons of sufficient size to facilitate analysis. Two samples (NZ03, NZ07) were selected from the WNG, these two samples being selected as they were the least affected by surface weathering effects, and are intended to provide an age for the formation of the West Nile Gneiss. Four samples were selected from the KGGB, three felsic igneous samples (MK01, AT4 and AMB1) and one metamorphic lithology (H1). The three felsic igneous lithologies are intended to provide a minimum age of formation for the belt (these lithologies being intrusive within the belt sediments) and in the light of the similarities between the geochemical data from the KGGB and UCG (See Chapter 5) establish a geochronological link between these two terranes. The single metamorphic sample (H1) is intended to provide data regarding the metamorphism of the eastern end of the belt and potentially provide a detrital estimate for the formation of the KGGB. Four samples have been selected from the UCG (W13, WP05, W10 and H4), these being sourced from three distinct generations of intrusive material. Samples W13 and WP05 are sourced from the Watsa-B granodiorite, the two samples being from opposite sides of the intrusion in order to establish if it represents a single intrusive generation. Sample W10 is a granite collected from within the poorly mapped undifferentiated intrusives and is intended to establish if these pre-date the lithologies of the Watsa igneous complex. Sample H4 has been chosen to represent the assumed 'late' boundary intrusives that are identified along the boundary between the two terranes and have been interpreted as stitching plutons, therefore dating the collision of the KGGB and UCG. In all cases the samples from the UCG are intended to examine the relationship between the igneous lithologies of the UCG and KGGB given the similarities observed in their geochemical characteristics.

Each sample consisted of 5-10 kg of fresh rock, weathered edges having been removed, and split into 2-4 cm fragments. Samples were crushed by Fritsch jaw crusher and sieved to isolate and remove the 50-250 μm fraction. The isolated 50-250 μm fraction was placed in an ultrasonic bath to remove fine particulates adhering to crystal surfaces and flushed with acetone and millicule water. Magnetic separation was performed by hand using an Nd:YAG magnet retaining the non-magnetic 50-250 μm fraction. The isolated fraction was density separated in sodium polytungstate liquid (Density 2.75 g/cm^3) to extract the heavy mineral phases. The heavy mineral fraction was flushed with acetone and millicule water to remove any sodium polytungstate residue retained on the crystal surfaces. Zircon crystals were extracted from the heavy

fraction by hand picking and mounted in resin blocks. Resin blocks were polished to produce a level surface and imaged by cathode luminescence to map the internal structure, identifying any distinct zones, and to act as a reference during analysis.

Zircon U-Pb data were acquired at the NERC Isotope Geoscience Laboratory (NIGL) by laser ablation (LA) multi-collector inductively coupled plasma mass spectrometry (MC-ICP-MS). Ablation was performed using a New Wave Research UP193SS (193 nm) Nd:YAG laser ablation system equipped with a custom low volume 'zircon ablation cell'. Ablated material was transported from the ablation cell to the ICP-MS by a 500 ml/min helium gas flow. Laser ablation protocol was calibrated at the beginning of each sample to achieve optimum signal intensity during ablation; settings for each sample are given in the discussion of results. Data was generated using a Nu Instruments, Nu Plasma HR multi-collector inductively coupled plasma mass spectrometer equipped with a multi-ion-counting array. The MC-ICP-MS was calibrated before each analytical session by simultaneously aspirating a 500 ppt ^{205}Tl - ^{235}U solution. Faraday gains were determined for each ion counter using a 100 ppt ^{205}Tl - ^{235}U solution cycling the ^{205}Tl through each ion counter, comparing to the equivalent faraday signal. Data acquisition was performed by Nu Instruments time resolved analysis software with instrument zero and on-peak zeros determined at the start of each run. Sample runs were conducted in batches of 10-15 analysis including standards with the laser fired for 40 seconds per sample. During acquisition the ^{205}Tl - ^{235}U solution was co-aspirated to facilitate measurement and correction of instrument mass bias and elemental fractionation. Coeval measurement of ^{202}Hg was used to correct for isobaric interference between ^{204}Hg and ^{204}Pb peaks. Internationally recognised standards 91500 (Wiedenbeck et al., 1995), GJ-1 (Jackson et al., 2004) and Plesovice (Slama et al., 2008) were analysed at the beginning of each sample run to act as matrix matched reference and secondary references to validate data for each analytical run. Data was normalised to the deviation of the average daily $^{207}\text{Pb}/^{206}\text{Pb}$ and $^{206}\text{Pb}/^{238}\text{U}$ values for the 91500 standard. Data was processed using a modified version of ISOPLOT (Ludwig, 2003). Data values recording $<<0.01$ mV ^{207}Pb and >300 cps ^{204}Pb after correction for isobaric ^{204}Hg interference have been rejected. All data has been plotted U-Pb concordia plots using the Wetherill method.

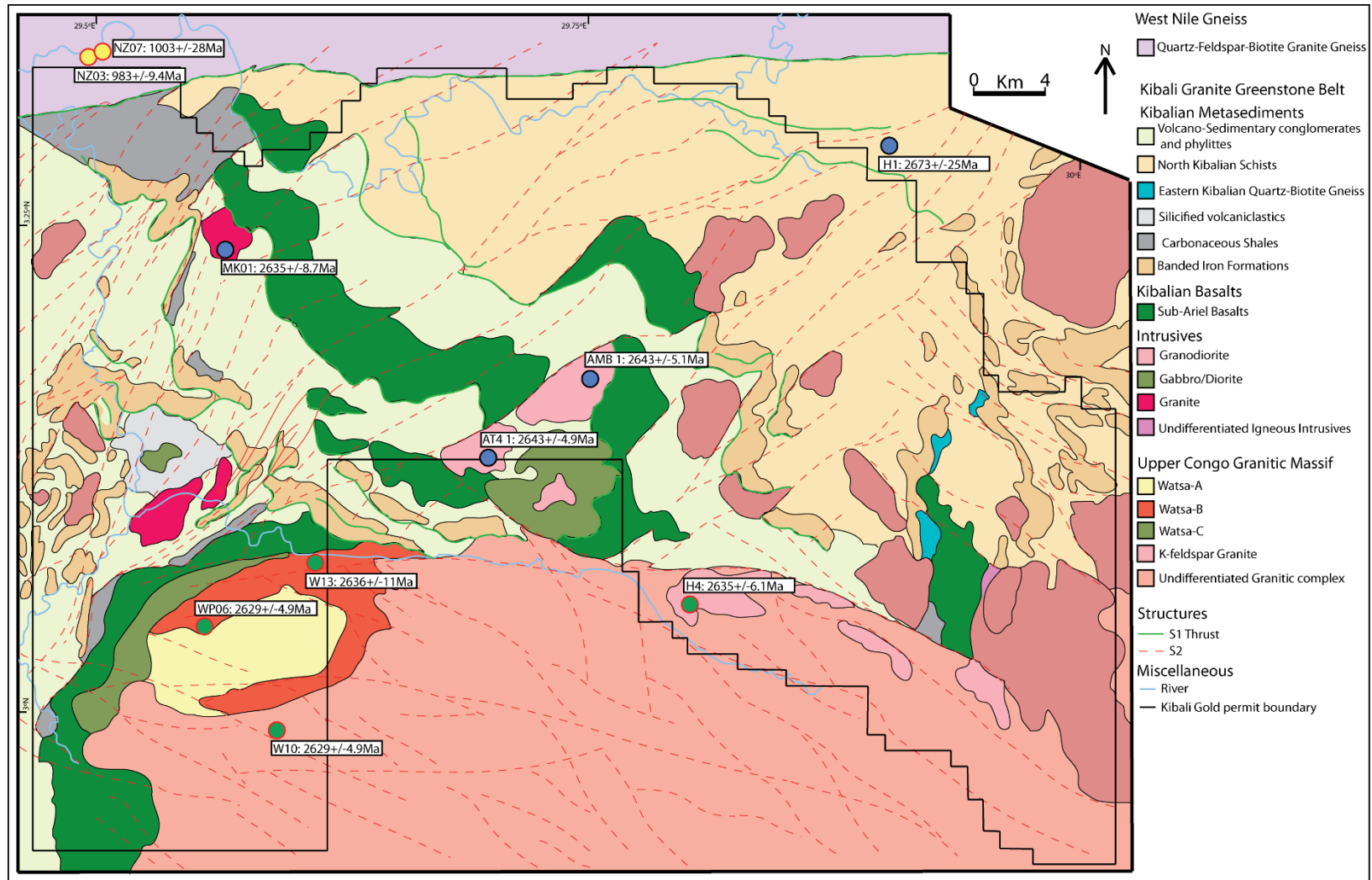


Figure 6.1: Locations of samples used in U: Pb zircon study

6.4 Results:

A full set of analytical data is presented in Appendix 4

6.4.1 Upper Congo Granite

6.4.1.1 Sample: W13

Sample W13 is a granodiorite from the Watsa igneous complex, composed of quartz (20%), feldspar (45% plagioclase, 15% orthoclase) and amphibole (10%) with minor amounts of hypersphene (~8%) and other minor phases (~2%). Late alteration has occurred within the sample with significant recrystallisation of K-feldspar edges to quartz and extensive alteration within the plagioclase phase, it being replaced by aluminoceladonite. Zircon crystals are prismatic euhedral to subhedral ranging in size from 150 – 300 μm long and 50 -100 μm wide, cathodoluminescence images show well-formed fine oscillatory zoning present within all crystals (Fig. 6.3). CL imaging also shows discontinuities within the internal zoning highlighted by bright spots and layers though no clear cross cutting between cores and rims is identified (Fig. 6.2). During analysis the laser system was set to spot size of 25 μm , frequency of 5 Hz delivering 2.00 Jcm^2 for duration 40 seconds. 40 spot analyses were performed on a total of 24 zircons with multiple analyses performed on 15 zircons. 2 analyses were rejected based on high common lead content. U-Pb Concordia show data to be discordant with an upper intercept at 2633.9 ± 7.7 Ma and a lower intercept at 516.5 ± 42 Ma (Fig. 6.3).

6.4.1.2 Sample WP06

Sample WP06 is a granodiorite from the Watsa igneous complex, composed of quartz (25%), feldspar (45% plagioclase, 10% orthoclase), hypersphene (~5%), amphibole (~5%) and chlorite (~5%) and other minor phases (~5%). Plagioclase feldspar displays significant alteration by aluminoceladonite, confined to the internal zoning within individual crystals. A proportion of the quartz component is secondary having formed from the recrystallisation of feldspar. Zircon crystals are prismatic euhedral ranging in size from 150 – 300 μm long and 50 -100 μm wide, with well-developed internal oscillatory zoning (Fig. 6.2). A subset of crystals displays a distinct contrast between core and rims of the zircon crystals. Homogenous cores containing no internal zoning are surrounded by oscillatory zoned rims and zoned cores where the surrounding oscillatory zoned rims cross cut the zoning present within the cores (Fig. 6.2). During analysis the laser was calibrated to a spot size of 25 μm , frequency of 10 Hz delivering 2.2J cm^2 for duration 40 seconds. 59 analyses were performed on a total of 39 zircons with multiple analyses performed on 14 zircons. 11 analyses were rejected based on high common lead values. U-Pb Concordia shows data is highly

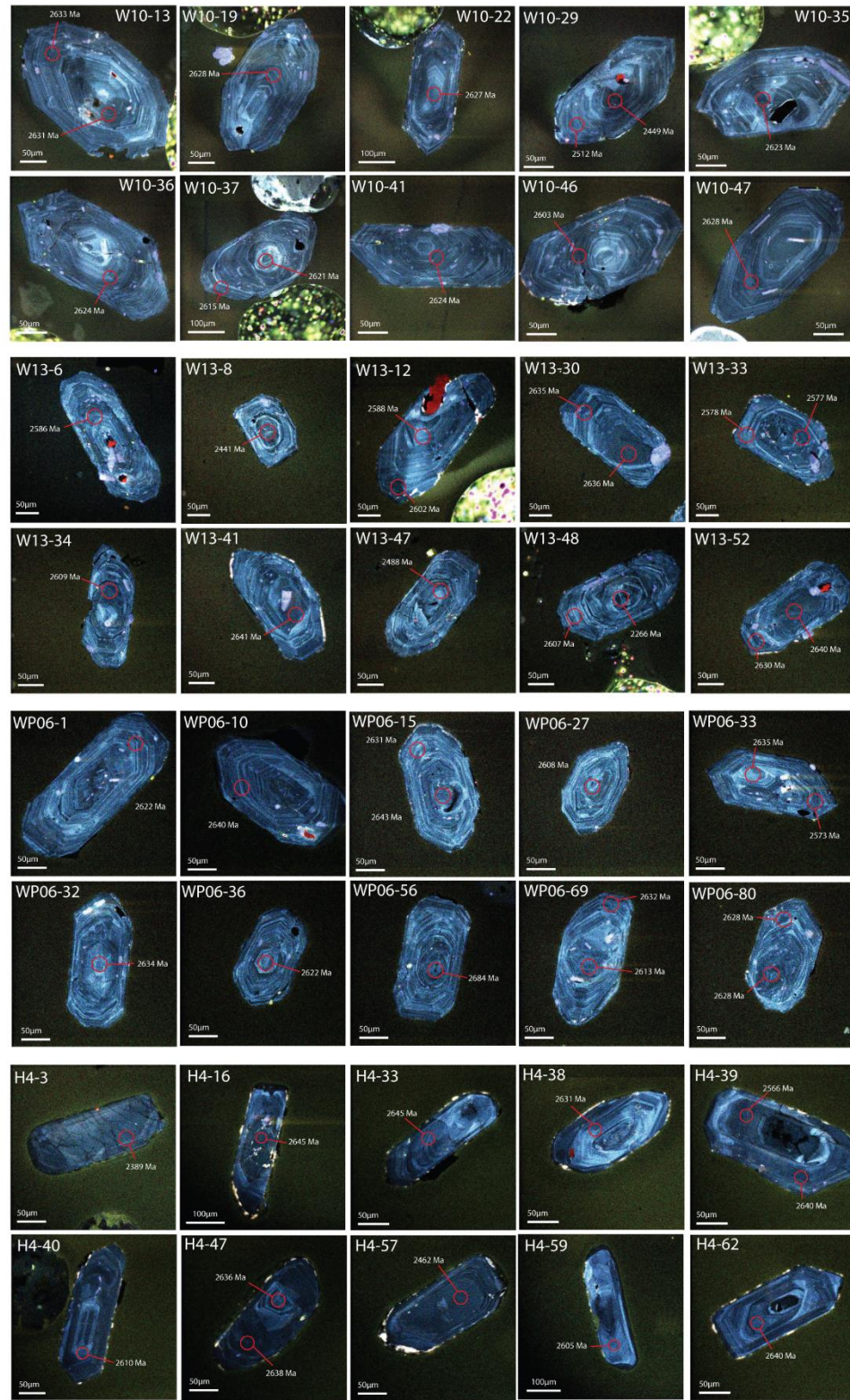


Figure 6.2: Cathodoluminescence images of selected zircons from samples W10, W13, WP06 and H4 from the Upper Congo Granitic Massif showing the range of morphologies and internal features identified within the samples.

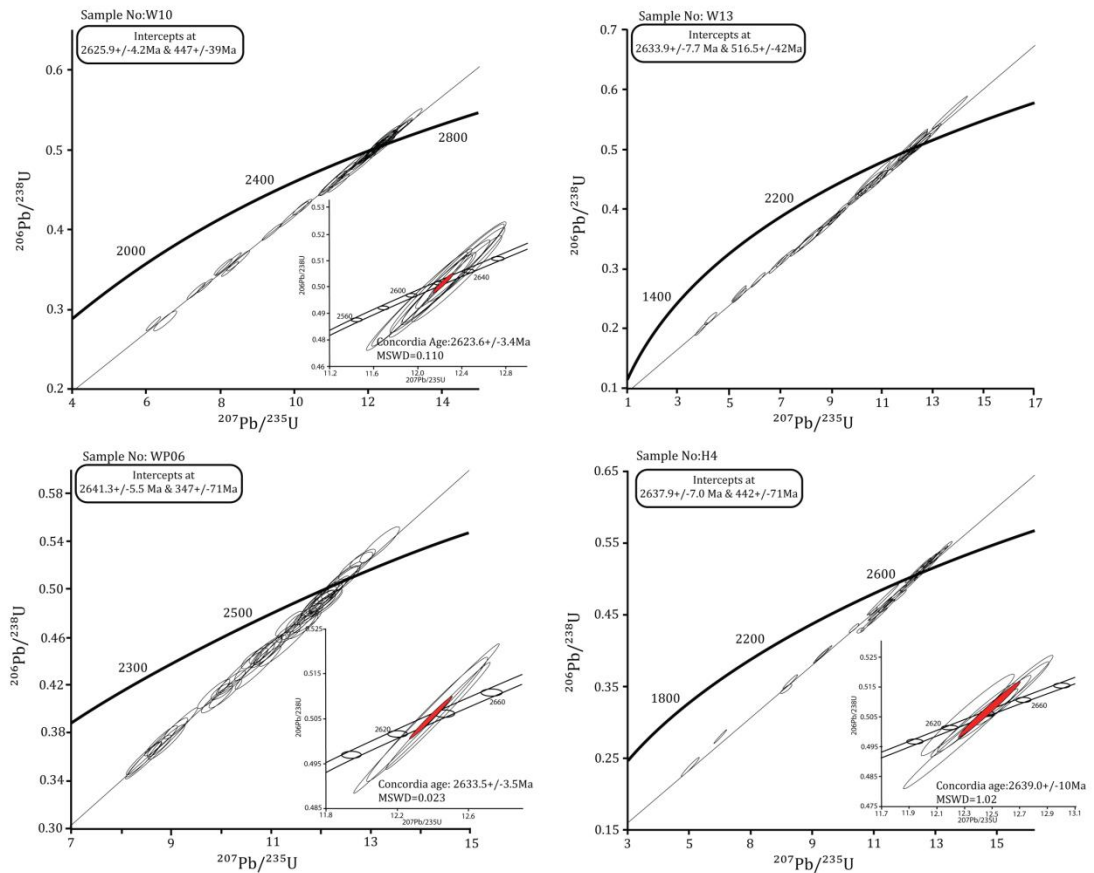


Figure 6.3: Wetherill concordia diagrams displaying data for samples analysed from the Upper Congo Granitic massif. Inset diagrams display concordia age calculated from samples with discordance <1%

discordant with an upper intercept at $2641 \pm 5.5 \text{ Ma}$ and lower intercept at $347 \pm 71 \text{ Ma}$ (Fig. 6.3). 3 data points are less than 1% discordant and yield a concordia age of $2633.5 \pm 3.5 \text{ Ma}$ (MSWD=0.023) (Fig. 6.3).

6.4.1.3 Sample H4

Sample H4 is a monzogranite from the isolated granitic massifs present along the boundary between the Upper Congo Granite Massif and the Kibali Granite-Greenstone Belt. The sample is composed of quartz (40%), feldspar (35% plagioclase, 20% orthoclase) with minor amounts of hypersphene and other minor phases (~5%). Large plagioclase feldspar phenocrysts display variable alteration by aluminoceladonite and some of the quartz within the groundmass displays characteristics that indicate it is a product of secondary recrystallization. Zircon crystals occur in two morphologies, elongate prismatic euhedral $300 \mu\text{m}$ long and $50 \mu\text{m}$ wide and a second ‘stubbier’ prismatic euhedral set ranging in size from $200 - 300 \mu\text{m}$ long and $\sim 100 \mu\text{m}$ wide. Internal features are variable though oscillatory zoning is identified to varying degrees within the

majority of the majority of the crystals (Fig.6. 2). Textural variations are noted with both homogenous cores surrounded by oscillatory zoned rims and zoned cores surrounded by homogenous rims identified. During analysis the laser was calibrated to a spot size of 25 μm , frequency of 10 Hz delivering 2.2 Jcm^2 for duration 40 seconds. 61 analyses were performed on a total of 36 zircons with multiple analysis performed on 18 zircons. 12 analysis were rejected based on high common lead content. Data yields U-Pb Concordia plots showing data is discordant with an upper intercept at $2637\pm 7.0\text{Ma}$ and a lower intercept at $442\pm 71\text{ Ma}$ (Fig. 6.3). 7 data points are less than 1% discordant and yield a concordia age of $2639\pm 10\text{ Ma}$ (MSWD=1.02) (Fig. 6.3).

6.4.1.4 Sample W10

Sample W10 is a granodiorite from the Watsa igneous complex, composed of quartz (25%), feldspar (45% plagioclase, 15% orthoclase), amphibole (5%) and hypersphene (5%) and other minor phases (~5%). Plagioclase feldspar has been extensively altered by aluminoceladonite with the outer edges of the plagioclase crystals also showing significant recrystallization to fine quartz. Zircon crystal morphologies range from prismatic euhedral to subhedral and in size from 150 – 300 μm long and 50 -150 μm wide. Internal structure is consistent across the crystal set with fine oscillatory zoning identified in all cases. The centres of the zircon crystals are commonly homogenous and vary in size from 25-50 μm in size though no significant discontinuity is observed between these cores and the surrounding oscillatory zoned areas (Fig. 6.2). During analysis laser was calibrated to a spot size of 20 μm , frequency of 10 Hz delivering 1.9 Jcm^2 for duration 40 seconds. 45 analyses were performed on a total of 37 zircons with 5 zircon crystals having multiple analysis performed. 2 analyses were rejected based on high common lead content. Analysis yields U-Pb Concordia plots showing majority of the data to be discordant with a calculated upper intercept at $2625\pm 4.2\text{ Ma}$ and lower intercept at $447\pm 39\text{ Ma}$ (Fig. 6.3). 9 data points are less than 1% discordant and yield a concordia age of $2623.6\pm 3.4\text{ Ma}$ (MSWD=0.110) (Fig. 6.3).

6.4.2 Kibali Granite-Greenstone Belt

6.4.2.1 Sample: MK01

Sample MK01 is a granodiorite from the Kalimva granitoid in the north west of the study area. The sample is composed of quartz (30%), feldspar (55% plagioclase, 10% orthoclase) with minor amounts of hypersphene and other minor phases (~5%). Plagioclase feldspar shows significant alteration by aluminoceladonite and a small proportion of the quartz present within the sample displays characteristics that indicate it is a secondary product formed through the recrystallisation of feldspar. Zircon crystals display two distinct lithologies, elongate prismatic crystals and more rounded irregular crystals, both phases

ranging in size from 150-250 μm in length and 50-150 μm in width. The internal structure of the zircon crystals is relatively uniform with both crystal morphologies displaying homogenous cores that are surrounded by oscillatory zoned rims, the individual zones being broader than noted within the other samples. A small subset of the zircons displays fine oscillatory zoning throughout the crystals (Fig. 6.4). During analysis the laser was calibrated to a spot size of 25 μm , frequency of 10 Hz delivering 2.00 Jcm^2 for duration 40 seconds 40 analyses were performed on a total of 30 zircons with multiple analysis performed on 9 zircons. 2 analyses were rejected based on high common lead content. Analysis yields U-Pb Concordia showing data to be highly discordant with an upper intercept at 2635.1 ± 7.0 Ma and lower intercept at 508 ± 55 Ma (Fig. 6.5). 7 data points are less than 1% discordant and yield a concordia age of 2634 ± 3.2 Ma (MSWD=2.9) (Fig. 6.5).

6.4.2.2 Sample: AT-4

Sample AT-4 is a quartz monzodiorite from the southern end of the Ambarau intrusion and is composed of quartz (10%), feldspar (55% plagioclase, 20% orthoclase), amphibole (5%) with minor amounts of hypersphene (~5%) and other minor phases (~5%). The plagioclase phase has been extensively altered by aluminoceladonite and recrystallised to quartz. Late chlorite alteration phase is also identified throughout the sample. Zircon crystals are prismatic euhedral to subhedral ranging in size from 50 – 100 μm long and 50 - 100 μm wide. CL images show internal structure is dominated by fine oscillatory zoning though this is often observed to be deformed in places (Fig. 6.4). A small subset of crystals display homogenous cores surrounded by thinly zoned rims (Fig. 6.4). During analysis the laser was calibrated to a spot size of 25 μm , frequency of 10 Hz delivering 2.00 Jcm^2 for duration 40 seconds 59 analyses were performed on a total of 51 zircons with multiple analysis performed on 7 zircons. 11 analysis were rejected based on high common lead content. Analysis yields U-Pb Concordia showing data to be highly discordant with an upper intercept at 2648 ± 6.2 Ma and a lower intercept at 344 ± 97 Ma (Fig. 6.5). 4 data points are less than 1% discordant and yield a concordia age of 2639.9 ± 3.4 Ma (MSWD=0.31) (Fig. 6.5).

6.4.2.3 Sample: AMB-1

Sample AMB-1 is a granodiorite from the Ambarau intrusion in the centre of the study region. The sample is composed of quartz (20%), Feldspar (55% plagioclase, 15% orthoclase) with minor amounts of hypersphene (~5%) and other minor phases (~5%). Significant aluminoceladonite alteration of the plagioclase phenocrysts has occurred throughout the sample and the edges of the crystals have commonly been replaced by to quartz. Zircon crystals are prismatic euhedral to subhedral in form and ranging in size from 150 – 300 μm long and 50 -150 μm wide. Zircon crystals are divided on the basis of their internal structure into two distinct groups, those displaying oscillatory zoning throughout the crystal and those with homogenous cores

and thin zoned rims (Fig. 6.4). Fracturing of the zircon crystals is noted principally within those zircons with homogenous cores. During analysis the laser was calibrated to a spot size of 25 μm , frequency 10 Hz delivering 2.2 Jcm^2 for duration 40 seconds. 45 analyses were performed on a total of 28 zircons with multiple analyses performed on 11 zircons. 5 analyses were rejected based on high common lead content. Data yields U-Pb Concordia showing data is highly discordant with an upper intercept at 2642.7 ± 5.1 Ma and a lower intercept at 265 ± 110 Ma (Fig. 6.5). 4 data points are less than 1% discordant and yield a concordia age of 2650.9 ± 3.2 Ma (MSWD=0.41) (Fig. 6.5).

6.4.2.4 Sample H1

Sample H1 is a paragneiss from the north east of the study area near to the contact with the West Nile Gneiss. The sample is composed of quartz (90%) with minor plagioclase feldspar (8%) and biotite (2%), the plagioclase feldspar being replaced by quartz. Two distinct morphologies of zircon are identified within the sample, narrow elongate crystals ranging in size from 100-150 μm long and 50 μm wide, and short rounded crystals ranging in size from 50-150 μm long and 50 to 100 μm wide. Internal crystal structure is variable though typified by alternating zoning with the width of the zones varying between zircons (Fig. 6.4). The zircons are frequently damaged and the internal zoning can range from poorly developed to strongly contrasting (Fig. 6.4). During analysis the laser was calibrated to a spot size of 20 μm , frequency 10 Hz, delivering 2.00 Jcm^2 for a duration of 40 seconds. 62 analyses were performed on a total of 44 zircons with multiple analyses performed on 12 zircons. 11 analyses were rejected based on high common lead values. Analysis yields U-Pb Concordia showing the data to be discordant with an upper intercept at 2662 ± 4.9 Ma and a poorly defined lower intercept at 159 ± 63 Ma (Fig. 6.5). Degree of discordance present within data was sufficient that no points displayed discordance less than 2%; as such it was not possible to calculate a concordia age.

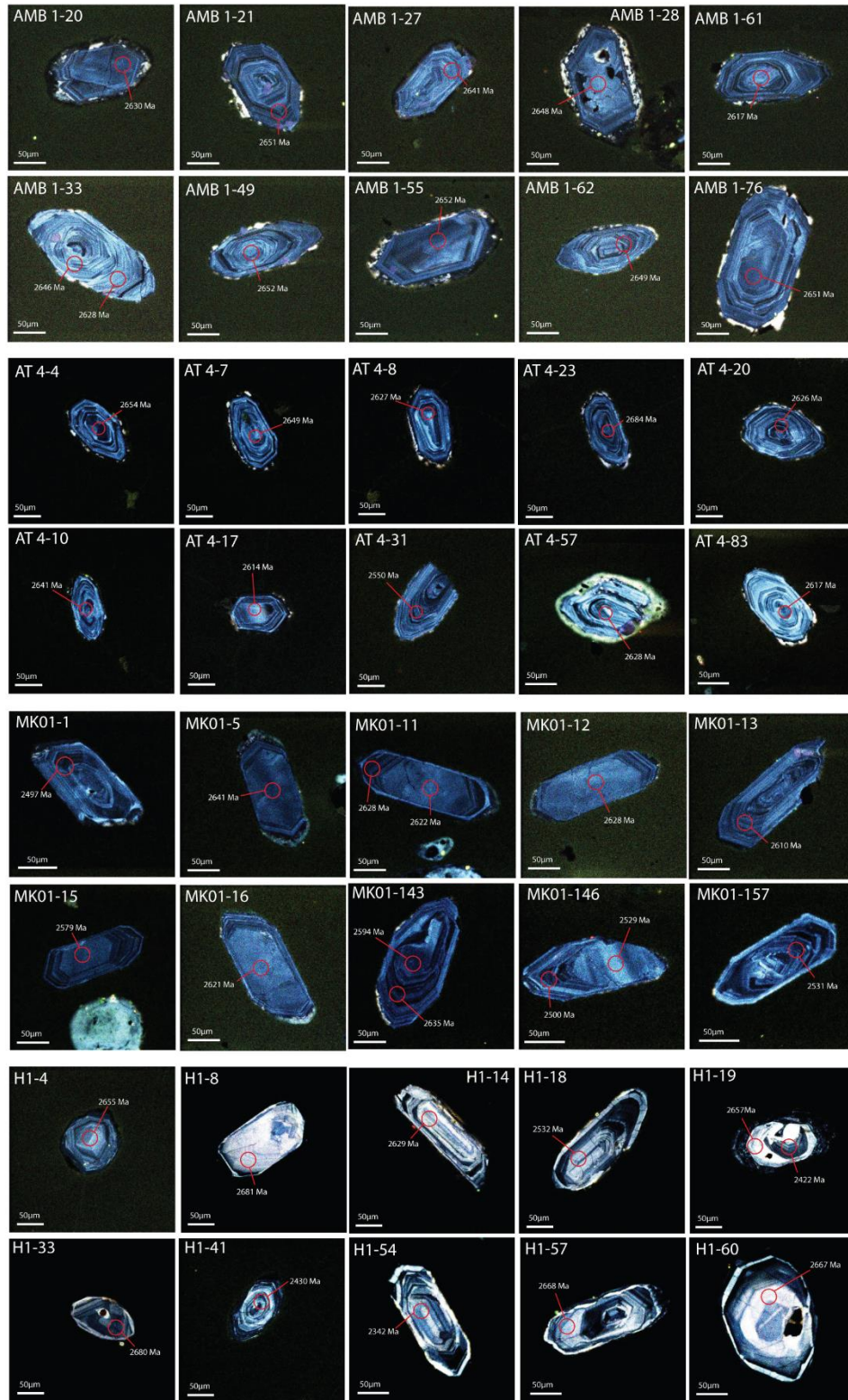


Figure 6.4: Cathode Luminescence images of selected zircons analysed in this study from the Kibali Granite-Greenstone Belt showing the range of morphologies and internal features identified within the samples.

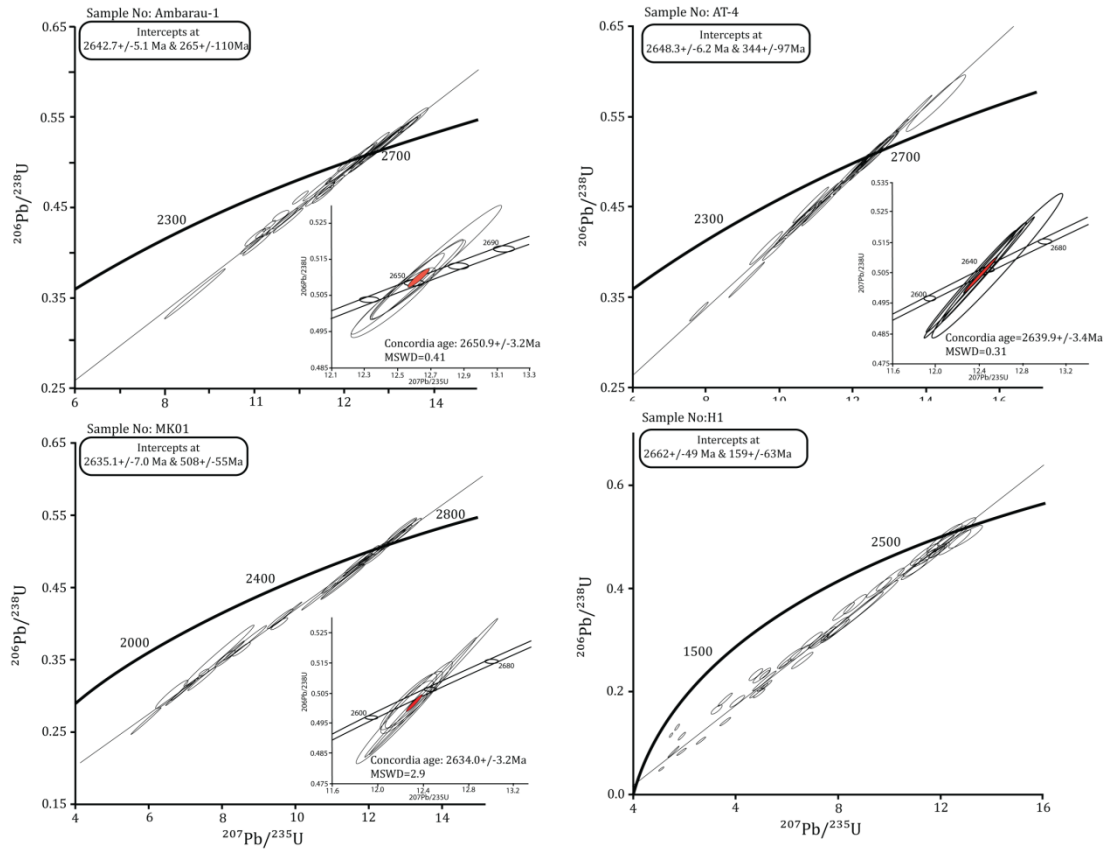


Figure 6.5: Wetherill concordia diagrams displaying data for samples analysed from the Kibali granite-Greenstone Belt Inset diagrams display concordia age calculated from samples with discordance <1%

6.4.3 West Nile Gneiss

6.4.3.1 Sample: NZ03

Sample NZ03 is a granite-gneiss from the West Nile Gneiss identified in the North West corner of the study area. The sample is composed of quartz (80%), orthoclase feldspar (15%) and biotite and other minor phases (5%). The sample is deformed with feldspar porphyroclasts surrounded by aligned quartz and biotite. The feldspar porphyroclasts are observed being replaced by aluminoceladonite in some instances. Zircons are elongate prismatic and euhedral ranging from 200-350 μm long and 50-150 μm wide. Two distinct internal morphologies are identified, the elongate crystals display homogenous cores with thin zoned rims while the shorter crystals display broad oscillatory zones throughout the crystal (Fig. 6.6). Zircons are frequently observed with substantial damage, the most common being cracks extending across the crystals (Fig. 6.6). During analysis the laser was calibrated to a spot size of 25 μm , frequency 10 Hz delivering 2.00 Jcm^2 for duration 40 seconds. 69 analyses were performed on a total of 65 zircons with multiple analyses performed on three zircons. 31 analyses were rejected based on high common lead content. Data yields U-Pb Concordia

showing data is discordant with an upper intercept at 983 ± 7 Ma and lower intercept at 140 ± 130 Ma (Fig. 6.7). 6 data points have discordance $< 1\%$, yielding a concordia age of 985 ± 2.8 Ma (MSWD=0.091) (Fig. 6.7).

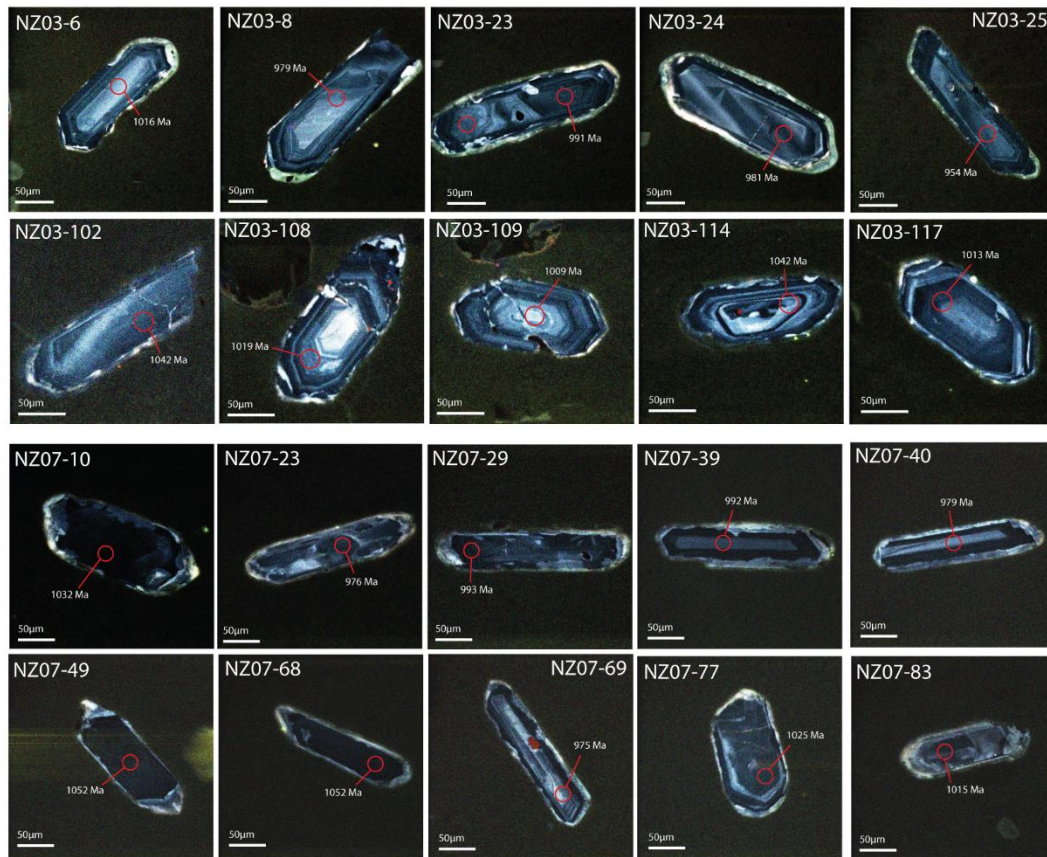


Figure 6.6: Cathodoluminescence images of selected zircons from samples NZ03 and NZ07 from the West Nile Gneiss showing the range of morphologies and internal features identified within the samples.

6.4.3.2 Sample: NZ07

Sample NZ07 is a granite-gneiss from the West Nile Gneiss in the north east of the study area. The sample is composed of quartz (75%), orthoclase feldspar (15% and biotite (5%) with negligible amounts of other minor phases. The sample is deformed with distinct quartz and biotite bands defining a planar fabric that wraps around large orthoclase feldspar porphyroclasts. The feldspar porphyroclasts show evidence of alteration by alluminoceladonite, though this is not extensive. Two distinct morphologies of zircon are identified within the sample, thin elongate prismatic crystals ranging in size from 200-350 μm in length and ~ 50 μm wide, and short euhedral crystals ranging in size from 100-150 μm in size. Cathodoluminescence imaging shows the crystals from this sample are dull with few internal features the crystals being dominated

by broad homogenous areas (Fig. 6.6). Internal zoning is limited; where visible the zones are wide with only small number of zones visible within individual crystals (Fig. 6.6). During analysis the laser was calibrated to a spot size of 25 μm , frequency 10 Hz delivering 2.2 Jcm^2 for duration 40 seconds. 57 analyses were performed on a total of 47 zircons with multiple analyses performed on 10 zircons. 26 analyses were rejected based on high common lead and high error. U-Pb Concordia show a cluster of discordant data points straddling the concordia at approximately 1000 Ma with a single data point sitting below the Concordia at approximately 600 Ma and a single value isolated near 2200 Ma, though this is data point is highly discordant. To yield an age the isolated upper value has not been included resulting in an upper intercept at 1014 ± 45 Ma and lower intercept at 417 ± 290 Ma (Fig. 6.7). Including the upper data point yields a highly discordant line with an upper intercept at 2786 ± 180 Ma and a lower intercept at 999 ± 49 Ma (Fig. 6.7). 5 data points display discordance less than 2%, these data yield a calculated concordia age of 991.2 ± 8.4 Ma (MSWD=0.46) (Fig. 6.7).

6.5 Discussion

All samples returned discordant data which yield an upper and lower intercept when plotted using the Wetherill concordia method, where possible concordia ages based on partial data sets have been determined. These concordia ages generally correlate well with the upper intercepts values but are preferred to the upper intercept due to their higher degree of accuracy. It is necessary to assess whether the generated dates, especially in the case of potential Pb loss events, possess any geological significance. The data from the three major geological terranes will be considered separately below before considering the wider regional implications of the data

6.5.1 The Upper Congo Granitic Massif

Samples from the Upper Congo granitic massif return concordant ages ranging from 2625 ± 4.2 Ma to 2641 ± 5.5 Ma (Fig. 6.3). The oscillatory zoning identified under cathode-luminescence imaging of all crystals from the Upper Congo Granite Massif is typical of zircons formed in igneous systems (Corfu et al., 2003) and as such the concordia ages are interpreted as representing crystallisation ages for the analysed samples. The distinct ‘core-rim’ characteristics observed within a subset of the zircons, most notably those in sample WP06, return similar ages (overlapping within error) for both core and rim. The observed ‘zoning’ is thought to be the result of fluctuations in the zircon saturation level in melt from which the crystals formed, The high fluorescence ‘zones’ frequently observed within the zircon crystals also being attributed to this process. The samples from the Watsa igneous complex (WP06, W10 and W13) are from different intrusive phases and indicate the complex developed over a short.

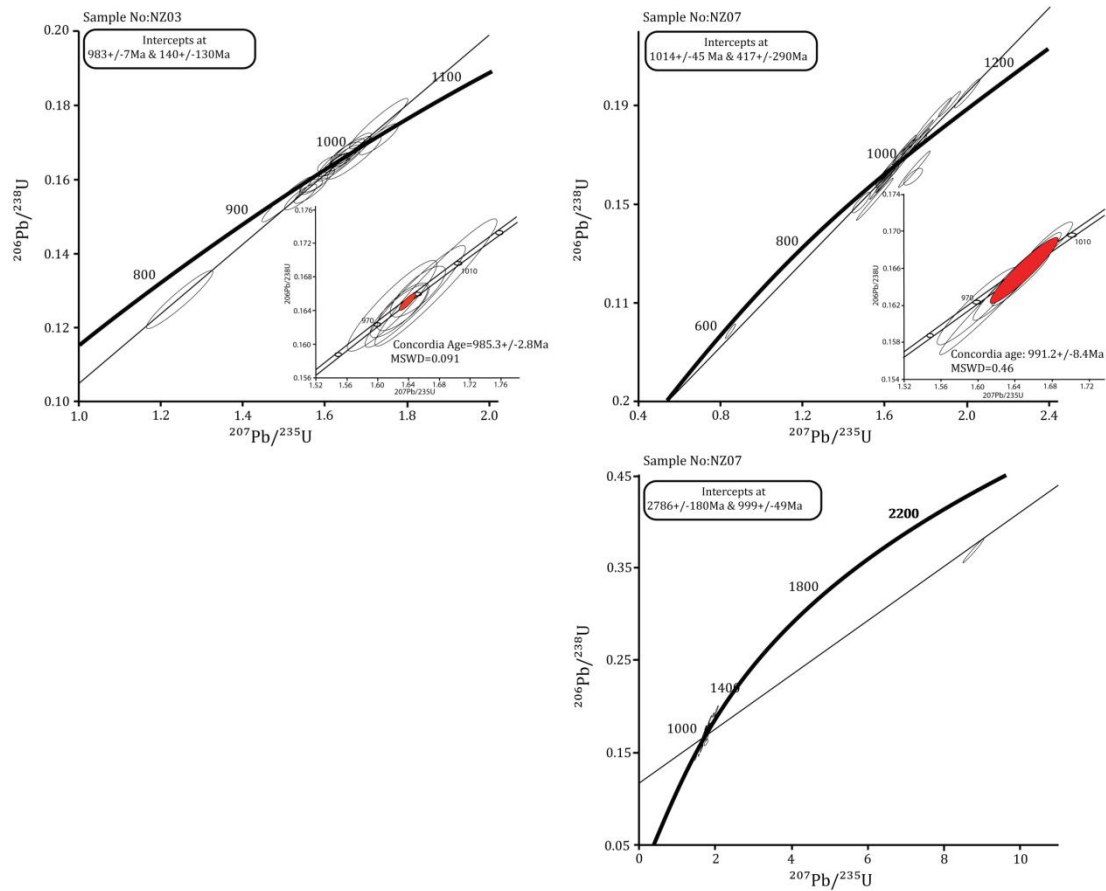


Figure 6.7: Wetherill concordia diagrams displaying data for samples analysed from the West Nile Gneiss Inset diagram display concordia age calculated from samples with discordance <1% (sample NZ03) and <2% (Sample NZ07)

period of approximately 16 Ma. Sample H4 shows that the formation of igneous material was not confined to the Watsa complex instead extending along the margin between the Upper Congo Granite Massif and the Kibali Granite-Greenstone belt. All samples display pronounced discordant data trends when plotted using the Wetherill method indicating that a significant perturbation of the uranium-lead isotope systems has occurred post crystallisation in the period between 347 ± 71 Ma to 516.5 ± 42 Ma (Fig. 6.3).

6.5.2 The Kibali Granite-Greenstone Belt

Samples from the Kibali Granite-Greenstone Belt yield concordia ages ranging from 2634.0 ± 3.2 Ma and 2650 ± 3.2 Ma (Fig. 6.5). The oscillatory zoning identified in cathode-luminescence imaging from the igneous samples are interpreted as showing that the ages represent igneous crystallisation ages. Sample H1 returns a significantly older upper intercept, at 2662 ± 49 Ma (Fig. 6.5), than the formation ages determined for the igneous lithologies from the Kibali Granite-Greenstone Belt. The zircons from sample H1 display

internal textures consistent with having formed through igneous crystallisation however as the sample is classified as a paragneiss these zircons might have been inherited through erosion of a Mesoarchean granitoid. The Wetherill concordia plot shows the igneous samples show data points distributed tightly along the discordia line however the data for sample H1, while aligning along the discordia line, are broadly distributed. This distribution can be explained through two distinct mechanisms; preferential loss of ^{206}Pb or ^{207}Pb during post formation lead loss or that the analysed zircons have a range of formation ages. The two lead species possess similar geochemical behaviour and mobility in hydrothermal systems and as such fractionation between the two species is considered unlikely. That the zircons possess a range of initial formation ages is consistent with the interpretation of this sample as having a sedimentary origin as potentially geological units from a range of ages will have been deposited into the basin in which it formed. The upper intercept age therefore is considered to represent an upper boundary on the deposition of material into the sedimentary basin; data is insufficient to constrain the hypothesised basin any further. All samples form discordia when modelled using the Wetherill method, indicating a significant lead loss event has occurred across the belt in the period between 508 ± 55 Ma and 159 ± 63 Ma (Fig. 6.5).

6.5.3 The West Nile Gneiss Complex

The samples from the West Nile Gneiss show a significantly different distribution of ages compared to the ages observed within the Kibali Granite-Greenstone Belt and Upper Congo Granitic Massif. The upper intercept generated for samples NZ03 and NZ07 define a window between 983 ± 7 Ma and 1014 ± 45 Ma (Fig. 6.7). As the sample is classified as an orthogneiss the zircon population can potentially be formed from a combination of primary magmatic zircons inherited from the original granite protolith and zircons formed during high grade metamorphism. The homogenous textures seen in the cathode-luminescence images are interpreted as zircons that formed through metamorphic processes or igneous zircons that have been extensively recrystallised during metamorphism. The zoned zircons identified in sample NZ03 are potentially relic igneous zircons; however as they yield similar ages to the homogenous zircons it would suggest that the isotope systems have been extensively modified during metamorphism but without significant anatexis. Sample NZ07 displays the most significant evidence for the inheritance of zircon with a single analysis returning a significantly older value than the other zircons analysed within from the sample. This analysis is highly discordant; however a regression line returns an upper intercept of 2786 ± 180 Ma. While the data is insufficient to draw firm conclusions regarding the origin of the gneisses it is suggestive of a Mesoarchean protolith. Based on the available data it is thought that the ages obtained from the West Nile Gneiss samples represent a metamorphic age, marking the deformation and metamorphism of a Mesoarchean granite. Both analysed samples yielded discordant data with the lower intercepts defining a

broad window extending from 140 ± 130 Ma to 417 ± 290 Ma (Fig. 6.7). This indicates that a second event has further perturbed the isotopic system in the West Nile Gneiss during the Phanerozoic.

6.5.4 Regional lead loss event

Evidence for perturbation of the uranium-lead isotope system was identified in all samples. It has been established that modifying the uranium-lead isotopic signature through thermal heating alone is precluded at temperatures below 900°C , although low temperature modification is possible during exposure to hydrothermal fluids (Lee et al., 1997; Schoene, 2014). Within all samples the alteration of the plagioclase feldspar phase to aluminoceladonite was identified. This alteration event postdates formation, is identified in all three terranes and is thought to correspond to the modification of the lead isotope signature within the samples. This hypothesis requires alteration and therefore lead loss to occur coevally in all three terranes. The intervals determined for the three terranes overlap within error, however they span a broad time period (140 ± 130 Ma to 516.5 ± 42 Ma (Fig. 6.3, 6.5 and 6.7)) which does not support the interpretation of a single geological event. Examining the error values and zircon textures shows a trend of increasing error northward across the study area with a broad trend of both increasing zircon damage and anatexis. The increased zircon ‘damage’ with increasing proximity to the terrane boundaries and in the north of the area is thought to relate to the relative intensity of the deformation and proximity to the tectonic ‘front’ present between the Kibali Granite-Greenstone Belt and the West Nile Gneiss. The higher degree of damage present within the zircons from the north of the study area will have allowed further modification of the isotopic system during uplift of the region and through surface processes resulting in enhanced Pb loss. The significant lead loss event is therefore hypothesised to have begun at approximately 500 Ma with progressive uplift resulting in steady modification of the lead isotope characteristics over the subsequent 500 Ma.

6.5.5 Geochronological Evolution of the Kibali Granite Greenstone Belt and Neighbouring Terranes

The differing geochronological characteristics of the three major terranes have identified four significant periods of geologic activity that have affected the region. An active basin system is hypothesised to have existed at approximately 2660 Ma with the sediments, basalts and ironstones that now constitute the Kibali Granite-Greenstone Belt forming in this environment, geochemical data indicated this was likely a back arc basin. A protracted period of igneous arc volcanic activity occurred from 2648-2625 Ma, this potentially corresponding to the accretion of the sediments of the Kibali Granite Greenstone Belt to the northern margin of the Congo craton. Similar formation ages are reported for the granite-greenstone belts of southern Uganda and northern Tanzania (Kabete et al., 2012a; 2012b; Lehto and Katto, 2014; Westerhoff et al., 2014) suggesting that the formation of the Kibali Granite-Greenstone Belt was part of a broader accretionary trend. At approximately 1 Ga (Corresponding to the Rodinian tectonic event) the West Nile Gneiss was subject to

a significant metamorphic event resulting in the resetting of the Uranium lead isotope system. The absence of evidence for this event in the Upper Congo Granite Massif and the Kibali Granite-Greenstone Belt is taken to indicate the West Nile Gneiss was still geographically separated from the other terranes during this event. The assembly of the terranes into their current configuration is linked to region wide lead loss event thought to have occurred at approximately 500 Ma. The north-south collision of the Saharan-Metacraton with the Congo craton and formation of the Oubanguide orogenic belt across central Africa is associated with the assembly of Gondwana c.600 Ma (Abdelsalam et al., 2002). While poorly constrained the Oubanguide orogeny is thought to have occurred in this region during the period 660-430 Ma (Pin and Poivedin, 1987; Abdelsalam et al., 2002; Westerhoff et al., 2014) which is supported by the data from the Kibali Granite-Greenstone Belt. The West Nile Gneiss is observed over-thrusting the Kibali Granite-Greenstone Belt along its northern edge. Based on the contrasting ages between the two terranes we suggest that this thrust surface marks the southern boundary of the Oubanguide orogeny in the region. The thrust surfaces identified along the upper edge of the Kalimva granitoid and associated ductile deformation indicate that the units of the Kibali Granite-Greenstone Belt were significantly remobilised and deformed during the Oubanguide orogenic event.

6.5.6 Implications for the Development of Au Mineralisation

Analysis of the geochronological characteristics of the major terranes within the study area has identified two distinct geological periods in which conditions favourable to the formation of orogenic gold mineralisation may have existed. The first is the initial formation of the Kibali Granite-Greenstone-Belt and its accretion to the northern margin of the Upper Congo Granite Massif during the closure of the hypothesised back arc basin system. The tectonothermal conditions present during arc accretion and back arc basin closure are considered favourable to the development of orogenic gold systems (Tomkins, 2010). The Archean greenstone belts of South Uganda and North Tanzania contain a number of notable gold deposits (Kabete et al., 2012b; Nyakecho and Hagemann, 2014) and the deposits within the Kibali belt may represent an extension of these processes. The second period of major regional scale fluid flow corresponds to the regional 'lead loss' event and fault remobilisation associated with the development of the Oubanguide orogeny and collision of the Saharan Metacraton and Congo craton.

6.6 Conclusion

Geochronological studies of the Kibali Granite-Greenstone Belt and its neighbouring terranes, the West Nile Gneiss and the Upper Congo Granite Massif, have shown a complex and prolonged history. Arc volcanism and associated terrane accretion occurred during the Neoproterozoic at approximately 2.64-2.63 Ga as part of a region wide crustal formation event. The West Nile Gneiss at this time is thought to have been

geographically separated from the units of the Congo craton and shows a distinct geological history having been significantly metamorphosed c. 1 Ga. The terranes were finally assembled as part of the Pan-African orogeny during the formation of Gondwana when the West Nile Gneiss was thrust over the units of the Kibali Granite-Greenstone Belt. This event is marked by a region wide lead loss event that significantly perturbed the U-Pb isotopic system and resulted in the region wide alteration by aluminoceladonite. The Geological history revealed through zircon dating of the terranes has significant implications for temporally constraining the development of orogenic gold mineralisation with two distinct time periods during which large scale regional fluid flow may have been active.

Chapter 7. Textural and compositional characteristics of wall rock alteration and sulphide mineral phases of the major gold deposits in the Kibali Granite-Greenstone Belt; Insights into the factors affecting the distribution of mineralisation

7.1 Introduction

The Kibali Granite-Greenstone Belt is host to significant gold mineralisation, gold deposits having been identified throughout the belt (Chapter 1). The most significant resource is located in the south west of the study area, focussed around the Karagba-Chaffeur-Durba (KCD) deposit. The KCD deposit constitutes the main gold resource with a number of significant satellite deposits, the largest of which are the Mengu, Pakaka and Pamao deposits, comprising a significant additional resource. The deposits are hosted in variably deformed and hydrothermally altered packages of the Kibalian metasediments, basalts and banded iron formations and display a range of mineralisation styles including; disseminated sulphides, vein hosted and ironstone sulphidisation. Here the textural and compositional characteristics of the KCD and its three main satellite deposits are examined, highlighting the significant characteristics of the host lithologies, hydrothermal alteration assemblages, mineralisation styles and ore mineralogy. These observations have then been used to establish a preliminary model for the formation of mineralisation within the Kibali Granite-Greenstone Belt.

7.2 Methodology

Samples used in this study were collected over the course of three field seasons between 2012 and 2014 and consist of standard NQ drill core from the KCD, Mengu, Pakaka and Pamao gold deposits (All sample data is displayed in Appendix 1). For each deposit samples representative of the differing hydrothermal alteration textures and styles of mineralisation were collected in order to provide the necessary information to complete the aims of this study. All samples were initially classified in hand specimen to establish their characteristics and a subset of these samples were selected for further textural and compositional analysis. Mineral identification and textural analysis of the alteration and sulphide mineral assemblages were performed through reflected and transmitted light microscopic study of polished thin sections by petrographic microscope. Mineral compositions were determined using a Zeiss EVO 50 Scanning Electron Microscope and X-ACT Energy Dispersive System (EDS) detector with data handling performed by the Oxford instruments INCA analytical suite. EDS analysis was performed with an accelerating voltage of 20 kV, beam current of 1.5 nA and detector process time of 4 seconds. Prior to each analytical session signal intensity was measured by faraday

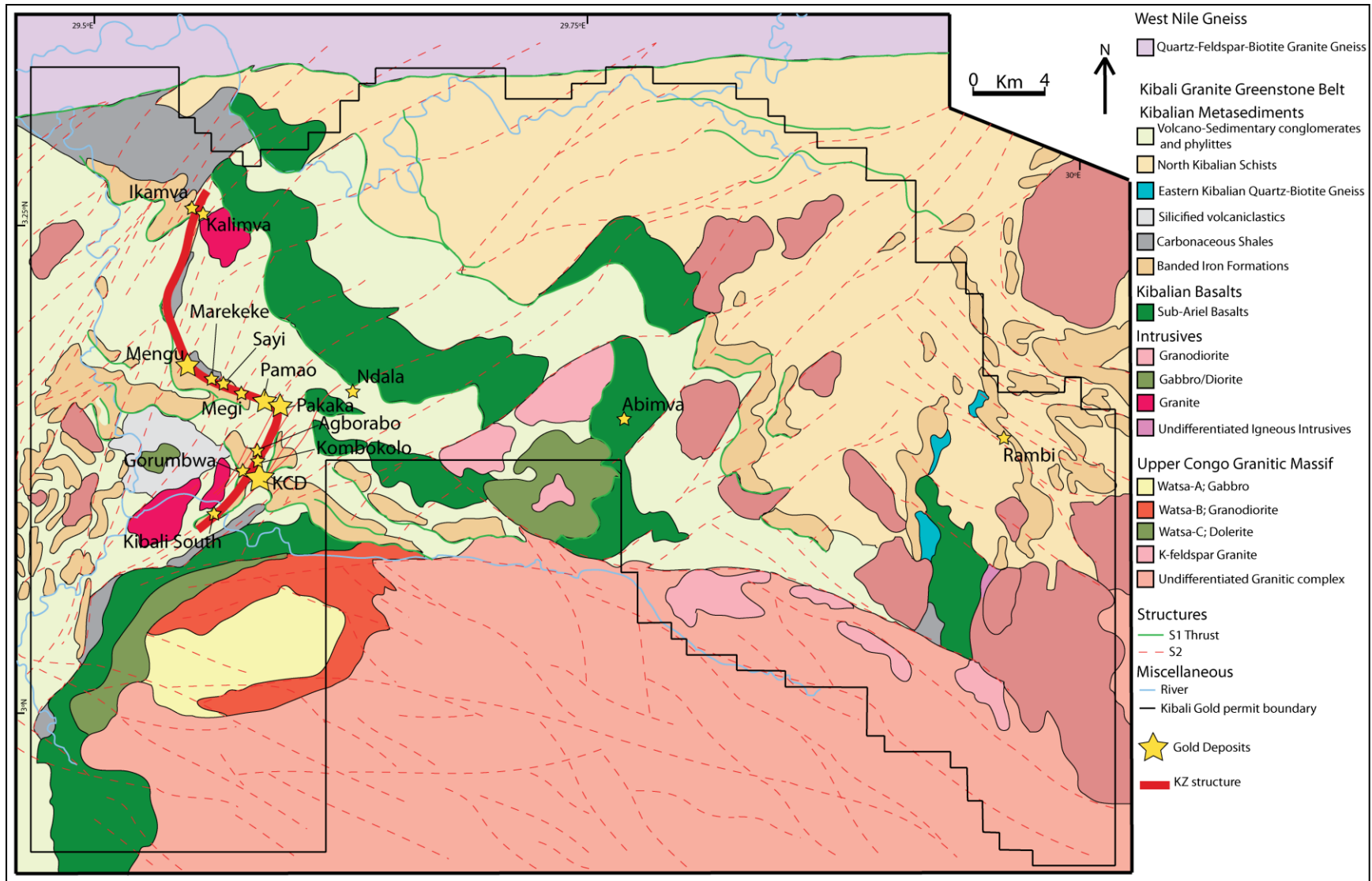


Figure 7.1: Geological map of the Kibali Granite-Greenstone Belt displaying the location of known gold occurrences and the hypothesized position of the KZ structure (Allibone, 2015)

cup until the variation in signal intensity fell below 1%. A pure albite standard was utilised to calibrate the detector at the beginning of each analytical session and a cobalt standard was periodically used to calibrate beam intensity throughout each analytical session. A full set of EDS analytical data is available in Appendix 5.

7.3 Structural setting and deposit morphology

Gold deposits within the Kibali Granite-Greenstone Belt are distributed along an approximately 20 km long structure referred to as the KZ Structure (Fig. 7.1) (Allibone, 2015). The KZ structure consists of a north-northeast striking segment, on which the Sessenge and KCD deposits are hosted, and a west-northwest striking segment on which the Pamao, Pakaka and Mengu deposits are hosted (Fig. 7.1) (Allibone, 2015). Through studying the KZ structure Allibone (2015) identifies seven distinct phases of deformation within the Kibali district:

- D₁: ductile faulting parallel, though locally cross cutting, lithological layering
- D₂: isoclinal recumbent folds dipping 25-30°NNE with associated layer parallel foliation
- D₃: upright folds plunging ca. 25°NE with steeply NW or SE dipping axial planes
- D₄: sericite 'rich' spaced foliation confined to altered lithologies within the KCD
- D₅: steeply dipping brittle faults striking NE parallel to the axis of F₃ (D₃) folds
- D₆: SSW dipping folds with sub-horizontal fold axes trending WNW or ESE with associated axial plane parallel crenulation cleavage
- D₇: SSW dipping normal faults and fractures associated with barren en-echelon veins

Events D₁-D₄ and D₆ are ductile in nature, resulting in the formation of ductile faults, folds and lineations (Allibone, 2015). The tectonic setting of events D₁ and D₄ is ambiguous however events D₂ and D₃ are considered to have formed in a contractional setting (Allibone, 2015). The D₆ event is associated with the thrusting of the West Nile Gneiss over the KGGB, the contact between the KGGB and WNG being approximately parallel to the F₆ fold axes, with limited data indicating top to the south-southwest displacement of the F₆ folds (Allibone, 2015). Events D₅ and D₇ are brittle in nature with D₇ being associated with tectonic relaxation after the D₆ event (Allibone, 2015).

The north-northeast orientated section of the KZ structure is structurally complex with two generations of co-axial folding and multiple generations of faulting being identified (Allibone, 2015). The KZ structure in this area is aligned with the hinge orientation of a major F₂ fold, D₁ faulting and a kilometre wide zone of F₃ folding (Allibone, 2015). The west-northwest striking part of the KZ structure is orientated parallel to the

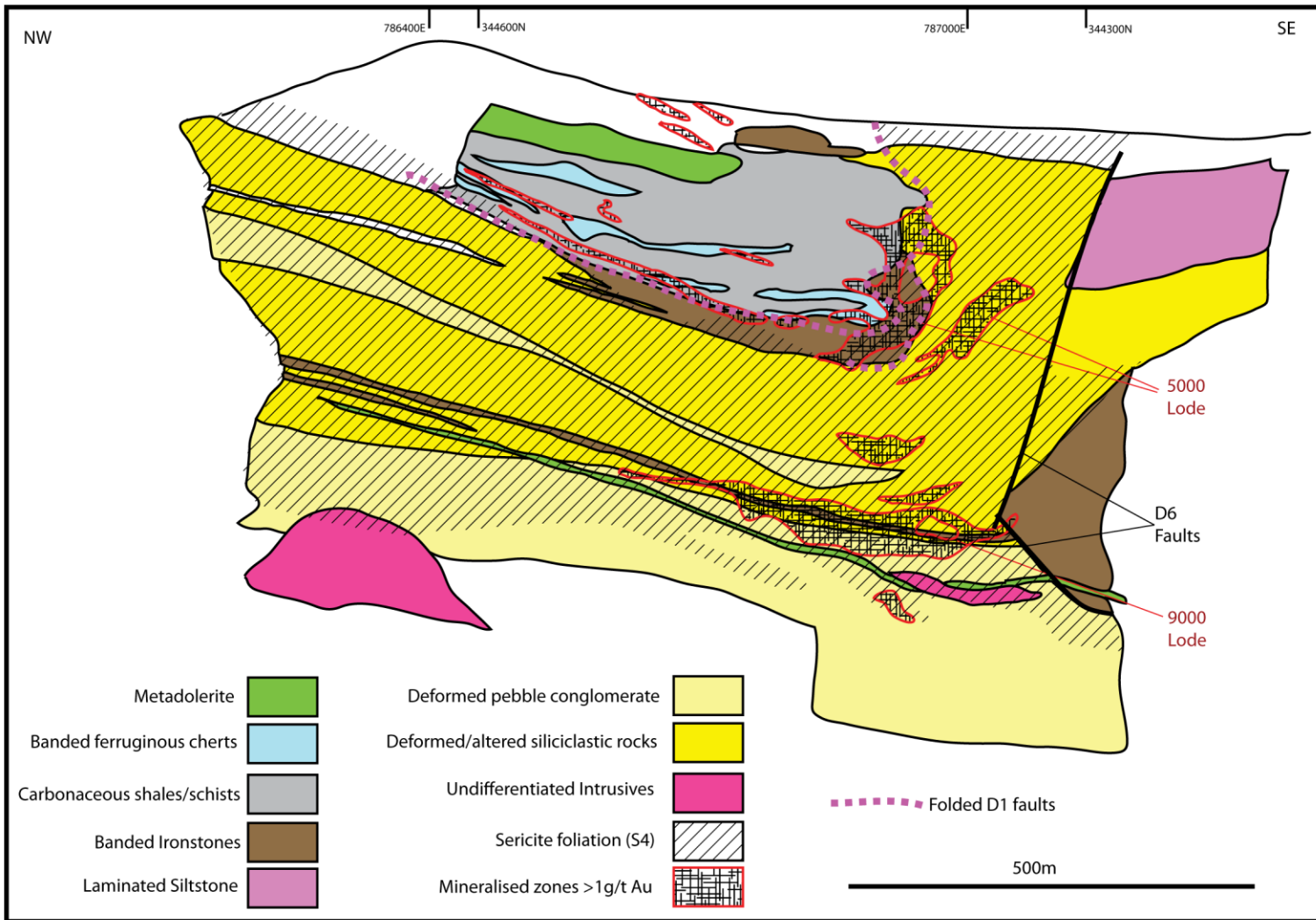


Figure 7.2: Cross section of the Karaba-Chaffeur-Durba (KCD) deposit displaying the position of major lithological units, alteration halo, faults and mineralised lodes. Redrawn after Allibone (2015)

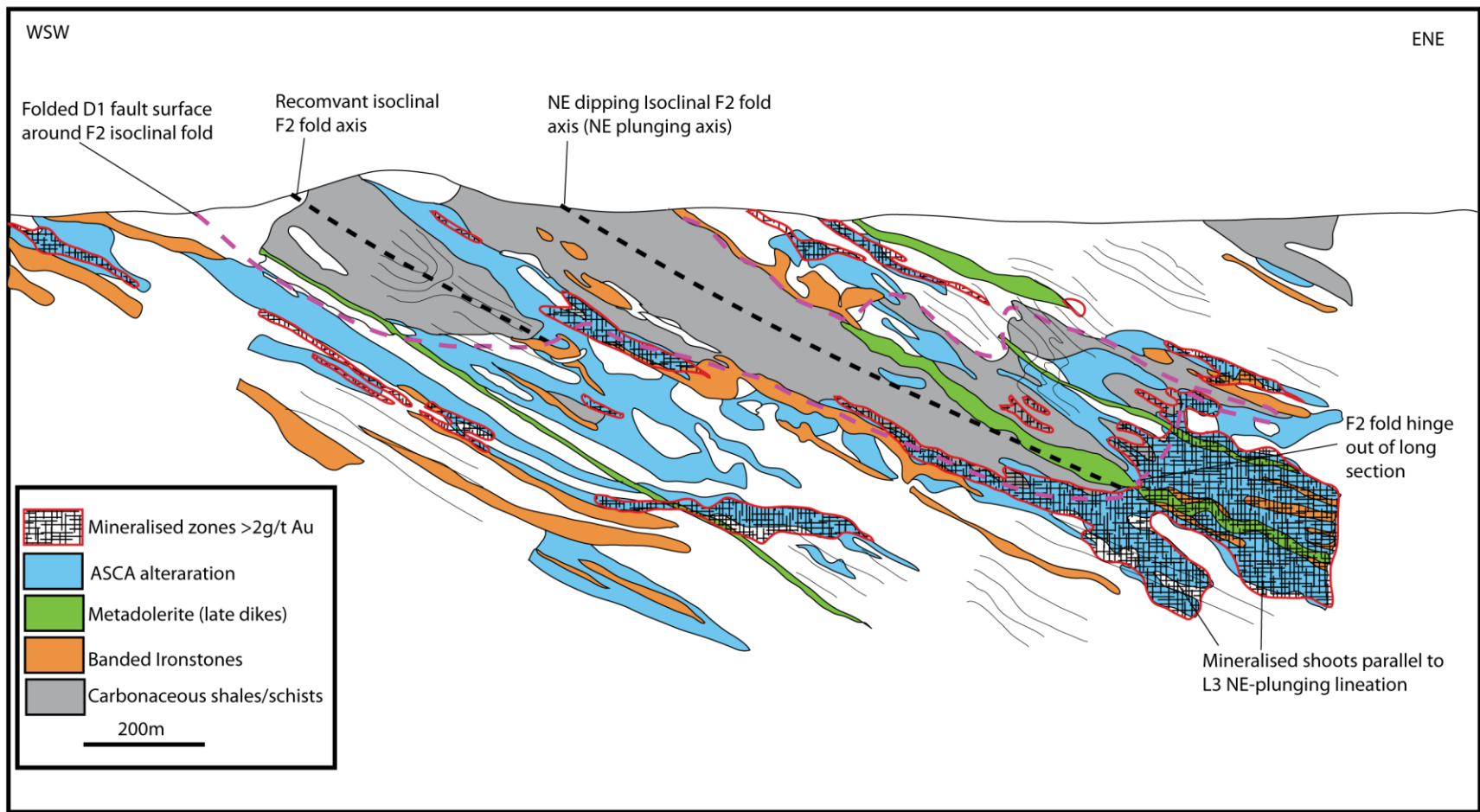


Figure 7.3: Long section through the Karagba-Chaffuer-Durba (KCD) deposit displaying the north east dipping attitude of the host lithologies, F2 fold axis and mineralised lodes.

Redrawn after Allibone (2015)

F₂ fold limbs, at a highly oblique angle to the axes of the F₂/F₃ folds, with F₃ fold being comparatively rare in this segment of the KZ structure (Allibone, 2015).

Mineralisation in both sections of the KZ structure, occurs as north-northeast plunging (~25°) lodes orientated parallel to the L₂/L₃ lineations and axes of the F₂/F₃ folds (associated with the D₂/D₃ events) (Fig. 7.3) (Allibone, 2015). The KCD consists of three stacked lodes; the 3000, 5000 and 9000 lodes (Fig. 7.2, 7.3); while the smaller satellite deposits consist of a single dipping lode. Mineralisation is thought to have developed between the D₄ and D₅ events (Allibone, 2015) with the similar orientations of the lodes and the F₂/F₃ axes (Fig. 7.3) leading Allibone (2015) to hypothesise that these structures have exerted a strong control on the formation of mineralisation. Allibone (2015) further links the structural complexity of the WNW orientated section of the KZ structure with the exceptional endowment of the KCD relative to the other deposits in the KGGB. The D₁ faults are thought to have acted as an active boundary along which the developing F₂ faults terminated resulting in the lithologies in the D₁ hanging wall being more extensively folded and establishing a rheological heterogeneity in the core of the KCD (Allibone, 2015). Subsequent deformation, during the D₃/D₅ events, being focused into this zone resulting in the observed structural complexity (Allibone, 2015).

7.4 Karagba-Chaffeur-Durba (KCD)

7.4.1 Host Lithologies

The Karagba-Chaffeur-Durba (KCD) deposit is hosted within a thrust stacked sequence (Allibone, 2015) composed of the Kibalian metasediments and banded ironstone lithologies that have been subjected to greenschist facies regional metamorphism characterised by a chlorite-muscovite-quartz assemblage (Chapter 2). The Kibalian metasediments at the KCD consist of volcano-sedimentary conglomerates with minor carbonaceous shales and carbonaceous--rich conglomerates. Two distinct types of banded iron formation are identified, deformed massive homogenous ironstone with a minor quartz component and 'Banded' material consisting of alternating quartz and magnetite-rich layers. The volcano-sedimentary conglomerates are the most abundant host lithology and are the principal host of mineralisation. These lithologies consist of quartz clasts, ranging in size from 0.2 mm to 5 cm, hosted in a phyllosilicate-rich groundmass, composed primarily of chlorite, with the relative proportions of the clast/groundmass varying between individual samples (Fig. 7.4). Where clasts are absent the lithology consists of fine crystalline quartz with discrete layers of aluminoceladonite. The host lithologies show a heterogeneous distribution of deformation (Fig. 7.4), localised areas being significantly deformed with a trend for increased deformation

in proximity to the mineralised horizons. Deformation is characterised by stretching and alignment of the quartz clasts and of the phyllosilicate groundmass with accompanying quartz recrystallisation of the clast material and enhanced chlorite growth in the inter clast areas (Fig. 7.5A). Stretching is sufficient that in places clast material attains a width greater than that of the core sample giving the appearance of alternating layers of fine crystalline quartz and thin dark bands composed of aligned chlorite crystals. Analysis of chlorite compositions from the inter-clast zones in the deformed lithologies show chlorite is predominantly the ripidolite variety with rare analyses of brunsvigite and daphnite (Table 7.1).

7.4.2 Hydrothermal Alteration

Two distinct phases of hydrothermal alteration are discerned within the deposit, an initial phase pre-dating mineralisation characterised by the development of ankerite+siderite±quartz±aluminoceladonite and a late phase characterised by the development of magnetite-rich horizons, overprinting both earlier alteration phases and mineralisation. Pre-mineralisation ankerite+siderite±quartz±aluminoceladonite assemblage is widespread forming a broad alteration halo around the mineralised lodes giving the lithologies a blurred white/yellow appearance (Fig. 7.4). Low intensity alteration is manifested as the formation of the Fe-carbonates+quartz+aluminoceladonite in the inter-clast areas (Fig. 7.5). With increasing intensity alteration assemblages are observed completely overprinting phyllosilicates in the inter-clast areas and progressively altering the quartz-rich clasts (Fig. 7.5). Alteration of clast material is dominated by Fe-carbonates+quartz with only minor aluminoceladonite component. At peak intensity this event is texture destructive (Fig. 7.4 and 7.5), overprinting the pre-alteration deformational textures and mineral phases. The Pre-mineralisation event is dominated by the Fe-carbonate minerals with both ankerite and siderite being widely identified, occurring as masses of interlocking >10 µm angular/sub-angular crystals. Individual samples may be ankerite dominated, siderite dominated or a mix of the two phases. Both ankerite and siderite phases display significant compositional variation with the abundance of iron being the main driver of variation between individual crystals (Table 7.2). These compositional variations are most pronounced in the ankerite phase, forming a range of compositions forming between the ideal compositions of ankerite and dolomite (Fig. 7.6). The phyllosilicates alteration, while being termed aluminoceladonite here, vary significantly in composition (Table 7.3). As was the case with the Fe-carbonates variation in the proportion of iron is the main source of compositional variation, the phyllosilicates ranging in composition from muscovite to ferro-celadonite (Fig. 7.7). Magnetite alteration occurs post mineralisation and is characterised by the development of 0.5-2 mm magnetite crystals, overprinting and occluding the regional metamorphic, pre-mineralisation and mineralisation related mineral assemblages. Magnetite alteration has a relatively restricted distribution, when compared to the pre mineralisation alteration, occurring as discrete horizons within the Kibalian metasediments.

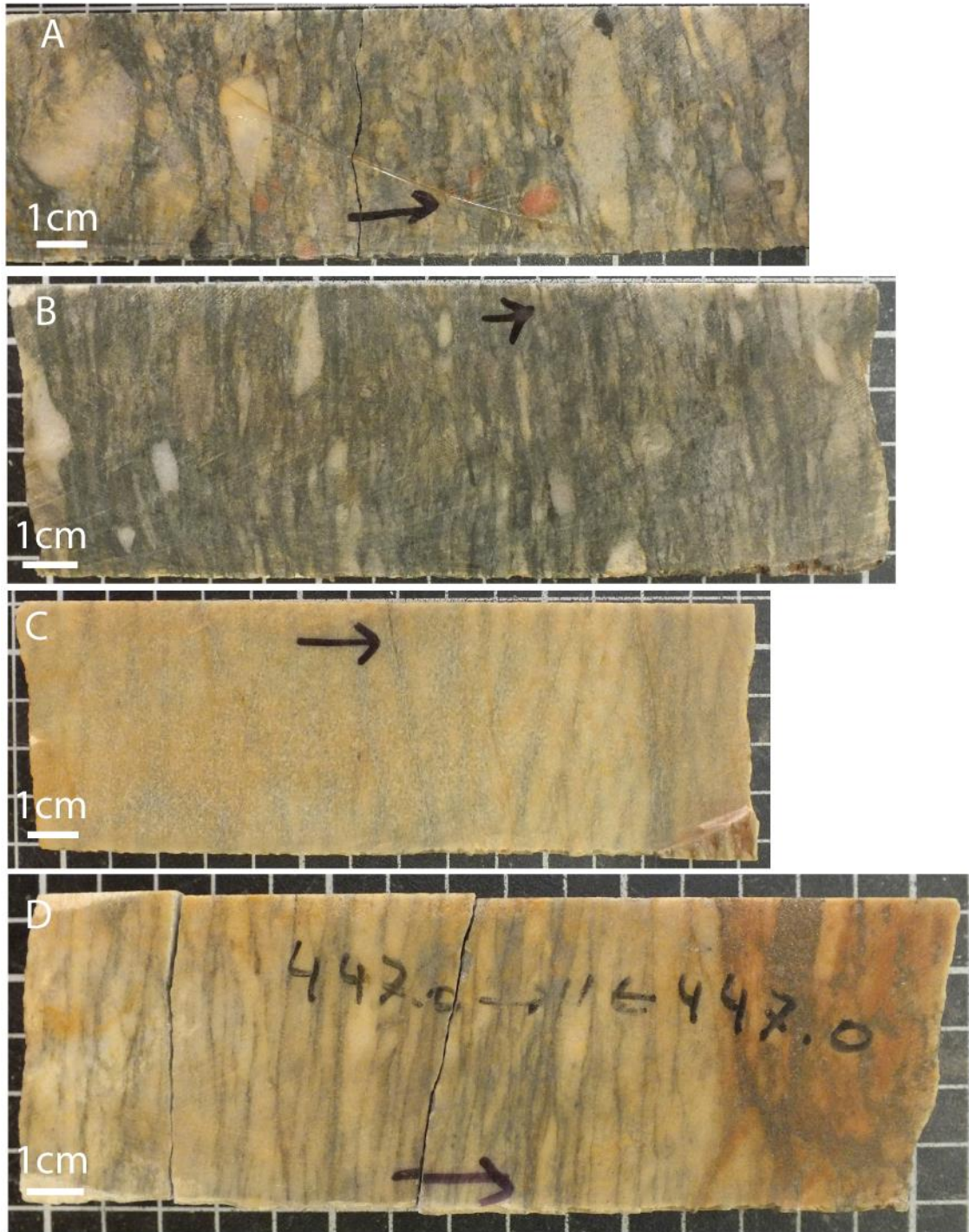


Figure 7.4: Core samples displaying the characteristics of the volcano-sedimentary conglomerate lithologies at the KCD deposit: A) Sample 2013-D84; Polymict clast-rich volcano-sedimentary conglomerate with minor deformation and stretching, B) Sample 2013-D25; Clast poor volcano-sedimentary conglomerate with minor deformation and poorly developed parallel layers in the phyllosilicate groundmass, C) Sample 2013-D114; Stretched volcano-sedimentary conglomerate consisting of deformed quartz clasts and parallel aligned phyllosilicate-rich inter-clast areas, white/yellow colour is caused by the extensive alteration and overprinting by Fe-carbonate±quartz alteration, D) Sample 2013-D97; Heavily deformed volcano-sedimentary conglomerate displaying characteristic clast-inter-clast texture, clasts attaining a width greater than the core, Pale yellow/white colour is the result of moderate Fe-carbonate±quartz alteration, Transition to mineralized horizon characterised by disseminated sulfides in the phyllosilicate-rich horizons.

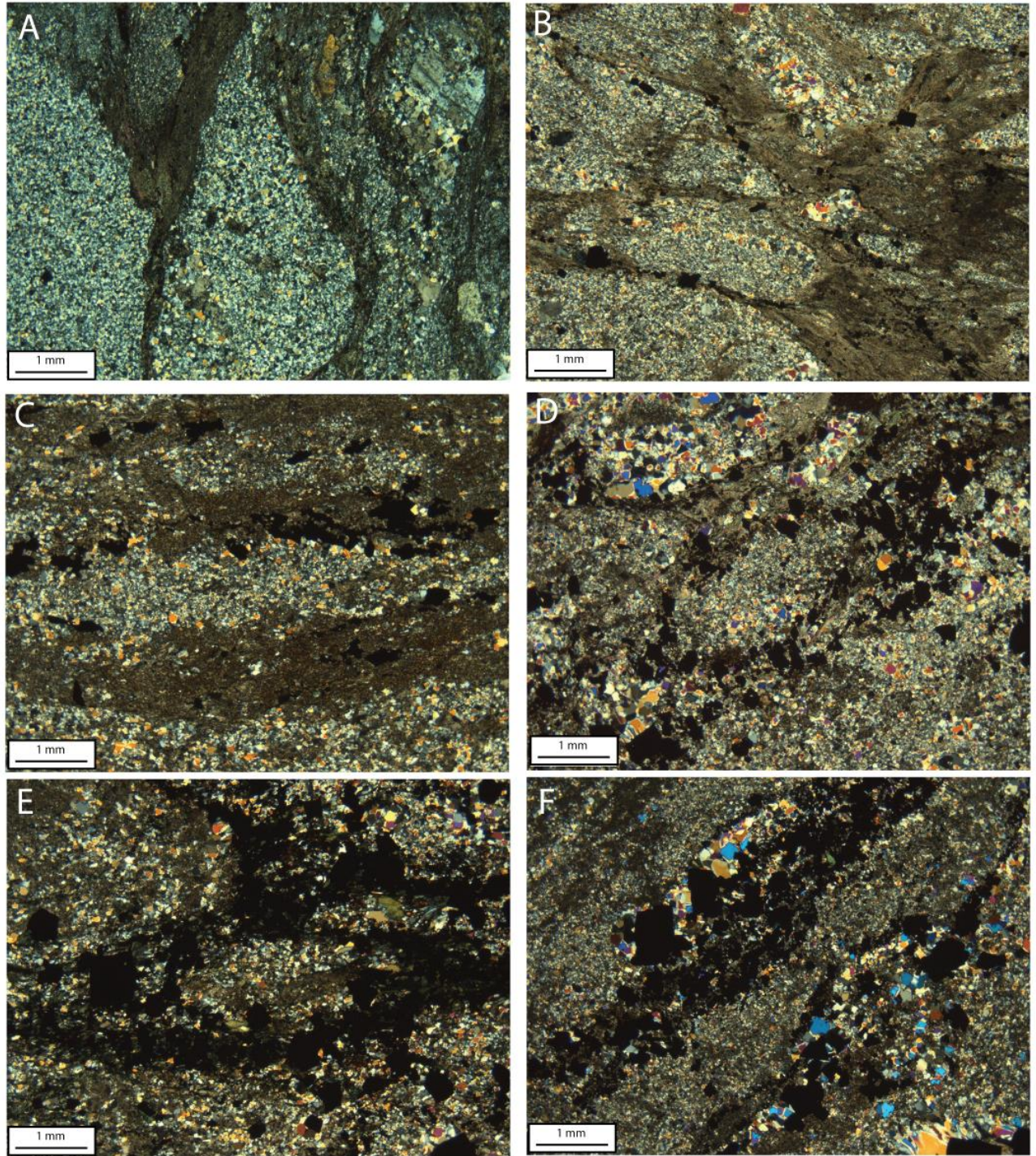


Figure 7.5: XPL Photomicrographs showing deformatinal and mineralisation characteristics in the lithologies at the KCD deposit: A) Sample 2013-D84; Deformed volcano-sedimentary conglomerate, quartz(±feldspar) stretched clasts with phyllosilicate (chlorite±aluminoceladonite) rich inter-clast areas. B) Sample 2013-D26; Deformed clast-rich volcano-sedimentary conglomerate with low intensity disseminated sulfides occurring in the inter-clast zones. C) Sample 2013-D40; Deformed volcano-sedimentary conglomerate with extensive Fe-carbonate alteration overprinting the former phyllosilicate-rich inter-clast areas with minor sulphide mineralisation. D) Sample PB12-D10: Fe-carbonate alteration and disseminated sulfide mineralisation occurring in the inter-clast phyllosilicate-rich zones. E) Sample 2013-D22: Fe-carbonate alteration and intense disseminated sulfide mineralisation in the phyllosilicate-rich inter-clast pathways. F) Sample 2013-D44: Sulfide minerals set in a quartz+Fe-carbonate gangue replacing iron-rich horizons in the quartz-rich banded ironstone lithologies.

Table 7.1: Representative analysis of chlorite from deformed volcano-sedimentary conglomerates at the Karagba-Chaffeur- Durba deposit.

Sample	2013-D22	2013-D22	2013-D22	2013-D22	2013-D22	2013-D22	2013-D26	2013-D84	2013-D90	2013-D14	2013-D14	2013-D14
Analysis	SITE 1D	SITE 1M	SITE 1 S	SITE 3 N	SITE 3 P	SITE 4 K	SITE 1 N	SITE 2 B	SITE 2 F	SITE 1 H	SITE 1 K	SITE 2 M
SiO ₂	22.56	22.69	21.54	21.81	24.95	23.57	24.33	24.55	22.78	22.53	23.83	24.71
TiO ₂	0.00	0.00	0.00	0.00	0.00	0.00	0.00	0.00	0.00	0.00	0.00	0.00
Al ₂ O ₃	19.83	19.62	19.20	18.71	19.04	19.95	21.47	21.13	21.63	20.34	20.95	20.41
FeO	34.47	34.99	34.56	35.54	30.39	33.97	31.13	33.46	40.10	35.76	36.15	36.51
MnO	0.00	0.00	0.00	0.00	0.00	0.00	0.00	0.00	0.00	0.00	0.00	0.00
MgO	6.37	6.47	5.70	5.88	6.20	6.42	8.92	7.58	2.52	5.99	6.41	6.80
CaO	0.00	0.00	0.00	0.00	0.00	0.00	0.00	0.00	0.00	0.00	0.00	0.00
Na ₂ O	0.00	0.00	0.00	0.00	0.00	0.00	0.00	0.00	0.00	0.00	0.00	0.00
K ₂ O	0.00	0.00	0.00	0.00	0.00	0.00	0.00	0.00	0.00	0.00	0.00	0.00
H ₂ O*	10.18	10.21	9.81	9.87	10.29	10.37	10.86	10.84	10.43	10.28	10.70	10.85
Total	93.81	94.24	90.98	91.80	93.34	95.24	97.73	98.68	98.41	95.18	98.67	100.00
Si	5.31	5.33	5.26	5.30	5.77	5.43	5.36	5.41	5.22	5.25	5.33	5.45
Al (iv)	2.69	2.67	2.74	2.70	2.23	2.57	2.64	2.59	2.78	2.75	2.67	2.55
Al (vi)	2.82	2.76	2.79	2.66	3.01	2.87	2.95	2.92	3.08	2.84	2.86	2.77
Ti	0.00	0.00	0.00	0.00	0.00	0.00	0.00	0.00	0.00	0.00	0.00	0.00
Fe ³⁺	0.07	0.05	0.03	0.00	0.43	0.17	0.17	0.18	0.17	0.05	0.11	0.12
Fe ²⁺	6.79	6.87	7.06	7.24	5.88	6.55	5.73	6.17	7.69	6.97	6.76	6.73
Mn	0.00	0.00	0.00	0.00	0.00	0.00	0.00	0.00	0.00	0.00	0.00	0.00
Mg	2.24	2.27	2.08	2.13	2.14	2.20	2.93	2.49	0.86	2.08	2.14	2.23
Ca	0.00	0.00	0.00	0.00	0.00	0.00	0.00	0.00	0.00	0.00	0.00	0.00
Na	0.00	0.00	0.00	0.00	0.00	0.00	0.00	0.00	0.00	0.00	0.00	0.00
K	0.00	0.00	0.00	0.00	0.00	0.00	0.00	0.00	0.00	0.00	0.00	0.00
OH*	16.00	16.00	16.00	16.00	16.00	16.00	16.00	16.00	16.00	16.00	16.00	16.00
Total	35.91	35.94	35.96	36.03	35.46	35.79	35.78	35.77	35.79	35.94	35.87	35.85
Fe/Fe+Mg	0.75	0.75	0.77	0.77	0.75	0.75	0.67	0.72	0.90	0.77	0.76	0.75
Variety	ripidolite	ripidolite	ripidolite	ripidolite	brunsvigite	ripidolite	ripidolite	ripidolite	daphnite	ripidolite	ripidolite	ripidolite
T (°C)-Cathelineau (1988)	371.16	368.62	379.00	373.02	296.65	351.37	363.14	354.63	385.59	380.97	367.89	348.89
T (°C)-Jowett (1991)	384.07	381.54	392.50	386.57	309.65	364.33	373.24	366.43	403.06	394.35	381.07	361.96

Table 7.2: Representative analysis of Fe-carbonate alteration minerals identified from the Karagba-Chaffeur-Durba deposit.

Sample	PB12-D01A	PB12-D09	2013-D22	2013-D26	2013-D84	2013-D103	2013-D97	2013-D92	2013-D8	2013-D90	2013-D96	2013-D102	2013-D14
Analysis	SITE 2 D	SITE 3 E	SITE 1 C	SITE 3 B	SITE 1 L	SITE 1 M	SITE 2 G	SITE 1 G	SITE 3 D	SITE 2 J	SITE 2 K	SITE 3 C	SITE 2 D
SiO ₂													
TiO ₂													
Al ₂ O ₃													
FeO	21.49	21.80	19.12	15.49	19.48	13.12	24.98	26.63	26.64	25.30	24.08	23.62	9.91
MnO	0.50	0.30		0.45	0.40	0.32							
MgO	7.07	7.01	7.44	9.53	8.27	12.72	5.28	3.91	4.79	4.02	5.70	4.88	14.46
CaO	26.96	26.44	24.58	25.12	25.94	27.87	26.21	25.99	26.24	24.49	25.37	26.79	27.40
Total	56.01	55.55	51.14	50.59	54.08	54.03	56.48	56.73	57.66	53.82	55.16	55.28	51.78
Mineral	Ankerite	Ankerite	Ankerite	Ankerite	Ankerite	Ankerite	Ankerite	Ankerite	Ankerite	Ankerite	Ankerite	Ankerite	Ankerite

Sample	PB12-D09	PB12-D02A	2013-D12	2013-D84	2013-D103	2013-D97	2013-D92	2013-D8	PB12-D02A	2013-D90	2013-D96	2013-D102	2013-D14
Analysis	SITE 2 D	SITE 3 F	SITE 5 B	SITE 2 L	SITE 2 M	SITE 1 F	SITE 2 C	SITE 1 K	SITE 1 I	SITE 1 G	SITE 2 H	SITE 2 D	SITE 2 I
SiO ₂													
TiO ₂													
Al ₂ O ₃													
FeO	48.86	52.94	49.38	47.98	49.30	52.87	55.21	53.85	53.22	53.04	51.80	49.96	48.94
MnO	0.52	0.30	0.31	0.73					0.35				0.43
MgO	5.97	3.22	5.49	8.86	7.31	5.28	3.69	3.81	4.12	3.56	4.66	5.13	7.70
CaO	0.55	0.33	1.05	0.39	0.80	0.52	0.66	0.59	0.44	0.43	0.45	0.46	0.56
Total	55.90	56.79	56.23	57.97	57.60	58.95	59.55	58.55	58.13	57.29	56.91	55.55	57.62
Mineral	Siderite	Siderite	Siderite	Siderite	Siderite	Siderite	Siderite	Siderite	Siderite	Siderite	Siderite	Siderite	Siderite

Table 7.3: Representative analysis of aluminoceladonite phyllosilicates identified in alteration assemblages at the Karagba-Chaffeur-Durba deposit

Sample	PB12-D01A	PB12-D09	PB12-D02A	2013-D12	2013-D26	2013-D84	2013-D103	2013-D97	2013-D92	2013-D8
Analysis	SITE 3 E	SITE 3 G	SITE 1 F	SITE 3 C	SITE 1 L	SITE 1 J	SITE 1 U	SITE 2 D	SITE 2 F	SITE 1 M
SiO ₂	48.81	47.67	47.43	47.29	46.17	49.09	49.22	48.49	47.59	47.67
TiO ₂	0.64	0.62	0.52	0.77		0.29	0.43	0.49	0.57	0.37
Al ₂ O ₃	30.69	32.65	27.80	30.88	33.64	32.14	28.02	31.36	33.48	34.65
FeO	4.72	3.79	8.23	5.07	1.78	3.32	6.21	4.59	3.07	2.86
MnO										
MgO	0.96	0.67	0.85	0.63	0.67	0.81	1.31	0.86	0.48	
CaO										
K ₂ O	10.08	9.97	10.19	10.28	9.37	9.59	10.18	10.36	10.11	9.38
Na ₂ O		0.55		0.34	0.66	0.67		0.38	0.51	0.89
Total	95.90	95.94	95.01	95.25	92.28	95.91	95.37	96.53	95.81	95.82
Mineral	Al-celadonite									

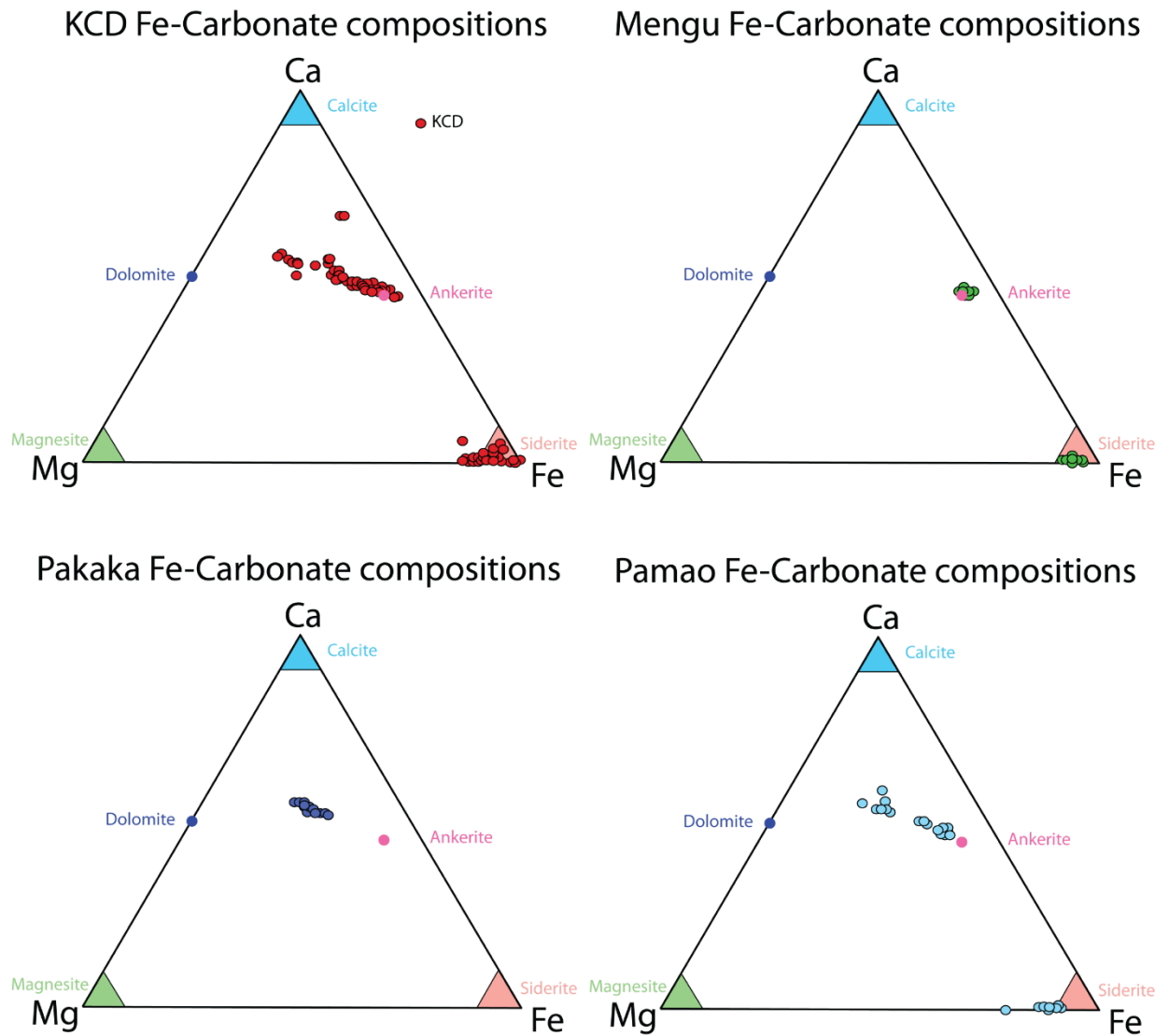
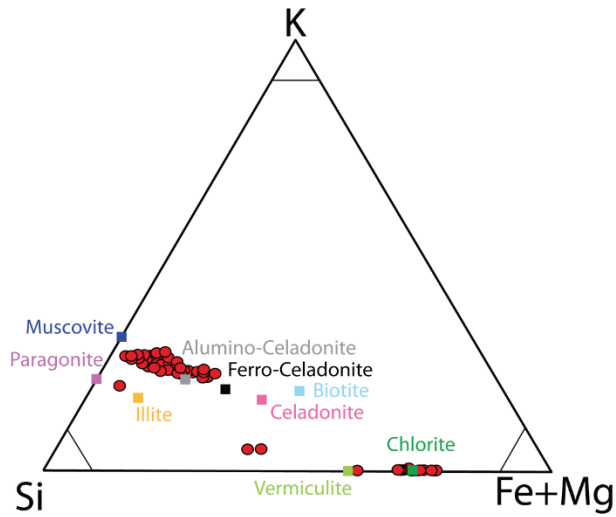
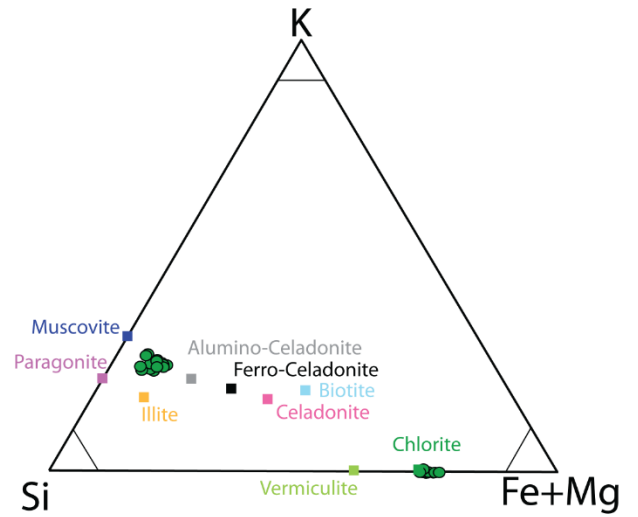


Figure 7.6: Ternary diagrams displaying compositional variations in Fe-Carbonate alteration minerals at the four major deposits. Values are Wt% values normalised to sum to 100%. Mineral reference values from Deer, Howie and Zussman (1966)

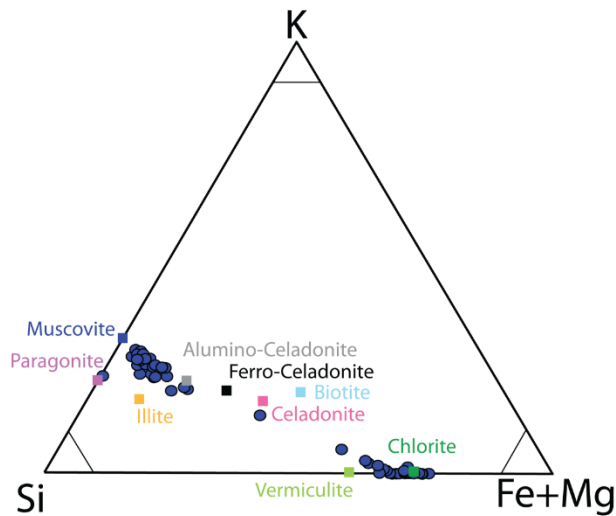
KCD: Phyllosilicate compositions



Mengu: Phyllosilicate compositions



Pakaka: Phyllosilicate compositions



Pamao: Phyllosilicate compositions

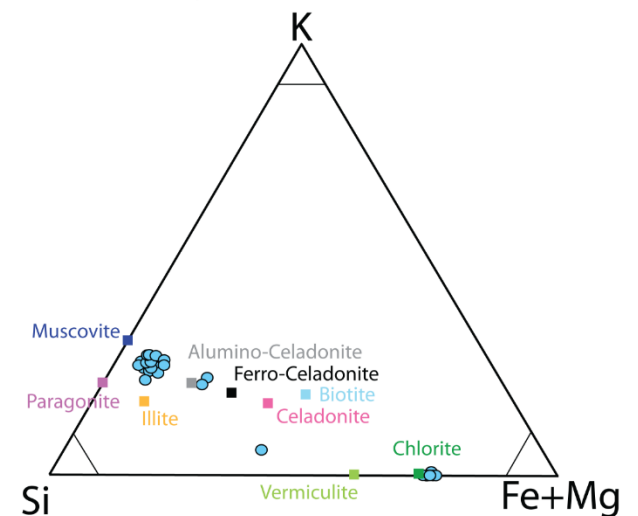


Figure 7.7: Ternary diagrams displaying compositional variations in phyllosilicate alteration minerals at the four major deposits. Values are wt% values normalised to sum to 100%. Mineral reference values from Deer, Howie and Zussman (1966)

7.4.3 Mineralisation Styles

Multiple styles of mineralisation are identified at the KCD deposit with disseminated sulphides and multiple vein styles being identified within the Kibalian metasedimentary lithologies in addition to vein and replacement style mineralisation within the ironstone lithologies. Within the Kibalian metasediments disseminated sulphide style mineralisation is associated with low intensity deformation and hydrothermal alteration of the host volcano-sedimentary conglomerates.

Disseminated sulphide mineralisation is identified in the phyllosilicate-rich interstitial areas between the deformed quartz-rich clasts with sulphide mineral phases observed overprinting and replacing chlorite and Fe-Carbonate phases (Fig. 7.8a and 7.8b-e). Sulphide hosting veins are identified in areas of intensive texture destructive hydrothermal alteration and the banded ironstone lithologies with three distinct types of vein having been identified (Fig. 7.8b-d).

Type-1 consist of 0.2-1 cm quartz±siderite±Al-celadonite veins with defined edges cross cutting relic structures in the altered volcano-sedimentary conglomerates and quartz/iron banding where observed in the ironstone lithologies (Fig. 7.8b and 7.10a-b). Type-2 veins are composed of fine quartz±siderite±Al-celadonite and run parallel to relic textures and foliation within the altered conglomerates forming dense vein nets across the sample material (Fig. 7.8c). These are discerned from the disseminated inter-clast hosted mineralisation by the abundance of quartz and lack of phyllosilicate minerals within the veins and the jagged angular appearance of the structures. Type-3 veins possess a quartz±siderite±Al-celadonite composition and occur as 1-5 cm irregular poorly masses of quartz and sulphides with poorly developed boundaries, appearing to blend into the surrounding Fe-carbonate alteration (Fig. 7.8c and 7.10c-d). Transitional styles, incorporating aspects of both disseminated and vein mineralisation are also identified.

Mineralisation within the banded ironstone occurs in two distinct styles, quartz+siderite+sulphide veins, matching the mineralogy and morphology to the type-1 veins distinguished in the Kibalian metasediments (Fig. 7.9a and 7.8f), and replacement style mineralisation with sulphides replacing iron-rich horizons (Fig. 7.9b). Within the Kibalian metasedimentary lithologies a relationship between the intensity of pre mineralisation alteration and the style of mineralisation is identified, with a corresponding variation in gold grade. Unaltered to low intensity Fe-carbonate+quartz alteration predominantly hosts low grade (<1 g/t) disseminated style mineralisation, though higher grade examples are also identified (Fig. 7.8). With increasing alteration intensity mineralisation style transitions to type-2 veins, where relic textures are still visible, and onto type-1 and type-3 veins where alteration intensity is at its maximum (Fig. 7.8). This transition to vein style mineralisation is generally accompanied by an increase in gold grade with samples displaying type-3 vein mineralisation possessing the highest gold grades.

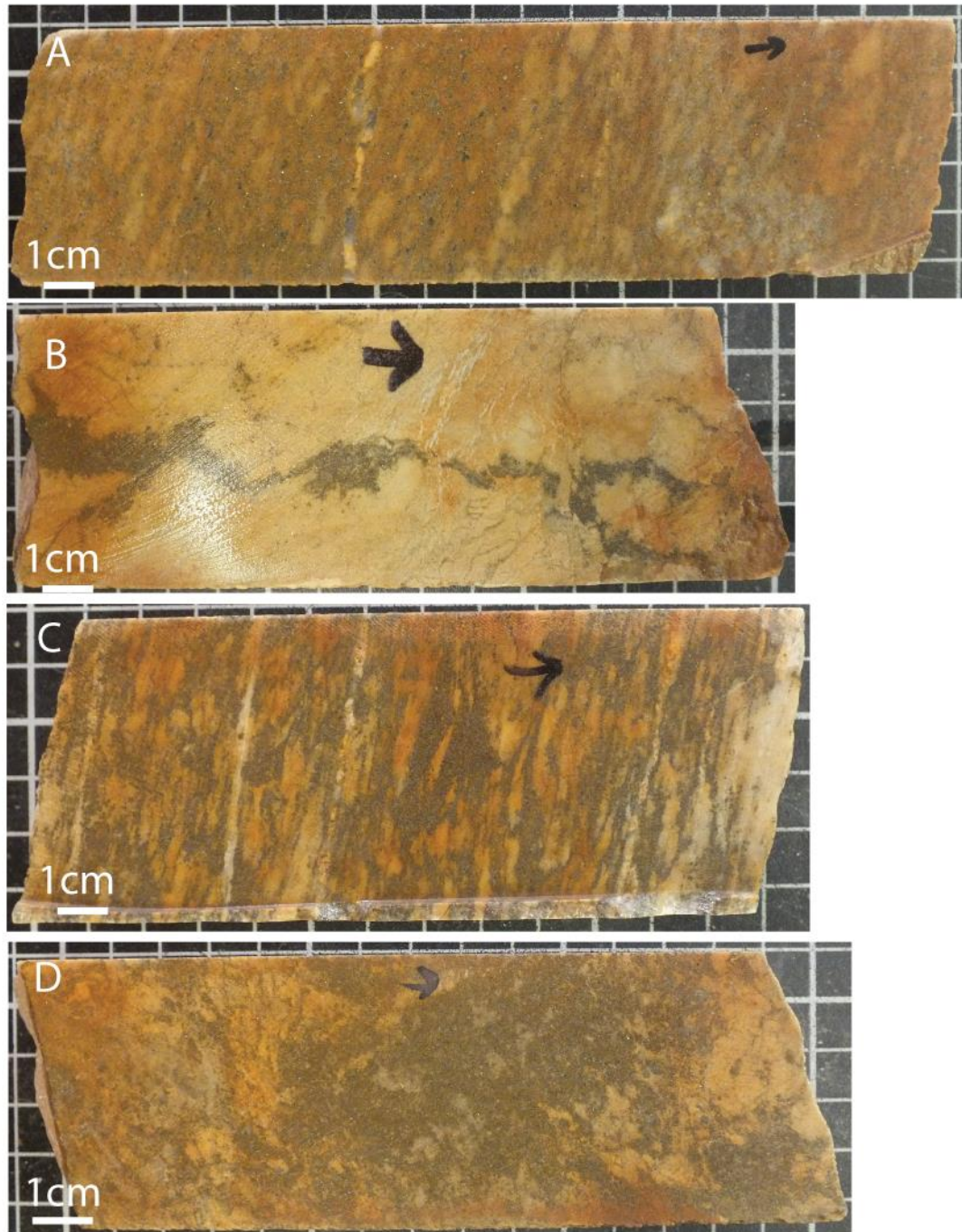


Figure 7.8: Mineralisation styles identified at the KCD gold deposit: A) Sample 2013-D8 (9.9g/t): Disseminated sulphide style mineralisation, sulphide minerals are identified in the inter-clast phyllosilicate-rich zones. B) Sample 2013-D14 (3.28g/t): Type 1 vein bisecting texture destructive Fe-carbonate+quartz alteration, Sulphide minerals are hosted in quartz±siderite gangue. C) Sample 2013-D38 (14g/t): Type 2 vein mineralisation in altered volcano-sedimentary conglomerates, vein structures run parallel to the stretching direction exploiting pre-existing planes of weakness. D) Sample 2013-D57 (25.42g/t): Type 3 vein mineralisation occurring in highly altered (Fe-carbonate±quartz) material, Sulphide minerals are hosted in a quartz±siderite gangue forming an amorphous mass in the centre of the sample

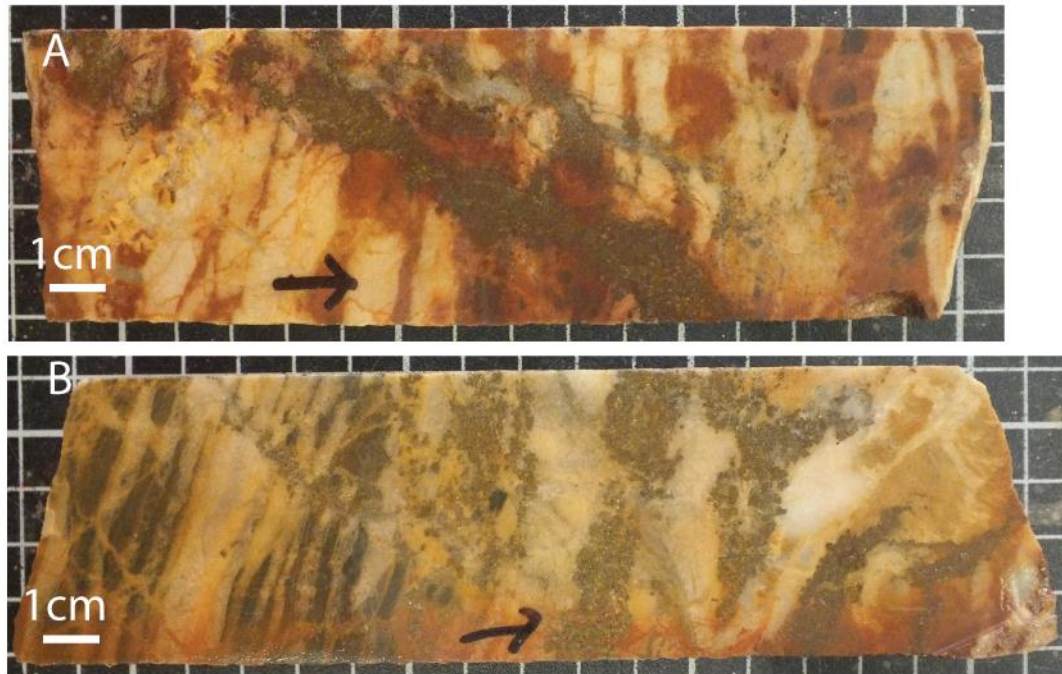


Figure 7.9: Vein and replacement style mineralisation identified in the banded iron formations: A) Sample 2013-D69 (7.1g/t); Sulphide minerals in quartz gangue cross cutting extensively altered banded ironstone. B) Sample 2013-D70 (7g/t); Sulphide mineralisation forming discrete layers replacing relic ironstone horizons in a highly altered (Fe-carbonate+quartz) banded ironstone.

7.4.4. Ore Mineralogy

The mineralogical characteristics of the major ore phases at the KCD deposit are here discussed, a paragenesis of their formation is displayed in Figure 7.11.

7.4.4.1 Pre-Ore stage

Arsenopyrite 1 (Asp-1) occurs as well formed 20-50 μm angular crystals (Fig. 7.12e), typically identified as inclusions within later sulphide phases. Pyrrhotite-1 (Po-1) is locally abundant, being the dominant sulphide phase in some of the examined samples. Where abundant pyrrhotite-1 displays two distinct morphologies, irregular interlocking vuggy masses of 200-100 μm crystals being the most common, and rarer angular homogenous 1-5 mm crystals. These large pyrrhotite masses are commonly observed occluding Asp-1. Chalcopyrite 1 (Cpy-1) is identified only rarely, occurring as rounded 10-50 μm masses occluded within the Py-1b phase (See below) (Fig. 7.12e).

7.4.4.2 Ore Stage

Pyrite is the main Au-bearing ore mineral at the KCD, with multiple generations being identified (Fig. 7.12a-f). Pyrite 1 (Py-1) is observed occluding and replacing the earlier sulphide phases, and as

‘disseminated’ aggregates of crystals. Disseminated Py-1 forms 100-1000 μm angular isometric cubic, rectangular crystals and deformed sub-hedral crystals (Fig. 7.12a-f). Pyrite 1 is distinguished by its distinct ‘zoned’ appearance with vuggy cores (Pyrite-1a (Py-1a)) surrounded by homogenous rims (Pyrite-1b (Py-1b)) (Fig. 7.12b). Vugs within Py-1a are sub-micron in size and contain inclusions of multiple mineral phases including pre-ore sulphide phases and hydrothermal alteration minerals. These vuggy areas define distinct growth zoning which is further reflected by compositional variations identified within Py-1a. Compositional analysis of the vuggy areas has shown them to be composed of alternating layers of arsenian pyrite. Pyrite 2 is observed as disseminated crystals within the groundmass and on the outer edges of the large well Py-1 crystals (Fig. 7.12 a,d and e). Py-2 forms variable 50-200 μm angular to subhedral crystals with a predominantly homogenous texture though less common vuggy examples are identified.

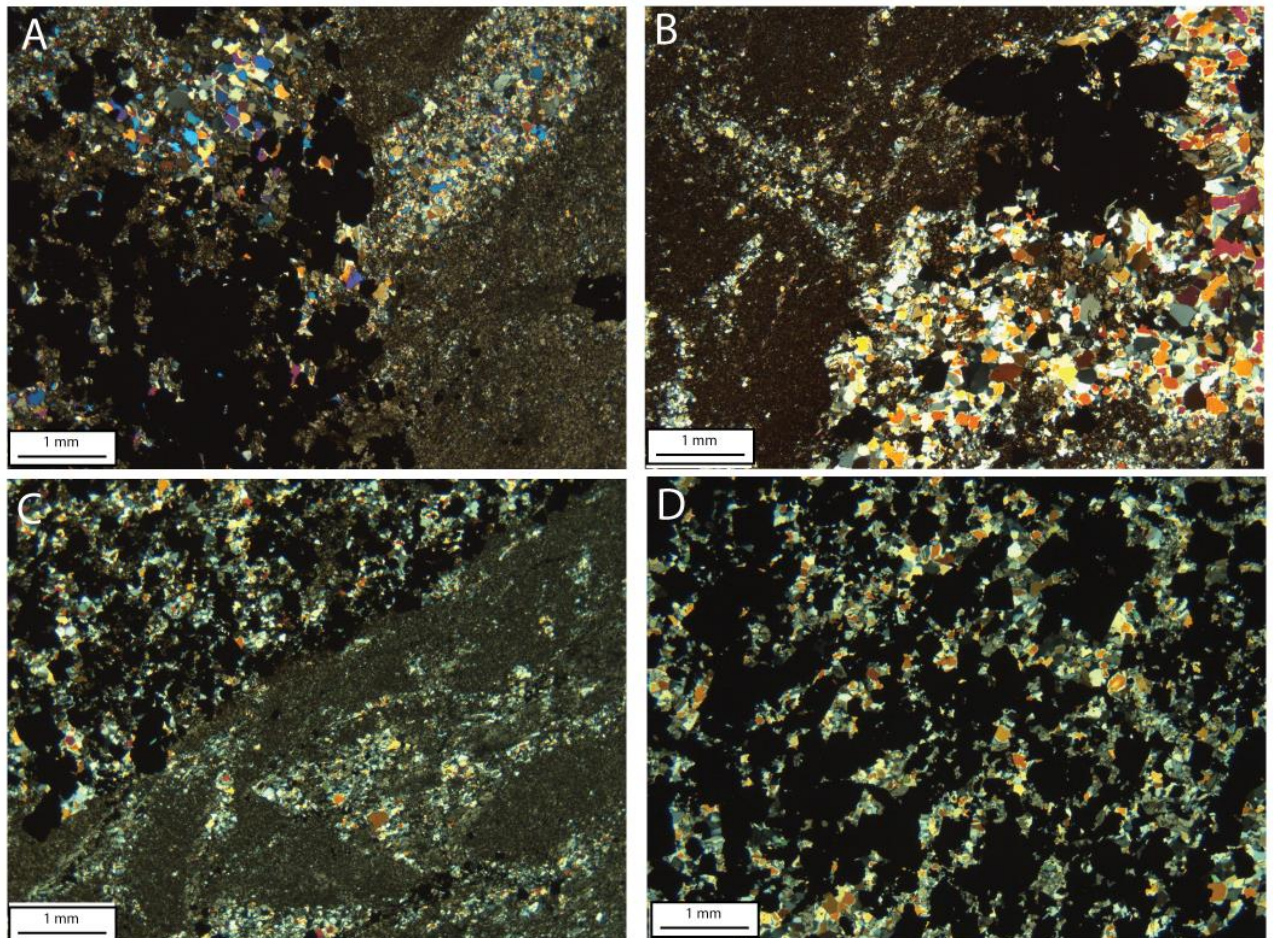


Figure 7.10: XPL Photomicrographs displaying selected examples of vein style mineralisation at the KCD gold deposit: A) Sample 2013-D44; Type 1 sulphide-bearing mineral vein cross cutting heavily stretched and altered volcano-sedimentary conglomerate. B) Sample 2013-D92; Type 3 quartz vein with minor sulphide mineralisation cutting across texture destructive alteration (Fe-carbonate±quartz). C) Sample 2013-D60; Type 1 sulphide-rich vein in highly altered (texture destructive Fe-carbonate+quartz) host. D) Sample 2013-D107; Abundant sulphide minerals hosted in a quartz-siderite gangue in a type 3 mineralised vein structure.

Mineral	Pre-Ore stage	Ore stage	Post ore stage
Deformation metamorphism			
Quartz	—————	-----	
Chlorite	—————	-----	
Alluminoceladonite	—————	-----	
Hydrothermal Alteration			
Ankerite	—————	-----
Siderite	—————	-----
Quartz	—————	-----
Magnetite			—————
Sulphides			
Arsenopyrite-1	—————		
Chalcopyrite-1		—————	
Pyrrhotite-1		—————	
Pyrite-1a		—————	
Pyrite-1b		—————	
Au-1		—————	
Tenantite 1		—————	
Pyrite 2			
Pyrrhotite-2			—————
Arsenopyrite-2			—————
Au-2			—————
Chalcopyrite-2			—————
Marcassite-1			—————
Galena-1			—————
Pyrite 3			—————
Accessory Phases			
Monazite		—————	
Fluorapatite	—————	-----	
Apatite	—————	-----	
Scheelite	—————	-----	
Rutile	—————	-----	

Figure 7.11: Paragenetic diagram illustrating the developmental sequence of the major mineral phases including alteration assemblages, sulphide mineralisation and selected accessory phases identified at the Karagba-Chaffeur-Durba deposit.

7.4.4.3 Gold mineralisation

Native gold is identified in three main textural settings at the KCD and is frequently associated with the Py-1 ore phase. Au-1 occurs as irregular sub-rounded to sub-angular crystals ranging in size from sub-micron to 200 μm . Au-1 is identified exclusively within the py-1 mineral phase. The majority of identified gold grains are confined to the outer homogenous Py-1b phase being only rarely identified in, and on the boundary of, the Py-1a phase (Fig. 7.13 a-f). Au-2 post-dates the formation of the Py-1 and Py-2 ore phases and is divided into two phases (Au-2a and Au-2b) based on morphology and mode of occurrence. Au-2a occurs as isolated crystals within the groundmass and nucleating on the edges, and partially enclosing, the Py1/Py2 phase (Fig. 7.13d-e). Au-2a crystals are irregular angular to-sub-angular in form and range in size from 10-200 μm . Au-2a crystals are observed nucleating on the edges of pyrite crystals their morphology is partially controlled by the existing pyrite crystal resulting in more irregular morphology. Au-2b is associated with fractures in the Py-1 crystal phase with grain morphology and size being controlled by fracture geometry (Fig. 7.13d-f). Au-2b is commonly observed intergrown with post ore stage Cpy-2 and Gal-1. The Au-2 (a/b) phase displays distinct relationship with the grade of the sample, only being observed in type-3 vein structures with the highest gold grades.

7.4.4.4 Post Ore stage

Arsenopyrite-2 (Asp-2) forms 50-200 μm angular diamond and rectangular crystals occurring as disseminated crystals within the groundmass and enclosing Pyrite-1 and Pyrite-2 (Fig. 7.12c). Post ore chalcopyrite (Chalcopyrite-2 (Cpy-2)) occurs in two distinct morphologies, being identified as crystals within the groundmass and as fracture filling within the Pyrite-1 mineral phase. Where identified within the groundmass Cpy-2 is observed forming highly irregular sub-rounded 100 μm crystals occurring as both isolated crystals within the quartz/carbonate groundmass and enclosing the Py-1 phase. Chalcopyrite-2 is commonly observed in association with Galena 2 (Gal-2) occurring as fracture filling within the Pyrite-1 mineral phase and are associated with the Au2 event (Fig. 7.13f). These phases are typically 10-100 μm irregular anhedral crystal forms with morphology being primarily controlled by crack geometry. These fracture fillings are associated with the Au-2 mineralisation event. Rare Marcasite-1 (Marc-1) is identified, occurring as 100-200 μm irregular angular material enclosing both Py-1 and Asp-2 mineral phases (Fig. 7.12e). The marcasite is similarly coloured to the pyrite material being primarily identified by its distinct finely speckled texture. Pyrrhotite-2 (Po-2) forms 20-200 μm irregular crystals enclosing the Pyrite-1 and Pyrite-2 phases (Fig. 7.12a and d). Pyrite-3 (Py-3) is rarely identified occurring as fine 'skeletal' crystals occupying space between pre-existing phases, most commonly within the fine quartz groundmass.

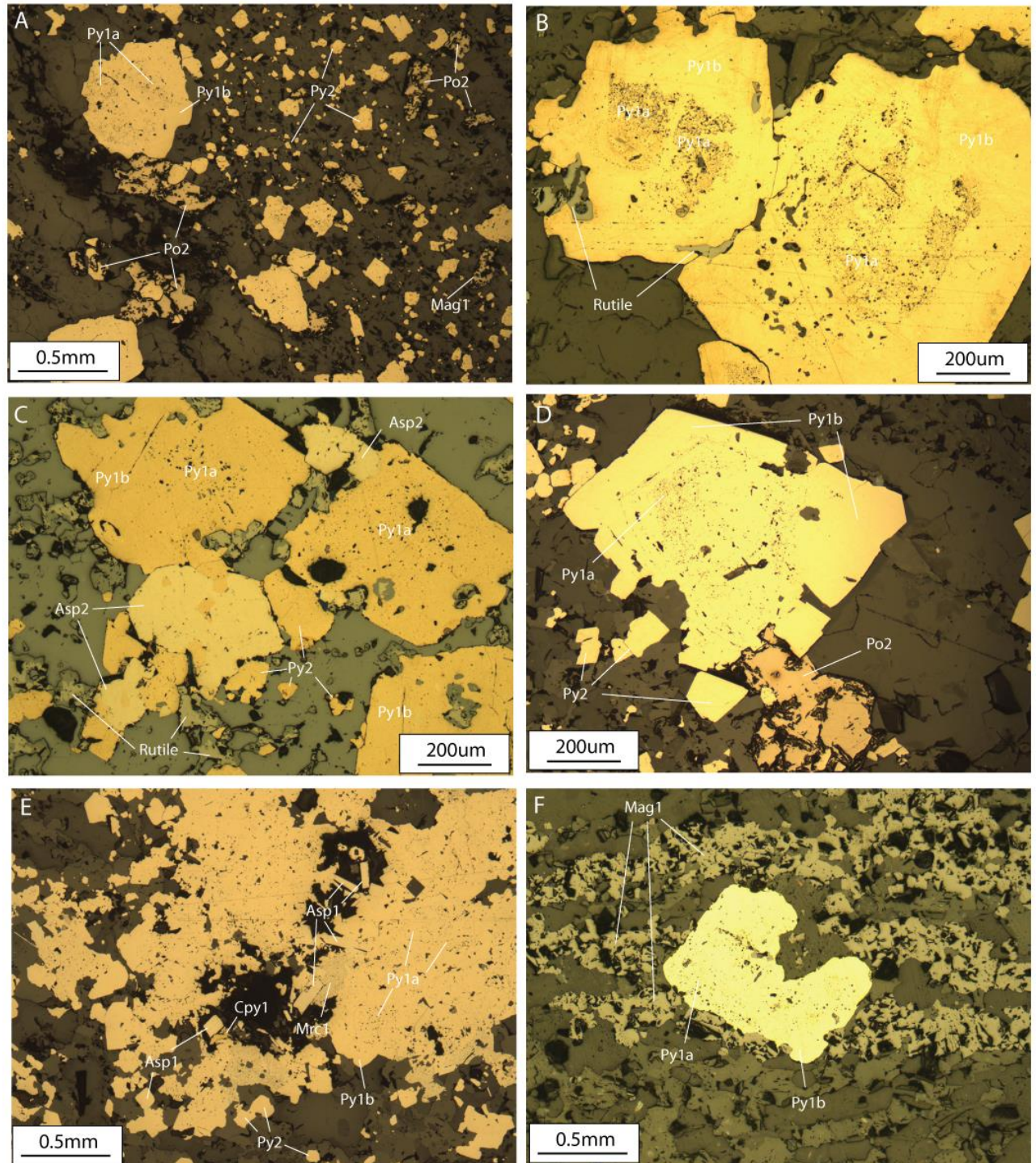


Figure 7.12: RFL Photomicrographs displaying the relationship between the major sulphide mineral phases at identified at the Karagba-Chaffeur-Durba (KCD) deposit. A) Sample 2013-D1; Pyrrhotite-1 occluding Pyrite-1 and Pyrite-2 phases. B) Sample PTS21; Zoned Py1a/b pyrite occluding early rutile. C) Sample KCD24; Post ore Arsenopyrite-2 partially occluding zoned Pyrite-1a/b and Pyrite-2 crystals. D) Sample 2013-D2; Post ore Pyrrhotite-2 partially occluding the Pyrite-1 and Pyrite-2 mineral phases. E) Sample D92; Multiple generations of arsenopyrite and pyrite with late chalcopyrite and marcasite. F) Sample KCD15; Zoned Pyrite-1a/b pyrite crystals partially occluded by late magnetite alteration.

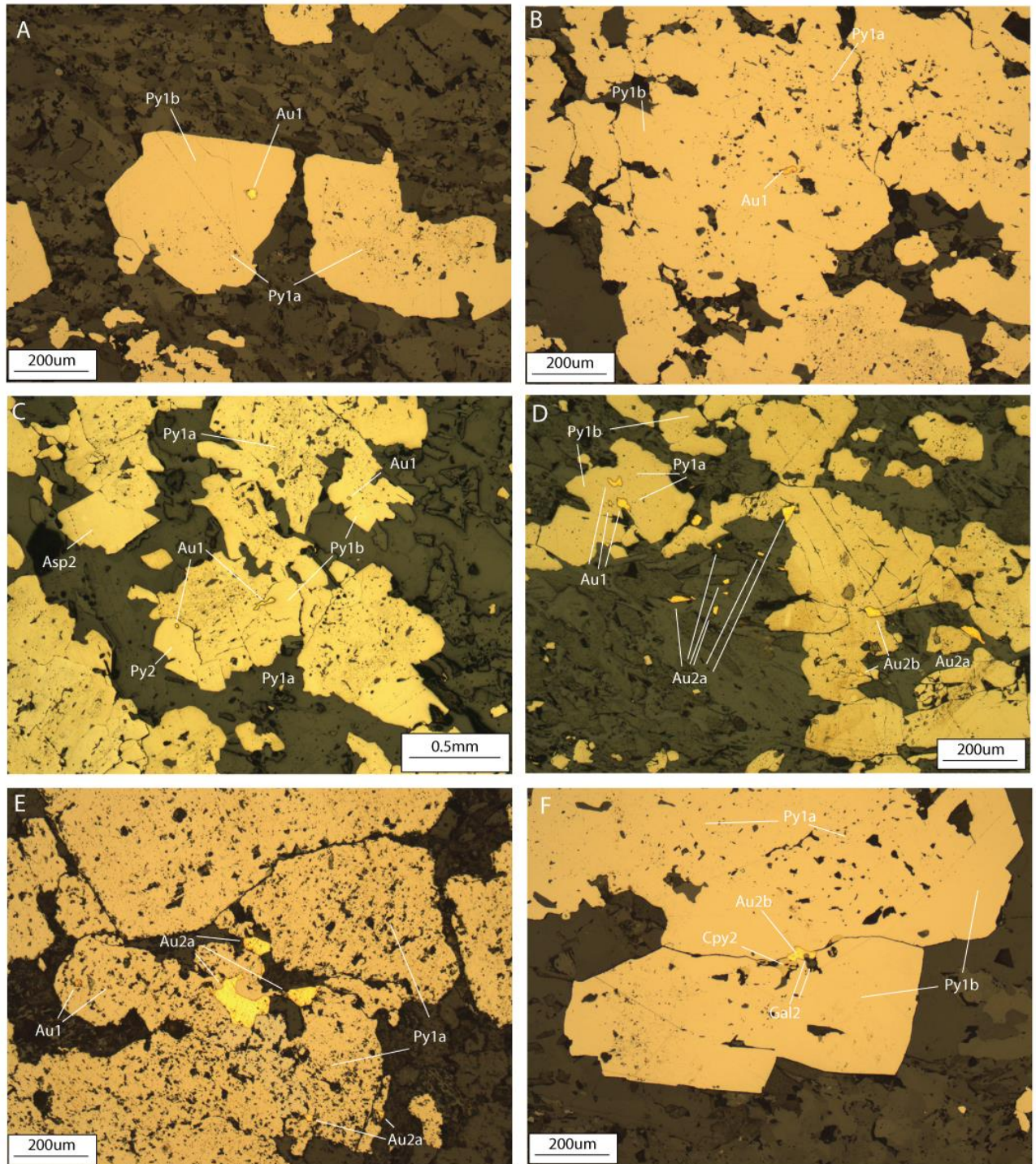


Figure 7.13: RFL Photomicrograph displaying the occurrences of gold and its relationship to the pyrite sulphide mineral phases at the Karagba-Chaffeur-Durba deposit. A) Sample 2013-D91; Au-1 occluded in Py-1b material. B) Sample 2013-D111; Irregular grain of Au-1 occluded in poorly formed mass of Py-1a/b sulphide. C) Sample KCD25; Au-1 occluded in Py-1b and Py-2 sulphide phases. D) Sample KCD12; Multiple generations of gold occurring in inclusions within sulphides (Au-1), As isolated grains in the groundmass and on the edges of sulphide crystals (Au-2a) and as fracture hosted grains (Au-2b). E) Sample 2013-D97; Au-2a grains partially occluding pyrite. F) Sample 2013-D97: Fracture hosted gold (Au-2b) intergrown with 'post ore' Chalcopyrite-2 and Galena-2.

7.5 Mengu

7.5.1 Host lithologies

Sampled host lithologies at the Mengu deposit consist of banded iron formations and variable members of the Kibalian metasediments. Banded iron formations occur in multiple horizons at the Mengu deposit occurring as massive homogenous ironstone containing randomly distributed silica masses. The majority of the examined samples are composed of units attributed to the Kibalian metasediments, with a significant degree of variability between individual samples. Volcano-sedimentary conglomerates consisting of Quartz-feldspar clasts hosted within a phyllosilicate-rich (chlorite/aluminoceladonite) groundmass are the most commonly identified lithology (Fig. 7.15a). The volcano-sedimentary conglomerates are compositionally diverse, the morphology and relative proportion of the clast material (ranging from clast poor/absent to clast supported) being highly variable. Fine laminated sediments, consisting of millimetre thick undulating layers, are also identified as interbedded horizons within the more abundant volcano-sedimentary conglomerate as part of the Kibalian metasediments. The host lithologies at the Mengu deposit have been deformed on a localised scale, this being most commonly observed in the clast-rich volcano-sedimentary conglomerates. Deformation is characterised by stretching and recrystallisation of the clasts resulting in fine crystalline quartz clasts that range from ellipsoid to thin highly attenuated 'bands' (Fig. 7.14 and 7.15b). Deformation of the quartz clasts is accompanied by recrystallisation and alignment of the chloritic phyllosilicate minerals parallel to the stretching orientation, the phyllosilicate minerals appearing to 'flow' around the quartz-rich clasts (Fig. 7.14 and 7.15b). Limited analyses of chlorite compositions show chlorite compositions vary between samples with both daphnite and ripidolite varieties being identified (Table 7.4).

7.5.2 Alteration

Two prominent alteration events are identified in the samples from the Mengu deposit, a pre-mineralisation event characterised by Fe-carbonate+quartz±aluminoceladonite and a post mineralisation event characterised by the formation of magnetite-rich layers. Fe-carbonate alteration is observed primarily in the volcano-sedimentary lithologies, occurring as <0.1 mm angular to sub-angular crystals overprinting both the phyllosilicate-rich inter-clast zones and quartz clast material (Fig. 7.52c). This event varies in intensity, ranging from benign, with only small isolated patches of carbonate, to texture destructive (Fig. 7.15d), the Fe-carbonates(+quartz) dominating the groundmass with no evidence of the primary volcano-sedimentary textures being identifiable. Two species of Fe-carbonate are identified, ankerite and siderite, with compositions being consistent throughout the examined samples (Table 7.5 and Fig. 7.6). Ankerite and siderite are identified in all samples, though specific sites are generally predominantly one mineral or the other. Unlike the aluminoceladonite in the samples from the KCD deposit, analyses from the Mengu



Figure 7.14: Core samples from the Mengu deposit displaying the localized deformation of the volcano-sedimentary conglomerate lithologies: A) Sample 2013-M11; Deformed clast-rich volcano-sedimentary conglomerate, densely packed stretched quartz clasts separated by thin chlorite-rich bands. B) Sample 2013-M17; Stretched volcano-sedimentary conglomerate consisting of quartz clasts and thick chlorite-rich bands, deformation is sufficient that clasts width has exceeded the core width.

deposit show aluminoceladonite mica compositions are restricted, clustering between the ideal compositions of aluminoceladonite and muscovite (Table 7.6 and Fig. 7.7). Late alteration at the Mengu deposit is identified in the Kibalian metasedimentary lithologies and is characterised by the formation of magnetite crystals of varying morphologies. Magnetite alteration occurs in association with sulphide mineralisation in the altered and deformed volcano-sedimentary conglomerates, forming large sub-hedral crystals that partially occlude auriferous pyrite. Magnetite alteration is also identified in the layered sediments, magnetite occurring as ~0.2 mm thick layers composed of densely interlocking <0.1 mm magnetite crystals (See Fig. 7.15f).

7.5.3 Mineralisation styles

Two prominent mineralisation styles are identified in the lithologies at the Mengu deposit, disseminated sulphide mineralisation and quartz+siderite±aluminoceladonite sulphide-bearing veins. Disseminated sulphide mineralisation is observed in the volcano-sedimentary conglomerates as sulphide minerals overprinting and replacing chlorites and Fe-carbonates in the inter-clast phyllosilicate-rich areas (Fig. 7.16a and c, Fig. 7.15c). The intensity of the disseminated sulphides varies from rare isolated sulphide crystals to abundant sulphides extensively overprinting the pre-existing mineral phases, at its most intense

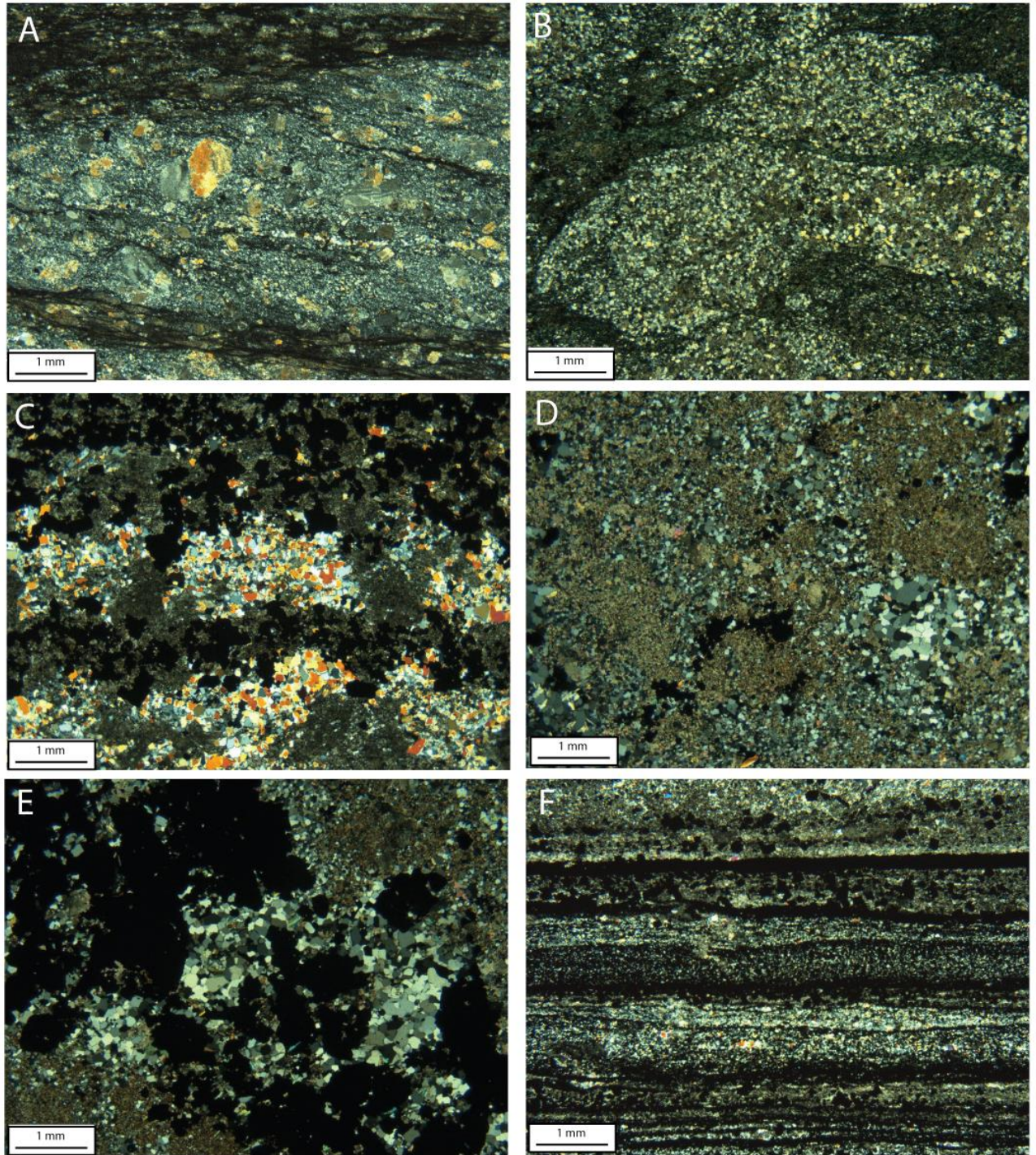


Figure 7.15: XPL Photomicrographs illustrating host lithology, alteration and mineralisation micro-textural characteristics in selected samples from the Mengu deposit: A) Sample 2013-M13; Deformed volcano-sedimentary conglomerate, a quartz-feldspar clast in a groundmass composed of micas aligned parallel to the stretching direction. B) Sample PB12-M05; Deformed quartz-rich clasts with minor Fe-Carbonate alteration set in a groundmass composed of aligned chlorite crystals. C) Sample PB12-M13; Mineralisation hosted in deformed and altered volcano-sedimentary conglomerate, phyllosilicate-rich zones between quartz clasts are altered by Fe-carbonates which host abundant sulphides. D) Sample PB12-M06; Texture destructive Fe-carbonate+quartz alteration. E) Sample PB12-M06; Mineralised vein (sulphides hosted in quartz) bisecting texture destructive alteration. F) Sample 2013-M15; Late magnetite alteration (dark bands) forming variable thickness parallel layers.

Table 7.4: Representative analyses of chlorite identified in deformed volcano-sedimentary conglomerates at the Mengu deposit

Sample	PB12-M02	PB12-M02	PB12-M02	PB12-M02	PB12-M05	PB12-M05	PB12-M05	PB12-M05	PB12-M05	PB12-M05
Analysis	SITE 2 C	SITE 2 H	SITE 3 D	SITE 4 H	SITE 1 F	SITE 1 L	SITE 2 G	SITE 2 Y	SITE 3 P	SITE 3 U
SiO ₂	22.98	24.23	23.87	23.44	24.34	23.60	23.20	24.15	23.39	24.12
Al ₂ O ₃	20.37	21.56	20.74	19.89	20.47	20.79	19.55	20.00	21.24	19.10
Fe ₂ O ₃	0.23	1.08	0.59	0.24	0.71	0.32	0.41	0.55	0.47	0.45
FeO	40.29	39.25	40.26	40.52	35.15	36.32	34.25	35.66	35.59	34.96
MnO	0.00	0.00	0.00	0.00	0.00	0.00	0.00	0.00	0.00	0.00
MgO	4.03	4.18	4.21	4.25	7.21	6.74	6.83	7.00	6.70	7.41
CaO	0.00	0.00	0.00	0.00	0.00	0.00	0.32	0.00	0.00	0.00
Na ₂ O	0.00	0.00	0.00	0.00	0.00	0.00	0.00	0.00	0.00	0.00
K ₂ O	0.00	0.00	0.00	0.00	0.00	0.00	0.00	0.00	0.00	0.00
H ₂ O*	10.44	10.83	10.69	10.49	10.75	10.68	10.32	10.65	10.66	10.51
Total	98.34	101.12	100.36	98.83	98.63	98.46	94.87	98.00	98.05	96.55
Si	5.28	5.35	5.35	5.36	5.42	5.30	5.39	5.43	5.26	5.50
Al (iv)	2.72	2.65	2.65	2.64	2.58	2.70	2.61	2.57	2.74	2.50
Al (vi)	2.79	2.98	2.83	2.72	2.80	2.80	2.74	2.74	2.89	2.64
Ti	0.00	0.00	0.00	0.00	0.00	0.00	0.00	0.00	0.00	0.00
Fe ³⁺	0.04	0.18	0.10	0.04	0.12	0.05	0.07	0.09	0.08	0.08
Fe ²⁺	7.74	7.25	7.54	7.74	6.54	6.82	6.65	6.71	6.69	6.67
Mn	0.00	0.00	0.00	0.00	0.00	0.00	0.00	0.00	0.00	0.00
Mg	1.38	1.38	1.40	1.45	2.39	2.26	2.36	2.34	2.24	2.52
Ca	0.00	0.00	0.00	0.00	0.00	0.00	0.08	0.00	0.00	0.00
Na	0.00	0.00	0.00	0.00	0.00	0.00	0.00	0.00	0.00	0.00
K	0.00	0.00	0.00	0.00	0.00	0.00	0.00	0.00	0.00	0.00
OH*	16.00	16.00	16.00	16.00	16.00	16.00	16.00	16.00	16.00	16.00
Total	35.95	35.78	35.88	35.95	35.85	35.93	35.91	35.88	35.90	35.90
Fe/Fe+Mg	0.85	0.84	0.84	0.84	0.74	0.75	0.74	0.74	0.75	0.73
Variety	daphnite	daphnite	daphnite	daphnite	ripidolite	ripidolite	ripidolite	ripidolite	ripidolite	ripidolite
T (°C)-Cathelineau (1988)	376.45	364.89	365.21	363.61	353.90	373.35	358.85	351.81	379.86	340.60
T (°C)-Jowett (1991)	392.39	380.67	381.07	379.47	366.33	386.21	371.41	364.53	392.58	352.95

Table 7.5: Representative analyses of Fe-carbonate alteration minerals identified at the Mengu deposit

Sample	PB12-M02	PB12-M02	PB12-M02	2013-M18	2013-M18	2013-M18	PB12-M06	PB12-M06	PB12-M06	PB12-M05	PB12-M05	PB12-M05
Analysis	SITE 1 F	SITE 2 F	SITE 4 E	SITE 2 A	SITE 2 B	SITE 4 E	SITE 1 E	SITE 4 C	SITE 5 F	SITE 1 D	SITE 2 E	SITE 3 C
SiO ₂												
FeO	25.40	25.19	24.74	25.21	25.43	24.57	24.71	25.12	54.39	20.33	20.48	20.26
MnO		0.35	0.34							0.79	0.61	0.53
MgO	3.80	4.67	4.88	4.74	4.83	5.53	4.88	5.05	2.57	8.44	7.16	7.79
CaO	26.37	26.28	26.40	26.57	26.48	26.49	26.16	26.07	0.29	26.30	25.37	26.03
Total	55.56	56.48	56.37	56.52	56.74	56.60	55.74	56.24	57.26	55.86	53.62	54.61
Mineral	Ankerite											
Sample	PB12-M02	PB12-M02	PB12-M02	2013-M18	2013-M18	2013-M18	PB12-M06	PB12-M06	PB12-M06	PB12-M05	PB12-M05	PB12-M05
Analysis	SITE 2 D	SITE 3 G	SITE 5 C	SITE 2 C	SITE 3 C	SITE 4 B	SITE 2 B	SITE 2 E	SITE 3 F	SITE 1 X	SITE 3 E	SITE 3 J
SiO ₂												
FeO	53.30	52.55	53.73	54.15	51.95	52.29	52.43	54.51	52.44	47.16	47.52	47.30
MnO		0.53					0.32		0.30	0.85	1.01	0.83
MgO	4.38	5.25	3.40	4.00	4.71	2.48	3.75	2.37	4.27	8.47	7.20	8.70
CaO	0.49	0.59	0.56	0.28	0.53	0.57	0.78	0.47	0.56	0.44	0.84	0.48
Total	58.17	58.91	57.68	58.43	57.18	55.78	57.29	57.35	57.57	57.08	56.91	57.56
Mineral	Siderite											

Table 7.6: Representative analyses of aluminoceladonite alteration minerals identified at the Mengu deposit

Sample	2013-M18	2013-M18	2013-M18	PB12-M06	PB12-M06	PB12-M06	PB12-M05	PB12-M05	PB12-M05	PB12-M05	PB12-M05
Analysis	SITE 1 E	SITE 2 E	SITE 3 E	SITE 1 G	SITE 2 C	SITE 4 H	SITE 1 U	SITE 2 N	SITE 2 Z	SITE 3 M	SITE 3 T
SiO ₂	47.74	47.31	43.18	47.48	47.34	47.10	48.26	47.36	47.80	47.06	46.57
TiO ₂		0.30							0.32	0.43	0.30
Al ₂ O ₃	34.99	34.22	32.38	32.93	34.10	33.08	30.27	30.35	30.58	30.60	32.22
FeO	2.26	3.34	2.15	3.24	2.70	3.68	3.59	3.49	3.76	2.59	3.23
MgO				0.53	0.39		1.31	1.05	1.05	1.11	0.69
K ₂ O	9.06	9.02	8.40	9.04	7.44	8.73	9.83	9.87	9.89	9.81	9.73
Na ₂ O	1.34	1.10	1.29	1.02	2.33	1.40	0.36	0.47	0.50	0.48	0.62
Total	95.39	95.30	87.39	94.24	94.30	93.99	93.63	92.60	93.89	92.07	93.37
Mineral	Al-Celadonite										

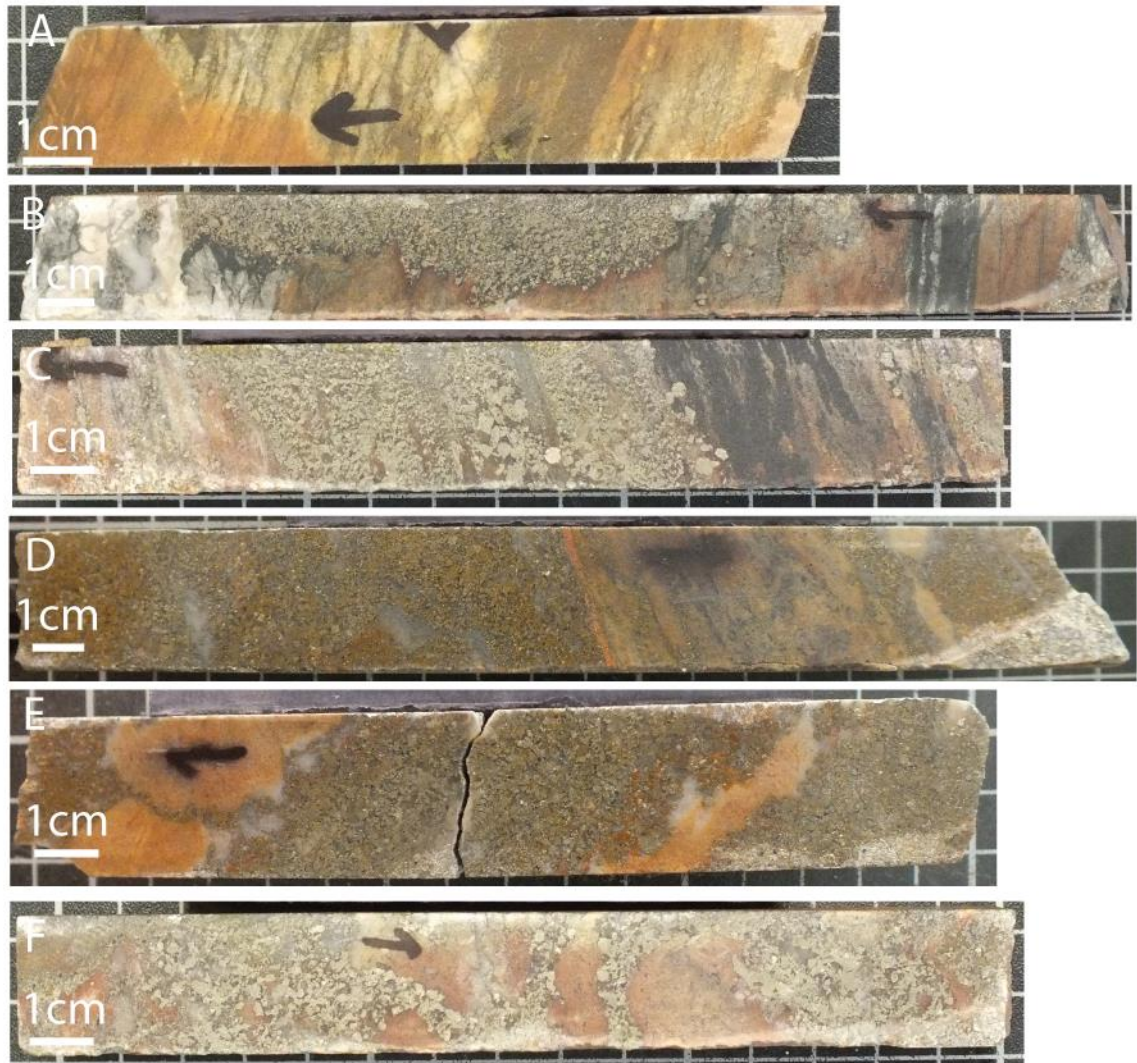


Figure 7.16: Core images displaying mineralisation styles identified in samples from the Mengu deposit: A) Sample PB12-M3 (3.75g/t) Disseminated sulphide mineralisation hosted in inter-clast phyllosilicate-rich areas. B) Sample PB12-M2 (5.99g/t); Irregular vein style mineralisation, sulphides hosted quartz gangue cutting across extensive Fe-carbonate alteration. C) Sample PB12-M17; Extensive disseminated sulphide mineralisation hosted within altered clast poor volcano-sedimentary conglomerate. D) Sample PB12-M16 (7.2g/t); Vein mineralisation consisting of sulphides hosted in a quartz gangue, wide vein running parallel to relic textures in the host. E) Sample PB12-M18 (8.91g/t); Sulphide+quartz vein cutting across texture destructive Fe-carbonate+quartz alteration. F) Sample PB12-M6 (15g/t); Mineralised vein structures cutting texture destructive Fe-carbonate+quartz alteration.

overprinting the edges of the relic quartz clasts. Vein style mineralisation is the most frequently observed mineralisation style at the Mengu deposit, veins being characterised by a quartz±siderite±aluminoceladonite gangue mineralogy ranging from >1 cm to approximately 10 cm in thickness (Fig. 7.15b, d-f). Vein style mineralisation is identified in material that has undergone intense texture destructive Fe-carbonate±quartz alteration (Fig. 7.15b, d-f, and Fig. 7.16e) while the disseminated sulphide style predominates in areas of low intensity alteration. Mineralisation style also shows a correlation with gold grade, vein style mineralisation possessing the highest gold grades within the available samples (Fig. 7.16).

7.5.4 Ore Mineralogy

The mineralogical characteristics and the major ore phases at the Mengu deposit are here discussed, a paragenesis of their formation is displayed in Fig. 7.17.

7.5.4.1 Pre-Ore Stage

Pre-ore sulphide phases are observed rarely within the sulphide mineral assemblage at the Mengu Hill deposit. Chalcopyrite-1 (Cpy-1), Pyrrhotite-1 (Po-1) and Arsenopyrite-1 (Asp-1) are identified as small inclusions within the later pyrite (Fig. 7.18a, d and f). All three phases display similar morphology, being rounded to sub-rounded 5-30 µm masses with no distinct crystal forms, instead being replaced by the enclosing pyrite material. Cpy-1 is commonly observed replacing Po-1 (Fig. 7.18a).

7.5.4.2 Ore stage

Pyrite is the dominant sulphide material at Mengu accounting for approximately 99% of the observed sulphide assemblage. Pyrite is the main ore-bearing phase, being the only phase with which gold mineralisation has been observed. Pyrite-1 occurs as well formed 100-1000 µm triangular, hexagonal and pyritoform crystals (Fig. 7.18 a-f). The Pyrite-1 phase is subdivided into Py-1a and Py-1b. Py-1a is distinguished by its vuggy texture, consisting of sub-micron to 2 µm vugs that are observed defining a series of growth zones within the py-1 crystals and as vuggy trails separating homogenous pyrite material (Fig. 7.18 b-c). Py-1b is distinguished by its textural homogeneity and is identified as rims of variable thickness around the outer edges of the Py-1a phase (Fig. 7.18 a-f). Pyrite-2 is the most abundant mineral phase identified within the sample from Mengu, forming irregular sub-rounded to sub-angular 5-100 µm crystals throughout the mineralised areas and as aggregate masses of intergrown crystals and as crystals nucleated on the outer margin of the Py-1 generation (Fig. 7.18 b-c). Pyrite-2 (Py-2) is predominantly texturally homogenous though areas of 'vugs' are present where Py-2 crystals interlock as aggregate masses.

7.5.4.3 Gold Mineralisation

Gold mineralisation is observed exclusively in association with the pyrite mineral phases outlined above with two distinct generations of native gold being identified. Au-1 occurs as rounded to sub-rounded grains ranging in size from sub-micron to 80 µm, identified exclusively within the outer homogenous Py-1b rims and the Py-2 phase (Fig. 7.19a-c). Au-2 is rare only being identified as rare irregular sub-rounded to sub angular 10-20 µm crystals along the outer edges of the Py-1 and Py-2 mineral phases, and displays an association with fractures in the pyrite mineral phases (Fig. 7.19 d).

Mineral	Pre-Ore stage	Ore stage	Post ore stage
Deformation metamorphism			
Quartz	—————		
Chlorite	—————		
Alluminoceladonite	—————		
Hydrothermal Alteration			
Ankerite	—————	As Gangue material	
Siderite	—————		
Quartz	—————		
Magnetite			—————
Sulphides			
Pyrrhotite-1	—————		
Arsenopyrite-1	—————		
Chalcopyrite-1	—————		
Pyrite-1a		—————	
Pyrite-1b		—————	
Au-1		—————	
Tenantite 1		—————	
Pyrite 2			—————
Pyrrhotite-2			—————
Au-2			—————
Accessory Phases			
Monazite		—————	
Fluoroapatite	—————		
Apatite	—————		
Scheelite	—————		
Rutile	—————		

Figure 7.17: Paragenetic diagram illustrating the developmental sequence of the major mineral phases including alteration assemblages, sulphide mineralisation and selected accessory phases identified at the Mengu deposit.

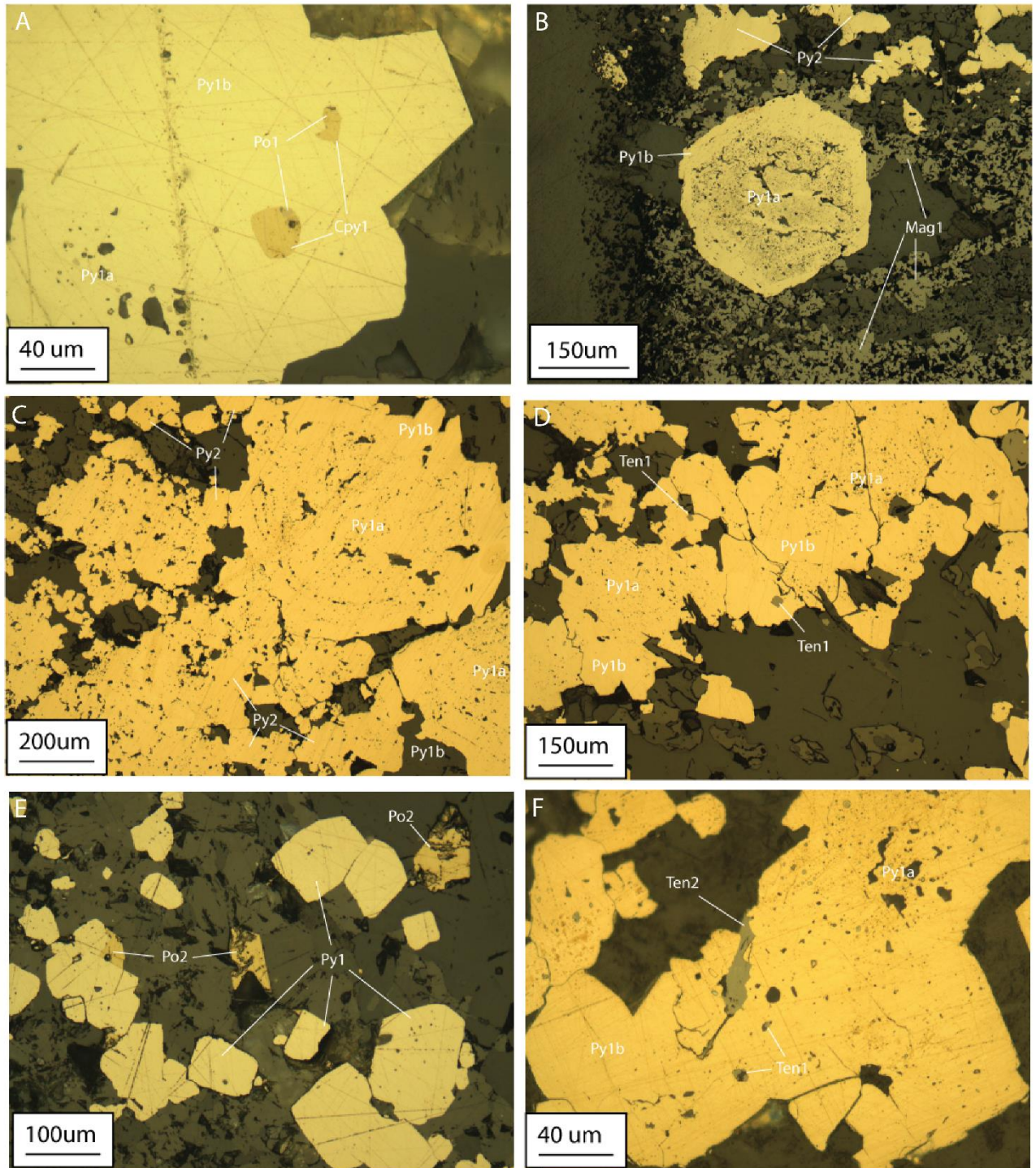


Figure 7.18: RFL Photomicrographs illustrating the relationship between sulphide phases observed at the Mengu Deposit. A) Sample 2013-M13; Early Chalcopyrite-1 and Pyrrhotite-1 occluded in poorly zoned Pyrite-1 (a/b) crystal. B) Sample PB12-M07; Two generations of pyrite being partially occluded by late magnetite alteration. C) Sample PB12-M02; Two generations of pyrite, Large Pyrite-1 crystals with vuggy cores (Py-1a) and thin homogenous rims (Py-1b) partially occluded by aggregate mass of poorly formed Py-2 crystals, Vugs in Py-1a loosely define a number of radial growth zones. D) Sample PB12-M07 Multiple generations of pyrite occluding tennantite crystals. E) Sample 2013-M13; Pyrrhotite-2 crystals partially occluding Py-1 crystals. F) Sample PB12-M02; Two generations of Tennantite associated with Py-1 (a/b) sulphide phase.

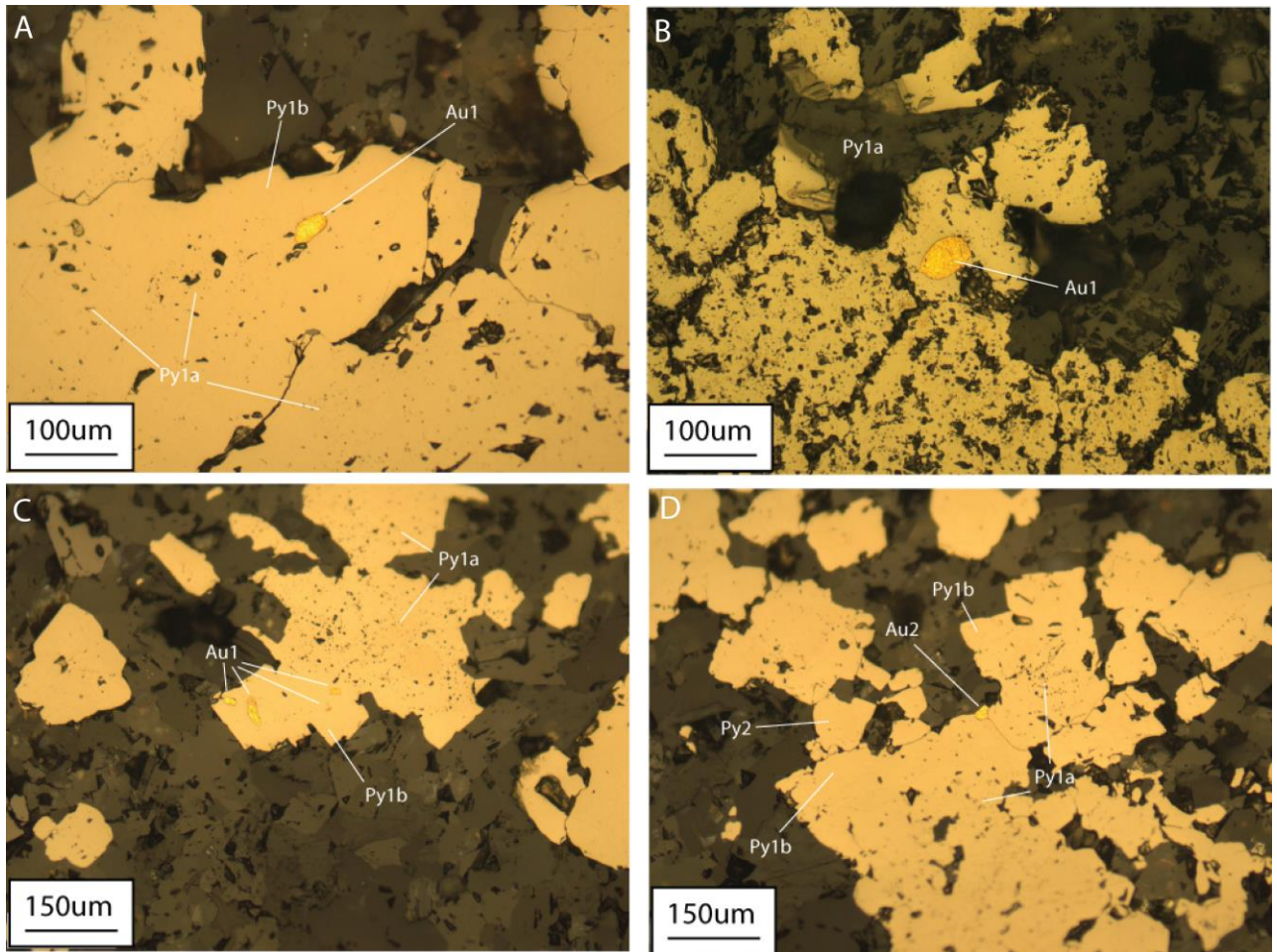


Figure 7.19: RFL Photomicrographs illustrating the relationship of gold mineralisation to the major pyrite phases; A) Sample MH005B, B) Sample MH002B and C) Sample MH001B; Rounded Au-1 crystals occluded in Py-1 (a/b) sulphide material. D) Sample MH001B; Sub-angular Au-2 crystal occurring on the edge of Py-1 crystals.

7.5.4.4 Post ore stage

Post ore sulphide phases are rarely identified within the samples from Mengu with only three species, Pyrrhotite-2 (Po-2), Chalcopyrite-2 (Cpy-2) and Tennantite-2 (Ten-2) being observed. Pyrrhotite-2 occurs as irregular angular 20-100 μm crystals, identified as isolated crystals within the groundmass (Fig. 7.18e). Chalcopyrite-2 occurs as 10-20 μm angular to sub-angular crystals observed in fractures in the Py-1 and Py-2 crystal phases. The morphology of the Cpy-2 phase is principally controlled by the morphology of the host fracture. Tennantite-2 occurs as irregular sub-rounded masses ranging in size from 20-150 μm nucleating along the edges of the Py-2 mineral phase and as rare highly irregular fracture filling material (Fig. 7.18f).

7.6 Pakaka

7.6.1 Host lithologies

The Pakaka deposit is hosted within a diverse sequence consisting of the Kibalian metasediments, Kibalian basalts and BIF sequences. Variable volcano-sedimentary conglomerates attributed to the Kibalian metasediments are the most commonly identified lithotype and consist of deformed quartz clasts hosted in a matrix composed of phyllosilicate minerals (aluminoceladonite and chlorite). The volcano-sedimentary conglomerates are highly variable with clast size ranging from >0.5 cm to 3 cm and ranging in proportion from 10% to 90% of the lithology. Where clasts are absent the observed volcano-sedimentary material consists of either fine crystalline homogenous quartz-rich material or fine millimetre scale parallel laminated fine crystalline material. Basaltic lithologies are identified in the upper part of the sequence and consist of fine crystalline grey to grey brown material with frequent 1-2 mm thick quartz parallel quartz veins. The basalts at Pakaka have been reported as pillowed basalts by the staff at the Kibali gold project though this has not been observed in the available samples. Ironstones (BIF) occur as thick layers of massive ironstone with faint internal laminations being sporadically visible. The host lithologies have been variably deformed prior to the development of mineralisation, this deformation being observed in the volcano-sedimentary conglomerate lithologies (Fig. 7.20). Deformation is characterised by stretching and recrystallisation of clasts to fine quartz and alignment of phyllosilicates in the inter-clast areas with associated recrystallisation of chlorite (Fig. 7.20 and Fig. 7.21 a-b). Deformation of the volcano-sedimentary lithologies is sufficient that in places the clast material has attained a width greater than the core section under examination giving the samples a banded appearance consisting of alternating quartz-rich and phyllosilicate-rich layers (Fig. 7.20d). Alignment and recrystallisation of the phyllosilicate minerals is also observed within the laminated sediments where the phyllosilicate and quartz crystals that make up each layer being parallel aligned (Fig. 7.21 d). Analyses of the compositions of the chlorite minerals (Table 7.7) in the deformed volcano-sedimentary conglomerates shows the greatest degree of variation in the examined deposits. Chlorite compositions vary significantly with daphnite, brunsvigite, pycnochlorite, ripidolite and diabantite varieties being identified, the proportion of iron and magnesium being the main source of compositional variation (Fig. 7.7).

7.6.2 Alteration

The host lithologies at the Pakaka deposit have been extensively altered pre-mineralisation with the widespread development of Fe-carbonate+quartz±aluminoceladonite (Table 7.8 and 7.9). Fe-carbonate minerals are comprised solely of ankerite (Table 7.8) occurring as sub 0.1 mm interlocking angular crystals (Fig. 7.21c-f).

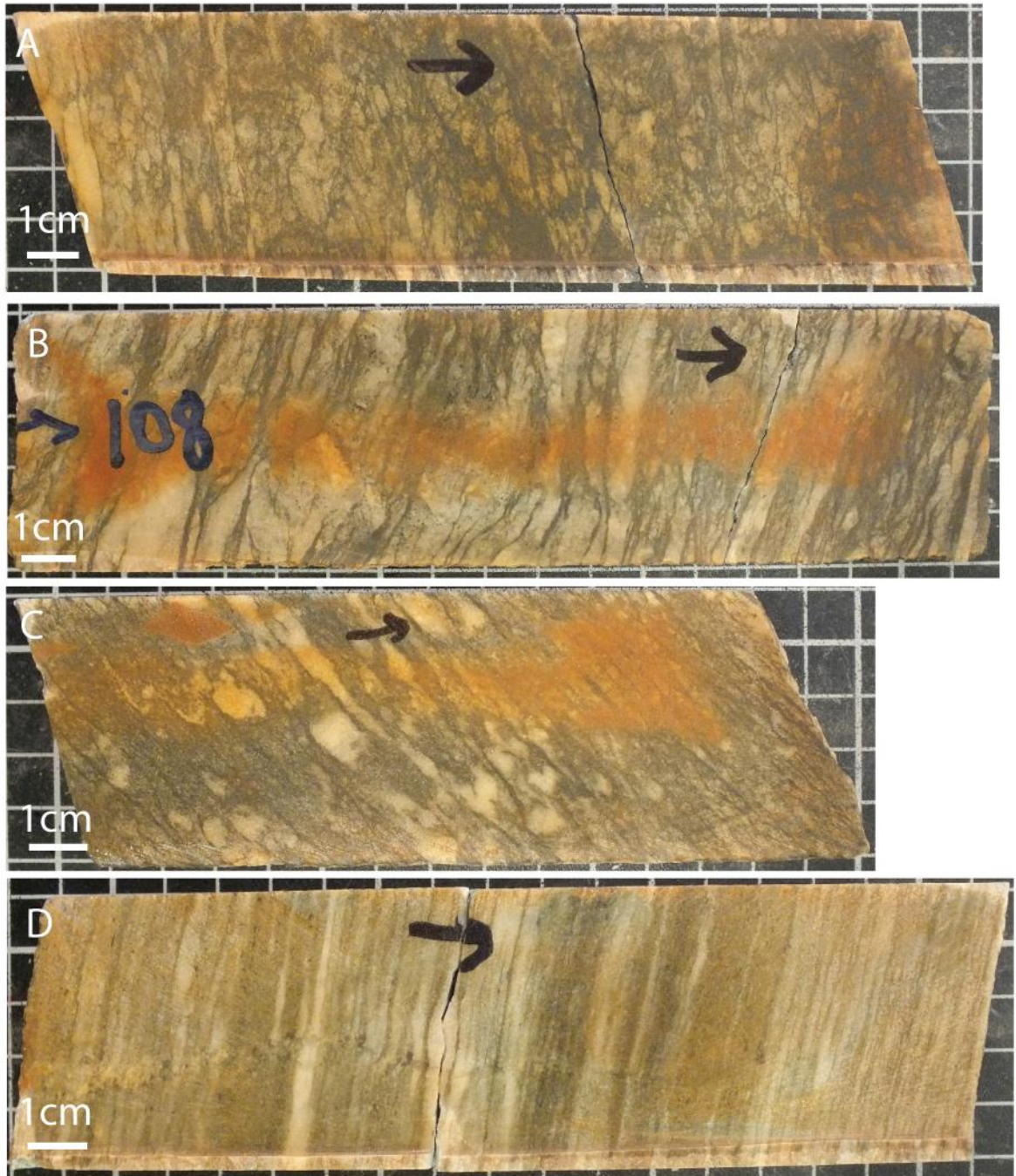


Figure 7.20: Core images displaying range of deformational characteristics identified in the volcano-sedimentary conglomerates at the Pakaka deposit. A) Sample 2013-P23; Quartz clasts and chlorite-rich groundmass displaying minor deformation. B) Sample PB12-PK59; Heavily deformed clast-rich volcano-sedimentary conglomerate consisting of highly attenuated quartz clasts with thin inter-clast bands of aligned chlorite. C) Sample 2013-P35; Heavily deformed phyllosilicate-rich volcano-sedimentary conglomerate consisting of variably attenuated quartz clasts in a chlorite-rich groundmass displaying strong alignment and shearing. D) Sample 2013-P20; Deformed and altered volcano-sedimentary conglomerate composed of highly attenuated quartz clasts and aligned phyllosilicate-rich zones, stretching exceeds core width giving the appearance of a layered sediment.

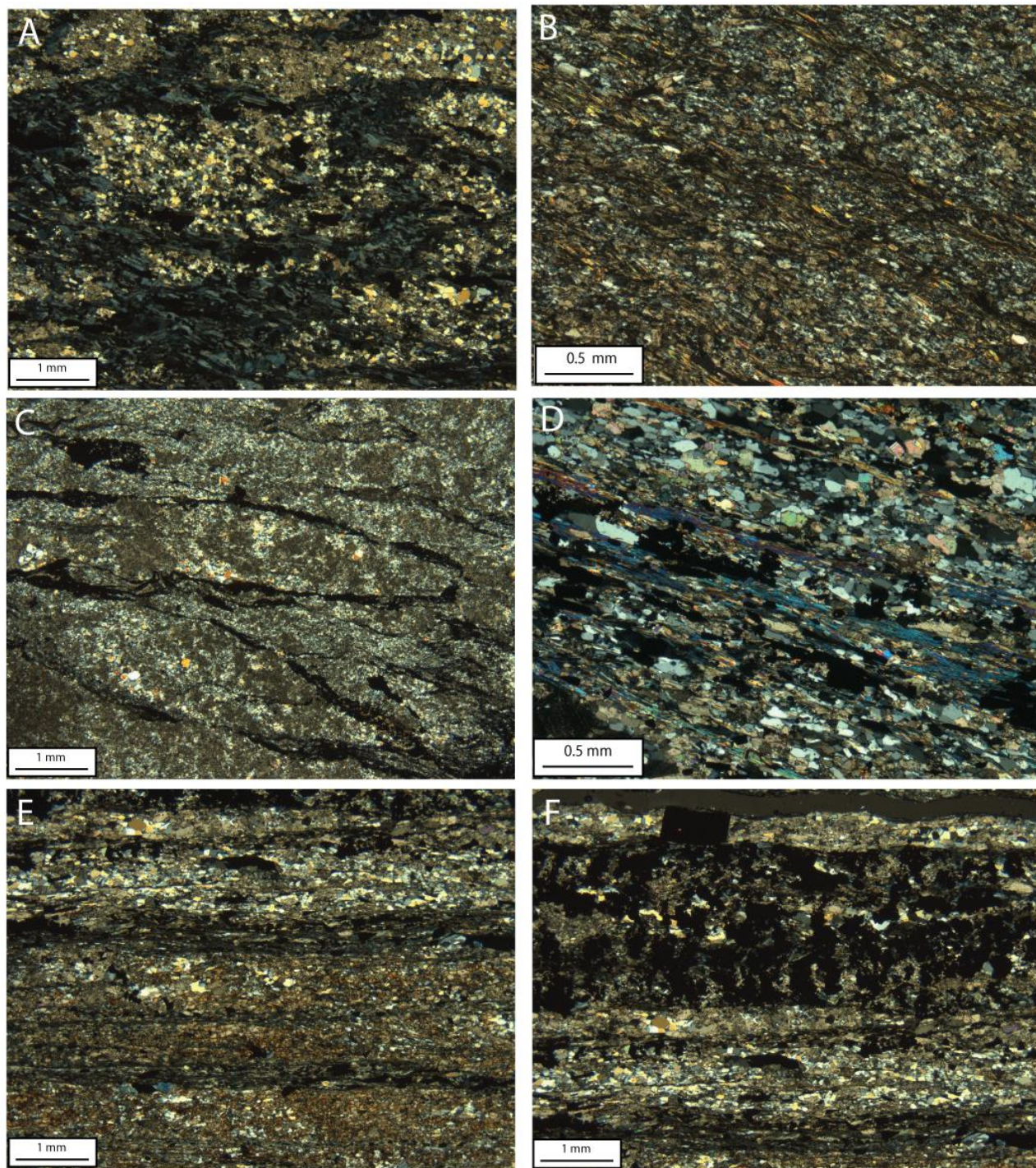


Figure 7.21: XPL Photomicrographs displaying deformation, alteration and mineralisation textures identified in the volcano-sedimentary units at the Pakaka deposit. A) Sample 2013-P23; Irregular quartz clasts and aligned chlorite-rich inter-clast zones, minor sulphide mineralisation occurs along the edges of the quartz clasts overprinting chlorite crystals. B) Sample 2013-P28; deformed 0.5-2 mm clasts and phyllosilicate-rich inter-clast zones, both clasts and phyllosilicates display minor Fe-carbonate alteration. C) Sample 2013-P24; Deformed quartz clasts altered by Fe-carbonate crystals, clasts are separated by ~0.1 mm thick chlorite-rich bands which are host to minor sulphide development. D) Sample PB12-PK09; Aligned quartz and chlorite layers in clast absent volcano-sedimentary conglomerate material, Fe-carbonate alteration in overprinting the host phases with sulphide minerals replacing chlorite. E) and F) Sample PB12-PK19; Heavily deformed quartz-rich clasts separated by bands of aligned chlorite crystals, Fe-carbonate alteration is heavily overprinting the deformed quartz clasts, Sulphide mineralisation is observed overprinting the chlorite-rich horizons.

Table 7.7: Representative analyses of chlorite minerals in deformed volcano-sedimentary conglomerates from the Pakaka deposit

Sample	PB12-PK14A	PB12-PK04	2013-P5	2013-P5	2013-P5	2013-P5	2013-P35	2013-P35	2013-P35	2013-P35	2013-P35
Analysis	SITE 4 C	SITE 1 H	SITE 1 C	SITE 1 P	SITE 1 W	SITE3 E	SITE 1 C	SITE 1 R	SITE 2 G	SITE 3 D	SITE 3 F
SiO ₂	23.27	25.40	29.61	26.77	26.58	26.57	26.38	26.40	25.02	25.96	24.44
Al ₂ O ₃	20.94	18.11	18.32	19.86	18.99	19.24	18.90	18.73	19.41	18.94	19.69
Cr ₂ O ₃	0.00	0.00	0.00	0.54	0.50	0.63	0.00	0.00	0.34	0.00	0.48
Fe ₂ O ₃	0.82	0.83	2.83	1.18	1.15	1.09	0.71	0.90	0.43	0.82	0.33
FeO	37.07	37.30	19.22	22.26	21.81	21.67	29.18	28.97	30.25	28.44	30.40
MgO	4.89	6.32	16.20	16.00	15.72	15.82	12.09	11.98	10.94	12.05	10.58
CaO	0.00	0.00	0.00	0.00	0.00	0.00	0.30	0.00	0.25	0.00	0.22
Na ₂ O	0.00	0.00	0.00	0.00	0.00	0.00	0.00	0.00	0.00	0.00	0.00
K ₂ O	0.00	0.00	0.00	0.00	0.00	0.00	0.00	0.00	0.00	0.00	0.00
H ₂ O*	10.49	10.63	11.48	11.40	11.13	11.19	11.09	11.02	10.88	10.94	10.79
Total	97.49	98.59	97.65	98.33	95.88	96.53	98.65	97.99	97.52	97.15	96.93
Si	5.31	5.72	6.14	5.61	5.71	5.68	5.69	5.73	5.51	5.68	5.43
Al (iv)	2.69	2.28	1.86	2.39	2.29	2.32	2.31	2.27	2.49	2.32	2.57
Al (vi)	2.95	2.54	2.65	2.53	2.54	2.53	2.51	2.53	2.56	2.57	2.59
Ti	0.00	0.00	0.00	0.05	0.00	0.00	0.00	0.00	0.00	0.00	0.00
Cr	0.00	0.00	0.00	0.09	0.08	0.11	0.00	0.00	0.06	0.00	0.08
Fe ³⁺	0.14	0.14	0.44	0.19	0.19	0.18	0.11	0.15	0.07	0.13	0.06
Fe ²⁺	7.07	7.02	3.33	3.90	3.92	3.87	5.27	5.26	5.57	5.20	5.65
Mg	1.66	2.12	5.01	5.00	5.04	5.04	3.89	3.88	3.59	3.93	3.50
Ca	0.00	0.00	0.00	0.00	0.00	0.00	0.07	0.00	0.06	0.00	0.05
Na	0.00	0.00	0.00	0.00	0.00	0.00	0.00	0.00	0.00	0.00	0.00
K	0.00	0.00	0.00	0.00	0.00	0.00	0.00	0.00	0.00	0.00	0.00
OH*	16.00	16.00	16.00	16.00	16.00	16.00	16.00	16.00	16.00	16.00	16.00
Total	35.82	35.82	35.44	35.76	35.76	35.78	35.85	35.81	35.91	35.83	35.93
Fe/Fe+Mg	0.81	0.77	0.43	0.45	0.45	0.45	0.58	0.58	0.61	0.58	0.62
Variety	daphnite	brunsvigite	pycnochlorite	pycnochlorite	pycnochlorite	pycnochlorite	brunsvigite	brunsvigite	ripidolite	brunsvigite	ripidolite
T (°C)-Cathelineau (1988)	371.69	305.49	237.65	322.63	306.44	312.32	309.32	303.49	338.68	312.32	352.22
T (°C)-Jowett (1991)	386.43	319.51	240.55	325.98	309.91	315.64	317.16	311.40	347.29	319.95	360.99

Table 7.8: Representative analyses of Fe-carbonate alteration minerals identified in samples from the Pakaka deposit

Sample	PB12-PK02B	PB12-PK02B	PB12-PK14A	PB12-PK14A	2013-P24	2013-P24	PB12-PK04	PB12-PK04	PB12-PK14	PB12-PK14	2013-P5	2013-P5	2013-P35	2013-P35
Analysis	SITE 2 B	SITE 5 F	SITE 1 E	SITE 4 E	SITE 1 C	SITE 2 G	SITE 1 F	SITE 2 N	SITE 1 J	SITE 3 H	SITE 3 V	SITE 3 X	SITE 1 N	SITE 2 U
SiO ₂														
TiO ₂														
FeO	12.58	13.62	12.69	13.59	11.59	12.51	15.01	16.31	14.02	11.30	11.19	11.19	14.12	2.43
MnO	0.46	0.55	0.49	0.48	0.52	0.51	0.36	0.56	0.72	0.49	1.00	1.19	0.66	0.45
MgO	12.94	11.97	12.41	12.07	14.08	13.29	11.60	10.70	12.74	13.50	12.74	12.62	11.75	0.81
CaO	27.39	27.35	27.22	27.08	28.09	28.43	27.46	27.80	27.81	27.65	28.38	28.58	28.01	49.44
Total	53.37	53.48	52.82	53.21	54.28	54.75	54.43	55.37	55.29	52.95	53.31	53.58	54.53	53.13
Mineral	Ankerite	Ankerite	Ankerite	Ankerite	Ankerite	Ankerite	Ankerite	Ankerite	Ankerite	Ankerite	Ankerite	Ankerite	Ankerite	Ankerite

Table 7.9: Representative analyses of aluminoceladonite alteration minerals at the Pakaka depos

Sample	PB12-PK02B	PB12-PK02B	PB12-PK14A	PB12-PK14A	2013-P24	2013-P24	PB12-PK04	PB12-PK04	PB12-PK14	2013-P5	2013-P5
Analysis	SITE 3 C	SITE 3 F	SITE 2 C	SITE 2 F	SITE 1 L	SITE 2 H	SITE 1 B2	SITE 2 K	SITE 4 C2	SITE 1 V	SITE 2 T
SiO ₂	48.82	47.33	47.05	46.16	48.56	49.10	48.22	47.80	49.93	47.36	45.12
TiO ₂	0.60	0.60	0.41	0.47	0.57	0.54	0.46	0.54	0.37	1.06	1.42
Al ₂ O ₃	30.72	33.28	34.16	33.45	31.90	31.42	31.87	34.10	31.41	28.83	25.32
FeO	1.72	0.94	0.96	0.89	1.78	1.73	1.44	0.79	1.37	2.52	4.89
MgO	1.80	0.94	0.74	0.90	1.49	1.66	1.15	0.92	1.31	1.87	3.97
CaO				0.40							
K ₂ O	10.27	10.02	9.61	9.44	9.88	10.08	9.60	9.72	9.74	8.74	8.04
Na ₂ O	0.42	0.52	0.71	0.73	0.40	0.38	0.84	0.83	0.52	0.46	
V ₂ O ₅	0.42			0.37		0.36		0.40	0.89		
Cr ₂ O ₃	0.56				0.70	0.70	0.51		0.42	0.78	0.88
Total	95.33	93.63	93.64	92.80	95.26	95.98	94.09	95.11	95.96	91.62	89.64
Mineral	Al-Celadonite										



Figure 7.22: Core images illustrating the mineralisation styles identified at the Pakaka deposit. A) Sample PB12-PK02a (3.14 g/t); Sulphide-bearing veins hosted in Quartz gangue cutting through the extensive quartz alteration. B) Sample PB12-PK09 (6.5 g/t); Disseminated sulphide mineralisation hosted in finely layered sediment. C) Sample PB12-PK15 (12.17 g/t) Volcano-sedimentary conglomerate consisting of irregular 1cm quartz clasts with extensive disseminated sulphide mineralisation overprinting the inter-clast areas. D) Sample PB12-PK17 (20 g/t); Irregular massive sulphide-bearing vein cutting across texture destructive Fe-carbonate+quartz alteration.

Fine quartz is associated with the ankerite phase, displaying a similar habit, occurring as sub 0.1 mm angular crystals (Fig. 7.21 c-f). The intensity of the Fe-carbonate+quartz±aluminoceladonite varies from benign (Fig. 7.21 a-b) to pervasive, overprinting significant proportions of the host mineralogy (Fig. 7.21 e-f). In the volcano-sedimentary conglomerates low intensity alteration is observed confined to the inter-clast phyllosilicate-rich zones with increasing intensity resulting in the overprinting of the clast and inter-clast areas. Where ankerite alteration is observed in the laminated sediments it is of low to moderate intensity with the quartz-rich layers being altered to a greater extent than the neighbouring chlorite-rich layers (Fig. 7.21 e). In addition to ankerite alteration widespread and pervasive calcite alteration is observed in both the basaltic and volcano-sedimentary conglomerates occurring as 0.5 cm to 1 cm diamond shaped crystals overprinting mineral phases and deformational textures.

7.6.3 Mineralisation styles

Sulphide mineralisation at the Pakaka deposit occurs as disseminated sulphides and as irregular vein structures. Disseminated sulphides are observed within the Kibalian metasedimentary lithologies, both the volcano-sedimentary conglomerates and the fine laminated sediments (Fig. 7.22 b and c). Where occurring within the volcano-sedimentary conglomerates the disseminated sulphides are identified in the phyllosilicate-rich inter-clast areas, overprinting and replacing the chlorite and Fe-carbonate mineral phases (Fig. 7.21 c). Intensity of the inter-clast disseminated sulphides varies from rare isolated sulphide crystals to extensive overprinting of the inter-clast areas (Fig. 7.21 a and c). Disseminated sulphides are observed throughout the laminated sediments (Fig. 7.21 d-f), though the sulphides are observed preferentially occurring in the phyllosilicate-rich layers replacing primarily chlorite and to a lesser extent the Fe-carbonates (Fig. 7.21 d-f). Where replacing the chlorite minerals the sulphides retain the primary crystal morphology, forming elongate crystals parallel to the stretching direction. Vein style mineralisation is observed in the deformed volcano-sedimentary conglomerates (Fig. 7.22 a, c and d), with vein structures displaying diverse morphologies. Veins range from 0.2 cm 'veinlets' to irregular 5cm masses, in all cases vein mineralogy consists of sub 0.1 mm quartz crystals with minor siderite and aluminoceladonite. Vein structures are observed exploiting the inter-clast areas of the volcano-sedimentary conglomerates in a similar style to the type 2 veins identified at the KCD deposit (Fig. 7.22 a, c and d).

7.6.4 Ore Mineralogy

The mineralogical characteristics are the major ore phases at the Pakaka deposit are here discussed, a paragenesis of their formation is displayed in Figure 7.23.

7.6.4.1 Pre-ore stage

Arsenopyrite-1 (Asp-1) is the most abundant of the pre-ore phases being identified throughout the ore samples from the Pakaka deposit. Asp-1 occurs as euhedral angular 20-200 μm rectangular and kite shaped crystals occurring as disseminated crystals within the groundmass and is frequently observed occluded by later sulphide phases (Fig. 7.24 a-c). Arsenopyrite-2 (Asp-2) occurs as 5-50 μm sub-angular crystals, forming dense aggregate crystal masses (Fig. 7.24a). These masses occur as disseminates within the groundmass and nucleating on the surfaces of the Asp-1 phase (Fig. 7.24 a). Pyrrhotite-1 (Po-1) is identified as irregular 10-40 μm rounded and sub rounded inclusions occluded within the Pyrite-1 phases (Fig. 7.24 c and e), and as larger crystals occluding arsenopyrite crystals attributed to the Asp-2 phase (Fig. 7.24 c).

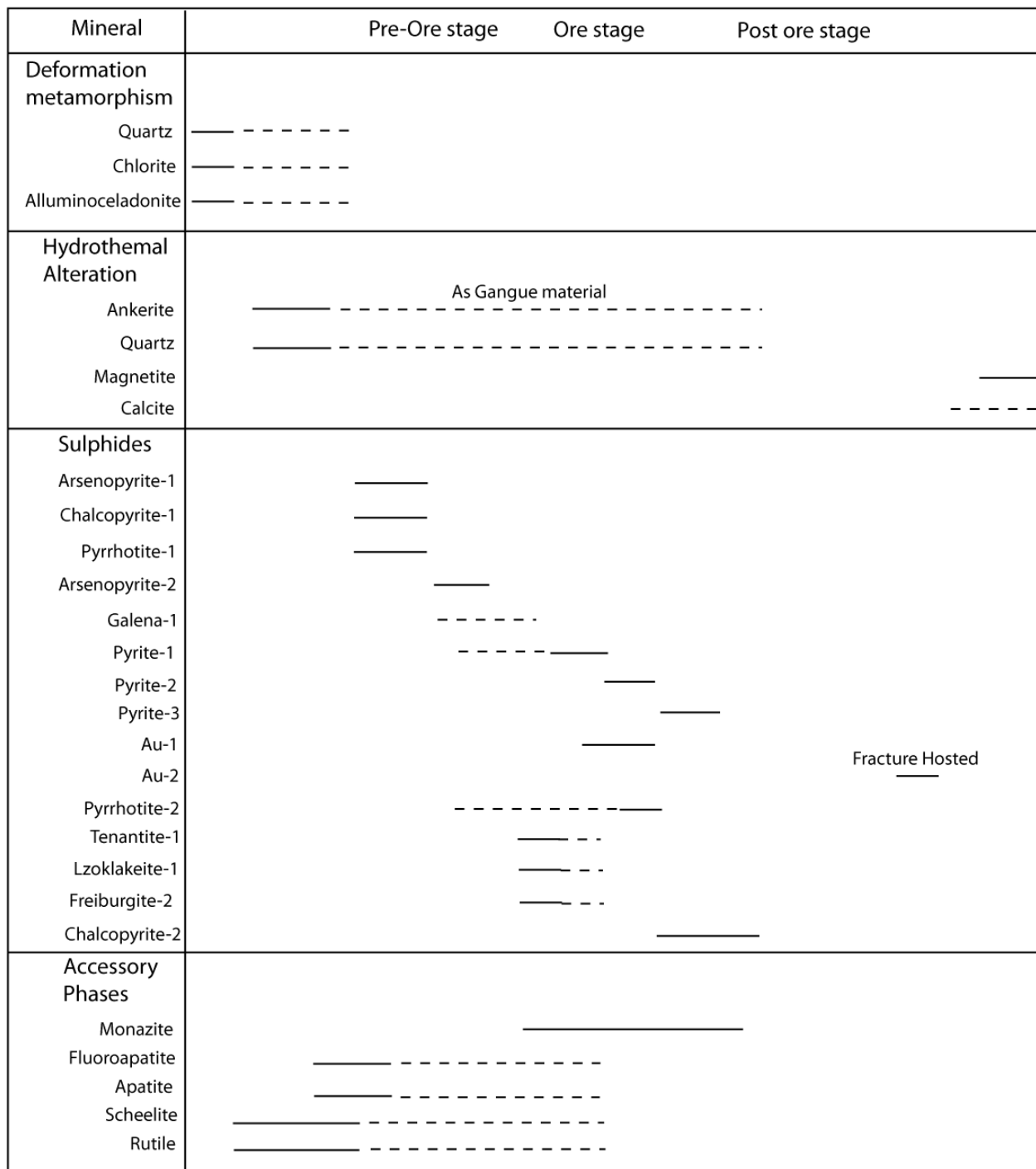


Figure 7.23: Paragenetic diagram illustrating the relative timing of the major alteration, sulphide and accessory minerals in the samples from the Pakaka deposit.

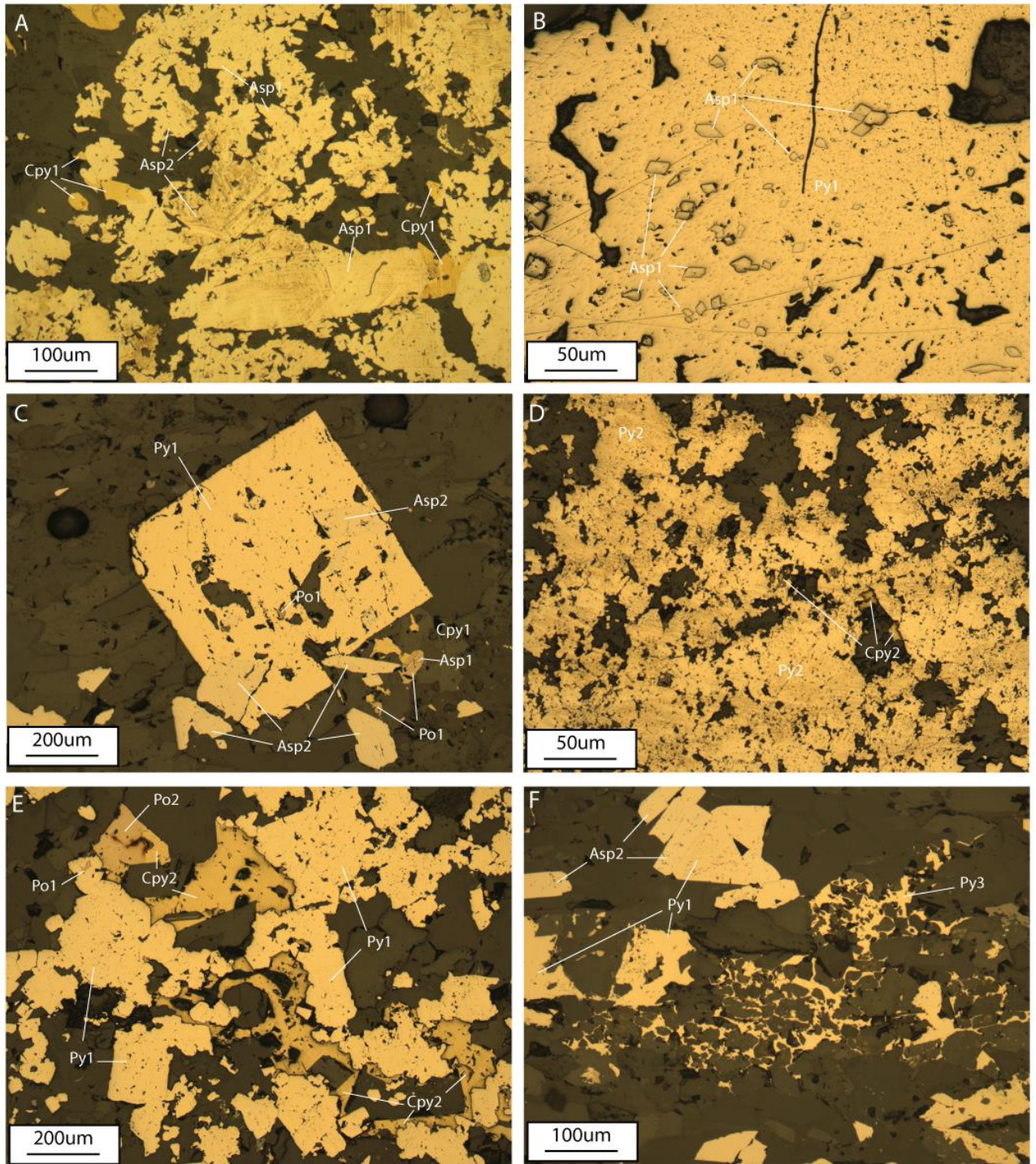


Figure 7.24: RFL Photomicrographs illustrating the relationship between the major sulphide phases identified at the Pakaka deposit. A) Sample PB12-PK07; Early pre-ore sulphide phases consisting of two generations of abundant arsenopyrite (Asp-1 and Asp-2) and rarer Chalcopyrite-1. B) Sample PB12-PK07; Well-formed Arsenopyrite-1 crystals occluded by massive vuggy Pyrite-1. C) Sample PB12-PK09; Interaction of multiple sulphide phases including Arsenopyrite-1 and Arsenopyrite-2, Pyrrhotite-1, Chalcopyrite-1 and Pyrite-1. D) Sample PB12-PK02; Massive aggregate mass of poorly formed irregular Pyrite-2 crystals with late Chalcopyrite-2 growing along crystal edges. E) Sample PB12-PK02; Late Pyrrhotite-2 and Chalcopyrite-2 phases partially occluding irregular Pyrite-1 crystals. F) Sample PK09; Late skeletal Pyrite-3 forming between quartz crystals within the groundmass.

Chalcopyrite-1 (Cpy-2) is observed in a range of different morphologies, forming irregular angular to sub-angular 20-150 μm crystals occluding Asp-1 and Asp-2 (Fig. 7.24 a), and as 10-100 μm irregular rounded inclusions within Py-1 (Fig. 7.24c).

7.6.4.2 Ore stage

Pyrite is the most abundant sulphide mineral phase and forms the primary ore-bearing mineral within the samples from Pakaka, being the only phase in which gold mineralisation has been identified. Three generations of pyrite are identified in the samples from Pakaka, displaying a diverse range of morphologies. Pyrite-1 (Py-1) is the most abundant of the three phases and occurs predominantly as 50-500 μm irregular sub-angular to sub-rounded crystals with abundant sub-micron vugs (Fig. 7.24 b,c and e). Pyrite-2 (Py-2) is discerned by its distinct morphological characteristics, forming aggregate masses up to a centimetre in size comprised of highly irregular 10-50 μm crystals (Fig. 7.24 d).

7.6.4.3 Gold Mineralisation

Two phases of gold mineralisation are identified at the Pakaka deposit, occurring exclusively in association with the Py-1 sulphide phase. Au-1 occurs as 1-5 μm rounded to sub-angular crystals occluded within the Py-1 sulphide phase and is the more abundant of the two identified phase of gold mineralisation, accounting for 90% of the observed Au grains. Au-2 is only rarely identified, occurring as 5-10 μm angular to sub-angular crystals within fractures in the Py-1 sulphide phase, its morphology and size being controlled by the morphology of the host fracture.

7.6.4.4 Post ore stage

Pyrrhotite-2 (Po-2) occurs as sub-hedral angular 150-200 μm crystals developed along crystal surfaces and of the Py-1 mineral phase (Fig. 7.24e). Pyrrhotite-2 has been extensively replaced by Chalcopyrite-2 (Cpy-2). Cpy-2 occurs as irregular angular to sub-angular 30-250 μm crystals partially occluding Py-1 and Po-2 in addition to quartz crystals in the groundmass. Pyrite-3 (Py-3) is sporadically identified within the samples, forming highly irregular skeletal crystal with morphology being controlled by inter-crystalline space restrictions (Fig. 7.24 f). While Py-3 is observed occluding the Asp-1 phase, its relationship to the other mineral phases is unknown.

7.7 Pamao

7.7.1 Host lithologies

The Pamao deposit is hosted within a sequence composed of variable units attributed to the Kibalian metasediments, banded iron formations and Kibalian basalts. The Kibalian metasediments and the basaltic material are the most significant lithologies with mineralisation having been identified to varying degrees in both lithologies. The Kibalian metasediments are dominated by volcano-sedimentary conglomerates, consisting of deformed quartz clasts hosted in a phyllosilicate-rich groundmass (Fig. 7.25 a-d). Clast size varies significantly between individual samples, ranging from >1 cm to 5 cm in size, in all cases the clasts being composed of fine >0.1 mm interlocking quartz crystals. Relative abundances of the quartz clasts and phyllosilicate groundmass material varies from clast poor matrix dominated lithologies to clast-rich (Fig. 7.25 a-d). Material of interpreted as basalts at Pamao consist of fine crystalline, >0.1 mm to 1 mm, quartz, plagioclase feldspar that has been extensively deformed and altered. The Kibalian metasediments and basalts have been significantly deformed prior to the development of mineralisation. Deformation of the volcano-sedimentary conglomerates is characterised by stretching of the quartz clasts and alignment of the inter-clast phyllosilicate minerals parallel to the stretching orientation (Fig. 7.26 a-b). Stretching of the volcano-sedimentary lithologies is variable ranging from relatively un-deformed, clasts retaining an oval morphology, to a maximum where stretching of the clasts is sufficient that they exceed the width of the core sample, the sample appearing to be alternating layers of quartz and sub-mm thick phyllosilicates (Fig. 7.25 a-d). Deformation is accompanied by recrystallisation of clast material to fine sub-mm interlocking quartz crystals and of the inter-clast phyllosilicates to chlorite. Chlorite compositions are consistent, with little compositional variation being identified (Fig. 7.7, Table 7.10). Two species of chlorite, ripidolite and daphnite, are identified within samples at Pamao (Table 7.10).

7.7.2 Alteration

Pre mineralisation alteration at the Pamao deposit is characterised by the development Fe-carbonates+quartz±aluminoceladonite overprinting the earlier metamorphic mineral assemblage. This alteration event is dominated by Fe-carbonates with two species of Fe-carbonates identified, Ankerite and siderite, occurring as <0.1mm angular to sub-angular interlocking crystals (Fig. 7.26b). Individual samples are generally dominated by either ankerite or siderite with only rare occurrences of the other phase and only being discernible through microprobe analysis. Fe-carbonate alteration is pervasive being



Figure 7.25: Core samples displaying the range of deformation identified within the volcano-sedimentary conglomerates at the Pamao deposit. A) Sample 2013-PM14; Volcano-sedimentary conglomerate consisting of large slightly attenuated quartz clasts hosted in a phyllosilicate-rich groundmass. B) Sample 2013-PM31; Heavily deformed and altered phyllosilicate-rich volcano-sedimentary conglomerate consisting of alternating bands consisting of stretched quartz clasts and chlorite-rich layers. C) Sample 2013-PM3; Deformed and altered clast-rich volcano-sedimentary conglomerate with sub mm inter-clast bands composed of aluminoceladonite. D) Sample 2013-PM4; Deformed and altered volcano-sedimentary conglomerate consisting of highly attenuated quartz clasts with thin sub mm to 2mm thick inter clast chlorite bands.

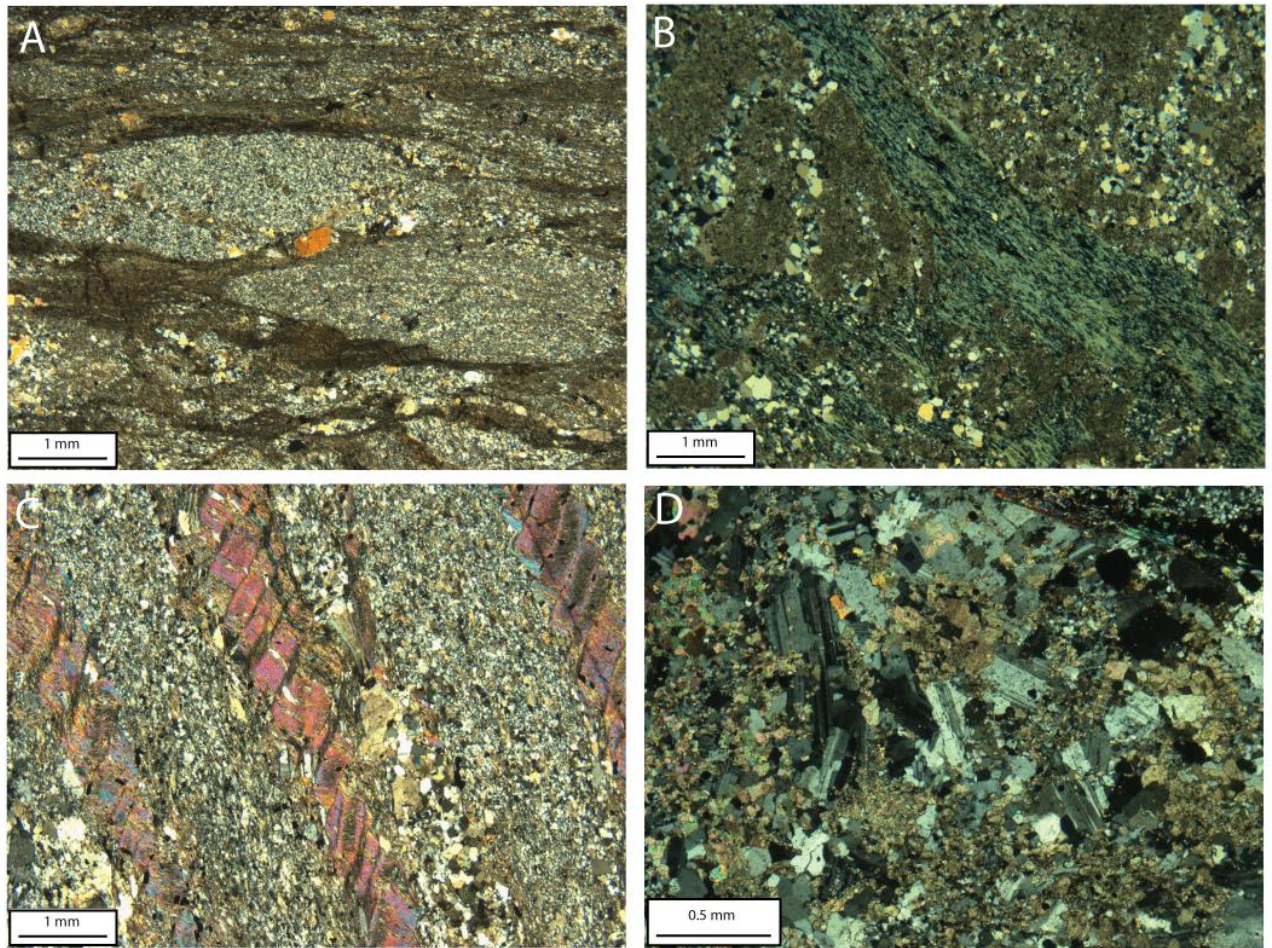


Figure 7.26: XPL Photomicrographs displaying deformation and alteration characteristics in the host lithologies at the Pamao deposit. A) Sample 2013-PM14; Deformed quartz clasts with rare feldspar crystals surrounded by aligned aluminoceladonite and chlorite inter-clast areas. B) Sample PB12-PM10; Deformed and altered volcano-sedimentary conglomerate, quartz clasts with extensive Fe-carbonate alteration and inter-clast areas composed of aligned chlorite. C- Sample 2013-PM4; Deformed volcano-sedimentary conglomerate consisting of highly attenuated quartz clasts separated by aluminoceladonite-rich layers display kink banding. D) Sample PB12-PM07; Altered Basalt consisting of quartz and feldspar crystals overprinted by Fe-carbonate alteration.

identified, at varying intensity's, in the majority of the sample material. In the deformed volcano-sedimentary conglomerates Fe-carbonate alteration is observed overprinting quartz clasts and ranges in intensity from sporadic patches of Fe-carbonate development to altering the majority of the clast with only small areas of quartz remaining (Fig. 7.26 b). Fe-carbonate alteration is also identified in phyllosilicate-rich inter-clast areas though only as sporadic crystals, these structures remaining dominated by parallel orientated chlorite and aluminoceladonite (Fig. 7.26 b). Fe-carbonate alteration is also widely identified in the basaltic lithologies, occurring as 0.1 mm sub-angular interlocking crystals recrystallising feldspar within the groundmass. The two species of Fe-carbonate display a degree of compositional variation (Table 7.11 and Fig. 7.26) with the proportion of iron being the most significant component in the observed variations (Fig. 7.26). The Fe-carbonate alteration is accompanied by the development of quartz, occurring as <math><10 \mu\text{m}</math>

sub-angular crystals intergrown with the Fe-carbonate mineral phases, and aluminoceladonite which occurs as acicular crystals growing between the other alteration phases. The aluminoceladonite alteration displays restricted compositions (Table 7.12) corresponding to an intermediate phase between the ideal compositions of aluminoceladonite and muscovite (Fig. 7.7). Late magnetite alteration is identified post-dating the development of mineralisation (Fig. 7.30 f), forming layers parallel to the orientation of deformation.

7.7.3 Mineralisation styles

Sulphide mineralisation in samples from the Pakaka deposit is identified occurring as two distinct styles: disseminated sulphides and as vein style mineralisation (Fig. 7.27). Disseminated sulphide style mineralisation is observed within the deformed volcano-sedimentary conglomerates and basaltic material, sulphide minerals replacing and overprinting chlorite, siderite and ankerite mineral phases in the phyllosilicate-rich areas (Fig. 7.27 and 7.28). Disseminated sulphide mineralisation intensity varies from rare isolated sulphide crystals to extensive overprinting of the host mineralogy (Fig. 7.28). Vein style mineralisation occurs as 0.2 cm to 2 cm thick veins orientated parallel to the stretching and only rarely cross cutting the pre-mineralisation structures within the host lithology (Fig. 7.27 b and d). Veins are composed of quartz±Fe-carbonate gangue consisting of sub 0.1 mm angular to sub-angular interlocking crystals. Sulphide crystals in the vein structures are coarser than the disseminated sulphides with Gold grades are generally increasing where significant vein style mineralisation is present.

7.7.4 Ore Mineralogy

The mineralogical characteristics are the major ore phases at the Pamao deposit are here discussed, a paragenesis of their formation is displayed in Figure 7.29.

7.7.4.1 Pre-Ore phase

Arsenopyrite-1 (Asp-1) is identified as isolated crystals occluded within the later Pyrite-1 (Py-1) mineral phase (Fig. 7.30 b and d). Asp-1 crystals display a range of morphologies, ranging from irregular sub-rounded 10 µm crystals to 40 µm angular kite shaped crystals. Pyrrhotite-1 (Po-1) forms irregular rounded to sub-rounded 10-100 µm masses occluded within the Py-1 mineral phase (Fig. 7.30 c) and is also observed in rare cases replacing Asp-1 inclusions within the Py-1 mineral phase (Fig. 7.30b). Chalcopyrite-1 (Cpy-1) forms irregular sub-angular to sub-rounded 10-50 µm masses occluded within the pyrite mineral phase (Fig. 7.30 b-d). Cpy-1 is observed replacing both the Asp-1 and Po-1 mineral phases (Fig. 7.30b).

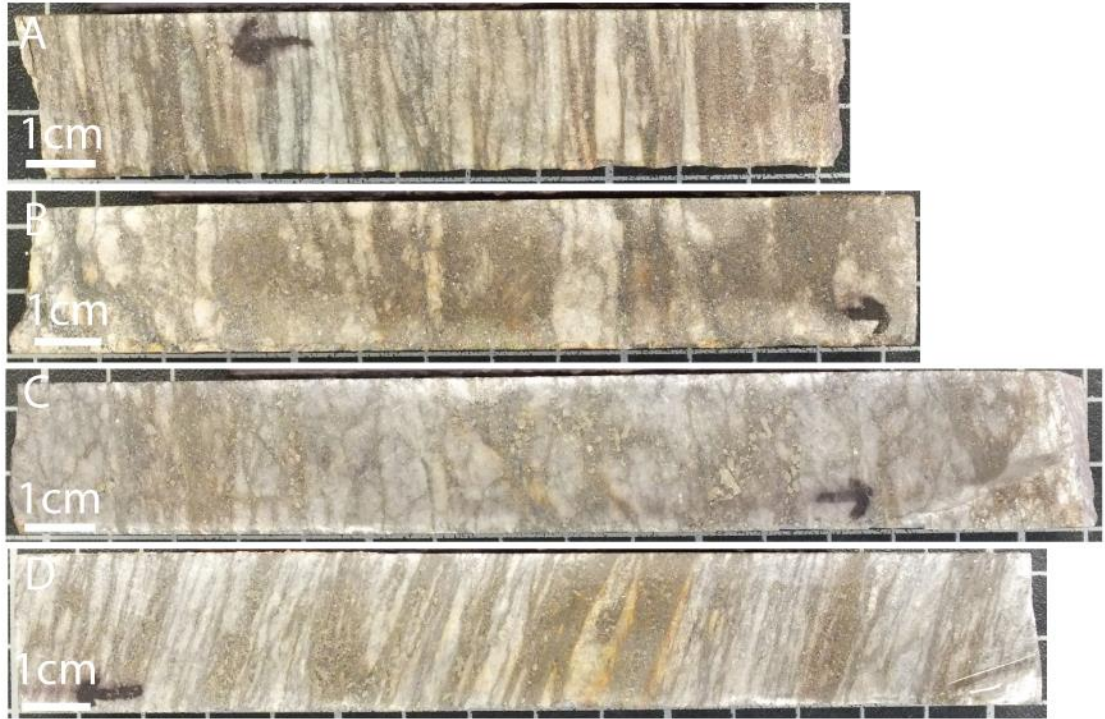


Figure 7.27: Core images displaying mineralisation styles identified in core from the Pamao deposit: A) Sample PB12-PM09 (0.44 g/t); Disseminated sulphide mineralisation occurring in the inter-clast phyllosilicate-rich areas between clasts. B) Sample PB12-PM03; Disseminated and vein style sulphide mineralisation, disseminated mineralisation occurs as thin layers in the inter-clast phyllosilicate-rich areas while vein style mineralisation forms 1-2 cm thick bands running parallel to the deformation orientation. C) Sample PB12-PM01 (3.16 g/t); Disseminated and vein style mineralisation within deformed and altered volcano-sedimentary conglomerate, Disseminated sulphides occur as fine sulphides in the thin phyllosilicate-rich inter-clast areas, vein mineralisation forms irregular zones of coarser sulphides with structures cutting across the host textures. D) Sample PB12-PM02 (7.2 g/t); Disseminated and vein style sulphide mineralisation in heavily deformed and altered volcano-sedimentary conglomerate, Disseminated sulphides are identified in the inter-clast phyllosilicate-rich areas, vein mineralisation forms two 1cm wide structures across the centre of the sample orientated parallel to deformation.

Table 7.10: Representative analyses of chlorite minerals in deformed volcano-sedimentary conglomerates at the Pamao deposit

Sample	PB12- PM08	PB12- PM08	PB12- PM03	PB12- PM03	2013-PM12	2013-PM12	PB12- PM10	PB12- PM10	2013-PM4	2013-PM4	2013- PM31	2013- PM31
Analysis	SITE 5 C	SITE 7 E	SITE 1 T2	SITE 2 J	SITE 1 P	SITE 2 Q	SITE 1 F	SITE 1 W	SITE 1 W	SITE 3 M	SITE 2 E	SITE 3 G
SiO ₂	23.05	23.70	21.53	23.03	23.73	24.47	23.75	24.04	22.95	23.54	22.11	22.88
Al ₂ O ₃	20.84	20.82	19.39	20.56	21.06	22.38	21.24	21.02	20.34	20.57	20.73	21.54
Fe ₂ O ₃	0.14	0.48	0.00	0.62	0.43	0.91	0.40	0.55	0.50	0.79	0.16	0.48
FeO	37.51	37.00	36.90	36.09	36.43	35.40	36.62	36.43	34.11	34.57	37.49	37.55
MgO	5.95	6.12	5.53	5.59	6.62	6.61	6.64	6.66	6.84	6.55	4.94	5.13
CaO	0.00	0.00	0.00	0.00	0.00	0.00	0.00	0.00	0.00	0.00	0.00	0.00
Na ₂ O	0.00	0.00	0.00	0.00	0.00	0.00	0.00	0.00	0.00	0.00	0.00	0.00
K ₂ O	0.00	0.00	0.00	0.00	0.00	0.26	0.00	0.00	0.00	0.00	0.00	0.00
H ₂ O*	10.56	10.68	9.97	10.40	10.74	11.03	10.78	10.80	10.36	10.51	10.25	10.56
Total	98.04	98.79	93.32	96.29	99.01	101.05	99.44	99.49	95.11	96.55	95.69	98.12
Si	5.23	5.32	5.16	5.30	5.29	5.30	5.28	5.33	5.30	5.36	5.17	5.19
Al (iv)	2.77	2.68	2.84	2.70	2.71	2.70	2.72	2.67	2.70	2.64	2.83	2.81
Al (vi)	2.81	2.83	2.66	2.89	2.84	3.03	2.85	2.83	2.85	2.89	2.88	2.96
Fe ³⁺	0.02	0.08	0.00	0.11	0.07	0.15	0.07	0.09	0.09	0.14	0.03	0.08
Fe ²⁺	7.12	6.94	7.48	6.95	6.80	6.41	6.80	6.76	6.59	6.58	7.33	7.12
Mg	2.01	2.05	1.98	1.92	2.20	2.13	2.20	2.20	2.36	2.22	1.72	1.73
Ca	0.00	0.00	0.00	0.00	0.00	0.00	0.00	0.00	0.00	0.00	0.00	0.00
Na	0.00	0.00	0.00	0.00	0.00	0.00	0.00	0.00	0.00	0.00	0.00	0.00
K	0.00	0.00	0.00	0.00	0.00	0.14	0.00	0.00	0.00	0.00	0.00	0.00
OH*	16.00	16.00	16.00	16.00	16.00	16.00	16.00	16.00	16.00	16.00	16.00	16.00
Total	35.97	35.90	36.11	35.87	35.91	35.87	35.92	35.89	35.89	35.83	35.96	35.90
Fe/Fe+Mg	0.78	0.77	0.79	0.79	0.76	0.75	0.76	0.76	0.74	0.75	0.81	0.81
Variety	ripidolite	ripidolite	ripidolite	ripidolite	ripidolite	ripidolite	ripidolite	ripidolite	ripidolite	ripidolite	daphnite	daphnite
T (°C)-Cathelineau (1988)	383.59	370.04	394.80	372.34	373.78	373.14	376.63	367.74	372.14	363.51	393.95	390.48
T (°C)-Jowett (1991)	397.26	383.60	408.72	386.23	386.76	385.97	389.60	380.74	384.55	376.34	408.49	404.87

Table 7.11: Representative analyses of Fe-carbonate alteration minerals identified at the Pamao deposit.

Sample	PB12-PM08	PB12-PM01A	PB12-PM03	2013-PM12	2013-PM12	PB12-PM07	PB12-PM07	PB12-PM10	PB12-PM10
Analysis	SITE 2 B	SITE 3 G	SITE 1 L	SITE 1 C	SITE 2 H	SITE 1 D	SITE 2 D	SITE 1 H	SITE 3 G
SiO ₂									
TiO ₂									
Al ₂ O ₃									
FeO	20.49	17.87	20.61	22.40	19.95	12.02	10.65	21.81	21.23
MnO	0.52	0.67	0.49	0.39		0.34		0.54	0.46
MgO	7.92	9.05	6.79	7.05	8.58	12.75	14.32	6.99	7.55
CaO	26.13	27.90	26.07	26.29	26.29	27.61	27.68	26.76	26.54
SrO							0.70		
Total	55.06	55.50	53.96	56.12	54.82	52.72	53.35	56.10	55.78
Min Name	ankerite	ankerite	ankerite	ankerite	ankerite	ankerite	ankerite	ankerite	ankerite

Sample	PB12-PM08	2013-PM12	2013-PM12	2013-PM12	2013-PM12	2013-PM31	2013-PM31	2013-PM31	2013-PM31
Analysis	SITE 7 D	SITE 1 D	SITE 1 J	SITE 2 B	SITE 3 E	SITE 1 B	SITE 1 G	SITE 1 N	SITE 1 U
SiO ₂									
TiO ₂									
Al ₂ O ₃									
FeO	51.57	50.00	48.76	49.32	49.56	53.95	53.72	54.00	53.40
MnO	0.52	0.58	0.54	0.47	0.43		0.50	0.28	
MgO	6.05	7.54	8.55	7.48	7.64	1.32	1.15	1.10	0.83
CaO	0.45	0.62	0.35	0.42	0.37	2.10	1.83	1.72	2.87
CoO ₂		0.36	0.21	0.27	0.44				
Total	58.58	59.10	58.41	57.96	58.44	57.37	57.20	57.10	57.10
Min Name	siderite								

Table 7.12: Representative analyses of aluminoceladonite alteration minerals at the Pamao deposit

Sample	PB12-PM08	PB12-PM08	PB12-PM01A	PB12-PM01A	PB12-PM12	PB12-PM12	PB12-PM07	PB12-PM07	PB12-PM10	2013-PM4	2013-PM4
Spectrum	SITE A C	SITE 6 B	SITE 4 B	SITE 6 G	SITE 1 W	SITE 3 L	SITE 1 J	SITE 3 K	SITE 2 Y	SITE 1 L	SITE 1 U
SiO ₂	46.99	47.58	48.42	47.98	47.50	48.37	48.03	51.78	47.01	48.21	46.91
TiO ₂	0.28	0.37	0.29		0.30	0.32	0.58	0.45	0.28	0.31	
Al ₂ O ₃	33.24	31.78	32.86	33.60	33.11	34.02	32.22	31.03	33.44	31.65	32.90
FeO	2.74	2.83	1.90	1.66	2.52	2.44	1.57	1.46	2.92	2.08	1.94
MgO	0.59	0.94	1.10	0.86	0.68	0.64	1.21	1.26	0.65	1.21	0.79
K ₂ O	9.98	9.77	9.65	9.85	9.25	9.10	9.24	8.98	9.01	9.95	10.00
Na ₂ O	0.54	0.52	0.82	0.84	0.83	0.71	0.66	1.78	0.51	0.55	0.58
V ₂ O ₅							0.35				
Cr ₂ O ₃							0.35				
Total	94.37	93.79	95.04	94.79	94.19	95.58	94.21	96.74	93.83	93.96	93.12
Min Name	Al-celadonite										

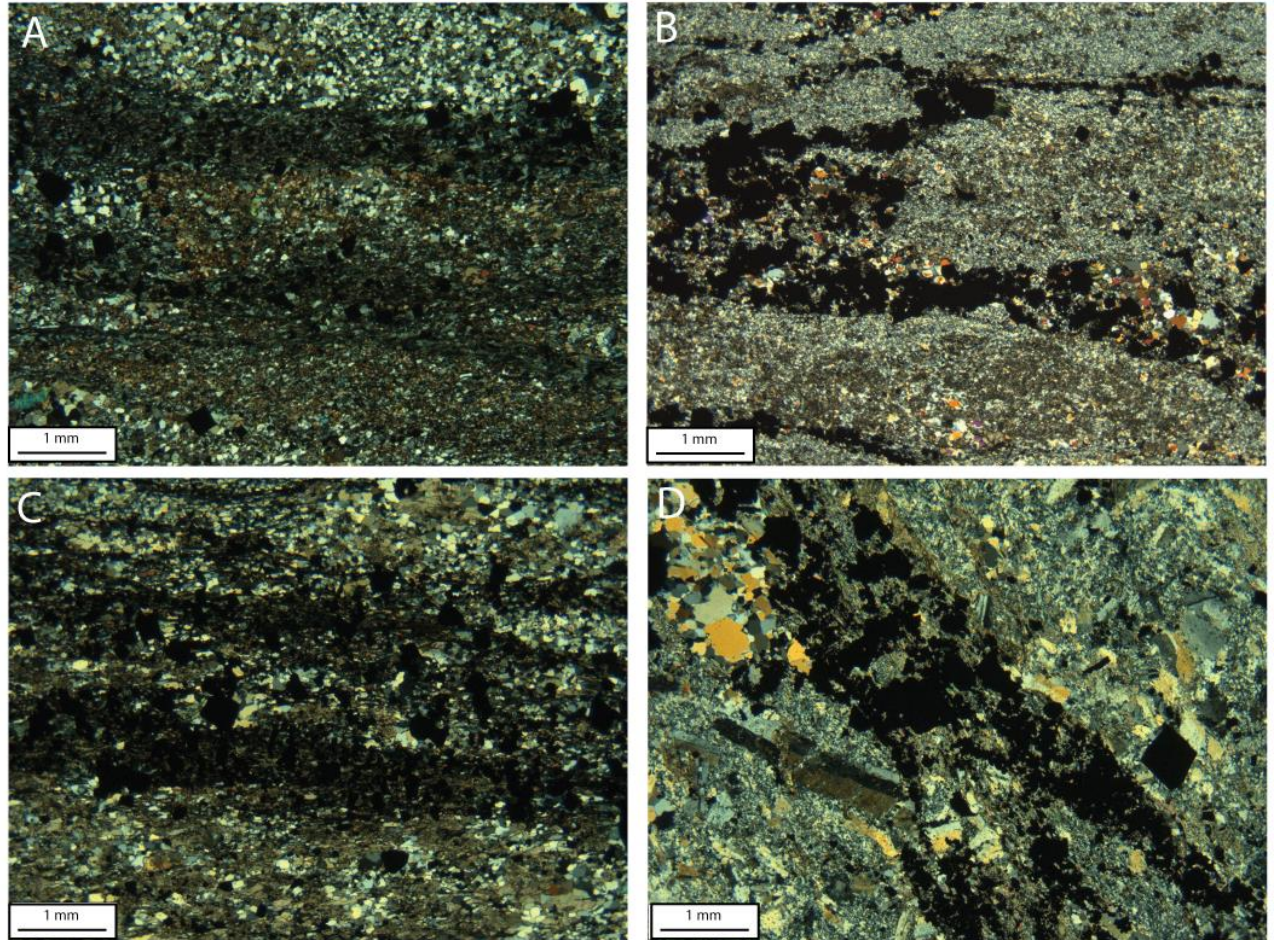


Figure 7.28: XPL Photomicrographs displaying alteration and mineralisation textures identified in samples from the Pamao deposit. A) Sample PB12-PM06: Fe-carbonate alteration overprinting deformed quartz clasts and chlorite-rich inter-clast areas, disseminated sulphide mineralisation is observed overprinting chlorite. B) Sample PB12-PM12; Vein style mineralisation running parallel to deformation orientation in volcano-sedimentary conglomerate that has been altered by Fe-carbonate, Sulphides are hosted in a quartz±siderite gangue. C) Sample PB12-PM09; Disseminated sulphide mineralisation overprinting chlorite-rich layers. D) Sample PB12-PM01; Sulphide-bearing quartz-aluminoceladonite vein cutting across altered basalt.

7.7.4.2 Ore Phase

Pyrite is the dominant sulphide mineral phase identified in the majority of samples at Pakaka and the sole phase with which gold mineralisation is associated. A single pyrite phase, Pyrite-1 (Py-1) is identified, occurring as angular to sub-angular isometric cubic, triangular and hexagonal crystals ranging in size from 10-100 μm (Fig. 7.30a-f). Py-1 is texturally homogenous with only small irregular areas within each crystal containing appreciable numbers of vugs. In rare examples the vugs are abundant and define zones within the Py-1 crystals. Where this occurs the Py-1 generation is divided into Py-1a (abundant vugs) and Py-1b (No vugs, homogenous texture) (Fig. 7.30 c)

Mineral	Pre-Ore stage	Ore stage	Post ore stage
Deformation metamorphism			
Quartz	—————	-----	
Chlorite	—————	-----	
Alluminoceladonite	—————	-----	
Hydrothermal Alteration			
Ankerite		—————	-----
Siderite		—————	-----
Quartz		—————	-----
Sulphides			
Galena-1	—————		
Sphalerite-1	—————		
Arsenopyrite-1		—————	
Pyrrhotite-1		—————	
Chalcopyrite-1		—————	
Pyrite-1a			—————
Pyrite-1b			—————
Au-1			—————
Arsenopyrite-2			—————
Chalcopyrite-2			—————
Accessory Phases			
Monazite		—————	
Fluorapatite	—————	-----	
Scheelite	—————	-----	
Rutile	—————	-----	

Figure 7.29: Paragenetic diagram illustrating the relative timing of the major alteration, sulphide and accessory phases in the samples from the Pamao deposit

7.7.4.3 Au Mineralisation

A single phase of Au-mineralisation (Au-1) is identified within the examined samples at Pakaka and is identified exclusively in association with the Py-1 mineral phase. Au-1 occurs as irregular sub-rounded to sub-angular masses ranging in size from sub-micron to 20 µm in size occluded within the Py-1 phase.

7.7.4.4 Post-Ore Phase

Two post ore sulphide phases are identified within the samples from Pamao. Chalcopyrite-2 (Cpy-2) and Arsenopyrite-2 (Asp-2). Chalcopyrite-2 occurs as rare sub angular to sub-rounded crystals ranging in size from 20-40 µm. Cpy-2 is observed nucleating on the margins of Py-1 (Fig. 7.30e-f). Arsenopyrite-2 is the most abundant of the post ore sulphide phases. Asp-2 occurs as irregular angular to sub-angular 10-20 µm crystals that form interlocking aggregate crystal masses, occluding small pyrite crystals attributed to the Py-1 phase (Fig. 7.30a) . The two post ore phases are not observed together and as such the relationship between them is unknown.

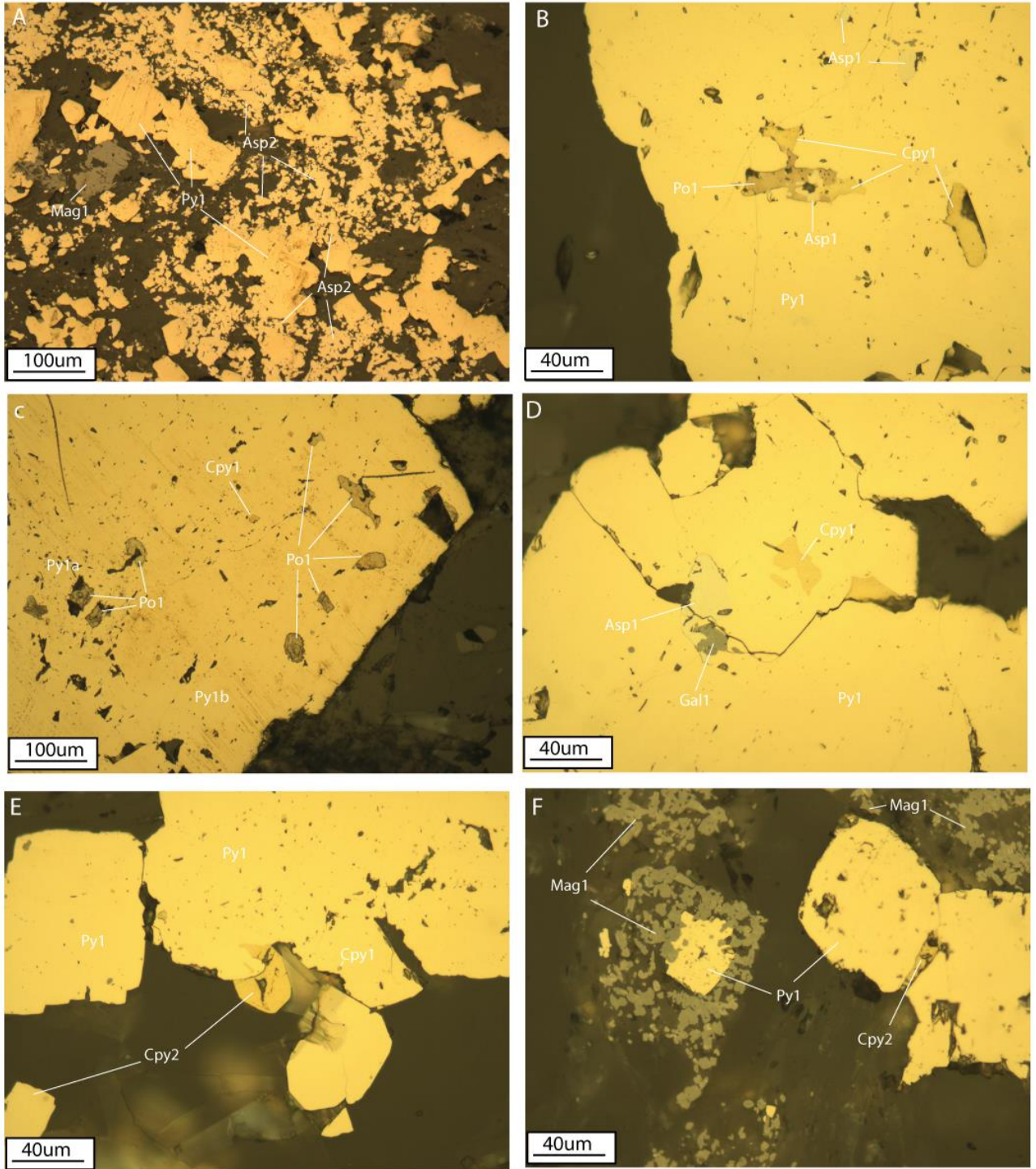


Figure 7.30: RFL Photomicrographs illustrating the relationship between the major sulphide phases in the samples from the Pamao deposit: A) Sample PB12-PM01; Arsenopyrite-2 ocluding Pyrite-1. B) Sample PB12-PM01; Pyrite-1 ocluding multiple early sulphide phases including Arsenopyrite-1, Pyrrhotite-1 and Chalcopyrite-1. C) Sample PB12-PM08; vuggy Pyrite 1a and homogenous pyrite 1b ocluding early Chalcopyrite-1 and Pyrrhotite-1. D) Sample PB12-PM01; Pyrite-1 ocluding early Arsenopyrite-1, Chalcopyrite-1 and Galena-1. E) Sample PB12-PM02; Chalcopyrite-2 partially ocluding Pyrite-1. F) Sample PB12-PM01; Late Magnetite-1 alteration ocluding Pyrite-1.

7.8 Discussion

7.8.1 Comparative mineralogy

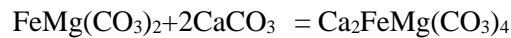
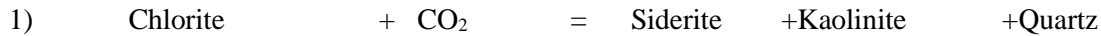
The characteristics of the four deposits (The KCD, Mengu, Pakaka and Pamao) discussed above are summarised in Table 7.13 and are here discussed in the context of developing of comparative mineralogical model.

Host lithologies are predominantly the geological units belonging to the Kibalian meta-sediments, with mineralisation primarily observed in interpreted volcano-sedimentary conglomerate lithologies. Other lithologies are identified hosting significant mineralisation, including the banded iron formations at the KCD and interpreted basaltic lithologies at the Pamao deposit, however these constitute a small percentage of the observed mineralisation. The host volcano-sedimentary conglomerates are in all cases metamorphosed, in line with the regional greenschist facies event (Chapter 4), but also display intense localised deformation in association with mineralisation. This deformation is characterised in all cases by pure shear and the variable stretching and recrystallisation of the volcano-sedimentary lithologies producing the distinct ‘clast-inter-clast’ texture (quartz-rich clasts hosted in a phyllosilicate-rich matrix).

Pre-mineralisation alteration is characterised by the development of Fe-carbonates + quartz + aluminoceladonite, with intensity varying throughout the deposits ranging from sporadic Fe-Carbonate crystals overprinting phyllosilicates in the inter-clast areas to texture destructive alteration, the alteration assemblages overprinting all pre-mineralisation textures and mineral assemblages. The hydrothermal alteration characteristics of orogenic gold deposits were reviewed in Chapter 3, but in brief are characterised by addition of CO₂, S, K, H₂O, SiO₂±Na under typically greenschist facies conditions (Ridley and Diamond, 2000). Alteration minerals are typically dominated by carbonate minerals and alkali-rich phases (K>Na) such as potassium-rich phyllosilicates (including aluminoceladonite) (Ridley and Diamond, 2000). The alteration characteristics of the Kibalian deposits are therefore consistent with those expected from orogenic gold deposits. The alteration assemblage and presentation displays particular similarities to those described at the Otago schist orogenic gold deposits outlined by Craw et al. (2009, 2013). Craw et al. (2009) developed a series of equations to describe the interaction of CO₂-rich fluids with the phyllosilicate host lithologies, the two equations most relevant to the alteration assemblages identified at the Kibalian gold deposits are;

Table 7.13: Summary of the major features of the KCD, Mengu, Pakaka and Pamao deposits

	Karagba-Chaffeur-Durba	Mengu	Pakaka	Pamao
Host lithologies	Deformed volcano-sedimentary conglomerates, Banded ironstone,	Deformed volcano-sedimentary conglomerates	Deformed volcano-sedimentary conglomerates	Deformed volcano-sedimentary conglomerates, Deformed basalts
Alteration	Fe-Carbonate (Ankerite+Siderite) + Quartz+Aluminoceladonite Late magneite	Fe-Carbonate (Ankerite+Siderite) + Quartz+Aluminoceladonite Late magneite	Fe-Carbonate (Ankerite) + Quartz+Aluminoceladonite	Fe-Carbonate (Ankerite+Siderite) + Quartz+Aluminoceladonite Late magnetite
Mineralisation Styles	Quartz+siderite vein hosted sulphides (three distinct styles) and disseminated interclast sulphides	Quartz+siderite vein hosted sulphides and disseminated interclast sulphides	Quartz+siderite vein hosted sulphides and disseminated interclast sulphides	Quartz+siderite vein hosted sulphides and disseminated interclast sulphides
Major Sulphides	Pyrite (~99%)	Pyrite (~99%)	Pyrite (~80%) and Arsenopyrite (~20%)	Pyrite (~99%)
Minor Sulphides	chalcopyrite + arsenopyrite + pyrrhotite + marcassite + tennantite + galena	chalcopyrite + pyrrhotite + tennantite	arsenopyrite + chalcopyrite + pyrrhotite + tenantite + lzoklakeite + freiburgite	chalcopyrite + arsenopyrite + galena + sphalerite + pyrrhotite
Accessory Phases	Fluoroapatite + apatite + monazite + scheelite + rutile	Fluoroapatite + apatite + monazite + scheelite + rutile	Fluoroapatite + apatite + monazite + scheelite + rutile	Fluoroapatite + monazite + scheelite + rutile
Gold occurrence	Occluded in Pyrite and as late native and fracture hosted gold	Occluded in Pyrite and as late fracture hosted gold	Occluded in Pyrite and as late fracture hosted gold	Occluded in Pyrite and as late fracture hosted gold



It is considered probable that similar processes to these are applicable to the Kibalian system, the main difference being the formation of aluminoceladonite instead of kaolinite in equation 1. The predominance of ankerite or siderite in individual samples and the compositional variations identified in the alteration phases across all four deposits (Fig. 7.4 and 7.5) would therefore be the result of variations in the abundance of Fe and Ca in individual sections of the host lithologies.

Sulphide mineralisation is dominated in all deposits by Fe-sulphides, pyrite being the most abundant mineral phase in all deposits, and the main gold host. All deposits also show varying proportions of chalcopyrite, arsenopyrite, and pyrrhotite with base metal sulphides being largely absent. This sulphide assemblage is typical of orogenic gold deposits (Ridley and Diamond, 2000). Multiple mineralisation styles are identified in all four deposits. Disseminated mineralisation is characterised by sulphide minerals overprinting and replacing chlorite and Fe-carbonate mineral phases in the phyllosilicate-rich inter-clast zones in the deformed volcano-sedimentary conglomerates, constituting the low-grade mineralisation in all deposits. Vein style mineralisation is also observed in all four deposits and is characterised by the formation of quartz+siderite(±aluminoceladonite)+sulphide veins in lithologies that have undergone extensive Fe-Carbonate alteration. Three distinct styles of vein mineralisation are observed across the four deposits 1) Veins parallel to relic clast-inter-clast structures exploiting relic inter-clast pathways (Fig. 7.8 c), 2) Well defined veins cross cutting relic structures in heavily altered lithologies (Fig. 7.8 b) and 3) Amorphous quartz-rich structures in heavily altered lithologies (Fig. 7.8 d). Further styles of mineralisation are identified in the banded iron formations at the KCD with cross cutting veins (Fig. 7.9 a), similar in characteristic to the type veins described above, and replacement style mineralisation (Fig. 7.9 b) in which iron sulphides replace the ironstone horizons. In all four deposits gold mineralisation is closely associated with the pyrite mineral phase, gold occurring principally as inclusions within the pyrite. A second phase of gold mineralisation is identified, occurring as fracture hosted gold grains and in the case of the KCD as isolated gold grains within the groundmass.

The similarities in the characteristics of the host, alteration and mineralisation mineralogy's between the individual deposits define a single style of mineralisation that has been active across the western part of the Kibali Granite-Greenstone Belt.

7.8.2 Geothermometry

Earlier in this study chlorite compositions were used to estimate formation temperatures of metamorphic chlorite in the Kibalian volcano-sedimentary conglomerates. Here the methods outlined by Cathelineau (1988) and Jowitt (1991) are again used to estimate chlorite formation temperatures in the highly deformed volcano-sedimentary conglomerate lithologies identified in association with mineralisation in all four deposits. Selected chlorite compositions and calculated temperature estimates are displayed in Tables 7.1, 7.4, 7.7 and 7.10. At the KCD chlorite formation temperatures range from 296 to 385°C (interquartile range= 355 to 375°C), with an average of 364°C (n=39) using the Cathelineau (1988) method and between 309 and 409°C (interquartile range=368 to 389°C), with an average of 377°C (n=39) using the method of Jowitt (1991). At Mengu chlorite formation temperatures range from 341 to 384°C (interquartile range=356 to 372°C), with an average of 364°C (n=31) using the Cathelineau (1988) method and between 353 and 399°C (interquartile range=369 to 386), with an average of 378°C (n=31) using the method of Jowitt (1991). At Pakaka chlorite formation temperatures range from 263 to 372°C (interquartile range=304 to 329°C), with an average of 314°C (n=31) using the Cathelineau (1988) method and between 267 and 386°C (interquartile range=309 to 333°C), with an average of 320°C (n=31) using the method of Jowitt (1991). At Pamao chlorite formation temperatures range from 356 to 405°C (interquartile range=369 to 380°C), with an average of 373°C (n=93) using the Cathelineau (1988) method and between 368 and 420°C (interquartile range=382 to 394°C), with an average of 386°C (n=93) using the method of Jowitt (1991). The estimated chlorite formation temperatures define a broad temperature range from 263 to 420°C with the temperature ranges for each deposit overlapping. Examining the interquartile ranges shows that the majority of the data from the KCD, Mengu and Pamao deposits fall in the 350 to 400°C range. The data from the Pakaka deposit yields significantly lower formation temperatures, the majority of data falling in the range 300 to 335°C.

The estimated metamorphic chlorite formation temperatures calculated for the 'undeformed' volcano-sedimentary conglomerates in Chapter 4 defined a range between 294 to 370°C with the majority of data falling in the interval 310 to 360°C. This data indicates that the localised deformation observed at the KCD, Mengu and Pamao deposits took place at temperatures slightly elevated in comparison to those present during the regional greenschist facies metamorphism. The Pakaka deposit is the exception, chlorite formation temperatures correlating well with the regional values.

The localised deformation predates the formation of mineralisation and while providing an insight into the conditions present at the deposits, does not provide a direct estimate for the iron sulphide phases. The arsenopyrite geothermometer allows estimation of the formation temperatures of the arsenopyrite mineral phase based on the systematic variations in the Atomic % arsenic in arsenopyrite (Kretschmar and Scott, 1976). Here the arsenic buffered diagram developed by Sharp et al. (1985) is used to estimate formation temperatures. Arsenopyrite at the deposits in the KGGB is frequently associated with pyrrhotite, the phases being observed intergrown and replacing each-other. As such the Aspy+Po field (Fig. 7.31-7.35) is the most suitable in estimating formation temperatures. The Aspy-Po is the broadest of the compositional fields and this is reflected in the arsenopyrite compositions from the deposits, which display significant variation in atomic % arsenic. In estimating temperatures the maximum possible range based on the atomic % As values are reported.

Arsenopyrites at the KCD vary in composition from 30.7 to 34.6 at% As (Interquartile range=32.5 to 33.5 at% As) with an average value of 33.0 at% As (n=46). These As compositions correspond to a formation temperature range of <300 to 540° C (Interquartile temperature range=370 to 505° C) (Fig. 7.31).

Arsenopyrites from the Mengu deposit vary in composition from 30.5 to 33.2 at% As (Interquartile range= 30.9 to 32.7 at% As) with an average value of 32.0 at% As (n=11). These As compositions correspond to a formation temperature range of <300 to 500° C (Interquartile range= <300 to 470° C) (Fig. 7.32).

Arsenopyrites from the Pakaka deposit vary in composition from 31.5 to 34.1 at% As (Interquartile range= 32.3 to 33.7 at% As) with an average value of 33.0 at% As (n=37). These arsenic compositions correspond to a formation temperature range of 315 to 525° C (Interquartile range= 360 to 510° C) (Fig. 7.33).

Arsenopyrites from the Pamao deposit vary in composition from 30.4 to 33.5 at% As (Interquartile range= 31 to 32.5 at% As) with an average value of 31.9 at% As (n=34). These As values correspond to a formation temperature range of <300 to 520° C (Interquartile range= 305 to 455° C) (Fig. 7.34). The temperature estimates based on the arsenic content of arsenopyrite from each deposit overlap to define a broad window of formation temperatures ranging from <300 to 540° C. While these temperature estimates are too broad to draw any firm conclusions they do overlap, and extend upward from, the chlorite formation temperatures from the deformed volcano sedimentary conglomerate. This possibly indicates that the processes that formed mineralisation were an extension of existing deformational processes within the Kibalian belt.

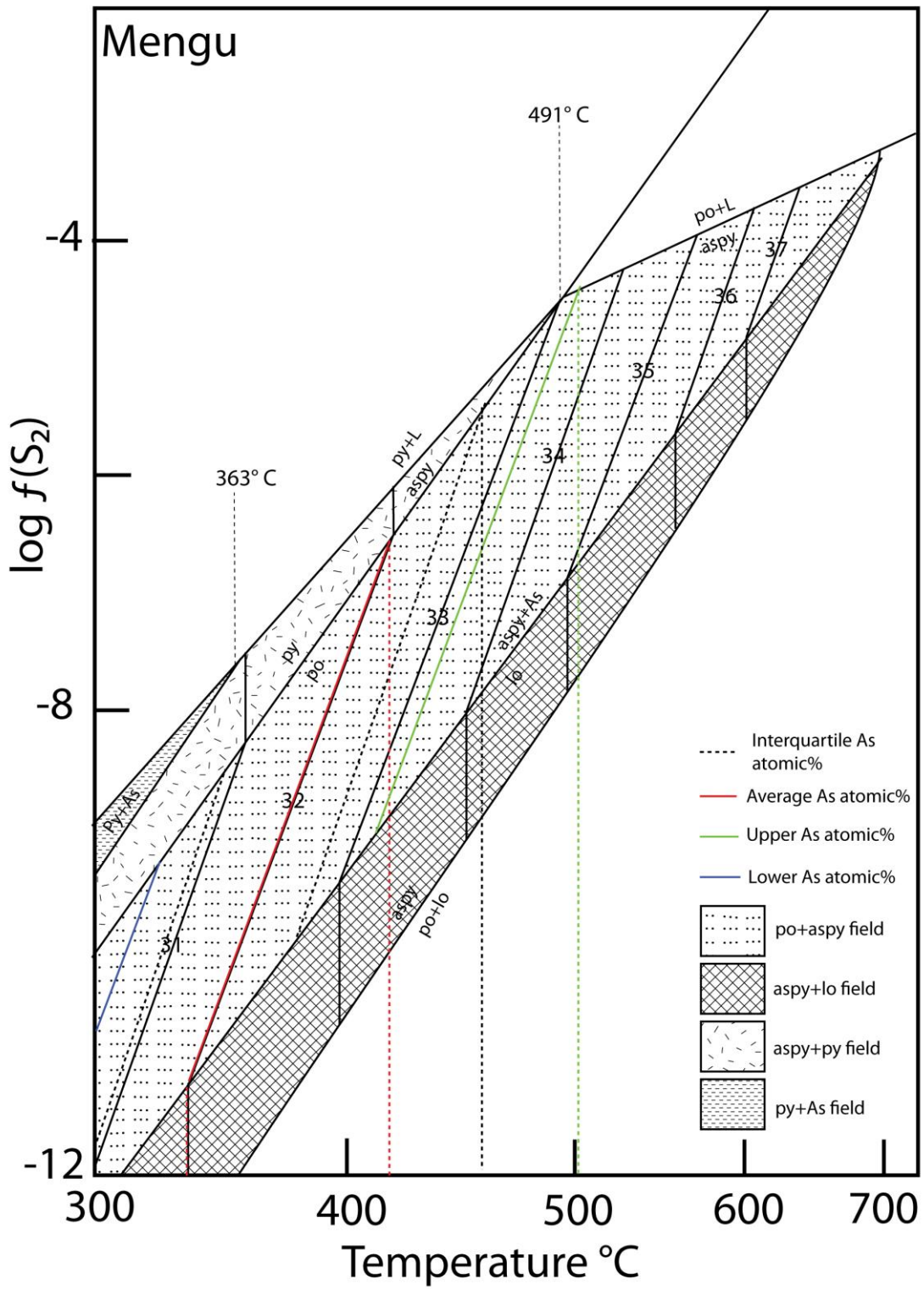


Figure 7.32: Arsenopyrite geothermometry diagram redrawn from Sharp et al. (1985) displaying data from the Mengu deposit.

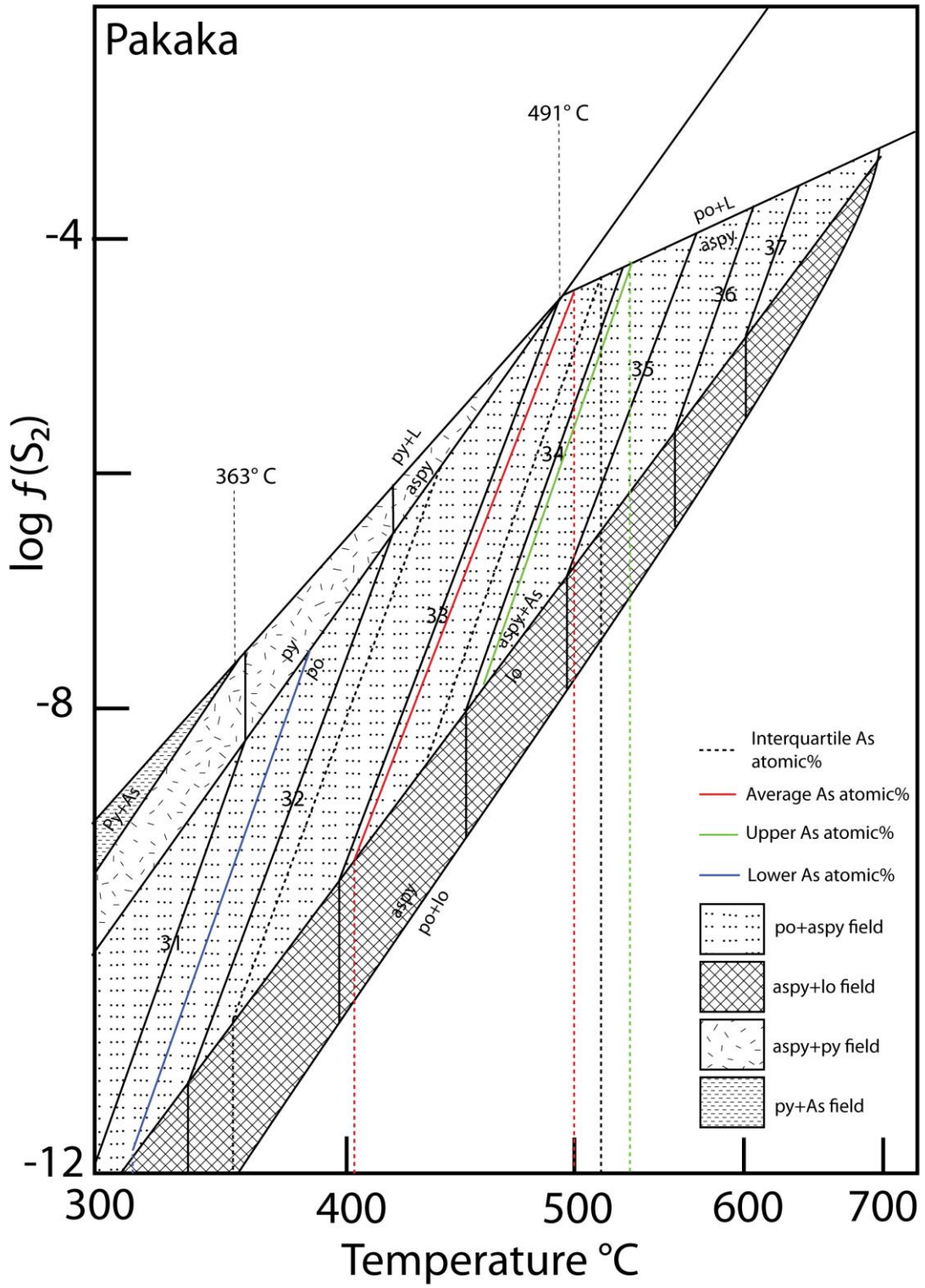


Figure 7.33: Arsenopyrite geothermometry diagram redrawn from Sharp et al. (1985) displaying data from the Pakaka deposit.

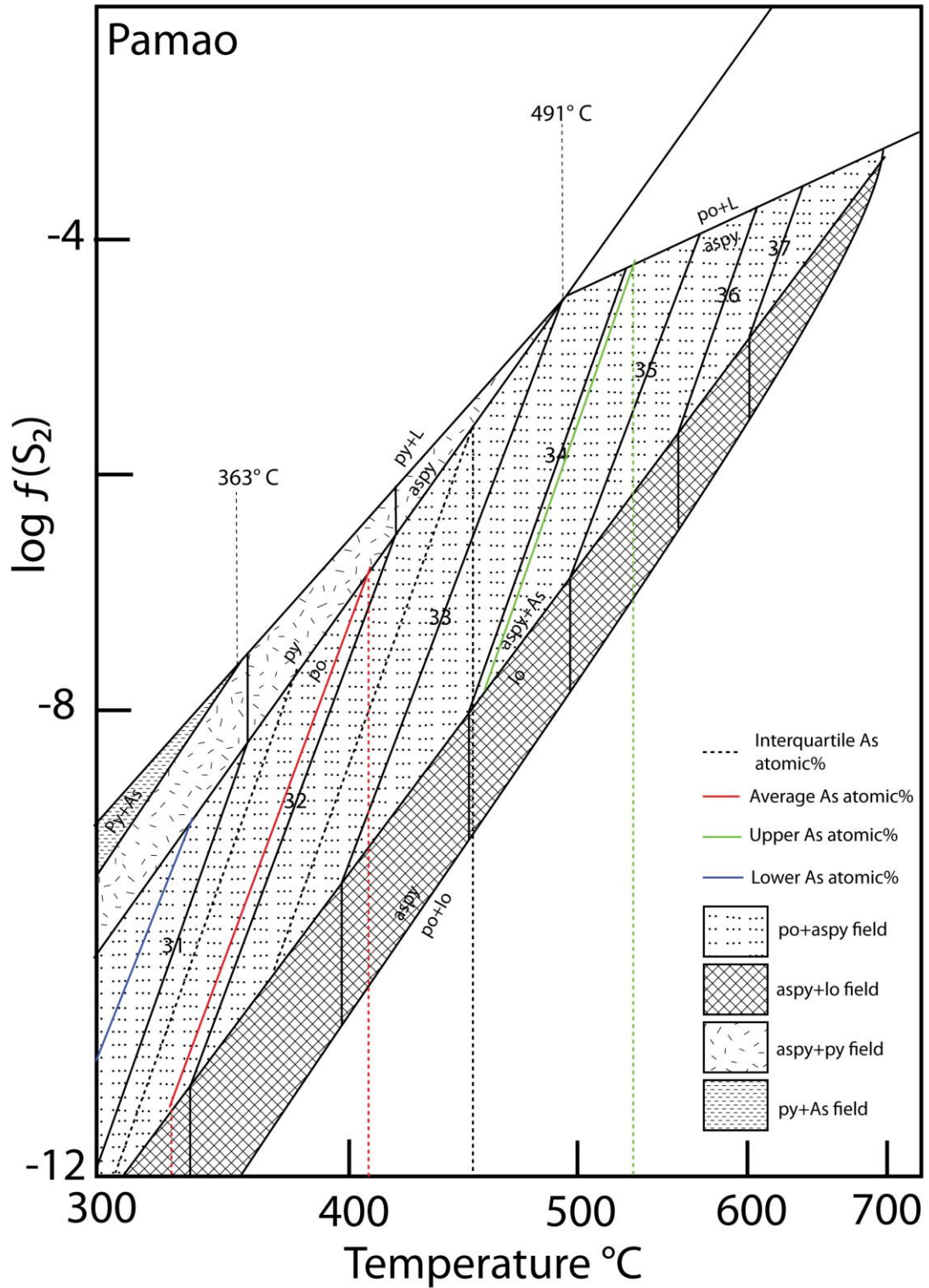


Figure 7.34: Arsenopyrite geothermometry diagram redrawn from Sharp et al. (1985) displaying data from the Pamao deposit.

7.8.3 Mineralisation model

In developing a model for the formation of mineralisation in the eastern part of the KGGB it is necessary to consider all of the aspects discussed above, ranging from the localised deformation of the Kibalian volcano-sedimentary conglomerates to the development of the contrasting disseminated and vein mineralisation styles.

Localised deformation of the host volcano-sedimentary lithologies occurred prior to the formation of mineralisation but is considered an important component in ‘preparing’ the host lithologies for the later alteration and mineralising events. The deformation of polymineralic rocks, such as the Kibalian volcano-sedimentary rocks, is controlled by the relative abundance and rheological properties of each mineral phase (Handy, 1990). The pre-deformation volcano-sedimentary conglomerates (Chapter 4) are characterised by quartz-feldspar clasts set in a phyllosilicate-rich matrix. Phyllosilicates are rheologically weaker than the quartz feldspar phases (Handy, 1990; Wintsch et al., 1995) and as a result strain is preferentially partitioned, though not totally, into the phyllosilicate matrix material (Handy, 1990). The application of strain to such a material results in the realignment and recrystallisation of both the phyllosilicate matrix minerals and the clast material (Handy, 1990; Wintsch et al., 1995; Zhang et al., 1999), a process referred to in the literature as either ‘reaction weakening’ or ‘strain softening’ (McCuaig and Kerrich, 1998). The resultant mineral phases, in particular the phyllosilicate material, will vary depending on the initial composition of the deforming lithology. Initially Fe+Mg-rich lithologies will form Fe+Mg-rich phyllosilicates (Wintsch et al., 1995), including chlorite, as are observed in the deformed volcano-sedimentary conglomerates. Under strain phyllosilicate crystals will form in orientations favourable to glide (Wintsch et al., 1995; Zhang et al., 1999) effectively lowering the rheological strength of these inter-clast zones (Wintsch et al., 1995). Further strain will be even more favourably partitioned into the inter-clast material. This said the deformed volcano-sedimentary conglomerates identified at the four ore deposits display significant deformation and attenuation of the quartz clast phase in addition to the phyllosilicate-rich zones. Partitioning of strain into the rheologically strong mineral phase, in this case the quartz clasts, may occur when the rheologically strong phase is abundant or under high strain conditions (Handy, 1990). The clast/matrix proportions of the volcano-sedimentary conglomerates are highly variable (see above and Chapter 4). Where clasts are abundant strain will have been more significantly affected this phase (Handy, 1990). Alternatively continued partitioning of strain into a phyllosilicate-rich phase may significantly increase the ‘length’ of these zones causing an associated reduction in volume (Wintsch et al., 1995; Zhang et al., 1999). This ‘lengthening’ would result in a transition from a phyllosilicate matrix dominated lithology to a clast dominated lithology and the partitioning of strain into the quartz clasts (Handy, 1990). This process of reaction softening may occur across a range of strain and temperature conditions, from greenschist to

amphibolite, increasing temperature and strain reducing the rheological strength of the mineral phases and further enhancing deformation (Handy, 1990). In the case of the Kibalian deposits it is hypothesised that this process was taking place under sub-greenschist to greenschist facies conditions at approximately 300-400°C. The reaction weakening process has a significant secondary effect, an increase in fluid interconnectivity and permeability of the deformed lithologies (Zhang et al., 1999). Aligned phyllosilicate-rich zones display permeability anisotropy with permeability being significantly enhanced parallel to foliation (Zhang et al., 1999). When this occurs permeability can rapidly rise to a plateau under even low strain rates (Zhang et al., 1999). This mechanism allows high permeability pathways to be maintained at high confining pressures (Wintsch et al., 1995). This increased permeability in the phyllosilicate-rich horizons is apparent when the distribution of the major alteration phases is examined. Low intensity Fe-Carbonate alteration was confined principally to the phyllosilicate-rich pathways, only at increasing intensities is it observed replacing the quartz clast material.

Greenschist facies fluids produced through metamorphic devolatilisation are typically considered to be CO₂-rich (Yardley and Cleverley, 2013). It is hypothesised that such a CO₂-rich fluid ascended through the crust being focused in to the zones of high permeability created by the reaction weakening process. The observed alteration assemblage is thus the product of interaction between the ascending CO₂-rich fluid and the Fe+Mg-rich phyllosilicates. Isotropic carbonate minerals such as Ankerite and Siderite are rheologically strong, in comparison to aligned phyllosilicates (Handy, 1990), and their precipitation inhibits further deformation and significantly reduces permeability. This effect, generally referred to in the literature as hydrothermal hardening (McCuaig and Kerrich, 1998), is thought to have inhibited deformation in the phyllosilicate-rich horizons sufficiently that continued application of strain will have begun to have deformed the quartz clasts. In fine interlocking crystalline structures such as the quartz clasts, deformation occurs by crystal plastic processes and is accompanied by dilatancy, increasing permeability (Peach and Spiers, 1996). This process would allow limited infiltration of the ascending fluids into the clast material resulting in the observed alteration. At its most intense alteration is texture destructive, overprinting all of the original litho-textures. At this point permeability will be at a minimum.

The varying levels to which the Fe-Carbonate alteration assemblages have developed play a significant role in the development of mineralisation, controlling the mineralisation style (Fig. 7.35). The abundance of iron sulphides, particularly pyrite, and the close association of gold with the pyrite phase, indicates that mineralising fluids were likely H₂S-rich (McCuaig and Kerrich, 1998; Williams-Jones et al., 2009). At the observed temperatures (400 to 500°C) H₂S-rich fluids are thought to transport gold as a bi-sulphide complex (Stefansson and Seward, 2004).

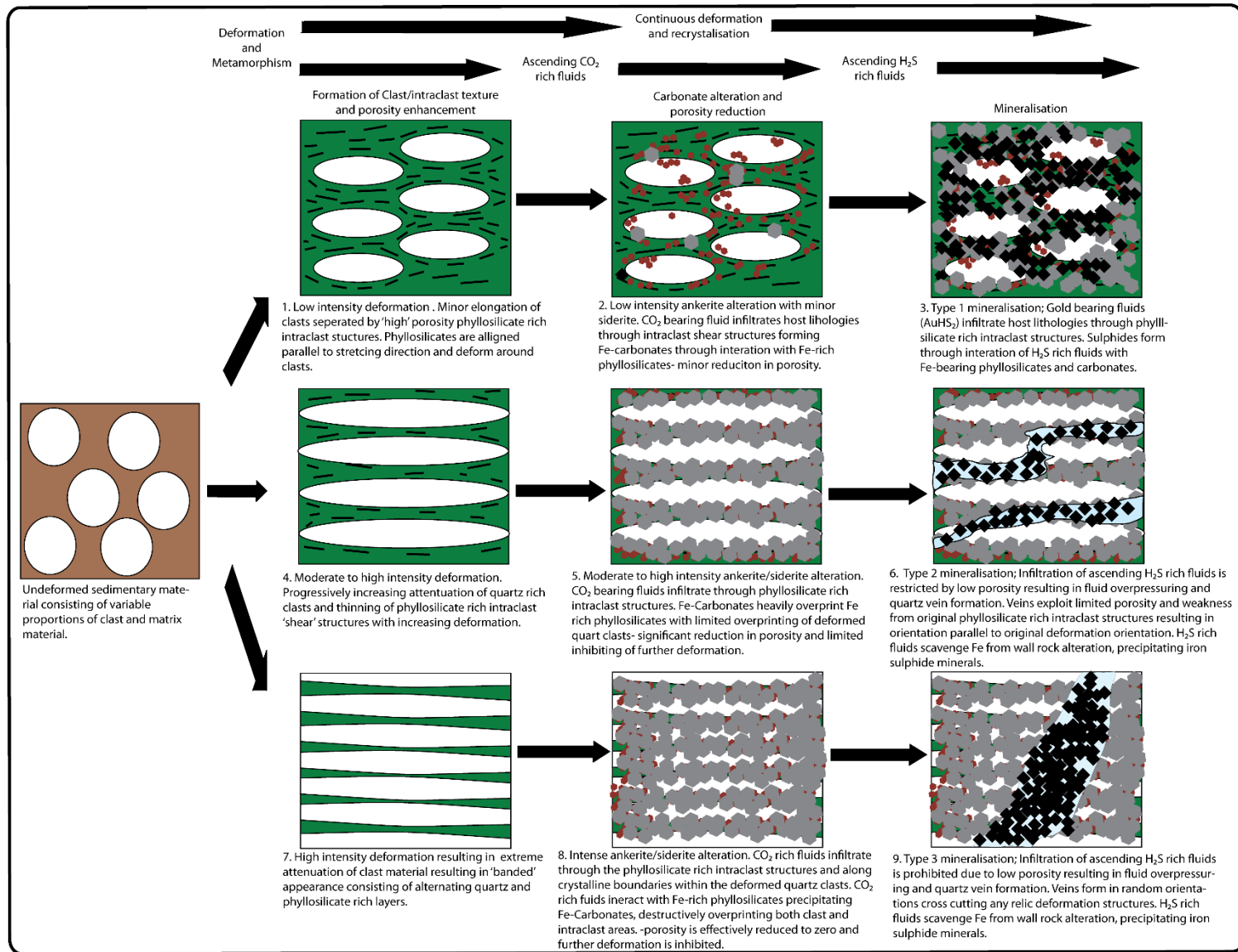


Figure 7.35: Schematic diagram illustrating the reaction weakening and hydrothermal hardening mechanisms hypothesised to have influenced the formation of mineralisation in the deposits at the

Kibali Gold Project

At the site of deposition these fluids are hypothesised to have acted differently depending on the intensity of the alteration (Fig. 7.35). Areas where only low level alteration is identified will have retained significant permeability allowing the infiltration of mineralising fluids through the phyllosilicate-rich zones, precipitating sulphides through interaction with the Fe-rich mineral phases (chlorite and ankerite/siderite) (Fig. 7.35). With increasing intensity of alteration, and corresponding reduction in permeability, the infiltration of fluids will be restricted and mineralisation style will therefore be dependent on fluid over-pressuring and fracture mesh propagation mechanisms (Fig. 7.35) (Cox, 2002; Sibson, 1996). In the case of the Kibali deposits this is represented by the three distinct styles of vein mineralisation with the mineralising fluids precipitating sulphides through interaction with Fe-rich alteration phases in the wall rock (Fig. 7.35). In order to retain permeability throughout the pre-mineralisation deformation, alteration and mineralisation processes the deposits must have been under continuous strain, strain being necessary for enhanced permeability in phyllosilicate-rich horizons (Wintsch et al., 1999; Zhang et al., 1999). Allibone (2015) (Section 7.3) hypothesised that mineralisation developed between the D4 and D5 deformation events. The model proposed here hypothesises that the observed alteration and mineralisation textures formed in a continuous ductile process. This may correspond to any of the ductile deformation events outlined by Allibone (2015) (D1-D4 or D6 events). The similarity in the attitude of the mineralised lodes and the F3/F4 folds (Allibone, 2015) suggests that these structures were the focus of the deformational processes that resulted in enhanced permeability but the exact timing of the mineralisation remains ambiguous and will require further work.

The secondary gold event, characterised by native and fracture hosted gold frequently associated with the post ore sulphide phases, indicate reactivation of the mineralised system after its initial formation. The fracture hosted nature of the majority of this gold suggests a brittle regime was predominant at the time. Allibone (2015) identified two brittle style deformation event D5 and D7. These both post date the formation of mineralisation, hypothesised to have occurred in association with the D3 and D4 events, and may be related to the observed secondary gold phase.

7.8. Conclusions

Mineralisation within the Kibali Granite-Greenstone Belt is characterised by multiple pyrite (>90%) +arsenopyrite+chalcopyrite+pyrrhotite+marcasite sulphide assemblages with multiple generations of each species having been identified. In all deposits pyrite is the dominant sulphide phase with the relative proportion of the other sulphide phases varying between deposits. Gold is hosted predominantly within the pyrite mineral phase though late secondary gold is identified, frequently associated with micro-fractures in

the pyrite mineral phase. Mineralisation is hosted within highly deformed examples of the Kibalian Metasediments with the volcano-sedimentary conglomerates and Banded Iron Formations being particularly notable host lithologies. The host lithologies have been variably altered by a localised Fe-carbonate (ankerite/siderite)+quartz±aluminoceladonite event that increases in intensity with proximity to the gold deposits. Mineralisation is hypothesised to have formed during regional greenschist facies metamorphism through a complex interaction between factors increasing permeability (reaction weakening), characterised by the development of aligned phyllosilicate-rich horizons, and those decreasing permeability (hydrothermal hardening), the formation of 'high resistance' mineral phases such as quartz and Fe-carbonates. These two factors exerted a significant control on the distribution of mineralisation by controlling the behaviour of mineralising fluids infiltrating the host lithologies and through 'prepping' the host lithologies making them chemically favourable for the formation of mineralisation.

Chapter 8. $\delta^{34}\text{S}$ characteristics of the Karagba-Chaffeur-Durba (KCD) gold deposit and other significant gold resources in the Kibali Granite-Greenstone Belt

8.1 Introduction

Sulfur isotope analysis has become a nearly ubiquitous tool in the investigation of orogenic gold deposits due to the abundance of sulphide gangue and ore minerals, and the relative ease and cost effectiveness which allows large data sets to be rapidly constructed. Furthermore, as it is thought that gold is predominantly transported as a bi-sulphide complex ($\text{Au}(\text{HS})_2$) (Groves et al., 2003; Goldfarb et al., 2005), the source of sulfur can yield information regarding the origin of the gold (Chang et al., 2008). Sulfur isotopes also provide a mechanism through which specific sulphide mineral phases can be compared and contrasted both within and between individual deposits while simultaneously providing a range of information regarding the origin and formation of the deposit. Due to the lack of research into the principle gold deposits within the Kibali Granite-Greenstone belt (The Karagba-Chaffeur-Durba (KCD), Mengu, Pakaka and Pamao deposits), the sulfur isotope characteristics of the auriferous sulphide assemblages are currently unknown. Here the $\delta^{34}\text{S}$ isotope characteristics of the main deposits within the Kibali granite-greenstone belt are examined with the aim of characterising and contrasting the individual deposits and drawing wider conclusions regarding the origins of the sulphide minerals.

8.2 The Sulfur Isotope System

Sulfur is the 14th most abundant element in the Earth's crust (Seal, 2006) and is widespread throughout the lithosphere, biosphere, hydrosphere and atmosphere (Faure and Mensing, 2005). Four naturally occurring stable isotopes of sulfur are identified, ^{32}S , ^{33}S , ^{34}S and ^{36}S , with relative abundances of 95.02, 0.75, 4.21 and 0.02% respectively (Lide and Frederiske, 1995; Seal, 2006). A single radioactive isotope, ^{35}S , is also identified with a half-life of 87 days making it insignificant in geological investigation (Seal, 2006). $\delta^{34}\text{S}$ expresses the ratio of $^{34}\text{S}/^{32}\text{S}$ in units of parts per thousand (‰) defined by the formula:

$$\delta^{34}\text{S} = \left\{ \left[\left(\frac{^{34}\text{S}}{^{32}\text{S}} \right)_{\text{sample}} - \left(\frac{^{34}\text{S}}{^{32}\text{S}} \right)_{\text{reference}} \right] / \left(\frac{^{34}\text{S}}{^{32}\text{S}} \right)_{\text{reference}} \right\} \times 1000$$

All sulfur isotope values are expressed relative to the Vienna Canyon Diablo Troilite (VCDT $\delta^{34}\text{S}=0.0\text{‰}$), with an absolute $^{34}\text{S}/^{32}\text{S}$ value of 4.50045×10^{-3} (Ault and Jensen, 1963). Due to the original VCDT material having been exhausted, the VCDT value is now defined relative to the IAEA-S-1 standard ($\delta^{34}\text{S} = -0.3\text{‰}$) (Seal, 2006). The VCDT is an effective standard as mafic igneous rocks possess $\delta^{34}\text{S}$ values close to zero and therefore the $\delta^{34}\text{S}$ values of terrestrial rocks will express changes in their $^{34}\text{S}/^{32}\text{S}$

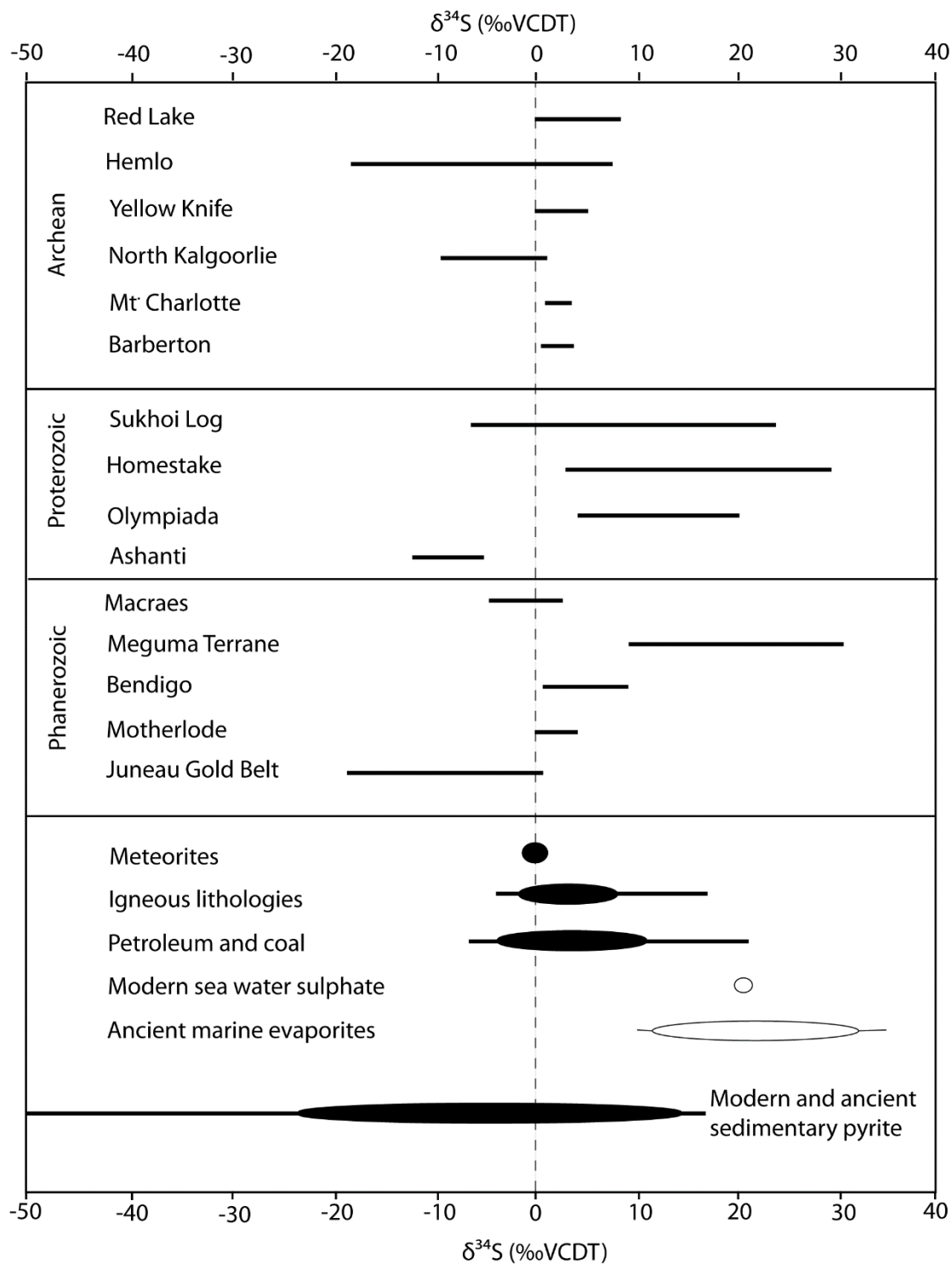


Figure 8.1: $\delta^{34}\text{S}$ ranges for terrestrial sulfur reservoirs and selected orogenic gold deposits from the Archean, Proterozoic and Phanerozoic. Reservoir values from Seal, 2006; Deposit values compiled from Rye and Ohmoto (1974), Kerrich (1987), Golding et al. (1990), Kontak et al. (1990), Goldfarb et al. (1991), De Ronde et al. (1992), Oberthur et al. (1996), and Chang et al. (2008 and references therein),

characteristics since they were introduced into the crust (Faure and Mensing, 2005; Seal, 2006). The $\delta^{34}\text{S}$ value is an easy ratio to measure due to the mass difference between the two isotopes: ^{34}S having a mass 6.2% greater than ^{32}S (Seal, 2005; Faure and Mensing, 2005). This mass difference is sufficient to allow significant mass dependent fractionation through biogenic sulphate reduction, isotope exchange reactions, sulphide precipitation mechanisms, and closed reservoir and reservoir mixing processes (Faure and Mensing, 2005; Seal, 2006). Mass independent fractionation of sulfur occurs through upper atmosphere photochemical processes (Seal, 2006). These are expressed by the value of $\Delta^{33}\text{S}$, but have had limited use in geological studies up to this point. The widespread use of sulfur isotopes to study multiple lithologies and environments has resulted in the various sulfur reservoirs being well defined (Fig. 8.1) allowing them to be utilised as a tracer for the source of sulfur within the system under investigation.

8.3 Sampling and Analytical Technique

Samples for analysis were selected from the suite of drill core collected from the KCD, Mengu, Pakaka and Pamao deposits and previously used in the study of the textural, petrographic and compositional characteristics of the four deposits. Petrographic observations identified a number of different sulphide phases within each deposit (Chapter 7) that could potentially be utilised in examining the $\delta^{34}\text{S}$ characteristics, including pyrite, arsenopyrite and chalcopyrite. With the exception of pyrite, the identified sulphides species were of too small a crystal size or too finely intergrown with other sulphide minerals to allow accurate analysis. As such analysis has restricted to the abundant pyrite mineral phases. Drill core from each of the four deposits was inspected to select those samples with suitable abundance of sulphide material. In the case of the KCD, drill core was selected in order to provide samples from the three major lodes at multiple depths and gold grade. In order to retain textural information, the samples were analysed through a combination of LA-ICP-MS and conventional analysis. Samples for LA-ICP-MS analysis were cut and mounted into polished resin blocks, where possible reusing sample stubs from the production of polished thin sections. Mounted blocks were examined and photographed by binocular microscope to identify relevant textures and to select sites for laser ablation. Samples for conventional analysis were crushed without metal contact and sieved to isolate the 63-500 μm fraction. The separated mineral fraction was washed in an ultrasonic bath to remove any material adhering to the surface before the pyrite fraction was isolated by hand picking. Care was taken during hand picking to select 'clean' pyrite crystals to which no additional sulphide or gangue material was attached.

Analysis of all samples was undertaken at the Scottish Universities Environmental Research Centre stable isotope facility, under a grant from the NERC Isotopes Geosciences Facilities (NIGL) Steering Committee. Conventional sample separates were converted to SO_2 gas by combustion with cuprous oxide using the

procedure outlined by Robinson and Kusakabe (1975). Combustion took place under vacuum conditions at a temperature of 1,070°C for a duration of 25 minutes, yielding SO₂ gas which was cryogenically purified using a CO₂-acetone slush trap to remove trace water vapour and a CO₂- n-pentane slush trap to remove trace CO₂. Sulfur isotope characteristics were determined by VG SIRA II gas mass spectrometer, raw δ⁶⁶SO₂ values converted to δ³⁴S by calibration with the NBS-123 and IAEA-S-3 international standard and the internal lab CP-1 standard.

Laser ablation of polished blocks was conducted by placing selected blocks in an evacuated chamber to which pure oxygen was added to allow laser induced combustion to take place. Previously selected ablation sites were located and combusted using a SPECTRON LASERS 902Q CW Nd-YAG laser (details of the laser setup and signal path are outlined in Wagner et al., 2002). For each ablation the beam was rastered across the sample medium, excavating an approximately 50µm wide strip between 3-5mm in length. As with the conventional analysis, the SO₂ gas was cryogenically purified and analysed by VG SIRA II gas mass spectrometer using the same method as outlined above. An additional correction was applied to the laser ablation data to correct for systematic fractionation of δ³⁴S in the SO₂ gas relative to δ³⁴S mineral values.

8.4 Results

The results of 95 analyses of pyrite from the KCD, Mengu, Pakaka and Pamao deposits are presented here. They are listed by deposit in tables 1-4 and presented as histograms in Fig. 8.2. Due to the small crystal size and the presence of micro-inclusions within the pyrite crystals, only a limited number of analysis from the Py-1a and Py-2 sulphide generations were collected, with the majority of analyses being from the Py-1b generation.

A total of 56 analyses were conducted on three generations of pyrite material from the KCD, consisting of 5 analyses of Py-1a, 47 analyses of Py-1b and 4 analyses of Py-2. Deposit wide δ³⁴S values range from 1.7‰ to 7.5‰ with an average value of 4.9‰. Examining the individual sulphide generations shows Py-1a ranging from 3.9‰ to 7.1‰ with an average value of 5.3‰, Py-1b ranging from 1.7‰ to 7.5‰ with an average value of 4.9‰ and Py-2 ranging from 3.8‰ to 6.6‰ with an average value of 5.2‰. A total of 17 analyses are reported from three generations of pyrite material from the Mengu deposit, consisting of 1 analysis of Py-1a, 14 analyses of Py-1b and 2 analyses Py-2. Deposit wide δ³⁴S values range from -1.4‰ to 5.6‰ with an average value of 2.6‰. The sole analysis of Py-1a yielded a value of 2.4‰, Py-1b ranged from 0.6‰ to 5.6‰ with an average value of 2.8‰ and analysis of Py-2 returned values of -1.4‰ and 3.9‰ with an average of 1.25‰. A total of 14 analyses are reported from two generations of pyrite from the Pakaka deposit, consisting of 12 analyses of Py-1b and 2 analyses of Py-2.

Table 8.1: Analytical data for material from the Karagba-Chaffeur-Durba (KCD) deposit. $\delta^{34}\text{S}$ values are presented as ‰ VCDT. L/C column indicates whether analysis was by Laser ablation (L) or conventional (C) analytical method.

Deposit	Analysis ID	Sample ID	Hole ID	Depth (m)	Lode	grade (g/t)	Sulphide Type	L/C	$\delta^{34}\text{S}$
KCD	PB12-D01A-a	PB12-D01A	DGT003	503.04	9000	\	Py-1a	L	5.5
KCD	PB12-D01A-b	PB12-D01A	DGT003	503.04	9000		Py-1b	L	4.7
KCD	PB12-D01B-a	PB12-D01A	DGT003	503.04	9000		Py-1a	L	5.1
KCD	PB12-D01B-b	PB12-D01A	DGT003	503.04	9000		Py-1b	L	5.6
KCD	PB12-D03	PB12-D03	DGT003	524	9000	\	Py-1	C	2.8
KCD	PB12-D08a	PB12-D08	DDD466	552.89	5000	\	Py-1	C	3.3
KCD	PB12-D08B	PB12-D08	DDD466	552.89	5000	\	Py-1	C	2.5
KCD	PB12-D09a	PB12-D09	DDD466	589.1	5000	\	Py-1b	L	4.0
KCD	PB12-D09b	PB12-D09	DDD466	589.1	5000	\	Py-1a	L	3.9
KCD	PB12-D09c	PB12-D09	DDD466	589.1	5000	\	Py-1b	L	3.6
KCD	PB12-D11	PB12-D11	DGT004	229.38	5000	\	Py-1	C	2.2
KCD	PB12-D12	PB12-D12	DGT004	522.91	9000	\	Py-1	C	2.5
KCD	2013-D1	2013-D1	DDD542	267.88	3000	10.1	Py-1b	L	5.0
KCD	2013-D2a	2013-D2	DDD542	274.48	3000	5.2	Py-1b	L	6.7
KCD	2013-D2b	2013-D2	DDD542	274.48	3000	5.2	Py-2	L	6.6
KCD	2013-D5a	2013-D5	DDD542	290.7	3000	5.4	Py-1b	L	6.5
KCD	2013-D5b	2013-D5	DDD542	290.7	3000	5.4	Py-2	L	3.8
KCD	2013-D8	2013-D8	DDD542	361.69	9000	9.9	Py-1b	L	4.2
KCD	2013-D10	2013-D10	DDD542	171.17	3000	0.1	Py-1b	L	7.5
KCD	2013-D12	2013-D12	DDD503A	311.94	9000	0.0	Py-1b	L	4.5
KCD	2013-D14	2013-D14	DDD503A	364.4	9000	11.1	Py-1b	L	6.3
KCD	2013-D22a	2013-D22	DDD503A	364.56	9000	11.1	Py-1a	L	7.1
KCD	2013-D22b	2013-D22	DDD503A	364.56	9000	11.1	Py-1b	L	6.8
KCD	2013-D24	2013-D24	DDD503A	290.56	9000	5.4	Py-1b	L	5.6
KCD	2013-D35	2013-D35	DDD333	296.95	5000	16.1	Py-1b	L	5.9
KCD	2013-D40	2013-D40	DDD333	342.13	9000	2.7	Py-1b	L	7.1
KCD	2013-D42	2013-D42	DDD333	353.55	9000	1.2	Py-1b	L	5.9
KCD	2013-D44	2013-D44	DDD333	358.6	9000	3.1	Py-1b	L	7.2

Table 8.1 (continued):

Deposit	Analysis ID	Sample ID	Hole ID	Depth (m)	Lode	grade (g/t)	Sulphide Type	L/C	34S
KCD	2013-D57	2013-D57	DDD423	155.24	5000	25.4	Py-1b	L	6.3
KCD	2013-D60	2013-D60	DDD423	171.48	5000	3.3	Py-1b	L	1.7
KCD	2013-D70a	2013-D70	DDD464	161.28	5000	7.0	Py-1a	L	5.0
KCD	2013-D70b	2013-D70	DDD464	161.28	5000	7.0	Py-1b	L	6.7
KCD	2013-D70c	2013-D70	DDD464	161.28	5000	7.0	Py-1b	L	6.4
KCD	2013-D87	2013-D87	DDD464	416.36	9000	/	Py-1b	L	3.5
KCD	2013-D90	2013-D90	DDD464	418.74	9000	2.0	Py-1b	L	4.2
KCD	2013-D92a	2013-D92	DDD464	420.6	9000	2.7	Py-1b	L	4.4
KCD	2013-D92b	2013-D92	DDD464	420.6	9000	2.7	Py-2	L	4.7
KCD	2013-D97a	2013-D97	DDD464	448.32	9000	27.7	Py-1b	L	6.4
KCD	2013-D97b	2013-D97	DDD464	448.32	9000	27.7	Py-2	L	5.9
KCD	2013-D98	2013-D98	DDD464	452.15	9000	7.4	Py-1b	C	4.4
KCD	2013-D102	2013-D102	DDD464	460.64	9000	0.2	Py-1b	L	4.9
KCD	2013-D108	2013-D108	DDD464	500.18	9000	1.8	Py-1b	L	3.9
KCD	2013-D111	2013-D111	DDD464	507.84	9000	1.0	Py-1b	L	6.6
KCD	KCD05	KCD05B	DDD531A	255.2	3000	\	Py-1b	L	4.7
KCD	KCD07	KCD07	DDD531A	433.6	9000	44.8	Py-1b	L	5.0
KCD	KCD11	KCD11	DDD531A	551.9	9000	23.6	Py-1b	L	5.4
KCD	KCD12	KCD12	DDD531A	566.9	9000	3.0	Py-1b	L	5.0
KCD	KCD15	KCD15	DDD531A	790	9000	1.8	Py-1b	L	5.2
KCD	KCD19	KCD19	DDD292	181	9000	1.5	Py-1b	L	2.6
KCD	KCD20	KCD20	DDD292	482	9000	4.1	Py-1b	L	4.3
KCD	KCD20b	KCD20	DDD292	482	9000	4.1	Py-1b	L	2.7
KCD	KCD21	KCD21	DDD292	537	9000	18.0	Py-1b	L	4.7
KCD	KCD22b	KCD22b	DDD292	538.8	9000	1.8	Py-1b	L	5.7
KCD	KCD23b	KCD23B	DDD292	544.6	9000	25.4	Py-1b	L	5.4
KCD	KCD23a	KCD23	DDD292	544.6	9000	25.4	Py-1b	L	3.3
KCD	KCD25	KCD25	DGT011	465	9000	36.5	Py-1b	L	3.8

Table 8.2: Analytical data for material from the Mengu deposit. $\delta^{34}\text{S}$ values are presented as ‰ VCDT. L/C column indicates whether analysis was by Laser ablation (L) or conventional (C) analytical method.

Deposit	Analysis ID	Sample ID	Hole ID	Depth (m)	grade (g/t)	Sulphide Generation	L/C	$\delta^{34}\text{S}$
Mengu	PB12-M02	PB12-M02	MDD036	168.71	5.99	Py-1b	L	3.2
Mengu	PB12-M04	PB12-M04	MDD036	186.12	6.78	Py-1b	L	2.4
Mengu	PB12-M06a	PB12-M06	MDD036	202.82	15.86	Py-1b	L	3.0
Mengu	PB12-M06b	PB12-M06	MDD036	202.82	15.86	Py-2	C	-1.4
Mengu	PB12-M06c	PB12-M06	MDD036	202.82	15.86	Py-1b	L	0.9
Mengu	PB12-M07-a	PB12-M07	MDD036	210.05	6.86	Py-1b	L	0.6
Mengu	PB12-M07-b	PB12-M07	MDD036	210.05	6.86	Py-1b	L	1.5
Mengu	PB12-M09	PB12-M09	MDD036	219.3	7.71	Py1b	L	2.2
Mengu	2013-M4-a	2013-M4	MDD019	57.85	4.17	Py-1b	L	2.6
Mengu	2013-M4-b	2013-M4	MDD019	57.85	4.17	Py-1b	L	1.4
Mengu	2013-M13A	2013-M13	MDD031	28.38	\	Py-1b	L	4.9
Mengu	2013-M13B-a	2013-M13	MDD031	28.38	\	Py-1b	L	5.4
Mengu	2013-M13B-b	2013-M13	MDD031	28.38	\	Py-1b	L	5.6
Mengu	2013-M18A-a	2013-M18	MDD031	69.9	\	Py-1b	L	3.1
Mengu	2013-M18A-b	2013-M18	MDD031	69.9	\	Py-2	L	3.9
Mengu	2013-M18B-a	2013-M18	MDD031	69.9	\	Py-1a	L	2.4
Mengu	2013-M18B-b	2013-M18	MDD031	69.9	\	Py-1b	L	2.7

Table 8.3: Analytical data for material from the Pakaka deposit $\delta^{34}\text{S}$ values are presented as ‰ VCDT. L/C column indicates whether analysis was by Laser ablation (L) or conventional (C) analytical method.

Deposit	Analysis ID	Sample ID	Hole ID	Depth (m)	grade (g/t)	Sulphide type	L/C	$\delta^{34}\text{S}$
Pakaka	2013-P11	2013-P11	PDD072	235.79	1.27	Py-1b	L	5.2
Pakaka	2013-P13	2013-P13	PDD072	236.22	15.32	Py-1b	L	3.5
Pakaka	2013-P15	2013-P15	PDD072	239.9	1.19	Py-1b	L	4.7
Pakaka	2013-P42	2013-P42	PDD058	171.04	6.79	Py-1b	L	4.4
Pakaka	PB12-PK02A-a	PB12-PK02	PDD084	132.62	3.18	Py-1b	L	4.8
Pakaka	PB12-PK02A-b	PB12-PK02	PDD084	132.62	3.18	Py-2	L	4.4
Pakaka	PB12-PK02B-a	PB12-PK02	PDD084	132.62	3.18	Py-1b	L	3.5
Pakaka	PB12-PK02B-b	PB12-PK02	PDD084	132.62	3.18	Py-2	L	4.8
Pakaka	PB12-PK11	PB12-PK11	PDD100	114.05	29.2	Py-1b	L	4.6
Pakaka	PB12-PK13	PB12-PK13	PDD088	159.7	5.27	Py-1b	L	5.9
Pakaka	PB12-PK14A	PB12-PK14	PDD088	167.15	12.16	Py-1b	L	6.2
Pakaka	PB12-PK14B	PB12-PK14	PDD088	167.15	12.16	Py-1b	L	4.4
Pakaka	2013-P12	2013-P12	PDD072	235.98	1.27	Py-1b	L	3.6
Pakaka	2013-P19	2013-P19	PDD140	330.54	-	Py-1b	L	4.6

Table 8.4: Analytical data for material from the Pamao deposit. $\delta^{34}\text{S}$ values are presented as ‰ VCDT. L/C column indicates whether analysis was by Laser ablation (L) or conventional (C) analytical method.

Deposit	Analysis ID	Sample ID	Hole ID	Depth (m)	grade (g/t)	Sulphide type	L/C	$\delta^{34}\text{S}$
Pamao	PB12-PM01	PB12-PM01	PMDD006	76.525	3.66	Py1b	L	4.3
Pamao	PB12-PM02	PB12-PM02	PMDD006	78.51	7.72	Py1b	L	4.0
Pamao	PB12-PM08-a	PB12-PM08-a	PMDD008	115.28	0.65	Py1b	L	6.4
Pamao	PB12-PM08-b	PB12-PM08-b	PMDD008	115.28	0.65	Py1b	L	4.5
Pamao	PB12-PM09	PB12-PM09	PMDD008	117.33	0.44	Py1b	L	5.0
Pamao	2013-PM7	2013-PM7	PMDD002	64.21	2.84	Py1b	L	4.1
Pamao	2013-PM8	2013-PM8	PMDD002	64.65	2.84	Py1b	L	4.2
Pamao	2013-PM12	2013-PM12	PMDD002	81	1.12	Py1b	L	3.2

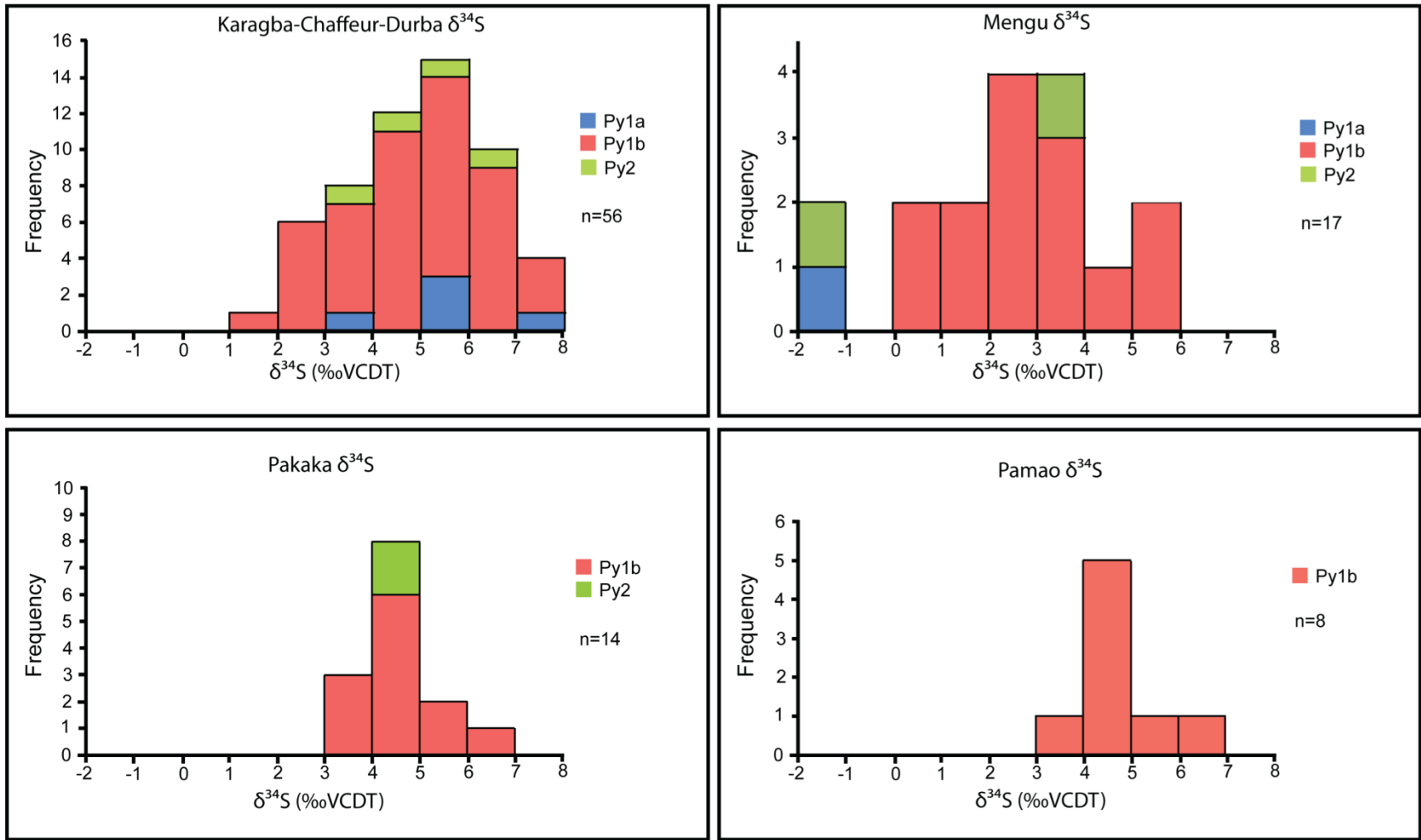


Figure 8.2: Histograms displaying $\delta^{34}\text{S}$ data from the KCD, Mengu, Pakaka and Pamao gold deposits

Across the Pakaka deposit $\delta^{34}\text{S}$ values range from 3.5‰ to 6.2‰ with an average value of 4.6‰. Examining the two sulphide generations individually shows Py-1b ranging in composition from 3.5‰ to 6.2‰ with an average value of 4.6‰, with the two analyses of Py2 returning values of 4.4‰ and 4.8‰ with an average value of 4.6‰. Eight analyses are presented from the Pamao deposit, all of these being from the Py-1b generation. Data for the Py-1b analyses ranges from 3.2‰ to 6.4‰ with an average value of 4.5‰.

8.5 Discussion

The $\delta^{34}\text{S}$ characteristics of the four deposits have a similar data distribution, with each deposit showing a significant degree of internal heterogeneity but with a strong degree of overlap with the other deposits (Fig. 8.2). The Pakaka and Pamao deposits display the strongest similarities, the data defining a relatively restricted range of $\delta^{34}\text{S}$ values between 3.5 and 6.2‰ (Pakaka) and 3.2 and 6.4‰ (Pamao), with similar internal distributions, the majority of data falling in the 3 to 4‰ interval. The KCD and Mengu deposits display a wider distribution of data, the KCD ranging from 1.7 to 7.5‰ and Mengu from -1.4 to 5.6‰. The data from the KCD shows a normal distribution peaking between 5 and 6‰, while Mengu defines a curve peaking in the interval 2 and 4‰. Though some slight differences in the $\delta^{34}\text{S}$ characteristics are identified, principally the marginal offset of the Mengu data towards lighter $\delta^{34}\text{S}$ values and the significant degree of overlap between all four data sets is interpreted as indicating the deposits formed from fluids with similar $\delta^{34}\text{S}$ isotope characteristics and a common sulfur source. The observed variations are considered to be the result of either variations in the composition of the source region or the effect of the differing sulfur isotope compositions of the host lithologies although, without direct measurement of the host rock $\delta^{34}\text{S}$ characteristics, this cannot be confirmed. Due to analytical restrictions, the distribution of data is heavily biased with the majority of data from the Py1b mineral phase. The limited number of measurements from the Py1a and Py2 mineral phases show a similar distribution of data to that displayed by the Py1b phase. This makes it probable that the three sulphide generations were formed from the same geological fluid, however further analysis and the construction of a more robust data set will be required to confirm this.

In considering the origin of the analysed sulfur, the broad range defined by the four deposits (-1.4‰ to 7.5‰) overlaps with the $\delta^{34}\text{S}$ characteristics of several known sulfur reservoirs (Fig. 8.1) including igneous lithologies, hydrocarbons and sedimentary sources (Faure and Mensing, 2005; Seal, 2006) and is comparable to $\delta^{34}\text{S}$ values reported from a range of Archean, Proterozoic and Phanerozoic orogenic gold deposits (Fig. 8.1). It was hypothesised in chapter 7 that metamorphic devolatilisation of the thrust stack was the source of the fluids from which the ore phases were derived. This thrust stack is likely composed of a range of lithologies similar to those identified in the modern Kibali Granite-Greenstone Belt, including basalts, carbonaceous shales and variable volcano-sedimentary conglomerates formed within an Archean

oceanic back arc basin (Chapters 4-6). In modern oceanic settings, biogenic processes result in the fractionation of $\delta^{34}\text{S}$ towards lighter values, although Cameron (1982) demonstrated that sulphate reducing bacteria only became significant in the fractionation of sulfur at approximately 2.3 Ga (Cameron, 1982). The U:Pb zircon data derived from the intrusive phases within the Kibali Granite-Greenstone belt bracketed the proto Kibalian basin at >2.63 Ga (Chapter 5). Sediments formed in the Kibalian basin will therefore not have been significantly affected by sulphate reducing bacteria. As a result, the isotopic components of the sediments should be expected to be heavily influenced by their primary source: in the case of the Kibalian meta-sediments a primarily igneous signature consistent with the observed values. The majority of the lithologies within the Kibali Granite-Greenstone Belt are considered to have formed in an oceanic back arc environment; as such a seawater sulfur component is likely to have had a significant influence of the $\delta^{34}\text{S}$ characteristics of the belt lithologies. The characteristics of Archean sea water are not well established and as such it is not possible to quantify their influence.

8.6 Conclusions

The data set presented is the first time the $\delta^{34}\text{S}$ isotopic characteristics of the auriferous sulphide phases at the major gold deposits in the Kibali Granite-Greenstone Belt have been investigated. The isotopic characteristics of the four deposits are strongly similar and are interpreted as indicating a common source of sulfur for the deposits, hypothesised to be the Kibalian meta-sediments and basalts.

The $\delta^{34}\text{S}$ study was predominantly restricted to the Py-1b mineral phase and as such the data is not representative of the deposits as a whole. Any further study of the deposits should focus on diversifying the data set and generating $\delta^{34}\text{S}$ values for the other sulphide generations (multiple generations of pyrite, chalcopyrite and arsenopyrite are present within all four deposits). This additional data would facilitate the modelling of the evolution of the $\delta^{34}\text{S}$ component and temperatures within the mineralising fluids and also provide a more meaningful contrast between the deposits, the proportions of the major sulphide phases being one of the major variables between the four deposits. Any further study of the $\delta^{34}\text{S}$ characteristics will also benefit from the determination of the $\delta^{34}\text{S}$ values of the major lithological units in the Kibali Granite-Greenstone Belt, this data providing realistic values for the $\delta^{34}\text{S}$ characteristics of the hypothesised source region with which to compare the values derived from the sulphides.

Chapter 9. Constraining the age of mineralisation at the Kibali Gold project: U-Th-Pb dating of monazite

9.1 Introduction

Investigation of the geochronological evolution of the Kibali Granite-Greenstone Belt (KGGB) and its neighbouring terranes identified two distinct windows of geological time in which orogenesis, with associated thermal flux and associated large scale fluid flow occurred (Chapter 6). To further our understanding of the regional evolution and place the development of mineralisation into this context it is necessary to geochronologically constrain the formation of mineralised lodes. Accurately dating mineralisation has historically been difficult due to a lack of suitable geochronometers and analytical techniques with sufficient spatial resolution and precision to allow in situ analysis of phases directly associated with mineralisation. In situ analysis of monazite within hydrothermal mineral systems has been utilised in multiple studies to provide accurate dates for the development of economic mineralisation in orogenic type gold deposits (Salier et al., 2004; Rasmussen et al., 2006; Vielreicher, 2010). Laser Ablation-ICP-MS analysis of the U-Th-Pb Monazite system has here been used here to generate ages for the growth of monazite associated with ore-bearing phases at the KCD, Pakaka and Pamao gold deposits. The dating of multiple deposits will allow us to additionally determine if mineralisation developed in each deposit as a discrete event or simultaneously as part of a district wide mineralising event.

9.2 Structure and Chemistry of Monazite

The U-Th-Pb decay system and the behaviour of Uranium and thorium within geological systems have been reviewed elsewhere (Chapter 6) and shall not be discussed any further here.

Monazite is an orthophosphate mineral that is commonly found as an accessory phase within igneous and metamorphic lithologies as well as mineralised systems such as quartz veins and pegmatites. Monazite occurs in the form $A(PO_4)$ where the A site is occupied by a range of light rare earth elements, La, Ce and Nd being common components (Boatner, 2002). The internal structure of monazite consists of chains of alternating PO_4 tetrahedra and polyhedra of rare earth cations in nine fold coordination with oxygen (Boatner, 2002). Inclusion of uranium and thorium within monazite occurs through two mechanisms, huttonic substitution through substitution of $REE^{3+}P^{5+}$ by $Th^{4+}Si^{4+}$ or $U^{4+}Si^{4+}$ and brabantite substitution through substitution of $2REE^{3+}$ by $Ca^{2+}Th^{4+}$ or $Ca^{2+}U^{4+}$ with a solid solution series hypothesised to exist with the two mechanisms of substitution forming the end members (Harrison et al., 2002). The A site in which radioactive elements are hosted is capable of hosting all daughter isotopes produced through the Uranium/Thorium-Lead decay series including the final Pb daughter elements (Boatner, 2002; Harrison et

al., 2002). The incorporation of common lead, ^{204}Pb , at the 'A' site during formation may also occur and must be corrected for during U-Pb analysis. As with other mineral phases that host radioactive nucleoids, lattice damage and metamictisation caused by alpha particle recoil during radioactive decay and its effect on the mobility of daughter elements within the monazite phase must be considered (Boatner, 2002; Harrison et al., 2002).

The capability of the monazite to retain both parent and daughter nucleoids has led to its widespread use in geochronological studies examining deformed and metamorphosed rocks (Pyle and Spear, 2003; Mahan et al., 2006) and hydrothermal gold systems (Salier et al., 2004; Rasmussen et al., 2006; Vielreicher, 2010). To properly utilise monazite in geochronological studies the stability and robustness of the U-Th-Pb isotope system within monazite must be considered. Recent studies have determined that the closure temperature of monazite, the temperature at which ion exchange with a surrounding medium no longer occurs, is approximately 900°C (Cherniak et al., 2004; Cherniak and Pyle, 2008; Cherniak, 2010) making it one of the most stable minerals.

Studies of monazite have observed that crystals primarily occur in highly crystalline form with little evidence of metamictization as would be expected from a mineral containing significant volumes of radioactive elements. This characteristic is attributed to a low temperature annealing process which acts to repair lattice damage. As such dissolution rates within monazite are low and the problems of radiation damage and metamictization experienced by other uranium-bearing mineral phases are less of a concern (Boatner, 2002). These characteristics have made monazite the preferred material for use in investigating deformed and metamorphosed material where monazite has retained its primary characteristics (Dumond et al., 2008; Mahan et al., 2006; Williams and Jercinovic, 2002) Recent studies have identified conditions under which U-Th-Pb compositions of monazite can be modified or reset resulting in incorrect age determinations with fluid moderated coupled dissolution reprecipitation reactions being the favoured mechanism by which this occurs (Teufel and Heinrich, 1997; Harlov et al., 2007, 2011; Cherniak and Pyle, 2008; Crowley et al., 2008; Harlov and Hetherington, 2010; Williams et al., 2011). The identification of this process has particular relevance for hydrothermal systems where the possibility of the monazites being exposed to high volumes of hydrothermal fluid are high.

9.3 Sample Preparation and Analytical Technique

Monazite was initially identified as an accessory phase in association with Au-bearing pyrite during the investigation of the petrological characteristics of the mineralised systems at the Karagba-Chaffeur-Durba (KCD), Mengu, Pakaka and Pamao Au deposits (Chapter 7). The suitability of samples for analysis was assessed by imaging polished thin sections using a Carl Zeiss EVO 50 scanning electron microscope at

Kingston University. Individual monazite crystals were identified and the size and relationship of the monazite to mineralisation was recorded. To be considered for dating samples were required to contain six or more monazite crystals greater than $15 \mu\text{m}^2$ in size, In addition crystal shape must be conducive to the placing of a $15 \mu\text{m}^2$ round spot on its surface. A total of 50 polished thin sections were assessed and while monazite was identified in the majority of the samples a subset of nine samples were identified as containing the necessary concentration of monazite crystals with the required morphology. Final sample selection consisted of 5 samples from the KCD, 2 samples from Pamao and a single sample from Pakaka. Monazite crystals were identified in samples from the Mengu deposit but no sample met the necessary criteria.

High contrast back scattered SEM imaging was used to identify any internal zoning within monazite crystals though in all cases this was not observed. U-Th-Pb concentrations in monazite were analysed at the NERC isotope Geosciences Laboratories (NIGL), UK by the laser ablation inductively coupled mass spectrometry technique (LA-ICP-MS). The laser ablation technique was selected to allow the analysis of monazite in situ, thereby retaining textural information on the relationship of monazite to the ore phases. Laser ablation was performed using a New Wave Research UP193ss (193 nm) Nd:YAG laser ablation system fitted with a large format cell using a spot size of $15 \mu\text{m}$ and laser parameters set to 5 Hz, 2.2 Jcm^2 , 25 second ablation time with a 10 second 'wash out' period between ablations. U-Pb concentrations were determined using a NuAtom Single collector inductively coupled mass spectrometer with measurements made on a MassCom secondary electron multiplier set to peak jumping mode. The following masses were measured during each analysis ^{202}Hg , $^{204}\text{Pb}+^{204}\text{Hg}$, ^{206}Hg , ^{207}Pb , ^{208}Pb , ^{232}Th and ^{235}U and measurement procedures were consistent with those outlined in Palin et al. (2013). Data processing used Nu instruments software time resolved function, data reduction and uncertainty propagation was performed using an in house spreadsheet. U-Th-Pb data were normalised to primary reference material 'Stern' monazite [$512 \pm 1.9 \text{ Ma}$ (Palin et al., 2013)] with materials 'Manangotry' [$559 \pm 1 \text{ Ma}$ (Palin et al., 2013)] and 'Moacyr' [$515.6 \pm 1.4 \text{ Ma}$ (Palin et al., 2013)] used as secondary reference materials. U-Pb and Th-Pb data was corrected using a ^{207}Pb based common lead correction and an additional correction was made to account for excess ^{206}Pb derived through the decay of ^{230}Th , produced during the ^{238}U - ^{206}Pb decay chain. Uncorrected data was processed and plotted as Terra-Wasserburg plots using the Isoplot V4.14 (Ludwig, 2003) Excel add on to account for the presence of variable amounts of common lead. Collection of U, Th and multiple Pb isotopes during all analyses allows the calculation of independent age determinations using the ^{238}U - ^{206}Pb and ^{232}Th - ^{208}Pb decay systems which are also presented.

9.4 Results

Here the results of the Monazite analysis are presented, a full set of the analytical data is available in Appendix 6.

9.4.1 Karagbe-Chaffeur-Durba (KCD)

9.4.1.1 Sample: PB12-D05

Sample PB12-D05A is composed of pyrite hosted in carbonaceous shale taken from drill hole DDD466. Mineralisation occurs as a series of pyrite-rich veins that cross cut the sample and range in thickness from sub mm to 2 cm in size. Sample D05A consists of a polished thin section across the largest of these mineralised veins. Hydrothermal monazite occurs in the mineralised veins in association with Au-bearing pyrite phases and as isolated crystals within the quartz groundmass. Where associated with pyrite, monazite is observed enclosed by pyrite and partially enclosing pyrite (Fig. 9.1 A-C). 20 monazite crystals matching the analytical criteria were identified. A total of 25 individual analyses were performed, 5 monazite crystals being of sufficient size for two analytical spots. 7 analyses were rejected due to high ^{204}Pb content. All data points are discordant (Fig. 9.2a) constituting a cluster just above concordia with discordance ranging from 7.6-19.5% and an array extending away from the concordia with discordance ranging from 26.3-58.8%. No correlation is observed between degree of discordance and Th/U ratios and as such the data is interpreted as representing a single population. A regression line of the data points yields an intercept age of 511 ± 20 Ma (MSWD=2.2) (Fig. 9.2 A). Individual spot ages show $^{206}\text{Pb}/^{238}\text{U}$ ages ranging from 504 ± 37 to 717 ± 65 Ma, $^{207}\text{Pb}/^{235}\text{U}$ ages ranging from 557 ± 31 to 1739 ± 144 Ma and $^{207}\text{Pb}/^{206}\text{Pb}$ ages ranging from 735 ± 50 to 3364 ± 125 Ma. Corrected $^{232}\text{Th}-^{208}\text{Pb}$ data yield ages ranging from 502.03 ± 30.7 to 567.97 ± 43.9 Ma with an average value of 518 ± 8.4 Ma (MSWD=0.77) (Fig. 9.3 B). Corrected $^{238}\text{U}-^{206}\text{Pb}$ data yield ages ranging from 435.6 ± 28.5 to 552.9 ± 31.9 Ma with an average value of 509 ± 16 (MSWD=3.4) (Fig. 9.3 A).

9.4.1.2 Sample: PB12-D10

Sample PB12-D10 is composed of deformed and mineralised volcano-sedimentary conglomerate from drill hole DGT004. Conglomerate consists of variably sized and stretched quartz clasts separated by mm scale intraclast bands of chlorite extensively replaced by ankerite/siderite. Mineralisation is confined to the intraclast areas and is dominated by Au-bearing pyrite. Hydrothermal monazite is identified exclusively within the mineralised intraclast chlorite bands, occurring in association with quartz, chlorite, ankerite/siderite and pyrite.

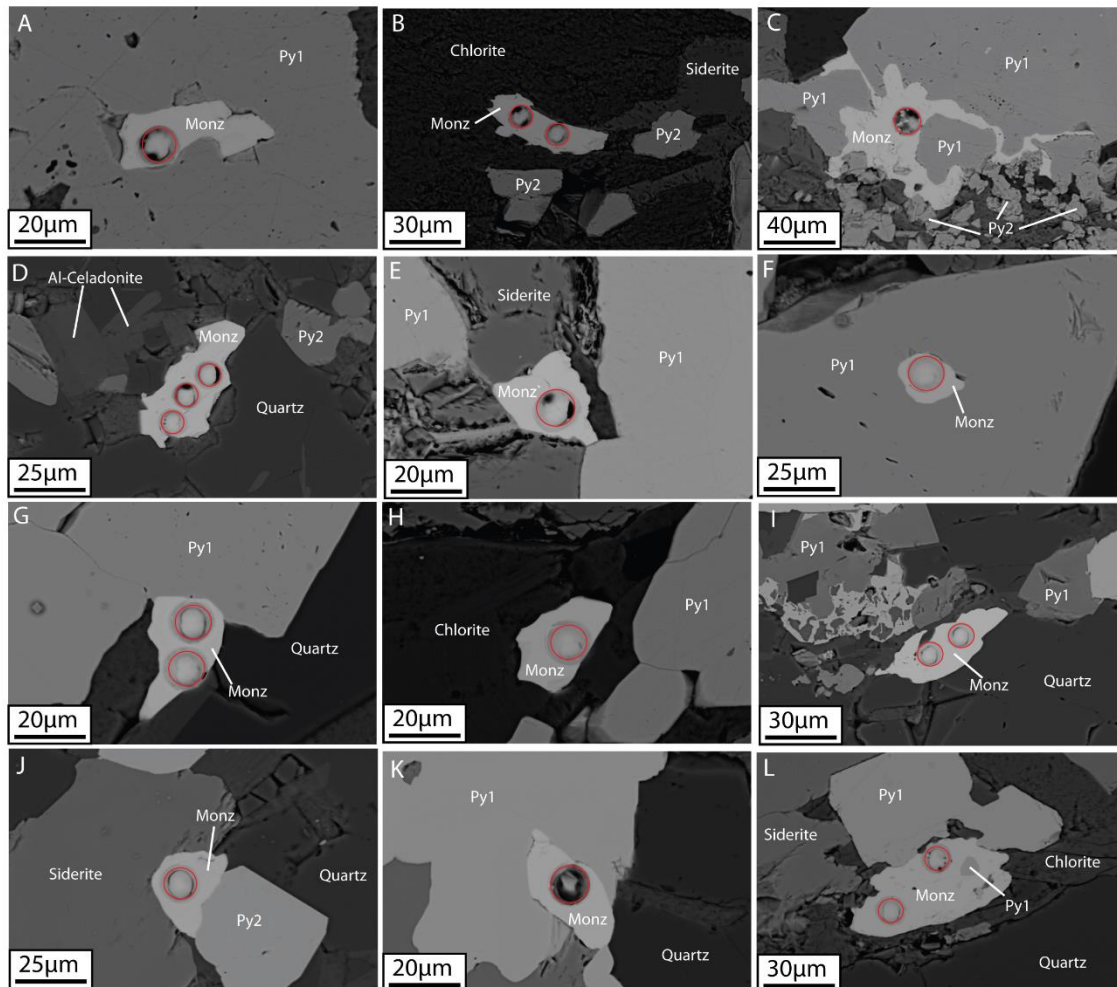


Figure 9.1:

Selected electron micrographs demonstrating mode of occurrence of monazite crystal phase within samples from the KCD deposit. (A-C); sample PB12-D05, (D-E); sample PB12-D10, (F-H); sample PB12-D12, (I-J); sample 2013-D39, K-M; Sample 2013-D57. Monazite is identified in four modes of occurrence, Enclosed or partially enclosed by Au-bearing pyrite (images A,F,G and K), enclosing auriferous pyrite (Images C and L), intergrown with pyrite (images E and J) and isolated within the groundmass in association with phyllosilicate (aluminoceladonite and chlorite)-rich zones (Images B,D,H and I). In all cases monazite was identified within areas interpreted as regions of high fluid flow related to the development of hydrothermal mineralisation. Red circles indicate ablation spots used in generating age data

Monazite is observed primarily as isolated crystals within the groundmass (Fig. 9.1 D) and as crystals on the edges of auriferous pyrite (Fig. 9.1 E). 7 monazite crystals matching the analytical criteria were identified. A total of 11 analyses were performed with two monazite crystals being of sufficient size to allow multiple analyses. All data points are included in the interpretation, none having been rejected. All data are discordant constituting a cluster of data points above the concordia line (discordance 10-57%) with a number of outliers (discordance 75-81%) (Fig. 9.2 C). Analyses with high discordance are noted as possessing higher Th/U values (Fig. 9.5) however separation from the lower discordance analyses is not

sufficient that they are interpreted as representing two distinct populations. A regression of this data yields an intercept age of 552 ± 35 Ma (MSWD=4.0) (Fig. 9.2 C). Individual spot ages yield $^{206}\text{Pb}/^{238}\text{U}$ ages ranging from 531 ± 24 to 646 ± 31 Ma, $^{207}\text{Pb}/^{235}\text{U}$ ages ranging from 612 ± 22 to 1597 ± 51 Ma and $^{207}\text{Pb}/^{206}\text{Pb}$ ages ranging from 669 ± 37 to 3275 ± 39 Ma. Corrected $^{232}\text{Th}/^{208}\text{Pb}$ ages yield ages ranging from 549.28 ± 19.3 to 693.02 ± 38.1 Ma with an average value of 587 ± 30 Ma (MSWD=10.5) (Fig. 9.3). Corrected $^{238}\text{U}/^{206}\text{Pb}$ ages yield ages ranging from 474.4 ± 19.9 to 595.1 ± 19.6 Ma with an average value of 537 ± 29 Ma (MSWD=19) (Fig. 9.3 C-D).

9.4.1.3 Sample: PB12-D12

Sample PB12-D12 is composed of deformed and mineralised conglomerate material from drill hole DGT004. Conglomerate consists of 0.5-1.5 cm stretched quartz clasts with intraclast material consisting of chlorite overprinted by extensive ankerite/siderite. Mineralisation dominates the sample occurring as both quartz veins aligned along foliation and as disseminated material within the intraclast areas. Mineralisation consists of Au-bearing pyrite. Hydrothermal monazite is identified within both types of mineralised structure occurring in association with quartz and pyrite in the quartz veins and with chlorite, ankerite/siderite, quartz and pyrite in the intraclast areas. In both mineralisation styles monazite crystals are observed occurring as isolated crystals (Fig. 9.1 H) within the groundmass and in association with Au-bearing pyrite (Fig. 9.1 F-G). Where associated with auriferous pyrite the monazite crystals are observed both partially and fully enclosed by pyrite (Fig. 9.1G-F) and as crystals on the edges of pyrite crystals. 17 monazite crystals matching the analytical criteria were identified, Due to problems locating monazite during analysis only 14 crystals were analysed. 18 analyses were performed with 2 crystals being of sufficient size to allow multiple analyses, 7 data points were rejected based on high common lead content. All data are discordant forming a diffuse cluster of data above the concordia line (discordance 34-64%) with three outliers (discordance 75-80%) (Fig. 9.2 C). A trend is noticed for increasing discordance with increasing Th/U ratio although the data form a continuous series and is considered one population (Fig. 9.5). A regression line through the data yields an intercept of 531 ± 23 Ma. Individual spot ages yield $^{206}\text{Pb}/^{238}\text{U}$ ages ranging from 689 ± 33 to 530 ± 26 Ma, $^{207}\text{Pb}/^{235}\text{U}$ ages ranging from 631 ± 17 to 1691 ± 73 Ma and $^{207}\text{Pb}/^{206}\text{Pb}$ ages ranging from 865 ± 24 to 3339 ± 60 Ma. Corrected $^{232}\text{Th}/^{208}\text{Pb}$ ages yield ages ranging from 537.07 ± 24.4 to 671.71 ± 33.2 Ma with an average age of 580 ± 21 Ma (MSWD=6.8) (Fig. 9.3 E). Corrected $^{238}\text{U}/^{206}\text{Pb}$ ages range from 504.4 ± 20.9 to 594.4 ± 21.1 Ma with an average age of 538 ± 19 Ma (MSWD=9.4) (Fig. 9.3 F).

9.4.1.4 Sample: 2013-D39

Sample 2013-D39 is composed of highly altered conglomeratic material with extensive mineralisation taken from drill hole DDD333. Host conglomerate consists of 0.5-1 cm stretched recrystallized quartz clasts with intraclast areas consisting of mica overprinted by ankerite/siderite. The sample is extensively mineralised with mineralisation focused in the inter-clast areas with additional areas of cross cutting vein type structures with both morphologies dominated by Au-bearing pyrite. Hydrothermal monazite is identified only within the mineralised areas occurring both as isolated crystals within the quartz groundmass (Fig. 9.1 I) associated with chlorite, alunoceladonite and siderite/ankerite, and intergrown with Au-bearing pyrite (Fig. 9.1 J). 10 monazite crystals fitting the analytical criteria were identified however problems identifying crystals during analysis resulted in only 8 crystals being analysed. A total of 12 analyses were performed with four crystals being of sufficient size to allow multiple analyses, 1 data point was rejected on the basis of high common lead content. Eleven data points are discordant with 1 analysis yielding a concordant age. Discordant data form a cluster of 4 points sitting adjacent to the concordia line (discordance 35-60%) with the remainder of the data points forming an increasingly discordant trend (discordance 67-80%) (Fig. 9.2d). The data is interpreted as being composed of a single population. The single concordant data point generates a concordia age of 581 ± 16 Ma (MSWD=0.00037) while a regression through all data points yields an intercept age of 531 ± 23 Ma (MSWD=2.6) (Fig. 9.2 D). Individual spot ages yield $^{206}\text{Pb}/^{238}\text{U}$ ages ranging from 512 ± 34 to 758 ± 55 Ma, $^{207}\text{Pb}/^{235}\text{U}$ ages ranging from 597 ± 30 to 1826 ± 94 Ma and $^{207}\text{Pb}/^{206}\text{Pb}$ ages ranging from 582 ± 46 to 3434 ± 67 Ma. Corrected $^{232}\text{Th}/^{208}\text{Pb}$ values return ages ranging from 549.98 ± 36.7 to 683.32 ± 51.9 Ma with an average age of 597 ± 22 Ma (MSWD=2.5) (Fig. 9.4 B).

9.4.1.5 Sample 2013-D57

Sample 2013-D57 is composed of fine crystalline quartz overprinted by extensive fine ankerite/siderite alteration taken from drill hole DDD423. Quartz and Fe-carbonate alteration is sufficient that it is not possible to determine the protolith. Mineralisation within the sample is extensive and is composed of 2-5 cm wide zones of fine quartz, hosting Au-bearing pyrite. Hydrothermal monazite is identified exclusively within the mineralised areas and is observed occurring as isolated crystals within the quartz groundmass and intergrown with pyrite (Fig. 9.1 K-L). Where intergrown with pyrite monazite is observed both partially enclosed by pyrite (Fig. 9.1k) and on the outer edges of pyrite crystals (Fig. 9.1 I). 11 monazites fitting the analytical criteria were identified. A total of 14 analyses were performed with 5 monazite crystals being of sufficient size to allow multiple analyses, 1 data point was rejected on the basis of high common lead content.

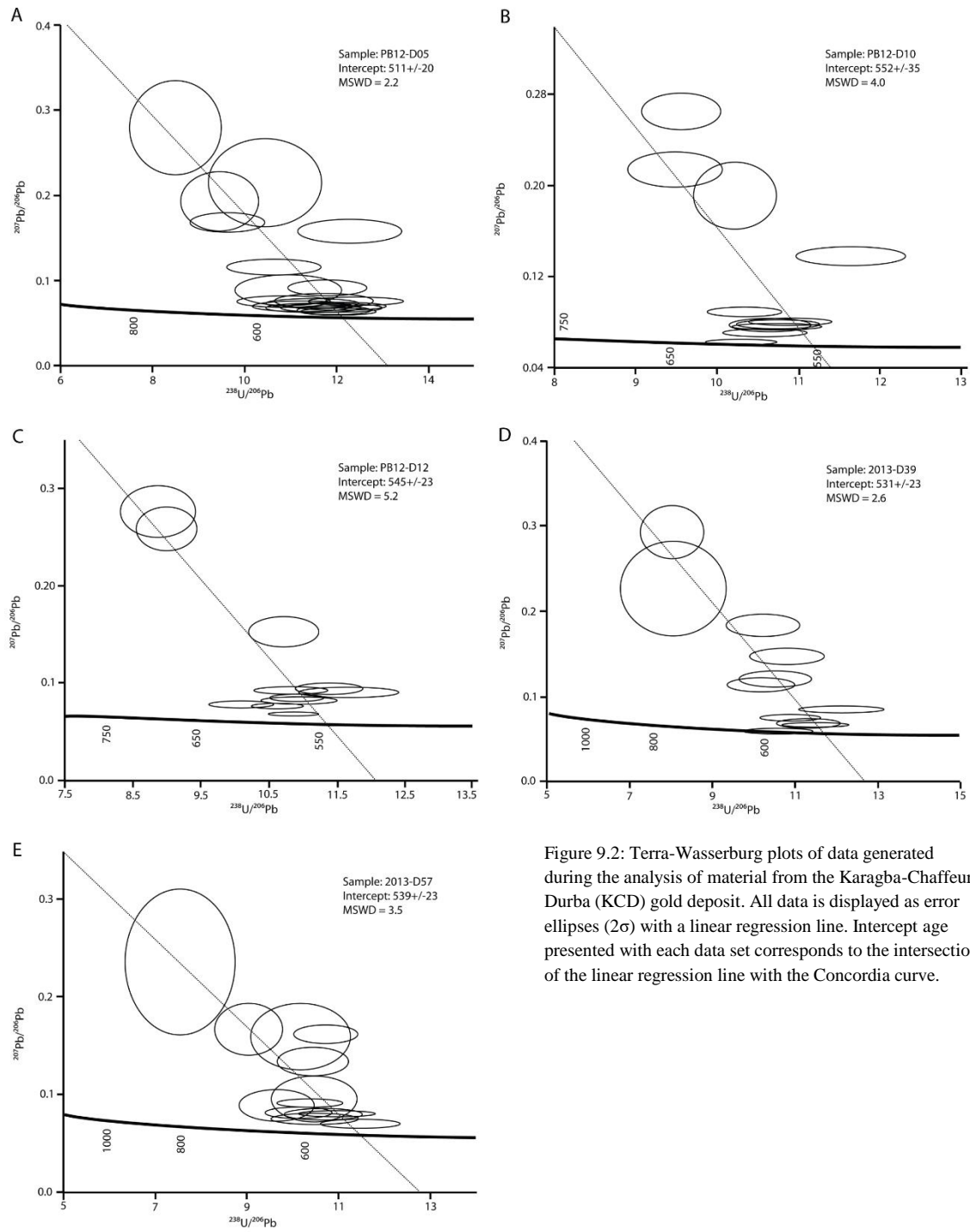


Figure 9.2: Terra-Wasserburg plots of data generated during the analysis of material from the Karagba-Chaffeur-Durba (KCD) gold deposit. All data is displayed as error ellipses (2σ) with a linear regression line. Intercept age presented with each data set corresponds to the intersection of the linear regression line with the Concordia curve.

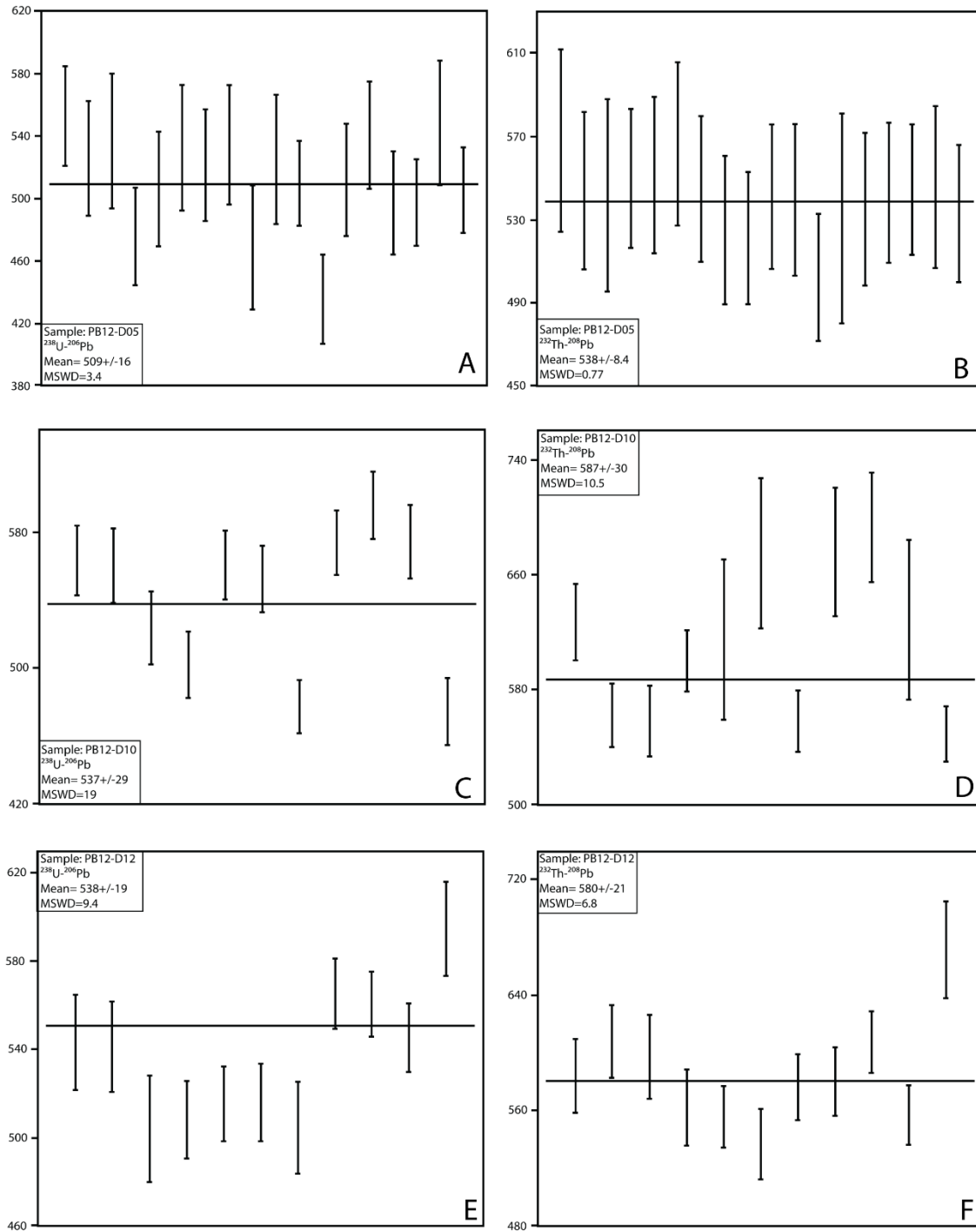


Figure 9.3: Mean Standard weighted distribution plots for samples PB12-D05, PB12-D10 and PB12-D12. Plots were generated from corrected $^{232}\text{Th}/^{207}\text{Pb}$ and $^{232}\text{U}/^{208}\text{Pb}$ ages using Isoplot excel add in (Ludwig, 2001)

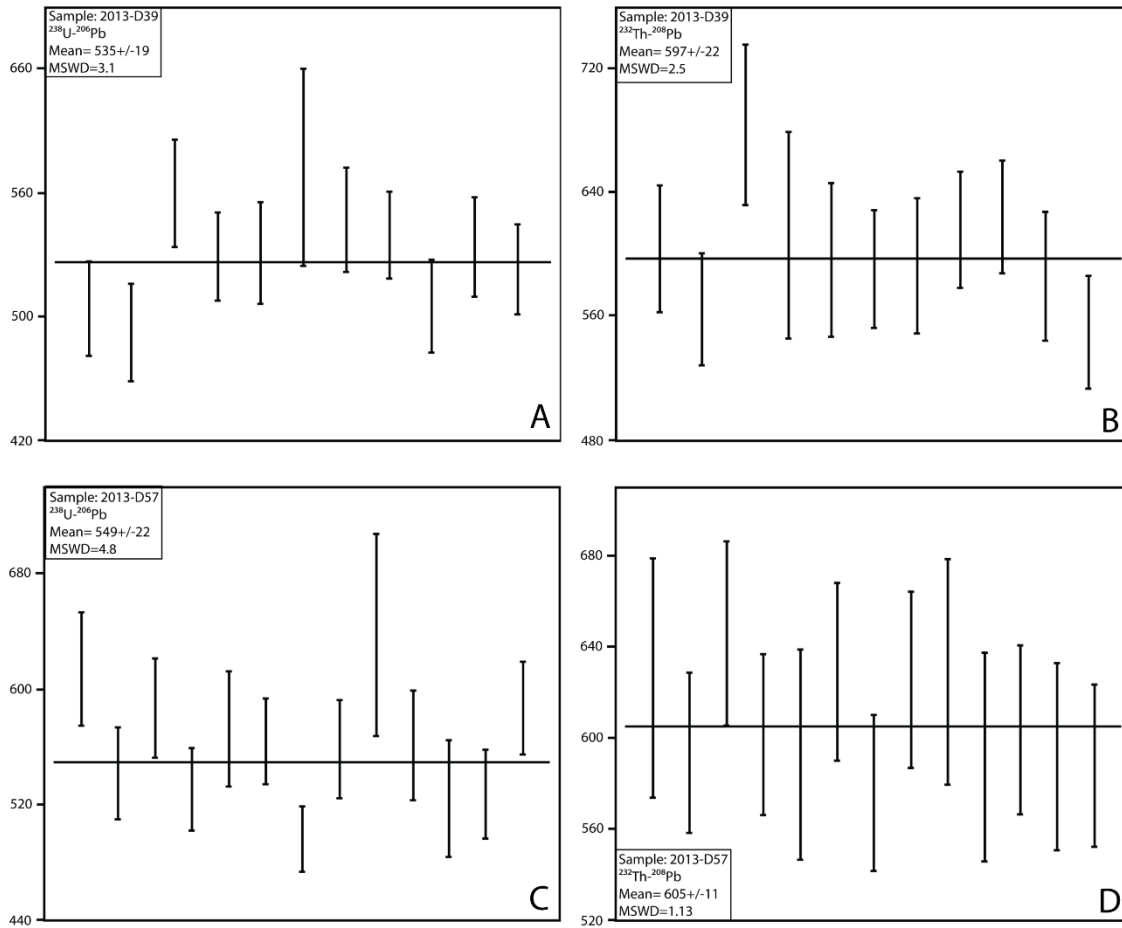


Figure 9.4: Mean Standard weighted distribution plots for samples 2013-D39 and 2013-D57. Plots were generated from corrected $^{232}\text{Th}/^{207}\text{Pb}$ and $^{232}\text{U}/^{208}\text{Pb}$ ages using Isoplot excel add in (Ludwig, 2001)

Corrected $^{238}\text{U}/^{206}\text{Pb}$ ages range from 489.5 ± 31.6 to 597.1 ± 63.9 Ma with an average value of 535 ± 19 Ma (MSWD=3.1) (Fig. 9.4 A).

All analyses return discordant data points consisting of a cluster of data sitting above the concordia line (discordance 41-61%) with the remainder of the analyses forming an array extending away from the concordia line (discordance 72-75%) (Fig. 9.2 E). The data is interpreted as representing a single population. Regression of the discordant data yields an intercept age of 539 ± 23 Ma (MSWD=3.5) (Fig. 9.2 E). Single spot analyses yield $^{206}\text{Pb}/^{238}\text{U}$ ages ranging from 539 ± 32 to 802 ± 97 Ma, $^{207}\text{Pb}/^{235}\text{U}$ ages ranging from 619 ± 37 to 1697 ± 214 Ma and $^{207}\text{Pb}/^{206}\text{Pb}$ ages ranging from 924 ± 55 to 3095 ± 206 Ma. Corrected $^{232}\text{Th}/^{208}\text{Pb}$ ages range from 576.02 ± 34.4 to 646.03 ± 40.5 Ma with an average value of 605 ± 11 Ma (MSWD=1.13) (Fig. 9.4 D). Corrected $^{238}\text{U}/^{206}\text{Pb}$ ages range from 496.2 ± 22.5 to 637.4 ± 70 Ma with an average value of 549 ± 22 Ma (MSWD=4.8) (Fig. 9.4 C).

9.4.2 Pakaka Deposit

9.4.2.1 Sample PB12-PK02

Sample PB12-PK02 is composed of massive quartz clasts set in a silicified fine quartz matrix with rare chlorite, aluminoceladonite and ankerite, sourced from drill hole PDD084. Mineralisation dominates the intraclast areas and is composed primarily of Au-bearing pyrite with other minor sulphide components. Hydrothermal monazite is confined to the mineralised areas occurring as rare isolated crystals embedded within the fine quartz groundmass (Fig. 9.6 A) and more frequently intergrown with pyrite (Fig. 9.6 B-C) occurring on the outer edges of the pyrite crystals. 25 monazites fitting the analytical criteria were identified. A total of 33 analyses were performed with four monazite crystals being of sufficient size to allow multiple analyses. 16 data points were rejected on the basis of high common lead content. All analyses yield discordant data points and form two distinct populations when displayed using the Terra-Wasserburg method (Fig. 9.7), the two populations are also apparent when the Th/U ratios (Fig. 9.5) are examined with population 1 (containing the majority of the data points) displaying lower Th/U ratios in comparison to the smaller population 2, the two populations are therefore considered separately. Population 1 yields a regression intercept age of 558 ± 10 Ma (MSWD=0.55) (Fig. 9.7) with single spot ages for $^{206}\text{Pb}/^{238}\text{U}$ ranging from 554 ± 23 to 643 ± 28 Ma, $^{207}\text{Pb}/^{235}\text{U}$ ages ranging from 576 ± 27 to 1138 ± 65 Ma and $^{207}\text{Pb}/^{206}\text{Pb}$ ages ranging from 652 ± 33 to 2265 ± 75 Ma. Corrected ages for population 1 yield $^{232}\text{Th}/^{208}\text{Pb}$ ages ranging from 530.50 ± 24.2 to 617.08 ± 68.7 Ma with an average of 560 ± 13 Ma (MSWD=1.7) (Fig. 9.8 B) and $^{238}\text{U}/^{206}\text{Pb}$ ages ranging from 540.3 ± 24.7 to 584.4 ± 31.7 Ma with an average value of 561 ± 7 Ma (MSWD=1.12) (Fig. 9.8 A). Population 2 is offset to younger ages relative to population one and yields a regression intercept age of 509 ± 13 Ma (MSWD=0.49) (Fig. 9.7). Single spot ages return values for $^{206}\text{Pb}/^{238}\text{U}$ ranging from 507 ± 19 to 633 ± 29 Ma, $^{207}\text{Pb}/^{235}\text{U}$ ages ranging from 554 ± 26 to 1497 ± 59 Ma and $^{207}\text{Pb}/^{206}\text{Pb}$ ages ranging from 754 ± 48 to 3098 ± 49 Ma. Corrected ages return $^{232}\text{Th}/^{208}\text{Pb}$ ages ranging from 513 ± 24 to 544.24 ± 27 Ma with an average of 525 ± 10 Ma (MSWD=0.84) (Fig. 9.8 C) and $^{238}\text{U}/^{206}\text{Pb}$ ages ranging from 482.2 ± 43 to 514.6 ± 23.1 Ma with an average age of 499.6 ± 8.8 Ma (MSWD=0.665) (Fig. 9.8 D).

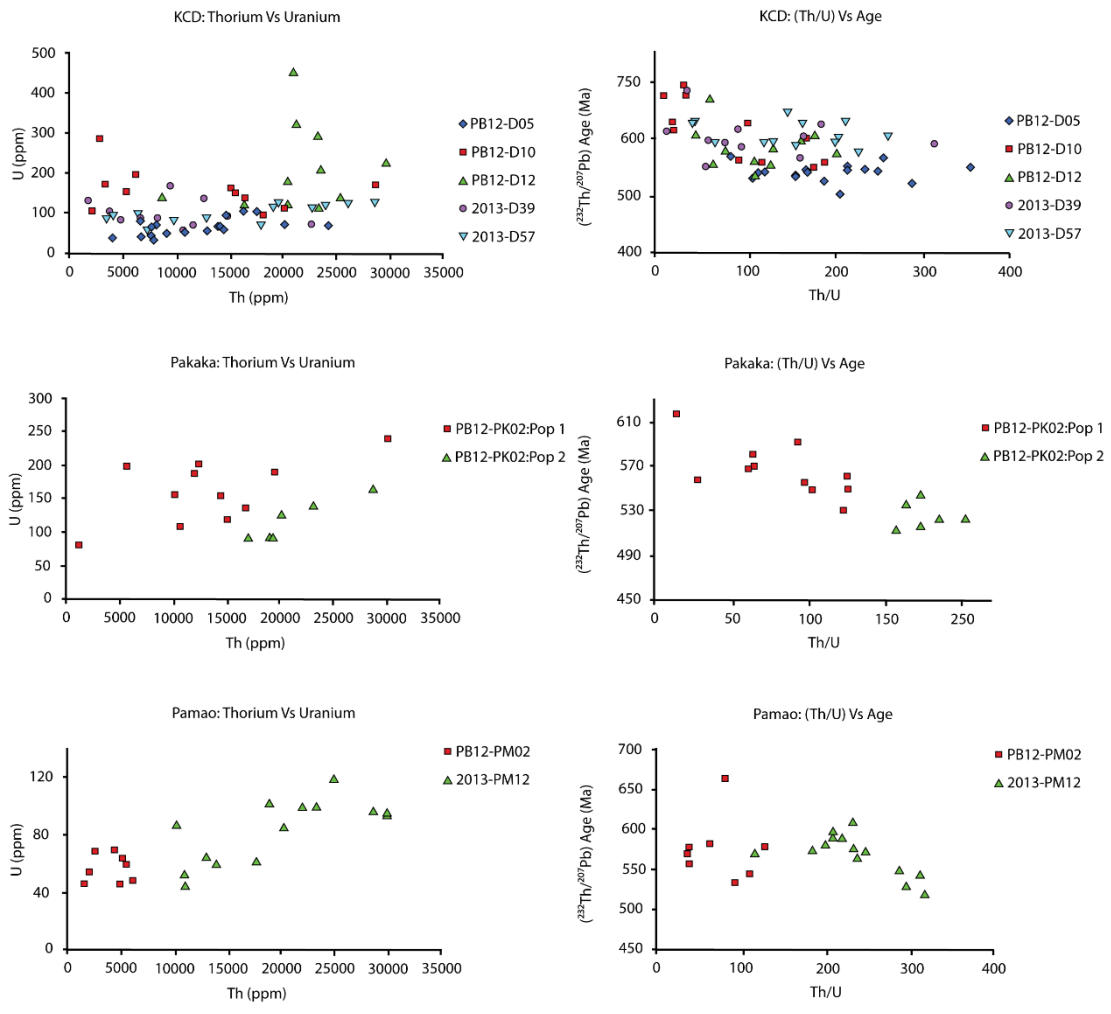


Figure 9.5: Thorium vs uranium and Th/U vs age plots for all data from KCD, Pakaka and Pamao deposits

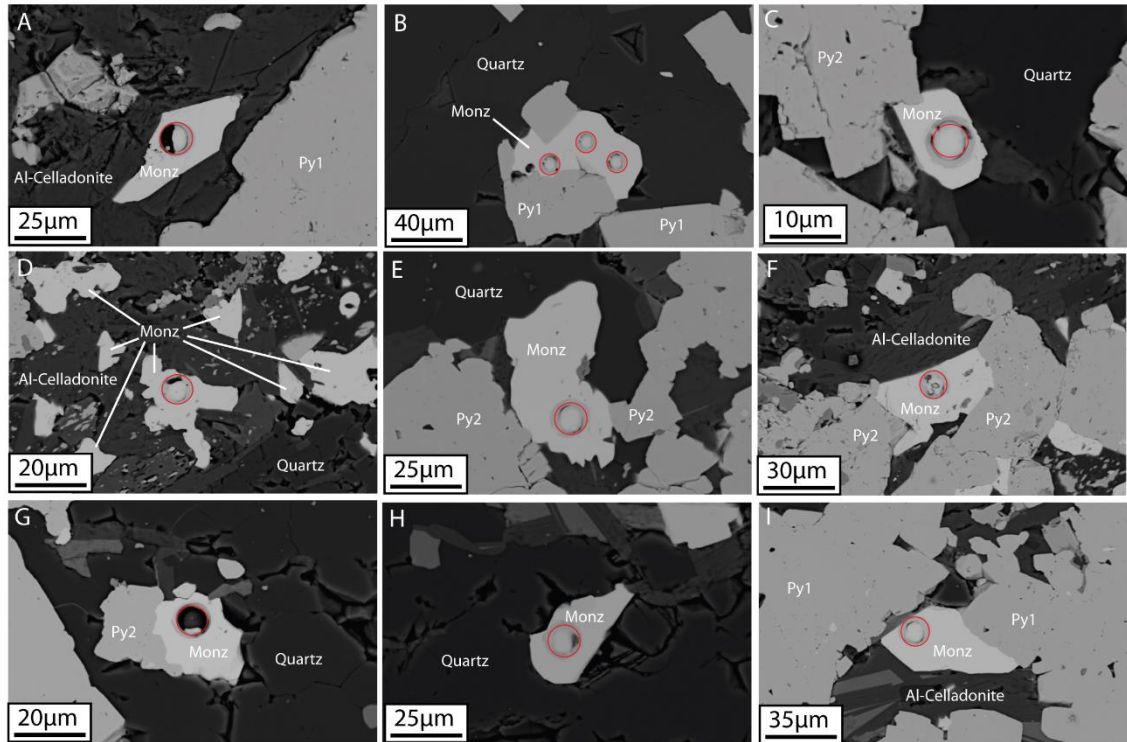


Figure 9.6: Electron micrographs showing the mode of occurrence of monazite phases within samples from Pakaka and Pamao. Images (A-B) sample PB12-PK02, (C-E) sample PB12-PM02, (F-H) sample 2013-PM12. Monazite phase occurs in two distinct modes of occurrence, Intergrown with auriferous pyrite (images B, D,E and H) and within the quartz-mica groundmass (images A, C and D). Image F shows monazite with features that could be interpreted as being enclosed by auriferous pyrite and partly enclosing the neighbouring pyrite crystal. Ablation sites used in age determinations are shown by red circles.

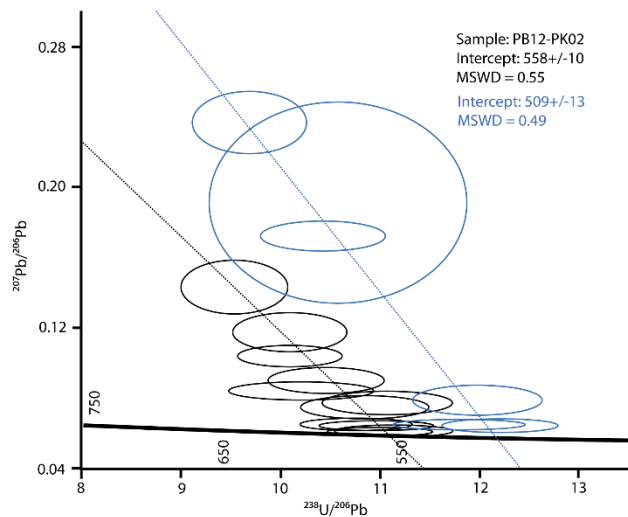


Figure 9.7: Terra-Wasserburg plots of uncorrected data generated during the analysis of material from the Pakaka gold deposit. All data is displayed as error ellipses (2σ) with a linear regression line. Intercept age presented with each data set corresponds to the intersection of the linear regression line with the Concordia curve.

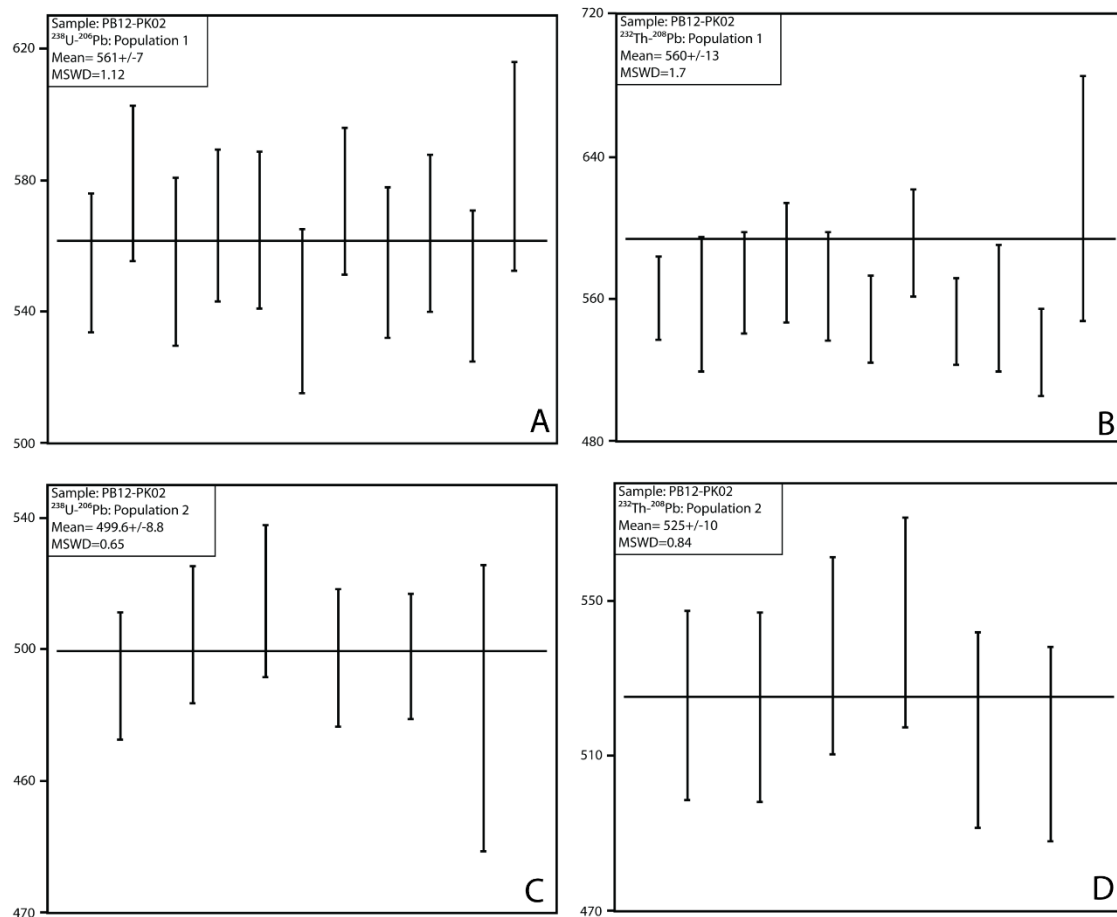


Figure 9.8: Mean Standard weighted distribution plots of data from the Pakaka gold deposit. Plots were generated from corrected $^{232}\text{Th}/^{207}\text{Pb}$ and $^{232}\text{U}/^{208}\text{Pb}$ ages using Isoplot excel add in (Ludwig, 2003)

9.4.3 Pamao Deposit

9.4.3.1 Sample PB12-PM02

Sample PB12-PM02 is composed of altered fine conglomeratic material from drill hole PMDD006. The sample is composed of densely packed, stretched 0.5mm quartz clasts separated by chlorite and aluminoceladonite-rich intraclast structures which vary in thickness from 0.1 to 1 cm. Mineralisation is confined to the intraclast bands occurring in association with chlorite and aluminoceladonite. Mineralisation is dominated by pyrite with minor occurrences of other sulphide species, with arsenopyrite being the most notable of these. Monazite is identified within the mineralised intraclast areas as isolated crystals associated with quartz and chlorite (Fig. 9.6 D) and intergrown with pyrite (Fig. 9.8 E-F). Monazite forms irregular angular to sub angular crystals ranging in size from 5-50 μm . 8 monazite crystals fitting the analytical criteria were identified, 8 analyses were performed with no data points rejected. Two populations are identified within the data based on Th/U ratios (Fig. 9.5). Population 1 displays Th/U ratios between 35 and

65 with population 2 displaying Th/U ratios of 82 to 129. The two populations form parallel arrays when plotted using the Tera-Wasserburg method with population 2 offset to younger $^{238}\text{U}/^{206}\text{Pb}$ values (Fig. 9.9 A). Regression lines for populations 1 and 2 return intercept ages of 581 ± 27 Ma (MSWD=0.015) and 528 ± 34 Ma (MSWD=0.33) respectively (Fig. 9.9 A).

Population 1 single spot ages give values for $^{206}\text{Pb}/^{238}\text{U}$ ranging from 608 ± 34 to 823 ± 54 Ma, $^{207}\text{Pb}/^{235}\text{U}$ ranging from 848 ± 44 to 1880 ± 71 Ma and $^{207}\text{Pb}/^{206}\text{Pb}$ ages ranging from 1541 ± 49 to 3397 ± 39 Ma. Corrected ages return $^{232}\text{Th}/^{208}\text{Pb}$ ages ranging from 556.66 ± 60.4 to 581.83 ± 37.5 Ma with an average value of 575 ± 24 Ma (MSWD=0.18) (Fig. 9.10 A) and $^{238}\text{U}/^{206}\text{Pb}$ ages ranging from 581.4 ± 31.1 to 604.4 ± 30.3 with an average value of 590 ± 16 Ma (Fig. 9.10 B). Population 2 single spot ages for $^{206}\text{Pb}/^{238}\text{U}$ range from 571 ± 37 to 691 ± 46 Ma, $^{207}\text{Pb}/^{235}\text{U}$ ages ranging from 835 ± 54 to 1500 ± 72 and $^{207}\text{Pb}/^{206}\text{Pb}$ ages ranging from 1624 ± 65 to 2957 ± 52 Ma. Corrected $^{232}\text{Th}/^{208}\text{Pb}$ ages range from 533.58 ± 38.8 to 663.37 ± 46.1 Ma with an average value of 575 ± 88 Ma (MSWD=7.1) (Fig. 9.10 C) and $^{238}\text{U}/^{206}\text{Pb}$ ages ranging from 528.1 ± 28.7 to 559.5 ± 31.4 with an average age of 540 ± 16 Ma (MSWD=0.80) (Fig. 9.10 D).

9.4.3.2 Sample 2013-PM12

Sample 2013-PM12 is consists of highly deformed and altered conglomeritic material from drill hole PMDD002. Sample consists of highly stretched and attenuated quartz masses separated by fine sub mm bands composed of quartz, chlorite and aluminoceladonite. Both deformed clasts and intraclast mica bands have been extensively modified by the development of Fe-carbonates prior to the development of mineralisation. Mineralisation is extensively developed within the phyllosilicate-rich intraclast structures and to a lesser degree in the outer edges of the quartz clasts. Mineralisation is dominated by Au-bearing pyrite with minor arsenopyrite also being noted. Monazite is identified solely within the mineralised areas and is confined to the mica-rich intraclast pathways. Monazite is observed occurring as isolated crystals (Fig. 9.6 H) within the phyllosilicate-rich structures associated with quartz and aluminoceladonite and intergrown with mineralised pyrite (Fig. 9.6 G and I). Monazite occurs as irregular angular to sub rounded crystals ranging in size from 20-40 μm in size. 15 monazite crystals fitting the analytical criteria were identified, 15 analyses were performed with one data point rejected due to high common lead values. Analyses form a highly discordant array (discordance ranging from 63 to 79%) when plotted using the Tera-Wasserburg method (Fig. 9.9 B). While several possible linear trends are apparent within the plotted data the data set is interpreted as being composed of a single population as no concurrent trends are observable within the Th/U ratios (Fig. 9.5). Regression of data yields an intercept age of 492 ± 31 Ma (MSWD=2.9) (Fig. 9.9 B), single spot ages yield ages for $^{206}\text{Pb}/^{238}\text{U}$ ranging from 491 ± 23 to 802 ± 52 Ma, $^{207}\text{Pb}/^{235}\text{U}$ ages ranging from 725 ± 55 to 1860 ± 86 Ma and $^{207}\text{Pb}/^{206}\text{Pb}$ ages ranging from 1518 ± 51 to 3274 ± 36 Ma. Corrected

data yields ages for $^{232}\text{Th}/^{208}\text{Pb}$ ranging from 519.56 ± 19.4 to 610 ± 53 Ma with an average value of 564 ± 16 Ma (MSWD=5.1) (Fig. 9.10 E) and $^{238}\text{U}/^{206}\text{Pb}$ ages ranging from 457.9 ± 21.4 to 583.9 ± 37.9 Ma with an average age of 517 ± 20 Ma (MSWD=7.2) (Fig. 9.10 F).

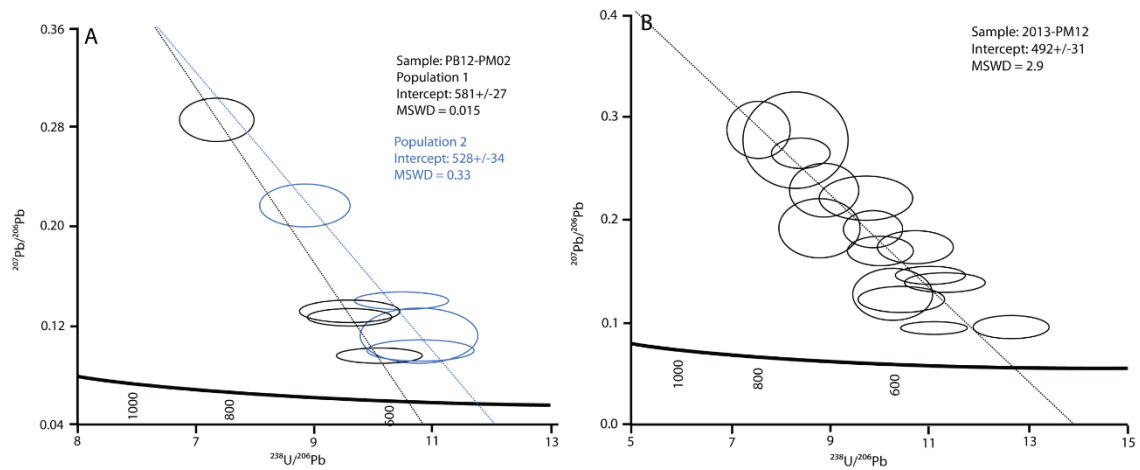


Figure 9.9: Terra-Wasserburg plots of uncorrected data generated during the analysis of material from the Pamao gold deposit. All data is displayed as error ellipses (2σ) with a linear regression line. Intercept age presented with each data set corresponds to the intersection of the linear regression line with the Concordia curve.

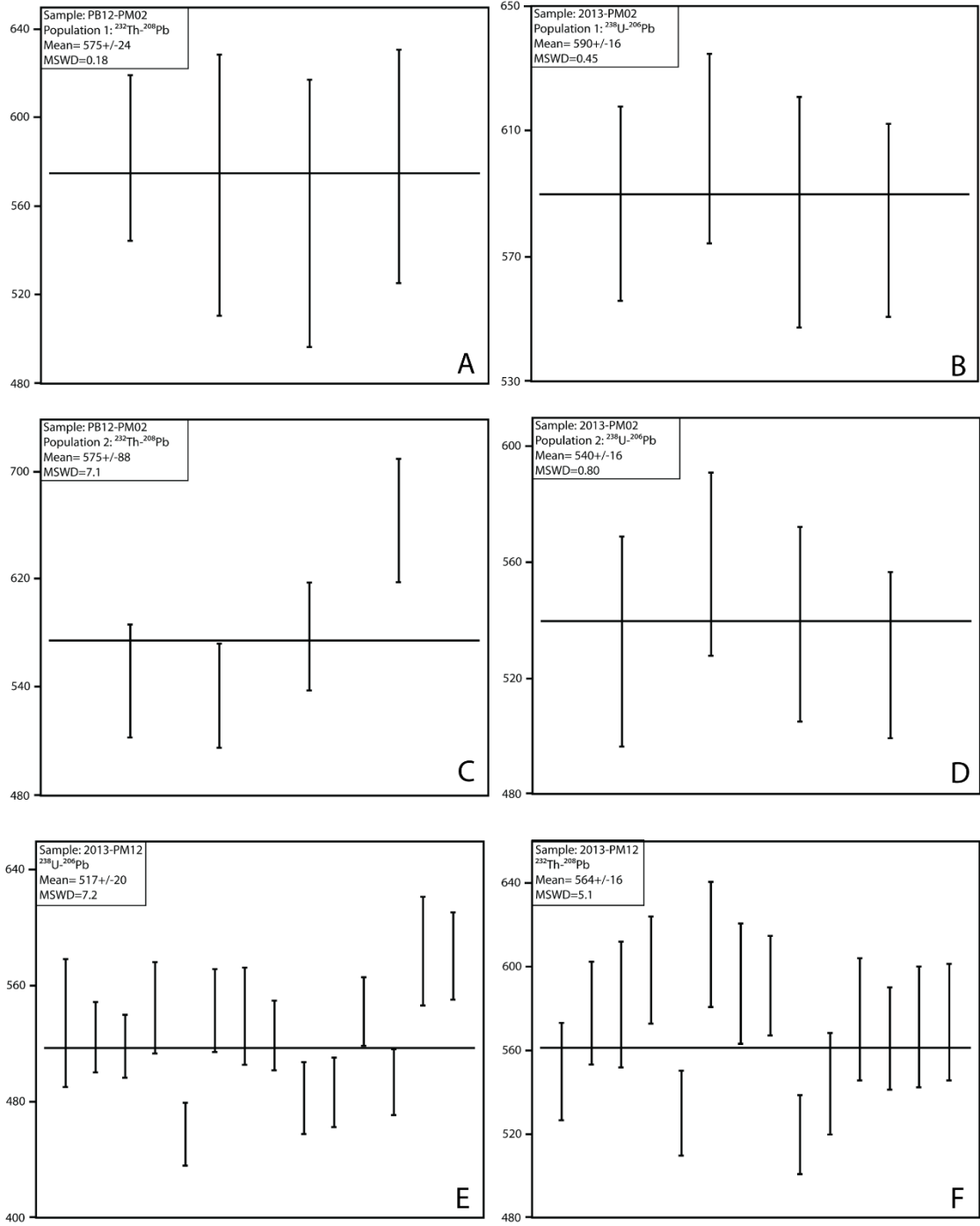


Figure 9.10: Mean Standard weighted distribution plots for samples from the Pamao gold deposit. Plots were generated from corrected $^{232}\text{Th}/^{207}\text{Pb}$ and $^{232}\text{U}/^{208}\text{Pb}$ ages using Isoplot excel add in (Ludwig, 2003)

9.5 Discussion

It is necessary to assess the data described above in the context of the accuracy of the multiple dates yielded by the analyses in order to ascertain a final age for the formation of monazite. All analytical points, with the exception of one, are highly discordant and as such initial age estimates were derived from regression lines. Examining the spot ages for all data it is observed that there is a high degree of variability in the $^{207}\text{Pb}/^{206}\text{Pb}$ and $^{207}\text{Pb}/^{235}\text{U}$ ages compared to the $^{206}/^{238}\text{U}$ values. The range of values identified in the isotope systems utilising ^{207}Pb is interpreted as indicating the ^{207}Pb content is the principle driver of variability and discordance within the data set. Due to this variability and the lack of concordant data points the intercept ages are not favoured. The weighted average ages generated from the corrected $^{232}\text{Th}/^{208}\text{Pb}$ and $^{238}\text{U}/^{206}\text{Pb}$ spot ages are preferred, being corrected for common lead and using isotope systems independent of ^{207}Pb concentrations.

In all cases except PB12-PM02:population 2 and PB12-PK02 population 1 the weighted average $^{232}\text{Th}/^{208}\text{Pb}$ age display a lower MSWD value, and therefore higher probability of a true fit, compared to the $^{238}\text{U}/^{206}\text{Pb}$ average ages (Fig. 9.3, 9.4, 9.8 and 9.10). In the case of PB12-PK02 population 1 the ages produced by both the $^{238}\text{U}/^{206}\text{Pb}$ and $^{232}\text{Th}/^{208}\text{Pb}$ methods are similar (561 ± 7 and 560 ± 13 Ma respectively (Fig. 9.8)). The $^{232}\text{Th}/^{208}\text{Pb}$ ages are considered more accurate and representative of the true formation age of the monazite. The method used for analysis typically produces more accurate $^{238}\text{U}/^{206}\text{Pb}$ age determinations however in this case the better accuracy observed in the $^{232}\text{Th}/^{208}\text{Pb}$ is attributed to the higher concentration of Thorium, typically 50-400 times enriched compared to U, within all analysed monazites (Fig. 9.5).

9.5.1 Age of monazite formation

9.5.1.1 Karagba-Chaffeur-Durba (KCD)

Analysed monazites within the KCD samples occur intergrown with Au-bearing pyrite, as enclosed masses and enclosing the pyrite (Fig. 9.1), and are interpreted to have formed synchronously with the pyrite gangue phase. Analysis of monazite in both occurrences produced no apparent delineation between the two morphologies and as such they are attributed to the same population. The determined weighted average $^{232}\text{Th}/^{208}\text{Pb}$ ages for samples from the KCD (Fig. 9.3 and 9.4) range from 538 ± 8.4 to 605 ± 11 Ma. The apparent trend of increasing age with increasing sample number is coincidental, the samples not having been analysed in this order and having been analysed over the course of two days removing the possibility of machine bias. Four of the determined age intervals overlap within error, extending from 587 ± 30 to 605 ± 11 Ma, and as such are considered part of a single event. Sample D05 yielded a $^{232}\text{Th}/^{208}\text{Pb}$ age of 538 ± 8.4 Ma falling outside the interval outlined by the other samples from the KCD. These data suggest that there may

have been two distinct events in which monazites were formed within the hydrothermal system. However examination of the Th/U ratios (Fig. 9.5) shows similar distributions indicating monazite formed from a single source. Assuming monazite represents a single generation an average value of the KCD data yields an age of 568.43 ± 43 Ma (Fig. 9.11).

9.5.1.2 Pakaka

The single sample analysed from the Pakaka deposit shows two distinct monazite populations yielding distinct ages with no error overlap. Both populations, delineated by strongly contrasting U/Th ratios, display a similar mode of occurrence, intergrown but postdating the development of auriferous pyrite (Fig. 9.2), and as such provide only a lower estimate for the development of mineralisation. Population 1 returns a weighted average $^{232}\text{Th}/^{208}\text{Pb}$ age of 560 ± 13 Ma while population 2 returns a $^{232}\text{Th}/^{208}\text{Pb}$ age of 525 ± 10 Ma (Fig. 9.11). The data would suggest two independent events in which monazites were formed within the sample. However this does not necessarily correlate to multiple sulphide forming events as the monazite textures do not conclusively tie the formation of the monazite and the development of auriferous sulphides.

9.5.1.3 Pamao

Analyses of the two samples from the Pamao deposit yielded $^{232}\text{Th}/^{208}\text{Pb}$ ages of 575 ± 24 and 564 ± 16 Ma. The samples show a high degree of correlation and yield an average $^{232}\text{Th}/^{208}\text{Pb}$ for the two of 567 ± 13 Ma (Fig. 9.8). The monazites identified within the sample texturally postdate the auriferous pyrite phase and as such the age estimate represents a lower bound for the development of mineralisation. As outlined above sample PB12-PM02 displayed distinct differences in the distribution of ages generated by the $^{232}\text{Th}/^{207}\text{Pb}$ and $^{238}\text{U}/^{206}\text{Pb}$ ages, the $^{232}\text{Th}/^{206}\text{Pb}$ system yielding a single age while the $^{238}\text{U}/^{206}\text{Pb}$ data divided the data in to two distinct events (Fig. 9.9a). Examining the Thorium and Uranium concentrations and ratios the data (Fig. 9.5) can be divided into two populations, those samples with a thorium concentration of approximately 5000 ppm and those with concentrations below 2500 ppm. However this division does not correspond to the observed split in ages displayed by the $^{238}\text{U}/^{206}\text{Pb}$ data with the uranium concentrations displaying no clear division. The split in ages observed within the $^{238}\text{U}/^{206}\text{Pb}$ is thought to be a result of the relatively large errors occurring as a result of the low concentrations of uranium within the sample (Fig. 9.5).

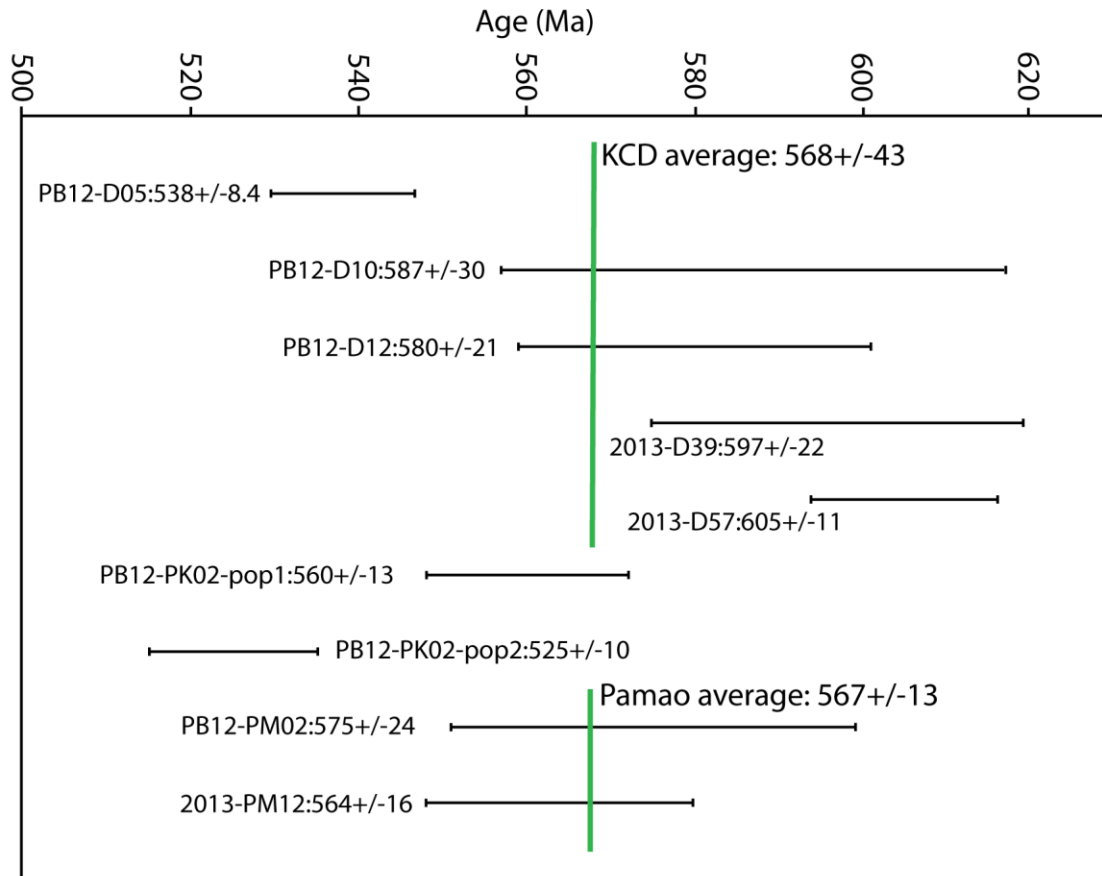


Figure 9.11: Ages and associated errors for all samples from the KCD, Pakaka and Pamao deposits. Determined average values from the KCD and Pamao data are shown by the green line and associated label.

9.5.2 Monazite Age as Proxy for Mineralisation Age

The monazite phases analysed within the samples were all identified within zones of interpreted high fluid flow and deformation that are associated with the development of auriferous mineralisation. The relative timing between the development of auriferous phases and monazite has been established by the morphological characteristics within each sample (Fig. 9.1 and 9.6). In the case of samples from the Durba deposit monazite is interpreted as forming synchronously with mineralisation, monazite texturally pre and postdating pyrite mineralisation. However in the case of the Pakaka and Pamao deposits the available evidence indicates that the monazite post-dates the formation of auriferous phases. Therefore monazite ages provide a lower bound for the development of mineralisation within these systems.

9.5.3 Single Region Wide Event vs Discrete Individual Events

A key question in modelling the development of orogenic gold mineralisation within the Kibali Granite-Greenstone Belt addresses whether mineralisation developed as a single region wide mineralising pulse or as a series of discrete events with the interpretation having significant implications for the developing model.

The data generated shows evidence for the formation of the monazite mineral phase within the KCD deposit from 538 ± 8.4 to 605 ± 11 Ma, within the Pakaka deposit from 525 ± 10 to 560 ± 12 Ma and at Pamao from 564 ± 16 to 575 ± 24 Ma (Fig. 9.11). The broad overlap observed between data from individual deposits indicates monazite developed broadly synchronously within the three systems in a relatively short time window, an approximately 100 Ma period extending from 515-615 Mya. The spread of data and the large errors present for individual sample dates prevents this window being constrained any further.

Micklethwaite et al. (2014) demonstrated that fluid systems in orogenic gold deposits only require a period of 10-40 Ka in order to form a supergiant gold deposit. As such the hypothesis of multiple active mineralising systems over a period of 100 Ma is unlikely with the broad age range probably a result of the relatively large error values.

If the hypothesis of a single prolonged event is rejected then it is logical to consider the formation of the monazite in terms of multiple discrete events. The data generated for the Pakaka deposit is interpreted as showing evidence of two distinct populations of monazite identified based on their U/Th content (Fig. 9.5) with each having formed in a distinct event, one at 560 ± 12 Ma and a second at 525 ± 20 Ma (Fig. 9.8 A-B). The data from the KCD deposit also shows evidence of two possible episodes of monazite formation, one at approximately 580 Ma and a second at 538 ± 8.4 Ma (Fig. 9.11). However the same contrast in Th/U ratios and concentrations as observed in the populations at the Pakaka deposit is not observed with all populations displaying overlapping Th/U concentrations (Fig. 9.5). The data generated by analysis of material from the Pamao shows a high degree of correlation between the samples when the $^{232}\text{Th}/^{207}\text{Pb}$ ages are considered despite a strong bimodal distribution being noted within the distribution of thorium and uranium between the two samples (Fig. 9.5). The potential for multiple phases of monazite formation within each deposit has been identified in the available data although the argument for distinct populations of monazite is not compelling.

9.5.4 Representative of True Mineralisation Age?

The U-Pb zircon data set (Chapter 6) identified a region wide lead loss event at approximately 500 Mya that was linked to a hypothesised collision between the West Nile Gneiss and the Kibali Granite-Greenstone Belt during the Oubanguide orogeny. The 515-615 Mya age bracket generated by the monazite data correlates

with the upper end of this region wide lead loss event and therefore provides independent correlation and establishes its geological significance. Orogenic gold systems in Archean greenstone belts are typically considered to have formed broadly coeval with the formation of the host belt (Groves et al., 1992, Groves et al., 2005; McCuaig and Kerrich, 1998). However the monazite data from the gold deposits in the Kibali Granite-Greenstone Belt indicates the mineralised systems were active approximately 2 Ga after the formation of the belt.

The processes by which isotope ratios within monazite may be modified post formation have been well established (Harlov et al., 2007, 2011; Teufel and Heinrich, 1997; Cherniak and Pyle, 2008; Crowley et al., 2008; Harlov and Hetherington, 2010; Williams et al., 2011) and must be considered here in light of the established region wide hydrothermal Oubanguide event. The region wide fluid flow during the Oubanguide event would have provided the necessary conditions by which monazite formed at approximately 2.63 Ga could be modified by coupled dissolution re-precipitation reactions resulting in them being isotopically reset between 0.5-0.6 Ga. If this process has occurred then it has serious implications for the interpretation of the data discussed above. Williams et al. (2011) identified that the process of coupled dissolution re-precipitation advances progressively along a reaction front within the monazite crystal resulting in distinct zones of alteration that are identifiable under high contrast back scattered electron imaging (Williams et al., 2011). Back scattered electron images of monazites used in this study show no evidence of this alteration zoning although the small crystal size leaves the possibility that the entire crystal has been modified, effectively resetting the isotope system. The similarity in spot ages generated by monazite crystals that are identified isolated within the groundmass/ along the outer edges of pyrite crystals (exposed to potential hydrothermal fluids) and those identified enclosed by pyrite suggest this process may not have occurred. The pyrite showing no distinct recrystallization textures may potentially have mantled and protected the enclosed monazite from exposure to hydrothermal fluids.

9.6 Conclusion

The available data are interpreted as showing that the monazite phase developed across the region during the period 515-615 Mya. The resolution of the data is insufficient to constrain the formation age any further and while evidence for multiple phases of monazite development is identified the large error values and small data set make establishing if multiple monazite forming events occurred unlikely. The determined window of monazite formation confirms the presence of active hydrothermal systems, initially hypothesised based on the lead loss event identified within the U-Pb zircon data, active during the Oubanguide orogeny. This data suggests a highly unusual orogenic system where the mineralised systems are active significantly after the formation of the greenstone belt (~2 Ga). While questions remain regarding whether the monazite dates

record primary formation ages or a secondary hydrothermal event, which modified the isotopic concentrations, it will require further isotopic analysis utilising more robust isotope systems to draw firm conclusions.

Chapter 10. Re:Os Pyrite constraints on the formation of mineralisation at the Karagba-Chaffeur-Durba (KCD) orogenic gold deposit, NE Democratic Republic of the Congo

10.1. Introduction

Earlier in this study, monazite age data were used to place geochronological constraints on the formation of gold mineralisation. This returned a formation age for the monazite mineral phase of approximately 600 Ma, corresponding to a regional lead loss event identified in the U:Pb zircon data (Chapter 6). While monazite is strongly associated with the Au-bearing sulphides, as an accessory phase it is not directly related to the Au mineralisation event. How robust these data are is unclear. The work of Williams et al. (2011) have highlighted potential mechanisms by which interaction with hydrothermal fluids can reset the U-Pb decay system in situ, without significant modification of the monazite crystal itself. Evidence for isotopic modification was not identified within the monazite data (Chapter 8). The application of the Re:Os isotope system to directly date the Au-bearing pyrite phase will further clarify the evolution of hydrothermal activity within the mineralised systems in the Kibali Granite-Greenstone Belt.

10.2. The Re:Os Isotopic System

The Rhenium-Osmium decay system has become an increasingly important technique in the study of the geochronological characteristics of hydrothermal sulphide-bearing ore systems, as it allows the direct analysis of ore and ore-bearing sulphide phases. The technique has been successfully applied to multiple orogenic gold systems, including the Sukhoi Log and Olympiada deposits (Yakubchuk et al., 2014); Muruntau, Uzbekistan (Morelli, 2007); the Meguma group gold deposits (Morelli et al., 2005); the Bendigo and Maldon goldfields, Australia (Arne et al., 2001); the Klondike gold district (Mather and Mortensen, 2013) and the Lupa Goldfield, Tanzania (Lawley et al., 2014).

Two naturally occurring isotopes of Re, ^{185}Re and ^{187}Re , are observed in nature. These constitute, respectively, 37.4% and 62.6 % of the total Re budget. ^{187}Re decays to one of the seven naturally occurring isotopes of Os, ^{187}Os , through β particle emission. This occurs with a half-life of $4.23 \pm 0.13 \times 10^{10}$ years. Both elements are strongly siderophile and are thought to have been sequestered into the earth's core early in its history, during the process of internal differentiation (Crocket, 1969; Morris and Short, 1969). As a result the crust possesses low concentrations of both elements, average concentrations in terrestrial igneous rocks being <1 ppb Re and <3 ppb Os (Faure and Mensing, 2005). Sulphide minerals, including molybdenite, chalcopyrite, pyrrhotite and pyrite naturally sequester Re and Os and therefore commonly display elevated concentrations of Re and Os with high Re/Os values. This makes them suitable for use in geochronological

studies (Faure and Mensing, 2005; Morelli et al., 2010). The substitution of Re and Os into the atomic lattice of molybdenite and chalcopyrite is linked to the similarity in valence and ionic radius of rhenium and osmium in their tetravalent state (ionic radii $\text{Re}^{4+}=0.71 \text{ \AA}$, $\text{Os}^{4+}=0.71 \text{ \AA}$) to Mo^{4+} (0.68 \AA) and Cu^{2+} (0.69 \AA) (Faure and Mensing, 2005)).

The habit of Re and Os in pyrite is less well constrained, the current consensus being that the two elements occur as sub-micron inclusions within pyrite, as opposed to substituting into the atomic lattice (Faure and Mensing, 2005). In addition to allowing the direct analysis of ore-bearing sulphide phases, the Re:Os isotope system in pyrite has been selected for use as it is considered extremely robust and is able to retain its original isotopic characteristics through post formation metamorphic events. This has been investigated by Morelli et al. (2007) who examined the Re:Os isotopic characteristics of low-level sulphide minerals (Pyrite, Pyrrhotite and Chalcopyrite) from volcanogenic massive sulphide deposits in the Trans-Hudson orogeny. Morelli et al. (2007) demonstrated that the Re-Os geochronometer in pyrite remains closed through metamorphic conditions up to 660°C (Morelli et al., 2007).

10.3. Sampling and Analytical Technique

Extensive sample preparation conducted during the early stages of this study, including the production of polished thin sections, polished blocks and mineral separates, left insufficient material from the original suite of mineralised material to extract the required volume of pyrite for a Re-Os study. An additional suite of mineralised material from the KCD was therefore collected in collaboration with the Kibali Gold project geology department (Table 10.1). This sample suite consisted of 32 samples of mineralised drill core, selected for the abundance of pyrite within the sample. Twenty five of these samples were selected for initial testing to determine whether sufficient Re and Os content was present to allow for a full analysis. To isolate the gold-bearing Py-1 mineral phase, the samples were crushed without metal contact and sieved to isolate the 60-250 μm fraction. The isolated fraction was washed in distilled water, using an ultrasonic bath to further remove particulate matter adhering to the surface of the mineralised material. Pyrite was extracted by hand picking under microscope, each crystal being examined to ensure no additional material, such as quartz, was adhering to the surface. The isolated pyrite material was then washed in an ultrasonic bath to ensure all particulate matter adhering to the surfaces of the pyrite crystals was removed. Following initial testing, six samples (Table 10.1) were selected for full analysis of their Re-Os abundances and isotopic compositions.

Sample analysis was performed at the Total Laboratory for Source Rock Geochronology and Geochemistry at Durham University, following the analytical protocol outlined in Selby et al. (2009). Approximately 0.4 g

Table 10.1: Samples collected and tested as part of the Re-Os study of the Karagba-Chaffeur-Durba (KCD) gold deposit, samples selected for final analysis are highlighted in bold

Sample No.	Hole I.D	Depth from (m)	Depth to (m)	Sample description
PB-1	DDD531A	419.53	419.83	Deformed Hematised Volcano-Sedimentary Conglomerate: Pyrite-rich veins
PB-2	DDD329	460.09	460.39	Heavily altered fine volcanoclastic conglomerate: Veins parallel to foliation
PB-3	DDD329	271.2	271.5	Fine volcanoclastic conglomerate: Sulphide veins cross cutting principle foliation
PB-4	DDD531A	674.74	675.05	Deformed Hematised Volcano-Sedimentary Conglomerate: Intraclast mineralisation
PB-5	DDD565	593.44	593.64	Altered and deformed volcano-sedimentary conglomerate: sulphides parallel to stretching foliation
PB-6	DDD564	473.25	473.45	Deformed Volcano-Sedimentary conglomerate: sulphide veins parallel to principle foliation
PB-7	DDD565	633.16	633.46	Stretched and deformed volcano-sedimentary Conglomerate: Intraclast mineralisation
PB-8	DDD329	366.17	366.47	Deformed volcano-sedimentary conglomerate: Intraclast mineralisation
PB-9	DDD531A	792.68	792.98	Heavily altered fine volcanoclastic conglomerate: sulphides parallel to foliation
PB-10	DDD011	261.27	261.57	Silicified volcano-sedimentary conglomerate: Intraclast mineralisation
PB-11	DDD531A	486.37	486.67	Fine volcanoclastic conglomerate: Sulphide veins cross cutting principle foliation
PB-12	DDD329	405.25	405.55	Silicified fine volcanoclastic conglomerate: Sulphide veins cross cutting stretching foliation
PB-13	DDD531A	551.31	551.61	Altered fine volcanoclastic: disseminated mineralisation
PB-14	DDD291	348.58	348.78	Clast-rich volcano-sedimentary conglomerate: Intraclast mineralisation
PB-15	DDD531A	768.84	769.14	Altered volcano-sedimentary conglomerate: Sulphide veins parallel and cross cutting principle foliation
PB-16	DDD565	385.19	385.39	Highly altered volcano-sedimentary conglomerate: cross cutting sulphide veins
PB-17	DDD291	318.61	318.91	Stretched and altered volcano-sedimentary conglomerate: Intraclast mineralisation
PB-18	DDD564	341.6	341.8	Silicified clast-rich volcano-sedimentary conglomerate: Intraclast mineralisation
PB-19	DDD011	314.52	314.82	Highly altered fine volcanoclastic: Sulphides bands across sample
PB-20	DDD531A	227.15	227.45	Heavily altered fine volcanoclastic conglomerate: Sulphide bands parallel to principle foliation
PB-21	DDD564	487.98	488.18	Carbonaceous Shale: Disseminated sulphides
PB-22	DDD213	570.37	570.7	Deformed and altered fine volcanoclastic: sulphides developed parallel to foliation
PB-23	DDD213	544.2	544.5	Highly altered and deformed volcanoclastic: sulphides cross cutting stretching foliation
PB-24	DDD213	485.18	485.48	Highly altered fine volcanoclastic material: Disseminated mineralisation
PB-25	DDD565	326.1	326.3	Stretched and deformed volcano-sedimentary Conglomerate: Massive cross cutting sulphides
PB-26	DDD213	440.95	441.25	Highly altered and deformed volcano-sedimentary conglomerate: Intraclast mineralisation
PB-27	DDD573	278.28	278.58	Highly altered and stretched volcano-sedimentary conglomerate: Abundant intraclast mineralisation
PB-28	DDD573	199.13	199.43	Highly altered fine volcanoclastic: sulphide veins parallel to stretching
PB-29	DDD213	187.57	187.87	Highly altered and deformed volcano-sedimentary conglomerate: Intraclast mineralisation
PB-30	DDD573	180.86	181.16	Deformed BIF and volcano-sedimentary conglomerate: Sulphide veins cross cutting internal layering
PB-31	DDD565	453.51	453.81	Altered clast-rich volcano-sedimentary conglomerate: intraclast mineralisation
PB-58	DDD423	163.1	163.24	Altered and deformed volcano-sedimentary conglomerate: Intraclast sulphides

of pyrite separate for each sample was accurately weighed into a carius tube and combined with a known amount of ^{185}Re - ^{190}Os tracer solution. The sample and tracer solution were digested and equilibrated by aqua regia (11N HCl (3 ml) and 15.5N HNO₃ (8 ml)) at 220°C for a period of 48 hours. Osmium was isolated and purified by CHCl₃ solvent extraction and micro-distillation while Re was isolated by anion exchange column and single bead chromatography. Purified Re and Os were loaded on Ni and Pt filaments and isotopic characteristics were analysed by negative-ion mass spectrometry using a ThermoElectron TRITON mass spectrometer and ion counting using a secondary electron multiplier. Os concentrations were determined with the electron multiplier in peak hopping mode while Re concentrations were measured statically by Faraday collectors. Uncertainties were determined through full propagation of errors from mass spectrometer measurement, blank abundances, isotopic compositions, spike calibrations and analysis from Re and Os standards.

10.4 Results

Six analyses of pyrite were performed and the results are reported in Table 10.2. Total Re and Os abundances are low, ranging from 0.31 to 1.10 ppb Re and 15.50 to 210.06 ppt Os. Common Os (^{192}Os) values are variable, ranging from 3.17 to 80.56 ppt, accounting for 11 to 38% of total Osmium within the samples. Resultant $^{187}\text{Re}/^{188}\text{Os}$ ratios are low, ranging from 13.02 to 463.23, with accompanying $^{187}\text{Os}/^{188}\text{Os}$ values being very low, ranging from 0.714 to 21.054. Sample PB16 possesses significantly different Re:Os isotopic characteristics to the other analysed samples with $^{187}\text{Re}/^{187}\text{Os}=463.23$ and $^{187}\text{Os}/^{188}\text{Os}=21.054$, with all other samples returning values for $^{187}\text{Re}/^{187}\text{Os}<120$ and $^{187}\text{Os}/^{188}\text{Os}<4$. Regression of data was performed using Isoplot V1.6 (Ludwig, 2003). Regression of the $^{187}\text{Re}/^{188}\text{Os}$ vs $^{187}\text{Os}/^{188}\text{Os}$ data for all samples (n=6) yields a poorly constrained age of 2705 ± 670 Ma (MSWD=282) with an initial $^{187}\text{Os}/^{188}\text{Os}=-0.8\pm 2.3$ (Table 10.1), calculated sample $\text{Os}_{\text{initial}}$ values ranging from -3.57 to 0.11 (Table 2: $\text{Os}_{\text{initial-a}}$). Sample PB16 possesses significantly different Re:Os isotopic characteristics with low total Os (=28.65ppt), with resultant high $^{187}\text{Re}/^{188}\text{Os}=463.23$ and $^{187}\text{Os}/^{188}\text{Os}=21.05$. These differences are most apparent in the regression diagram displayed in Fig. 10.1. Here sample PB16 plots in the upper right part of the diagram, while sample PB58 lies off the main trend and is offset to the right of the other samples due to its relatively high $^{187}\text{Re}/^{187}\text{Os}$ value (115.33) and low $^{187}\text{Os}/^{188}\text{Os}$ value (1.732). Excluding these two samples produces a regression line with Age= 2053 ± 700 Ma (MSWD=44) and initial $^{187}\text{Os}/^{188}\text{Os}=0.33\pm 0.74$ (Table 10.2) with calculated sample $\text{Os}_{\text{initial}}$ values ranging from 0.19 to 0.52 (Table 10.2: $\text{Os}_{\text{initial-b}}$). The four samples are further divided into two groups, samples PB04 and PB11 plot, respectively, on and above the regression line with calculated $\text{Os}_{\text{initial}}>0.3$, and samples PB17 and PB19 plot below the regression line with calculated $\text{Os}_{\text{initial}}<0.3$. Two point regressions of samples PB17 and PB19 give an age of 1966 ± 39 Ma (MSWD=0.0) with initial $^{187}\text{Os}/^{188}\text{Os}=0.28\pm 0.018$ (Fig. 10.3).

Table 10.2: Re-Os analytical data for samples from the KCD gold deposit

Sample	Re (ppb)	±(ppb)	Os (ppt)	±(ppt)	¹⁹² Os (ppt)	±(ppt)	% ¹⁹² Os	¹⁸⁷ Re/ ¹⁸⁸ Os	±(ppt)	¹⁸⁷ Os/ ¹⁸⁸ Os	±(ppt)	rho	Os _{initial-a}	Os _{initial-b}
PB04	0.79	0.02	57.74	0.45	16.19	0.13	28.04	97.62	2.01	3.748	0.034	0.317	-0.74	0.35
PB11	0.32	0.02	47.26	0.31	15.84	0.12	33.52	39.78	1.92	1.902	0.017	0.137	0.07	0.52
PB16	0.74	0.02	28.65	0.58	3.17	0.10	11.07	463.23	17.64	21.054	0.685	0.830	-0.26	4.94
PB17	0.53	0.02	210.06	0.79	80.56	0.35	38.35	13.02	0.38	0.714	0.004	0.108	0.11	0.26
PB19	1.10	0.02	109.83	0.65	35.12	0.18	31.97	62.47	0.93	2.360	0.016	0.265	-0.51	0.19
PB58	0.31	0.02	15.50	0.17	5.29	0.11	34.14	115.33	6.10	1.732	0.035	0.355	-3.57	-2.28

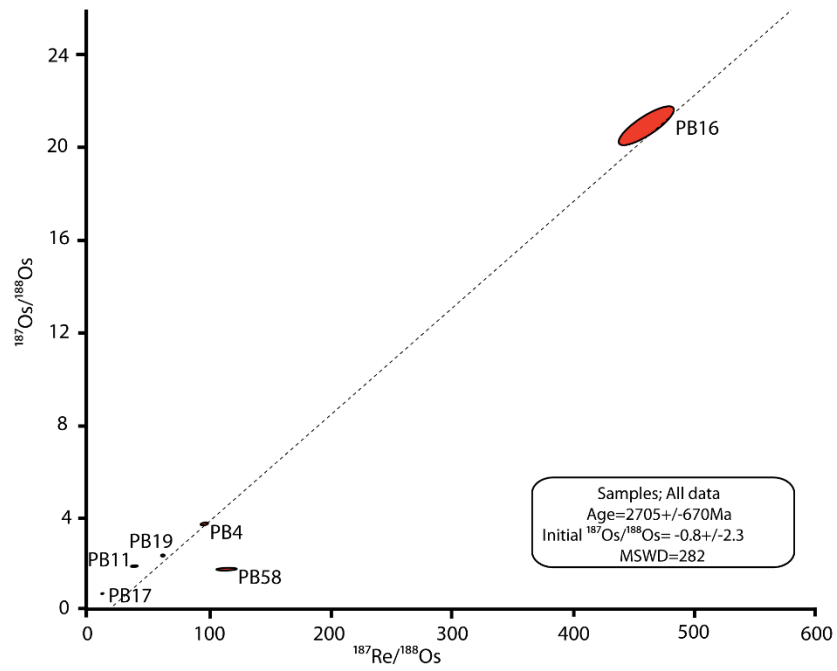


Figure 10.1: Model-1 regression for all samples from the KCD gold deposit

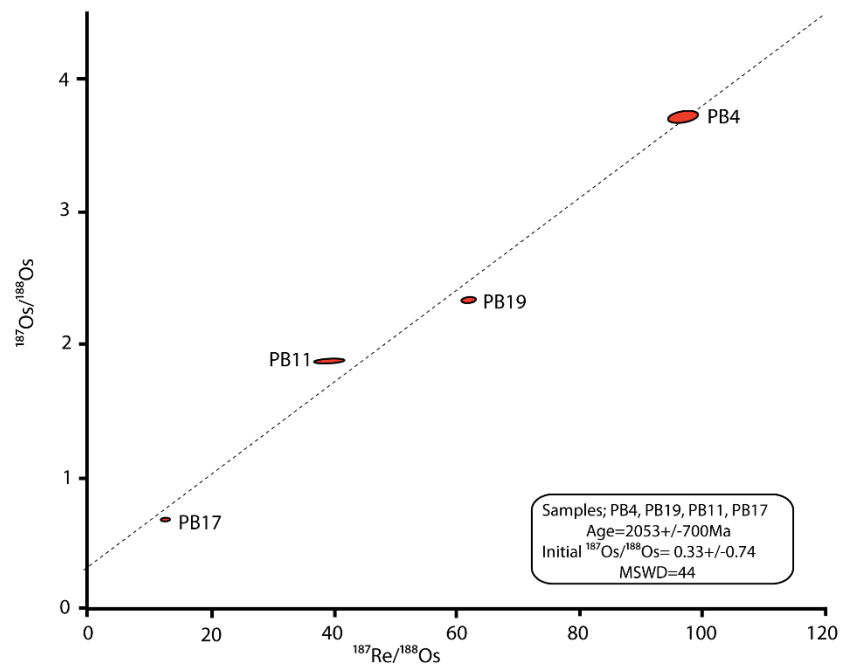


Figure 10.2: Model-1 regression of selected data from the KCD gold deposit

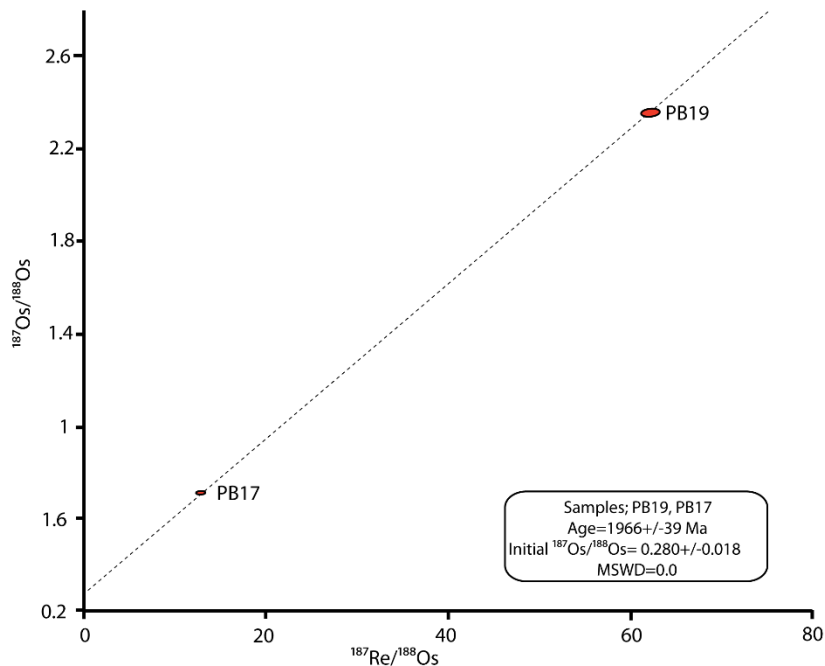


Figure 10.3: Model-1 regression of analytical data for samples PB17 and PB19

10.5 Discussion

The Re:Os isotopic data of mineralised pyrite from the KCD deposit are complex and have been used above to generate a series of regressions each yielding a different formation age. In accessing the validity of these ages it is necessary to consider two principle aspects: firstly whether the sample set represents a single suite with a common origin or are they the product of multiple discrete pyrite forming events and secondly, whether the calculated formation ages are geologically significant.

Regression of all data (Fig. 10.1) yielded a poorly constrained age of 2705 ± 670 Ma; the large error value makes determining any geological significance of the data impossible. Samples PB16 and PB58 display significantly different isotopic characteristics to the other analysed samples, and plot off the trend defined by the remainder of the data. The negative initial osmium value calculated from regression of all data points would indicate post-formation modification of the Re-Os isotopic characteristics of all samples. In this case however, the influence of sample PB16, and to a lesser extent sample PB58, is thought to have significantly affected the regression, resulting in incorrect age and initial osmium calculation. The difference in the isotopic characteristics of these two samples is interpreted to indicate that they either represent two separate discrete pyrite forming events or that these two samples have had their isotopic characteristics significantly

modified post formation. Excluding samples PB16 and PB58 from the regression yields an age of 2053 ± 700 Ma (Fig. 10.2). As was the case with the regression of all data points, this is insufficiently accurate to tie to a particular geological event. The data points display a significant degree of scatter around the regression line, exceeding that which was expected by the determined analytical errors. Cardon et al. (2008) identified several possible mechanisms that may account for this scatter; underestimation of analytical error, formation of mineralisation over a protracted period of time, perturbation of the Re:Os isotope systematics through supergene alteration and the diffusive redistribution of radiogenic ^{187}Os . The underestimation of errors is considered unlikely in this case, although cannot be conclusively excluded. However, as the samples were collected from drill core below the oxide zone, the effects of supergene alteration can be discounted. The diffusion of radiogenic ^{187}Os had been highlighted as the principle cause of $^{187}\text{Os}/^{187}\text{Re}$ heterogeneity within molybdenite by multiple studies, ^{187}Os being more prone to diffusion as it is less easily incorporated into the structure of molybdenite than rhenium (Kosler et al., 2003; Selby and Creaser, 2004; Stein et al., 2003). The diffusion of ^{187}Os is thought to be particularly significant in sample material with low Re concentrations such as pyrite (Cardon et al., 2008; Selby and Creaser, 2004). The diffusion of ^{187}Os is principally a concern with micro-analytical techniques such as LA-ICP-MS, the acid digestion method being less susceptible to internal variations in ^{187}Os . Initial sampling was conducted under the assumption that the KCD deposit formed during a single discrete event. However, if mineralisation formed over a long period of time or as a series of discrete mineralising events, then the selected samples may not represent a single coherent data set. Samples PB17 and PB19 display the most similar $\text{Os}_{\text{initial}}$ values, 0.26 and 0.19 respectively (Table 10.2). These samples originate from two separate drill holes separated by approximately 50 m and from similar depths. It is reasonable therefore to consider samples PB17 and PB19 as being part of the same individual mineralised lode within the wider KCD deposit. Samples PB04 and PB11 display less similar Re-Os characteristics with calculated $\text{Os}_{\text{initial}}$ values of 0.35 and 0.52 respectively. These samples originate from the same drill hole; sample PB04 was collected at a depth of 674.74 m and PB11 was collected at a depth of 486.37 m. Due to the spatial separation of these two samples it is unlikely they are part of the same mineralised lode. Regression of the data from samples PB17 and PB19 yielded a more tightly constrained age of 1966 ± 39 Ma with an initial $^{187}\text{Os}/^{188}\text{Os} = 0.280 \pm 0.018$. The Rwenzori-Eburnean tectonic episode (Chapter 2), involving the closure of a series of rift basin between the Congo and Tanzanian cratons, has been constrained through U:Pb zircon dating to the period 2.0-1.85 Ga (Mantarri, 2014; Westerhoff et al., 2014), correlating well with the 1966 ± 39 Ma age. Furthermore Cahen et al. (1984) presented Rb:Sr ages for pegmatites in the Upper Congo Granitic Massif between 2075 ± 60 Ma to 1850 ± 55 Ma and common lead ages (galena) for auriferous galena-quartz veins in the Kibali Granite-Greenstone Belt of 1810 Ma (Zambula mine) and 2025 Ma (Dila Mine). Cahen et al. (1984) utilised these ages to link the formation of mineralisation to the reactivation of northeast-southwest orientated shear structures during the Rwenzori

tectonic episode (as part of the broader Eburnean orogeny) (Cahen et al., 1984). While the determined age displays some encouraging correlation with significant regional tectonic events, as a two point regression it lacks statistical robustness and will require further assessment to establish a firm date for the formation of this specific mineralised lode. The differences between samples PB17 and PB19 in comparison to the remainder of the data raises the possibility that different 'lodes' within the deposit may have formed during discrete individual events.

10.6 Conclusions

The most significant information that can be drawn from the available data is that the mineralisation within the KCD formed prior to the 600 Ma age previously hypothesised on the basis of the monazite U:Pb data. Though not providing an accurate date, these new data indicate that the gold hosting pyrite formed at approximately, or prior to, 2 Ga. This would suggest that either the monazite phase was formed during the regional event previously identified at ~600 Ma or underwent significant modification and resetting of its isotopic characteristics at this time. The variability between individual samples, both in terms of the distribution of data points on regression diagrams and the variations in resultant calculated initial Osmium values, raises the possibility that the individual mineralised lodes within the KCD formed not as one large mineralising event but as a series of discrete events with distinct Re:Os characteristics.

To determine an accurate age for the development of auriferous pyrite will require further analysis. Careful sampling of mineralised core must be taken to ensure all samples are collected from a single discrete mineralised 'lode'. To complement the existing data, sampling from boreholes in the vicinity of holes DDD011 and DDD291 at a depth of approximately 310-320 m should be considered favourable, as this material will correspond to the same mineralised lode as samples PB17 and PB19.

Chapter 11. Evolution of the Kibali Granite-Greenstone Belt, NE Democratic Republic of the Congo, and Controls on Gold Mineralisation at the Kibali Gold Deposit

At the beginning of this study, a working hypothesis was presented for the evolution of the Kibali Granite-Greenstone Belt in which the belt was formed during the Archaean when southward moving West Nile Gneiss (WNG) was thrust over the top of the Kibali Granite-Greenstone Belt (KGGB) and Upper Congo Granitic Massif (UCG). Gold mineralisation was hypothesised to have formed during this accretionary event. The data presented in this study has significantly advanced the geological knowledge of the KGGB and its neighbouring terranes, as well as the potential mechanisms by which gold mineralisation was formed. Here the data are brought together and used to present a new synthesis for the formation and evolution of the Kibali Granite-Greenstone Belt and some of the factors affecting the development of gold mineralisation.

11.1 Formation and Evolution of the Kibali-Granite-Greenstone Belt and Neighbouring Terranes

Investigation of the geochemical characteristics of the igneous lithologies from the KGGB and UCG returned a range of trace element compositions that display characteristics similar to lithologies produced in modern arc/ back-arc geotectonic settings. The lithologies that make up the KGGB are therefore hypothesised to have formed in an evolving arc/back-arc environment, along the northern margin of the Bomu-Kibalian block. The volcano-sedimentary, chemo-sedimentary and basaltic lithologies that now make up the KGGB were deposited into this evolving back-arc environment.

U:Pb zircon dating of the felsic igneous intrusions from the KGGB and UCG defined a major cycle of felsic igneous production in the period 2.62 to 2.64 Ga across the Kibalian back-arc system and on the northern margin of the UCG. This constrains the deposition of the Kibalian metasediments and formation of the Kibalian basalts to >2.64 Ga (a single age determination from the north Kibalian schists returned an age of 2.66 Ga). This 2.64 Ga event is thought to coincide with the accretion of the Kibalian metasediments onto the northern margin of the UCG. This arc system is hypothesised to represent the north-east extension of the craton-wide period of crustal accretion and formation along the northern margin of the Bomu-Kibalian block (Congo craton) during the Neoproterozoic. This has been well documented in Uganda and Tanzania (Kabete et al., 2012a, 2012b; Westerhoff et al., 2014) and this study provides the first evidence for it in the Northeast DRC.

The lithologies of the KGGB have been extensively metamorphosed, with the metamorphic grade varying across the belt from sub-greenschist facies in the west characterised by the development of chlorite and epidote (chlorite geo-thermometry indicating temperatures of approximately 310-360°C), to amphibolite

grade in the west characterised by biotite-rich folded schists. Metamorphism is assumed to have occurred during the period of terrane accretion at 2.64 Ga. The position of the West Nile Gneiss during this Archean crust forming event is unknown, but it is considered to have been geographically distant at this time. The WNG displays an independent geological history to the other major terranes with a high-grade metamorphic event recorded in the period 937-1014 Ma that is not observed in the other terranes. The West Nile Gneiss is now regarded as being the southernmost extension of the enigmatic Saharan-Metacraton (Abdelsalam et al., 2002). Collision of the Saharan Metacraton with the northern margin of the Congo Craton is hypothesised to have occurred during the Oubangide orogeny at approximately 600-450 Ma (Westerhoff et al., 2014) and this is reflected in the zircon data with a region-wide lead loss event, affecting all three terranes, being identified in the period 140-516 Ma.

The West Nile Gneiss is hypothesised to have over-thrust the Kibalian Granite-Greenstone Belt re-activating pre-existing structures in addition to developing new thrust surfaces (as seen by the significant deformation within the Kalimva granite). This event is associated with regional fluid flow, manifesting as the widespread development of aluminoceladonite alteration in all three terranes. This fluid flow is also hypothesised to be responsible for the observed zircon lead loss. This lead loss event as recorded in the KGGB and neighbouring terranes covers a wide time period and this is attributed to continued lead loss during uplift and surface processes.

11.2 Controls on Gold Mineralisation

The Karagba-Chaffeur-Durba (KCD), Mengu, Pakaka and Pamao deposits display many similarities and are classified together as 'Kibalian' style mineralisation. Kibalian mineralisation is characterised by a pyrite dominated sulphide assemblage with varying amounts of arsenopyrite+chalcopyrite+pyrrhotite(±marcasite) and other minor phases. The sulphides occur as both disseminated and vein style mineralisation in variably altered (Fe-carbonate+quartz±aluminoceladonite) and deformed host lithologies belonging to the Kibalian metasediments, Kibalian basalts and banded iron formations.

Deformation weakening of the host lithologies is hypothesised to have created a series of high permeability phyllosilicate rich zones in the Kibalian metasediments that acted to focus deformation and fluid flow. This deformation is hypothesised to have occurred during the broader regional greenschist facies event (chlorite geothermometry indicate a formation temperature range of 304-394°C) and are correlated with the D₄ event of Allibone (2015).

It is thought that CO₂-rich fluids produced at depth ascended through these high permeability structures interacting with the Fe-rich phyllosilicates to precipitate a Fe-carbonate rich alteration assemblage.

Continued metamorphic devolatilisation at depth is hypothesised to have produced H₂S-rich fluids that scavenged gold from the Kibali thrust stack. At the depositional site lithologies with low level alteration retained sufficient permeability that gold-bearing fluids could flow through them and interacted with the Fe-rich chlorite and Fe-carbonate lithologies depositing iron sulphides and gold. In heavily altered lithologies, where the Fe-carbonate+quartz±aluminoceladonite alteration has been texture destructive, fluid overpressuring and vein mesh formation is hypothesised to have occurred, with the H₂S-bearing fluids scavenging Fe from the wall-rocks to precipitate iron sulphides and associated gold.

The timing of mineralisation relative to the evolution of the KGGB was one of the main questions postulated at the beginning of this study and remains a key factor in modelling the formation of the gold deposits. While the similarities in the mineral alteration and sulphide mineral assemblages in addition to their similar $\delta^{34}\text{S}$ values are interpreted to indicate the deposits formed in a single region-wide mineralisation event, the exact timing of this event is still uncertain.

On the basis of the U:Pb zircon data two potential time periods in which large scale fluid flow may have been occurring were suggested: (1) the period of terrane accretion and metamorphism at 2.64 Ga; and (2) the region-wide lead loss event at approximately 500 Ma when the West Nile Gneiss over-thrust the KGGB and UCG during the Oubanguide orogenic event. Re:Os analysis of gold-bearing pyrite, while not producing a conclusive age, has indicated that the gold-bearing pyrite phase formed at approximately 2 Ga. Whether this represents the true age of mineralisation is unclear and will require further work, but does suggest that a currently unknown geological event at 2 Ga is related to the development of mineralisation.

U:Pb monazite ages from the minor monazite phase, occurring in the mineralised horizons intergrown with auriferous pyrite, returned formation ages that defined a window between 515-615 Ma, corresponding with the interpreted Oubanguide orogenic event (Allibone (2015) D6 event). These data shows that the mineralising systems were reactivated during the Oubanguide event with fluid flow being sufficient to either precipitate new mineral phases or recrystallise pre-existing phases. Whether any gold mineralisation occurred during this event is unknown, although the secondary gold remobilisation (observed as native and fracture hosted gold in all deposits) may have taken place during this time.

11.3 Conclusions

The main aims of this study (Chapter 1) were to characterise the formation and evolution of the Kibali Granite-Greenstone Belt and its neighbouring terranes, and to characterise gold mineralisation at the KCD, Mengu, Pakaka and Pamao deposits, while utilising radioisotopes to place the formation of mineralisation in the context of the regional evolution. The data presented in this study have directly addressed these aims,

significantly advancing the knowledge base of the Kibali Granite-Greenstone Belt and its neighbouring terranes. The main findings of this study are as follows;

- The Kibali Granite-Greenstone Belt is composed of thrust stacked meta-sediments; consisting principally of variable volcano-sedimentary conglomerates and biotite schists, banded iron formations and tholeiitic basalts. The metasedimentary lithologies are intruded by a number of igneous plutons ranging in composition from gabbro to granite.
- The Upper Congo Granitic Massif is composed of multi-phase intrusive plutons with 4 distinct phases identified, in addition to a number of currently undifferentiated intrusions. These intrusions are compositionally diverse ranging from layered mafic intrusions (dominated by plagioclase feldspar) to K-feldspar-rich granites.
- The West Nile Gneiss over-thrusts the Kibali Granite-Greenstone Belt along its northern edge and is classified as a granite-gneiss. The gneiss is variably deformed, with a noted increase in deformation towards the contact with the Kibali Granite-Greenstone Belt.
- The Kibali Granite-Greenstone Belt and the Upper Congo Granite Massif formed in an arc/back-arc environment, the back arc-basin forming the proto-Kibali basin into which the metasediments were deposited. This is thought to be the north east extension of a regional accretionary trend along the northern margin of the Proto-Congo Craton during the Neoproterozoic. U:Pb zircon data has been used to constrain this accretionary event to the period 2.63-2.64 Ga.
- U:Pb zircon data identified a significant metamorphic event in the West Nile Gneiss at 1 Ga that is not observed in the other terranes. This has been interpreted as showing that the two terranes were separate at this time.
- Collision and accretion of the West Nile Gneiss with the Kibali Granite-Greenstone Belt is constrained by U:Pb zircon and U:Pb monazite to the period 600-400 Ma. This is correlated with the Pan-African Oubanguidic orogenic event and is thought to have been accompanied by region wide fluid flow and alteration.
- Mineralisation at the four deposits (KCD, Mengu, Pakaka and Pamao) display similar characteristics, being characterised by a pyrite(±gold) +arsenopyrite+ chalcopyrite+ pyrrhotite ±marcasite sulphide assemblage occurring as both disseminated and vein style sulphides.
- In all cases mineralisation is identified in deformed volcano-sedimentary conglomerates, basalts and Banded Iron formations that have been extensively altered prior to mineralisation by Fe-carbonate (ankerite±siderite)+quartz±aluminoceladonite.
- The formation of mineralisation is linked to an interplay between ‘reaction weakening’ and ‘hydrothermal hardening’ of the host lithologies. These processes resulted in the localised

fluctuation of permeability focusing deep sourced CO₂ and H₂S-rich fluids into the deposition site and led to the range of mineralised textures identified in the deposits.

- The similarities between the deformation, alteration and mineralisation of each deposit, in addition to the similar $\delta^{34}\text{S}$ values [-1 – 8‰ (VCDT)] is interpreted as indicating mineralisation formed in a single region-wide event, occurring during the development of greenschist facies metamorphism in the Kibali Granite-Greenstone Belt.
- Re:Os pyrite data indicate mineralisation formed at approximately 2 Ga, however further data are required to confirm this.
- U:Pb monazite dating showed monazite associated with the auriferous pyrite was either formed or had its isotopic characteristics reset during the period 600-500 Ma. This indicates that the mineralised systems were reactivated during the Oubanguide orogeny (collision of the West Nile Gneiss and Kibali Granite-Greenstone Belt).

11.4 Further Work

This study has significantly developed the understanding of the formation and evolution of the Kibali Granite-Greenstone Belt, the Upper Congo Granitic massif and the West Nile Gneiss and has begun to place the formation of gold mineralisation into a regional context. Further study is however required to achieve a better understanding of the evolution of the KGGB and the controls on the formation of gold mineralisation, several prominent themes that require further investigation are outlined below;

1. Age of mineralisation. Accurately constraining the age of mineralisation will provide additional information regarding the evolution of the region as a whole, and also increase understanding of the evolution of the mineralised systems. Current data indicates, several periods of high fluid flow through the mineralising systems, with the current best estimate for the formation of mineralisation being approximately 2 Ga. Continuing with the rhenium-osmium dating should be the focus, with the aim of augmenting the existing data set, by sampling from lithologies adjacent to the analysed samples, to generate a conclusive age for the formation of auriferous pyrite.
2. Fluid composition. Establishing the composition of the fluids involved in the formation of alteration and gangue phases would provide essential data, allowing the determination of accurate formation temperatures and pressures. To achieve this, detailed fluid inclusion and complimentary isotopic studies ($\delta^{18}\text{O}$, δD) should be undertaken. These techniques were investigated during this study, but pilot studies produced no usable data. Difficulties in separating the quartz, ankerite and siderite

mineral phases with the available equipment precluded the use of $\delta^{18}\text{O}$ and δD , while small inclusion size and interpreted deformation of the quartz host (deformation modifies inclusion shape and alters the volume of the inclusion) raised concerns regarding the validity of fluid inclusion data. If these challenges can be overcome, by either the availability of more suitable sample material or improved preparation techniques, fluid composition data would prove invaluable.

3. Metamorphic characteristics of the Kibali Granite-Greenstone Belt. While significant progress has been made in the understanding of the formation and evolution of the KGGB, the metamorphic characteristics of the belt, and in particular the eastern end of the belt, are relatively poorly known. In particular, accurate P-T data would significantly advance the understanding of the evolution of the belt. Garnet-mica schists have been reported in the eastern end of the belt and would provide an ideal medium, using the garnet compositions, to estimate the P-T conditions that these lithologies formed under.

Chapter 12: References

Abdelsalam, M.G., Liegeois, J.P., Stern, R., 2002. The Saharan Metacraton. *Journal of African Earth Sciences*, v.34, p. 119-136.

Abdelsalam, M.G., Gao, S.S., Liegeois, J.P., 2011. Upper Mantle Structure of the Saharan Metacraton. *Journal of African Earth Sciences*. v.60, p. 328-336.

Allibone, A., 2015. The KZ Structure, Controls on Mineralization in the Kibali District. Unpublished report to Randgold Resources LTD.

Anhaeusser, C.R., 2010. Magmatic and structural characteristics of the ca.3440 Ma Theespruit Pluton, Barberton Mountain Land, South Africa. *American Journal of Science*, v.310, p. 1136-1167.

Anhaeusser, C.R., 2014. Archaean greenstone belts and associated granitic rocks-A review. *Journal of African Earth Sciences*, v.100, p. 684-732.

Arne, D.C., Bierlein, F.P., Morgan, J.W., Stein, H.J., 2001. Re-Os dating of sulphides associated with gold mineralization in central Victoria Australia. *Economic Geology*, v.96, p. 1455-1499.

Ault, W.U., Jensen, M.L., 1963. Summary of sulfur isotope standards. In: *Biogeochemistry of Sulfur Isotopes*. Jensen, M.L. (ed) National Science Foundation, Symp Proc, Yale University.

Barley, M.E., and Groves, D.I., 1990. Deciphering the tectonic evolution of Archean greenstone belts: The importance of contrasting histories to the distribution of mineralization in the Yilgarn Craton, Western Australia: *Precambrian Research*, v.46, p. 3-20.

Barley, M.E., 1997. The Pilbara Craton. In: De Wit, M.J., Ashwal, L.D., (Eds.). *Greenstone Belts*, v. 5.12. Clarendon Press, Oxford, p. 657-664.

Begg, G.C., Griffin, W.L., Natapov, L.M., O'Reilly, S.Y., Grand, S.P., O'Neill, C.J., Hronsky, J.M.A., Poudjom Djomani, Y., Swain, C.J., Deen, T., Bowden, P., 2009. The lithospheric architecture of Africa: Seismic tomography, mantle petrology and tectonic evolution. *Geosphere*, v. 5, p. 23-50.

Bierlein, F.P., Crowe, D.E., 2000. Phanerozoic Orogenic Lode Gold Deposits. *SEG Reviews*, v. 13, p. 103-139.

Bierlein, F.P., Groves, D.I., Cawood, P.A., 2010. Metallogeny of accretionary orogens: The connection between lithospheric processes and metal endowment. *Ore Geology Reviews*, v. 36, p. 282-292.

Bierlein, F. P., Groves, D. I., Goldfarb, R. J., Dubé, B. 2006. Lithospheric controls on the formation of provinces hosting giant orogenic gold deposits. *Mineralium Deposita*, v. 40, p. 874-886.

Blenkinsop, T., Martin, A., Jelsma, H.A., Vinyu, M.L., 1997. The Zimbabwe Craton. In: De Wit, M.J., Ashwal, L.D. (Eds.). *Greenstone Belts*, v. 5.12. Clarendon Press, Oxford, pp. 567-580.

Block, S., Moyen, J-F., Zeh, A., Poujol, M., Jaguin, J., Paquette, J-L., 2013. The Murchinson greenstone belt, South Africa: Accreted slivers with contrasting metamorphic conditions. *Precambrian Research*. v. 227, p. 77-98.

Boatner, A.L., 2002. Synthesis, structure and properties of monazite, pretulite and xenotime, *in* *Phosphates-Geochemical, Geological and Materials Importance*, 2002, Kohn, J.M., Rakovan, J., Hughes, J.M., eds., Mineralogical Society of America, *Reviews in Mineralogy and Geochemistry*, v. 48, p. 87-121., ISBN: 0-93995060-X.

Borg, G., Krogh, T., 1999. Isotopic age data of single zircons from the Archaean Sukumaland Greenstone Belt, Tanzania, *Journal of African Earth Sciences*. v. 29, p. 301-312.

Borg, G., Shackleton, R.M., 1997. The Tanzania and NE Zaire Cratons. In: De Wit, M.J., Ashwal, L.D. (Eds.). *Greenstone Belts*, v. 5.9, Clarendon Press, Oxford, p. 608-619.

Brandl, G., Cloete, M., Anhaeusser, C.R., 2006. Archaean Greenstone belts In: Johnson, M.R., Anhaeusser, C.R., Thomas, R.J. (Eds.). *The Geology of South Africa*. Geological Society of South Africa, Johannesburg and Council for Geoscience, Pretoria, p. 5-9.

Buchwaldt, R., Toulkerides, T., Todt, W., Ucauwun, E. K. 2008. Crustal age domains in the Kibaran belt of SW-Uganda: Combined zircon geochronology and Sm-Nd isotopic investigation. *Journal of African Earth Sciences* v. 1, p. 4-20.

Burrows, D.R., Spooner, E.T.C., 1989. Relationships between Archaean gold vein-shear zone mineralization and igneous intrusions in the Val d'Or and Timmins areas, Abitibi subprovince, Canada. *Economic Geology Monograph*, v. 6, p. 424-444.

Cahen, L., Snelling, N.J., 1966. *The Geochronology of Equatorial Africa*. North-Holland Publishing Company. Amsterdam.

Cahen, L., Snelling, N.J., Delhal, J., Vail, J.R., 1984. *The geochronology and evolution of Africa*. Oxford Science Publishing., Clarendon press, Oxford. UK.

Cameron, E.M., 1982. Sulphate and sulphate reduction in early Precambrian oceans. *Nature*, v. 296, p. 145-148.

Cameron, E.M., 1988. Archean gold: relation to granulite formation and redox zoning in the crust. *Geology*, v. 16, p. 109-112.

Cann, J. R., 1970. Rb, Sr, Y, Zr and Nb in some ocean floor basaltic rocks. *Earth and Planetary Science Letters*, v. 10, p. 7-11.

Cardon, O., Reisberg, L., Andre-Mayer, A., Leroy, J., Milu, V., Zimmermann, C., 2008. Re-Os systematics of pyrite from the Bolcana porphyry copper deposit, Apuseni Mountains, Romania. *Economic Geology*, v. 103, p. 1695-1702.

Cathelineau, M., 1988. Cation occupancy in chlorites and illites as a function of temperature. *Clay Miner.* v. 23, p. 471-485.

Cawood, P. A., Hawkesworth, C. J., Dhuime, B. 2013. The continental record and the generation of continental crust. *Geological Society of America Bulletin*, v. 125, p. 14-32.

Chamberlain, C.M., Tosdal, R.M., 2007. U-Pb Geochronology of the Lake Victoria Greenstone Terrane, Tanzania. Mineral Deposit Research Unit, The University of British Columbia (Research Program on World-class Gold Deposits and Advanced Exploration Projects Owned and/or Joint Ventured to Barrick Gold, Placer Dome, Anglo-Gold Ashanti, Resolute Mining NL as Main sponsors).

Chang, Z., Large, R. R., & Maslennikov, V., 2008. Sulfur isotopes in sediment-hosted orogenic gold deposits: Evidence for an early timing and a seawater sulfur source. *Geology*, v. 36, p. 971-974.

Cherniak, D.J., 2010. Diffusion in accessory minerals: zircon, titanite, apatite, monazite and xenotime. *Reviews in Mineralogy and Geochemistry*, v. 72, p. 827-869.

Cherniak, D.J., Pyle, J.M., 2008. Th diffusion in monazite. *Chemical Geology*, v. 256, p. 52-61.

Cherniak, D. J., Watson, E.B., Grove, M., Harrison, T.M., 2004. Pb diffusion in monazite: a combined RBS/SIMS study. *Geochemica et Cosmochimica Acta*, v. 68, p. 829-840.

Cline, J.S. Bodnar, R.J., 1991. Can economic porphyry copper mineralization be generated in a typical calc-alkaline melt? *Journal of Geophysical Research*, v. 96, p. 8113-8126.

Condie, K.C., 1998. Episodic continental growth and supercontinents: A mantle avalanche connection? *Earth and Planetary Science Letters*, v. 163, p. 97-108.

Condie, K.C., 2005. High Field Strength element ratios in Archean basalts: a window to evolving sources of mantle plumes? *Lithos*, v. 79, p. 491-504.

Condie, K., 2015. Changing tectonic settings through time: Indiscriminate use of geochemical discriminant diagrams. *Precambrian Research*, v. 266. p. 587-591.

Condie, K. C., Aster, R. C., 2010. Episodic zircon age spectra of orogenic granitoids: the supercontinent connection and continental growth. *Precambrian Research*, v. 180, p. 227-236.

Cook, Y.A., Sanisla, I.V., Hammerli, J., Blenkinsop, T.G., Dirks, P.H.G.M., 2015. A primitive mantle source for the Neoproterozoic mafic rocks from the Tanzania Craton. *Geoscience Frontiers*, v. 1-16, p. 1-16.

Corfu, F., Hanchar, J.M., Hoskin, P.W.O., Kinny, P., 2003. Atlas of Zircon Textures. *Reviews in Mineralogy and Geochemistry*, v. 53, p. 469-500.

Cox, S.F., 2002. Fluid flow in mid- to deep crustal shear systems: Experimental constraints, observations on exhumed high fluid flux shear systems, and implications for seismogenic processes. *Earth Planets Space*, v. 54, p. 1121-1125.

Craw, D., Upton, P., Horton, T., Williams, J. 2013. Migration of hydrothermal systems in an evolving collisional orogeny, New Zealand. *Mineralum Deposita*, v. 48, p. 233-248.

Craw, D., Upton, P., Mackenzie, D. J. 2009. Hydrothermal alteration in ancient and modern orogenic gold deposits, New Zealand. *New Zealand Journal of Geology and Geophysics*, v. 52:1, p. 11-26.

Crocket, J.H., 1969. Platinum Metals. In Wedepohl, W.H., (Ed.), *Handbook of Geochemistry*. II-5. Springer-Verlag, Heidelberg.

Crowley, J.L., Brown, R.L., Gervais, F., Gibson, H.D., 2008. Assessing inheritance of zircon and monazite in granitic rocks from the Monashee Complex, Canadian Cordillera. *Journal of Petrology*, v. 49 (11), p. 1915-1929.

Davidson, J., Turner, S., Handley, H., Dosseto, A., 2013. Dy/Dy* Variations Arising from mantle Sources and Petrogenetic Processes. *Journal of Petrology*, v. 54, p. 525-537.

Deer, W.A., Howie, R.A., Zussman, J., 1966. *An Introduction to the Rock Forming Minerals*. Longmans, Green & Co. Ltd., London. ISBN 10: 0582442109

De Ronde, C.E.J., Faure, K., Bray, C.J., Whitford, D.J., 2000. Round Hill shear zone-hosted gold deposit, Macraes Flat, Otago, New Zealand: Evidence of a magmatic ore fluid: *Economic Geology*, v. 95, p. 1025-1048.

De Ronde, C.E.J., Spooner, E.T.C., de Wit, M.J., Bray, C.J., 1992. Shear zone-related, Au quartz vein deposits in the Barberton greenstone belt, South Africa: field and petrographic characteristics, fluid properties, and light stable isotope geochemistry. *Economic Geology*. v. 87, p. 366-402.

Dumond, G., McLean, N., Williams, M.L., Jercinovic, M.J., Bowring, S.A., 2008. High-resolution dating of granite petrogenesis and deformation in a lower crustal shear zone: Athabasca granulite terrane, western Canadian Shield. *Chemical Geology*, v. 254, p. 175-196.

Drake, M. J., Well, D.F., 1973. Europium anomaly in plagioclase feldspar: Experimental results and semiquantitative model. *Science*, v. 180, p. 1059-1060.

Elliott, T., 2003. Tracers of the Slab. Inside the subduction factory. *Geophysical Monograph Series*, v. 138, p. 23–45.

Erikson, K.A., Krapez, B., Fralick, P. W., 1997. Sedimentology aspects In: De Wit, M.J., Ashwal, L.D. (Eds.). *Greenstone Belts*, v. 2.1. Clarendon Press, Oxford, p. 33-45.

Escuder Viruete, J., Contreras, F., Stein, G., Urien, P., Joubert, M., Pérez-Estaun, A., Friedman, R., Ullrich, T., 2007. Magmatic relationships and ages between adakites, magnesian andesites and Nb-enriched basalt-andesites from Hispaniola: Record of a major change in the Caribbean island arc magma sources. *Lithos*, v. 99, p. 151–177.

Escuder Viruete, J., Pérez-Estaún, A., Joubert, M., Weis, D., 2011. The Pelona-Pico Duarte basalts Formation, Central Hispaniola: an on-land section of Late Cretaceous volcanism related to the Caribbean large igneous province. *Geologica Acta*, v. 9, p. 307–328.

Faure, G., Mensing, T. M., 2005. *Isotopes: principles and applications*. John Wiley & Sons Inc. ISBN: 0-471-38437-2

Finch, R.J., Hanchar, J.M., 2003. Structure and Chemistry of Zircon and Zircon-Group Minerals. *Reviews in mineralogy and geochemistry*, v. 53, p. 1-26.

Fitton, J.G., Saunders, A.D., Norry, M.J., Hardarson, B.S., Taylor, R.N., 1997. Thermal and chemical structure of the Iceland plume. *Earth and Planetary Science Letters*, v. 153, p. 197–208.

Foley, S., Tiepolo, M and Vannucci, R., 2002. Growth of early continental crust controlled by melting of amphibolite in subduction zones. *Nature*, v. 417, p. 837-840.

Frimmel, H. E., 2008. Earth's continental crustal gold endowment. *Earth and Planetary Science Letters*, v. 267, p. 45-55.

Gabourey, D., 2013. Does gold in orogenic deposits come from pyrite in deeply buried carbon rich sediments? Insight from volatiles in fluid inclusions. *Geology*, v. 41, p. 1207-1210.

Goldfarb, R.J., Baker, T., Dube, B., Groves, D.I., Hart, C.J.R., Gosselin, R., 2005. Distribution, character, and genesis of gold deposits in metamorphic terranes, in Hedenquist, J.W., Thompson, J.F.H., Goldfarb, R.J., Richards, J.P., (eds), *Economic Geology 100th Anniversary Volume*, p. 407-450.

Goldfarb, R.J., Groves, D.I., Gardoll, S., 2001, Orogenic gold and geologic time: A global synthesis: *Ore Geology Reviews*, v. 18, p. 1-75.

Goldfarb, R.J., Newberry, R.J., Pithorn, W.J., Gent, C.A., 1991. Oxygen, hydrogen, and sulphur isotope studies in the Juneau gold belt, southeastern Alaska: constraints on the origin of hydrothermal fluids. *Economic Geology*, v. 86, p. 66-80.

Golding, S.D., Clark, M.E., Keele, R.A., Wilson, A.F., Keays, R.R., 1990. Geochemistry of Archean epigenetic gold deposits in the Eastern Goldfields Province, Western Australia. *Geol. Dept. Univ. Extension, Univ. West. Aust. Publ.* v. 23, p. 141-176.

Gray, D. R., Foster, D. A., Meert, J. G., Passchier, C. W., 2008. A Damara orogeny perspective on the assembly of Southwestern Gondwana. *Geological Society London Special Publication*, v. 295, p. 257-278.

Gross, G.A. 1996. Algoma-type Iron formation, in *Selected British Columbia Mineral Deposit Profiles, Volume 2- Metallic Deposits*, Lefebure, D.V. and Hoy, T., (Eds.), *British Columbia Mineral of Employment and Investment, Open File 1996-13*, p. 25-28.

Groves, D.I., Barley, M.E., Barnicoat, A.C., Cassidy, K.F., Fare, R.J., Hagemann, S.G., Ho, S.E., Hronsky, J.M.A., Mikucki, E.J., Mueller, A.G., McNaughton, N.J., Perring, C.S., Ridley, J.R., Vearncombe, J.R., 1992. Sub-Greenschist- to granulite-hosted Archean lode gold deposits of the Yilgarn Craton: a depositional continuum from deep-sourced hydrothermal fluids in crustal-scale plumbing systems. In: Glover, J.E., Ho, S.E. (Eds.), *The Archaean: Terrains Processes and Metalogeny*. *Geol. Dep. Univ. Extension, Univ. West. Aust. Publ. No. 22*, p. 325-337.

Groves, D.J., Goldfarb, R.J., Robert, F., Hart, C.J.R., 2003. Gold deposits in metamorphic belts: Overview of current understanding, Outstanding problems, Future research, and Exploration significance: *Economic Geology*, v. 98, p. 1-29.

Groves, D.I., Vielreicher, R.M., Goldfarb, R.J., Condie, K.C., 2005. Secular changes in global tectonic processes and their influence on the temporal distribution of gold-bearing mineral deposits. *Economic Geology*, v. 100, p. 203-224.

Handy, M.R., 1990. The Solid-State Flow of Polymineralic Rocks. *Journal of Geophysical Research*, v. 95 (6), p. 8647-8661.

Harlov, D.E., Wirth, R., Hetherington, C.J., 2007. The relative stability of monazite and huttonite at 300-900 degrees C and 200-1000 MPa: metasomatism and the propagation of metastable mineral phases. *American Mineralogist*, v. 92 (10), p. 1652-1664.

Harlov, D.E., Wirth, R., Hetherington, C.J., 2011. Fluid-mediated partial alteration in monazite: the role of coupled dissolution-precipitation in element redistribution and mass transfer. *Contributions to Mineralogy and Petrology*. v. 162 (2), p. 329-348.

Harlov, D.E., Hetherington, C.J., 2010. The relative Partial high-grade alteration of monazite using alkali-bearing fluids: experiment and nature. *American Mineralogist*, v. 87, p. 245-261.

Harrison, T.M., Catlos, E.J., Montel, J.M., 2002. U-Th-Pb of phosphate minerals. *in* Kohn, J.M., Rakovan, J., and Hughes, J.M. (Eds.), *Phosphates- Geochemical, geological, and materials importance: Reviews in Mineralogy and Geochemistry*, v. 48, p. 523-558.

Hastie, A.R., 2009. Is the Cretaceous primitive island arc (PIA) series in the circum-Caribbean region geochemically analogous to the modern island arc tholeiites (IAT) series? *In*: James, K.H., Lorente, M.A., Pindell, J. (Eds.), *Geology of the area between North and South America, with focus on the origin of the Caribbean Plate: Geological Society of London, Special Publication*, v. 328, p. 397-409.

Hastie, A.R., Kerr, A.C., Pearce, J.A., Mitchel, S. F., 2007. Classification of altered volcanic island arc rocks using immobile trace elements: Development of the Th-Co discrimination diagram. *Journal of Petrology*, v. 48, p. 2341-2357.

Hastie, A.R., Mitchel, S.F., Treloar, P.J., Kerr, A.C., Neill, I., Barfod, D.N., 2013. Geochemical components in a Cretaceous island arc: The Th/La-(Ce/Ce*)_{nd} diagram and implications for subduction initiation in the inter-American region. *Lithos*, v. 162-163, p. 57-69.

Hickman, A.H., 2012. Review of the Pilbara Craton and Fortescue Basin, Western Australia: Crustal evolution providing environments for early life. *Island Arc*. v. 21, p. 1-31.

Hickman, A.H., Van Kranendonk, M.J., 2012. Early Earth evolution: evidence from the 3.5-1.8Ga geological history of the Pilbara region of Western Australia. *Episodes*, v. 35, p. 283-297.

Human Rights Watch, 2005. *The Curse of Gold*. <http://www.hrw.org>.

Hoskin, P. W., Schaltegger, U., 2003. The composition of zircon and igneous and metamorphic petrogenesis. *Reviews in Mineralogy and Geochemistry*, v. 53, p. 27-62.

Jackson, S. E., Pearson, N. J., Griffin, W. L., Belousova, E. A., 2004. The application of laser ablation-inductively coupled plasma-mass spectrometry to in situ U-Pb zircon geochronology. *Chemical Geology*, v. 211, p. 47-69.

Jenkin, G.R.T., Craw, D., Fallavk, A.E., 1994. Stable isotopic and fluid inclusion evidence for meteoric fluid penetration into an active mountain belt; alpine schist, New Zealand. *Journal of Metamorphic Geology*, v.12, p. 429-444.

Jolly, W.T., Lidiak, E.G., Dickin, A.P., 2006. Cretaceous to Mid-Eocene pelagic sediment budget in Puerto Rico and the Virgin Islands (northeast Antilles Island arc). *Geologica Acta*, v. 4, p. 35–62.

Jowitt, E.C., 1991. Fitting Iron and Magnesium into the hydrothermal chlorite geothermometer. GAC/MAC/SEG Joint Annual Meeting (Toronto, May 27-29, 1991), Program with Abstracts 16, A62. Toronto.

Kabete, J.M., Groves, D.I., McNaughton, N.J., Mruma, A.H., 2012a. A New tectonic framework for the Tanzanian Shield: Implications for gold metallogeny and undiscovered endowment. *Ore Geology Reviews*, v. 48, p. 88-124.

Kabete, J.M., McNaughton, N.J., Groves, D.I., Mruma, A.H., 2012b. Reconnaissance SHRIMP U-Pb zircon geochronology of the Tanzania Craton: Evidence for Neoproterozoic granitoid-greenstone belts in the Central Tanzania region and the Southern East African Orogen. *Precambrian Research*, v. 216-219, p. 232-266.

Kerrick, R., 1987. The stable isotope geochemistry of Au-Ag vein deposits in metamorphic rocks. In: Kyser, T.K. (Ed.), *Mineralogical Association of Canada. Short Course 13*, p. 287-336.

Kerrick, R., Allison, I., 1978. Flow mechanisms in rocks: microscopic and mesoscopic structures and their relation to physical conditions of deformation in the crust. *Geoscience Canada*, v. 5, p. 110-118.

Kisangani, E.F., Bobb, F.S., 2010. *Historical Dictionary of the Democratic Republic of the Congo*, Third edition. *Historical Dictionaries of Africa*, no. 112. Scarecrow Press, Inc. Plymouth, United Kingdom.

Kontak, D.J., Smith, P.M., Kerrich, R., Williams, P.F., 1990. An integrated model for Meguma Group lode gold deposits, Nova Scotia, Canada. *Geology*, v. 18, p. 238-242.

Koons, P.O., Craw, D., 1991. Gold mineralization as a consequence of continental collision; an example from the Southern Alps, New Zealand. *Earth and Planetary Science Letters*, v. 103, p. 1-9.

Kosler, J., Simonetti, A., Sylvester, P.J., Cox, R.A., Tubrett, M.N., and Wilton, D.H.C., 2003. Laser Ablation ICP-MS measurements of Re/Os in molybdenite and implications for Re-Os geochronology: *Canadian Mineralogist*, v. 41, p. 307-320.

KPMG Global Mining Institute, 2014. Democratic Republic of Congo; Country mining guide. <http://www.kpmg.com/mining>.

Kretschmar, U. Scott, S.D., 1976. Phase relations involving arsenopyrite in the system Fe-As-S and Their Application. Ph.D. thesis, University of Toronto, Toronto, Ontario.

Labidi, J., Cartigny, P., Hamelin, C., Moreira, M., Dosso, L., 2014. Sulfur isotope budget (^{32}S , ^{33}S , ^{34}S and ^{36}S) in Pacific-Antarctic ridge basalts: A record of mantle source heterogeneity and hydrothermal sulphide assimilation. *Geochemica et Cosmochimica acta*, v. 133, p. 47-67.

Large, R.R., Bull, S.W., Maslennikov, V.V., 2011. A Carbonaceous sedimentary source-rock model for Carlin-type and orogenic gold deposits. *Economic Geology*, v. 106, p. 331-358.

Large, R. R., Danyushevsky, L., Hollit, C., Maslennikov, V., Meffre, S., Gilbert, S., & Foster, J., 2009. Gold and trace element zonation in pyrite using a laser imaging technique: implications for the timing of gold in orogenic and Carlin-style sediment-hosted deposits. *Economic Geology*, v. 104, p. 635-668.

Lawley, C.J., Selby, D., Condon, D., Imber, J., 2014. Palaeoproterozoic orogenic gold style mineralization at the Southwestern Archaean Tanzanian cratonic margin, Lupa Goldfield, SW Tanzania: Implications from U-Pb titanite geochronology. *Gondwana Research* v. 26, p. 1141-1158.

- Lavreau, J., 1984. Vein and stratabound Gold Deposits of Northern Zaire. *Mineralum Deposita*, v. 19, p. 158-165
- Lavreau, J. J., 1973. New data about the Kilo-Moto Gold Deposits (Zaire). *Mineralum Deposita*, v. 8, p. 1-6.
- Le Bas, M.J., Le Maitre, R.W., Steckeisen, A., Zanetti, B. 1986. A chemical classification of volcanic rocks based on the total alkali-silica diagram. *Journal of Petrology*, v. 27, p. 745-750.
- Lee, J.K.W., Williams, I.S., Ellis, D.J., 1997. Pb, U and Th diffusion in natural zircon. *Nature*, v. 390, p. 159-161.
- Lehto, T., Katto, E., 2014. GTK Consortium Geological Surveys in Uganda 2008-2012 Sustainable Management of Mineral Resources Project. Geological Survey of Finland, Special Paper 56.
- Li, Z. X., Zhang, L., Powell, C. M. 1995. South China in Rodinia: part of the missing link between Australia-East Antarctica and Laurentia? *Geology*, v. 23, p. 407-410.
- Lide, D.R., Frederiske, H.P.R., 1995. Handbook of chemistry and physics, 76th ed. CRC press, Boca Raton, Florida.
- Link, K., Koehn, D., Barth, M.G., Tiberindwa, J.V., Barifailo, E., Aanyu, K., Foley, S., 2010. Continuous cratonic crust between the Congo and Tanzania blocks in western Uganda: *International Journal of Earth Sciences (Geol Rundach)*, v. 99, p. 1559-1573.
- Ludwig, K., 2003, Isoplot/Ex, version 3.0: A geochemical toolkit for Microsoft Excel: Berkeley, Geochronology Center, Special Publication 4.

Mahan, K.H., Gonclaves, P., Williams, M.L., Jercinovic, M.J., 2006. Dating metamorphic reactions and fluid flow: application to exhumation of high-P granulites in a crustal scale shear zone, Western Canadian Shield. *Journal of Metamorphic Geology*, v. 24, p. 193-217.

Makitie, H., Harma, P., Virransalo, P., Kock, G. de., Lugaizi, I., Tumwine, A., 2014. The Granite batholith of Mubende, Uganda: preliminary results on its petrography, geochemistry and construction rock potential. In: Lehto, T., Katto, E. (Eds). *GTK Consortium Geological Surveys in Uganda 2008-2012. Geological Survey of Finland, Special Paper 56.*

Mantarri, I., 2010. Mesoarchean to Neoproterozoic U-Pb and Sm-Nd ages from Uganda. In: Lehto, T., and Katto, E. (Eds). *GTK Consortium Surveys in Uganda 2008-2012. Geological Survey of Finland, special Paper 56.*

Mantarri, I., Kigereigu, F., Huhma, H., Kock, G. S. de., Koistinen, T., Kuosmanen, E. T., Lahaye, Y., Lehtonen, M. I., Makitie, H., Manninen, T., O'Brien, H., Saalman, K., Virransalo, P., Westerhoff, A. B., 2011. New Precambrian rock ages from Uganda. *23rd Coll. Afr. Geol. (CAG23)*, 8-14 Jan. 2011, Univ. of Johannesburg, Abstract volume, 260.

Mantarri, I., 2014. Mesoarchean to Neoproterozoic U-Pb and Sm-Nd ages from Uganda. In: Lehto, T. and Katto, E. (Eds). *GTK Consortium Geological Surveys in Uganda 2008-2012. Geological Survey of Finland, Special Paper 56.*

Manya, S., 2002. Geochemistry and petrogenesis of volcanic rocks of the Neoproterozoic Sukumaland Greenstone Belt, Northwestern Tanzania. *Journal of African Earth Sciences*, v. 40, p. 269-279.

Manya, S., Kobayashi, K., Maboko, M.A.H., Nakamura, E., 2006. Ion microprobe zircon U-Pb of the late Archaean metavolcanics and associated granites of the Musoma-Mara Greenstone Belt, Northeast Tanzania: Implications for the geological evolution of the Tanzania Craton. *Journal of African Earth Sciences*, v. 45, p. 355-366.

Manya, S., Maboko, M.A.H., 2003. Dating basaltic volcanism in the Neoproterozoic Sukumaland Greenstone Belt of the Tanzania Craton using the Sm-Nd method: implications for the geological evolution of the Tanzania Craton, *PreCambrian Research*, v. 121, p. 35-45.

Manya, S., Maboko, M.A.H., 2008. Geochemistry and geochronology of Neoproterozoic volcanic rocks of the Iramba–Sekenke greenstone belt, central Tanzania. *Precambrian Research*, v. 163, p. 265-278.

Mather, R., Mortensen, J., 2013. Re-Os dating of gold in gold-bearing orogenic vein systems in the Klondike district. In: *Yukon Exploration and Geology 2012*, MacFarlane, K.E., Nordling, M.G., Sack, P.J. (Eds), Yukon Geological Survey, p. 65-72.

McCuaig, T.C., Kerrich, R., 1998. P-T-t-deformation-fluid characteristics of lode-gold deposits: Evidence from alteration systematics: *Ore Geology Reviews*, v. 12, p. 381-453.

McDonald, I., Viljoen, K. S., 2006. Platinum-group element geochemistry of mantle eclogites: a reconnaissance study of xenoliths from the Orapa kimberlite, Botswana. *Applied Earth Science (Transactions of the Institution of Mining and Metallurgy B)*, v. 115, p. 81-93

Mickelthwaite, S., Ford, A., Witt, W., and Sheldon, H.A., 2014. The where and how of faults, fluids and permeability-insights from fault stepovers, scaling properties and gold mineralisation, *Geofluids*, v. 15, p. 240-251

Mikucki, E.J., 1998. Hydrothermal transport and depositional processes in Archean lode-gold systems: A review: *Ore Geology Reviews*, v. 13, p. 307-321.

Morelli, R.M., 2007. Testing the robustness of Re-Os low level sulphide chronometers: An example from metamorphosed VMS ores, Trans Hudson Orogen, Canada. 2007 GSA Denver Annual Meeting abstract volume.

Morelli, R.H., Bell, C.C., Creaser, R.A., Simonetti, A., 2010. Constraints on the genesis of gold mineralization at the Homestake Gold Deposit, Black Hills, South Dakota from rhenium-osmium sulphide geochronology. *Mineralum Deposita*, v. 45, p. 461-480.

Morelli, R.M., Creaser, R.A., Selby, D., Kontak, D.J., Horne, R.J., 2005. Rhenium-Osmium arsenopyrite geochronology of Meguma Group gold deposits, Megumaterrane, Nova Scotia, Canada: Evidence for multiple gold mineralizing events. *Economic Geology*, v. 100, p. 1229-1242.

Morelli, R., Creaser, R.A., Seltmann, R., Stuart, F.M., Selby, D., Graupner, T., 2007. Age and source constraints for the giant Muruntau gold deposit, Uzbekistan, from coupled Re-Os-He isotopes in arsenopyrite. *Geology*, v. 35, p. 795-798.

Morris, D.F.C., Short, E.L., 1969. Rhenium. In K.H. Wedepohl (Eds.) *Handbook of Geochemistry*, v. II-I. Springer-Verlag, Heidelberg.

Nagudi, B., Koeberl, C., Klotzli, U., 2001. Determination of the petrogenetic history and age of the Singo granite using zircons. *GSU newsletter* 1, p. 36-37. Abstract Volume, Regional Conference GSU and GSAF, Kampala, 10-12 September 2001.

Nesbitt, B.E., 1988. Gold deposit continuum; a genetic model for lode Au mineralization in the continental crust. *Geology*, v. 16, p. 1044-1048.

Nijman, W., Clevis, Q., de Vries, S.T., 2010. The waning stage of a greenstone belt: the mesoarchaeon Mosquito Creek Basin of the East Pilbara, Western Australia. *Precambrian Research*, v. 180, p. 251-271.

Nyakecho, C., Hagemann, S.G., 2014. An overview of gold systems in Uganda, *Australian Journal of Earth Sciences*, v. 61.

Oberthur, T.U., Mumm, A.S., Vetter, U., Simon, K., Amanor, J.A., 1996. Gold mineralization in the Ashanti belt of Ghana: genetic constraints of the stable isotope geochemistry. *Economic Geology*, v. 91, p. 289-301.

Padgham, W.A., 1985. Observations and speculations on supracrustal successions in the Slave Structural Province. In: Ayres, L.D., Thurston, P.C., Card, K.D., Weber, W. (Eds.). *Evolution of Supracrustal sequences*. Geological association of Canada Special Paper 28, p. 133-151.

Palin, R., Searle, M., Waters, D., Parrish, R., Roberts, N., Horstwood, M., Yeh, M.W., Chung, S.L., Anh, T., 2013. A Geochronological and Petrological study of anatectic paragneiss and associated granite dykes from the Day Nui Con Voi metamorphic core complex, North Vietnam: constraints on the timing of metamorphism within the Red River shear zone. *Journal of Metamorphic Geology*, v. 31 (4), p. 359-387.

Peach, C.J., Spiers, C.J., 1996. Influence of crystal plastic deformation on dilatancy and permeability development in synthetic salt rock. *Tectonophysics*, v. 256, p. 101-128.

Pearce, J. A., 1996. A users guide to basalt discrimination diagrams. In: Wyman, D. A. (Eds) *Trace Element Geochemistry of Volcanic Rocks: Applications for Massive Sulphide Exploration*. Geological Association of Canada, Short Course Notes 12, p. 79-113.

Pearce, J. A., 2008. Geochemical fingerprinting of oceanic basalts with applications to ophiolite classification and the search for Archean oceanic crust. *Lithos*, v. 100, p. 14-28.

Pearce, J.A., Peate, D.W., 1995. Tectonic implications of the composition of volcanic arc magmas. *Annual Reviews Earth and Planetary Science Letters*, v. 23, p. 251–285.

Pearce, J.A., Stern, R.J., 2006. Origin of back-arc basin magmas. Trace element and isotope perspectives. *Geophysical Monograph Series*, v. 166, p. 63–86.

Peccerillo, R., Taylor, S. R., 1976. Geochemistry of Eocene calc-alkaline volcanic rocks from the Kastamonu area, Northern Turkey. *Contributions to Mineralogy and Petrology*, v. 58, p. 63-81.

Pedreira, A. J., Waele, B. De., 2008. Contemporaneous evolution of the Paleoproterozoic-Mesoproterozoic sedimentary basins of the Sao-Francisco-Congo Craton. *Geological Society., London, Special Publication*, v. 294, p. 33-48.

Philips, G.N., Powell, R., 2010. Formation of gold deposits: A metamorphic devolatilization model. *Journal of Metamorphic Geology*, v. 28, p. 689-718.

Pin, C., Poivedin, J.L., 1987. U-Pb zircon evidence for a Pan-African granulite facies metamorphism in the Central African Republic. A new interpretation of the high grade series of the northern border of the Congo Craton. *Precambrian Research*, v. 36, p. 303-312.

Pinna, P., Cocherie, A., Thieblemont, D., Jezequel, P., Kayogoma, E. 2004. The Making of the East African Craton 2.93-2.53 Ga. 20th Coll. Afr Geol. (CAG20), 2-7 June 2004, BGRM, Orleans, 336.

Pitcairn, I. K., Craw, D., Teagle, D.A.H., 2015. Metabasalts as sources of metals in orogenic gold deposits. *Mineralum Deposita*, v. 50, p. 373.

Pitcairn, I. K., Olivo, G. R., Teagle, D. A., Craw, D., 2010. Sulfide evolution during prograde metamorphism of the Otago and Alpine Schists, New Zealand. *The Canadian Mineralogist*, v. 48, p. 1267-1295.

Pitcairn, I. K., Teagle, D. A., Craw, D., Olivo, G. R., Kerrich, R., Brewer, T. S. (2006). Sources of metals and fluids in orogenic gold deposits: insights from the Otago and Alpine Schists, New Zealand. *Economic Geology*, v. 101, p. 1525-1546.

Powell, R., Will, T.M., Phillips, G.N., 1991. Metamorphism in Archean greenstone belts: calculated fluid compositions and implications for gold mineralisation. *Journal of Metamorphic Geology*, v. 9, p. 141-150.

Pyle, J.M., Spear, F.S., 2003. Four generations of accessory-phase growth in low-pressure migmatites from SW New Hampshire. *American Mineralogist*, v. 88, p. 338-351.

Randgold Resources Ltd, 2010. Technical Report (NI 43-101); Kibali Gold Project in the Democratic Republic of Congo.

Randgold Resources Ltd, 2013. Kibali Gold Mine Annual Report 2013. <http://www.rangoldresources.com>.

Rasmussen, B., Sheppard, S., Fletcher, I.R., 2006. Testing ore deposit models using in situ U-Pb geochronology of hydrothermal monazite: Paleoproterozoic gold mineralization in northern Australia. *Geology*, v. 34, p. 77-80.

Ries, A., Vearncombe, J.R., Price, R.C., Shackleton, R. M., 1992. Geochronology and geochemistry of the rocks associated with a late Proterozoic ophiolite in West Pokot, NW Kenya: *Journal of African Earth Sciences*, v. 14, p. 25-36.

Ridley, J.R., Diamond, L.W., 2000. Fluid chemistry of orogenic lode-gold deposits and implications for genetic models: *Reviews in Economic Geology*, v. 11, p. 265-290.

Robb, L.J., Robb, V.M., 1986. Archaean pegmatite deposits in the north eastern Transvaal. In: Anhaeusser, C.R., Maske, S., (Eds.). *Mineral deposits of Southern Africa*, vol. 1. Geological Society of South Africa, Johannesburg. p. 437-449.

Robinson, B.W., Kusakabe, M., 1975. Quantitative preparation of sulfur dioxide for $^{34}\text{S}/^{32}\text{S}$ analyses from sulphides by combustion with cuprous oxide: *Analytical Chemistry*, v. 47, p. 1179-1181.

Rock, N.M.S., Groves, D.I., Perring, C.S., Golding, S.D., 1989. Gold lamprophyres, and porphyries; what does their association mean? In: Keays, R.R., Ramsey, W.R.H., Groves, D.I. (Eds), *The Geology of Gold deposits: the perspective in 1988*. *Economic Geology Monogram*, v. 6, p. 609-625.

Rollinson, H., 2003. *Using Geochemical data: evaluation, presentation, interpretation*. Pearson Education Limited, Essex, UK. ISBN: 978-0-582-06701-1

Ruotoistenmaki, T., 2014. Geophysical characteristics of ASWA shear, Nagasongola discontinuity and Ring dyke complex in Uganda. *Journal of African Earth Sciences*, v. 93, p. 23-41.

Rye, R.O., Ohmoto, H., 1974. Sulfur and carbon isotopes and ore genesis: a review. *Economic Geology*, v. 69, p. 826-842.

Salier, B.P., Groves, D.I., McNaughton, N.J., Fletcher, I., 2004. The world class Wallaby gold deposit, Laverton, Western Australia: an orogenic-style overprint on magmatic-hydrothermal magnetite-calcite alteration pipe? *Mineralum Deposita*, v. 39, p. 473-494.

Sanislav, I. V., Kolling, S. L., Brayshaw, M., Cook, Y. A., Dirks, P. H. G. M., Blenkinsop, T. T., Mturi, M. I., Ruhega, R., 2015. The geology of the giant Nyankanga gold deposit, Geita Greenstone Belt, Tanzania. *Ore Geology Reviews*, v. 69. p. 1-16.

Sanislav, I. V., Wormald, R. J., Dirks, P. H. G. M., Blenkinsop, T. G., Salamba, L., Joseph. D., 2014. Zircon U-Pb ages and Lu-Hf isotope systematics from late-tectonic granites, Geita Greenstone Belt: Implications for crustal growth of the Tanzania Craton. *Precambrian Research*, v. 242, p. 187-204.

Sarma, D.S., Fletcher, I.R., Rasmussen, B., McNaughton, N.J., Ram Mohan, M., Groves, D.I., 2011. Archean gold mineralization synchronous with late cratonization of the Western Dharwar Craton, India: 2.52 Ga U-Pb ages of hydrothermal monazite and xenotime in gold deposits. *Mineralum Deposita*, v. 46, p. 273-288.

Schoene, B., 2013. U-Th-Pb Geochronology, In, Holland, H.D., and Turekian, K.K., *Treatise on Geochemistry* 2nd edition, v. 4, p. 341-378.

Schumann, A., Sschenk, V., Kulyanyingi, P. K., Morelli, C., Barton, E., Garbe-Schonberg, D., 2004. Evidence for the widespread occurrence of neo-Archean GGM-type granitoids in eastern Uganda: Orleans, Abstracts, 20th Colloquium of African Geology, 366.

Seal, R.R., 2006. Sulfur Isotope Geochemistry of Sulfide Minerals. *Reviews in Mineralogy and Geochemistry*. v. 61, p. 633-677.

Selby, D., Creaser, R.A., 2004. Macroscale NTIMS and microscale LA-MC-ICP-MS Re-Os isotopic analysis of molybdenite: Testing spatial restrictions for reliable Re-Os age determinations, and implications for the decoupling of Re and Os within Molybdenite: *Geochemica et Cosmochimica Acta*, v. 68, p. 3897-3908.

Selby, D., Kelley, K. D., Hitzman, M.W., Ziec, J., 2009. Re-Os Sulfide (Bornite, Chalcopyrite, and Pyrite) systematics of the carbonate-hosted copper deposits at Ruby Creek, southern Brooke Range, Alaska. *Economic Geology*. v. 104, p. 437-444

Sharp, Z.D., Essne, E.J., Kelly, W.C., 1985. The Re-examination of the arsenopyrite geothermometer: Pressure considerations and application to natural assemblages. *Canadian Mineralogist*, v. 23, p. 517-534.

Sibson, R. H., Robert, F., Poulsen, K. H., 1988. High-angle reverse faults, fluid-pressure cycling, and mesothermal gold-quartz deposits. *Geology*, v. 16, p. 551-555.

Sibson, R.H., 1990. Faulting and fluid flow: Mineralogical Association of Canada, Short Course 18, p. 93-132.

Sibson, R.H., 1996. Structural permeability of fluid-driven fault-fracture meshes. *Journal of Structural Geology*, v. 18, p. 1031-1042.

Sibson, R. H., 2004. Controls on maximum fluid overpressure defining conditions for mesozonal mineralisation. *Journal of structural geology*, v. 26, p. 1127-1136.

Slama, J., Kosler, J., Condon, D.J., Crowley, J.L., Gerdes, A., Hanchar, J.M., Horstwood, M.S.A., Morris, G.A.M., Nasdala, L., Norberg, N., Schaltegger, U., Schoene, B., Tubrett, M. N., Whitehouse, M.J., 2008. Plesovice zircon- A new natural reference material for U-Pb and Hf isotopic microanalysis. *Chemical Geology*, v. 249, p. 1-35.

Stefansson, A., and Seward, T.M., 2004. Gold (I) complexing in aqueous sulphide solutions to 500°C at 500 bar. *Geochimica et Cosmochimica acta*, v. 68, no. 20, p. 4121-4123.

Stein, M., Hoffmann, A.W., 1994. Mantle plumes and episodic crustal growth. *Nature*, 372, 63-68.

Stein, H.J., Schersten, A., Hannah, J., Markey, R., 2003. Subgrain-scale decoupling of Re and ¹⁸⁷Os and assessment of laser ablation ICP-MS spot dating in molybdenite: *Geochimica et Cosmochimica acta*, v. 67, p. 3673-3686.

Stolz, A.J., Jochum, K.P., Spettel, B., Hofmann, A.W., 1996. Fluid- and melt-related enrichment in the subarc mantle: evidence from Nb/Ta variations in island-arc basalts. *Geology*, v. 24, p. 587-590.

Sun, S., McDonough, W.F., 1989. Chemical and isotope systematics of oceanic basalts: implications for mantle composition and processes. *Magmatism in the Ocean Basins*. Geological Society of London, Special Publication 42, p. 313–345.

Sylvester, P.J., Harper, G.D., Byerly, G.R., Thurston, P.C., 1997. Volcanic aspects. In: De Wit, M.J., Ashwal, L.D. (Eds.). *Greenstone Belts*, vol. 2.2 Clarendon Press, Oxford, p. 55-90.

Tack, L., Wingate, M.T.D., Waele, B. De, Meert, J., Belousova, E., Griffin, B., Tahon, A., Fernandez-Alonso, M., 2010. The 1375 Ma “Kibaran event” in Central Africa: Prominent emplacement of bimodal magmatism under extensional regime. *Precambrian Research*, v. 180, p. 63-84.

Taylor, H.P., 1979. Oxygen and hydrogen isotope relationships in hydrothermal mineral deposits: In Barnes, H.I., (Ed), *Geochemistry of hydrothermal ore deposits*. New York: Wiley-Interscience, p. 236-277.

Taylor, S.R., and McLennan, S.M., 1985. *The continental crust: its composition and evolution*. Blackwell Scientific Publication, Carlton.

Teufel, S., Heinrich, W., 1997. Partial resetting of the U-Pb isotope system in monazite through hydrothermal experiments: an SEM and U-Pb isotope study. *Chemical Geology*, v. 137, p. 273-281.

Tilton, G.R., 1960. Volume diffusion as a mechanism for discordant lead ages. *Journal of Geophysical Research*, v. 65, p. 2933-2945.

Tomkins, A. G., 2010. Windows of metamorphic sulfur liberation in the crust: implications for gold deposit genesis. *Geochimica et Cosmochimica Acta*, v. 74, p. 3246-3259.

Tomkins, A. G., 2013. On the source of orogenic gold. *Geology*, v. 41 (12), p. 1255-1256.

United Nations, Division for Public Administration and Development Management, Department of Economic and Social Affairs., 2007. *Democratic Republic of the Congo; Public administration country profile*.

United Nations Development Programme, 2014. *Human development report 2014: Sustaining Human Progress: Reducing Vulnerabilities and Building Resistance*.

United Nations, 2011. Map No. 4007 Rev 10, Department of Field Support; Cartographic Section.

Vearncombe, J.R., 1983. A proposed continental margin in the Precambrian of Western Kenya. *International Journal of Earth Sciences, Geol. Rundschau*, v. 72, p. 663-670.

Vearncombe, J.R., Barton, J.M., Cheshire, P.E., De Beer, J.H., Stettler, E.H., Brandl, G., 1992. Geology, geophysics and mineralization of the Murchinson schists belt, Rooiwater Complex and surrounding granitoids. *Geological Survey of South Africa Memoir 81*, p.139.

Vielreicher, N.M., Groves, D.I., Fletcher, I.R., McNaughton, N.J., Rasmussen, B., 2003. Hydrothermal monazite and xenotime geochronology: a new direction for precise dating of orogenic gold mineralization., *Economic Geology Newsletter*, v. 53, p. 9-16.

Vielreicher, N.M., Groves, D.I., Snee, L.W., Fletcher, I.R., McNaughton, N.J., 2010. Broad Synchronicity of three gold mineralization styles in the Kalgoorlie Gold Field: SHRIMP U-Pb and $^{40}\text{Ar}/^{39}\text{Ar}$ geochronological evidence. *Economic Geology*, v. 105, p. 187-227.

Viljoen, M.J., 1979. The geology and geochemistry of the "Antimony Line" in the United Jack Complex, Murchinson range. In: Anhaeusser, C.R., Foster, R.P., Stratten, T., (Eds.). *A Symposium on Mineral deposits and the transportation and Deposition of Metals*, Geological Society of South Africa special Publication 5, p. 133-158.

Wagner, T., Boyce, A.J., Fallick, A.E., 2002. Laser combustion analysis of $\delta^{34}\text{S}$ of sulfosalt minerals: Determination of the fractionation systematics and some crystal-chemical considerations. *Geochimica et Cosmochimica Acta*, v. 66, p. 2855-2863.

Westerhoff, A.B., Harma, P., Isabirye, E., Katto, E., Koistinen, T., Kuosmanen, E., Lehto, T., Lehtonen, M.I., Makitie, H., Manninen, T., Manttari, I., Pekkala, Y., Pokki, J., Saalman, K., Virransalo, P., 2014. Geology and Geodynamic development of Uganda with explanation of the 1:1,000,000- Scale Geological Map. Geological Survey of Finland, Special Paper 55.

Wiedenbeck, M. Alle, P., Corfu, F., Griffin, W.L., Meier, M., Oberli, F., Von Quadt, A., Roddick, J.C., Spiegel, W., 1995. Three natural zircon standards for U-Th-Pb Lu-Hf trace element and REE analysis. *Geostandards Newsletter*, v. 19, p. 1-23.

Williams, M.L., Jercinovic, M.J., 2002. Microprobe monazite geochronology: putting absolute time into microstructural analysis. *Journal of Structural Geology*, v. 24, p. 1013-1028.

Williams, M.L., Jercinovic, M.J., Harlov, D.E., Budzyn, B., Hetherington, C.J., 2011. Resetting monazite ages during fluid-related alteration. *Chemical Geology*, v. 283, p. 218-225.

Williams-Jones, A. E., Bowell, R. J., Migdisov, A. A., 2009. Gold in solution. *Elements*, v. 5(5), p. 281-287.

Wintsch, R.P., Christofferson, R., Kronenberg, A.K., 1995. Fluid-rock reaction weakening of fault zones. *Journal of Geophysical Research*, v. 100, No.B7, p. 13,021-13,032.

Woodtli, R., 1961. Gold Impregnation Deposits in the Moto Area. *Economic Geology*, v. 56, p. 603-607.

Xue, Y., Campbell, I., Ireland, T. R., Holden, P., Armstrong, R., 2013. No mass-independent sulfur isotope fractionation in auriferous fluids supports a magmatic origin for Archean gold deposits. *Geology*, v. 41, p. 791-794.

Yakubchuk, A., Stein, H., Wilde, A., 2014. Results of pilot Re-Os dating of sulphides from the Sukhoi Log and Olympiada orogenic gold deposits, Russia. *Ore Geology reviews*, v. 59, p. 21-28.

Yardley, B.W.D., and Cleverley, J.S., 2013. The role of metamorphic fluids in the formation of ore deposits. *In*, Jenkin, G.R.T., Lusty, P.A.J., McDonald, I., Smith, M.P., Boyce, A.J., Wilkinson, J.J., (Eds). *Ore deposits in an Evolving Earth*. Geological society, London, Special Publications, 393.
DOI:10.1144/SP393.5.

Zhang, S., Tullis, T.E., Scruggs, V.J., 1999. Permeability anisotropy and pressure dependency of permeability in experimentally sheared gouge materials. *Journal of Structural Geology*, v. 21, p. 795-806.

Zhao, G., Sun, M., Wilde, S. A., Li, S. Z., 2004. A Paleo-Mesoproterozoic supercontinent: assembly, growth and breakup. *Earth-Science Reviews*, v. 67, p. 91-123.